99 | Springer Proceedings in Physics

J. M. Marcaide
K. W. Weiler
(Eds.)

Cosmic Explosions

On the 10th Anniversary of SN1993J (IAU Colloquium 192)

Springer

SPRINGER PROCEEDINGS IN PHYSICS 99

SPRINGER PROCEEDINGS IN PHYSICS

75 **Computer Simulation Studies in Condensed-Matter Physics V**
Editors: D.P. Landau, K.K. Mon, and H.-B. Schüttler

76 **Computer Simulation Studies in Condensed-Matter Physics VI**
Editors: D.P. Landau, K.K. Mon, and H.-B. Schüttler

77 **Quantum Optics VI**
Editors: D.F. Walls and J.D. Harvey

78 **Computer Simulation Studies in Condensed-Matter Physics VII**
Editors: D.P. Landau, K.K. Mon, and H.-B. Schüttler

79 **Nonlinear Dynamics and Pattern Formation in Semiconductors and Devices**
Editor: F.-J. Niedernostheide

80 **Computer Simulation Studies in Condensed-Matter Physics VIII**
Editors: D.P. Landau, K.K. Mon, and H.-B. Schüttler

81 **Materials and Measurements in Molecular Electronics**
Editors: K. Kajimura and S. Kuroda

82 **Computer Simulation Studies in Condensed-Matter Physics IX**
Editors: D.P. Landau, K.K. Mon, and H.-B. Schüttler

83 **Computer Simulation Studies in Condensed-Matter Physics X**
Editors: D.P. Landau, K.K. Mon, and H.-B. Schüttler

84 **Computer Simulation Studies in Condensed-Matter Physics XI**
Editors: D.P. Landau and H.-B. Schüttler

85 **Computer Simulation Studies in Condensed-Matter Physics XII**
Editors: D.P. Landau, S.P. Lewis, and H.-B. Schüttler

86 **Computer Simulation Studies in Condensed-Matter Physics XIII**
Editors: D.P. Landau, S.P. Lewis, and H.-B. Schüttler

87 **Proceedings of the 25th International Conference on the Physics of Semiconductors**
Editors: N. Miura and T. Ando

88 **Starburst Galaxies**
Near and Far
Editors: L. Tacconi and D. Lutz

89 **Computer Simulation Studies in Condensed-Matter Physics XIV**
Editors: D.P. Landau, S.P. Lewis, and H.-B. Schüttler

90 **Computer Simulation Studies in Condensed-Matter Physics XV**
Editors: D.P. Landau, S.P. Lewis, and H.-B. Schüttler

91 **The Dense Interstellar Medium in Galaxies**
Editors: S. Pfalzner, C. Kramer, C. Straubmeier, and A. Heithausen

92 **Beyond the Standard Model 2003**
Editor: H.V. Klapdor-Kleingrothaus

93 **ISSMGE**
Experimental Studies
Editor: T. Schanz

94 **ISSMGE**
Numerical and Theoretical Approaches
Editor: T. Schanz

95 **Computer Simulation Studies in Condensed-Matter Physics XVI**
Editors: D.P. Landau, S.P. Lewis, and H.-B. Schüttler

96 **Electromagnetics in a Complex World**
Editors: I.M. Pinto, V. Galdi, and L.B. Felsen

97 **Fields, Networks and Computations**
A Modern View of Electrodynamics
Editor: P. Russer

98 **Particle Physics and the Universe**
Proceedings of the 9th Adriatic Meeting, Sept. 2003, Dubrovnik
Editors: J. Trampetić and J. Wess

99 **Cosmic Explosions**
On the 10th Anniversary of SN1993J (IAU Colloquium 192)
Editors: J. M. Marcaide and K. W. Weiler

Homepage: springeronline.com

Volumes 46–74 are listed at the end of the book.

J. M. Marcaide K. W. Weiler (Eds.)

Cosmic Explosions

On the 10th Anniversary of SN1993J (IAU Colloquium 192)

With 199 Figures and 15 color plates

Springer

Professor Juan-María Marcaide
Universidad de Valencia
Depto. Astronomia y Astrofisica
Calle Dr. Moliner 50
46100 Burjassot
Spain

Dr. Kurt W. Weiler
Naval Research Laboratory, Code 7213
Washington, DC 20375-5320
USA

ISSN 0930-8989

ISBN 3-540-23039-4 Springer Berlin Heidelberg New York

Library of Congress Control Number: 2004111216

Springer is a part of Springer Science+Business Media

springeronline.com

Printed in Germany

Typesetting by the authors/editors
Cover concept: eStudio Calamar Steinen
Cover production: *design & production* GmbH, Heidelberg

Printed on acid-free paper 62/3141/ts 5 4 3 2 1 0

Preface

Supernovae are among the most energetic phenomena in the Universe and related to almost all aspects of modern astrophysics including starburst galaxies, cosmic ray acceleration, neutron star and black hole formation, nucleosynthesis and ISM chemical enrichment, energy input to the ISM, cosmic distance scale determination, dark energy related cosmological acceleration, gamma-ray bursts, extra-solar system neutrino burst detection, gravity wave generation, and many more. Additionally, the past 15 years have been particularly productive with many new results and new understanding due in particular to the closest SN in 400 years in SN 1987A in the Large Magellanic Cloud, and the unusually bright and close SN 1993J and SN 1994I in the nearby galaxies M81 and M51, respectively. In addition, the discovery of the γ-ray burst GRB 980425 and its related supernova SN 1998bw, and the confirmation of GRB 030329/SN 2003dh, tied the study of SNe and GRBs inextricably together. With the many developments since the last major supernova meeting in La Serena, Chile in 1997, we felt that it was an appropriate time to bring together experts and students interested in the subject for a meeting where SN and GRB properties and interrelationships could be discussed. The tenth anniversary of SN 1993J provided such an opportunity and, appropriately, the meeting was held in Spain where SN 1993J was discovered on the early morning of 28 March 1993 by a Spanish amateur astronomer, Francisco García.

The conference covered all aspects of supernova and GRB research: theoretical aspects like nucleosynthesis and explosion mechanisms, progenitor stars, pulsar and SNR formation, interaction with the circumstellar medium, and particle acceleration mechanisms, as well as observational aspects including radio, IR, optical, X-ray, and gamma-ray studies. Cosmology and Dark Energy were also extensively discussed. The conference consisted of 17 reviews, 17 invited talks, 58 contributed papers and 50 posters. Wider public interest in astrophysics in general and supernovae in particular was shown by the large attendance at the excellent open lectures given by the renown scientist, lecturer, and author Sir Martin Rees from Cambridge, UK, by Francisco García from Lugo, Spain, and by the world's most successful amateur supernova hunter, Rev. Robert Evans from Hazelbrook, New South Wales, Australia.

In order to preserve and more widely disseminate the information presented at the meeting, we have prepared the present volume and accompanying CD-ROM. The CD additionally includes poster descriptions and meeting photographs not printed here.

Such a valuable meeting would not have been possible without the support of many people and institutions. There is no way that we can list all the people who contributed to making the meeting a success, but we would particularly like to thank M. Toharia, Director of the Museo de las Ciencias Príncipe Felipe, Prof. F. Tomás, Rector of the Universitat de Valencia, and Prof. J. Quesada, Head of the Oficina de Ciencia y Tecnología de la Generalitat Valenciana. Very special thanks are also due to the members of the Local Organizing Committee and, in particular, to its co-chairman Dr. J. C. Guirado and to the staff of the Museo de las Ciencias.

The conference could not have taken place without the financial and technical support of many Valencian, Spanish, European, American, and international agencies and institutions: Ciudad de las Artes y de las Ciencias de Valencia, Universitat de Valencia, Generalitat Valenciana, Ayuntamiento de Valencia, Ministerio de Ciencia y Tecnología, Consejo Superior de Investigaciones Científicas, Sociedad Española de Astronomía, European Commission, International Astronomical Union, International Union of Radio Science, National Aeronautics and Space Administration, National Science Foundation, American Astronomical Society, and the Naval Research Laboratory all contributed to its success.

We would also like to thank Viajes Iberia Congresos for the efficient conference organization and Springer for the continuous support and patience with the editors of these proceedings. KWW wishes to thank the Office of Naval Research for the 6.1 funding supporting his research.

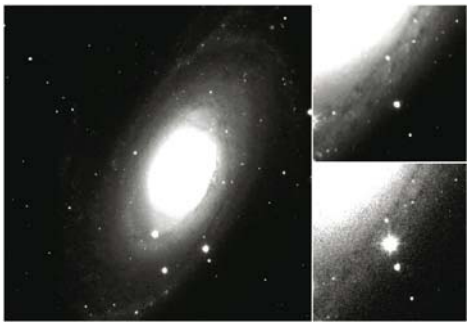

Fig. 1. Photographs (courtesy of Brian P. Schmidt) of the galaxy M81 with SN1993J readily apparent (left), the area of the SN before explosion (right, top), and the area with SN1993J near maximum brightness (right, bottom).

Valencia – Washington, *J.M. Marcaide*
August 2004 *K.W. Weiler*

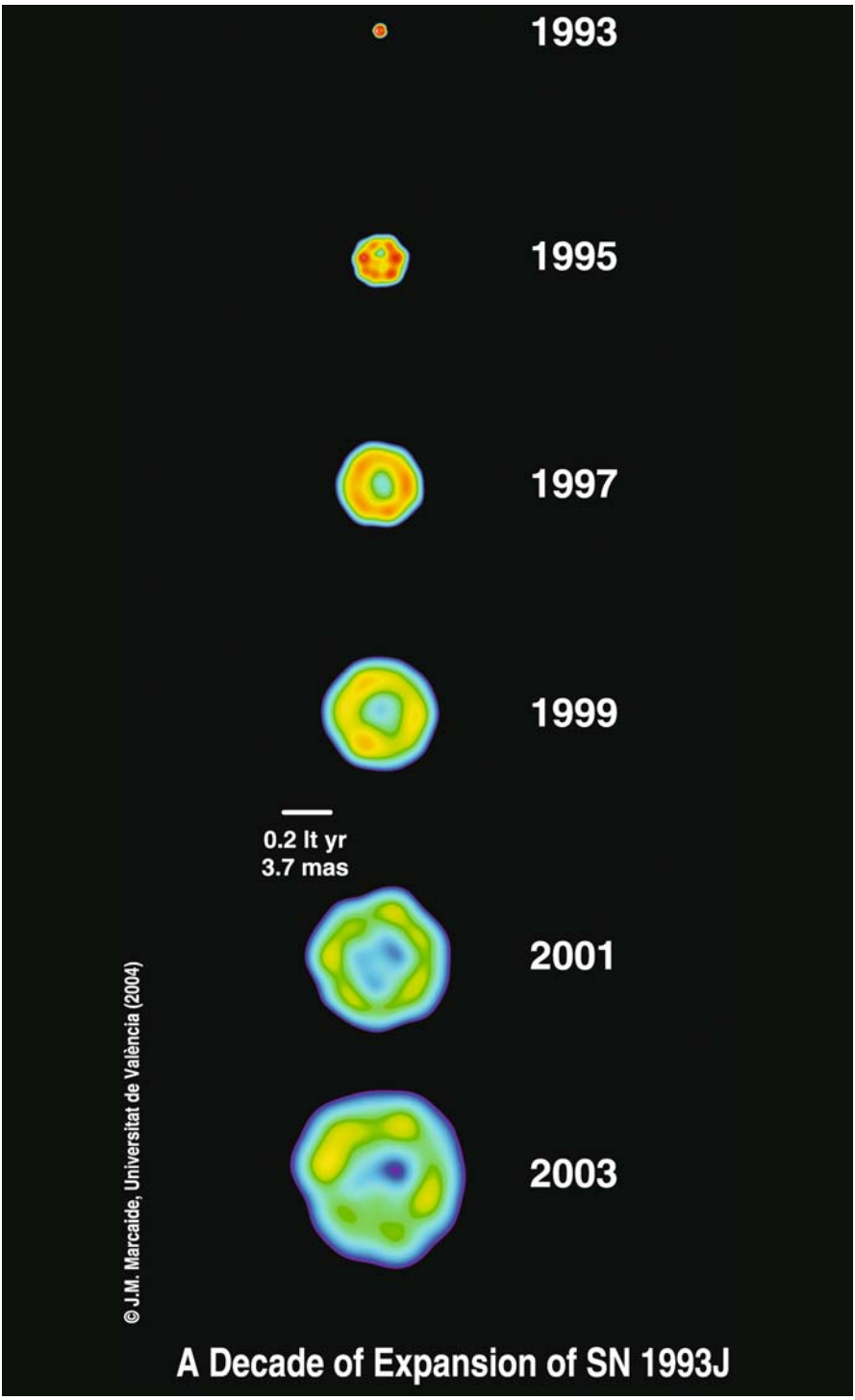
1993
1995
1997
1999
0.2 lt yr
3.7 mas
2001
2003
© J.M. Marcaide, Universitat de València (2004)
A Decade of Expansion of SN 1993J

Contents

Part VII Gamma-Ray Bursters

Part VIII Supernovae, Gamma-Ray Bursters, and Cosmology

List of Contributors

Antxon Alberdi
IAA-CSIC
Apdo. Correos 3004
18080 Granada, Spain
antxon@iaa.es

Miguel A. Aloy
Max-Planck-Institut für Astrophysik
Karl-Schwarzschild-Str. 1
85741 Garching, Germany
maa@mpa-garching.mpg.de

Carles Badenes
Institut d'Estudis Espacials de Catalunya
Gran Capitá 2-4
08034 Barcelona, Spain
badenes@ieec.fcr.es

Norbert Bartel
York University
Toronto, Canada
bartel@yorku.ca

Edo Berger
Division of Physics, Mathematics and Astronomy, 105-24
California Institute of Technology
Pasadena, CA 91125, USA
ejb@astro.caltech.edu

Michael F. Bietenholz
York University
Toronto, Canada
mbieten@yorku.ca

G.S. Bisnovatyi-Kogan
Space Research Institute
Russian Academy of Sciencs
Profsoyuznaya 84/32
Moscow 117997, Russia
gkogan@mx.iki.rssi.ru

A. Blanchard
LAOMP
14, Av. E. Belin
31 400 Toulouse, France
alain.blanchard@ast.obs-mip.fr

Joshua S. Bloom
Harvard-Smithsonian Center for Astrophysics, MC 20
60 Garden Street
Cambridge, MA 02138, USA
jbloom@tdc.harvard.edu

Eduardo Bravo
Departament de Física i Enginyeria Nuclear
Universitat Politècnica de Catalunya
Av. Diagonal 647
Barcelona, Spain
eduardo.bravo@upc.es

Enrico Cappellaro
INAF - Osservatorio Astronomico di Capodimonte
via Moiariello 16
80181 Napoli, Italy
cappellaro@na.astro.it

Alberto J. Castro-Tirado
Instituto de Astrofísica de Andalucía
(IAA-CSIC)
P.O. Box 03004
E-18080 Granada, Spain
ajct@iaa.es

Roger A. Chevalier
Department of Astronomy
University of Virginia
P.O. Box 3818
Charlottesville, VA 22903, USA
rac5x@virginia.edu

Nikolai N. Chugai
Institute of Astronomy, RAS
Pyatnitskaya 48
109017 Moscow, Russia
nchugai@inasan.rssi.ru

Massimo Della Valle
INAF-Arcetri Astrophysical
Observatory
Largo E. Fermi 5
I-50125, Firenze, Italy
massimo@arcetri.astro.it

Inma Dominguez
Universidad de Granada
Granada, Spain
inma@ugr.es

Vikram V. Dwarkadas
ASCI FLASH Center
Univ of Chicago
5640 S. Ellis Ave
Chicago IL 60637, USA
vikram@flash.uchicago.edu

Abouazza Elmhamdi
SISSA/ISAS
via Beirut 4
34014 Trieste, Italy
elmhamdi@sissa.it

Alexei V. Filippenko
Department of Astronomy
University of California
601 Campbell Hall
Berkeley, CA 94720-3411, USA
alex@astro.berkeley.edu

Dale A. Frail
National Radio Astronomy
Observatory
Socorro, NM 87801, USA
dfrail@nrao.edu

Claes Fransson
Department of Astronomy
Stockholm University, AlbaNova
SE-106 91 Stockholm, Sweden
claes@astro.su.se

Filippo Frontera
University of Ferrara
Physics Dept.
Via Paradiso 12
I-44100 Ferrara, Italy
frontera@fe.infn.it

Avishay Gal-Yam
School of Physics and Astronomy
Tel Aviv University
Tel Aviv, Israel
avishay@wise.tau.ac.il

Wlodzimirerz Godlowski
Astronomical Observatory
Jagiellonian University
30-244 Krakow, Orla 171, Poland
godlows@.oa.uj.edu.pl

Mario Hamuy
The Observatories
Carnegie Institution of Washington
mhamuy@ociw.edu

Wolfgang Hillebrandt
Max-Planck-Institut für Astrophysik
D-85748 Garching, Germany
wfh@mpa-garching.mpg.de

Raphael Hirschi
Observatoire de Genève
CH-1290 Sauverny, Switzerland
raphael.hirschi@obs.unige.ch

Peter Hoeflich
Dept. of Astronomy
University of Texas
Austin, TX 78681, USA
pah@astro.as.utexas.edu

Kevin Hurley
University of California Space Sciences Laboratory
Berkeley, CA 94720-7450, USA
khurley@sunspot.ssl.berkeley.edu

H.-Th. Janka
Max-Planck-Institut für Astrophysik
Postfach 1317
D-85741 Garching, Germany
thj@mpa-garching.mpg.de

J. G. Kirk
Max-Planck-Institut für Kernphysik
Postfach 10 39 80
D-69029 Heidelberg, Germany
john.kirk@mpi-hd.mpg.de

Koichi Iwamoto
Nihon University
Japan
iwamoto@phys.cst.nihon-u.ac.jp

Hans Janka
Max-Planck Institute fuer Astrophysik
Germany
hjanka@mpa-garching.mpg.de

Saurabh Jha
University of California
USA
saurabh@astron.berkeley.edu

John Kirk
Max-Plank Institute fuer Kernphysik
Germany
John.Kirk@mpi-hd.mpg.de

Volodymir Kryvdyk
Kyiv National University
av. Glushkova 6
Kyiv 03022, Ukraine
kryvdyk@mail.univ.kiev.ua

William H. Lee
Instituto de Astronomía, UNAM
Apdo. Postal 70-264
Cd. Universitaria, México
wlee@astroscu.unam.mx

Bruno Leibundgut
European Southern Observatory
Karl-Schwarzschild-Strasse 2
D-85748 Garching, Germany
bleibundgut@eso.org

Weidong Li
Department of Astronomy
University of California
Berkeley, CA 94720-3411, USA
weidong@astron.berkeley.edu

Abraham Loeb
Astronomy Department
Harvard University
60 Garden Street
Cambridge, MA 02138, USA
aloeb@cfa.harvard.edu

Andrew I. MacFadyen
Theoretical Astrophysics
California Institute of Technology
MC 130-33
Pasadena, CA 91125, USA
andrew@tapir.caltech.edu

Hideki Madokoro
RIKEN
Hirosawa 2-1
Wako 351-0198, Japan
madokoro@postman.riken.go.jp

Filippo Manucci
IRA-CNR
Largo E. Fermi 5
50125 Firenze, Italy
filippo@arcetri.astro.it

D. Maoz
School of Physics and Astronomy
Tel Aviv University
Tel Aviv, Israel
dani@wise.tau.ac.il

J.M. Marcaide
Departamento de Astronomía
Universitat de València
46100 Burjassot, Spain
J.M.Marcaide@uv.es

Gabriel Martínez-Pinedo
Institut d'Estudis Espacials de Catalunya
Barcelona, Spain
martinez@ieec.fcr.es

Thomas Matheson
Harvard-Smithsonian Center for Astrophysics
60 Garden Street
Cambridge, MA 02138, USA
tmatheson@cfa.harvard.edu

Paolo A. Mazzali
INAF - Osservatorio Astronomico di Trieste
Via Tiepolo, 11
Trieste, Italy
mazzali@ts.astro.it

Richard McCray
JILA
University of Colorado
Boulder, CO 80309-0440, USA
dick@jila.colorado.edu

Peter A. Milne
Steward Observatory
University of Arizona
Tucson, AZ, USA
pmilne@as.arizona.edu

Sergey G. Moiseenko
Space Research Institute
Profsoyuznaya str. 84/32
Moscow 117997, Russia
moiseenko@iki.rssi.ru

Thomas Morris
Department of Astrophysics
Oxford University
Oxford, OX1 3RH
UK
tsm@astro.ox.ac.uk

Thomas W.B. Muxlow
Jodrell Bank Observatory
University of Manchester
Macclesfield, Cheshire SK11 9DL, UK
twbm@jb.man.ac.uk

Ken'ichi Nomoto
Department of Astronomy
University of Tokyo
Tokyo, Japan
nomoto@astron.s.u-tokyo.ac.jp

Nino Panagia
Space Telescope Science Institute
3700 San Martin Drive
Baltimore, MD 21218, USA
panagia@stsci.edu

A. Pastorello
Dipartimento di Astronomia
Università di Padova
Vicolo dell' Osservatorio 2
I-35122 Padova, Italy
pastorello@pd.astro.it

Ferdinando Patat
European Southern Observatory
Garching, Germany
fpatat@eso.org

Alan Pedlar
Jodrell Bank Observatory
University of Manchester
Cheshire SK11 9DL, UK
ap@jb.man.ac.uk

Miguel A. Pérez-Torres
IAA - CSIC
Apdo. Correos 3004,
18008 Granada, Spain
torres@iaa.es

David Pooley
MIT Center for Space Research
70 Vassar St.
Cambridge, MA 02139, USA
dave@mit.edu

Dovi Poznanski
School of Physics & Astronomy
Tel-Aviv University
Tel-Aviv 69978, Israel
dovip@wise.tau.ac.il

Alak Ray
Tata Institute of Fundamental Research
Mumbai, India
akr@tifr.res.in

F.K. Röpke
Max-Planck-Institut für Astrophysik
Karl-Schwarzschild-Str. 1
D-85741 Garching, Germany
fritz@mpa-garching.mpg.de

Stephan Rosswog
Dept. Physics & Astronomy
University of Leicester
Leicester LE1 7RH, UK
sro@astro.le.ac.uk

Stuart D. Ryder
Anglo-Australian Observatory
P.O. Box 296
Epping, NSW 1710, Australia
sdr@aaoepp.aao.gov.au

Daniel N. Sauer
Max-Planck-Institut für Astrophysik
Garching, Germany
dsauer@mpa-garching.mpg.de

Brian Schmidt
Research School of Astronomy and Astrophysics
Mt. Stromlo Observatory
The Australian National University
via Cotter Rd
Weston Creek, ACT 2611, Australia
brian@mso.anu.edu.au

Miguel Sirera
Departamento de Astronomia y Astrofísica
Universidad de Valencia
46100 Burjassot (Valencia), Spain
Miguel.Sirera@uv.es

Stephen J. Smartt
IoA
University of Cambridge
Cambridge, UK
sjs@ast.cam.ac.uk

Alicia M. Soderberg
Palomar Observatory, 105-24
California Institute of Technology
Pasadena, CA 91125, USA
ams@astro.caltech.edu

Elena Sorokina
SAI
Universitetskij pr. 13
119992 Moscow, Russia
sorokina@sai.msu.su

Richard A. Sramek
National Radio Astronomy Observatory
PO Box O
Socorro, NM, USA
dsramek@aoc.nrao.edu

Lister Stavely-Smith
Australia Telescope National Facility
CSIRO
PO Box 76
Epping, NSW 1710, Australia
Lister.Staveley-Smith@csiro.au

Mathias Stehle
Max-Planck-Institut für Astrophysik
P.O. Box 1317
D-85741 Garching, Germany
mstehle@mpa-garching.mpg.de

Mark Sullivan
University of Durham
South Road
Durham, DH1 3LE, UK
mark.sullivan@durham.ac.uk

V.V. Tikhomirov
Institute for Nuclear Problems
Belarus State University
Bobrujskaya str. 11
Minsk 220050, Belarus,
tikh@inp.minsk.by

Claudia Travaglio
Max-Planck Institut für Astrophysik
Karl-Scwarzschild Str. 1
D-85741 Garching bei München,
Germany
claudia@mpa-garching.mpg.de

Dmitri Yu. Tsvetkov
Sternberg Astronomical Institute
Universitetski pr.13
119992, Moscow, Russia
tsvetkov@sai.msu.su

Massimo Turatto
Osservatorio Astronomico di Padova, INAF
vicolo dell'Osservatorio 5
35122 Padova, Italy
turatto@pd.astro.it

Schuyler Van Dyk
IPAC/Caltech
Pasadena, CA, USA
vandyk@ipac.caltech.edu

Hitoshi Yamaoka
Department of Physics
Kyushu University
812-8581 Japan
yamaoka@rc.kyushu-u.ac.jp

Luca Zampieri
INAF-Osservatorio Astronomico di Padova
Vicolo dell'Osservatorio 5
I-35122 Padova, Italy
zampieri@pd.astro.it

H.-U. Zimmerman
Max-Planck-Institut für extraterrestrische Physik
Postfach 1312
D-85471 Garching, Germany
zim@mpe.mpg.de

Part I

Supernovae: Individual

A Decade of Radio and X-ray Observations of SN 1993J

Schuyler D. Van Dyk[1], Kurt W. Weiler[2], Richard A. Sramek[3], Nino Panagia[4], Christopher Stockdale[5], Christina Lacey[6], Marcos Montes[2], and Michael Rupen[3]

[1] IPAC/Caltech, Pasadena, CA, USA;
vandyk@ipac.caltech.edu
[2] NRL, Washington, DC, USA;
Kurt.Weiler@nrl.navy.mil, Marcos.Montes@nrl.navy.mil
[3] NRAO, Socorro, NM, USA;
dsramek@aoc.nrao.edu, mrupen@aoc.nrao.edu
[4] STScI, Baltimore, MD, USA & Astrophys. Div., Space Sci. Dept., ESA;
panagia@stsci.edu
[5] Marquette Univ., Milwaukee, WI, USA;
Christopher.Stockdale@marquette.edu
[6] U. of South Carolina, Columbia, SC, USA;
lacey@sc.edu

Summary. We review ten years of radio continuum and X-ray monitoring of the Type IIb SN 1993J in M81. The supernova (SN) has been observed continuously, since only a few days after explosion, by our group with the Very Large Array at a number of radio frequencies, as well as by other groups. As a result, it is among the best-studied radio supernovae. The observed synchrotron radio emission is thought to arise from the interaction of the SN shock with the pre-SN wind-established circumstellar medium around the progenitor star. We describe the properties of the circumstellar interaction, based on the more fully-developed dataset, and compare this to our earlier characterization made in 1994. SN 1993J has also been a target of X-ray satellites, and we briefly discuss the nature of the X-ray emission and, together with the radio emission, describe the implications for the nature of the SN's progenitor.

1 Introduction

The radio emission from supernovae (SNe) serves as an excellent, and often the only, probe of the final stages of the evolution of the massive progenitor star. Radio SNe (RSNe) are characterized by nonthermal synchrotron emission, S_ν, at very high brightness temperature (T_B); "turn on" of the emission, first, at high radio frequencies and, subsequently, at lower frequencies; a power-law decline after maximum radio light at each frequency, with index β; and, transition from an optically thick spectral index, α (where $S_\nu \propto \nu^\alpha$). Type Ib/c RSNe turn on, reach maximum, and decline rapidly, e.g., at 6 cm, within tens of days, while Type II (mostly II-linear; II-L) RSNe require several hundred days to rise to 6 cm maximum and then decline much more

slowly than do the Type Ib/c RSNe. The Type II-narrow (IIn) RSNe evolve even more slowly, taking more than 1000 days to reach 6 cm maximum, before a slow decline over many years to decades. Observing most RSNe requires one to be a "sedentary gentle person of leisure," but this allows one to analyze these objects far more carefully and accurately as they evolve, compared to those who hastily and perfunctorily analyze various faster-evolving objects.

The radio emission has been interpreted via the Chevalier "mini-shell" model [3, 4], where the relativistic electrons and enhanced magnetic field necessary for synchrotron emission arise from the SN shock interacting with a relatively high-density circumstellar medium (CSM) which has been ionized and heated ($> 10^4$–10^5 K) by the initial X-ray/UV flash. This CSM is presumed to have been established by a constant mass-loss ($\dot{M}$) rate, constant velocity ($w_{\rm wind}$) wind from a massive progenitor star or stellar system. The ionized CSM, then, is the source of free-free absorption of the synchrotron emission. A rapid rise in the observed radio flux density results from a decrease in absorption as the radio emitting region expands.

In this model, the spectral index $\alpha = (1-\gamma)/2$, where γ is the relativistic particle index, and the decline index $\beta = -(\gamma+5-6m)/2$, where the SN shock radius evolves with time as $R_{\rm shell} \propto t^m$. The SN ejecta have density profile $\rho_{\rm ejecta} \propto r^{-n}$, while $\rho_{\rm CSM} = \dot{M}/(4\pi\ v_{\rm wind}\ r^{-s})$, such that $m = (n-3)/(n-s)$ (for a spherically-symmetric wind, $s = 2$).

Chevalier [5] has said that "the expected time evolution of the physical parameters is not well understood and the predicted light curves are only plausible estimates of the evolution." Therefore, we have analyzed the observed data in terms of parameterized light curves. Originally, the parameterization was relatively simple and provided an adequate reproduction of the objects known at that time; see [25]:

$$S(\mathrm{mJy}) = K_1 \left(\frac{\nu}{5\ \mathrm{GHz}}\right)^{\alpha} \left(\frac{t-t_0}{1\ \mathrm{day}}\right)^{\beta} e^{-\tau_{\rm external}} \tag{1}$$

where

$$\tau_{\rm external} = K_2 \left(\frac{\nu}{5\ \mathrm{GHz}}\right)^{-2.1} \left(\frac{t-t_0}{1\ \mathrm{day}}\right)^{\delta}. \tag{2}$$

K_1 and K_2 correspond formally to the flux density and uniform f-f absorption (FFA) at 5 GHz one day after the explosion date t_0. The absorption decline index $\delta = -3m = \alpha - \beta - 3$.

With the discovery of the RSN IIn 1986J, another layer of complexity was added to the parameterization, allowing for a clumpy or filamentary, mixed internal emission/absorption mechanism, which leads to a slower radio turn-on; see [26]:

$$S(\mathrm{mJy}) = K_1 \left(\frac{\nu}{5\ \mathrm{GHz}}\right)^{\alpha} \left(\frac{t-t_0}{1\ \mathrm{day}}\right)^{\beta} e^{-\tau_{\rm external}} \left(\frac{1-e^{-\tau_{\rm filament}}}{\tau_{\rm filament}}\right) \tag{3}$$

where

$$\tau_{\rm filament} = \tau' = K_3 \left(\frac{\nu}{5\ {\rm GHz}}\right)^{-2.1} \left(\frac{t-t_0}{1\ {\rm day}}\right)^{\delta'}, \quad (4)$$

K_3 is the clumpy or filamentary absorption at 5 GHz one day after explosion, and $\delta' = 5\delta/3$.

From the uniform, external FFA one can estimate the progenitor's mass-loss rate [25, 26, 27] as

$$\frac{\dot{M}({\rm M}_\odot {\rm yr}^{-1})}{(w_{\rm wind}/10\ {\rm km\ s}^{-1})} = 3.0\times10^{-6}\ \tau_{\rm FFA}^{0.5}\ m^{-1.5} \left(\frac{v_{\rm i}}{10^4\ {\rm km\ s}^{-1}}\right)^{1.5} \times \left(\frac{t_{\rm i}}{45\ {\rm days}}\right)^{1.5} \left(\frac{t}{t_{\rm i}}\right)^{1.5m} \left(\frac{T}{10^4\ {\rm K}}\right)^{0.68} \quad (5)$$

where $t_{\rm i}$ is the measurement date of the initial ejecta velocity $v_{\rm i}$, and T is the wind (CSM) temperature.

2 Radio Emission from SN 1993J

2.1 Ancient History

SN 1993J in M81 was monitored with the Ryle Telescope [18] and Very Large Array (VLA[1]; [24]), respectively, from just a few days after explosion up to the first 300 days. (We do not include discussion of the early mm data here.) Whereas Pooley & Green [18] observed only at 2 cm, Van Dyk et al. [24] provide data from 1.3 to 20 cm and found that the standard form of the Weiler et al. [26] parameterization did not provide an adequate fit to the data. Specifically, it became apparent, with $\delta = -1.99$ and $\delta' = -2.02$ ($\simeq 2$), that the assumptions of $\delta = \alpha - \beta - 3$ and $\delta' = 5\delta/3$ did not apply to SN 1993J.

With the results of the then-available VLBI data, that the SN was essentially in free expansion [1, 12], i.e., $m \simeq 1$, and with $\tau_{\rm FFA} \propto \int {n_e}^2 dr \propto r^{(-2\eta+1)}$, $n_e \propto r^{-\eta}$ ($\propto \rho_{\rm CSM}$) and $\tau_{\rm FFA} \propto r^{-2}$, then $\eta = 1.50$. That is, $\rho_{\rm CSM} \propto r^{-1.5}$, which is a shallower profile than for a spherically symmetric wind (see also [7]). Such a CSM profile could be explained by either a decreasing mass-loss rate, $\dot{M}$, or increasing wind speed, $w_{\rm wind}$, prior to the progenitor's explosion. Such variation might also result in a clumpy wind.

[1] The VLA telescope of the National Radio Astronomy Observatory is operated by Associated Universities, Inc. under a cooperative agreement with the National Science Foundation.

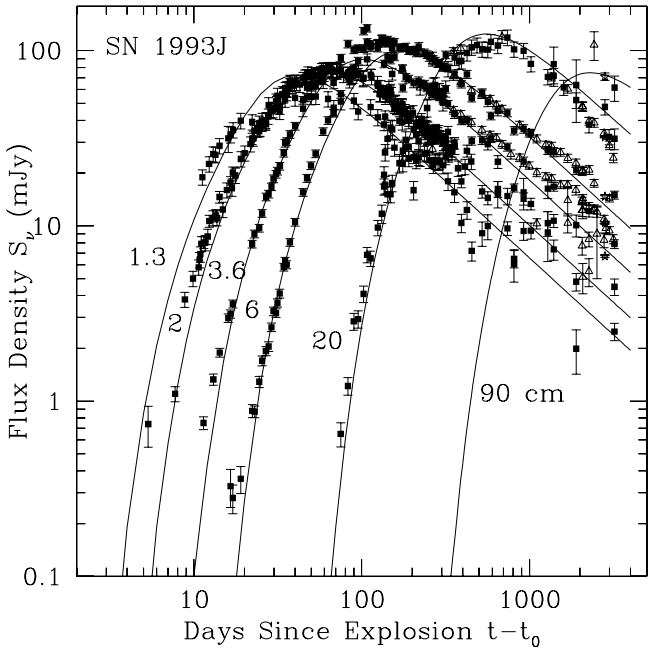

Fig. 1. Preliminary best-fit model to the SN 1993J VLA data. This model fit includes a clumpy, external absorbing medium and SSA.

2.2 Alternate Views

It has been proposed that synchrotron self-absorption (SSA) may play a role in some objects [5]. Fransson & Bjornsson [8] and Chevalier [5] independently interpreted the SN 1993J data, assuming that the CSM profile was spherically symmetric (i.e., no shallow profile, no clumps) and that absorption is due to a combination of pure FFA and SSA. The model provided a good fit to the data. However, in this model the wind electron temperature, T_e, varies with radius, so that the FFA power law changes with radius and, therefore, with time. Although such an assumption is not physically unrealistic, an assumption of $T_e(r)$ has not been necessary to interpret any other RSN to date.

Similarly, Perez-Torres et al. [16] also model SN 1993J assuming pure FFA plus SSA and $T_e(r)$, but with $\rho_{\rm CSM} \propto r^{-1.66}$ (that the exponent is no longer assumed to be -1.5 is discussed below) and the assumption that the synchrotron emission is not optically thin. Again, their model provides a reasonable fit to the data.

2.3 Modern Times

We have continued monitoring SN 1993J with the VLA at a number of frequencies, including 90 cm, to >4000 days. The SN has also been observed at late times with the VLA by Bartel et al. [2] and Perez-Torres et al. [17]. SN 1993J continues to be, with the sole exception of SN 1987A, the best-studied RSN ever. However, the old fit [24] ceases to reproduce the data well, systematically overestimating the flux densities at late times. It has become necessary to refit our parameterization to the more complete dataset.

In recent times the parameterization has taken on additional complexity levels. A clumpy external medium plane-parallel absorption term has been included. Along with the mixed FFA/nonthermal emission internal to the interaction region, we also now include SSA in the formalism of $\tau_{\rm internal}$. Additionally, we also allow for the presence of a distant line-of-sight ionized medium, which results in a time-independent FFA component to $\tau_{\rm external}$ and additional spectral turn-over at low frequencies (see [15]). The parameterization is now (see [27]):

$$S(\mathrm{mJy}) = K_1 \left(\frac{\nu}{5\ \mathrm{GHz}}\right)^{\alpha} \left(\frac{t-t_0}{1\ \mathrm{day}}\right)^{\beta} e^{-\tau_{\rm external}} \left(\frac{1-e^{-\tau_{\rm CSM_{clumps}}}}{\tau_{\rm CSM_{clumps}}}\right) \times \left(\frac{1-e^{-\tau_{\rm internal}}}{\tau_{\rm internal}}\right) \quad (6)$$

where the new terms are

$$\tau_{\rm CSM_{clumps}} = \tau' = K_3 \left(\frac{\nu}{5\ \mathrm{GHz}}\right)^{-2.1} \left(\frac{t-t_0}{1\ \mathrm{day}}\right)^{\delta'} \quad (7)$$

$$\tau_{\rm internal_{SSA}} = K_5 \left(\frac{\nu}{5\ \mathrm{GHz}}\right)^{\alpha-2.5} \left(\frac{t-t_0}{1\ \mathrm{day}}\right)^{\delta''} \quad (8)$$

and

$$\tau_{\rm distant} = \tau'' = K_4 \left(\frac{\nu}{5\ \mathrm{GHz}}\right)^{-2.1} \quad (9)$$

and where K_3 is now the clumpy external absorption, K_5 is the internal SSA, and K_4 is the external time-independent FFA, all at 5 GHz one day after explosion. (Of course, in addition to clumps or filaments, the CSM may be structured with significant density irregularities, such as rings, disks, or shells.)

In Fig. 1 we show a preliminary best fit to the more complete data, including both an external clumpy medium and SSA, with χ^2/dof=5.48. The simpler assumption of wind T_e = const is adopted. In Table 1 (column 2) we list the best-fit model parameters. The main point emphasized here is that,

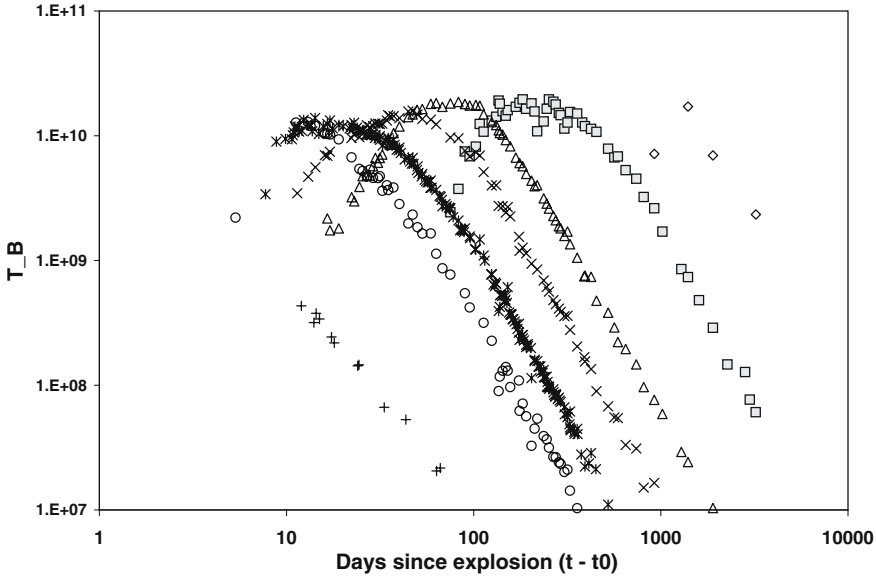

Fig. 2. Brightness temperature of SN 1993J based on VLA data, assuming $v_{\rm exp} = 10^4$ km s^{-1}.

for SN 1993J, SSA is not important, except for very early times, and SN 1993J bears no relationship at all to a sGRB. To further illustrate this, in Fig. 2 we show T_B as a function of time, based on the data at all frequencies and assuming $v_{\rm exp} = 10^4$ km s^{-1}. One can see that SN 1993J comes nowhere near experiencing any "inverse Compton catastrophe," and $T_B < 10^{11}$ K is well under even the equipartition T_B [19] that presumably sets a hard limit. SSA is simply not essential for SN 1993J. Based on this best-fit model, in Fig. 3 we show the absorption with time, and one can readily see that the SSA declines far more rapidly than the FFA and generally does not contribute substantially to the overall absorption.

Therefore we also can apply a preliminary best-fit model (χ^2/dof=5.69) to the data which leaves out SSA completely, but instead includes only FFA from the CSM (both uniform and clumpy). We show the fit in Fig. 4. As one can see, both models fit equally well (due to the relatively negligible SSA); both models also do not quite fit the peaks of the light curves well. In Table 1 (column 3) we list the best-fit model parameters. What can be seen is what was found in the past [24]: $\delta \simeq \delta' \simeq 2$. Using the more recent VLBI results, i.e., $m = 0.86$ [2, 13], following similar arguments as above, one finds $s = 1.66$, i.e., $s \neq 2$ (see also [14]). The main conclusions from the past [7, 24] still apply for the more complete dataset.

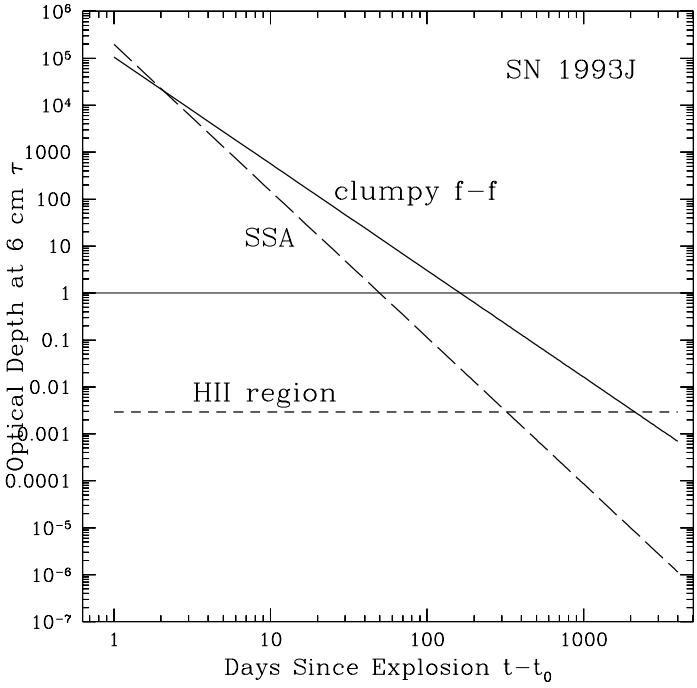

Fig. 3. Evolution of absorption of synchrotron radio emission from SN 1993J, based on a preliminary best-fit model. Shown are the clumpy FFA, SSA, and time-independent FFA from a distant line-of-sight HII region.

Table 1. Best-Fit Parameters

Parameter	Value(1)	Value(2)
K_1	1.39×10^4	1.36×10^4
α	-1.04	-1.05
β	-0.88	-0.88
K_2	...	9.14×10^2
δ	...	-1.88
K_3	9.98×10^4	8.33×10^4
δ'	-2.27	-2.26
K_4	2.76×10^{-3}	2.76×10^{-3}
K_5	1.78×10^5	...
δ''	-3.12	...

2.4 A New Wrinkle?

As can be seen in both Figs. 1 and 4, α appears to be changing, from ≈ -1 to ≈ -0.6 or -0.7 (see [2, 17]); at late times the overall model, with $\alpha \simeq -1$, underestimates the flux densities. We are investigating this change in our

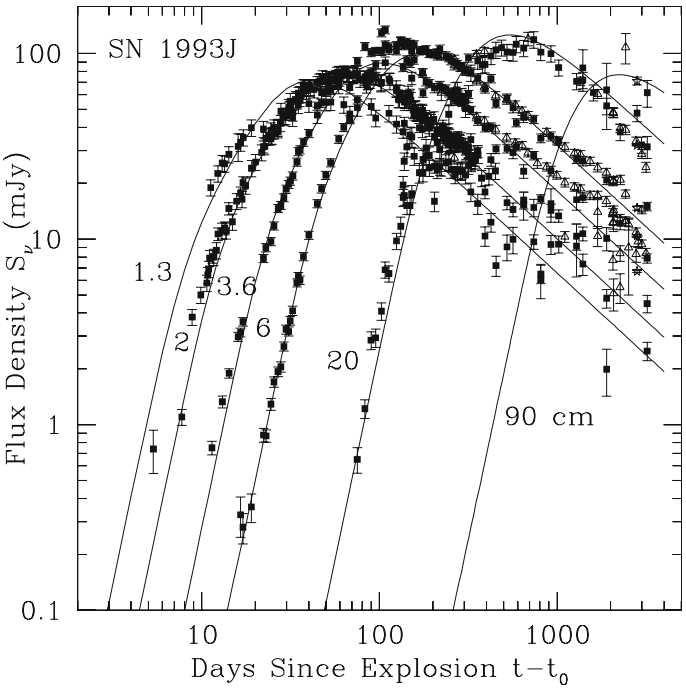

Fig. 4. Preliminary best-fit model to the SN 1993J VLA data. This model fit includes both a clumpy and uniform external absorbing medium, but no SSA.

continued VLA monitoring. The change could be due to increased adiabatic cooling and Coulomb losses [17] or the shock expanding into a region of CSM with a steeper density profile [2].

3 X-ray Emission from SN 1993J

Space does not afford a full discussion of X-rays from SN 1993J. Fortunately, this topic is discussed in more detail by Immler, Zimmermann, and Pooley in this volume. The SN was observed early using *ROSAT* at 0.1–2.4 keV [28, 29], *ASCA* at 1–10 keV [10, 22], and *CGRO/OSSE* at 50–150 keV [11], and at late times using *Chandra* at 0.3–8.0 keV [21] and *XMM* [30]. The main result is that X-rays were hard early and have become progressively softer. (See, e.g., the hardness index from the *ASCA* data [23].) This can best be explained by the hard X-rays emerging from the adiabatically expanding forward shock at $\sim 10^9$ K, and the softer X-rays from the radiative reverse shock at $\sim 10^7$ K. At early times a cool shell, at $< 10^4$ K at the shock contact discontinuity, absorbed most of the soft X-rays from within; see [6, 7]. From the linear decline of the *ROSAT* light curve Immler et al. [9] also find that $s = -1.63$,

confirming the earlier radio results [24] (see also [20]; although Swartz et al. [21] find a break in the light curve) and conclude that either $w_{\rm wind}$ was increasing and/or $\dot{M}$ was decreasing, as the progenitor transitioned from a red to blue supergiant prior to explosion.

The study of this fascinating SN at both radio and X-ray wavelengths continues.

Acknowledgement. We thank C. Williams for assistance in the VLA data analysis. KWW wishes to thank the Office of Naval Research (ONR) for the 6.1 funding supporting this research. Additional information and data on RSNe can be found on *http://rsd-www.nrl.navy.mil/7213/weiler/* and linked pages.

References

1. N. Bartel et al. : Nature **368**, 610 (1994)
2. N. Bartel et al. : Astrophys. J. **581**, 404 (2002)
3. R.A. Chevalier: Astrophys. J. **259**, 302 (1982)
4. R.A. Chevalier: Astrophys. J. Lett. **258**, L63 (1984)
5. R.A. Chevalier: Astrophys. J. **499**, 810 (1998)
6. R.A. Chevalier, C. Fransson: Astrophys. J. **420**, 268 (1994)
7. C. Fransson, P. Lundqvist, R.A. Chevalier: Astrophys. J. **461**, 993 (1996)
8. C. Fransson, C.-I. Björnsson: Astrophys. J. **509**, 861 (1998)
9. S. Immler, B. Aschenbach, Q.D. Wang: Astrophys. J. Lett. **561**, L107 (2001)
10. Y. Kohmura et al. : Pub. Astron. Soc. Japan **46**, L157 (1994)
11. M.D. Leising et al. : Astrophys. J. Lett. **431**, L95 (1994)
12. J. Marcaide et al. : Astrophys. J. Lett. **424**, L25 (1994)
13. J.M. Marcaide et al. : Astrophys. J. Lett. **486**, L31 (1997)
14. A.J. Mioduszewski, V.V. Dwarkadas, L. Ball: Astrophys. J. **562**, 869 (2001)
15. M.J. Montes, K.W. Weiler, N. Panagia: Astrophys. J. **488**, 792 (1997)
16. M.A. Pérez-Torres, A. Alberdi, J.M. Marcaide: Astron. Astrophys. **374**, 997 (2001)
17. M.A. Pérez-Torres, A. Alberdi, J.M. Marcaide: Astron. Astrophys. **394**, 71 (2002)
18. G.G. Pooley, D.A. Green: Mon. Not. R. Astron. Soc. **264**, 17P (1993)
19. A.C.S. Readhead: Astrophys. J. **426**, 51 (1994)
20. T. Suzuki, K. Nomoto: Astrophys. J. **455**, 658 (1995)
21. D.A. Swartz et al. : Astrophys. J. **144**, 213 (2003)
22. Y. Tanaka: IAUC 5753 (1993)
23. S. Uno et al. : Astrophys. J. **565**, 419 (2002)
24. S.D. Van Dyk, K.W. Weiler, R.A. Sramek, M.P. Rupen, N. Panagia: Astrophys. J. Lett. **432**, L115 (1994)
25. K.W. Weiler et al. : Astrophys. J. **301**, 790 (1986)
26. K.W. Weiler, N. Panagia, R.A. Sramek: Astrophys. J. **364**, 611 (1990)
27. K.W. Weiler, N. Panagia, M.J. Montes, R.A. Sramek: Ann. Rev. Astron. Astrophys. **40**, 387 (2002)
28. H.-U. Zimmermann, W. Lewin, E. Magnier, et al. : IAUC 5748 (1993)
29. H.-U. Zimmermann, W. Lewin, P. Predehl, et al. : Nature **367**, 621 (1994)
30. H.-U. Zimmermann, B. Aschenbach: Astron. Astrophys. **406**, 969 (2003)

Imaging of SN 1993J

A. Alberdi[1] and J.M. Marcaide[2]

[1] IAA-CSIC, Apdo. Correos 3004, 18080 Granada, Spain
antxon@iaa.es
[2] Departamento de Astronomía, Universidad de Valencia, 46100 Burjassot, Spain

Summary. SN 1993J has been imaged with VLBI, and its angular expansion monitored, for almost ten years. The images show shell-like radio structures with almost circular symmetry. SN 1993J expands according to models of shock excited emission. The angular expansion has a changing deceleration rate and is best modeled with two different slopes. The swept-up mass estimate at an age of 3159 days ($\sim$0.4 $M_\odot$), comparable to the low-mass envelope, favors a binary scenario. The observed spectral index of SN 1993J has slowly flattened since age 1000 days onward (α has changed from -1 to -0.67 at an age of 2820 days).

1 Introduction

SN 1993J is the radio supernova whose evolution has been monitored in greatest detail. It exploded on March 28th, 1993 and its radio emission was discovered a few days later (April 2 [22]; April 5 [15]). Its brightness and proximity has permitted unprecedented VLBI studies since the explosion.

It was first detected with VLBI on 25 April 1993. The observations were performed at 8.4 GHz on the baseline between the Madrid DSN antenna DSS63 and Westford, with a fringe spacing of 1.4 milliarcseconds ([8, 9]; on the second IAU Circular, the position of the supernova was established with a precision better than 10 mas).

1.1 Early Radio Size Estimates of SN 1993J

Marcaide et al. [10] provided estimates for the angular size of SN 1993J 29 and 36 days after explosion (0.28$\pm$ 0.06 mas on May 1, 1993), using an optically thick uniform disk model to analyze their data.

Bartel et al. [1] made a series of VLBI observations at 8.4 and 22 GHz, from one to three months after the supernova explosion, and found that the supernova was circularly symmetric and its expansion showed no signs of deceleration. Using uniform disk models, they determined an expansion velocity of 2.98$\pm$0.08 μas/day, which they found consistent with the maximum optical line velocities (18,000$\pm$1,000 km/s) [21], thus indicating that the radio emission arose from the shock front resulting from the interaction between the SN-ejecta and the circumstellar medium.

1.2 Discovery of the Shell-like Radio Structure

Marcaide et al. [11], at a supernova age of 239 days, showed that SN 1993J had a shell-like radio structure, the youngest ever discovered in a supernova. As seen in the Plate 1 (Fig. a), the radio shell was almost circularly symmetric, suggesting for the supernova explosion and the expanding radio shell a nearly spherical symmetry. The brightness distribution around the shell was quite uniform with enhanced emission in the south eastern part of the ring. Our estimate for the radio shell radius for 22 November 1993 (age 239 days) was 581±35 μas and yielded, assuming a zero-size at explosion, an average expansion rate for the shell radius of 2.43±0.15 μas/day, lower than the value previously estimated by Bartel et al. [1]. We determined a ratio of shell thickness to outer radius of 0.3±0.1.

The discovery of the shell structure was in agreement with the "Standard Interaction Model" (SIM) [5, 6]. In this model, the radio emission is assumed to be produced in a region of circumstellar gas (density profile $\rho_{csm} \propto r^{-s}$; s=2 corresponds to a steady wind) shocked by the outgoing ejecta (density profile $\rho_{ej} \propto r^{-n}$), thus giving rise to a "mini-shell" emission. For n>5, self-similar solutions are possible: the radii of the discontinuity surface, forward shock and reverse shock are related and all evolve in time with the power law R$\propto t^m$, where t is the time after explosion and the deceleration parameter, m, is given by (n-3)/(n-s).

2 Expansion of SN 1993J: An Exploding Star in Motion

After the discovery of the shell-like radio structure, we initiated a VLBI observing program to monitor the supernova expansion in a manner free from modeling uncertainties. Our first results [12] provided the first movie of the angular expansion of a radio supernova. The movie included observations from day 182 to day 541 (see Plate 1, Fig. b). SN 1993J expanded with circular symmetry and a self-similar evolution: at the radio frequency of 8.4 GHz, the structure relative to the outer radius remained time invariant even though the outer radius was expanding. Assuming a free expansion, we found an average angular expansion rate of 2.39±0.03 μas/day. We also found that the region of enhanced emission at the south-eastern part of the ring persisted with time and that the region had the steepest spectral index ($\alpha \leq -1.5, S \propto \nu^{\alpha}$).

Further observations at 5 GHz over 1304 days showed that the expansion was decelerating (m=0.86±0.02) [13]. Rupen et al. [19] found a similar result (m=0.837±0.025). All images had a circular shape, and the azimuthal changes in the brightness distribution could be attributed to inhomogeneities in the CSM (clumping in the wind), irregularities in the ejecta or changes in the magnetic field. After 1304 days, the velocity of the shock front had decreased to 9000 km/sec.

3 Deceleration in the Expansion of SN 1993J

Two research groups, one led by N. Bartel and the other by J.M. Marcaide, have monitored the angular expansion of SN 1993J for almost ten years [2, 3, 4, 12, 13]. The following conclusions can be drawn from their efforts:

3.1 Evolution of the Radio Shell

Along these years, the supernova has expanded rather isotropically (at least as seen in a 2D sky projection) showing a circular shell-like structure (deviations from circularity of the outer radius are smaller than 3%). However, the brightness distribution has been systematically changing both with time and azimuth around the source center. We show in the Plate 1 (Fig. c) two images of SN 1993J obtained on 22 September 1999 (age 2369 days) and 7 November 2002 (age 3511 days). For comparison, both images are shown convolved with a circular beam of 2 mas. In the first map, there is enhanced emission at the south-eastern part of the ring and a gap at the north-western part, whereas in the second the brightness distribution has become more complex with hot spots formed within the shell, even at position angles where the emission was very low in the first map (i.e. at the south-western part of the shell). Part of these changes are due to artifacts of the image reconstruction process, but part of them might be real. However, one should emphasize that, despite those enhancements and hot spots, the shell emission is rather uniform.

One common characteristic for all epochs (published, and those shown in the Plate still unpublished), is that the emission in the central part of the shell is much lower than that corresponding to a spherical optically thin shell with uniform emissivity. This indicates the existence of an important absorption in the central part of the source [4, 14], likely due to intervening ionized ejecta [7].

3.2 Determination of the Deceleration

In their published work, the group led by Marcaide has based their determinations on measurements of the supernova size on the image plane. In this case, the source size inferred from a map depends on how the map is produced. Because of the finite beam size, a positive bias is introduced in the size estimate: the size measured is larger than the true size. The fractional bias would systematically decrease for a source increasing in size if the same beam were used for all observations. This would cause an spurious contribution to the deceleration. Such undesirable contribution can be largely avoided by using a "dynamical beam," that is, using each time a beam of size proportional to the actual source size [13]. Considering all the observing epochs at 3.6 and 6cm (more than 25 observing epochs ranging from 72 to 3511 days), and fitting a single parameter to the data, Marcaide et al. have obtained

a deceleration parameter of m=0.87±0.01 (Supernova Radius R$\propto t^m$; using a convolving beam $\theta_b \propto t^{1.0}$) and m=0.83±0.02 (using a convolving beam $\theta_b \propto t^{0.8}$).

Adding the results for 30≤ t ≤ 175 days as given by Bartel et al. [2] to our data set, and using a dynamical beam that goes as $\theta_b \propto t^{0.8}$, we have reanalyzed our data through day 3511 allowing for a change of deceleration rate in the expansion of SN1993J (implying two deceleration parameters), that is, two straight lines and a time break in a log-log plot. We obtain the best fit with the following parameters: $m_1 = 0.93\pm0.06$, $m_2 = 0.82\pm0.01$, and $t_{\rm br} = 383 \pm 121$ days (see Fig. 1). This fit has a reduced χ^2_ν=2.18. Analyzing the same data set with only one deceleration parameter we obtain $m = 0.83 \pm 0.01$, with a reduced χ^2_ν=2.76. Though the latter result is compatible with our earlier estimate [13], it has a slightly larger reduced χ^2_ν than the fit with two deceleration regimes. It should be noted though that including the data from [2] affects *very* much the solution and that their data and ours have been obtained in different ways. See also [14] for a completely new approach. Their conclusions differ from those presented in this review.

The change in the angular growth rate of SN 1993J, if true, could be due to: i) a change in the density profile of the CSM caused by a changing mass loss rate of the progenitor and/or ii) a change in the density profile of the supernova ejecta (since $m = (n-3)/(n-s)$ in the SIM). Combining the deceleration rate determinations with the time dependence of the opacity due to an external medium ($\tau \propto t^\delta$, with $\delta = -(2s-1)m$, $\delta = -1.99^{+0.38}_{-0.16}$ [20]) and assuming that δ has not changed with time, we found that for early epochs in the expansion (t≤400 days) s=1.52 (density profile for the presupernova wind) and n=22.7 (ejecta density profile), while for later epochs s=1.71 and n=8.9. This result indicates that the density profile of the CSM has changed with time, thus suggesting that the fast circumstellar wind was probably not steady.

However, there is increasing evidence that, besides free-free absorption, synchrotron self-absorption (SSA) is also relevant for SN 1993J [7, 16, 17]. In fact, Fransson and Björnsson (1998) [7] can explain the light curves assuming a standard $s = 2$ density profile for the presupernova wind. In this case, the expansion deceleration could be associated with n (ejecta density profile) changing from 14.9 to 7.6 from early to late times. The supernova emission is becoming progressively more dominated by swept-up material, with the evolution of the supernova governed by the interaction of the high energy particles in the shell with the surrounding medium.

Assuming s=2 and typical values for the mass-loss rate and wind velocity ($\dot{M}= 5 \times 10^{-5}$ M$_\odot$ yr^{-1}, v_w= 10km/s), the swept-up mass after 3157 days, $\sim$ 0.4 M$_\odot$, is comparable to the low-mass envelope, thus favoring a binary scenario.

Bartel et al. [2, 4] have also imaged SN 1993J and measured the supernova size. Their results are based on model fitting of the two-dimensional

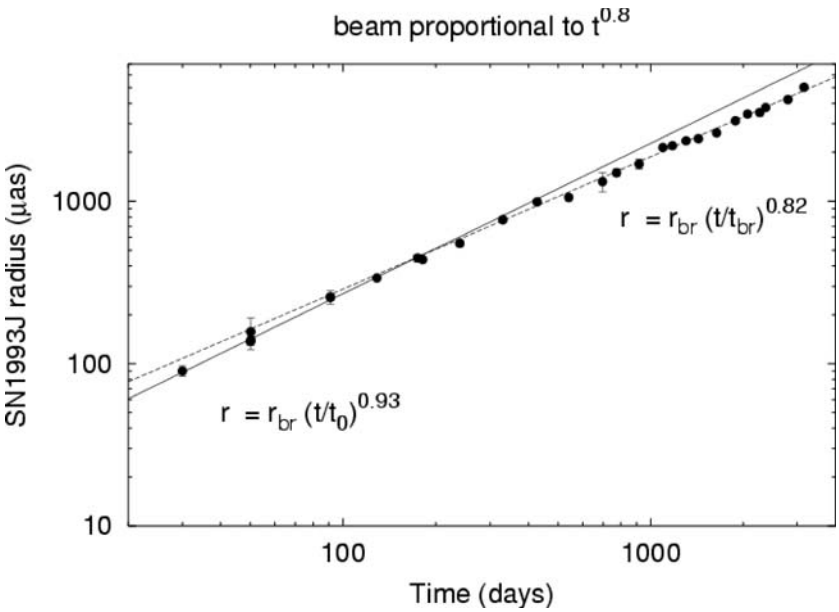

Fig. 1. Weighted least squares fit to the outer shell radius of SN1993J as a function of time since explosion, allowing for a change in its deceleration rate. The VLBI data up to $t \leq t_{\rm br}$=403 days (where the solid and dashed lines in the figure cross each other) can be well fitted by a power-law with index m_1=0.93±0.06 (solid line), while for $t \geq t_{\rm br}$ the best fit is given by a power-law of index m_2=0.82±0.01 (dashed line). Note that the scale is logarithmic. Our data and data from Bartel et al. [2] have been combined. The Bartel et al. data greatly affect the fit in the early days. See also the text for details about the dynamical beam used.

projection of a three-dimensional spherical shell of uniform emissivity to the calibrated uv-data set. They have also determined the supernova expansion, and have even claimed the detection of decreasing deceleration from age 1900 days onward. They find three different slopes: m=0.919±0.019 (age 30-300 days), m=0.781±0.009 (age 582-1893 days) and m=0.860±0.011 (age 1893-3164 days). According to them, these changes indicate that the evolution of SN 1993J is not self-similar, and are simultaneous with structural changes, line velocity changes and changes in the light curve decline. This time-dependent deceleration was predicted by Mioduszewski et al. [16], who calculated the time evolution of the expansion parameter from hydrodynamical simulations using an specific explosion model. In their interpretation, the interaction of features in the ejecta density structure with the reverse shock is relevant for the angular expansion.

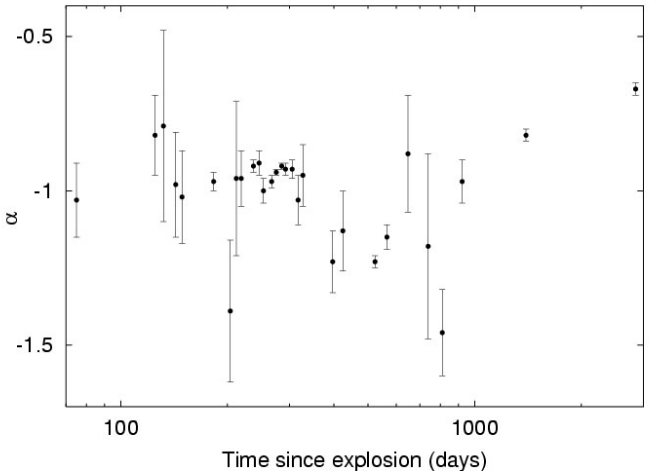

Fig. 2. Observed spectral index, α, of SN1993J from t ∼70 days up to t=2820 days, as obtained from fitting at each epoch the available VLA data to a synchrotron spectrum, partially suppressed by free-free absorption. After t ∼1000 days, the spectrum is flattening. The data used for the fits come from K. Weiler (private communication), except for the last data point which is from [18].

3.3 Determination of the Shell Width

The thickness of the shell has been found to be 30±10 % [11] (based on fits on the images) and 25±3 % [4] (based on fits in the uv plane, taking into account the central absorption) of its outer radius. See [14] in this proceedings volume for a detailed account on this matter.

4 Spectral Evolution of SN 1993J

We have fitted the available radio continuum data of SN 1993J for the period from ∼70 up to 2820 days after the explosion [18]. For all epochs, the spectra follow a power-law within the errors. The fit shows that the observed spectral index of SN 1993J has been slowly evolving since t∼1000 days onward, with α flattening from a value close to -1 to a value of -0.67±0.02 on day 2820 (see Fig. 2). A similar spectral evolution has also been reported by Bartel et al. [3].

The spectral evolution might suggest that radiative losses (mainly synchrotron), adiabatic cooling and ionization losses at the lowest frequencies contribute significantly to the integrated electron spectrum. Preliminary results from our group confirm the ongoing SN 1993J spectrum evolution, becoming progressively less steep (at least, up to age 3500 days where $\alpha \sim -0.55$).

For a power-law relativistic electron distribution, the spectral index of the electron distribution (γ) is related to the observed spectral index by $\gamma = 1 - 2\alpha$. Our value of α on day 2820, translates into γ=2.34±0.04, which agrees well with the injected electron spectrum predicted by [7], γ=2.1, consistent with diffusive shock acceleration. These authors propose that a constant fraction of the shocked thermal electrons, characterized by a constant spectral index $\alpha = -0.55$, are injected and accelerated. At early stages, synchrotron losses dominate the cooling of the electrons, steepening the integrated electron spectrum up to a value of ∼-1. For epochs t≥ 1000 days, radiative losses become less relevant and the observed spectral index flattens progressively, getting closer to the spectral index associated with the injected electron population, which seems consistent with the observational results.

Fransson and Björnsson [7] have modeled the SN 1993J light curves assuming a standard r^{-2} circumstellar medium and considering both free-free absorption and synchrotron self-absorption (SSA) (the importance of SSA was also discussed by other authors [17, 16]). They determine a magnetic field of B∼ $64(R_s/10^{15}cm)^{-1}$G, which argues strongly for a turbulent amplification behind the shock. Fransson and Björnsson also determine that the number density of relativistic electrons scales as a fixed fraction of the thermal energy density behind the shock.

5 Summary

SN 1993J is to date the radio supernova whose evolution has been monitored in greatest detail and the one which holds best promise for a comprehensive theoretical-observational analysis. SN 1993J has been imaged, and its angular expansion monitored, for almost 10 years. The results obtained by the two groups carrying out VLBI observations of SN1993J show a general agreement and can be summed up and summarized as follows:

- The shell-like radio structure of SN 1993J has expanded according to models of shock excited emission, showing almost circular symmetry, thus suggesting that the shock front is expanding almost isotropically. The brightness distribution changes with azimuth around the source center and with time. No protrusions have been detected.
- The angular expansion may not be self-similar. The expansion may be best modeled with two slopes.
- The swept-up mass estimate (0.4 $M_\odot$at 3157 days), comparable to the low-mass envelope, favors the binary scenario.
- A fit to the radio spectra of SN 1993J from ∼70 up to 2820 days shows a clear, albeit slow, evolution with α changing from $\simeq -1$ to $\simeq -0.67$.
- Free-free absorption from the CSM and Synchrotron Self-Absorption are relevant in SN 1993J.

References

1. N. Bartel et al. : Nature **368**, 610 (1994)
2. N. Bartel et al. : Science **287**, 112 (2000)
3. N. Bartel et al. : Astrophys. J. **581**, 404 (2002)
4. M.F. Bietenholz, N. Bartel, M.P. Rupen: Astrophys. J. **368**, 610 (2003)
5. R.A. Chevalier: Astrophys. J. **258**, 790 (1982)
6. R.A. Chevalier: Astrophys. J. **259**, 302 (1982)
7. C. Fransson, C.I. Björnsson: Astrophys. J. **509**, 861 (1998)
8. J.M. Marcaide et al. : IAUC 5785 (1993)
9. J.M. Marcaide et al. : IAUC 5820 (1993)
10. J.M. Marcaide et al. : Astrophys. J. Lett. **424**, L25 (1994)
11. J.M. Marcaide et al. : Nature **373**, 44 (1995)
12. J.M. Marcaide et al. : Science **270**, 1475 (1995)
13. J.M. Marcaide et al. : Astrophys. J. Lett. **486**, L31 (1997)
14. J.M. Marcaide et al. : In: This proceedings
15. G.G. Pooley, D.A. Green: IAUC 5751 (1993)
16. A.J. Mioduszewski, V.V. Dwarkadas, L. Ball: Astrophys. J. **562**, 869 (2001)
17. M.A. Pérez-Torres, A. Alberdi, J.M. Marcaide: Astron. Astrophys. **374**, 997 (2001)
18. M.A. Pérez-Torres, A. Alberdi, J.M. Marcaide: Astron. Astrophys. **394**, 71 (2002)
19. M.P. Rupen et al. : In: *Radio Emission from Galactic and Extragalactic Compact Sources - IAU Coll. 64*, ed. by J.A. Zensus, G.B. Taylor, J.M. Wrobel (ASP Conf. Series, Vol. 144, 1998) pp. 353-354
20. S.D. Van Dyk et al. : Astrophys. J. Lett. **432**, L115 (1994)
21. J.C. Wheeler et al. : Astrophys. J. Lett. **417**, L71 (1993)
22. K.W. Weiler, R.A. Sramek, S.D. van Dyk, N. Panagia: IAUC 5752 (1993)

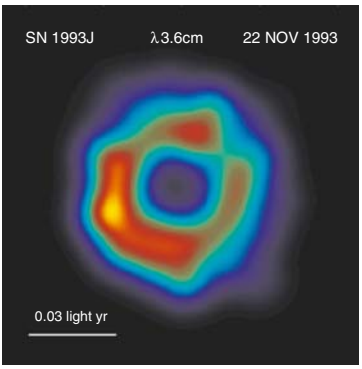

a) Discovery of shell−like radio structure in SN 1993J. False−color image obtained from 3.6cm VLBI observations 239 days after explosion. (From Marcaide et al. (1995), Nature 373, 44)

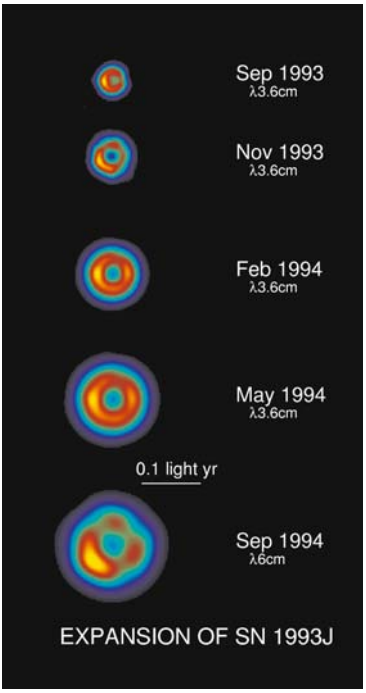

b) Sequence of images of SN 1993J from VLBI observations obtained 182, 239, 330, 427, and 541 days after the explosion. All but the last image were obtained from 3.6cm data. The image on day 541 was obtained from 6cm data. (From Marcaide et al. (1995), Science 270, 1475)

c) Preliminary images of SN 1993J obtained from 6 cm VLBI observations 2396 days (left) and 3511 days (right) after the explosion.

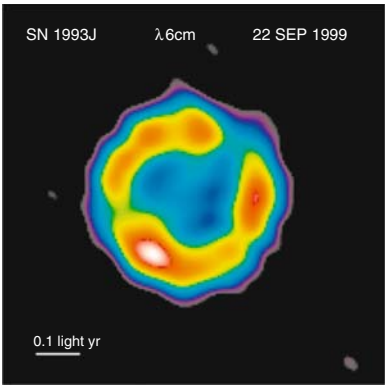

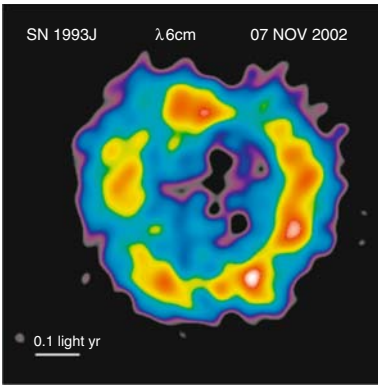

Plate (Alberdi & Marcaide)

Plate 1.

Nine Years of VLBI Imaging of Supernova 1993J

M. F. Bietenholz[1], N. Bartel[1], M. P. Rupen[2], A. J. Beasley[3], D. A. Graham[3], Altunin, V. I.[4], T. Venturi[5], G. Umana[5], W. H. Cannon[6], and J. E. Conway[8]

[1] York University, Canada
[2] National Radio Astronomy Observatory, USA
[3] CARMA, Owens Valley Radio Observatory, USA
[4] Max-Planck-Institut für Radioastronomie, Germany
[5] Jet Propulsion Laboratory, Caltech, USA
[6] Instituto di Radioastonomia, CNR, Italy
[7] York University & Space Geodynamics Lab/CRESTech, Canada
[8] Onsala Space Observatory, Sweden

Summary. We present a selection of our VLBI images of SN 1993J, along with our latest results on its expansion and its shell structure.

1 Introduction

Supernova 1993J is the most comprehensively monitored radio supernova to date. Our extensive campaign of VLBI observations [1, 2, 3, 4], at 35 epochs, at frequencies between 1.7 and 22 GHz, using up to 18 antennas in a global array, has allowed us to make images from 30 d to 9 yr after the explosion (see [5] for parallel observations). Our images are all phase-referenced to the stationary core, $M81^*_{\rm core}$, of the nuclear source in the host galaxy, M81 [3], which allows us to display them relative to the supernova's explosion center.

2 Model Fitting

At every epoch, we fit a spherical shell model directly to the u-v data in order to estimate the position of the geometrical center, the size, and for later epochs, the shell thickness of SN 1993J. We determined the projected motion of the center of SN 1993J relative to $M81^*_{\rm core}$ to be < 480 km s^{-1}, which is much smaller than the expansion velocities of 17,200 km s^{-1} at $t = 30$ d and 8900 km s^{-1} at $t = 1600$ d after shock breakout (1993 Mar. 28: $t = 0$ d)[2]. SN 1993J is still very circular 9 years after the explosion, and its expansion from the explosion center is isotropic to within 5.5% [3].

We show the expansion curve of SN 1993J in Fig. 1 (see [6] for parallel results). The expansion is more complex than a simple power-law. From almost free expansion at $t < 300$ d, the deceleration grows until $t \sim 1600$ d,

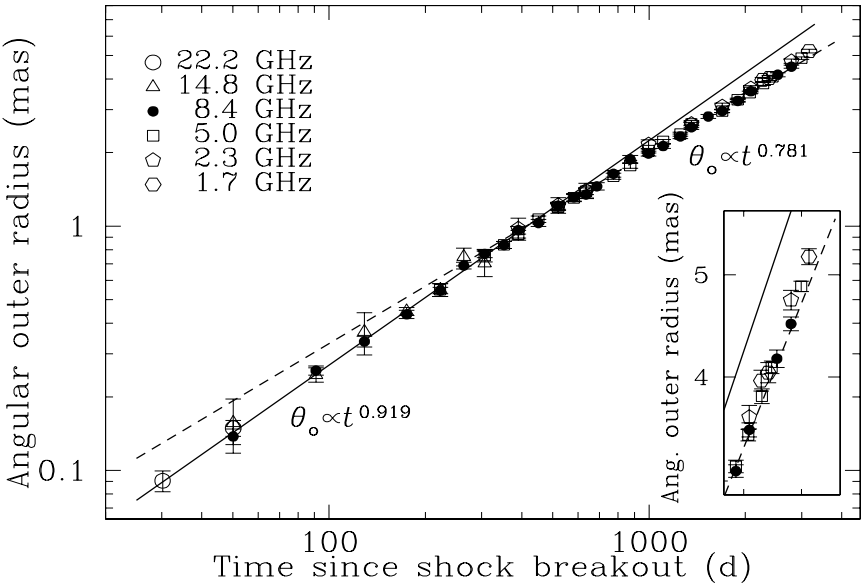

Fig. 1. The expansion curve of SN 1993J derived from 34 epochs of VLBI observations at frequencies between 1.7 and 22 GHz. The angular outer radii, θ_o, are derived from a spherical shell model fit directly to the u-v data. The inset shows outer radii for the latest epochs in more detail. The solid and dotted lines are power-law fits to the expansion, showing a change in the power-law index from 0.919 to 0.781 at $t \sim 600$ d. A further change in the index is visible in the inset (see [2] for more detail).

and then decreases again. For details and the interpretation of this behavior we refer the reader to [2].

3 Images

We present a selection of our images of SN 1993J at 8.4 and 5.0 GHz in Fig. 2 (see [1, 4] for more images). The shell structure first becomes visible at $t = 175$ d. Already at this stage the brightness was modulated around the ridge, with a distinct minimum to the west and a maximum to the east-south-east. Over the next ~ 300 d, this pattern appears to rotate, and by $t = 451$ d the maximum is to the south and the minimum to the north. The pattern of modulation then becomes more complex, with two hot spots appearing to the east and west by $t = 774$ d, and a third in the south by $t = 1107$ d. By the end of our observing period at $t = 3345$ d, the opening in the north had become a hot spot and there were two further hot spots, to the south-southeast, and the west-southwest. At that time, the radius of SN 1993J was $\sim 12,000$ AU.

With the increasing relative angular resolution we were able to determine the shell thickness, again using model-fitting. The best fit model had a shell thickness of $25 \pm 3\%$ of the shell's outer radius, and also had some absorption in the center of the shell. Models without absorption result in a thinner shell but also a poorer fit [4]. The best visual indication of the shell thickness is given by a composite image, also shown in Fig. 2, made from our last three 8.4 GHz data sets scaled and combined (see [4] for details).

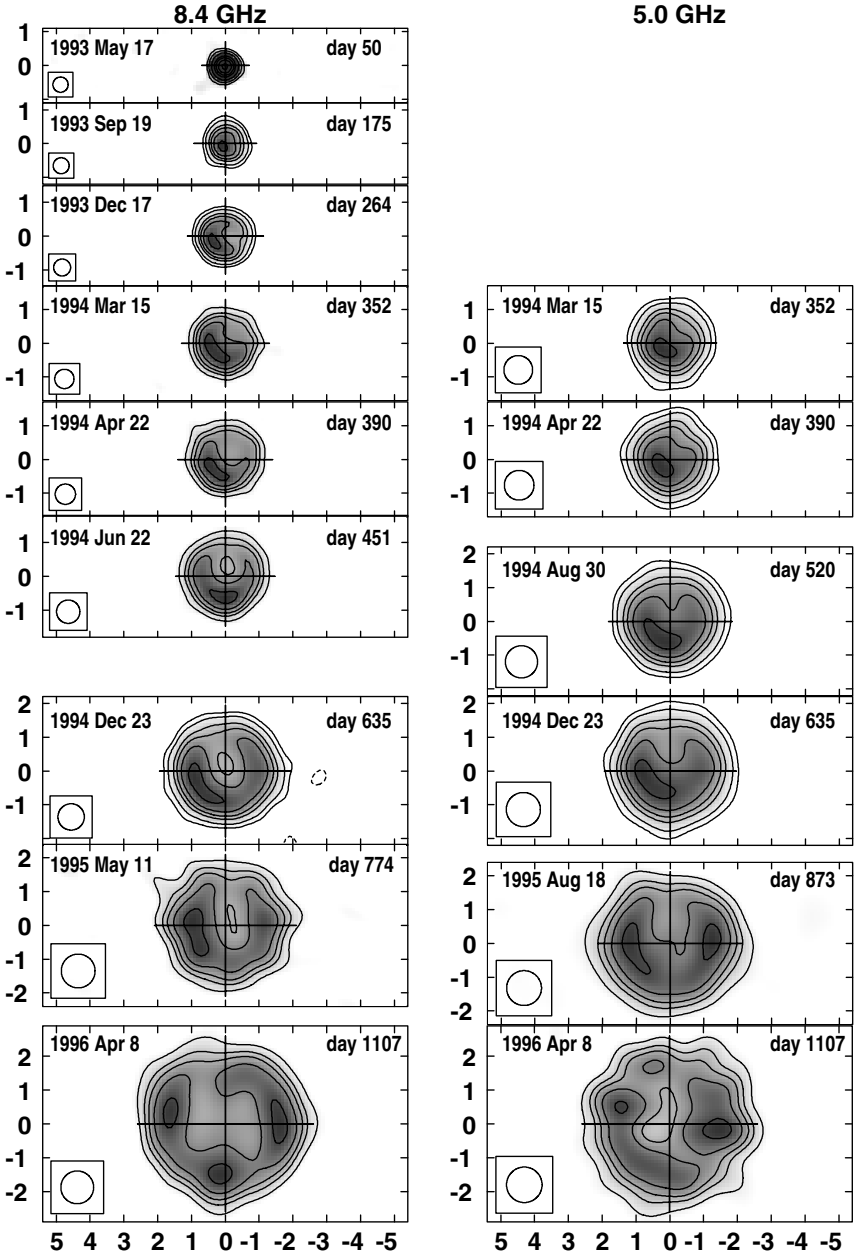
8.4 GHz
5.0 GHz
1993 May 17
day 50
1993 Sep 19
day 175
1993 Dec 17
day 264
1994 Mar 15
day 352
1994 Apr 22
day 390
1994 Jun 22
day 451
1994 Aug 30
day 520
1994 Dec 23
day 635
1995 May 11
day 774
1995 Aug 18
day 873
1996 Apr 8
day 1107
5 4 3 2 1 0 -1 -2 -3 -4 -5

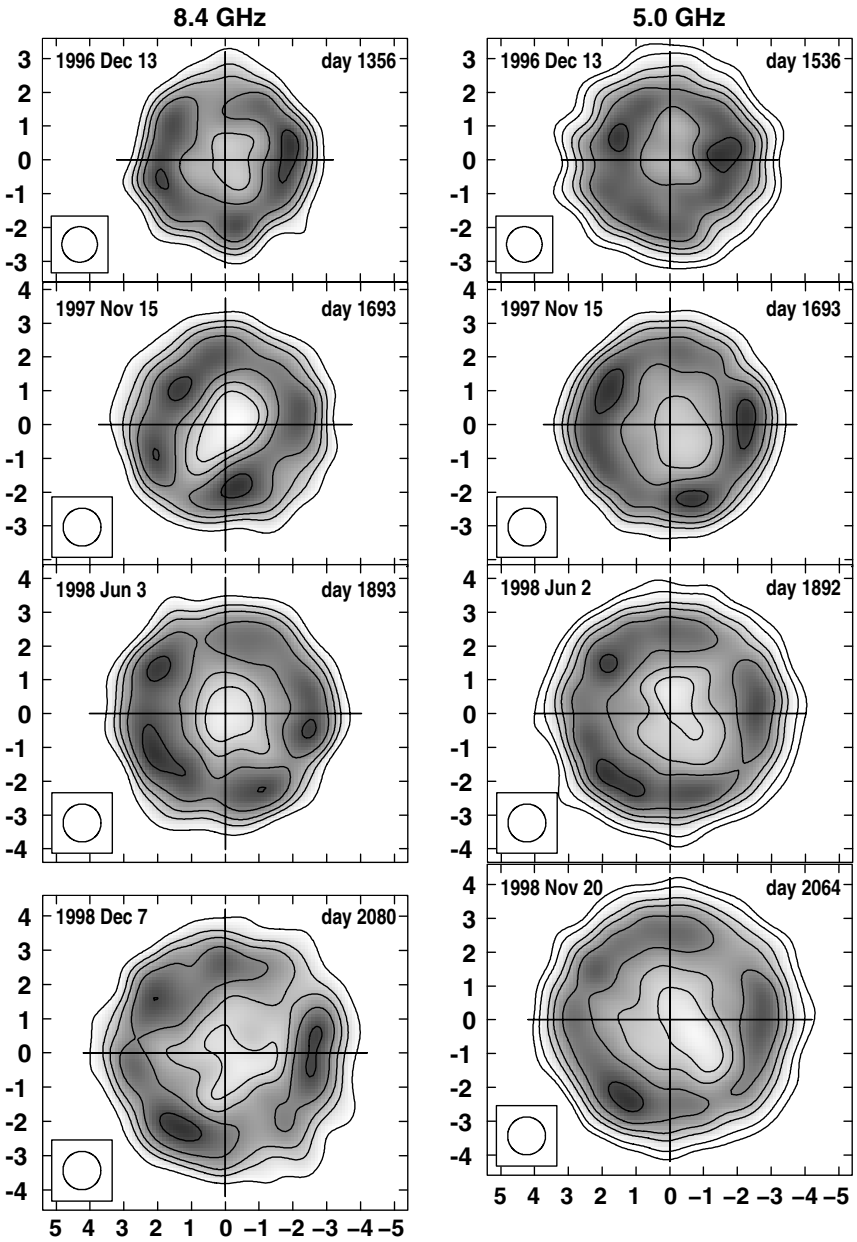
8.4 GHz
5.0 GHz
1996 Dec 13
day 1356
1996 Dec 13
day 1536
1997 Nov 15
day 1693
1997 Nov 15
day 1693
1998 Jun 3
day 1893
1998 Jun 2
day 1892
1998 Dec 7
day 2080
1998 Nov 20
day 2064
5 4 3 2 1 0 −1 −2 −3 −4 −5

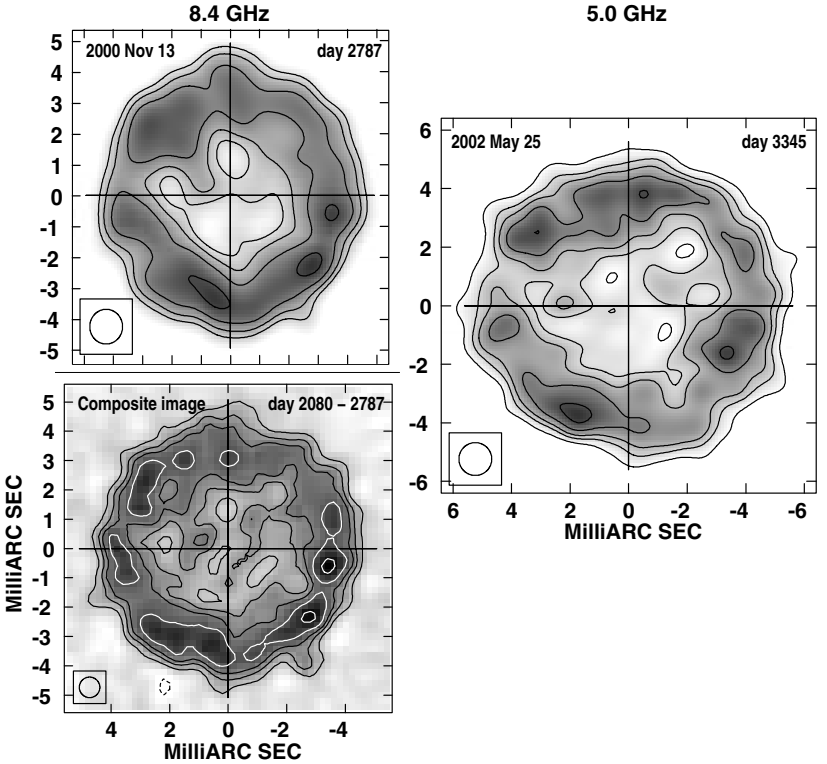

Fig. 2. Selected 8.4 and 5.0 GHz radio images of SN 1993J. The contours are drawn at 1, 2, 4, ..., 32, 45, 64, and 90% of the peak brightness, but only if they are $> 3\times$ the rms background noise. North is up and east is to the left. In each panel, the large cross indicates the position of the explosion center, and the resolution (FWHM) is indicated at lower left. The last 8.4 GHz image is at higher resolution (0.7 mas), and is a composite image, made from the data at $t = 2080$, 2525 and 2787 d (1998 Dec. to 2000 Nov.), scaled in outer radius to 4.49 mas (i.e. $t = 2787$ d).

References

1. N. Bartel et al. : Science **287**, 112 (2000)
2. N. Bartel et al. : Astrophys. J. **581**, 404 (2002)
3. M.F. Bietenholz, N. Bartel, M.P. Rupen: Astrophys. J. **557**, 770 (2001)
4. M.F. Bietenholz, N. Bartel, M.P. Rupen: Astrophys. J. **597**, 374 (2003)
5. J.M. Marcaide et al. : Astrophys. J. Lett. **486**, L31 (1997)
6. J.M. Marcaide et al. : In: *Proceedings. of the 6^{th} VLBI Network Symposium, 2002*, ed. by E. Ros et al. pp. 239–242

On the SN 1993J Radio Shell Structure

J.M. Marcaide[1], I. Martí-Vidal[1], E. Ros[2], A. Alberdi[3], J.C. Guirado[1], L. Lara[3,4], M.A. Pérez-Torres[3], and K.W. Weiler[5]

[1] Departamento de Astronomía, Universitat de València, 46100 Burjassot, Spain; J.M.Marcaide@uv.es
[2] Max-Planck-Institut für Radioastronomie, 53121 Bonn, Germany
[3] IAA-CSIC, Apdo. Correos 3004, 18080 Granada, Spain
[4] Universidad de Granada, 18071 Granada, Spain
[5] Naval Research Laboratory, Code 7213, Washington DC 20375-5320, USA

Summary. An accurate measurement of the expansion deceleration of SN 1993J depends on how well the shell size and its emission structure are known. With the goal of determining the emission structure of the shell, we have developed a new approach, which we call "Green Function Deconvolution" (GFD), based on iterative use of Green functions on the sky plane to reconstruct the radial emission profiles of spherically symmetric sources. This approach works reasonably well in the case of optically thin emitting sources, which is not the case for SN 1993J since, as we find, the emission from the central part of SN 1993J further away from us is strongly or totally absorbed. We describe the GFD method and present our findings about the emission structure of the shell. We also present the expansion of SN 1993J based on a method complementary to GFD, which will be described elsewhere.

1 Introduction

The determination of the characteristics of expansion of SN 1993J require accurate measurements of the true size of SN 1993J at each epoch. The images of SN 1993J obtained over 10 years are all circularly symmetric to a great extent and suggest an isotropic expansion. Actually, expansion decelerations have been determined [2, 3, 6, 10]. However, although compatible with each other, these determinations have been obtained differently. The group led by Marcaide has made the size measurements directly on the radio images, that is on the sky plane, while the group led by Bartel has made those size measurements on the Fourier plane assuming a shell model for the source with a given shell width and optically thin emission [4]. As shown by Alberdi and Marcaide [1] (see their Fig. 4) and [4] systematic trends in the expansion measurements are present.

In principle, the determination of the size of the radio supernova SN 1993J depends on the shell model used and there are no a priori reasons to assume a particular shell model. In practice, the determination of the external radius of the radio supernova is easier than the determination of the shell model, but the former determination is contaminated by lack of determination of the latter. The best approach would be to determine both accurately and

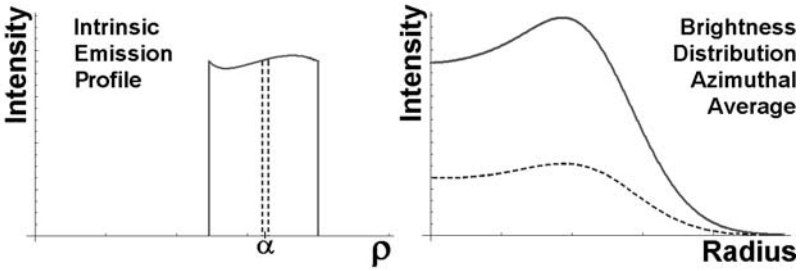

Fig. 1. (Left) A schematic of an arbitrary radial emission profile, indicating that it consists of a sum of very narrow profiles (dashed), which in turn correspond to the emission of very narrow 3D spherical shells; (Right) Schematic of the azimuthal average of the 2D brightness distribution generated by the emission of the 3D-shell corresponding to the radial profile given at left. It corresponds to the sum of Green Functions of very narrow profiles (dashed line, $G_\sigma(r,\alpha)$, see text) which add up to the given emission profile.

simultaneously. We have developed a tool for such purpose. The method, presented in this contribution, should be a good tool for cases of circular structures resulting from optically thin emission and in conditions of high signal to noise.

2 GFD Method

Let us consider the brightness distribution $I_{\alpha,\sigma}(r,\theta)$ due to a very (infinitesimally) thin spherical shell of radius α with uniform volume emissivity, once convolved by a beam of size σ. Let us indicate schematically such emission by a dotted profile on Fig. 1 (left). The azimuthally averaged emission $I_{\alpha,\sigma}(r)$ can thus be analytically expressed as:

$$G_\sigma(r,\alpha) = \exp\left(\frac{-r^2}{2\sigma^2}\right) \int_{\rho=0}^{\alpha} \rho d\rho \frac{\alpha}{(\alpha^2-\rho^2)^{\frac{1}{2}}} \exp\left(\frac{-\rho^2}{2\sigma^2}\right) BesselI\left(0,\frac{r\rho}{\sigma^2}\right)$$

where $BesselI(0,x)$ is the zeroth order modified Bessel Function of the First Kind. The above expression is thus a Green Function $G_\sigma(r,\alpha)$ which takes us from the emission profile on Fig. 1 (left) to the azimuthal average of the corresponding brightness distribution given on Fig. 1 (right).

The brightness distribution due to any optically thin shell of finite width will thus be a linear sum of the brightness distributions from a large number of very thin shells as indicated by the profile on Fig. 1 (left). In other words, as shown in Fig. 1 (right), the emission $I_{\mathrm{shell},\sigma}(r)$ from a finite width shell will be a weighted sum of elementary contributions $I_{\alpha,\sigma}(r)$, that is, a weighted sum

of Green functions $G_\sigma(r,\alpha)$, where the weights can be chosen to reproduce any emission profile by the appropriate $S(\alpha)$ in the expression

$$I_{\mathrm{shell},\sigma}(r) = \int_{\alpha_1}^{\alpha_2} S(\alpha) G_\sigma(r,\alpha) d\alpha$$

Let us now consider a map of a radio source of circular symmetry (reconstructed with a beam of size σ) described by the brightness distribution $B_\sigma(x,y)$ in Cartesian coordinates, or equivalently, $B_\sigma(r,\Theta)$ in polar coordinates. The azimuthal average of $B_\sigma(r,\Theta)$ yields $B_\sigma(r)$, which is equivalent to $I_\sigma(r)$ conceptually but is degraded with respect to it by radio noise, data calibration errors, image reconstruction errors, etc, say in a VLBI observation.

The basic idea of GFD is that $B_\sigma(r)$ can be "deconvolved" using functions of the type $G_\sigma(r,\alpha)$ to obtain an emission profile of the type of $S(\alpha)$.

3 GFD on Test Maps

We have generated a noiseless map which corresponds to the emission of an optically thin spherical shell of finite width (30% of outer radius) and we have made the azimuthal average of the map. The resulting intensity profile and the schematic of the shell emission profile (flat profile within the shell boundaries) is shown in Fig. 2 as the continuous line and light-shaded profile, respectively. Also in Fig. 2 the shell emission profile recovered after a GFD and the residuals are shown as a dark-shaded profile and a dashed line, respectively. As it can be seen, the GFD recovers the original emission profile rather well.

In order to further test the goodness of the GFD method we have generated the same model as in Fig. 2 but now we have added noise to the synthetic data. The added amount of noise (corresponding to random Gaussian errors of 10% in amplitude and 10 degrees in phase) simulates realistic observational conditions in VLBI. The resulting intensity profile, GF-deconvolved emission profile, and intensity residuals after GFD are shown in Fig. 3. The reconstruction of the shell profile is not as reliable as before now that noise and calibration errors are present. The level of emission appears enhanced in the inner part, the outer profile appears depleted, and the width of the shell appears much narrower. It is not a satisfactory reconstruction. The difficulties of the method have to do with the asymmetry of the Green Functions of the very narrow shells which are used as basic elements in the deconvolution. This asymmetry causes biases and some of them can be accounted for in a proper deconvolution strategy.

However, we have also found that in deconvolutions of real maps (see below in Sect. 4 and Fig. 5) we always obtain large negative residuals at the source center region which indicate that our maps contain less emission at

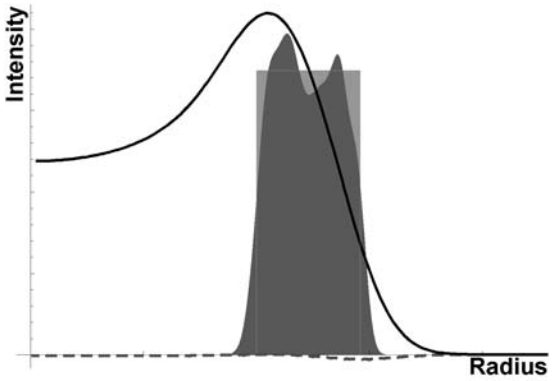

Fig. 2. Intensity profile (continuous line) corresponding to an azimuthal average of the brightness distribution due to a shell of flat radial emission profile (light-shaded) and finite width (30% of outer radius) and reconstructed emission profile (dark-shaded) using GFD. No noise has been added to the synthetic data which produce the brightness distribution. The residuals of the GFD (dashed line) are almost zero, as expected. The beam sizes used also correspond to 30% of the outer radius.

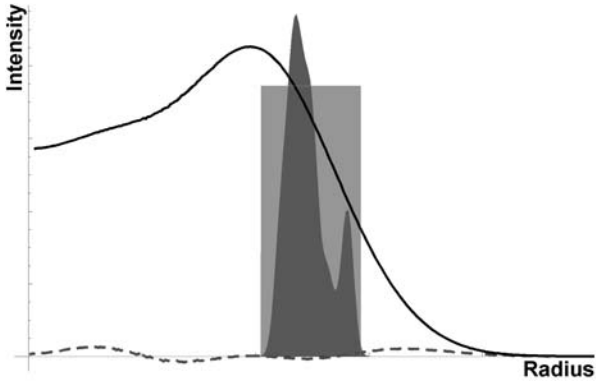

Fig. 3. Same as Fig. 2, but with realistic random noise and calibration errors. Notice the outward shift of the inner part of the reconstructed profile and the bias towards overestimating the emission in the inner region and underestimating it in the outer region.

the source center than expected for spherical shells of optically thin emission. Notice that, as said in Sect. 1, the Green Functions used in our GFD assume optically thin emission for the spherical shell. In order to further understand the implications of such central absorption (i.e. missing central emission at the source center with respect to what is expected for spherical shells of optically thin emission), and aware of the present limitation of our GFD method, we introduced central absorption in our synthesized noisy maps. Fig. 4 shows

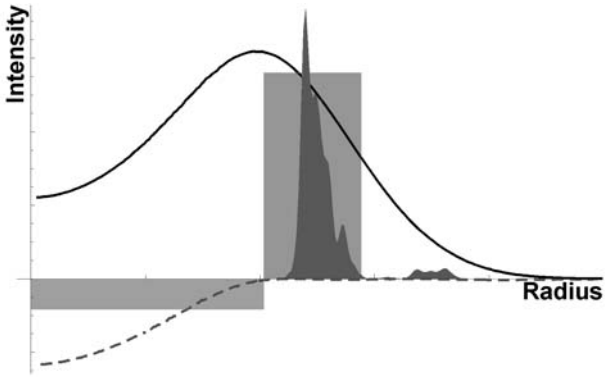

Fig. 4. Same as Fig. 3 but with a central absorber. The schematic of the central absorption indicates a complete blockage of the emission from the rear side of the shell for the extent of the drawing. In this case, the reconstructed profile is further biased towards larger radii and the reconstructed shell appears narrower than without the central absorber.

a schematic of the shell emission and the central absorption, the generated intensity profile and the deconvolved emission profile. The schematic of the central absorption in Fig. 4 indicates a complete blockage of the emission from the rear side of the shell for the extent of the drawing. The residuals are small everywhere, as before, but in the central region. These large central region residuals indicate the presence of the central absorption, as indeed we know is the case in this simulation. As it can be seen in Fig. 4, the recovered emission profile is not, under these conditions, a reliable representation of the shell profile. It bears resemblance to the shape of the profile recovered for the case without central absorption but the width of the profile is even narrower.

4 GFD of Real Maps

In Fig. 5 we use real data of SN 1993J from day 541. Without knowledge of the tests conducted and presented in the previous section one would not know how reliable this reconstruction is and how the true emission profile of the SN 1993J might be. However, the similarity of Figs. 4 and 5 is remarkable. From this similarity one is led to infer with caution that the emission profile of SN 1993J is probably that of a shell of width about 30% of size of the outer radius or somewhat less, since the deconvolved emission in Fig. 5 appears somewhat narrower than that in Fig. 4. Such a conclusion is in accord with previous experimental estimates but it does not help much to clarify further the situation. With respect to using the GFD method to determine the size of the radio supernova SN 1993J accurately, the prospects are not as good as expected but the application of the GFD method in SN 1993J reveals the

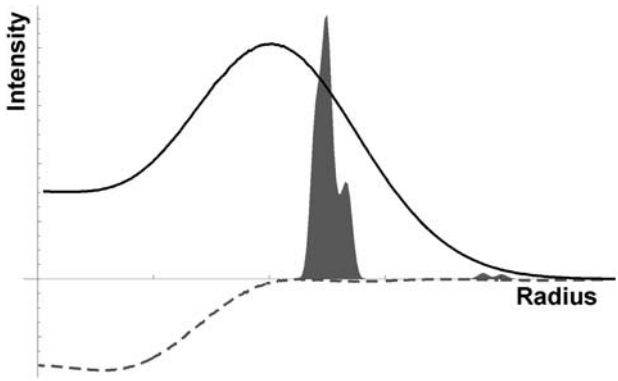

Fig. 5. Radial emission profile obtained from data of SN 1993J from day 541 after explosion. Notice its similarity to the profile reconstructed in Fig. 4.

presence of a strong absorption of emission at the source center with respect to what is expected for an optically thin spherically symmetric source.

5 Other Radio Sources

We have also applied the GFD to VLBI maps of 43.31+592 in M 82 (maps courtesy of A. Pedlar) and we have obtained size estimates for 43.31+592 very similar to those estimated with a different method [8, 9]. For 43.31+592 the GFD method seems to work better than for SN 1993J, perhaps because there is no central absorption. Another interesting case is SN 1987A where the specific geometry is known. The analytic expression for $G_\sigma(r, \alpha)$ in this case would be a different one to that given in Section 1 since it corresponds to a planar and tilted emitter but, once determined, the GFD should work reasonably well unless absorption intervenes again.

6 Expansion of SN 1993J

Having found that the GFD method is not as well-suited as we had expected for determining the outer radius of SN 1993J accurately, we have developed other methods to determine the source size and shell width, abandoning hope of determining the profile of the emission within the shell. Of the new methods, which cannot be presented here, the best is one which we call the Common-Point Method [7] and which yields outer radius estimates accurate within 2% for cases when the shell size relative to the source size is not very different between observations (actually, changes in shell size map into changes in measured outer radius scaled down by a factor of 4). Combining these methods we have been able to produce a reliable expansion graph with data at 6 cm which is presented in Fig. 6.

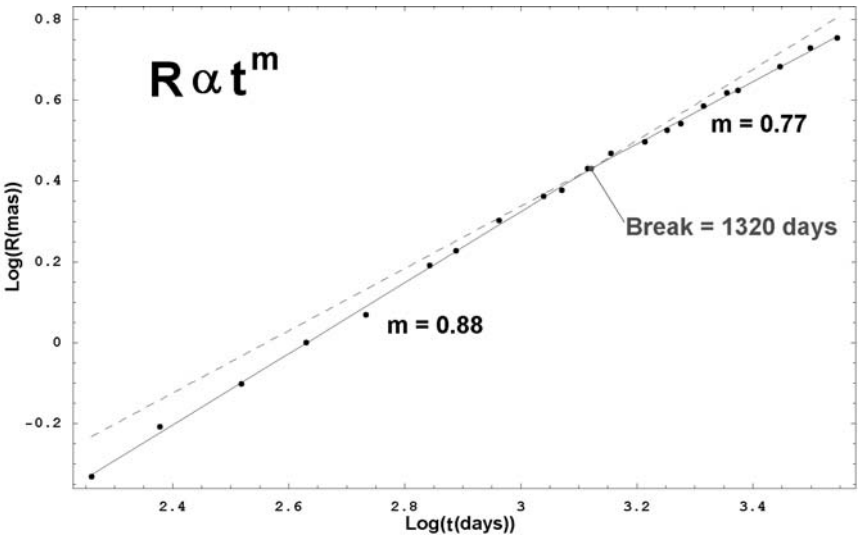

Fig. 6. Expansion of SN 1993J at 6 cm, determined with the Common-Point Method [7]. $R \propto t^m$, where R, t, and m are outer radius, age, and deceleration parameter, respectively.

7 Conclusions

A new method designed to determine the emission structure of a radio supernova works well for noiseless synthesized maps but does not work as well for noisy maps and for real maps. However, the method has been used to determine reliably the absorption in the central region of SN 1993J with respect to emission expected from an optically thin spherical shell. This absorption manifests itself as large systematic residuals in the GFD procedure. This result, also reported by [4], is not due to any shape in the emission profile of the shell as pointed out earlier [3], but rather to absorption of the emitting sphere further away from us, the radiation of which is likely absorbed by the intervening ionized ejecta as pointed out by [5]. The GFD method, used with maps obtained from our observations and with simulated maps, gives support to emission from a shell, the width of which appears to be somewhat less than 30% of the outer radius of SN 1993J. The GFD method might work reasonably well in cases like SN 1987A whose geometry is known and the maps might soon have very high dynamic range.

Acknowledgement. JMM wishes to acknowledge support of this research from the Spanish Ministry of Science and Technology under contract AYA2002-00897. KWW wishes to thank the Office of Naval Research (ONR) for the 6.1 funding supporting this research.

References

1. A. Alberdi and J.M. Marcaide: In: These proceedings
2. N. Bartel, et al. : Science **287**, 112 (2000)
3. N. Bartel, M.F. Bietenholz, M.P. Rupen et al. : Astrophys. J. **581**, 404 (2002)
4. M.F. Bietenholz, N. Bartel, M.P. Rupen: Astrophys. J. **368**, 610 (2003)
5. C. Fransson and C.I. Björnsson: Astrophys. J. **509**, 861 (1998)
6. J.M. Marcaide, A. Alberdi, E. Ros et al. : Astrophys. J. Lett. **486**, L31 (1997)
7. J.M. Marcaide et al. : In preparation (2004)
8. A. Pedlar et al. : In preparation (2004)
9. A. Pedlar, T. Muxlow, and J. Riley: In: These proceedings
10. M.P. Rupen, A.J. Beasley, N. Bartel et al. : In: *Radio Emission from Galactic and Extragalactic Compact Sources - IAU Coll. 164*, eds. J.A. Zensus, G.B. Taylor, J.M. Wrobel (ASP Conf. Series **144**, 1998) pp. 353-354

Optical, Ultraviolet, and Infrared Observations of SN 1993J

Alexei V. Filippenko[1] and Thomas Matheson[2]

[1] Department of Astronomy, University of California, 601 Campbell Hall, Berkeley, CA 94720-3411, USA;
alex@astron.berkeley.edu

[2] Harvard-Smithsonian Center for Astrophysics, 60 Garden Street, Cambridge, MA 02138, USA
tmatheson@cfa.harvard.edu

Summary. We review the existing set of optical/UV/IR observations of Supernova 1993J, concentrating heavily on optical data because these are by far the most plentiful. Some results from theoretical modeling of the observations are also discussed. SN 1993J has provided the best observational evidence for the transformation of a SN from one spectral type to another, thereby providing a link between Type II and Type Ib supernovae (SNe). This has strengthened the argument that SNe Ib (and, by extension, SNe Ic) are core-collapse events. SN 1993J has remained relatively bright for 10 years; its late-time emission comes from the collision of supernova ejecta with circumstellar gas that was released by the progenitor prior to the explosion. The circumstellar material shows strong evidence of CNO processing.

1 Introduction

Supernova (SN) 1993J was visually discovered in the nearby galaxy M81 (NGC 3031; $d = 3.6$ Mpc; [25]) by Francisco García on 1993 March 28.906 UT [54]. Ten years later, we still vividly remember our excitement after receiving by fax a rough finding chart from the discoverers, via the AAVSO. Ever since SN 1987A, those of us in the northern hemisphere had been eagerly waiting for a supernova in M31, or (more likely) in a somewhat more distant galaxy. What a golden opportunity! Unfortunately, our own robotic SN search, at that time being conducted with a 0.76-m telescope at Leuschner Observatory, missed discovery of SN 1993J because its field of view was somewhat too small to include the position of the supernova when centered on the galaxy nucleus, and because of bad weather [18]. It was a pleasure for both of us to finally meet Mr. García, at this conference.

SN 1993J reached $V = 10.8$ mag (e.g., [52]), becoming the brightest SN in the northern hemisphere since SN 1954A ($m_{\rm pg} = 9.95$; [2, 71]). In terms of observational coverage, both in temporal consistency (almost nightly observations at early times) and in the details of individual observations (including observations with signal-to-noise ratios, spectral resolutions, and wavelength regions not typically found in studies of supernovae), SN 1993J is surpassed

only by SN 1987A. Early spectra showed an almost featureless blue continuum, possibly with broad, but weak, Hα and He I λ5876 lines. This led to a Type II classification [21, 26] (see [23] for a general discussion of SN types). Wheeler & Filippenko [70] present a thorough review of the early work on SN 1993J.

Both the spectra and the light curves of SN 1993J quickly began to indicate that this was not a typical Type II SN. Indeed, the initially unusual light curves and the appearance of He I lines in the spectra were interpreted as evidence that SN 1993J was similar to a SN Ib, with a low-mass outer layer of hydrogen that gave the early impression of a SN II (see discussion and references below). Following [72], it was described as a "Type IIb" SN. This transformation from SN II to nearly SN Ib indicates a common mechanism (core collapse) for these two observationally defined subclasses. SN 1993J is thus one of the most significant SNe ever studied, not only for its role in linking Types II and Ib (and possibly Ic), but also because it was observed with such great detail.

Here we review observations of SN 1993J at optical, ultraviolet (UV), and infrared (IR) wavelengths, concentrating on optical because of the vast amount of data obtained in this wavelength range. Because of time and space constraints, we exclude light echoes and interstellar absorption lines, which have been used to probe the interstellar medium near SN 1993J. A recent optical spectrum of SN 1993J, obtained with the Keck-I 10 m telescope 9 years and 11 months after the explosion, is shown in Fig. 1. This is very close to 10 years, so we shall dub this the official "Valencia spectrum of SN 1993J."

2 Photometry of SN 1993J

The evolution of the light curve of SN 1993J did not follow either of the two typical paths for SNe II. SN 1993J did not remain at a relatively constant brightness after a slight decline from maximum, as a normal Type II plateau SN would, nor did the brightness decline in the pattern of a Type II linear SN. (For representatives of these Type II light curves, see, for example, [13].) Instead, SN 1993J rose quickly, then rapidly declined for $\sim$1 week, only to brighten a second time over the next two weeks. This led to another rapid decrease in brightness for $\sim$3 weeks, followed by an approximately exponential decline. For a complete discussion of the photometry of SN 1993J, see [3, 7, 14, 35, 46, 49, 52, 53, 56, 64, 69].

The unusual initial behavior of the light curve rapidly led many SN modelers to conclude that SN 1993J was the result of a core-collapse explosion in a progenitor that had lost a significant fraction of its hydrogen envelope, leaving only $\sim$0.1–0.5 $M_\odot$ of hydrogen. The original envelope could have been lost through winds [29] from a fairly massive star (25–30 $M_\odot$). Another possibility explored by [28] (see also, [43]) is that SN 1993J was the result of

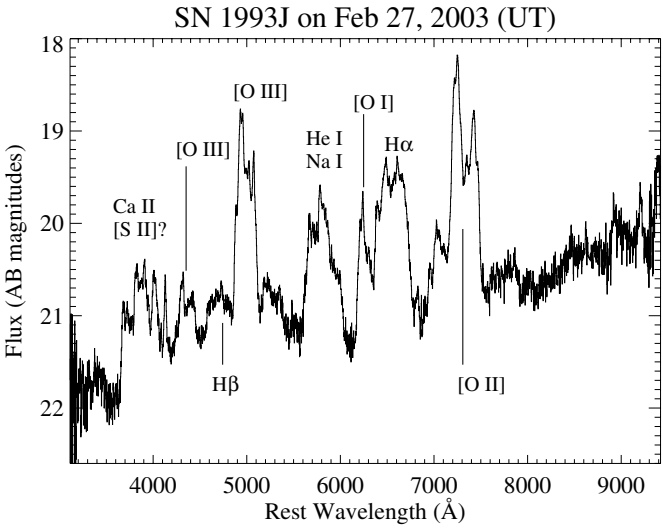

Fig. 1. Keck-I LRIS [45] spectrum of SN 1993J, obtained by A. V. Filippenko and R. Chornock nearly 10 years after the outburst. The absolute flux scale is only approximate, but relative fluxes should be accurate. Plausible line identifications are labeled. AB mag $= -2.5 \log f_\nu - 48.6$, on the ordinate scale. (Also known as the "Valencia spectrum of SN 1993J.")

the explosion of an asymptotic giant branch star having main-sequence mass $M_{ms} \approx 7$–$10\ M_\odot$, with a helium-rich envelope.

A more likely solution is that the progenitor of SN 1993J was a member of a binary system and the companion had stripped away a considerable amount of hydrogen. The progenitor was observed during prior studies of M81. Aldering, Humphreys, & Richmond [1] analyzed several sets of pre-existing images and deduced that the photometry was inconsistent with a single star at the position of SN 1993J. They found that the best fit for the progenitor itself was a K0 I star with $M_{\rm bol} \approx -7.8$ mag and $V - R \approx 0.7$ mag. Cohen, Darling, & Porter [12] derived a similar color from a five-month series of images of M81 from 1984; there was no apparent variability.

Using the scenario of a star that had been stripped of most of its hydrogen envelope, Nomoto et al. [43] and Shigeyama et al. [55] found a best fit to the light curve from their model of a $4M_\odot$ helium core, although a range of 3–6 $M_\odot$ for the core is reasonable. The main-sequence mass of the star would have been 15 $M_\odot$, while the residual hydrogen envelope is less than $\sim 0.9M_\odot$. Starting with a star of initial mass of 13–16 $M_\odot$, Woosley et al. [73] could reproduce the light curve from the explosion of a remaining helium core with mass $4.0 \pm 0.5 M_\odot$ and hydrogen envelope with mass $0.20 \pm 0.05 M_\odot$. A similar model by Podsiadlowski et al. [48] had $0.2M_\odot$ of hydrogen remaining on a

star of initial mass $M_i \approx 15M_\odot$. Ray, Singh, & Sutaria [51] also invoked a binary system for SN 1993J with a residual hydrogen envelope mass of $0.2M_\odot$. Utrobin [62] used an envelope mass of $0.1M_\odot$ remaining on a $3M_\odot$ helium core from an initial mass of $12M_\odot$. Bartunov et al. [6] achieved a good fit to the light curve with a helium core mass of 3.5 $M_\odot$, but a larger hydrogen envelope ($M_{env} \approx 0.9M_\odot$). Later studies continued to conclude that a low-mass envelope of hydrogen on a helium core was the most likely scenario for the progenitor [63, 74]. Intercomparison of two methods also indicated that the results were robust [8]. Houck & Fransson [32] used a non-local thermodynamic equilibrium (NLTE) synthetic spectrum code to fit nebular spectra and found that the Nomoto et al. [43] models could explain the late-time spectra. They found a best fit with a 3.2 $M_\odot$ helium core with a 0.2–0.4 $M_\odot$ hydrogen envelope. Patat, Chugai, & Mazzali [47] also used the late-time spectra, specifically the Hα line, to derive an ionized hydrogen mass of 0.05–0.2 $M_\odot$; this is a lower limit to the envelope mass.

3 Spectroscopy of SN 1993J

Woosley et al. [72] had already considered the above possibility for core-collapse SNe, giving them a new name: SNe IIb. The low-mass outer layer of hydrogen would give the initial appearance of a SN II, but the spectrum would slowly change to one more similar to that of a SN Ib, dominated by helium lines with the hydrogen either appearing weakly or completely gone. Indeed, Nomoto et al. [43] predicted that the spectrum of SN 1993J would show this behavior. This was first confirmed by [19], followed rapidly by [56] and [58]. Studies of the early optical spectra include those of [20, 27, 42, 44, 49, 59, 69].

Jeffery et al. [34] present an early UV spectrum of SN 1993J taken with the *Hubble Space Telescope (HST)* on 1993 April 15 UT. The other core-collapse SNe that had been observed in the UV to that point were compared with SN 1993J, and there were striking differences. SN 1993J had a relatively smooth UV spectrum and was more similar to SN 1979C and SN 1980K, both of which are radio sources and thus likely to have thick circumstellar envelopes (e.g., [68]). The UV spectra of SN 1987A, in contrast, showed broad absorption features. The illumination from circumstellar interaction may reduce the relative strengths of line features compared to the continuum and thus produce the featureless UV spectra of SNe 1979C, 1980K, and 1993J [9].

SN 1993J then evolved fairly rapidly into the nebular phase. The nebular-phase spectra were similar to those of a typical SN Ib, but the hydrogen lines never faded completely. In fact, Hα began to dominate the spectrum at late times, certainly the result of circumstellar interaction. There were several other papers that considered the nebular-phase spectra (and some relatively late-time spectra). Filippenko, Matheson, & Barth [22] show the transition to the nebular phase with spectra from Lick Observatory. Lewis et al. [35] present the complete La Palma archive covering days 2 through

125. Li et al. [37] discuss the nebular-phase spectra observed from the Beijing Astronomical Observatory. Barbon et al. [3] show the first year of observations from Asiago; the transformation of the SN from Type II to IIb is evident, as is the return of Hα at late times (by $\sim$ 200 days). A longer baseline ($\sim$ 500 days) for the spectra is found in the work of Finn et al. [24].

There were optical spectropolarimetric observations of SN 1993J. Trammell, Hines, & Wheeler [60] found a continuum polarization of $P = 1.6\% \pm 0.1\%$ on day 24 (assuming 1993 March 27.5 UT as the explosion date). Trammell et al. [60], as well as later considerations of the same data [30, 31], argued that this polarization implied an overall asymmetry, but the source of this asymmetry was undetermined. The presence of SN 1993J in a binary system was implicated as a potential source for the asymmetry. With more epochs of observation, [61] also found a polarization in the continuum of $\sim$ 1%, but a different level for the interstellar polarization. Nevertheless, they also concluded that SN 1993J was asymmetric. It is interesting to note that a subsequent SN IIb, SN 1996cb, showed substantially similar polarization of its spectra [67].

The analysis of individual aspects of the spectra has yielded some interesting results. Both Wang & Hu [66] and Spyromilio [57] found evidence for clumpy ejecta with blue shifted emission lines. Houck & Fransson [32] argue that the lines are not actually blue shifted, but that contamination from other lines appears to shift them. Nonetheless, the lines do show substructure that indicates clumpy ejecta.

Models of the early spectra could reproduce their overall spectral shape, but the line strengths were problematic. Baron et al. [4] found a photospheric temperature of $\sim$8000 K for day 10, but the predicted hydrogen and helium lines were too weak, possibly indicating unusual abundances or non-thermal effects. A later analysis including the *HST* UV spectrum was fit well by including enhanced helium abundance and NLTE effects [5]. Jeffery et al. [34] also had difficulties fitting line strengths for transitions that are susceptible to NLTE effects. Clocchiatti et al. [11] studied the early spectra to follow the evolution of color temperature and to calculate a distance to M81 ($\sim$ 3.5 Mpc) using the expanding photosphere method (e.g., [15]. The NLTE treatment of calcium is explored by [75], who found a best fit with a reduced calcium abundance.

4 Recent Studies of SN 1993J

Most of the above papers were published before year 2000, but in this section we discuss several more recent studies.

Matheson et al. [39] present a series of 42 Lick and Keck low-resolution optical spectra of SN 1993J from day 3 after explosion to day 2454, as well as one Keck high-dispersion spectrum from day 383. The spectra are studied in detail by [40]. Spectra during the nebular phase, but within the first two

years after explosion, exhibit small-scale structure in the emission lines of some species, notably oxygen and magnesium, showing that the ejecta of SN 1993J are clumpy. On the other hand, a lack of structure in emission lines of calcium implies that the source of calcium emission is uniformly distributed throughout the ejecta. These results are interpreted as evidence that oxygen emission originates in clumpy, newly synthesized material, while calcium emission arises from material pre-existing in the atmosphere of the progenitor [36, 37]. Spectra spanning the range 433–2454 days after the explosion show box-like profiles for the emission lines, clearly indicating circumstellar interaction in a roughly spherical shell. This is interpreted within the Chevalier & Fransson [10] model for SNe interacting with mass lost during prior stellar winds. At very late times, the emission lines have a two-horned profile, implying the formation of a somewhat flattened or disk-like structure that is a significant source of emission.

Matthews et al. [41] conducted IR photometry (windows in the interval 1.25–3.7 μm) and IR spectroscopy (windows in the interval 1.2–2.4 μm) of SN 1993J at early times, through about day 250. As in the case of the optical bands, the IR brightness rose to a secondary maximum and then dropped exponentially. However, the L' (3.7 μm) light curve exhibited an excess, beginning at day 130, which Matthews et al. [41] interpret as thermal emission from dust, as in the SNe II 1987A and 1998S. At early times, during the rise to the secondary maximum, the spectral energy distribution (SED) of SN 1993J could be fitted with black bodies, but such fits were too broad for the observed SEDs during the exponential decline. Though initially featureless, the IR spectra subsequently (during the exponential decline) became dominated by H, He, and probably Fe line emission.

The *HST* SINS collaboration (Supernova INtensive Study) obtained a series of UV spectra of SN 1993J over the course of about 7 years (Fransson et al. in preparation). It is quite clear that at late times, the emission is almost entirely coming from the shock interaction between the ejecta and circumstellar gas. The model fit to the observed spectrum is quite good, and its total luminosity is fixed by the observed X-ray emission from the shock – it is not a free parameter. Moreover, the detailed line profiles show that the emission is coming from a finite shell rather than a centrally peaked distribution of gas. There are strong, broad emission lines of N II], N III], and N IV], but only weak lines of C III] and C IV — characteristic of CNO processing. Indeed, a model spectrum having C:N = 1:13 by number in the circumstellar gas (with which the ejecta collide) gives a relatively good fit to the observations. CNO abundance ratios have previously been measured for a number of SNe II, with similar (but perhaps less extreme) results.

From *HST* images with $0\farcs05$ resolution, Van Dyk et al. [65] identify four stars brighter than $V = 25$ mag within $2\farcs5$ of SN 1993J that contaminated previous ground-based brightness estimates for the supernova progenitor. Correcting for the contamination, they find that the energy distribution of

the progenitor is consistent with that of an early K-type supergiant star with $M_V \approx -7.0 \pm 0.4$ mag and an initial mass of 13–22 $M_\odot$. The brightnesses of the nearby stars are sufficient to account for the excess blue light seen from the ground in pre-explosion observations [1]. Therefore, the SN 1993J progenitor did not necessarily have a blue companion, although by 2001, fainter blue stars are seen in close proximity to the supernova. These observations do not strongly limit the mass of a hypothetical companion. A blue dwarf star with a mass up to 30 $M_\odot$ could have been orbiting the progenitor without being detected in the ground-based images.

Explosion models and observations show that the SN 1993J progenitor had a helium-rich envelope. To test whether the helium abundance could influence the energy distribution of the progenitor, Van Dyk et al. [65] calculated model supergiant atmospheres with a range of plausible helium abundances. The models show that the pre-supernova colors are not strongly affected by the helium abundance longward of 4000 Å, and abundances ranging between solar and 90% helium (by number) are all consistent with the observations.

Recent optical spectra of SN 1993J (e.g., Fig. 1) show that the optical continuum is still very bright ($B \approx V \approx 21$ mag), certainly from the circumstellar interaction. Van Dyk et al. [65] suggest that the putative, blue companion star has $B > 23$ mag and $U > 22$ mag, so perhaps the most likely spectral region in which it might be observed is in the U band, where the actual observed continuum has $U \approx 22$ mag (Figure 1). At this conference, Stephen Smartt and collaborators reported the possible detection of hydrogen Balmer lines from the putative companion. Given the complexity of the SN spectrum (blends of emission lines, uncertain continuum level), however, this must be verified with future observations; most or all of the claimed Balmer lines may have other explanations. It is also not clear whether the Balmer lines, if real, come from a physical companion star or from an unrelated star along the same line of sight; the *HST* images shown by Van Dyk et al. [65] reveal several possible contaminants.

5 Final Remarks

Although SN 1993J has provided the best observational evidence for the transformation of a SN from one type to another, there have been other examples. The early spectra of SN 1987K showed hydrogen lines, but the late-time spectra more closely resembled those of SNe Ib [16]. The transition itself was not observed, occurring while SN 1987K was in conjunction with the Sun. SN 1996cb underwent a very similar metamorphosis from SN II to SN Ib; Qiu et al. [50] present a complete spectroscopic record of the transformation. A number of other examples of genuine SNe IIb have been found in recent years. In addition, there were some suggestions of hydrogen in spectra of the Type Ic SN 1987M [17, 33] and the SN Ic 1991A (and perhaps SN Ic

1990aa [17]). SN 1993J is clearly a significant object in the study of SNe. By providing a link between SNe II and SNe Ib, it has strengthened the argument that SNe Ib (and, by extension, SNe Ic) are also core-collapse events.

Acknowledgement. A.V.F.'s research on SN 1993J is currently supported by NSF grant AST-0307894, as well as by NASA grants AR-9529 and GO-9114 from the Space Telescope Science Institute, which is operated by AURA, Inc., under NASA contract NAS5-26555. We thank the conference organizers for partial travel funds. We are grateful to the staffs of the Lick and Keck Observatories for help with the observations. The W. M. Keck Observatory is operated as a scientific partnership among Caltech, the University of California, and NASA; the Observatory was made possible by the generous financial support of the W. M. Keck Foundation.

References

1. G. Aldering, R.M. Humphreys, M. Richmond: Astron. J. **107**, 662 (1994)
2. R. Barbon, F. Ciatti, L. Rosino: Astron. Astrophys. **25**, 241 (1973)
3. R. Barbon, S. Benetti, E. Cappellaro, F. Patat, M. Turatto, T. Iijima: Astron. Astrophys. Suppl. **110**, 513 (1995)
4. E. Baron, P.H. Hauschildt, D. Branch, R.M. Wagner, S.J. Austin, A.V. Filippenko, T. Matheson: Astrophys. J. Lett. **416**, L21 (1993)
5. E. Baron, P.H. Hauschildt, D. Branch: Astrophys. J. **426**, 334 (1994)
6. O.S. Bartunov, S.I. Blinnikov, N.N. Pavlyuk, D.Yu. Tsvetkov: Astron. Astrophys. **281**, L53 (1994)
7. P.J. Benson et al. : Astron. J. **107**, 1453 (1994)
8. S.I. Blinnikov, R. Eastman, O.S. Bartunov, V.A. Popolitov, S.E. Woosley: Astrophys. J. **496**, 454 (1998)
9. D. Branch, D.J. Jeffery, M. Blaylock, K. Hatano: Pub. Astron. Soc. Pacific **112**, 217 (2000)
10. R.A. Chevalier, C. Fransson: Astrophys. J. **420**, 268 (1994)
11. A. Clocchiatti, J.C. Wheeler, E.S. Barker, A.V. Filippenko, T. Matheson, J.W. Liebert: Astrophys. J. **446**, 167 (1995)
12. J.G. Cohen, J. Darling, A. Porter: Astron. J. **110**, 308 (1995)
13. J.B. Doggett, D. Branch: Astron. J. **90**, 2303 (1985)
14. V.T. Doroshenko, Yu.S. Efimov, N.M. Shakhovskoi: Astron. Lett. **21**, 513 (1995)
15. R.G. Eastman, B.P. Schmidt, R. Kirshner: Astrophys. J. **466**, 911 (1996)
16. A.V. Filippenko: Astron. J. **96**, 1941 (1988)
17. A.V. Filippenko: Astrophys. J. Lett. **384**, L37 (1992)
18. A.V. Filippenko: Sky & Tel. **86**, 30 (1993)
19. A.V. Filippenko, T. Matheson: IAUC 5787 (1993)
20. A.V. Filippenko, T. Matheson, L.C. Ho: Astrophys. J. Lett. **415**, L103 (1993)
21. A.V. Filippenko, R.R. Treffers, Y. Paik, M. Davis, E. Schlegel: IAUC 5731 (1993)
22. A.V. Filippenko, T. Matheson, A.J. Barth: Astron. J. **108**, 2220 (1994)
23. A.V. Filippenko: Ann. Rev. Astron. Astrophys. **35**, 309 (1997)

24. R.A. Finn, R.A. Fesen, G.W. Darling, J.R. Thorstensen, G.S. Worthey: Astron. J. **110**, 300 (1995)
25. W.L. Freedman et al. : Astrophys. J. **427**, 628 (1994)
26. P. Garnavich, H.B. Ann: IAUC 5731; corrigendum: IAUC 5733 (1993)
27. P.M. Garnavich, H.B. Ann: Astron. J. **108**, 1002 (1994)
28. M. Hashimoto, K. Iwamoto, K. Nomoto: Astrophys. J. Lett. **414**, L105 (1993)
29. P. Höflich, N. Langer, M. Duschinger: Astron. Astrophys. **275**, L29 (1993)
30. P. Höflich: Astrophys. J. **440**, 821 (1995)
31. P. Höflich, J.C. Wheeler, D.C. Hines, S.R. Trammell: Astrophys. J. **459**, 307 (1996)
32. J.V. Houck, C. Fransson: Astrophys. J. **456**, 811 (1996)
33. D.J. Jeffery, D. Branch, A.V. Filippenko, K. Nomoto: Astrophys. J. Lett. **377**, L89 (1991)
34. D.J. Jeffery et al. : Astrophys. J. Lett. **421**, L27 (1994)
35. J.R. Lewis et al. : Mon. Not. R. Astron. Soc. **266**, L27 (1994)
36. H. Li, R. McCray: Astrophys. J. **387**, 309 (1992)
37. A. Li, J. Hu, L. Wang, X. Jiang, H. Li: Astrophys. Space Sci. **211**, 323 (1994)
38. H. Li, R. McCray: Astrophys. J. **405**, 730 (1993)
39. T. Matheson et al. : Astron. J. **120**, 1487 (2000)
40. T. Matheson, A.V. Filippenko, L.C. Ho, A.J. Barth, D.C. Leonard: Astron. J. **120**, 1499 (2000)
41. K. Matthews, G. Neugebauer, L. Armus, B.T. Soifer: Astron. J. **123**, 753 (2002)
42. N.V. Metlova, D.Yu. Tsvetkov, S.Yu. Shugarov, V.F. Esipov, N.N. Pavlyuk: Astron. Lett. **21**, 598 (1995)
43. K. Nomoto, T. Suzuki, T. Shigeyama, S. Kumagai, H. Yamaoka, H. Saio: Nature **364**, 507 (1993)
44. K. Ohta, H. Maemura, T. Ishigaki, K. Aoki, H. Ohtani: Pub. Astron. Soc. Japan **46**, 117 (1994)
45. J.B. Oke et al. : Pub. Astron. Soc. Pacific **107**, 375 (1995)
46. M. Okyudo, T. Kato, T. Ishida, N. Tokimasa, H. Yamaoka: Pub. Astron. Soc. Japan **45**, L63 (1993)
47. F. Patat, H. Chugai, P.A. Mazzali: Astron. Astrophys. **299**, 715 (1995)
48. Ph. Podsiadlowski, J.J.L. Hsu, P.C. Joss, R.R. Ross: Nature **364**, 509 (1993)
49. T.P. Prabhu et al. : Astron. Astrophys. **295**, 403 (1995)
50. Y. Qiu, W. Li, Q. Qiao, J. Hu: Astron. J. **117**, 736 (1999)
51. A. Ray, K.P. Singh, F.K. Sutaria: Astrophys. Astron. **14**, 53 (1993)
52. M.W. Richmond, R.R. Treffers, A.V. Filippenko, Y. Paik, B. Leibundgut, E. Schulman, C.V. Cox: Astron. J. **107**, 1022 (1994)
53. M.W. Richmond, R.R. Treffers, A.V. Filippenko, Y. Paik: Astron. J. **112**, 732 (1996)
54. J. Ripero, F. García, D. Rodríguez: IAUC 5731 (1993)
55. T. Shigeyama, T. Suzuki, S. Kumagai, K. Nomoto, H. Saio, H. Yamaoka: Astrophys. J. **420**, 341 (1994)
56. B.P. Schmidt et al. : Nature **364**, 600 (1993)
57. J. Spyromilio: Mon. Not. R. Astron. Soc. **266**, L61 (1994)
58. D.A. Swartz, A. Clocchiatti, R. Benjamin, D.F. Lester, J.C. Wheeler: Nature **365**, 232 (1993)
59. Y. Taniguchi, T. Murayama, Y. Sato, Y. Yadoumaru, Y. Ohyama, G. Kosugi, M. Yoshida, T. Kurakami: Pub. Astron. Soc. Japan **45**, L43 (1993)

60. S.R. Trammell, D.C. Hines, J.C. Wheeler: Astrophys. J. Lett. **414**, L21 (1993)
61. H.D. Tran, A.V. Filippenko, G.D. Schmidt, K.S. Bjorkman, B.T. Jannuzi, P.S. Smith: Pub. Astron. Soc. Pacific **109**, 489 (1997)
62. V. Utrobin: Astron. Astrophys. **281**, L89 (1994)
63. V.P. Utrobin: Astron. Astrophys. **306**, 219 (1996)
64. W. van Driel et al. : Pub. Astron. Soc. Japan **45**, L59 (1993)
65. S.D. Van Dyk, P.M. Garnavich, A.V. Filippenko, P. Höflich, R.P. Kirshner, R.L. Kurucz, P. Challis: Pub. Astron. Soc. Pacific **114**, 1322 (2002)
66. L. Wang, J. Hu: Nature **369**, 380 (1994)
67. L. Wang, D.A. Howell, P. Höflich, J.C. Wheeler: Astrophys. J. **550**, 1030 (2000)
68. K.W. Weiler, R.A. Sramek, N. Panagia, J.M. van der Hulst, M. Salvati: Astrophys. J. **301**, 790 (1986)
69. J.C. Wheeler et al. : Astrophys. J. Lett. **417**, L71 (1993)
70. J.C. Wheeler, A.V. Filippenko: "Review of the Contributions to the Workshop on SN 1993J." In: *Supernovae and Supernova Remnants*, ed. R.A. McCray, Z. Wang (Cambridge, Cambridge University Press 1996) p. 241
71. P. Wild: Pub. Astron. Soc. Pacific **72**, 97 (1960)
72. S.E. Woosley, P.A. Pinto, P.G. Martin, T.A. Weaver: Astrophys. J. **318**, 664 (1987)
73. S.E. Woosley, R.G. Eastman, T.A. Weaver, P. Pinto: Astrophys. J. **429**, 300 (1994)
74. T.R. Young, E. Baron, D. Branch: Astrophys. J. Lett. **449**, L51 (1995)
75. Q. Zhang, Z.R. Wang: Astron. Astrophys. **307**, 166 (1996)

Simulated Radio Images and Light Curves of SN 1993J

Vikram V. Dwarkadas[1], Amy J. Mioduszewski[2], and Lewis T. Ball[3]

[1] ASCI FLASH Center, Univ of Chicago, 5640 S. Ellis Ave, Chicago IL 60637
vikram@flash.uchicago.edu
[2] NRAO, P.O. Box O, Socorro, NM 87801, USA;
amiodusz@nrao.edu
[3] CSIRO ATNF Parkes Observatory, P.O. Box 276, Parkes NSW 2870, Australia
lewis.ball@csiro.au

Summary. We present calculations of the radio images and light curves from supernovae, based on high-resolution numerical simulations of the hydrodynamics and radiation transfer in a spherically symmetric medium. As a specific example we model the emission from SN1993J. This supernova does not appear to be expanding in a self-similar fashion, and cannot be adequately fitted with the often-used analytic mini-shell model. We present a good fit to the radio evolution at a single frequency. Both free-free absorption and synchrotron self-absorption are needed to fit the light curve at early times, and a circumstellar density profile of $\rho \sim r^{-1.7}$ provides the best fit to the later data. Comparisons of VLBI images of SN1993J with synthetic model images suggest that internal free-free absorption completely obscures emission at 8.4 GHz passing through the center of the supernova for the first few tens of years after explosion.

1 Introduction

Radio Supernova (RSN) light curves are characterized by an initial rapid increase of radio flux to maximum, followed by a power-law decrease with time. High brightness temperature indicates a non-thermal origin for the emission, and it is now accepted that the emission is synchrotron in origin, due to the spiraling of relativistic electrons in a magnetic field. The wavelength-dependent turn-on suggests that the initial rise in the light curve is due to decreasing absorption as the shock expands in an optically thick medium.

In the past, the computation of SN radio light curves has been accomplished mainly via semi-empirical methods, primarily the mini-shell model developed by Chevalier [3] and extended by Weiler et al. [9]. These empirical methods assume a self-similar evolution for the SN shock front, with the shock radius expanding as a power law in time $\mathrm{r}_s \propto t^m$, where m is a constant [3]. The energy distribution of the relativistic electrons is assumed to be a power law of constant spectral index, and the energy density of the relativistic electrons and that of the magnetic field are assumed to each be a constant fraction of the thermal energy density behind the expanding supernova shock.

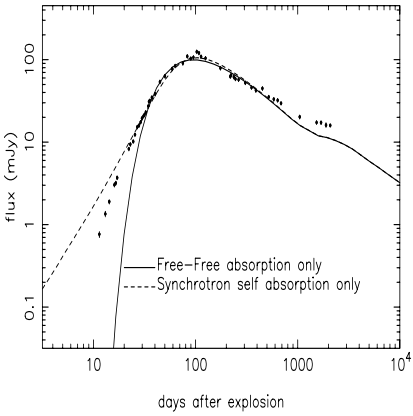

Fig 1a

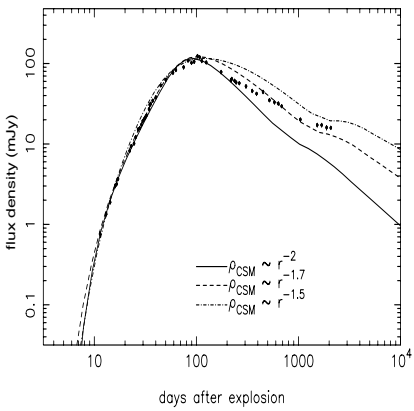

Fig 1b

In this article we outline a more robust and general technique for computing the radio light curves of young SNe. Details of our method are outlined in Mioduszewski et al. [5]. Herein we briefly describe the technique and the major results for the well-studied SN 1993J, as well as update the results with comparisons to more recent data.

2 Methods and Techniques

- We start with a computation of the hydrodynamic evolution of the SN remnant, calculated using VH-1, a 3-dimensional, finite-difference, high resolution, shock-capturing code based on the Piecewise Parabolic Method. This step immediately distinguishes our method from the mini-shell model, since we do not need to assume a self-similar expansion for the SN shock. Our technique is applied to SN 1993J, where the observations indicate that the expansion is not self-similar.
- The light curves are produced by calculating the transfer of radiation along a line-of-sight through the SN.
- We assume that the injection of relativistic particles at the shock follows a power-law, $N(E) \propto E^{-\gamma}$.
- We start with spherically symmetric simulations. These give pressure, density and temperature at each grid point and every time step.
- The code takes the simulations and rotates them to form a 3D sphere embedded in a Cartesian grid.
- The synchrotron emission and absorption is computed along each ray. If $N(E) = KE^{-\gamma}$, then emissivity j and opacity κ are given by

$$j \sim K\ B^{(\gamma+1)/2}\ \nu^{-(\gamma-1)/2.}$$

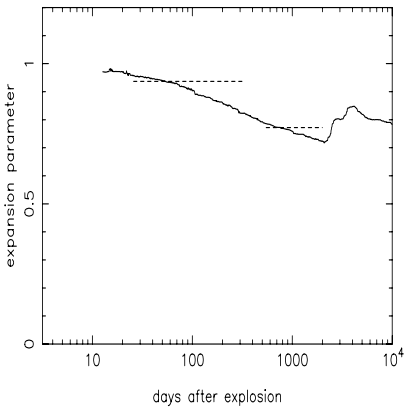

Fig 2a

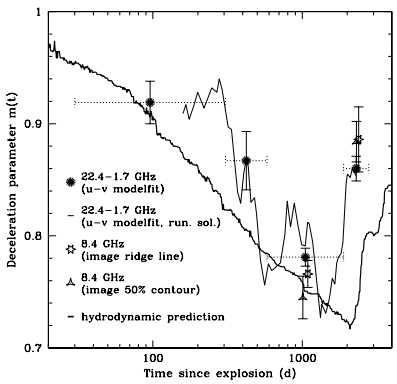

Fig 2b

$$\kappa \sim K\ B^{(\gamma+2)/2}\ \nu^{-(\gamma+4)/2.}$$

– In this work we assume that both magnetic energy density u_B and relativistic particle energy density u_{rel} are proportional to the thermal energy density.

$$u_B = \xi_B\ u_{th}, \qquad\qquad u_{rel} = \xi_{rel}\ u_{th}$$

– We take into account the external free-free absorption, which depends on the temperature and density profile of the ambient medium.
– The emissivity and absorption are used to calculate the optical depth τ, and finally the intensity $I_\nu(r)$. Integration is carried out using the trapezoidal rule.
– The result is a 2D array of surface brightness, which is used to make an image of the source and calculate the total flux.

3 SN1993J

As a first example we focus on SN 1993J - one of the brightest and best studied SNe in the Northern Hemisphere. The radio flux evolution of SN 1993J has been followed in detail by Bartel et al. [1, 2] and Pérez-Torres et al. [6, 7] using VLBI.

If shock radius $R_s \propto t^m$, then m is called expansion parameter. For power-law models, m is constant with time. But for SN 1993J, m decreases with time [1, 2]. Therefore the evolution is NOT self-similar, which perhaps implies that power-law density ejecta are not a reasonable assumption. For the ejecta structure we have therefore used Model 4H47 of Suzuki & Nomoto [8]. In this

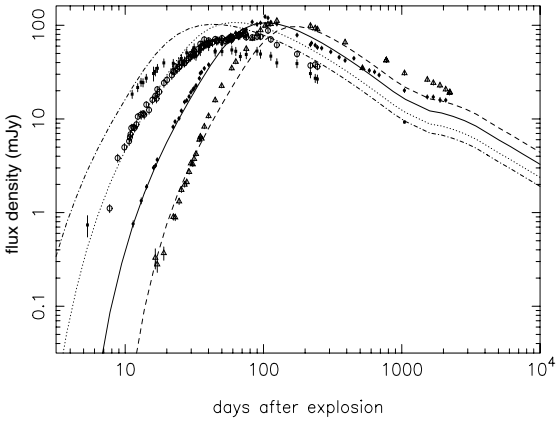

Fig 3

case the ejecta density shows considerably more structure than the commonly used "power-law" models.

In order to fit the X-ray and optical light curves, Nomoto et al. find that the CSM density profile must decrease more slowly than r^{-2}, which would be the case for a steady wind. Fransson and Bjornsson [4], however find that an r^{-2} profile is adequate to fit the radio light curve. Therefore we have tried 3 CSM density profiles, with density decreasing as $r^{-1.7}$, $r^{-1.5}$ and $r^{-2.}$.

Free-free absorption (FFA) alone results in an exponential rise of the light curve while synchrotron self absorption (SSA) alone results in a power-law increase (Fig. 1a). In order to fit the light curve we find that both FFA and SSA must be included, and that a CSM density profile of $r^{-1.7}$ provides the best fit to the observed light curve at 8.4 GHz (Fig. 1b). The data is represented by dots in the figure.

As mentioned above, the expansion parameter m (where $\mathrm{R}_s \propto t^m$) is not constant for SN 1993J, implying a non-self-similar evolution. Fig. 2a shows the evolution of the expansion parameter with time from our simulation of the interaction of a SN with an ejecta density profile described by the 4H47 model evolving in a medium whose density varies with radius as $\mathrm{r}^{-1.7}$. The dashed lines in the figure are error bars for the expansion parameter measured by Bartel et al. [2]. Our simulations are broadly consistent with these observations.

The model 4H47 exhibits local density maxima in the ejecta density profile. Impact of the reverse shock with one of these local density maxima results in a sudden increase in the expansion parameter around day 2300 (see Fig. 2a). Observations by Bartel et al. [2] show a similar rise in the expansion parameter (Fig. 2b), albeit somewhat earlier. It is possible that the change in the observed deceleration is due to a change in the CSM density or some other cause unrelated to the ejecta structure, but the coincidence is

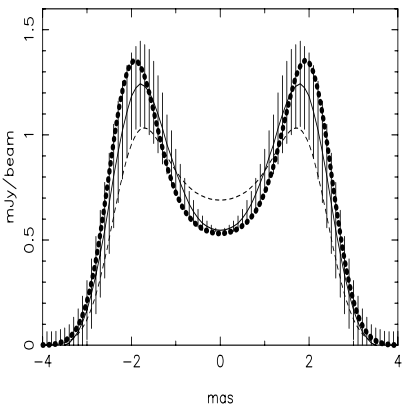

Fig 4a

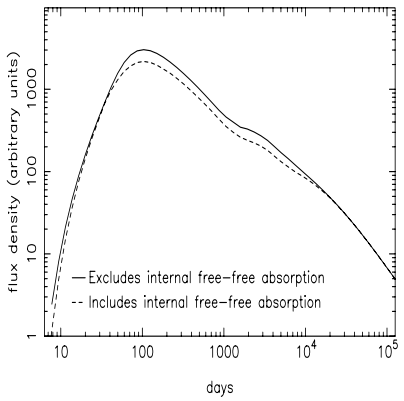

Fig 4b

striking nevertheless. It is also possible that in a more realistic multidimensional simulation any local density maxima would be unstable and would quickly smooth out.

3.1 SN1993J Light Curves

Our technique is to fit the observed light curve at one fiducial frequency 8.4 GHz. The frequency dependence at all epochs is simply $\nu^{-\alpha}$ (where $\alpha = 0.55$ is the spectral index determined by this best fit model of the light curve), and so the light curve at any other frequency has the same shape as that at the fiducial frequency. The observed flux densities from SN1993J and the corresponding model light curves are shown in Fig. 3. The different frequencies indicated are: 22.5 GHz (filled boxes, dot-dashed line), 15.0 GHz (open circles, dotted line), 8.4 GHz (filled circles, solid line), and 4.9 GHz (open triangles, dashed line)

3.2 Internal Absorption

In the early stages, the internal free-absorption was found to be important in order to match the surface brightness profile obtained from our simulated images to that observed. Fig. 4a shows the azimuthally averaged profile of the observed 8.4 GHz emission from SN 1993J on day 1349 (solid line with error bars), compared to that obtained from our simulations, excluding (dashed line) and including (dotted line) internal free-free absorption, convolved with the same beam as the image. The improvement in the fit when the internal free-free absorption is taken into account is readily apparent. Fig. 4b shows the change in the light curve when the internal absorption is taken into account. Our model suggests that the optical depth at 1 GHz does not fall to

unity until around 150 years after the explosion. This suggests that a central radio pulsar would be undetectable for many tens of years at frequencies below 1 GHz, although multidimensional effects, especially instabilities, that have not been included here may allow the radiation to escape somewhat earlier. Further details can be obtained from Mioduszewski et al. [5].

Acknowledgement. VD is supported by the US. Department of Energy grant number B341495 to the ASCI Flash Center (U Chicago), and by Award # AST-0319261 from the National Science Foundation.

References

1. N. Bartel et al. : Science **287**, 112 (2000)
2. N. Bartel et al. : Astrophys. J. **581**, 404 (2002)
3. R.A. Chevalier: Astrophys. J. **258**, 790 1982
4. C. Fransson, C.-I. Bjornsson: Astrophys. J. **509**, 861 (1998)
5. A.J. Mioduszewski, V.V. Dwarkadas, L. Ball: Astrophys. J. **562**, 869 (2001)
6. M.A. Perez-Torres, A. Alberdi, J.M. Marcaide: Astron. Astrophys. **394**, 71 (2002)
7. M.A. Perez-Torres, A. Alberdi, J.M. Marcaide: Astron. Astrophys. **374**, 997 (2001)
8. T. Suzuki, K. Nomoto: Astrophys. J. **455**, 658 (1995)
9. K.W. Weiler, R.A. Sramek, N. Panagia: In: *IAU Colloq. 145, Supernovae and Supernova Remnants*, ed. by R. McCray, Z. Wang (Cambridge: Cambridge Univ. Press, 1996) p. 283

X-ray Observations of SN 1993J

H.-U. Zimmermann

Max-Planck-Institut für extraterrestrische Physik, Postfach 1312,
85471 Garching, Germany;
zim@mpe.mpg.de

Summary. In April 2001 SN1993J was observed with both the PN and MOS cameras of the XMM-Newton observatory. A 2-component thermal emission model assuming ionization equilibrium provides a good fit to the spectrum in the 0.3 to 11 keV energy band, but fits to shock models show also acceptable results. The development of the X-ray temperatures over the first 8 years after the explosion is discussed in the light of the standard SN model. The long term X-ray lightcurve shows a general decline of the luminosity with $L_x \propto t^{-0.30}$.

1 Introduction

Results from spectral and lightcurve analysis as derived from X-ray observations – with special emphasis given to a recent XMM-Newton observation – during the first 8 years of this SN are presented and discussed. Part of the work has been done in collaboration with Bernd Aschenbach.

From the XMM-Newton observation in April 2001 we used for our analysis data of about 70 ks from the EPIC PN camera, run in small window mode, and of a similar amount from the MOS2 camera run in imaging mode.

2 XMM-Newton Spectral Results

Emission lines of highly ionized Mg, Si, S, Ar, Ca and the complex of the Fe lines dominate the SN spectrum (Fig. 1) at higher energies.

Table 1 shows a compilation of spectral fits to the PN camera, the MOS2 camera, and to a combined spectrum. The differences between the PN and the MOS2 spectra point to residual uncertainties in the spectral cross calibration. Time dependencies observed with the MOS2 calibration and the superior statistics of the PN spectrum with its 7515 counts compared to the 2593 counts in the MOS2 spectrum, let us use for the following spectral discussion only the fitting parameters of the PN spectrum.

The best fit over the whole energy band between 0.3 up to about 11 keV was achieved with a 2-temperature equilibrium model with variable abundances, called vmekal in XSPEC. We have also tested different shock models and found that a Sedov model with variable abundances, called vsedov

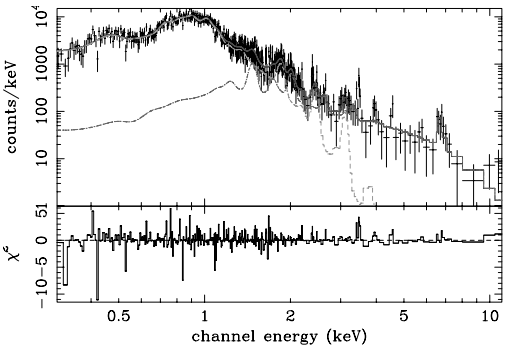

Fig. 1. XMM-Newton spectrum as observed with the PN camera and the best fit thermal 2-component model with kT_1=0.34 keV and kT_2=6.54 keV. The dashed curves show the low and high temperature component.

Table 1. Selected best fit parameters of different spectral models. 2vmekal is a 2-component thermal model with variable element abundances, 2vmekal1 is the same model but with identical element abundances for the 2 temperature components, and vsedov is a shock model with variable abundances.

instrument	model	$kT_1[keV]$	$kT_2[keV]$	$N_{H1}[10^{22}cm^{-2}]$	N_{H2}	dof	χ^2_r
PN	2vmekal	$0.34^{+0.05}_{-0.03}$	6.54^{+4}_{-4}	0.55±0.21	0.33±1.80	360	0.90
PN	2vmekal1	$0.35^{+0.04}_{-0.04}$	$4.24^{+3.8}_{-1.8}$	0.45±0.13	0.18±0.75	371	0.94
PN	vsedov	$0.51^{+0.04}_{-0.04}$	$7.0^{+0.2}_{-0.2}$	0.17±0.037		376	1.01
MOS2	2vmekal	$0.59^{+0.03}_{-0.04}$	$3.48^{+1.2}_{-1.2}$	0.25±0.25	0.0±0.54	113	1.25
PN+MOS2	2vmekal	$0.33^{+0.46}_{-0.46}$	$4.09^{+1.2}_{-1.2}$	0.59±0.25	0.2±0.8	505	0.99

in XSPEC, produces also acceptable chi-2 values, although all tested shock models reproduce not so well the different line complexes visible in the spectra.

Looking at the abundances of the low temperature component, in the fit C, N, and Al are not required, Mg and O are under abundant compared to solar, Fe is about solar, and the other elements show clear overabundances.

The high temperature component is determined almost solely by the line complexes of highly ionized Ar, Ca, and Fe. The temperature of $6.5 \pm 4keV$ is poorly restricted, because every temperature change is immediately compensated in the fit by changes in the abundances of these elements. Therefore the element abundances have errors typically much larger than the parameter values themselves. All the elements above Ne, which is not required in the fit, show a clear overabundance, with a moderate value only for the Fe abundance.

3 Spectral Development

While the first ROSAT PSPC spectra ([7, 8] reanalyzed for this work [9]) as well as the ASCA measurements [6] did only allow to set lower limits for the

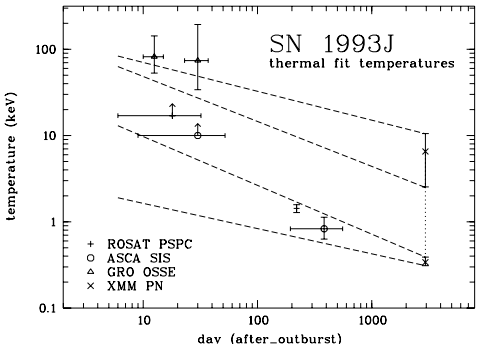

Fig. 2. X-ray determined emission temperatures. The dashed lines outline the time evolution of the low and high temperature component using the standard model. For each component there are two lines bracketing the range of the temperatures allowed by the *XMM-Newton* data using the 2vmekal model.

temperature of a thermal model, the hard X-ray instrument OSSE on GRO [4] could determine a temperature of approximately 80 keV at these times. ROSAT and ASCA measurements half a year later revealed a strong decrease from the initial high values to temperatures around 1 keV (Fig. 2).

In terms of the standard model proposed by Chevalier [2] it was assumed that the observed emission initially came from the fast forward shock, while emission from the reverse shock region was blocked by absorbing material due to fast cooling processes in the denser environment of this region. For the enormous temperature drop observed it was assumed that the initial absorption disappeared on a time scale of order 100 days so that half a year later the measured flux was dominated by the emission from the reverse shock region.

In the similarity solution of the standard model [3] the ratio between the temperatures in the forward and the reverse shock depend only on s, characterizing the circumstellar density profile and n, describing the density profile of the ejecta. Assuming that the two temperature components from the XMM spectrum represent emission from the reverse and forward shock regions and taking the circumstellar density profile s = 1.65 derived from the ROSAT light curve (see Section 4), we obtain n = 8.9 for the density profile of the ejecta. We can now enter n and s into the expression that describes the temporal development of the temperatures and extrapolate the XMM temperatures backward in time up to the ROSAT, ASCA and GRO results (dashed lines in Fig. 2). Despite the fact that strictly speaking the prior conditions to apply the similarity solution are no more fulfilled at these late times, the temperature development is not too badly described. But we do not think that this can be taken as final proof that we observe X-ray emission from both a forward and a reverse shock region.

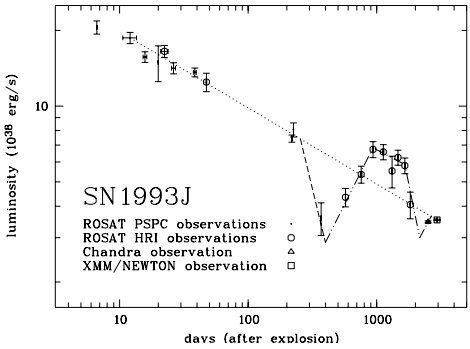

Fig. 3. X-ray light curve showing the development of the X-ray luminosity in the 0.3-2.4 keV energy range. The dotted line indicates a decline rate with $t^{-0.30}$. The dashed lines result from model calculations involving time limited decrease and increase of the density in the ambient matter.

4 X-ray Lightcurve

The X-ray lightcurve (Fig. 3), showing the 19 ROSAT observations since day 6, the Chandra observation of 2000 [5] and the XMM observation of 2001, covers now the first 8 years of this SN.

The tendency over the first half year is characterized by a decline of the luminosity with $t^{-0.30}$ where t is the time since the outburst. Thereafter the lightcurve shows a bump and 5 years after the outburst, the luminosity appears to return to the initial decline profile. The Chandra and XMM observations, scaled to the ROSAT data, support the view of a general trend.

In the standard model the circumstellar matter is assumed to originate from the stellar wind of the supergiant progenitor star producing a circumstellar density profile proportional to r^{-s}. From the measured time dependence of the luminosity, that is roughly proportional to the square of the density integrated over the emitting volume, we can derive the circumstellar density profile to follow an $r^{-1.65}$ behavior.

In the interpretation that the dominating emission region changed during the first half year from the forward shock to the reverse shock region it is somewhat surprising that the luminosity development does not reflect that dramatic change, but suggests rather a smooth transition maintaining the same gradient. Also the fact that the early ASCA spectrum showed already the Fe complex between 6 and 7 keV, demonstrating the existence of material at much lower temperatures than the observed and expected 80 keV, shows that reality is certainly more complex.

Dips and bumps in the X-ray lightcurve suggest local density changes above the general power-law profile of the circumstellar matter density, possibly caused by transient changes in the wind parameters of the progenitor or by asymmetries in a possible binary scenario.

If we correlate the ROSAT light curve with the expansion velocity of the SN shell derived from high resolution radio images of this object [1], we notice around the time of the onset of the bump (around day 350) a break in the

expansion rate. Both features may independently indicate a change of the density profile in the circumstellar medium.

The X-ray lightcurve shows a rapid decline between day 225 and 370, followed by a rapid increase up to day 935. A similar behavior could have occured between day 1126 and 1464, but there is just one data point consistent with no change. The rapid decline after day 1655 is evident and recovery indicated by the Chandra and XMM points after day 2500. The evidence of the latter 2 dips is statistically not too convincing, but they may be real.

If the shock wave runs into a sufficiently low density regime, matter heated so far will simply expand. For isothermal (adiabatic) expansion the lightcurve will go down with t^{-2} (with $t^{-8/3}$, as long as the temperature is higher than about 2 keV). When thereafter the shock wave encounters a density jump to significantly higher values, the luminosity increases linearly with t.

The times when we see after a dip increases of the luminosity in the X-ray lightcurve agree surprisingly well with the 3 parts in the radio expansion curve with maximum deceleration. This is interpreted as the moment when the shock hits a step like wall of denser circumstellar material.

We conclude that these changes in the X-ray lightcurve reflect changes of the density in the ambient matter profile, which appear to show some repetitive pattern like in a wave. Whether this characterizes the activity of the progenitor star with respect to mass loss or wind velocity remains to be seen.

5 Conclusions

The new data points in the X-ray lightcurve suggest a general decline rate with $L_x \propto t^{-0.30}$ with luminosity dips and bumps being intermediate phenomena. The suggested correlation of increases of the X-ray luminosity with the steepest deceleration seen in the expansion of the radio shell and the fact that the circularity of the radio images is not affected by these events, suggests that the observed increases are probably due to density changes in a more or less isotropic circumstellar matter distribution. There is, although statistically weak, an indication of further dips in the X-ray lightcurve, which could be due to repetitive activity changes in the progenitors wind history.

The XMM spectrum is best fitted by a 2-component thermal model that assumes ionization equilibrium. Although the standard model predicts the temperature development not too badly, even at these late times, there remains the question whether in X-rays we really see emission from two locally distinct regions, produced by a forward and a reverse shock.

References

1. N. Bartel et al. : Astrophys. J. **581**, 404 (2002)

2. R.A. Chevalier: Astrophys. J. **259**, 302 (1982)
3. C. Fransson, P. Lundqvist, R.A. Chevalier: Astrophys. J. **461**, 993 (1996)
4. M.D. Leising et al. : Astrophys. J. Lett. **431**, L95 (1994)
5. D.A. Swartz et al. : Astrophys. J. Suppl. **114**, 213 (2003)
6. S. Uno et al. : Astrophys. J. **565**, 419 (2002)
7. H.-U. Zimmermann et al. : Nature **367**, 621 (1994)
8. H.-U. Zimmermann, W.H.G. Lewin, B. Aschenbach: In: *Röntgenstrahlung from the Universe.* eds. H.-U. Zimmermann, J. Trümper, H. Yorke (MPE Report) **263** 289 (1996)
9. H.-U. Zimmermann, B. Aschenbach: Astron. Astrophys. **406**, 969 (2003)

Modeling the Radio and X-ray Emission of SN 1993J and SN 2002ap

Claes Fransson[1] and Claes-Ingvar Björnsson[1]

Department of Astronomy, Stockholm University, AlbaNova, 106 91 Stockholm, Sweden
claes@astro.su.se, bjornsson@astro.su.se

Summary. Modeling of radio and X-ray observations of supernovae interacting with their circumstellar media are discussed, with special application to SN 1993J and SN 2002ap. We emphasize the importance of including all relevant physical mechanisms, especially for the modeling of the radio light curves. The different conclusions for the absorption mechanism (free-free or synchrotron self-absorption), as well as departures from an $\rho \propto r^{-2}$ CSM, as inferred by some authors, are discussed in detail. We conclude that the evidence for a variation in the mass loss rate with time is very weak. The results regarding the efficiencies of magnetic field generation and relativistic particle acceleration are summarized.

1 Introduction

The interaction of supernovae (SNe) with their circumstellar medium (CSM) offer important clues to both the nature of the SN progenitors, the hydrodynamics of the explosion, the environment of the SN, and the physics of high velocity shock waves. The now convincing connection of Type Ic SNe and GRB's has also made the study of the SN environment especially interesting. Basically, the standard picture of the SN interaction with the surroundings is only a non-relativistic version of the standard afterglow scenario (e.g., Chevalier, these proceedings). We will discuss a few issues related to the SN interaction. For a more detailed exposition see the recent review in [8].

2 The Standard Model

Supernova progenitors come in basically two flavors: extended red supergiants, or compact, hot stripped stellar cores. The former are thought to be related to Type IIP SNe, while the latter are most likely related to Type Ib and Ic SNe. Type IIL, IIn and IIb SNe probably represent a decreasingly massive hydrogen envelope. It is also tempting to identify this as a sequence of increasing ZAMS mass, with the Type IIP representing the most common low mass progenitors, and the Type Ic's originating from the most massive Wolf-Rayet stars. A complication is the fact that a large fraction of stars are in close binary systems. Mass transfer between the companions can in this case lead to strong mass loss even for stars of comparatively low mass.

Massive stars have in general strong stellar winds. On the main sequence the blue supergiants have fast winds with a wind velocity of $500-3000$ km s^{-1}. As the star evolves to the red supergiant stage the escape velocity decreases dramatically and consequently the wind velocity to $10-30$ km s^{-1}. In most of this stage the mass loss rate is $10^{-6}-10^{-5}$ M$_\odot$ yr^{-1}. There are, however, indications, both from the observations of SNe (see below), and from stellar evolution calculations [14] that the star in some cases can undergo a stage with a superwind, similar to what occurs in AGB's, with mass loss rates of $\sim 10^{-4}$ M$_\odot$ yr^{-1}. The duration of this stage must be very short, $\sim 10^4$ yrs. Finally, if mass loss is important enough, the star may evolve to the Wolf-Rayet (WR) stage, with mass loss rate $\sim 10^{-5}$ M$_\odot$ yr^{-1} and a wind velocity of $1000-5000$ km s^{-1}, depending on the evolutionary stage of the WR star [30]. For single stars this occurs only for stars more massive than $\sim 22-40$ M$_\odot$ for solar metallicity, depending on rotation [27]. In a binary system this may, however, occur at considerably lower mass. Because the CS density is $\rho_{\rm cs} = \dot{M}/(4\pi u_{\rm w} r^2)$, where $\dot{M}$ is the mass loss rate, $u_{\rm w}$ the wind velocity and r the distance from the star, the CS density into which the SN explodes can differ by several orders of magnitude, depending on the evolutionary stage in which it explodes.

The collision of the supernova ejecta with the surrounding gas generates a strong shock wave, which expands with a velocity $20-30\%$ larger than the maximum velocity of the ejecta. The temperature behind this forward shock is $\sim 10^9$ K. The pressure behind the shock will send a reverse shock back into the ejecta. Because of the higher density, the velocity of the reverse shock will only be $V_{\rm cs}/(n-2) \sim 500-1000$ km s^{-1}, depending on the density gradient of the ejecta, $\rho_{\rm ej} \propto r^{-n}$ [5]. For polytropic envelopes the outer parts of the ejecta have $n \sim 10$ [24]. Departures from such a structure may, however, lead to both steeper and shallower gradients. For typical ejecta gradients the temperature will only be 10^7-10^8 K behind this shock. Therefore, and because of the high ejecta density, cooling will in general be important for the reverse shock [7, 10]. This will create a thin shell of cool gas between the reverse and CS shocks, often referred to as the cool, dense shell. The forward shock will in contrast usually be adiabatic, unless the CS density is very high.

During the last two decades radio, optical and X-ray observations have greatly added to our understanding of the SN environment (see the papers by Immler, Filippenko and Van Dyk). Of these, the radio provides the cleanest signature of CS interaction. Because of this, and also because the interpretation of these observations have generated some confusion, we will discuss these observations in some detail, as well as the complications going into the analysis.

2.1 Radio Emission and Absorption

The radio emission arises as a result of relativistic electrons accelerated in the shock region and emitting synchrotron radiation in the magnetic field. The

exact mechanism of the acceleration is not well known, although a first order Fermi mechanism would be natural across the shock. Particle acceleration may, however, also occur behind the shock, close to the contact discontinuity, separating the shocked ejecta and shocked CSM. The generation of the magnetic field is not much better understood, although there has been recent progress in this area. In particular, numerical simulations [13, 29] based on ideas of Medvedev & Loeb [26] for GRB's, have shown that the Weibel instability, which is a particular version of the two-stream instability, can give rise to a strong magnetic field at the shock. Although the simulations have mainly been done in the context of relativistic shocks, the same mechanism should work also for non-relativistic shocks. An important issue for this type of simulations is to determine the efficiency of conversion of the thermal energy of the shock into magnetic field and relativistic electron energy. The latter two are usually characterized by $\epsilon_{\rm e} = u_{\rm e}/u_{\rm therm}$ and $\epsilon_{\rm B} = u_{\rm B}/u_{\rm therm}$, where $u_{\rm therm} = 9/8\rho V_s^2$. Most likely, these parameters depend on both the shock velocity, the CSM density and chemical composition.

The radio emission may be affected by free-free absorption from the surrounding CSM and synchrotron-self absorption (SSA) by the same relativistic electrons that emit the radiation. Assuming the relativistic electrons to be injected behind the forward shock with an energy distribution given by $dn_{\rm e}(\gamma)/d\gamma \propto \gamma^{-p}$ for $\gamma_{\rm min} \leq \gamma \leq \gamma_{\rm max}$, the synchrotron spectrum is given by $F_\nu = \pi R^2 S_\nu[1 - \exp(-\tau_\nu)]$ where $S_\nu \propto \nu^{5/2}/B^{1/2}$ and $\tau_\nu \propto B^{3/2+\alpha} N_{\rm e} \nu^{-\alpha-5/2}$. Here $\alpha = (p-1)/2$ and $N_{\rm e}$ is the column density of relativistic electrons. In the case of negligible cooling $N_{\rm e} \propto R n_{\rm e} \propto R u_{\rm e}$. At low frequencies the optically thick spectrum is given by

$$F_\nu \propto R^2 \nu^{5/2} B^{-1/2}, \tag{1}$$

and at high frequencies

$$F_\nu \propto R^2 N_{\rm e} B^{1+\alpha} \nu^{-\alpha} \propto R^3 n_{\rm e} B^{1+\alpha} \nu^{-\alpha}. \tag{2}$$

A fit to the spectrum, covering the peak frequency ($\nu \equiv \nu_{\rm peak}$), therefore allows a determination of both the magnetic field and the density of relativistic electrons, if the radius of the emitting region is known. As we discuss below, this can usually be determined from optical line widths or in rare cases from VLBI.

From these expressions we can derive an estimate of the brightness temperature at the peak of the spectrum (i.e., where $\tau \sim 1$) given by

$$T_{\rm b} \approx 8.2 \times \times 10^{10} g(p)^{2/17} (\epsilon_{\rm e}/\epsilon_{\rm B})^{2/17} (F_\nu/10^{29} {\rm erg\ Hz^{-1}})^{1/17} {\rm K}, \tag{3}$$

independent of the value of $\nu_{\rm peak}$. The value of $g(p)$ varies slowly with the parameters specifying the energy distribution of the relativistic electrons, for example, $g(2) = 1/\ln(\gamma_{\rm max}/\gamma_{\rm min})$. The corresponding Lorentz factor is

$$\gamma_{\rm peak} \approx 1.0 \times 10^2 (\epsilon_{\rm e}/\epsilon_{\rm B})^{2/17} (F_\nu/10^{29}\ {\rm erg\ Hz^{-1}})^{1/17}, \quad (4)$$

showing that $\gamma_{\rm peak}$ is fairly insensitive to various parameters, and is expected to vary by less than an order of magnitude.

The second possibility, free-free absorption, is decoupled from the emission region, and only depends on the properties of the CSM. For an $\rho \propto r^{-2}$ CSM density, the free-free optical depth is

$$\tau_{\rm ff} \propto \nu^{-2} (\dot{M}/u_{\rm w})^2 T^{-3/2} R_{\rm s}^{-3}. \quad (5)$$

Here, $R_{\rm s} = V_{\rm s} t$. To estimate the relative importance of these mechanisms we determine the frequency of optical depth unity. For free-free absorption, we obtain

$$\nu_{\rm ff} \propto (\dot{M}/u_{\rm w}) T^{-3/4} V_{\rm s}^{-3/2} t^{-3/2}. \quad (6)$$

With

$$B^2/8\pi \propto \epsilon_{\rm B} \rho V_{\rm s}^2 \propto \epsilon_{\rm B} (\dot{M}/u_{\rm w}) V_{\rm s}^2 / R_{\rm s}^2 \propto \epsilon_{\rm B} (\dot{M}/u_{\rm w})/t^2 \quad (7)$$

and $N_{\rm e} \propto \epsilon_{\rm e} R_{\rm s} B^2/\epsilon_{\rm B}$ we obtain for the SSA frequency

$$\nu_{\rm SSA} \propto (\epsilon_{\rm B}\epsilon_{\rm e})^{1/3} (\dot{M}/u_{\rm w})^{2/3} V_{\rm s}^{1/3} t^{-1}. \quad (8)$$

The ratio of these is

$$\nu_{\rm ff}/\nu_{\rm SSA} \propto (\epsilon_{\rm B}\epsilon_{\rm e})^{-1/3} (\dot{M}/u_{\rm w})^{1/3} V_{\rm s}^{-11/3} T^{-3/4} t^{-1/2}. \quad (9)$$

Therefore, the relative importance of the two absorption mechanisms depends strongly on the wind velocity of the progenitor, the efficiencies of producing relativistic electrons and the strength of the magnetic field, the CSM temperature and especially the shock velocity. The latter point has been emphasized by Chevalier [6], who find that most Type Ic SNe fall into the SSA category, because of their high expansion velocities and high wind velocities.

For a consistent modeling it is crucial to include all relevant energy loss mechanisms for the relativistic electrons. These include the usual synchrotron losses, Compton losses on the photospheric and/or the synchrotron photons, and Coulomb losses. While the former two mainly act on the high energy electrons, and steepen the spectrum, the latter is most important at low energies, and lead to a flattening of the spectrum. Even with a constant value for p, this will lead to a curved optically thin spectrum. In practice, the kinetic equation for the electron distribution should be solved at each energy. More details on these processes can be found in [11].

When the cooling time starts to become comparable to the dynamical time (i.e., t), radiation losses will affect the emitted synchrotron spectrum. For synchrotron cooling

$$t_{synch}/t = 0.47(t/10\,\mathrm{days})(\gamma\,\epsilon_\mathrm{B})^{-1}(\dot{M}/10^{-5}\ \mathrm{M}_\odot\ \mathrm{yr}^{-1})^{-1}(u_\mathrm{w}/10\ \mathrm{kms}^{-1}). \quad (10)$$

Since $\gamma \gtrsim 10^2$, synchrotron cooling is expected to be important for supernovae with a red supergiant progenitor, unless $\epsilon_\mathrm{B} \ll 1$. However, cooling in supernovae with a Wolf-Rayet star progenitor cannot be excluded, since the cooling time may be shortened due to inverse Compton losses. This can occur in situations where $\epsilon_\mathrm{e} \gg \epsilon_\mathrm{B}$ (synchrotron self-Compton) or for very luminous supernovae for which scattering of photospheric photons may become important. As mentioned above, knowing ν_peak and R_s makes it possible to deduce individual values for ϵ_B and ϵ_e. The occurrence of cooling provides an extra constraint on the model; for example, the underlying assumption of a spherically symmetric source geometry can be tested. The source properties can be further refined if the Compton scattered radiation is observed. Furthermore, if a low frequency flattening due to Coulomb losses is not properly accounted for, it is likely that model fitting will give a value of ν_peak, and hence B, which is too large.

If free-free absorption is important, the epoch of optical depth unity allows us to determine the important density parameter, $\dot{M}/u_\mathrm{w}$. Because $R_\mathrm{s} = V_\mathrm{s}t$, one can determine the ratio $\dot{M}/u_\mathrm{w}$ from the time of optical depth unity at a given frequency, *if* the shock velocity and the temperature of the CSM are known. The shock velocity can either be estimated from the maximum extent of the optical line widths, usually the Hα line, or in more rare cases, like for SN 1993J, directly from the radius as inferred from VLBI observations.

The temperature of the CSM is even more difficult to determine. At the time of shock break-out a burst of soft X-rays heats and ionizes the CSM. The spectrum and luminosity of this burst depends on the nature of the progenitor, and has recently been discussed by Matzner & McKee [24]. A compact progenitor has a very brief burst of hard radiation with a low total energy, while a red supergiant has a longer burst, but considerably softer and with a larger energy. The ring of SN 1987A offers a spectacular example of a circumstellar structure heated and ionized by the outburst of the SN. In this case the initial temperature of the ring was $\sim 2 \times 10^5$ K, cooling on a time scale of years [21, 22]. At the smaller distances relevant for the free-free absorption of the radio supernovae during the first months ($10^{15} - 10^{16}$ cm), these effects will be even larger.

Unfortunately, with the exception of SN 1987A, little direct information on the temperature of the CSM is available. Instead, one has to rely on theoretical calculations. Because of the low density the recombination and ionization time scales are long compared to the evolution of the ionizing spectrum and one has to calculate the evolution of the temperature and ionization of the CSM from the out-break until the epoch of interest. This has only been done for a few cases, the Type IIL SN 1979C [20], SN 1987A [21, 22] and SN 1993J [12]. In all cases the CSM temperatures close to the shock are $10^5 - 10^6$ K immediately after shock break-out. The temperature

then decreases on a time scale of months, but can be $\gtrsim 2 \times 10^4$ K even a year after the explosion. This result is in sharp contrast to the simplified analyses of the radio light curves which assume a *constant* temperature of in most cases $\sim (1-3) \times 10^4$ K, and obviously leads to large errors in the estimated mass loss rates. Moreover, the decreasing temperature can mimic a change in the mass loss rate with time, as has been claimed for some of the radio supernovae. These effects are discussed in detail in [20].

3 SN 1993J

3.1 Synchrotron Self-absorption or Free-free Absorption?

The radio observations of SN 1993J [4, 32, 38] are to date by far the best ones available. Equally important, the VLBI observations [1, 23] give direct information about the size of the radio emitting region, and therefore the shock velocity, as function of time. From this combination a detailed modeling of the spectra have been possible [11, 12, 31, 38]. The conclusions with regard to the mechanism behind the absorption, as well as the structure of the CSM, however, differ substantially.

The analysis in both [12] and [38] were based on modeling the radio observations by free-free absorption in a CSM. As was shown in [11], this alone cannot reproduce the turn-off of the spectrum at low frequencies, which, especially at late epochs, is considerably shallower than the exponential cutoff expected for free-free absorption. Instead, it agrees well with the standard $F_\nu \propto \nu^{5/2}$ spectrum expected from synchrotron self-absorption. Only at early epochs was free-free absorption found to be important, and then only for the longest wavelengths.

The main reason why free-free is only marginally important is that the temperature of the CSM inferred from modeling of the heating and ionization by the radiation from the shock break-out is likely to have been very high, $\sim 10^5 - 10^6$ K [12]. The parametric fits by Van Dyk et al., on the other hand do not determine the temperature either observationally or theoretically, and simply assume a constant temperature. Because $\tau_{\rm ff} \propto T^{-3/2}$, this partly explains the different importance of the free-free absorption in [38] and [11]. Furthermore, Van Dyk et al. do not use the dynamical evolution from the VLBI observations. Finally, their fits do not include any cooling processes which affect the electron spectrum, and only assume a constant power law for this. Both Coulomb and synchrotron were shown to be important in [11], which flatten the low energy spectrum and steepen it at high energies. The effect of this can be seen especially in the lack of agreement between the fits and the observations at the peak of the lowest frequency, caused by Coulomb cooling, which flattens the electron spectrum.

The modeling in [31] is also based on SSA. They do, however, not include a self-consistent calculation of the electron spectrum, for example Coulomb

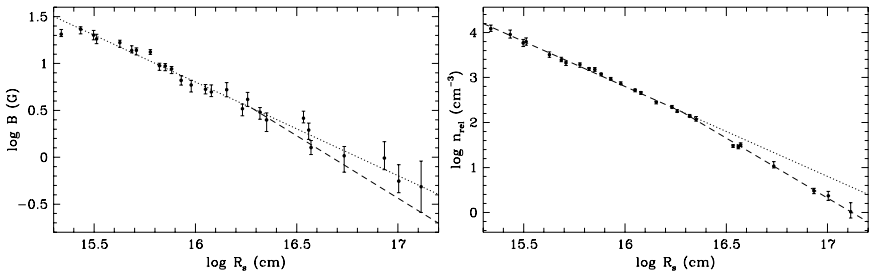

Fig. 1. Magnetic field (left) and density of relativistic electrons (right) as a function of the shock radius for SN 1993J. The dashed lines show the expected evolution if the magnetic energy density and relativistic particle density scale with the thermal energy density, $B^2/8\pi \propto \rho V_s^2 \propto n_{rel} \propto t^{-2}$, while the dotted lines show the case when $B \propto r^{-1}$ and $n_{rel} \propto r^{-2}$[11].

cooling is not accounted for, and invoke an arbitrary cutoff of the electron spectrum at low energies. This explains the different quantitative conclusions from [11]; in particular, the neglect of Coulomb cooling in the model fitting causes the deduced value of the synchrotron self-absorption frequency to be too high. This, in turn, results in an overestimation of the strength of the magnetic field.

A test of the SSA model was provided by the new low frequency observations with VLA in [32] and the VLA and GMRT in [4]. The fluxes of both these sets of observations agreed well with the fluxes predicted in [11]. In addition, the combined VLA and GMRT spectrum at 3200 days in [4] nicely showed the break in the spectrum caused by the synchrotron cooling to evolve as expected.

One of the most interesting results of the modeling of SN 1993J was that not only could individual values for the energy densities in magnetic field and relativistic particles be derived but also their evolution with time could be determined (see Fig. 1). Both of these energy densities scaled with the thermal energy density behind the shock (i.e., ϵ_B and ϵ_e are constants) but the conditions are far from equipartition since $\epsilon_B \approx 0.14$ and $\epsilon_e \sim 5 \times 10^{-4}$.

3.2 X-rays

X-ray emission from SN 1993J were observed with OSSE on Compton/GRO [18], ROSAT [15, 39], ASCA [37], Chandra [35] and XMM [40]. During the first two months, the OSSE and ASCA observations showed a very hard spectrum with $kT \sim 100$ keV. This agreed well with that expected from the forward, circumstellar shock $\sim 1.1 \times 10^2 (V_s/10^4 \text{ km s}^{-1})^2$ keV [12].

Because of the proximity to the Sun, it could then not be observed until $\sim$ 200 days after explosion. The temperature was now only $\sim$ 1 keV, and the column density had increased by a large factor [37, 39]. This transition

was explained in [12] as a natural consequence of the radiative reverse shock and the presence of the cool, dense shell. As the SN expanded the column density of the CDS decreases $\propto t^{-1}$, and therefore gradually becomes optically thin. Because the luminosity below $\sim$ 10 keV is dominated by the reverse shock, there will be a hard to soft transition, once the CDS becomes transparent. From the X-ray flux the mass loss rate was estimated to be $\sim 4 \times 10^{-5}$ $M_\odot$ yr^{-1}, in agreement with that estimated from the radio.

3.3 Structure of the CSM

There has been considerable confusion also with regard to the structure of the CSM of SN 1993J. In several papers [12, 15, 36, 38] there have been claims of a CSM density varying as $\rho \propto r^{-1.5-1.7}$. This has in turn been taken as evidence for a mass loss varying with time. Only in [11] was an $\rho \propto r^{-2}$ found to reproduce the observations. It is therefore of interest to examine the arguments on which these quite different conclusions rest.

As has already been discussed, the analysis in [12] and [38] both neglected the effects of SSA, and are therefore not physically consistent. Their conclusions from the radio modeling with regard to the CSM should therefore be ignored.

The X-ray analysis by Immler et al. [15] assumes that the X-ray emission emerges from the forward, circumstellar shock. This is directly contradicted by the low temperature, $\sim$ 1 keV, and high column density found from the ASCA observations later than 200 days [37]. As was discussed above, the X-ray flux and temperature at late phases are instead consistent with those expected from the reverse shock [12, 36].

The analysis by Suzuki & Nomoto [36] is based on a hydrodynamical, consistent modeling of the interaction of the ejecta and CSM, and the results should therefore be taken seriously. The fact that they obtain a CSM density at small radii varying as $\rho \propto r^{-1.7}$ and a clumpy medium at large radii, however, depends on the ejecta structure they use. The specific model they use, 4H47, was designed to reproduce the early light curve, and had for this purpose to be mixed artificially. More detailed modeling [16] also showed that these 1-D models are hydrodynamically unstable. A further problem with this model is that it does not reproduce the velocity evolution of the shock, as inferred by the VLBI observations. More detailed calculations of the X-ray evolution using an ejecta model which does reproduce the VLBI observations indeed show that a satisfactory reproduction of the X-ray observations can be obtained for an $\rho \propto r^{-2}$ CSM density.

In conclusion, *the only self-consistent modeling of the CSM of SN 1993J are those in [11] using radio observations and [36] using X-rays.* Because of the insensitivity of the radio observations to the ejecta structure, in contrast to the X-rays, we believe the former is the more reliable, and that an $\rho \propto r^{-2}$ CSM density is the most likely.

4 SN 2002ap

Type Ic SNe are of special interest because of their relation to the GRBs. The recent SN 2002ap is together with SN 1998bw the best observed objects of this class, and we discuss some issues related to this.

A special property of the Type Ic SNe is their high expansion velocities. Although this varies by a large factor from the relatively slow SN 1994I to SN 1998bw, they are in all cases much faster than the Type II's and also SN 1993J. A problem here is the fact that the expansion velocity of the radio emitting region is difficult to estimate directly from observations. The optical spectrum shows few clear line features at early time, implying that blending is very important. This only allows a lower limit to the velocity to be determined. For SN 1998bw this was $\sim 60,000$ km s^{-1}[28], and for SN 2002ap $\sim 30,000$ km s^{-1}[25].

Because of the high expansion velocities SSA dominates the radio absorption. The radio observations of SN 1998bw [17] have been discussed in [19]. The most important conclusions was the high expansion velocity, $V_{\rm s}/c \gtrsim 0.9$, and the large energy in relativistic ejecta. Unfortunately, the radio observations of this and other Type Ic's did not allow a determination of the mass loss rate, because this depends on the unknown values of $\epsilon_{\rm e}$ and $\epsilon_{\rm B}$. While these are often assumed to be close to equipartition, there is little theoretical motivation for this.

SN 2002ap is interesting in this respect because, in addition to good radio observations [2], it was also observed with XMM [33, 34]. The X-ray emission is most naturally explained as a result of inverse Compton scattering of the photospheric radiation by the same relativistic electrons which are responsible for the radio emission [3]. This process also leads to cooling of the relativistic electrons, and thereby a steepening of the emitted spectrum, which agrees with the fact that the optically thin radio spectrum is as steep as $F_\nu \propto \nu^{-0.9}$.

By modeling the radio light curves of the different frequencies one can determine the expansion velocity of the radio emitting region, as well as the relative values of $\epsilon_{\rm e}$ and $\epsilon_{\rm B}$. We find that $V_{\rm s} \sim 70,000$ km s^{-1}, and that $\epsilon_{\rm e}$ and $\epsilon_{\rm B}$ are roughly equal (i.e., the magnetic field and relativistic electrons are in approximate equipartition). The exact value of their ratio depends on the upper and lower cut-offs in the electron distribution, which are not directly observable. This is in contrast to SN 1993J, where we found that $\epsilon_{\rm B} \gg \epsilon_{\rm e}$. It is also interesting to note that in both 1993J and 2002ap the injected distribution of relativistic electrons has $p \approx 2$, which is the theoretical value expected from first order Fermi-acceleration at a non-relativistic shock. This is not directly apparent from the observations, since cooling alters the emitted spectrum so that the simple relation $\alpha = (p-1)/2$ cannot be used to deduce the value of p. It could be that an electron distribution with $p = 2$ is valid for most supernovae and that the range of observed values for α is due to cooling.

5 Conclusions

The VLA radio observations of SN 1993J are unique in terms of both the temporal coverage and the quality of the observations. The fact that also VLBI observations exist adds to this characterization, and means that the size of the radio emitting plasma can be determined without further assumptions. This combination makes a detailed spectral analysis possible, and from this a determination of the magnetic field and relativistic electron density as functions of time. For this a consistent physical model is necessary, which includes both the radiative transfer and the effects of different energy loss processes on the electron spectrum. There is no need to invoke arbitrary parameterized models, which only hides the real physical parameters, and may result in misleading conclusions with regard to physical mechanisms as well as the structure of the CSM.

Acknowledgement. We are grateful to Peter Lundqvist and Roger Chevalier for comments and collaborations on several of these issues.

References

1. N. Bartel et al. : Science **287**, 112 (2000)
2. E. Berger, S.R. Kulkarni, R.A. Chevalier: Astrophys. J. Lett. **577**, L5 (2002)
3. C.-I. Björnsson, C. Fransson: astro-ph 0401196 (2004)
4. P. Chandra, A. Ray, S. Bhatnagar: astro-ph 0402391 (2004)
5. R.A. Chevalier: Astrophys. J. **258**, 790 (1982)
6. R.A. Chevalier: Astrophys. J. **499**, 810 (1998)
7. R.A. Chevalier, C. Fransson: Astrophys. J. **420**, 268 (1994)
8. R.A. Chevalier, C. Fransson: In: *Supernovae and Gamma-Ray Bursters,* LNP **598**, ed. K. Weiler (Springer: Berlin 2003) p. 171
9. L. Ensman, A. Burrows: Astrophys. J. **393**, 742 (1992)
10. C. Fransson: Astron. Astrophys. **133**, 264 (1984)
11. C. Fransson, C.-I. Björnsson: Astrophys. J. **509**, 861 (1998)
12. C. Fransson, P. Lundqvist, R.A. Chevalier: Astrophys. J. **461**, 993 (1996)
13. J.T. Frederiksen, C.B. Hededal, T. Haugboelle, A. Nordlund: astro-ph 0308104 (2003)
14. A. Heger, L. Jeannin, N. Langer, I. Baraffe: Astron. Astrophys. **327**, 224 (1997)
15. S. Immler, B. Aschenbach, Q.D. Wang: Astrophys. J. Lett. **561**, L107 (2001)
16. K. Iwamoto, T.R. Young, N. Nakasato, T. Shigeyama, K. Nomoto, I. Hachisu, H. Saio: Astrophys. J. **477**, 865 (1997)
17. S.R. Kulkarni et al. : Nature **395**, 663 (1998)
18. M.D. Leising et al. : Astrophys. J. Lett. **431**, L95 (1994)
19. Z. Li, R.A. Chevalier: Astrophys. J. **526**, 716 (1999)
20. P. Lundqvist, C. Fransson: Astron. Astrophys. **192**, 221 (1988)
21. P. Lundqvist, C. Fransson: Astrophys. J. **380**, 575 (1991)
22. P. Lundqvist, C. Fransson: Astrophys. J. **464**, 924 (1996)
23. J.M. Marcaide et al. : Astrophys. J. Lett. **486**, L31 (1997)

24. C.D. Matzner, C.F. McKee: Astrophys. J. **510**, 379 (1999)
25. P.A. Mazzali et al. : Astrophys. J. Lett. **572**, L61 (2002)
26. M.V. Medvedev, A. Loeb: Astrophys. J. **526**, 697 (1999)
27. G. Meynet, A. Maeder: Astron. Astrophys. **404**, 975 (2003)
28. T. Nakamura, P.A. Mazzali, K. Nomoto, K. Iwamoto: Astrophys. J. **550**, 991 (2001)
29. K.-I. Nishikawa, P. Hardee, G. Richardson, R. Preece, H. Sol, G.J. Fishman: astro-ph 0305091 (2003)
30. T. Nugis, H.J.G.L.M. Lamers: Astron. Astrophys. **360**, 227 (2000)
31. M.A. Pérez-Torres, A. Alberdi, J.M. Marcaide: Astron. Astrophys. **374**, 997 (2001)
32. M.A. Pérez-Torres, A. Alberdi, J.M. Marcaide: Astron. Astrophys. **394**, 71 (2002)
33. P. Soria, E. Pian, P. Mazzali: Astron. Astrophys. **413**, 107 (2004)
34. F.K. Sutaria, P. Chandra, S. Bhatnagar, A. Ray: Astron. Astrophys. **397**, 1011 (2003)
35. D.A. Swartz, K.K. Ghosh, M.L. McCollough, T.G. Pannuti, A.F. Tennant, K. Wu: Astrophys. J. Suppl. **144**, 213 (2003)
36. T. Suzuki, K. Nomoto: Astrophys. J. **455**, 658 (1995)
37. S. Uno et al. : Astrophys. J. **565**, 419 (2002)
38. S.D. Van Dyk, K.W. Weiler, R.A. Sramek, M.P. Rupen, N. Panagia: Astrophys. J. Lett. **432**, L115 (1994)
39. H.U. Zimmermann et al. : Nature **367**, 621 (1994)
40. H.U. Zimmermann, B. Aschenbach: Astron. Astrophys. **406**, 969 (2003)

Detection of the Binary Companion to the Progenitor of SN 1993J

S.J. Smartt[1], J.R. Maund[1], R.P. Kudritzki[2], P. Podsiadlowski[3], G. Gilmore[1]

[1] IoA, University of Cambridge, Cambridge, UH;
sjs@ast.cam.ac.uk,jrm@ast.cam.ac.uk
[2] IfA, University of Hawaii, Honolulu, HI, USA;
kud@ifa.hawaii.edu
[3] University of Oxford, Oxford, UK;
podsi@astro.ox.ac.uk

Summary. We present a detailed late-time photometric and spectroscopic study of SN1993J with HST/ACS and Keck LRIS-B. We find a clear signature of a hot star component in the spectra of SN1993J which cannot be explained by the surrounding faint blue stars. This is the first detection of the expected massive binary companion to the red supergiant progenitor and confirms that SN1993J did indeed arise in an interacting binary system.

1 The Late-time Lightcurve of 1993J

The progenitor site of SN1993J was studied in detail shortly after discovery of the SN [1, 3]. A progenitor star was identified with a measured spectral energy distribution (SED) in $UBVRI$. The VRI colors were consistent with a K-type supergiant, but the UB-band fluxes were too high. This suggested there was flux from either a hot binary companion star, or a tight unresolved host OB association. Models of the supernova evolution at the time suggested the double peak in the lightcurve and the spectral transformation to a SN Ib could be explained if the K-type supergiant had lost almost all of its hydrogen envelope to a massive main-sequence (or near main-sequence) companion [6, 7, 9]. This would elegantly explain both the anomalous progenitor SED and the SN evolution. Several authors suggested that this binary companion could become visible within a few years after the SN faded. In this contribution we present a summary of our search for the companion of the progenitor star.

Figure 1 shows the UB lightcurves of SN1993J (and SN1987A for comparison) to illustrate how the SN has faded and when we might likely be able to identify a progenitor star. Although these are very different types of SNe, we don't have such continuous and late time coverage for any other SNe so our comparison data are limited. One difference is startlingly clear, after about 400 days SN1987A fades rapidly whereas SN1993J seems to plateau out at absolute magnitudes of around -8. Late-time low resolution spectra of 1993J (see the Filippenko & Matheson contribution in these proceedings)

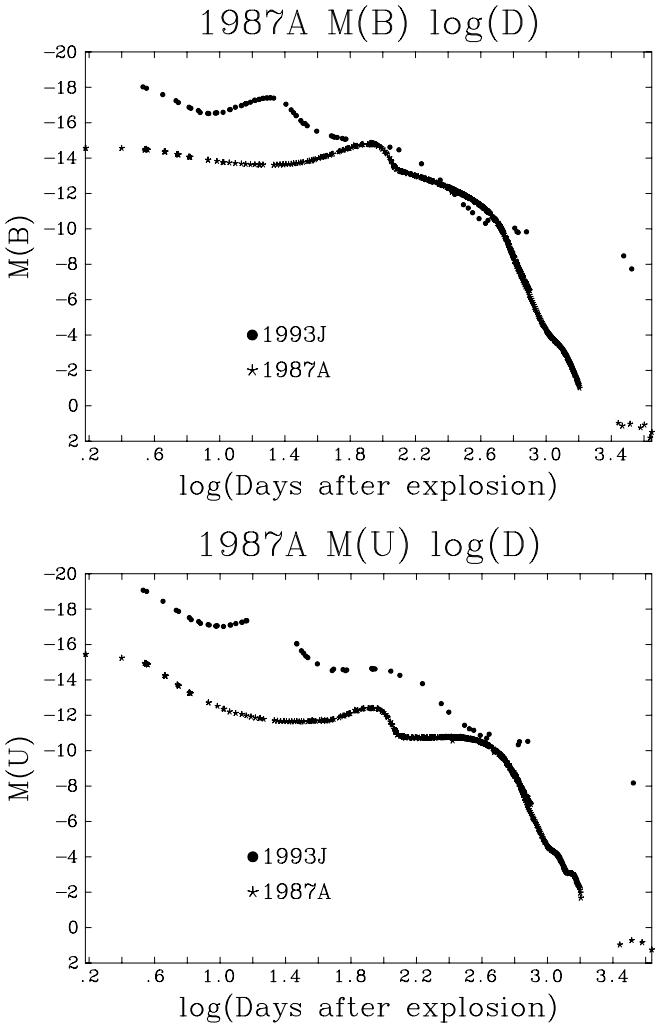

Fig. 1. Compilation of UB-band photometry for SN1993J and SN1987A. Note that at late times SN1993J seems to plateau out at very bright absolute magnitudes whereas SN1987A fades rapidly. The data come from mostly [2] (SN1987A) and [4] (SN1993J) with the points at $\log(D) > 3.4$ from our measured magnitudes in HST archive images.

illustrate evidence for strong interaction of the ejecta with a dense circumstellar medium. Hence the plateau effect may just be due to the strong emission line flux from this interaction. However it could also be due to the fact that there is an underlying stellar component, for example a supergiant star with an absolute magnitude in the range $-6 < M_B < -8$.

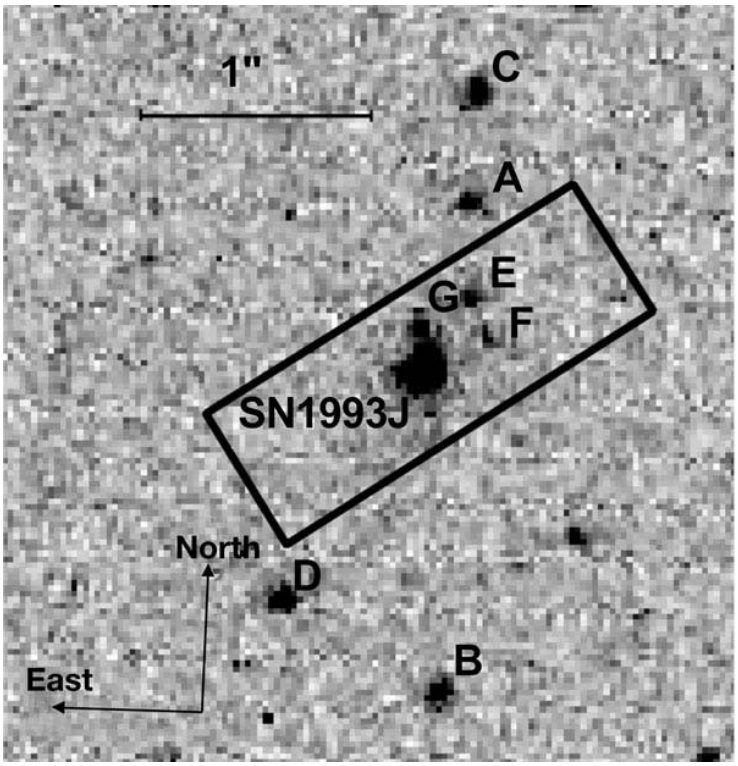

Fig. 2. HST ACS F330W image of SN1993J and its surrounding stellar population. This is a 1200s exposure taken 28 May 2002 (9.2yr after explosion). We follow the nomenclature of [8] and add an extra detected star in the ACS image (star G). The box is an example of the sky area sampled in the ground-based spectra from KeckI LRIS-B. The width is $0.7''$ (the slit-width) and length is $1.8''$ which is the aperture size used in the spectral reductions. The full photometry results are presented in [5].

2 Searching for the Companion Star

To search for signs of a hot companion star at the position of 1993J we took HST ACS images in the UV and deep, medium resolution spectra at Keck (full details are in [5]). Our idea was to take high signal-to-noise spectra in the near-UV to look for the spectral signature of an OB-supergiant or massive main-sequence star i.e. HI, HeI or HeII absorption features. The ACS image is shown on Fig. 2. SN1993J has several neighboring blue stars (G-F are at distances of 3-6 pc from the SN), but there is no dense OB-association.

We took a 5.5hr spectrum with Keck using a $0.7''$ slit and we estimate that the ground-based spectrum samples the region within the box in Fig. 1 (the seeing was between $0.7 - 1.2''$). The spectrum is shown in Fig. 3. The

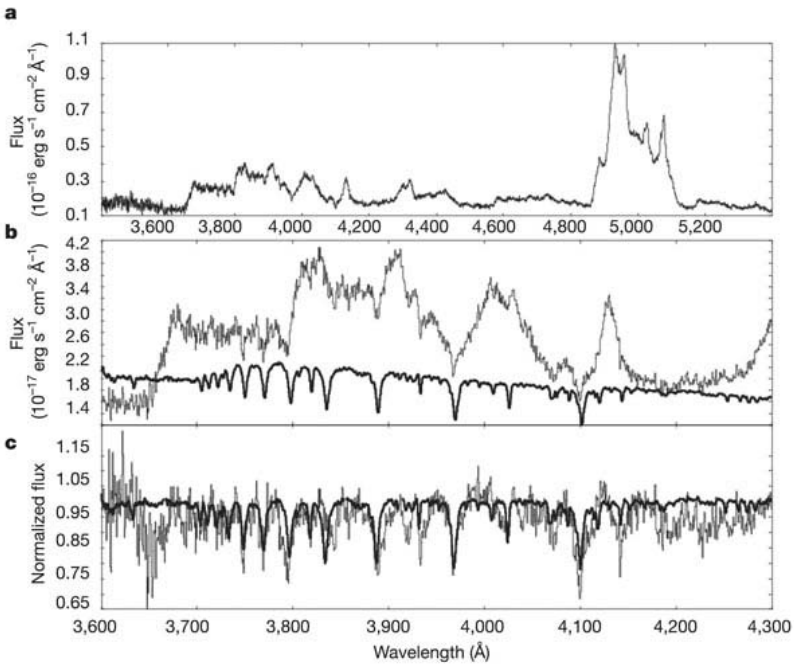

Fig. 3. Upper panel: flux calibrated spectrum of SN1993J 9.93yrs after explosion. Resolution 2.4Å, S/N ratio between 15-30. Middle Panel: the near UV spectrum of SN1993J and a B1Ia supergiant spectrum (HD168489) which has been scaled to the distance of M81 with a reddening of $E(B-V) = 0.2$ and a velocity shift of -120 km s^{-1}applied. The sharp absorption features seen on 1993J are coincident with the H I and He I wavelengths. Bottom Panel: Normalized spectra of SN1993J and the B-type supergiant. The SN spectrum was normalized using short spline fits to attempt to remove the broad emission-line component and allow the stellar spectral contribution to be estimated. The absorption lines are best matched with an early type B-supergiant (B0-B4) with a B2Ia spectrum giving the most consistent fit to all constraints.

broad emission lines characteristic of the strong circumstellar interaction are clearly visible but there are some striking, narrow absorption features superimposed on the continuum of the supernova. These features are all coincident with HI or HeI lines in an OB-star. This spectrum is a composite between the emission flux from the SN ejecta interaction and flux from an OB-star or stars. Clearly the important issue is whether or not the flux from the surrounding stars we see in the ACS images can contribute enough to cause these lines. Using the ACS photometry, we simulated the effect of the surrounding stars using a Gaussian weighting function (weighting the contributions by the distance from the centroid of SN1993J in a similar manner to [8]) and determined the maximum contribution of the surrounding stars to the flux of the

ground-based spectrum of SN1993J to be 18% [5]. We took some representative normalized spectra of OB-supergiants and diluted the continuum to 18%. The calculated line strengths are much too weak to match the observed features in Fig. 3.

To match the strength of these lines we took B-type supergiant spectra, added excess continuum to the stellar spectra (simulating the effect of the SN flux contribution) and renormalized. We varied the flux ratio until the renormalized H I line strengths matched those observed in the SN1993J spectrum. In a similar manner we matched the He I lines at 3819Å and 4026Å, assuming a normal He abundance. Early B-type supergiant spectra in the range B0-B4 provided the most consistent fit. Each line was fitted individually and the final ratios were calculated from the mean of all features. After accounting for the 18% contamination for the surrounding stars we estimate that the following continua ratios for each spectral type would give a consistent match SN/B0Ia=1, SN/B1Ia=1.9, SN/B2Ia=1.9, SN/B3Ia=2.3, SN/B4Ia=3. The pre-explosion UB photometry was used to further constrain the luminosity of the progenitor and our best estimate of a star that could produce the narrow lines and match the prediscovery photometry is $\log T_{\rm eff} = 4.3 \pm 0.1$ and $\log L/L_{\odot} = 5 \pm 0.3$ (which is approximately B2Ia). Using these values and the prediscovery photometry of [1] we further restrict the progenitor to be a K-type supergiant with parameters $\log T_{\rm eff} = 3.63 \pm 0.05$ and $\log L/L_{\odot} = 5.1 \pm 0.3$.

These results confirm that the progenitor of SN1993J was indeed a member of a binary system. A binary system of components with initial masses $14M_{\odot}$ and $15M_{\odot}$ is consistent with the observations. The $15M_{\odot}$ becomes a red-supergiant, loses almost all its envelope ($\sim 8M_{\odot}$) to its companion and then explodes when it has a mass of $\sim 5.4M_{\odot}$ (and helium exhausted core of $\sim 5.1M_{\odot}$). A full discussion is available in [5].

References

1. G. Aldering, R.M. Humphreys, M. Richmond: Astron. J. **107**, 662 (1993)
2. J.A. Caldwell et al. : Mon. Not. R. Astron. Soc. **262**, 313 (1993)
3. J.G. Cohen, J. Darling, A. Porter: Astron. J. **110**, 308 (1995)
4. J. Lewis et al. : Mon. Not. R. Astron. Soc. **266**, 27 (1994)
5. J.R. Maund, S.J. Smartt, R.P. Kudritzki, P. Podsiadlowski, G.F. Gilmore: Nature **427**, 129 (2004)
6. K. Nomoto et al. : Nature **364**, 507 (1993)
7. P. Podsiadlowski, J.J.L. Hsu, P.C. Joss, R.R. Ross: Nature **364**, 509 (1993)
8. S.D. Van Dyk et al. : Pub. Astron. Soc. Pacific **114**, 1322 (2003)
9. S.E. Woosley, R.G. Eastman, T.A. Weaver, P.A. Pinto: Astrophys. J. **429**, 300 (1994)

Supernova 1987A: The Birth of a Supernova Remnant

Richard McCray

JILA, University of Colorado, Boulder, CO 80309-0440, USA;
dick@jila.colorado.edu

Summary. I describe and interpret observations of the rapidly developing impact of the debris of SN1987A with its circumstellar ring.

1 Introduction

Today, we are observing SN1987A approximately 16 years after its initial outburst. During the first 10 years, the radiation from SN1987A was dominated by energy deposited in the interior by the decay of newly synthesized radioisotopes. From observations at many wavelengths, we learned a great deal about the dynamics and thermodynamics of the expanding debris. With the *Hubble Space Telescope*, we have also observed a remarkable system of three circumstellar rings, the origin of which remains a mystery.

About 7 years ago, the blast wave from the supernova began to strike the inner circumstellar ring, resulting in the appearance of a rapidly brightening "hot spot" on the ring. Today, many more hot spots have appeared, and the radio, infrared, optical, and X-ray radiation from of the supernova is now dominated by the impact of the supernova debris with its circumstellar matter. This impact marks the birth of a supernova remnant, SNR1987A.

Here, I discuss what we know about the circumstellar matter and rings, and what we are learning from observations of the interaction of the supernova debris with the circumstellar matter. Finally, I will hazard a few guesses about what we can expect to learn from SNR1987A during the next decade or so.

2 The Circumstellar Rings

The first evidence for circumstellar matter around SN1987A appeared a few months after outburst in the form of narrow optical and ultraviolet emission lines seen with the *International Ultraviolet Explorer* [9]. Even before astronomers could image this matter, they could infer that:

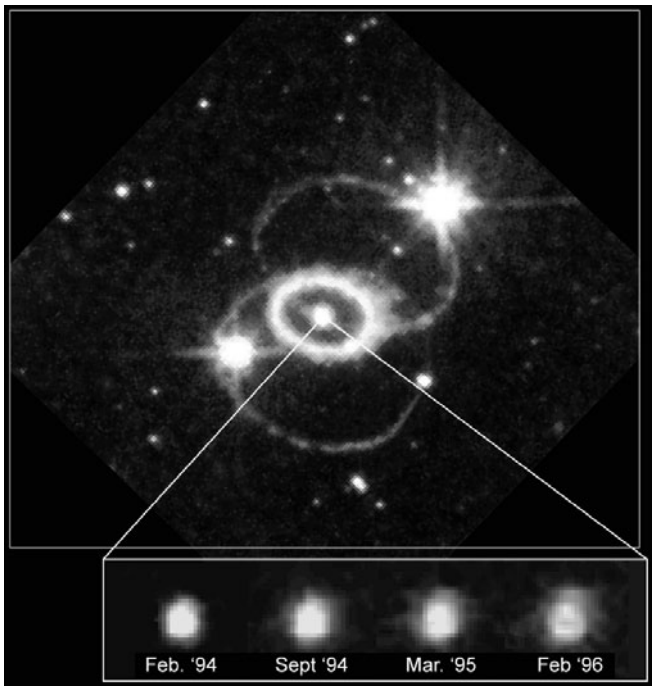

Fig. 1. HST image of SN1987A and its circumstellar rings. The inset at the bottom shows the evolution of the glowing center of the supernova debris.

- the gas was nearly stationary (from the linewidths);
- it was probably ejected by the supernova progenitor (because the abundance of nitrogen was elevated);
- it was ionized by soft X-rays from the supernova flash (from emission lines of NV and other highly ionized elements in the spectrum);
- it was located at a distance of about a light year from the supernova (from the rise time of the light curve of these lines); and
- the gas had atomic density $\sim 3 \times 10^3 - 3 \times 10^4$ cm^{-3} (from the fading timescale of the narrow lines [10]).

Figure 1 shows an image of the circumstellar rings of SN1987A taken with the WFPC on the *Hubble Space Telescope*. Dividing the radius of the inner ring (0.67 lt-year) by the radial expansion velocity of the inner ring (≈ 10 km s^{-1} [7]) gives a kinematic timescale $\approx 20,000$ years since the gas in the ring was ejected, assuming constant velocity expansion. The more distant outer loops are expanding more rapidly, consistent with the notion that they were ejected at the same time as the inner ring.

The rings observed by *HST* are glowing by virtue of the ionization and heating caused by the flash of EUV and soft X-rays emitted by the supernova during the first few hours after outburst. But calculations [8] show that this

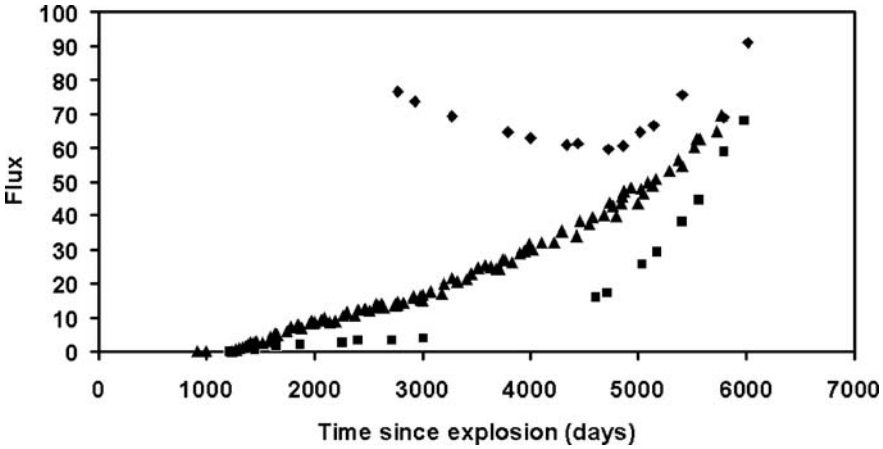

Fig. 2. Light Curves of SNR1987A. Diamonds – optical (Hα, 10^{-15} erg cm^{-2}s^{-1}, courtesy P. Challis); triangles – radio (4.7 GHz, mJy, courtesy R.N. Manchester); squares – X-rays (2.0 – 5 keV, 10^{-14} erg cm^{-2}s^{-1}, courtesy Sangwook Park).

flash was a feeble one. The glowing gas that we see in the triple ring system is probably only the ionized inner skin of a much greater mass of unseen gas that the supernova flash failed to ionize. For example, the inner ring has a glowing mass of only about ~ 0.04 M$_\odot$, just about what one would expect such a flash to produce.

In fact, ground-based observations of optical light echoes during the first few years after outburst provided clear evidence of a much greater mass of circumstellar gas within several light years of the supernova that did not become ionized [6, 22]. The echoes were caused by scattering of the optical light from the supernova by dust grains in this gas. They became invisible a few years after outburst.

What accounts for this circumstellar matter and the morphology of the rings? I suspect that the supernova progenitor was originally a close binary system, and that the two stars merged some 20,000 years ago. The inner ring might be the inner rim of a circumstellar disk that was expelled during the merger, perhaps as a stream of gas that spiraled out from the outer Lagrangean (L2) point of the binary system. Then, during the subsequent 20,000 years before the supernova event, ionizing photons and stellar wind from the merged blue giant star eroded a huge hole in the disk. Finally, the supernova flash ionized the inner rim of the disk, creating the inner ring that we see today.

The binary hypothesis provides a natural explanation of the bipolar symmetry of the system, and may also explain why the progenitor of SN1987A was a blue giant rather than a red giant [18]. But we still lack a satisfactory explanation for the outer loops. If we could only see the invisible circumstellar

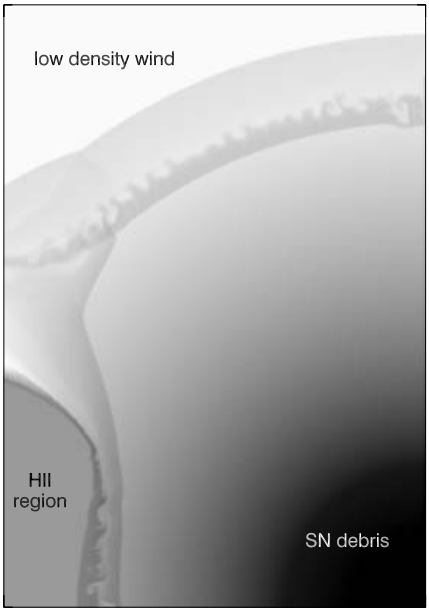

Fig. 3. Schematic illustrating the hydrodynamics of SNR1987A. As the freely expanding supernova ejecta first crosses a reverse shock, its temperature is elevated to $\gtrsim 10^7$ K. This high pressure X-ray-emitting gas drives a forward shock (blast wave) ahead into an HII region of low density ($n \sim 100$ cm^{-3}) gas. Optical hot spots appear behind the transmitted shock where the blast wave strikes an inward protrusion of the high density ($n \sim 10^4$ cm^{-3}) circumstellar ring.

matter that lies beyond the loops, we might have a chance of reconstructing the mass ejection episode.

Fortunately, SN1987A will give us another chance. When the supernova blast wave hits the inner ring, the ensuing radiation will cast a new light on the circumstellar matter. As I describe below, this event is now underway.

3 The Crash Begins

The first evidence that the supernova debris was beginning to interact with circumstellar matter came from radio and X-ray observations. As Fig. 2 shows, SN1987A became a detectable source of radio and soft X-ray emission about 1200 days after the explosion and has been brightening steadily in both bands ever since. Shortly afterwards, astronomers imaged the radio source with the *Australia Telescope Compact Array* (*ATCA*) and found that the radio source was an elliptical annulus inside the inner circumstellar ring observed by *HST* (Plate 2). From subsequent observations, they found that the annulus was expanding with a radial velocity $\sim 3,000$ km s^{-1} [12].

The radio emission most likely comes from relativistic electrons accelerated by shocks formed inside the inner ring where the supernova debris struck relatively low density circumstellar matter, and the X-ray emission comes from the shocked circumstellar matter and supernova debris. [4, 5]

Until 1996, the circumstellar ring continued to fade as it cooled and recombined [10]. But then, the first "hot spot" appeared and began to brighten on the ring (Plate 2). Evidently, this spot marks the place where the supernova blast wave first strikes an inward protrusion of the ring (Fig. 3). Since then, many more hot spots have appeared and now encircle the entire ring. As this interaction develops, the newborn supernova remnant is brightening at an accelerating rate at optical, radio, and X-ray wavelengths (Fig. 2).

4 The Reverse Shock

Borkowski et al. [1] used a 2-D hydro code to simulate the impact of the outer atmosphere of the supernova with the circumstellar matter. Their model predicted that Lα and Hα emitted by hydrogen atoms crossing the reverse shock should be detectable with the STIS. Then, in May 1997, only three months after these predictions were published, the first STIS observations of SN1987A were made, and broad ($\Delta V \approx \pm 12,000$ km s^{-1}) Lα emission lines were detected [20]. Within the observational uncertainties, the flux was exactly as predicted [14].

The broad Lα and Hα emission lines are not produced by recombination. Instead, they are produced by neutral hydrogen atoms in the supernova debris as they cross the reverse shock and are excited by collisions with electrons and protons in the shocked gas. The observed flux of broad Lα is a direct measure of the flux of hydrogen atoms that cross the shock. Moreover, since the outer supernova envelope is expected to be nearly neutral, the observed flux is a measure of the mass flux across the shock.

These Lα and Hα emission lines give us a powerful tool to map this shock. Since any hydrogen in the supernova debris is freely expanding, its line-of-sight velocity, $V_{\|} = z/t$, where z is its depth measured from the mid-plane of the debris and t is the time since the supernova explosion. Therefore, the Doppler shift of the Lα line will be directly proportional to the depth of the reverse shock: $\Delta\lambda/\lambda_0 = z/ct$. Thus, by mapping the L$\alpha$ or Hα emission with STIS, we can generate a 3-dimensional image of the reverse shock.

Figure 4 illustrates this procedure. Panel **a** shows the location of the slit superposed on an image of the inner circumstellar ring, with the near (**N**) side of the tilted ring on the lower left. Panel **b** shows the actual STIS spectrum of Lα from this observation. The slit is black due to geocoronal Lα emission. The bright blue-shifted streak of Lα extending to the left of the lower end of the slit comes from hydrogen atoms crossing the near side of the reverse shock, while the fainter red-shifted streak at the upper end of the slit comes from the far side of the reverse shock.

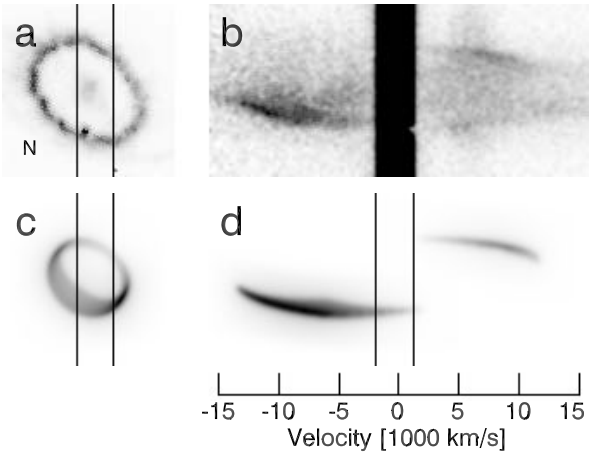

Fig. 4. STIS spectrum of Lα emission from the reverse shock [14].

From this and similar observations with other slit locations we have constructed a map of the reverse shock surface, shown in panel **c**. Note that the emitting surface is an annulus that lies inside the inner circumstellar ring. Presumably, the reverse shock in the polar directions lies at a greater distance from the supernova, where the flux of atoms in the supernova debris is too low to produce detectable emission. Panel **d** is a model of the STIS Lα spectrum that would be expected from hydrogen atoms crossing the shock surface illustrated in panel **c**. By comparing such model spectra with the actual spectra (e.g., panel **b**), we may refine our model of the shock surface [16].

5 The Hot Spots

In April 1997, Sonneborn et al. [20] obtained the first STIS spectrum of SN1987A. Images of the circumstellar ring were seen in several optical emission lines. No Doppler velocity spreading was evident in the ring images (Plate 2) except at one point, located at $P.A. = 29°$ (E of N), which we now call "Spot 1," where a Doppler-broadened streak was seen in Hα and other optical lines.

Spot 1 evidently marks the location where the supernova blast wave first touches an inward protrusion of the dense circumstellar ring (Fig. 3). When a blast wave propagating with velocity $V_b \approx 4,000$ km s^{-1} through circumstellar matter (density $n_0 \approx 150$ cm^{-3}) encounters the ring (density $n_r \approx 10^4$ cm^{-3}), one would expect the transmitted shock to propagate into the ring with $V_r \approx (n_0/n_r)^{1/2} V_b \approx 500$ km s^{-1} if it enters at normal incidence, and more slowly if it enters at oblique incidence.

The emission line spectrum of Spot 1 resembles that of a radiative shock, in which the shocked gas has had time to cool from its post-shock temperature $T_1 \approx 1.6 \times 10^5 [V_r/(100 \text{ km s}^{-1})]^2$ K to a final temperature $T_f \approx 10^4$ K. As the shocked gas cools, it is compressed by a density ratio $n_f/n_r \approx (T_1/T_f) \approx 160[V_r/(100 \text{ km s}^{-1})]^2 \ [T_f/(10^4\text{K})]^{-1}$. We see evidence of this compression in the observed ratios of forbidden lines, such as [NII]$\lambda\lambda$6548, 6584 and [SII]$\lambda\lambda$6717, 6731, from which we infer electron densities in the range $n_e \sim 10^6$ cm^{-3} using standard nebular diagnostics [19].

The fact that the shocked gas in Spot 1 was able to cool and form a radiative layer within a few years sets a lower limit, $n_r \gtrsim 10^4$ cm^{-3}, on the density of unshocked gas in the protrusion. Given that limit, we can estimate an upper limit on the emitting surface area of Spot 1, from which we infer that Spot 1 should have an actual size no greater than about one pixel on the HST Wide Field Planetary Camera (WFPC2). This result is consistent with the imaging observations.

The cooling timescale of shocked gas is sensitive to the postshock temperature, hence shock velocity. For $n_r = 10^4$ cm^{-3}, shocks faster than 250 km s^{-1} will not be able to radiate and form a cooling layer within a few years. It is likely that such fast non-radiative shocks are present in the protrusions. For example, I estimated above that a blast wave entering the protrusion at normal incidence might have velocity ~ 500 km s^{-1}. Faster shocks would be invisible in optical and UV line emission, but we are probably seeing evidence of such shocks in soft X-rays (§6). We would still see the optical and UV line emission from the slower oblique shocks on the sides of the protrusion, however.

Spot 2 did not appear until November 1998, but shortly thereafter, several more spots appeared [21]. By summer 2003, the entire ring was encircled by hot spots (Plate 2). The hot spots are brightening rapidly, with doubling timescales ranging from a few months to 2 years.

6 The X-ray Source

As I have already mentioned in §2, we believe that the X-ray emission from SNR1987A seen by *ROSAT* (Fig. 2) comes from the hot shocked gas trapped between the supernova blast wave and the reverse shock. But *ROSAT* could not image this emission; nor was it able to obtain a spectrum.

Our ability to analyze the X-rays from SNR1987A advanced dramatically with the launch of the *Chandra* observatory [3, 17]. Plate 2 shows the Chandra images at three epochs. We see immediately that the X-rays images have brightened and changed dramatically in the nearly 4 year interval spanned by these observations. The brightest regions of the early X-ray images were well within the optical ring and correlated rather well with the radio images; but as the optical hotspots brightened, the X-ray images were brightest along arcs that correlated well with the locations of the optical hot spots. Evidently,

in 1999 the X-ray emission was dominated by the shocked gas between the blast wave and the reverse shock, but today it is dominated by the shocked gas in the denser hot spots.

The fact that the X-ray and radio images are both brighter on the **E** (left) side than on the **W** could be explained by a model in which either: (a) the circumstellar gas inside the inner ring had greater density toward the **E**; or (b) the outer supernova debris had greater density toward the **E**. But the fact that most of the hot spots appeared first on the **E** side favors the latter hypothesis. If the circumstellar gas had greater density toward the **E** side and the supernova debris were symmetric, the blast wave would have propagated further toward the **W** side, and the hot spots would have appeared there first.

This conclusion is also supported by observations of Hα and Lα emission from the reverse shock (§3), which show that the flux of mass across the reverse shock is greater on the **W** side.

These observations highlight a new puzzle about SN1987A: why was the explosion so asymmetric? We might explain a lack of spherical symmetry by rapid rotation of the progenitor, but how do we explain a lack of azimuthal symmetry?

With the grating spectrometer on *Chandra*, we have also obtained a spectrum of the X-rays from SNR1987A [15]. It is dominated by emission lines from helium- and hydrogen-like ions of O, Ne, Mg, and Si, as well as a complex of Fe-L lines near 1 keV, as predicted (Borkowski et al 1997b). The characteristic electron temperature inferred from the spectrum, $kT_e \sim 3$ keV, is much less than the proton temperature, $kT_p \sim 30$ keV for a blast wave propagating with $V_b \approx 4,000$ km s^{-1} and that inferred from the widths of the X-ray emission lines. This result is a consequence of the fact that Coulomb collisions are too slow to raise the electron temperature to equilibrium with the ions.

The *Chandra* observations (Fig. 2) show that the X-ray flux is now brightening exponentially with an e-folding timescale ~ 2.4 years. The X-ray flux is expected to increase by another order of magnitude during the coming decade as the blast wave overtakes the inner circumstellar ring [2].

7 The Future

SNR1987A has been tremendous fun so far but the best is yet to come. During the next ten years, the blast wave will overtake the entire circumstellar ring. More hot spots will appear, brighten, and eventually merge until the entire ring is blazing brighter than Spot 1. We expect that the Hα flux from the entire ring will increase to $F_{\rm H\alpha} \gtrsim 3 \times 10^{-12}$ erg cm^{-2}s^{-1}, or $\gtrsim 30$ times brighter than it is today [11].

As we have already begun to see, observations at many wavelength bands are needed to tell the entire story of the birth of SNR1987A. Fortunately,

powerful new telescopes and technologies are becoming available just in time to witness this event.

Large ground-based telescopes equipped with adaptive optics will provide excellent optical and infrared spectra of the hot spots. We need to observe profiles of several emission lines at high resolution in order to unravel the complex hydrodynamics of the hot spots. These telescopes also offer the exciting possibility to image the source in infrared coronal lines of highly ionized elements (e.g., [Si IX] $2.58, 3.92\mu$m, [Si X] 1.43μm) that may be too faint to see with *HST*. Observations in such lines will complement X-ray observations to measure the physical conditions in the very hot shocked gas.

The observations with the *ATCA* have given us our first glimpse of shock acceleration of relativistic electrons in real time, but the angular resolution of *ATCA* is not quite good enough to allow a detailed correlation of the radio image with the optical and X-ray images. It will be wonderful to see images of SNR1987A from the *Atacama Large Millimeter Array* (*ALMA*), which should be available before the end of this decade. The images, which will have angular resolution better than the HST images, will give us a unique opportunity to test our theories of relativistic particle acceleration by shocks.

Of course, we should continue to map the emission of fast Lα and Hα from the reverse shock with *STIS*. Such observations give us a three-dimensional image of the flow of the supernova debris across the reverse shock, providing the highest resolution map of the asymmetric supernova debris. We expect this emission to brighten rapidly, doubling on a timescale $\sim$ 1 year. Most exciting, such observations will give us an opportunity to map the distribution of nucleosynthesis products in the supernova debris. We know that the debris has a heterogeneous composition. The early emergence of gamma rays from SN1987A showed that some of the newly synthesized ^{56}Co (and probably also clumps of oxygen and other elements) were mixed fairly far out into the supernova envelope by instabilities following the explosion [13]. When such clumps cross the reverse shock, the fast Hα and Lα lines will vanish at those locations, to be replaced by lines of other elements. If we keep watching with *STIS*, we should see this happen during the coming decade.

The shocks in the hot spots are surely producing ionizing radiation, roughly half of which will propagate ahead of the shock and ionize heretofore invisible material in the rings. The effects of this precursor ionization will soon become evident as brightening of narrow emission lines in the vicinity of the hot spots.

In §1 I pointed out that the circumstellar rings of SN1987A represent only the inner skin of a much greater mass of circumstellar matter, and that we obtained only a fleeting glimpse of this matter through ground-based observations of light echoes. The clues to the origin of the circumstellar ring system lie in the distribution and velocity of this matter, if only we could see it clearly. Fortunately, SNR1987A will give us another chance. Although it will take several decades before the blast wave reaches the outer rings, the impact

with the inner ring will eventually produce enough ionizing radiation to cause the unseen matter to become an emission nebula. We have estimated [11] that the fluence of ionizing radiation from the impact will equal the initial ionizing flash of the supernova within a few years after the ring reaches maximum brightness. I expect that the circumstellar nebula of SNR1987A will be in full flower within a decade. In this way, SN1987A will be illuminating its own past.

References

1. K.J. Borkowski, J.M. Blondin, R. McCray: Astrophys. J. Lett. **476**, L31 (1997)
2. K.J. Borkowski, J.M. Blondin, R. McCray: Astrophys. J. **477**, 281 (1997)
3. D.N. Burrows, et al: Astrophys. J. Lett. **543**, L149 (2000)
4. R.A. Chevalier: Nature **355**, 617 (1992)
5. R.A. Chevalier, V.I. Dwarkadas: Astrophys. J. Lett. **452**, L45 (1995)
6. A.P.S. Crotts, W.E. Kunkel, P.J. McCarthy: Astrophys. J. Lett. **347**, L61 (1989)
7. A. Crotts, S.R. Heathcote: Nature **350**, 683 (1991)
8. L. Ensman, A. Burrows: Astrophys. J. **393**, 742 (1992)
9. C. Fransson, et al.: Astrophys. J. **336**, 429 (1993)
10. P. Lundqvist, C. Fransson: Astrophys. J. **464**, 924 (1996)
11. D. Luo, R. McCray, J. Slavin: Astrophys. J. **430**, 264 (1994)
12. R.N. Manchester, et al: Pub. Astron. Soc. Australia **19**, 207 (2002)
13. R. McCray: Ann. Rev. Astron. Astrophys. **31**, 175 (1993)
14. E. Michael, et al: Astrophys. J. Lett. **509**, L117 (1998)
15. E. Michael, et al: Astrophys. J. **574**, 166 (2002)
16. E. Michael, et al: Astrophys. J. **593**, 809 (2003)
17. S. Park, et al: Astrophys. J. **567**, 314 (2002)
18. P. Podsiadlowski: Pub. Astron. Soc. Pacific **104**, 717 (1992)
19. C.S.J. Pun, et al: Astrophys. J. **572**, 906 (2002)
20. G. Sonneborn, et al: Astrophys. J. Lett. **492**, L143 (1998)
21. B.E.K. Sugerman, et al: Astrophys. J. **572**, 209 (2002)
22. L. Wang, E.J. Wampler: Astron. Astrophys. **262**, L9 (1992)

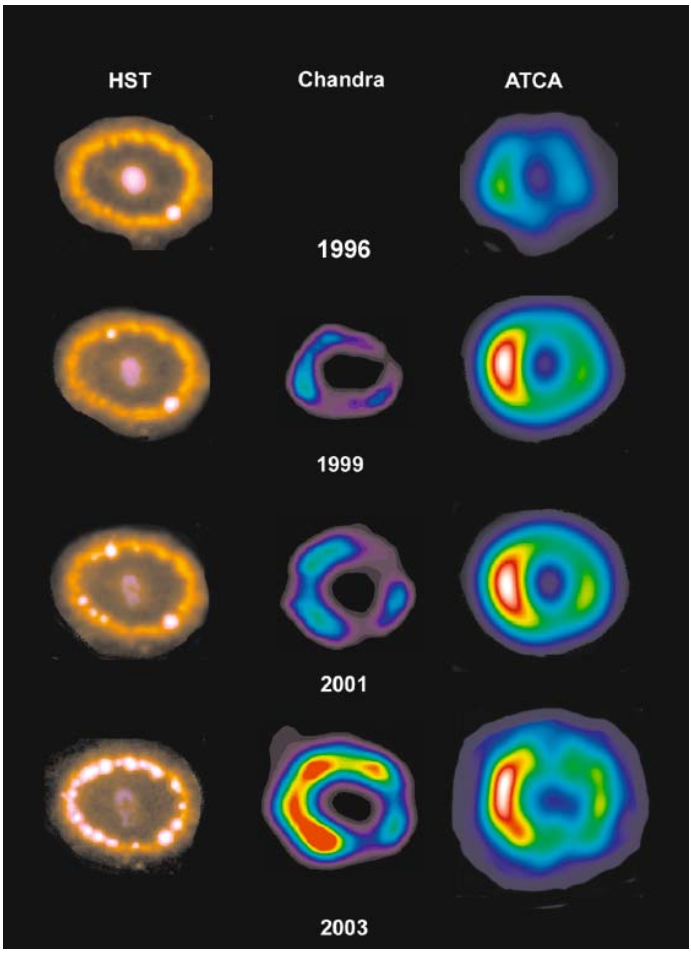

Optical, X−ray, and radio images of SNR 1987A at four epochs. The optical images in the first column are taken with broad Hα filter on the Hubble Space telescope (courtesy Peter Challis). The second column shows broadband (0.3−3.8 keV) images from Chandra (courtesy Sangwook Park), and the third column shows non−thermal radio images from the Australia Telescope Compact Array (courtesy Dick Manchester). The 1996, 1999, and 2001 radio images are taken at 8.7 GHz, while the 2003 image is taken at 18.5 GHz. In 1996, no hot spots are evident. The bright spot in the SW quadrant of the ring is a foreground star. In 1999, Spot 1, has appeared on the NE quadrant (position angle 29 deg) of the inner circumstellar ring. In 2001, Spots 2, 3, and 4 are evident in the SE quadrant. In 2003, the entire ring is encircled by hot spots.

Plate (McCray)

Plate 2.

SN 1987A at Radio Wavelengths

L. Staveley-Smith[1], R.N. Manchester[1], B.M. Gaensler[2], M.J. Kesteven[1], A.K. Tzioumis[1], N.S. Bizunok[3], and V.C. Wheaton[4]

[1] Australia Telescope National Facility, CSIRO, PO Box 76, Epping, NSW 1710, Australia;
Lister.Staveley-Smith@csiro.au
[2] Harvard-Smithsonian Center for Astrophysics, 60 Garden St. MS-6, Cambridge, MA 02138, USA
[3] Boston University, Boston, MA 02215, USA
[4] School of Physics, University of Sydney, NSW 2006, Australia

Summary. SN1987A has an intrinsic radio luminosity some four orders of magnitude less than SN1993J at maximum, largely a reflection of the tenuous wind from the progenitor of SN1987A before explosion. Both remnants have an edge-brightened, ring-like morphology though, in the case of SN1987A, the expansion rate is currently only around 3500 km s^{-1}. The flux density of the remnant of SN1987A continues to rise at all measured radio frequencies. Its spectral index is gradually flattening, indicating its transition into the supernova remnant phase. A campaign to increase the resolution of radio imaging by observing at higher frequencies is underway with the *Australia Telescope Compact Array* (ATCA).

1 Introduction

Radio observations of young supernovae are able to provide valuable information on stellar ejecta – its expansion rate, structure and kinetic energy. However, the most valuable and quantitative information relates to the structure of the surrounding medium with which this ejecta interacts. The density and structure of this medium is normally dominated by winds from the progenitor star, but its temperature and ionization state is strongly influenced by the ultraviolet flash created when the supernova shock erupts through the stellar photosphere. The minishell model [2] has been used with some success to explain radio observations of nearby supernovae, and appears to work reasonably well for SN1993J, the subject of this conference [8, 14]. However, the minishell model requires serious modification in order to account for clumpy progenitor mass-loss [25], the recently identified hypernovae/Gamma-Ray burst events [11] and, as we shall see, the late-time evolution of SN1987A.

2 Radio Luminosity Evolution

2.1 Early Times (< 1000 Days)

Radio emission from SN1987A in the Large Magellanic Cloud was detected immediately after outburst, with the 0.8 GHz flux density peaking at 140 mJy

on day 3 [22]. The rapid flux density evolution and low radio luminosity was consistent with interaction of the shock wave with a fast low-density wind from the blue supergiant progenitor Sk−69°202. If the delay in the low-frequency radio emission was due to free-free absorption, the progenitor mass-loss rate was $\sim 10^{-5} M_{\odot}$ [3]. If due to synchrotron self-absorption [5, 10, 21], the progenitor mass loss was smaller. VLBI observations indicated a fast > 19000 km s^{-1} shock front [9], consistent with early optical spectroscopy.

The early phase of the radio emission was consistent with the minishell model, albeit the radio luminosity was very low, and only detected because of its proximity. The peak 5 GHz luminosity of SN1987A was about four orders of magnitude smaller than SN1993J in M81, and about five orders of magnitude smaller than SN1986J or SN1988Z [26].

2.2 Late Times ($\geq$ 1000 Days)

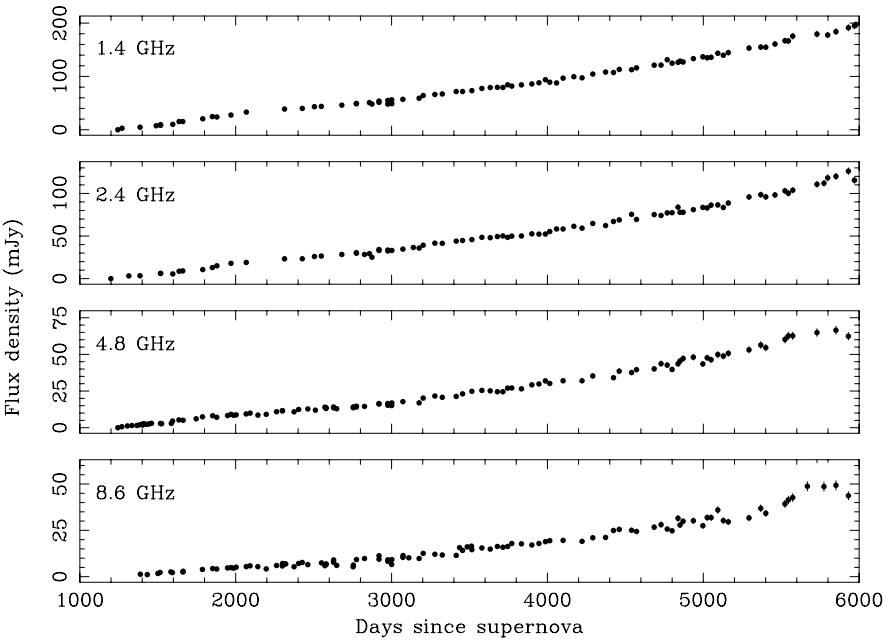

Fig. 1. The late-time evolution of the remnant of SN1987A at four different radio frequencies from 1.4 to 8.6 GHz. The flux density has increased in an approximately linear manner since day 1200. Some flux density fluctuations can be seen. All observations are from the ATCA.

SN1987A re-emerged as a radio source in 1990.5, first at low frequency (0.8 GHz) and, a month later, at higher frequencies (5 GHz) [19]. High resolution

imaging (see also section 4) confirmed that this emission was edge-brightened [20], and therefore due to an interaction of the shock front with a density jump. This increase was not unexpected because of the inferred pre-outburst evolution of Sk−69°202 and the high density of the beautiful arcsecond-scale structure of the circumstellar nebula imaged by the NTT and HST [24].

Figure 1 shows the evolution of SN1987A from day 1000 at frequencies from 1.4 to 8.6 GHz, based on observations with the ATCA. These observations, and the even more closely spaced MOST observations at 0.8 GHz [1], indicate an approximate linear increase to date, with a 1.4 GHz flux density of around 200 mJy at day 5900. At frequencies less than 2 GHz, the flux density of the SN1987A remnant now exceeds the peak flux density reached at early times. In comparison to the peak flux density of SN1993J of 100 mJy at 5 GHz (day 200) [23], the flux density of SN1987A at day 5900 is still only 65 mJy at 5 GHz. This implies that, intrinsically, SN1987A is still 8000 times fainter than SN1993J at maximum. There are significant deviations from the simple picture of a linear increase which are discussed elsewhere [1, 12].

The spectrum of SN1987A is non-thermal with an index ($S_\nu \propto \nu^\alpha$) of $\alpha \approx -0.8$ (see section 3). This is consistent with optically-thin synchrotron emission with an differential electron energy spectral index of -2.6. The source of this emission is the accelerated electrons and compressed magnetic field produced at the shock front. The favored mechanism is ion-modified diffusive shock acceleration which heats the upstream plasma, producing a precursor shock and lowering the compression ratio for the main shock [7]. However, the time-dependence of the resultant synchrotron emissivity depends on the density structure of the circumstellar nebula. Whilst the high emission measure component of this is easily traced by high-resolution forbidden-line and hydrogen recombination-line observations, the structure of the lower density regions only becomes apparent once its energy density has been raised by the passing shock front. Thus the radio (and X-ray) light curves of SN1987A are difficult to predict.

However, if not able to produce detailed predictions, models of the structure of the nebula around SN1987A and inside the circumstellar ring are useful in providing a general picture of what might happen in the future, and at what stage rapid increases in thermal and non-thermal emission at various wavelengths might begin to happen [4, 6, 15]. A common feature of these models is that the triple-ring circumstellar structure was created by asymmetric outflow during the red supergiant phase of the progenitor star in a manner similar to the formation of planetary nebulae from red giants. However, the inner part of this nebula has been modified and pre-shocked by the fast wind from the later blue supergiant phase, therefore creating several discontinuities and transition zones. At this stage, the (mainly thermal) X-ray light curve appears to be rising exponentially [16], indicating that the shock front is very close to the ring.

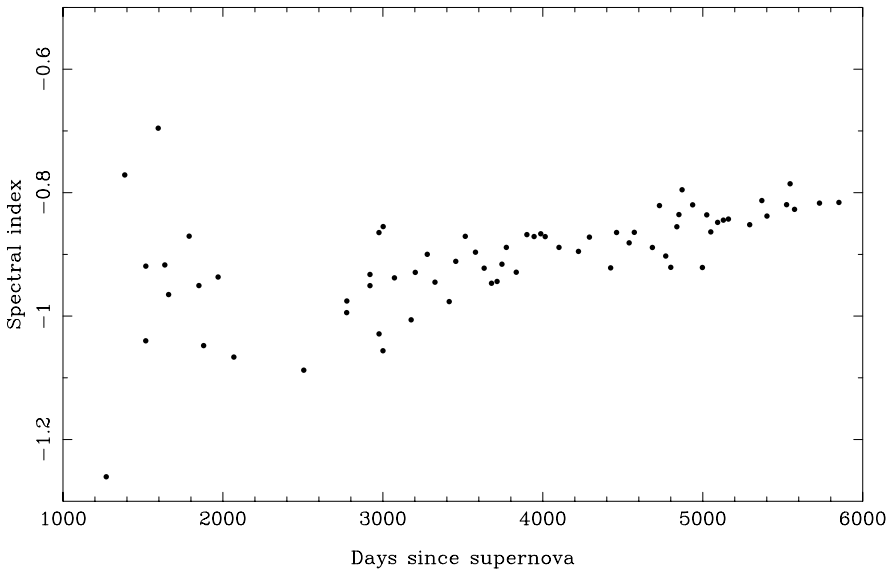

Fig. 2. The late-time spectral index evolution of the remnant of SN1987A derived from ATCA observations at 1.4 and 4.8 GHz, where the measurements are within a week of each other. After day 3000, a clear flattening of the spectral index is seen.

3 Spectral Evolution

As already shown for radio observations up to day 5000 [12], the spectral index of the SN1987A remnant is flattening with time. The index ($S_\nu \propto \nu^\alpha$) is currently $\alpha \approx -0.8$ and increasing at a rate of $\dot{\alpha} = 0.02$ yr^{-1} (Fig. 2). It may therefore reach the canonical -0.5 spectral index for shell-like remnants within 15 years. However, given the exponential evolution of the X-ray flux at the current time, it is likely that the radio evolution will not remain as regular as it has over the past few years.

It is interesting to note that, although the properties of SN1987A and SN1993J are in general quite different, the latter also appears to have a spectral index which is flattening with time [18]. The common implication is that the compression ratio of supernova shock fronts increases with time.

4 Structure in the Remnant of SN 1987A

A high resolution ATCA image taken at a frequency of 9 GHz in 2003 January is shown in Fig. 3. A ring-like structure is present, which has been modeled as a thin spherical shell and a number of hotspots [12]. In comparison with previous images, the east-west asymmetry is growing, and there appears to be enhanced emission in the southern part of the remnant. The latter feature

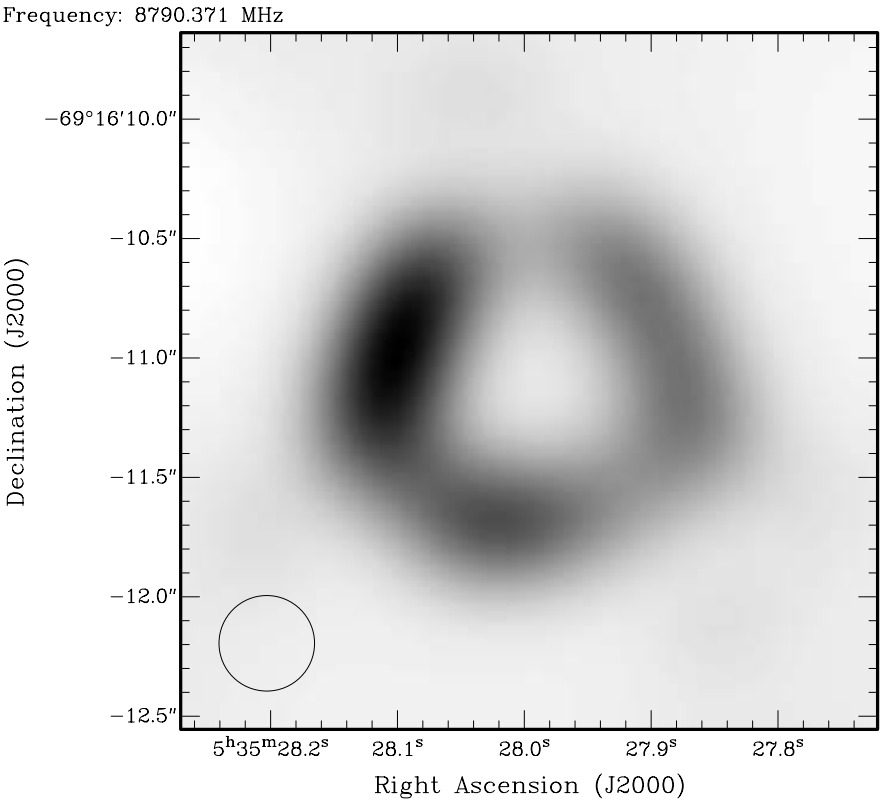

Fig. 3. An image of the radio remnant of SN1987A at day 5810. This image is a maximum entropy reconstruction of ATCA data at a frequency of 9 GHz, convolved with a beam (shown in the bottom left-hand corner) of 0.4 arcsec, resulting in an effective resolution of about 0.5 arcsec. A clear ring-link structure is seen.

may also be present in Chandra 1.2–8.0 keV data from late-2002 [16]. The remnant continues to expand at a rate of 3500 ± 100 km s^{-1} [12], which is similar to the newly derived X-ray expansion velocity of 5000 ± 1000 km s^{-1} [17].

The general picture that is emerging for the evolution of the remnant is that of a fast shock front interacting with gas of increasing density and, along with the increasing shock front area, producing increased levels of synchrotron and non-thermal X-ray emission. Asymmetries in the explosion and the circumstellar gas are responsible for the present-day shape of the remnant, though the general picture remains an almost-spherical shock front impinging on the interior of an hour glass-shaped nebula. Close to the equator, and along the rim of the hour glass, circumstellar densities are very high, and the shock is dramatically slowed down, giving rise to the thermal X-ray emission and the optical emission-line structure seen by HST.

5 Summary and Future Work

Radio emission from SN1987A and SN1993J, the latter being the subject of this conference, are different manifestations of the same basic physics – i.e. a subluminal shock front interacting with a circumstellar nebula. There are clear differences in the history and binarity of the progenitors which go a long way in explaining the very substantial observational differences. Principally these differences are in luminosity (SN1987A is still four orders of magnitude less bright than SN1993J at maximum), and evolution (the radio luminosity of SN1987A is increasing whilst that of SN1993J is decreasing). These difference arise from the fact that SN1987A is embedded in a complex planetary nebula-type structure, whereas SN1993J appears to have a simple r^{-2} circumstellar density profile.

Whilst optical and X-ray monitoring will remain valuable probes of the expanding shock front, a new regime of high-resolution radio imaging of SN1987A is opening up after the recent (2003) installation of 20 GHz receivers on the ATCA. This will allow images of resolution 0.2 arcsec to be regularly obtained, thus improving markedly on existing images such as in Fig. 3. Preliminary observations, which have been reported elsewhere, look promising [13].

References

1. L. Ball, D.F. Crawford, R.W. Hunstead, I. Klamer, V.J. McIntyre: Astrophys. J. **549**, 599 (2001)
2. R.A. Chevalier: Astrophys. J. **259**, 302 (1982)
3. R.A. Chevalier, C. Fransson: Nature **328**, 44 (1987)
4. R.A. Chevalier, V.V. Dwarkadas: Astrophys. J. **452**, 45 (1995)
5. R.A. Chevalier: Astrophys. J. **499**, 810 (1998)
6. K.J. Borkowski, J.M. Blondin, R. McCray: Astrophys. J. **477**, 281 (1997)
7. P. Duffy, L. Ball, J.G. Kirk: Astrophys. J. **447**, 364 (1995)
8. C. Fransson, C.-I. Björnsson: Astrophys. J. **509**, 861 (1998)
9. D.L. Jauncey, A. Kemball, N. Bartel, I.I. Shapiro, A.R. Whitney, A.E.E. Rogers, R.A. Preston, T.A. Clark: Nature **334**, 412 (1988)
10. J.G. Kirk, M. Wassman: Astron. Astrophys. **254**, 167 (1992)
11. Z.-Y. Li, R.A. Chevalier: Astrophys. J. **526**, 716 (1999)
12. R.N. Manchester, B.M. Gaensler, V.C. Wheaton, L. Staveley-Smith, A.K. Tzioumis, N.S. Bizunok, M.J. Kesteven, J.E. Reynolds: Pub. Astron. Soc. Australia **19**, 207 (2002)
13. R.N. Manchester, L. Staveley-Smith, B.M. Gaensler, M.J. Kesteven, A.K. Tzioumis: "The highest resolution image from the Compact Array: SNR 1987A at 12mm." In: *ATNF News*, issue 51, (ATNF October 2003), pp. 17-19 (also at `http://www.atnf.csiro.au/news/newsletter/oct03`)
14. J.M. Marcaide et al. : Science **270**, 1475 (1995)
15. R. McCray: Supernova 1987A: "The Birth of a Supernova Remnant." In: *These proceedings*

16. S. Park, D.N. Burrows, G.P. Garmire, S.A. Zhekov, D. McCray: "Monitoring the Evolution of SNR 1987A with Chandra." In: *Young Neutron Stars and their Environments*, IAU Symposium 218, ed. by F. Camilo, B. Gaensler (ASP, San Francisco 2004)
17. S. Park, S.A. Zhekov, D.N. Burrows, E. Michael, G.P. Garmire, G. Hasinger: astro-ph 0308220
18. M.A. Pérez-Torres, A. Alberdi, J.M. Marcaide: Astron. Astrophys. **394**, 71 (2002)
19. L. Staveley-Smith et al. : Nature **355**, 147 (1992)
20. L. Staveley-Smith, D.S. Briggs, A.C.H. Rowe, R.N. Manchester, J.E. Reynolds, A.K. Tzioumis, M.J. Kesteven: Nature **366**, 136 (1993)
21. M.C. Storey, R.N. Manchester: Nature **329**, 421 (1987)
22. A.J. Turtle, D. Campbell-Wilson, J.D. Bunton, D.L. Jauncey, M.J. Kesteven, Nature **327**, 38 (1987)
23. S.D. Van Dyk, K.W. Weiler, R.A. Sramek, M.P. Rupen, N. Panagia: Astrophys. J. Lett. **432**, L115 (1994)
24. E.J. Wampler, L. Wang, D. Baade, K. Banse, S. D'Odorico, C. Gouiffes, M. Tarenghi: Astrophys. J. Lett. **362**, L13 (1990)
25. K.W. Weiler, S.D. Van Dyk, J.E. Pringle, N. Panagia: Astrophys. J. **399**, 672 (1992)
26. K.W. Weiler, S.D. Van Dyk, M.J. Montes, N. Panagia, R.A. Sramek: Astrophys. J. **500**, 51 (1998)

High-Resolution Radio Imaging of Young Supernovae: SN 1979C, SN 1986J, and SN 2001gd

M.A. Pérez-Torres[1], J.M. Marcaide[2], A. Alberdi[1], E. Ros[3], J.C. Guirado[2], L. Lara[1,4], F. Mantovani[5], C.J. Stockdale[6], K.W. Weiler[6], P.J. Diamond[7], S.D. Van Dyk[8], P. Lundqvist[9], N. Panagia[10], I.I. Shapiro[11], and R. Sramek[12]

[1] IAA - CSIC, Apdo. Correos 3004, 18008 Granada, Spain; torres@iaa.es
[2] Departamento de Astronomía, Universidad de Valencia, 46100 Burjassot, Spain
[3] Max-Planck-Institut für Radioastronomie, 53121 Bonn, Germany
[4] Dpto. de Física Teórica y del Cosmos, Universidad de Granada, Spain
[5] Istituto di Radioastronomia/CNR, via P. Gobetti 101, 40129 Bologna, Italy
[6] Naval Research Laboratory, Code 7213, Washington, DC 20375-5320, USA
[7] MERLIN/VLBI National Facility, Jodrell Bank Observatory, UK
[8] IPAC/Caltech, Mail Code 100-22, Pasadena, CA 91125, USA
[9] Department of Astronomy, AlbaNova 106 91 Stockholm, Sweden
[10] ESA/Space Telescope Science Institute, Baltimore, MD 21218, USA
[11] Harvard-Smithsonian Center for Astrophysics, Cambridge, MA 02138, USA
[12] National Radio Astronomy Observatory, P.O. Box 0, Socorro, NM 87801, USA

Summary. The high resolution obtained through the use of VLBI gives an unique opportunity to directly observe the interaction of an expanding radio supernova with its surrounding medium. We present here results from our VLBI observations of the young supernovae SN 1979C, SN 1986J, and SN 2001gd.

1 Introduction

In the standard model of radio emission from supernovae, a blast wave is driven into an ionized, dense, slowly expanding wind. As a result, a high-energy-density shell is formed. The relativistic electrons present in this shell spiral along the magnetic field and respond for the observed radio synchrotron emission. The supernova quickly increases its radio brightness with time, due to the increasingly smaller electron column density in the line of sight. When the optical depth at cm-wavelengths is about unity, the supernova reaches its maximum of emission, after which the emission monotonically decreases due to expansion losses. Very-Long-Baseline Interferometry (VLBI) observations of radio supernovae are a powerful tool to probe the circumstellar interaction that takes place after a supernova explodes. Indeed, high-resolution radio observations permit us to trace the presupernova mass loss history by directly imaging the structure of the supernova as it expands. The wealth of information includes also a direct estimate of the deceleration of the supernova

expansion, estimates of the ejecta and circumstellar density profiles (which has implications on the progenitor system), distortion of the shock front, and the potential observation of Rayleigh-Taylor instabilities. Unfortunately, the usually large distances to radio supernovae makes their VLBI imaging a challenging task, and only radio supernovae that are young, bright, nearby, and rapidly expanding are appropriate VLBI targets.

2 SN 1979C

SN1979C was discovered on 19 April 1979 in the galaxy M100. It was classified as a Type II Linear supernova, and had an expansion velocity of 9200 km/s, at an age of about 45 days [14]. Its radio emission has been interpreted within the minishell model [3] with some modifications [13]. Recent studies of the environment of the supernova carried out in the optical [20] have put a possible constraint on the mass of the progenitor of 17 to 18 $M_{\odot}$. Previous VLBI observations of SN 1979C did not resolve the radio structure of the supernova [1]. Nevertheless, the modeling of these radio data showed the observations to be consistent with an undecelerated expansion of the supernova ($r \propto t^m, m = 1$) for the first five years.

The radio light curves of SN 1979C are rather odd, showing a wiggling behavior for almost 20 yr. Recently, the radio brightness of SN 1979C has stopped declining (or even started to increase) and has apparently entered a new stage of evolution [13]. This new trend in the radio light curves of SN 1979C is interpreted as being due to the supernova shock wave having entered a denser region of material near the progenitor star.

Prompted by this apparent new trend in the radio light curves of SN 1979C, we observed the supernova on June 1999 with a very sensitive four-antenna VLBI array at a wavelength of 18 cm. Unfortunately, the VLBI array could not fully resolve the radio structure of SN1979C, and we therefore determined model-dependent sizes for the supernova and compared them with previous results. We estimated the size of the supernova by using three different models: First, an optically thick, uniformly bright disk; second, an optically thin shell of width 30% the outer shell radius; and third, an optically thin ring. (We refer the reader to [10] for details of the modeling.) The best-fit model was an optically thin shell model, which has an angular size of 1.80 milliarcseconds for the outer shell supernova radius, corresponding to a linear size of $\sim 4.33 \times 10^{17}$ cm. The combination of our VLBI observations ($t \sim 20$ yr, M02 in Fig. 1) and previous ones [1] ($t \sim 5$ yr, B85 in Fig. 1), plus optical observations [5] at $t \sim 14$ yr (F99 in Fig. 1) allowed us to get an estimate of the epoch at which the deceleration started. We estimate that the supernova shock was initially in free expansion ($m = 1.0$) for the first 6 ± 2 yr and then experienced a very strong deceleration, characterized by a value of the deceleration parameter of $m = 0.62$.

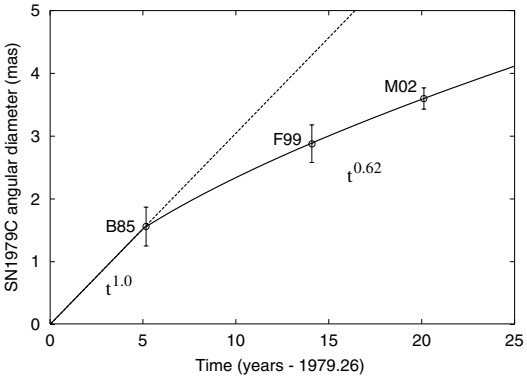

Fig. 1. Angular diameter of SN 1979C, in milliarcseconds, against time since explosion. The solid line indicates a possible expansion, which goes undecelerated ($m = 1$) for the first five years, and strongly decelerated ($m = 0.62$) from then on. See [10] for details.

If this deceleration is solely due to increased resistance from the circumstellar medium (CSM), the mass of the CSM swept up by the shock front, $M_{\rm swept}$, must be comparable to or larger than the mass of ejected hydrogen-rich envelope, $M_{\rm env}$. We estimate $M_{\rm swept} \sim 1.6\,{\rm M}_\odot$, assuming a standard density profile for the CSM ($\rho_{wind} \propto r^{-2}$). Momentum conservation arguments then suggest that the mass of the hydrogen-rich envelope ejected at explosion, $M_{\rm env}$ is no larger than about $0.9\,{\rm M}_\odot$. Those results favor a binary star scenario for SN 1979C, as previously suggested (e.g. [21]). The low value of the hydrogen-rich envelope suggests that the companion of the progenitor star stripped off most of the hydrogen-rich envelope mass of the pre-supernova star prior to the explosion, similar to the situation in SN 1993J.

Another point worth mentioning is the magnetic field in SN 1979C. If we assume equipartition between fields and particles, one expects a minimum magnetic field in the range of 10–80 mG to explain the observed level of radio emission. Since the energy density of the wind magnetic field is not larger than the kinetic energy density in the wind, it follows that $B_w \lesssim (\dot{M} v_w)^{1/2}\, r^{-1}$ for a standard wind. Using a mass-loss rate of $\sim 1.2 \times 10^{-4}$ ${\rm M}_\odot$ ${\rm yr}^{-1}$ for the progenitor of SN 1979C [9, 23] and a standard pre-supernova wind velocity v_w of 10 km ${\rm s}^{-1}$, we obtain $B_w \lesssim 0.2\,{\rm mG}$, which is a factor of 50–400 lower than needed. Therefore, if particles and fields are not very far from equipartition, then compression of the wind magnetic field due to the passage of the supernova shock is not enough to explain the high magnetic fields in the supernova, and another amplification mechanism must be acting. Turbulent amplification, as seems to be the case of SN1993J [15], is likely the most promising mechanism.

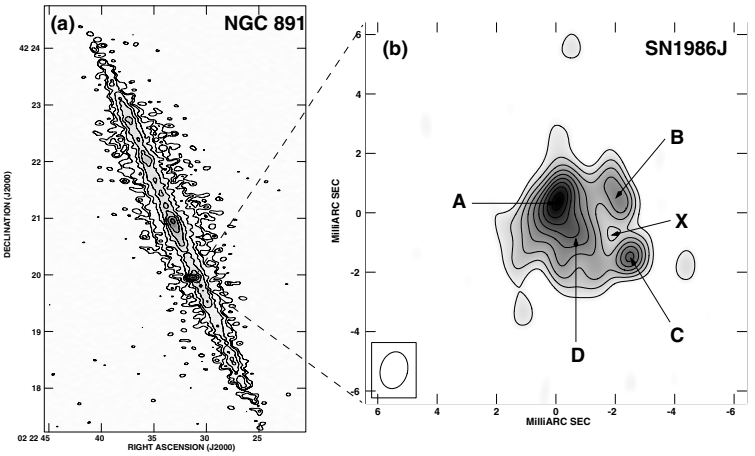

Fig. 2. VLA image (left) of the galaxy NGC 891 and its supernova SN 1986J, at the same frequency (5 GHz) and epoch of the global VLBI observations (right). See [15] for details.

3 SN 1986J

The type II SN 1986J exploded in the galaxy NGC891 ($D \approx 10$ Mpc). Unlike most supernovae, it was serendipitously discovered in the radio more than three years after the explosion. Modeling of the existing observations set the time of the explosion at the end of 1982 or the beginning of 1983 [17, 22]. The supernova reached a peak luminosity at $\lambda 6$ cm of about 8 times larger than that of SN 1979C, and about 13 times larger than the peak for SN 1993J, becoming one the brightest radio supernovae ever. Based upon its large radio luminosity, the progenitor star was probably a red giant with a main-sequence mass of $20 - 30$ $M_\odot$ that had lost material rapidly ($\dot{M} \gtrsim 2 \times 10^{-4}$ $M_\odot$ yr^{-1}) in a dense stellar wind [22].

VLBI observations made at $\lambda 3.6$ cm at the end of 1988 showed a shell-like structure for SN 1986J [2]. The authors claimed the existence of several protrusions at distances of twice the shell radius, and with apparent expansion velocities as high as ~ 15000 km s^{-1}. Since these protrusions were twice as far as the mean radius of the shell, it then follows that the main bulk of the shell expanded at roughly 7500 km s^{-1}. Such protrusions have been successfully invoked [4] to explain the coexistence of velocities smaller than 1000 km s^{-1} implied from the observed narrow optical lines [8, 17], and the large velocities indicated from the VLBI measurements.

We used archival VLA and global VLBI observations of supernova 1986J at $\lambda 6$ cm, taken about 16 yr after the explosion, to obtain the images shown in Fig. 2 (see [16] for a comprehensive discussion). The right panel corresponds to the $\lambda 6$ cm VLBI image of SN1986J. It shows a highly distorted

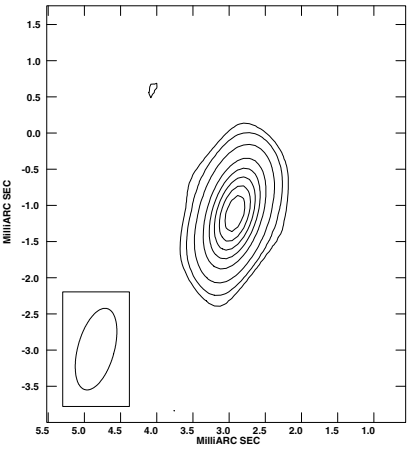

Fig. 3. Radio image of SN 2001gd obtained with GBT+Effelsberg+VLBA on 26 June 2002 (total flux $\sim$ 3.9 mJy; peak $\sim$ 3.3 mJy beam^{-1}; rms noise $\sim$ 20μJy; beam 1.16 $\times$ 0.50 mas, P.A. $\sim -15^{\circ}$).

shell of radio emission, indicative of a strong deformation of the shock front. The apparent anisotropic brightness distribution is very suggestive of the forward shock colliding with a clumpy, or filamentary wind. Note that there are several "protrusions" outside the shell, though just above three times the noise level and at different position angles from those previously reported [2]. Therefore, these protrusions could not be real, but must be just artifacts of the image reconstruction procedure. If this is the case, the disappearance of the protrusions seen in the previous VLBI observations [2] would imply a change in the density profile of the circumstellar wind.

The angular size of the shell of SN 1986J on 21 February 1999 is $\sim$4.7 mas, corresponding to a linear size of 0.22 pc at the distance of SN 1986J. Therefore, the average speed of the shell has decreased from around 7500 km s^{-1} at the end of 1988 down to about 6300 km s^{-1} at the beginning of 1999, indicating just a mild deceleration in the expansion of the supernova ($m \approx 0.90$). We find a swept-up mass by the shock front of $\sim$ 2.2 M$_{\odot}$ for a standard wind density profile. This large swept-up mass, coupled with the mild deceleration suffered by the supernova, suggests that the mass of the hydrogen-rich envelope ejected from the explosion was as large as $\sim$ 12 M$_{\odot}$. This enormous value strongly indicates that the supernova progenitor likely kept intact most of its hydrogen-rich envelope by the time of explosion, and favors a single, massive star progenitor scenario for SN 1986J.

We found a minimum total energy for the supernova (at the epoch of our VLBI observations) in the range $(2 - 90) \times 10^{48}$ erg, depending on the ratio of the heavy particle energy to the electron energy. The corresponding values for the magnetic field should then lie in the range (13 – 90) mG, while the

Table 1. VLBI results for radio supernovae

	SN 1979C	SN 1986J	SN 2001gd	SN 1993J
Distance (Mpc)	16.1 ± 1.3	9.6	21.6?	3.63 ± 0.34
Time since explosion[1](yr)	~ 20.1	~ 16	$\lesssim 1$	~ 8.6
$(L/L_{\rm SN\ 1993J})_{\rm 6cm\ peak}$	~ 1.6	~ 13	~ 2	1
Optically thin phase?	Yes	Yes	Likely yes	Yes
Radio brightness structure	Shell (likely)	Distorted shell	?	Smooth shell
$\dot{M}/10^{-5}$ M$_\odot$ yr^{-1}	$\sim (12-16)$	~ 20	?	~ 5
Deceleration parameter (m)	~ 0.62	~ 0.90	?	~ 0.82
$t_{\rm break}$ (years)	6 ± 2	Not yet	?	~ 0.5
Asymmetric expansion?	No	Yes	?	No ($\lesssim 5\%$)
Circumstellar medium	?	Clumpy	?	Approx. smooth
$M_{\rm swept}/\dot{M}$	~ 1.6	~ 2.2	?	~ 0.4
$M_{\rm env}/\dot{M}$	~ 0.9	~ 12	?	~ 0.6
Explosion scenario	Binary	Single	?	Binary
Magnetic field amplification	Turbulent?	Turbulent?	?	Turbulent?

[1]Time since explosion when the VLBI observations were carried out. The tabulated entries below refer to that time.

circumstellar wind magnetic field cannot exceed ~ 0.3 mG, i.e., it is 40 to 300 times smaller than necessary to explain the observed radio emission. As in the case of SN 1979C, turbulent amplification seems the most promising mechanism.

4 SN 2001gd

SN 2001gd was discovered on 24 November 2001 in the galaxy NGC 5033 [6], but its exact explosion date is uncertain. A spectrum of SN 2001gd showed the supernova to be a type IIb event well past maximum light [12]. The spectrum was almost identical to one of SN 1993J obtained on day 93 after explosion [11]. The similarities of the optical spectra of SN 2001gd and SN1993J drove us to observe SN 2001gd at the beginning of February 2002 with the VLA [18]. These and subsequent VLA observations confirmed the suggestion that SN 2001gd was a SN 1993J-like event, displaying a $\lambda 6$ cm peak luminosity of about twice that of SN 1993J [19].

We carried out high resolution VLBI observations of SN 2001gd at $\lambda 3.6$ cm, aimed at resolving the supernova structure. Figure 3 shows the image of SN 2001gd obtained from our VLBI observations on June 2002. Since the VLBI observations did not resolve the radio structure of SN 2001gd, we determined an angular size for the supernova using model-dependent estimates. We used the same three models as for SN 1979C. However, none of the models was favored at this stage and we only inferred an upper limit on the expansion speed of the radio photosphere, which should lie in the range ~ 23000 km s^{-1} to ~ 26000 km s^{-1} at the epoch of our observations

($\sim$ 306 days after explosion) and for an assumed distance to the supernova of 21.6 Mpc.

We plan to follow the evolution of this "twin" of SN 1993J via VLBI observations of SN 2001gd, the first radio supernova for which such monitoring is possible since the SN 1993J event in M 81. Those future observations will likely allow us to determine the deceleration and degree of self-similarity of the supernova expansion, constrain the range of density profiles for the supernova progenitor and the pre-supernova wind, and disentangle its radio emitting structure as it interacts with the circumstellar medium.

We summarize in Table 1 below the most remarkable results obtained from VLA and VLBI studies conducted on the radio supernovae we have discussed here and, for comparison, those obtained on SN1993J (see Alberdi & Marcaide in these Proceedings).

Acknowledgement. MAPT, AA, and ER thank the organizers for funding to attend the conference. This research has been supported by the Spanish DGICYT grants AYA2001-2147-C02-01 and AYA2001-2147-CO2-02. KWW wishes to thank the Office of Naval Research for the 6.1 funding supporting this research.

References

1. N. Bartel et al. : Nature **318**, 25 (1985)
2. N. Bartel et al. : Nature **350**, 212 (1991)
3. R.A. Chevalier: Astrophys. J. **258**, 790 (1982)
4. N.N. Chugai & M.L. Belous: Astron. Rep. **43**, 89 (1999)
5. R.A. Fesen et al. : Astron. J. **117**, 725 (1999)
6. K. Itagaki: IAUC 7761 (2001)
7. R. Kushida: IAUC 7761 (2001)
8. B. Leibundgut et al. : Astrophys. J. **372**, 531 (1991)
9. P. Lundqvist & C. Fransson: Astron. Astrophys. **192**, 221 (1988)
10. J.M. Marcaide et al. : Astron. Astrophys. **384**, 408 (2002)
11. T. Matheson et al. : Astron. J. **120**, 1487 (2000)
12. T. Matheson et al. : IAUC 7765 (2001)
13. M.J. Montes et al. : Astrophys. J. **532**, 1124 (2000)
14. N. Panagia et al. : Mon. Not. R. Astron. Soc. **192**, 861 (1980)
15. M.A. Pérez-Torres, A. Alberdi & J.M. Marcaide: Astron. Astrophys. **374**, 997 (2001)
16. M.A. Pérez-Torres et al. : Mon. Not. R. Astron. Soc. **335**, L23 (2002)
17. M.P. Rupen et al. : Astron. J. **94**, 61 (1987)
18. C.J. Stockdale et al. : IAUC 8018 (2002)
19. C.J. Stockdale et al. : Astrophys. J. **592**, 900 (2003)
20. S.D. Van Dyk et al. : Pub. Astron. Soc. Pacific **111**, 313 (1999)
21. K.W. Weiler et al. : Astrophys. J. **301**, 790 (1986)
22. K.W. Weiler, N. Panagia, & R.A. Sramek: Astrophys. J. **364**, 611 (1990)
23. K.W. Weiler et al. : Astrophys. J. **380**, 161 (1991)

VLBI Observations of SN 1979C and SN 1986J

N. Bartel and M.F. Bietenholz

York University, Toronto, Canada,
bartel@yorku.ca

Summary. We summarize our results on multi-epoch VLBI observations of SN 1979C in the galaxy M100 in Virgo, and of SN 1986 in the galaxy NGC 891. From $t = 3.7$ to 22 yr after the explosion, SN 1979C expands $\propto t^m$, almost freely, with $m = 0.95 \pm 0.03$. For a total kinetic energy of 3×10^{51} erg, the expansion result requires a mass-loss to wind-velocity ratio for the progenitor of only 1×10^{-5} $M_\odot$ yr^{-1}per 10 km s^{-1}, an order of magnitude smaller than estimated from radio light-curve fitting. We show a first image with slightly discernible structure of the supernova. For SN 1986J we present five images from 1987 to 2002 and show our result on moderately to strongly decelerated expansion with $m = 0.71 \pm 0.11$. We comment on our result of an inversion of the radio spectrum in terms of the emergence of a possible pulsar nebula.

The supernovae, SN 1979C [3] and SN 1986J [4] are, after SN 1993J , the next most comprehensively monitored radio supernovae with VLBI to date.

SN 1979C: In Fig. 1 we show a radio image of M100 with SN 1979C located at the southern edge of a spiral arm. We also show an image of SN 1979C at $t = 22$ yr after the explosion revealing for the first time structure, namely along the minor axis of the beam. SN 1979C was the first supernova whose radius and expansion could be determined with VLBI [2]. Our latest results (Fig. 2) show an expansion of the size $\propto t^m$ which is, with $m = 0.95 \pm 0.03$, almost consistent with being free. This result is in conflict with a recent report of strong deceleration starting at $t = 6 \pm 2$ yr [5]. For our solution for m, the ratio of the mass of the shocked ejecta to that of the swept up wind, $M_{\rm shock-ej}/M_{\rm sw} = 7^{+13}_{-3}$ for a density profile of the circumstellar medium (CSM) of $\rho_{CSM} \propto r^{-2}$. With the mass-loss to wind-velocity ratio taken from radio light-curve fits of $\dot{M}_w/w = 1.6{\times}10^{-4}$ $M_\odot$ yr^{-1} per 10 km s^{-1} [6], we get $M_{\rm shock-ej} = 25^{+50}_{-10}$ $M_\odot$ at $t = 22$ yr. This value is excessively large. In fact, with the velocity derived from the expansion curve, we get for the kinetic energy of the shells of the shocked ejecta and the shocked CSM, $E_{\rm kin,shock} = 1.5^{+3}_{-0.5}{\times}10^{52}$ erg. The total kinetic energy, including the kinetic energy of the unshocked ejecta, is even larger, about a factor of three.

With the explosion energy for a type II supernova of $\sim 3{\times}10^{51}$ erg, we can assume a typical value for $E_{\rm kin,shock}$ of $\sim 1{\times}10^{51}$ erg. We therefore think that $\dot{M}_w/w \sim 1{\times}10^{-5}$ $M_\odot$ yr^{-1} per 10 km s^{-1}. This value is about an order of magnitude smaller than that estimated from radio light-curve fitting. Values

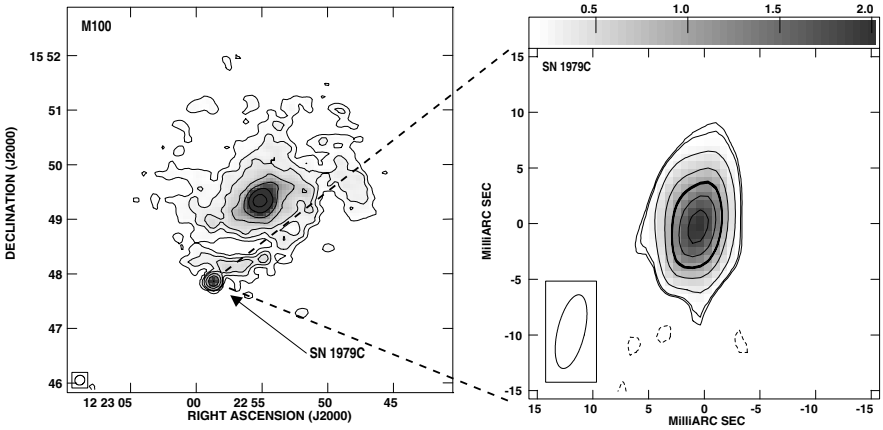

Fig. 1. Left panel: VLA image of the spiral galaxy M100 in the Virgo cluster with SN 1979C in it, at 1.7 GHz on 1996 March 15. Right panel: VLBI image of SN 1979C at 1.7 GHz on 2001 February 24. The beam (FWHM, 6.8 mas × 2.4 mas at a p.a. of −14 deg) is shown at lower left. The grey scale is labeled in mJy beam^{-1}.

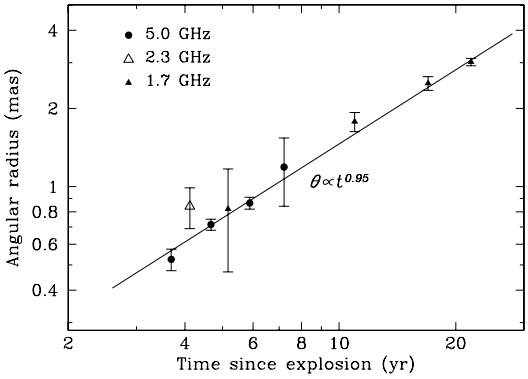

Fig. 2. The expansion of the angular radius, θ, of a uniform sphere model fit to the u-v data. The solid line gives the weighted least-squares power-law fit.

of $\dot{M}_w/w$ obtained from radio light-curve fitting should therefore be treated with caution.

The Expanding Shock Front Method (ESM) of combining the transverse radio expansion velocities with the radial optical velocities gives direct distance estimates, with standard errors, of 16.5 ± 2.5 to 19.8 ± 3.0 Mpc depending on whether the supernova has a bright center or is a shell without such a center.

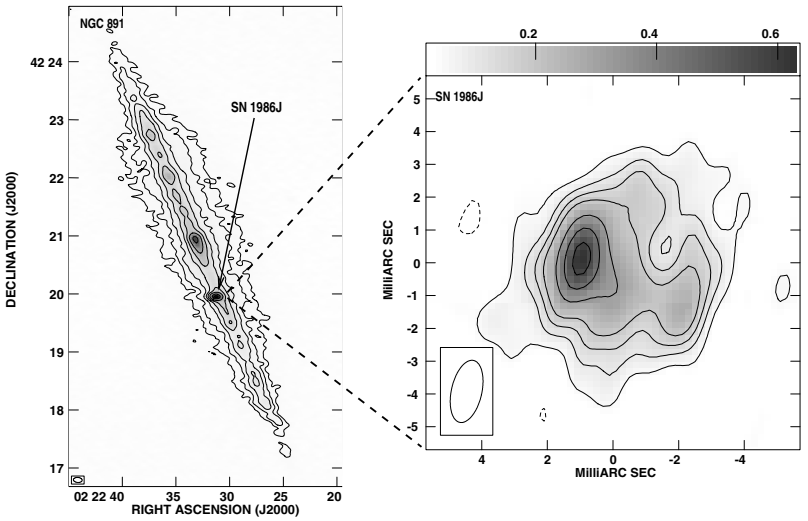

Fig. 3. Left panel: VLA image of NGC 891 with SN 1986J in it, at 5 GHz on 1999 February 22. Right panel: VLBI image of SN 1986J at 5.0 GHz at epoch 2002 November 11. The beam is shown at lower left. The grey scale is labeled in mJy beam^{-1}. In addition, contours are drawn at -7.4, 7.4, 10, 15, 20, 25, 30, 40, 50, 70, and 90% of the peak brightness of 0.57 mJy beam^{-1}.

SN 1986J: In Fig. 3 we show a radio image of the edge-on galaxy NGC 891 with SN 1986J located prominently in the southwestern part of it. We also show the latest image of SN 1986J at $t = 20$ yr, which reveals the complex structure of the supernova.

The full sequence of one model and four subsequent images is displayed in Fig. 4. The source structure is rather complex. It may be a composite with large brightness modulations across the source and with protrusions. Apart from an early high-resolution image [1], Fig. 5 gives the best indication so far that some components of shell structure are present.

The radio spectrum (Fig. 6, left panel) is inverted above ~ 10 GHz and may indicate the emergence of a pulsar nebula. Perhaps component C1* in Fig. 5 is a candidate for such a nebula. The expansion (Fig. 6, right panel) is moderately to strongly decelerated with $m = 0.71 \pm 0.11$. Note, that this result is in conflict with that reported by [7].

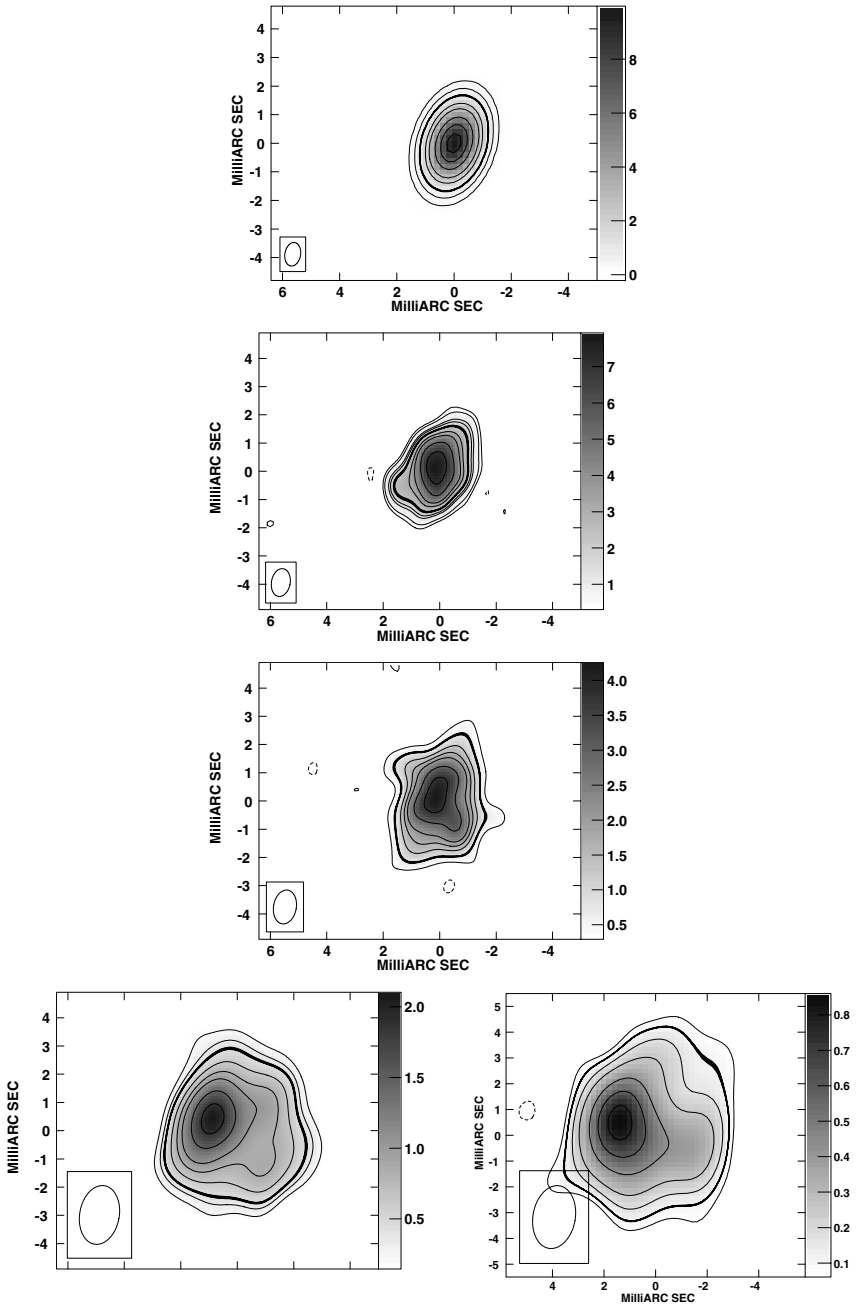

Fig. 4. One model (first panel, 1987 Feb., 10.7 GHz) and four images (1988 Sep., 8.4 GHz; 1990 Jul., 8.4 GHz; 1999 Feb., 5.0 GHz; 2002, Nov., 5.0 GHz) of SN 1986J. The heavier contour is that which contains 90% of the flux density. The brightness is given on the right margin in each panel in mJy beam^{-1}. The dynamically evolving beam is given in the lower left.

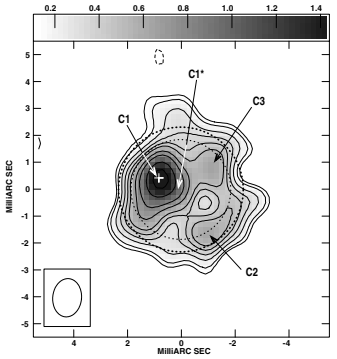

Fig. 5. VLBI image of SN 1986J at 5.0 GHz at epoch 1999 February 22. Contours are drawn at −7.4, 7.4, 10, 15, 20, 25, 30, 40, 50, 70, and 90% of the peak brightness of 1.64 mJy beam^{-1}. The dotted circles indicate the inner and outer radii of a spherical shell fit to the u-v data. Note, that the brightest portion of a projected shell of uniform volume emissivity is along the inner circle. See [7] for an independent analysis of our observations.

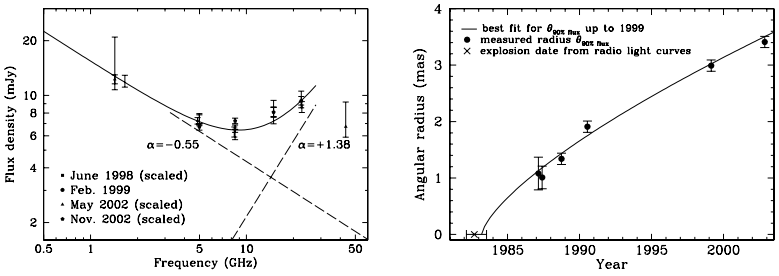

Fig. 6. Left panel: The radio spectrum of SN 1986J. The measurements in 1998 and 2002 were scaled to those of 1999. The dashed lines show the decomposition into two spectral power-law components. Right panel: An expansion power-law fit to all but the last measurements (from 90% flux density contours).

References

1. N. Bartel, M.P. Rupen, I.I. Shapiro, R.A. Preston, A. Rius: Nature **350**, 212 (1991)
2. N. Bartel, A.E.E. Rogers, I.I. Shapiro, M.V. Gorenstein, C.R. Gwinn, J.M. Marcaide, and K.W. Weiler: Nature **318**, 25 (1985)
3. N. Bartel and M.F. Bietenholz: Astrophys. J. **591**, 301 (2003)
4. M.F. Bietenholz, N. Bartel, M.P. Rupen: Astrophys. J. **581**, 1132 (2002)
5. J.M. Marcaide et al. : Astron. Astrophys. **384**, 408 (2002)
6. M.J. Montes, K.W. Weiler, S.D. Van Dyk, N.Panagia, C.K. Lacey, R.A. Sramek, R. Park: Astrophys. J. **532**, 1124 (2000)
7. M.A. Pérez-Torres, A. Alberdi, J.M. Marcaide, J.C. Guirado, L. Lara, F. Mantovani, E. Ros, K.W. Weiler: Mon. Not. R. Astron. Soc. **335**, L23 (2002)

SN 1994W: Evidence of Explosive Mass Ejection a Few Years Before Explosion

Nikolai N. Chugai[1], Robert J. Cumming[2], Sergei I. Blinnikov[3], Peter Lundqvist[2], Alexei V. Filippenko[4], Aaron J. Barth[4], Angela Bragaglia[5], Douglas C. Leonard[6], Thomas Matheson[7], and Jesper Sollerman[2]

[1] Institute of Astronomy, RAS, Pyatnitskaya 48, 109017 Moscow, Russia; nchugai@inasan.rssi.ru
[2] Stockholm Observatory, AlbaNova University Center, 106 61 Stockholm, Sweden. robert@astro.su.se, peter@astro.su.se
[3] ITEP, 117218 Moscow, Russia. blinn@sai.msu.su
[4] Department of Astronomy, University of California at Berkeley, Berkeley, CA 94720-3411, USA.
[5] Osservatorio Astronomico di Bologna, via Ranzani 1, 40127 Bologna, Italy
[6] Department of Astronomy, University of Massachusetts, 710 North Pleasant Street, Amherst, MA 01003-9305, USA.
[7] Harvard-Smithsonian Center for Astrophysics, Mail Stop 20, 60 Garden Street, Cambridge, MA 02138, USA.

Summary. We present and analyze spectra of the Type IIn supernova 1994W obtained between 18 and 202 days after explosion. During the first 100 days the line profiles are composed of three major components: (i) narrow P Cygni lines with absorption minima at -700 km s^{-1}; (ii) broad emission lines with blue velocity at zero intensity ~ 4000 km s^{-1}; (iii) broad, smooth, extended wings most apparent in Hα. These components are identified with the expanding circumstellar (CS) envelope [5], shocked cool gas in the forward postshock region, and multiple Thomson scattering in the CS envelope, respectively. The absence of broad P Cygni lines from the supernova (SN) is the result of the formation of an optically thick, cool, dense shell at the interface of the ejecta and the CS envelope. Models of the SN deceleration and Thomson scattering wings are used to recover the Thomson optical depth of the CS envelope, $\tau_{\rm T} \geq 2.5$ during first month, its density ($n \sim 10^9$ cm^{-3}) and radial extent, $\sim (4-5)\times 10^{15}$ cm. The plateau-like SN light curve, which we reproduce by a hydrodynamical model, is powered by a combination of internal energy leakage after the explosion of an extended presupernova ($\sim 10^{15}$ cm) and subsequent luminosity from circumstellar interaction. We recover the pre-explosion kinematics of the CS envelope and find it to be close to homologous expansion with outmost velocity ≈ 1100 km s^{-1} and a kinematic age of ~ 1.5 yr. The high mass ($\approx 0.4\ M_\odot$) and kinetic energy ($\approx 2\times 10^{48}$ erg) of the CS envelope combined with small age strongly suggest that the CS envelope was explosively ejected only a few years before the SN explosion.

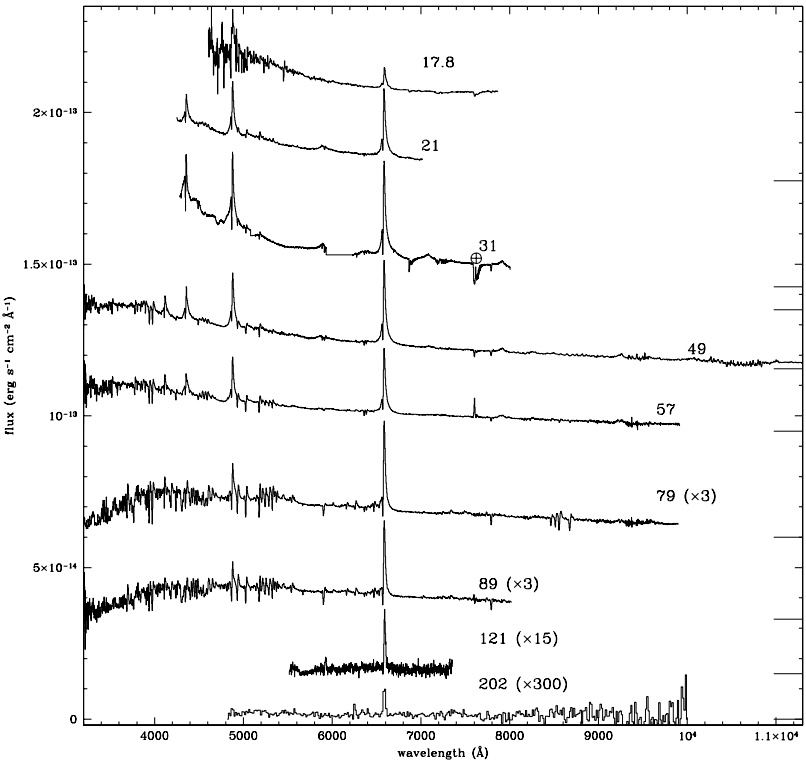

Fig. 1. Spectra of SN 1994W: days 18-202. The spectra have been shifted vertically for clarity. The ticks on the right hand side mark the zero level for each. The spectra from day 79 and later have been multiplied by a constant, noted in brackets. Note the change in relative intensity of the Balmer lines, a sign of temperature evolution.

1 Introduction

Type IIn supernovae are believed to arise from massive stars exploding into a dense circumstellar environment. Often highly luminous, they offer us an intriguing new window on the final stages of the progenitor's evolution.

SN 1994W, discovered on 1994 July 29 in NGC 4041, was a luminous Type IIn supernova whose light curve dropped dramatically at 110 days. The low luminosity after this point has been used to derive a very low mass of nickel in the ejecta ($M_{\rm Ni}$ <0.003 $M_\odot$; [5]). In a forthcoming paper [2], we present and analyze all the SN 1994W spectra and model the circumstellar interaction.

2 Observations

The spectra were taken between 1994 July and 1995 February using BFOSC on the BAO 1.5-m telescope, the IDS on the Isaac Newton Telescope, ISIS

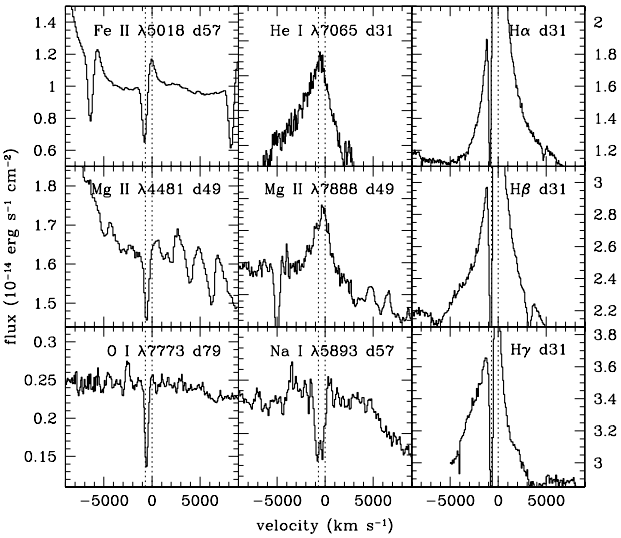

Fig. 2. Selected line profiles. The left hand panel shows examples of narrow P Cygni profiles, the middle panel shows broad lines (note the extended wings in Na I on day 57), and the right hand panel shows the wings of the H I lines on day 31. The dotted vertical lines mark velocities of 0 and -700 km s^{-1}.

on the William Herschel Telescope (La Palma), the Kast spectrograph at Lick Observatory's Shane 3-m reflector, and the LDS at the Nordic Optical Telescope on La Palma.

3 Spectral Evolution

No broad ejecta absorption lines are seen (Fig. 1). Together with high luminosity at maximum, this suggests an extended progenitor interacting with a circumstellar (CS) envelope, and the presence of a cool dense shell (CDS), which should form in SN II with extended envelopes [3, 4].

The spectra show persistent narrow P Cygni lines of H I with broad bases (Fig. 2). Triangular profiles with $v_{\rm FWHM} \sim 2500$ km s^{-1} are seen in He I and Mg II. Black body fits to the continuum show that the temperature declines from 15000 K on day 31 to 7200 K on day 89. From day 121 onward, only narrow emission lines are clearly seen.

We see broad lines with maximum velocity 4000 km s^{-1}, which we take to be the expansion velocity of the CDS. We think the broad lines come from Rayleigh-Taylor fingers from the interface of the radiative forward shock and the CS envelope (Fig. 3). The persistent, narrow P Cygni lines with maximum blue velocity 1100 km s^{-1} indicate the maximum velocity of the circumstellar envelope, which is overrun by the ejecta at 110 days. Broad wings on H I,

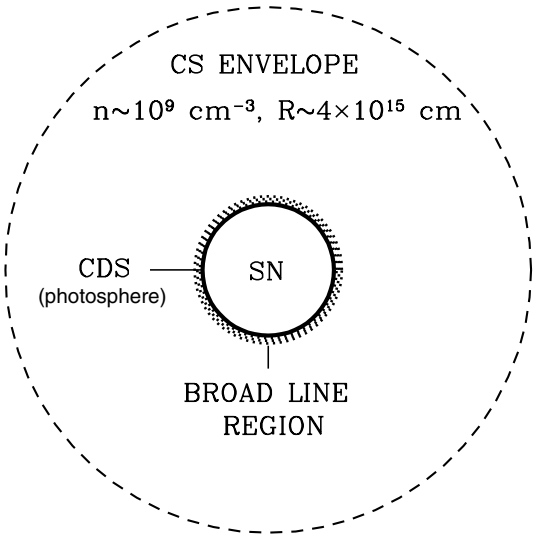

Fig. 3. A visualization of SN 1994W at around day 30. The SN ejecta is bounded by an opaque cool dense shell (CDS), which is responsible for the continuum radiation. The broad line region is a narrow mixing layer attached to the CDS, made up of Rayleigh-Taylor fragments of the CDS matter and possibly of shocked CS clouds. The SN ejecta expands into a dense CS envelope with Thomson optical depth of order unity. The CS envelope is responsible for both narrow lines and the extended Thomson wings seen in Hα.

and nearly inverse Balmer decrement on day 31 point to a high optical depth for Thomson scattering, from which we estimate that the density in the CS envelope is as high as $\sim 10^9$ cm^{-3}.

4 Light Curve Models

We model the broad band light curves using the multi-energy group radiation hydrodynamic code STELLA. The best fit model is for a 1.5×10^{51} erg explosion, $M_{\rm Ni}$ =0.015 M$_\odot$ and $M_{\rm ej}$ = 7 M$_\odot$ ejecta, with circumstellar envelope extending out to $R_{\rm out} = 4.5 \times 10^{15}$ cm (Fig. 4). A similar model, with the same bulk mass but no CS envelope, fails to reproduce the bright plateau up to 110 days.

5 Hα Profile Model

We have also modeled the evolution of the Hα line profile. The CS envelope is ionized by radiation from the forward shock, leading to line emission from

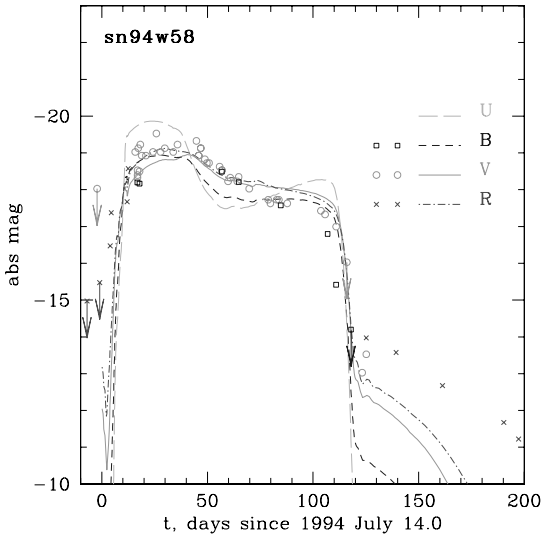

Fig. 4. Light curves for a model of SN 1994W characterized by $E = 1.5 \times 10^{51}$ erg, $M_{\rm Ni} = 0.015$ $M_\odot$ and $M_{\rm ej} = 7$ $M_\odot$.

recombination and collisional excitation. Our best fit is for a model with free expansion in the CS envelope and a boundary velocity of 1100 km s^{-1}. This suggests a mass ejection ∼1.5 yr before explosion.

Some SN IIn seem to be due to interaction with a superwind. SN 1994W, on the other hand, like SN 1995G [1], seems instead to have been preceded by a violent ejection event shortly before explosion, perhaps due to a Ne flash [1, 6].

References

1. N.N. Chugai, I.J. Danziger: astro-ph 0306330)
2. N.N. Chugai et al. : In preparation
3. S.W. Falk, W.D. Arnett: Astrophys. J. Suppl. **33**, 515 (1977)
4. E.K. Grasberg, V.S. Imshennik, D.K. Nadyozhin: Astrophys. Space Sci. **10**, 28 (1971)
5. J. Sollerman, R.J. Cumming, P. Lundqvist: Astrophys. J. **493**, 933 (1998)
6. S.E. Woosley, T.A. Weaver: Ann. Rev. Astron. Astrophys. **24**, 205 (1986)

A Most Energetic Type Ic Supernova: SN 2003L

Alicia M. Soderberg

Palomar Observatory, 105-24, California Institute of Technology, Pasadena, CA 91125, USA;
ams@astro.caltech.edu

Summary. We present extensive radio observations of SN2003L, the most luminous and energetic Type Ic radio supernova with the exception of SN 1998bw. Using radio data, we are able to constrain the physical parameters of the supernova, including the velocity and energy of the fastest ejecta, the temporal evolution of the magnetic field, and the density profile of the surrounding medium. We highlight the extraordinary properties of the radio emission with respect to the supernova's normal characteristics within optical bands. We find that although the explosion does not show evidence for a significant amount of relativistic ejecta, it produces a radio luminosity which is comparable to that seen in the unusual SN1998bw. Using SN2003L as an example, we comment briefly on the broad diversity of type Ic properties and the associated implications for progenitor models.

1 Introduction

Despite active campaigns to study radio emission from type Ib/c supernovae, only a small number of events have been successfully detected. Among the class of radio bright supernovae is SN1998bw, an unusually bright type Ic discovered within the error box of the nearby gamma-ray burst GRB 980425. Reaching a peak radio luminosity ~ 100 times higher than all other radio bright type Ib/c supernovae (SNe), it has been proposed that SN1998bw was powered by a central engine, similar to the popular model for gamma-ray bursts (GRBs) [3].

In this paper we present observations of the first radio bright type Ib/c supernova with energetics comparable to those shown in SN1998bw. SN2003L was optically discovered on 2003 Jan 12.15 UT [2] and spectroscopically identified on 2003 Jan 25.0 UT [5, 8]. The supernova was seen to bear strong resemblance to the typical type Ic SN1994I at maximum light, showing low average expansion velocities of 5900 km/s as derived from the Si II line. The optical lightcurve peaks at $m_V \approx 16$ which places SN2003L among the brightest optical type Ic's observed to date.

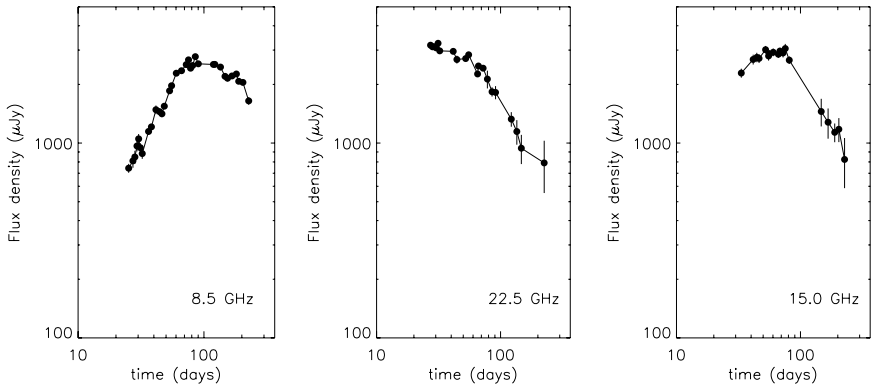

Fig. 1. Radio lightcurves for type Ic SN 2003L at 8.5, 15., and 22.5 GHz for the time period 2003 Jan 26 - 2003 Aug 15 UT.

2 Observations with the VLA

On 2003 Jan 26.23 UT we detected a radio transient coincident with the optical position of SN2003L. We subsequently initiated an intense radio monitoring campaign at the Very Large Array (VLA) to trace the evolution of the radio emission from the supernova. Data were taken in standard continuum observing mode with a bandwidth of 2×50 MHz centered on frequencies 8.5, 15.0 and 22.5 GHz. Flux density measurements were derived using calibrator 3C286 and phase referenced against calibrators J1118+125, J1120+134, and J1103+119. Data were reduced using standard packages within the Astronomical Image Processing System (AIPS). At 8.5 GHz (our most densely sampled light-curve) typical flux uncertainties were ~ 60 μJy for an average integration time of 10 minutes. The results of our radio monitoring campaign of SN2003L are summarized as Fig. 1. These observations demonstrate a broad spectrum, similar to that observed for SN 1998bw.

3 Robust Constraints

Here we discuss the constraints imposed by the radio observations for SN2003L. As a preliminary constraint on the total energy of the source, we estimate the brightness temperature (T_b) of the supernova and compare it with the robust constraints imposed by equipartition arguments and the inverse Compton catastrophe (ICC). From [6], the brightness temperature is defined as a function of the observed flux density, the peak frequency, and the angular size of the source. As an initial estimate for the physical size of the SN ejecta, we first assume the optical expansion velocity of 5900 km s^{-1} [8] can be used as an average speed to describe the motion of the radio bright

ejecta. Using an approximate explosion date of 2003 Jan 1 UT based on optical light-curves [7], we estimate the shock radius to be $r \approx 4.3 \times 10^{15}$ cm at $t \approx 85$ days when the observed flux density peaked at 8.5 GHz. Using the observed peak flux of $F_{8.5\ \mathrm{GHz}} \approx 2.8$ mJy and adopting a source distance of 91.7 Mpc ($\Omega_M = 0.27$, $\Omega_\Lambda = 0.73$, $H_0 = 71$ km s^{-1} Mpc^{-1}), we find a brightness temperature of $T_b \approx 1.8 \times 10^{12}$ K which is dangerously near the ICC limit of $T_b < 10^{12}$ K. This suggests that the radio ejecta expanded with a velocity significantly higher than that observed at optical frequencies. In fact, an ejecta velocity of $\sim 16,000$ km s^{-1} (~ 3 times larger than that derived from optical spectroscopy) would be necessary to avoid violating the ICC constraint.

Assuming equipartition of energy places a further constraint on the brightness temperature limit and reduces it to $T_b < 5 \times 10^{10}$ K. Using the equipartition arguments of [6] and [3], we derive the minimum energy for the radio supernova. Assuming that the observed radio flux is produced by synchrotron emission, the total energy of the source (U) can be expressed as the sum of the energy in relativistic electrons (U_e) and the energy in the magnetic field (U_B). At equipartition, the fraction of total energy in electrons equals the fraction of total energy in magnetic fields ($\epsilon_e = \epsilon_B = 1$) and the total energy is minimized at U_eq [6]. This occurs when the emitting source reaches an equipartition radius denoted by the angular size, θ_eq. The minimum energy of the source can be thus be parameterized in terms of the synchrotron peak flux and the equipartition size.

Using our most densely sampled light-curve, we fit for the peak flux (S_p) over the observed ~ 200 day evolution and find $S_p \approx 2.8$ mJy at $\nu_p = 8.5$ GHz on 2003 Mar 27 UT (≈ 85 days since explosion). For this epoch we estimate an angular size $\theta_\mathrm{eq} \approx 19\mu$as (with $\beta \approx -1.0$) which implies an average shock velocity of $v \approx 0.1c$ and an equipartition brightness temperature of $T_{b_\mathrm{eq}} \approx 5.0 \times 10^{10}$ K. By setting $U = U_\mathrm{eq}$ we find the energy is minimized at the equipartition value of $U_\mathrm{eq} \approx 4.3 \times 10^{47}$ erg with an associated magnetic field strength of $B_{p_\mathrm{eq}} \approx 0.6$ G. As shown by [6], synchrotron emission systems which diverge from equipartition necessitate a huge increase in total energy. Consequently, it is possible that the total energy contained within the fast moving ejecta of SN2003L is in fact much larger than 4.3×10^{47} ergs.

These preliminary constraints allow us to make two robust conclusions:

1. The velocity of the radio bright SN ejecta must be at least 16,000 km s^{-1} to avoid violating the inverse Compton catastrophe limit and $\sim 30,000$ km s^{-1} assuming equipartition.
2. The energy of the supernova must be $> 4.3 \times 10^{47}$ erg and could be significantly larger depending on the proximity of the system to equipartition.

These conclusions imply that there was a considerable amount of energy released at high velocities in the type Ic supernova explosion of SN2003L. In fact, these equipartition constraints alone demand that SN2003L is among the

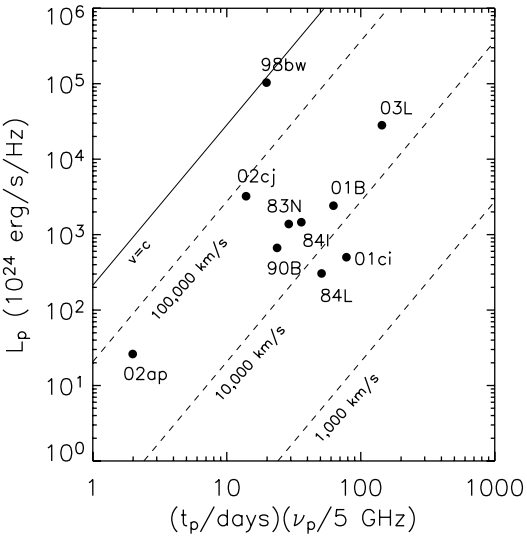

Fig. 2. The diversity of peak luminosities and observed time of the peak is shown above for all radio bright type Ib/c supernova. By assuming equipartition, the expansion velocity for each event can be estimated (dashed lines). Note the radio ejecta of SN2003L is relatively slow and luminous.

most energetic type Ib/c supernovae observed to date, second only to the unusual event of SN1998bw/GRB980425. Fig. 2 is a compilation of all the radio bright type Ib/c supernovae observed to date. By comparing the peak radio luminosity to the observed time of peak flux, the diversity in equipartition derived expansion velocities can be examined. Note that although SN2003L peaks later, it is among the brightest radio supernovae.

4 Implications and Physical Parameters

Assuming equipartition values of $\epsilon_B = \epsilon_e = 1$ and adopting synchrotron self-absorption as the dominant absorption process, we determine the temporal evolution of the total energy and radius of the ejecta for SN2003L. For observations spanning $t = 25 - 200$ days, the total energy increases from $E \approx 3.0 \times 10^{47}$ to 1.1×10^{48} ergs. Over the same period, the shock radius scales as $r \propto t^{0.67}$ from $r \approx 1.45 \times 10^{16}$ to 5.0×10^{16} cm. Assuming an explosion date of 2003 Jan 1 UT, the average velocity decreases from $v \approx 0.22c$ to $0.10c$. In comparison to SN1998bw where it was observed that $v \approx c$, it is clear that SN 2003L does not have a significant amount of material moving at relativistic speeds. However, the total energy within the radio bright ejecta remains quite high at $\sim 10\%$ that of SN1998bw (on similar timescales) and $10 - 100$ times greater than other radio supernovae.

Using the values derived for the total energy and radius, we predict the magnetic field decreased from $B \approx 0.75$ G to 0.23 G over the period $t = 25 - 200$ days. We find an temporal evolution of $B \propto t^{-0.63}$, such that $B \propto r^{-0.93}$. Extrapolating, we find $B(t) \approx 10$ G at $r \approx 10^{15}$ cm. For comparison, type IIb SN1993J exhibited a similar evolution with $B \approx 60$ G at $r \approx 10^{15}$ cm and a radial scaling of $B(r) \propto r^{-1}$.

Environmental properties can also be predicted based on our radio observations. From 25 days to 200 days, we find that the electron density, $n_e(t)$, drops by a factor of ~ 10 from $n_e \approx 340$ cm^{-3} to 36 cm^{-3}. Expressed in terms of a radial dependence, $n_e \propto r^{-1.8}$; similar to the density profile expected from a massive stellar wind, $n_e \propto r^{-2}$. This was also seen in the case of SN1998bw/GRB980425 [4], although solid evidence for a wind environment has yet to be detected for the majority of observed gamma-ray bursts.

Directly coupled to the electron number density is the mass loss rate, $\dot{M}$ of the progenitor star. For an assumed stellar wind velocity of $w = 10^3$ km s^{-1}, we find a roughly constant mass loss rate of $\dot{M}(t) \approx 5 \times 10^{-6} M_\odot$ yr^{-1}. This is $\sim$10 percent larger than values derived for SN1998bw and SN2002ap, of $\dot{M}(t) \approx 2.5 \times 10^{-7}$ and $5 \times 10^{-7} M_\odot$ yr^{-1}, respectively [1, 4]. It should be noted that these rates are consistently smaller than the predicted mass loss rate for Wolf-Rayet stars ($\dot{M}(t) \approx 10^{-4} - 10^{-5} M_\odot$ yr^{-1}), which are thought to be the progenitors of type Ic supernovae.

5 Discussion

Although the constraints provided by equipartition arguments are robust, they are also preliminary. The extensive radio data set for SN2003L warrants a full modeling effort to accommodate the effects of multiple absorption processes including synchrotron self-absorption and free-free absorption. Results from our radio modeling study of SN2003L will be presented along with extensive broadband data for this event [7]. We will show that the highly energetic supernovae SN2003L is becoming one of the best studied radio supernovae to date, thereby offering new insights on the diversity of cosmic explosions.

References

1. E. Berger, S.R. Kulkarni, R.A. Chevalier: Astrophys. J. Lett. **577**, L5 (2002)
2. T. Boles: IAUC 8048 (2003)
3. S.R. Kulkarni et al. : Nature **295**, 663 (1998)
4. Z. Li, R.A. Chevalier: Astrophys. J. **526**, 716 (1999)
5. T. Matheson, P. Challis, R.P. Kirshner, P.M. Garnavich: GCN 1846 (2003)
6. A.C. Readhead: Astrophys. J. **426**, 51 (1994)
7. A.M. Soderberg: in preparation
8. S. Valenti et al. : IAUC 8057 (2003)

Radio Monitoring of Supernova 2001ig: The First Year

Stuart D. Ryder[1], Elaine Sadler[2], Ravi Subrahmanyan[3], Kurt W. Weiler[4], Nino Panagia[5] and Christopher Stockdale[4,6]

[1] Anglo-Australian Observatory, P.O. Box 296, Epping, NSW 1710, Australia; sdr@aaoepp.aao.gov.au
[2] School of Physics, University of Sydney, NSW 2006, Australia; ems@physics.usyd.edu.au
[3] Australia Telescope National Facility, CSIRO, Locked Bag 194, Narrabri, NSW 2390, Australia; Ravi.Subrahmanyan@csiro.au
[4] Naval Research Laboratory, Code 7213, Washington, DC 20375-5320, USA; Kurt.Weiler@nrl.navy.mil
[5] ESA/Space Telescope Science Institute, 3700 San Martin Drive, Baltimore, MD 21218, USA; panagia@stsci.edu
[6] Physics Dept., Marquette University, P.O. Box 1881, Milwaukee, WI 53201, USA; Christopher.Stockdale@marquette.edu

Summary. Supernova 2001ig in NGC 7424 has been observed with the Australia Telescope Compact Array at ∼2 week intervals since its discovery, making this the best-studied Type IIb radio supernova since SN 1993J. We present radio light curves for frequencies from 1.4 to 20 GHz, and preliminary attempts to model the observed behavior. Since peaking in radio luminosity at 8.6 and 4.8 GHz some 1-2 months after the explosion, SN 2001ig has on at least two occasions deviated significantly from a smooth decline, indicative of interaction with a dense circumstellar medium and possibly of periodic progenitor mass-loss.

1 Introduction

On the evening of 2001 December 10, the Rev. Robert Evans found his 39th supernova from his home in the Blue Mountains, west of Sydney [4]. SN 2001ig lies in the outskirts of the SAB(rs)cd galaxy NGC 7424, at a distance of 11.5 Mpc [17]. Early optical spectroscopy with the 6.5 m Baade Telescope by Matheson and Jha [8] highlighted several similarities between SN 2001ig and the Type IIb SN 1987K [5]. In the months following, the spectral evolution of SN 2001ig began to resemble more and more that of the "prototypical" Type IIb SN 1993J, as the H recombination lines faded [2, 3], and eventually disappeared [6].

During a Director's Discretionary Time observation, SN 2001ig was detected by the ACIS-S instrument on board the *Chandra* X-ray Observatory

on 2002 May 22 UT. A total of 30 counts was recorded in 23400 sec of integration, corresponding to a 0.2-10.0 keV luminosity $\sim 10^{38}$ erg s^{-1} [14].

Since its commissioning, the Australia Telescope Compact Array (ATCA)[1] has played a leading role in the monitoring of several supernovae at radio wavelengths, most notably SN 1987A [16], SN 1978K [11, 13], and SN 1998bw/GRB980425 [22]. As SN 2001ig was too far south to allow effective monitoring with the Very Large Array (VLA) in its most compact (D) configuration at the time, we commenced observations with the ATCA within a week of its discovery, and have been following it on a regular basis since then.

2 Radio Light Curves

Our first ATCA observations of SN 2001ig over 6 hours on 2001 Dec 15 UT yielded a positive detection at 8.64 GHz, and a marginal detection at 4.79 GHz [12]. On 2001 Dec 31 UT, we detected SN 2001ig using a prototype 18.8 GHz receiver system on just three ATCA antennas. Observations have been carried out with a 128 MHz bandwidth, centered on the primary frequencies of 8.64, 4.79, 2.37, and 1.38 GHz, supplemented by some higher frequency data from both the ATCA and the VLA. The primary flux calibrator for the ATCA data is PKS B1934-638, while the source PKS B2310-417 serves as the secondary gain and phase calibrator. The primary beam around SN 2001ig happens to include an adjacent background source just 20″ away, which has also proved useful for gain calibration when phase stability was poor, or hour-angle coverage limited. Fig. 1 presents our entire dataset up to 2003 March 16.

The radio "light curve" of a supernova typically proceeds through three phases – a rapid turn-on, with a spectral index which is inverted ($\alpha = 2$ or steeper, where $S_\nu \propto \nu^\alpha$) due to absorption along the line-of-sight; followed by a peak in the flux density, firstly at the higher frequencies; then a more gradual decline in the optically-thin phase, with a non-thermal spectral index. By the end of February 2002, SN 2000ig had already peaked at frequencies of 8.64 GHz and 4.79 GHz. However, in early March, the fluxes at these two frequencies jumped by a factor of 2, and remained almost constant for the next two months, before resuming their decline. In August 2002, there was another short but significant pause in the decline. Similar, but less-pronounced deviations are also apparent in the data at 2.37 and 1.38 GHz.

Superimposed on Fig. 1 are model fits to the multi-frequency dataset, based on the "minishell" model of [1], as parameterized by [21]:

[1] The Australia Telescope is funded by the Commonwealth of Australia for operation as a National Facility managed by CSIRO.

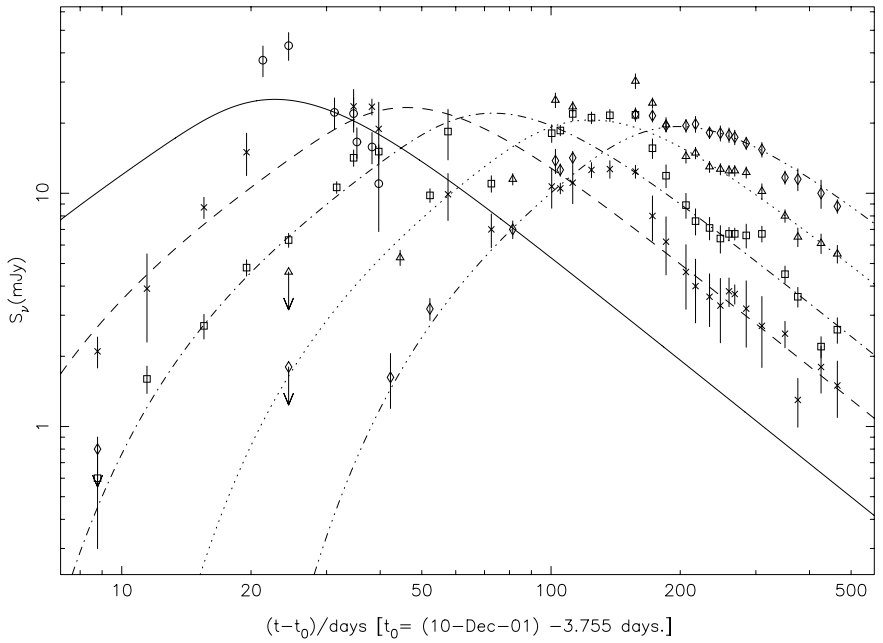

Fig. 1. Radio "light curves" for SN 2001ig at frequencies of 22.5/18.8 GHz (*circles, solid line*); 8.6 GHz (*crosses, dashed line*); 4.8 GHz (*squares, dash–dotted line*); 2.4 GHz (*triangles, dotted line*); and 1.4 GHz (*diamonds, dash–triple dotted line*). The curves are model fits to the data, as described in the text.

$$S(\mathrm{mJy}) = K_1\Big(\frac{\nu}{5\ \mathrm{GHz}}\Big)^{\alpha}\left(\frac{t-t_0}{1\ \mathrm{day}}\right)^{\beta} e^{-\tau}\left(\frac{1-e^{-\tau'}}{\tau'}\right),$$

$$\text{where}\quad \tau = K_2\Big(\frac{\nu}{5\,\mathrm{GHz}}\Big)^{-2.1}\left(\frac{t-t_0}{1\,\mathrm{day}}\right)^{\delta}$$

$$\text{and}\quad \tau' = K_3\Big(\frac{\nu}{5\,\mathrm{GHz}}\Big)^{-2.1}\left(\frac{t-t_0}{1\,\mathrm{day}}\right)^{\delta'}$$

Here K_1 is the flux density, K_2 and K_3 the attenuation by a homogeneous, and a clumpy absorbing medium respectively, at a frequency of 5 GHz one day after the explosion date t_0; α is the spectral index; β the rate of decline in the optically-thin phase; while δ and δ' describe the time dependence of the optical depths in the homogeneous, and clumpy circumstellar medium (CSM) respectively. By constraining the model fits using only the data leading up to the high-frequency turnover, as well as the late-time decay, we can at least compare the global characteristics of this event with those of the best-studied Type IIb supernova, SN 1993J (Table 1, [19]). We note that despite the temporary "boosts" in the radio flux, the overall rate of decline β in SN 2001ig is still much faster than SN 1993J. Furthermore, while the model

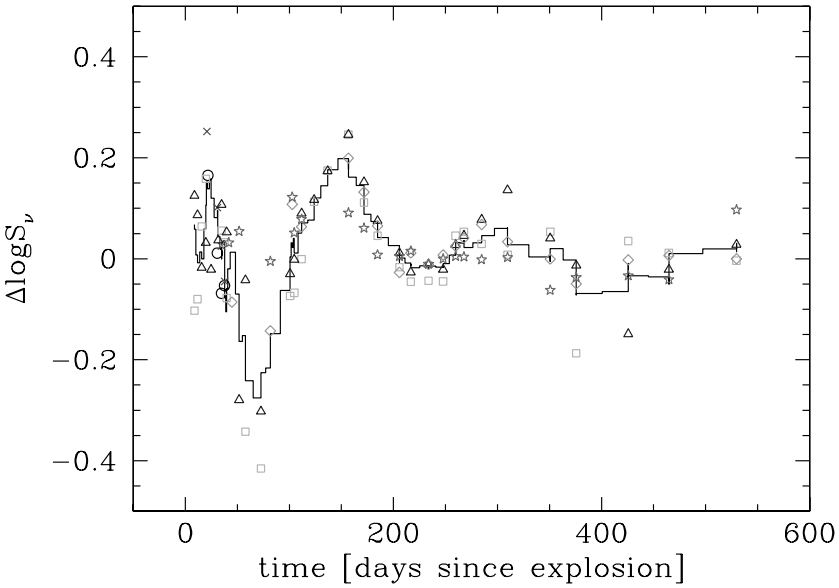

Fig. 2. Deviations of the observed flux of SN 2001ig about the best-fit model. The symbols are the same as in Fig. 1. The solid line is a 4-point boxcar average of the mean deviation over all frequencies at each epoch.

Table 1. Comparison of radio light curve model parameters.

Parameter	SN 2001ig	SN 1993J
K_1 (mJy)	2.47×10^4	1.36×10^4
α	-1.07	-1.05
β	-1.50	-0.88
K_2	1.13×10^2	9.14×10^2
δ	-1.94	-1.88
K_3	1.26×10^5	8.33×10^4
δ'	-2.69	-2.26
$L_{5\ \mathrm{GHz\ peak}}$ (erg s^{-1} Hz^{-1})	3.5×10^{27}	1.4×10^{27}

correctly predicted a 5 GHz peak luminosity twice that of SN 1993J, it was not actually attained until after day 100.

3 Periodic Mass-loss

Bumps and dips in the radio light curve can arise from modulations in either the optical depth, or the CSM density structure (both of which are coupled to some extent) via enhanced mass-loss. Throughout all these events, the spectral index α is relatively unaffected, which leads us to favor the latter

mechanism. A constant α implies that the percentage change in flux is the same at all frequencies, and this is illustrated in Fig. 2 on which is plotted the fractional deviation of the observed flux density from the best-fit model curves in Fig. 1, as a linear function of time. Fig. 2 also highlights an apparent periodicity in CSM density enhancements, with the shock wave reaching the peak of the first at $t \sim$150 days, a second peak near 300 days, and hints of a third peak between 400 and 500 days. For an ejecta expansion velocity of 15000 km s^{-1} and a stellar wind velocity of 10 km s^{-1}, this would imply a series of shells ~ 0.006 pc apart, ejected every 600 years or so. This is much longer than standard stellar pulsation timescales, but is not inconsistent with the period between thermal pulses (C/He shell flashes) in $5 - 10$ M$_\odot$ AGB stars [7].

Only SN 1979C has shown such regular structure in its radio light curve [20], though these variations eventually ceased [10]. The proposed explanation was modulation of the red supergiant progenitor wind due to eccentric orbital motion with a 4000 year period about a massive companion. Acceleration of the progenitor near periastron would result in wind density enhancements superimposed on a pinwheel-like CSM structure, which can account for the periodicity in the radio emission [15]. However, the variations will only be pronounced if the orbital plane is viewed from close to edge-on, which would then naturally account for why so few supernovae display such regular variations in their radio light curves.

Direct evidence for the existence of binary-generated spiral shocks comes from near-infrared aperture-masking interferometry on the Keck I telescope of the Wolf-Rayet stars WR 104 [18] and WR 98a [9]. Both sources show pinwheel-shaped nebulae, which are attributed to dust forming where the stellar winds of the WR star and an OB-type companion collide, then splaying outward. These sources may represent local, compact analogs of the CSM structure that is currently being swept up by the expanding blast wave from SN 2001ig.

Acknowledgement. We are grateful to the staff of the ATNF Paul Wild Observatory for their assistance with the ATCA observations.

References

1. R. Chevalier: Astrophys. J. **259**, 302 (1982)
2. A. Clocchiatti, J.L. Prieto: IAUC 7781 (2001)
3. A. Clocchiatti: IAUC 7793 (2002)
4. R.O. Evans: IAUC 7772 (2001)
5. A.V. Filippenko: Astron. J. **96**, 1941 (1988)
6. A.V. Filippenko, R. Chornock: IAUC 7988 (2002)
7. I. Iben, A. Renzini: Ann. Rev. Astron. Astrophys. **21**, 271 (1983)
8. T. Matheson, S. Jha: IAUC 7772 (2001)

9. J.D. Monnier, P.G. Tuthill, W.C. Danchi: Astrophys. J. Lett. **525**, L97 (1999)
10. M.J. Montes et al. : Astrophys. J. **532**, 1124 (2000)
11. S.D. Ryder et al. : Astrophys. J. **416**, 167 (1993)
12. S.D. Ryder, K. Kranz, E. Sadler, R. Subrahmanyan: IAUC 7777 (2001)
13. E.M. Schlegel et al. : Astron. J. **118**, 2689 (1999)
14. E.M. Schlegel, S.D. Ryder: IAUC 7913 (2002)
15. D.H. Schwarz, J.E. Pringle: Mon. Not. R. Astron. Soc. **282**, 1018 (1996)
16. L. Staveley-Smith et al. : Nature **355**, 147 (1992)
17. R.B. Tully: In: *Nearby Galaxies Catalog* (Cambridge Univ. Press: Cambridge, 1988)
18. P.G. Tuthill, J.D. Monnier, W.C. Danchi: Nature **398**, 487 (1999)
19. S. Van Dyk: In: these Proceedings
20. K.W. Weiler, S.D. Van Dyk, J.E. Pringle, N. Panagia: Astrophys. J. **399**, 672 (1992)
21. K.W. Weiler, N. Panagia, M. Montes, R.A. Sramek: Ann. Rev. Astron. Astrophys. **40**, 387 (2002)
22. M.H. Wieringa, S.R. Kulkarni, D.A. Frail: Astron. Astrophys. Suppl. **138**, 467 (1999)

Synthetic Spectra of the Type Ia SN 2002bo

M. Stehle[1,2] and P.A. Mazzali[3,1]

[1] Max-Planck-Institut für Astrophysik, P.O. Box 1317 85741 Garching, Germany; mstehle@mpa-garching.mpg.de
[2] Universitäts-Sternwarte München, Scheinerstr. 1, 81679 München, Germany
[3] INAF - Osservatorio Astronomico di Trieste, Via Tiepolo, 11, 34131 Trieste, Italy; mazzali@ts.astro.it

Summary. SN 2002bo, a type Ia supernova in NGC 3190, is the first object of the European Supernova Collaboration (ESC). It was discovered on 09 March 2002 and is one of the earliest observed SNe. An almost complete set of spectra and photometry is available from 13 days before maximum B light until a few days after. An analysis using synthetic spectra is presented, focusing on the controversial issue of the reddening of SN 2002bo.

1 Introduction

Thermonuclear (type Ia) supernovae are believed to originate from the thermonuclear disruption of a white dwarf composed of carbon and oxygen. It is generally accepted that when the degenerate mass reaches the Chandrasekhar limit (1.4 $M_\odot$), explosive carbon ignition occurs and burning to nuclear statistical equilibrium ensues, forming mostly radioactive ^{56}Ni. This decays to ^{56}Co and hence to ^{56}Fe, emitting γ-rays and positrons which power the observed optical display of the SN. Intermediate-mass nuclei, e.g. ^{28}Si, are produced in the outer, lower-density regions. These elements give rise to the typical observed spectra of SNe Ia, which are dominated by lines of Fe, Si and S. Improving our understanding of SNe Ia is important because they offer insight to astrophysical processes under extreme conditions and are of great use to measure cosmological distances. Theoretical models must be tested and constrained through comparison with observed light curves and spectral evolution. Modeling very early spectra is a powerful tool to determine certain parameters, e.g. the epoch, since parameters change significantly and quickly at that time. They not only yield information about the physical properties of the SN ejecta, such as temperature, chemical composition, etc., but also they can be used to verify observational-based estimates of parameters such as reddening, distance and epoch. Here we focus in particular on the reddening estimate.

2 Modeling

We use a Monte Carlo code originally developed by Abbot and Lucy [1] to treat multi-line transfer in the expanding envelopes of hot stars. This code was further developed and adapted to SNe by Mazzali and Lucy [3, 4, 5]. It uses as input a model of the explosion (ρ v. v), the emergent luminosity L, the epoch t (time since explosion), the estimated velocity of the photosphere v_{ph} and a set of abundances. The SN envelope is divided into a number of shells. Homologous expansion is assumed and the temperature in the various shells is computed assuming radiative equilibrium. The Sobolev approximation is adopted and all the radioactive decay and fast-electron energy is deposited below a sharply-defined radius, the "photosphere" (Schuster-Schwarzschild approximation). This energy is distributed equally among packets, which represent "collective photons". Each packet is characterized by a specific frequency and propagates through the envelope where it can interact with electrons and atoms. Interaction with electrons is treated as scattering, while if a packet is absorbed by a line it is re-emitted in one of the allowed downward transitions. The packet is assigned a new frequency and a random direction and the MC procedure continues until the packet either escapes the ejecta or is absorbed back in the photosphere. Finally, the emergent spectrum is computed using the formal integral [3].

The observations of SN 2002bo are discussed by Benetti et al. in this book. Here, we present and discuss synthetic spectra for two different epochs. In view of the somewhat unusual properties of SN 2002bo (e.g. the high velocity of several lines at early epochs), we computed models for the earliest spectrum (13 days before maximum) to determine whether or not the outer abundances are peculiar. We also computed models for a spectrum observed near maximum light in order to check the consistency of our results. We adopted a distance modulus $\mu = 31.67$. The density structure was taken from the W7 model [6], and so were the initial abundances, which are assumed to be uniform above the momentary photosphere. The radius of the "photosphere", the emergent luminosity and the abundances were adjusted within a reasonable range until the best match for each spectrum was achieved.

We consider first the early (–13 d) spectrum. In order to constrain the epoch and the reddening we computed a grid of models, varying the epoch between 4 and 7 days post-explosion and the reddening $E(B-V)$ between 0.00 and 0.45. From this grid we derived best-match values of $t = 5 \pm 1$ days post-explosion and $E(B-V) = 0.30$. Thus the maximum-light spectrum corresponds to an epoch of 18 ± 1 days post-explosion. With a higher reddening of $E(B-V) = 0.45$, the best (but poorer) match was achieved with an epoch of 6 ± 1 days post-explosion. Since the observations indicate a value viz. $E(B-V) = 0.43 \pm 0.10$, we conservatively adopt $E(B-V) = 0.30 \pm 0.15$, and computed models with both $E(B-V) = 0.45$ and 0.30.

Figure 1 shows this spectrum plus the two models. The best match to the data was obtained using a bolometric luminosity of $log_{10}L = 41.94$ [erg s^{-1}] at

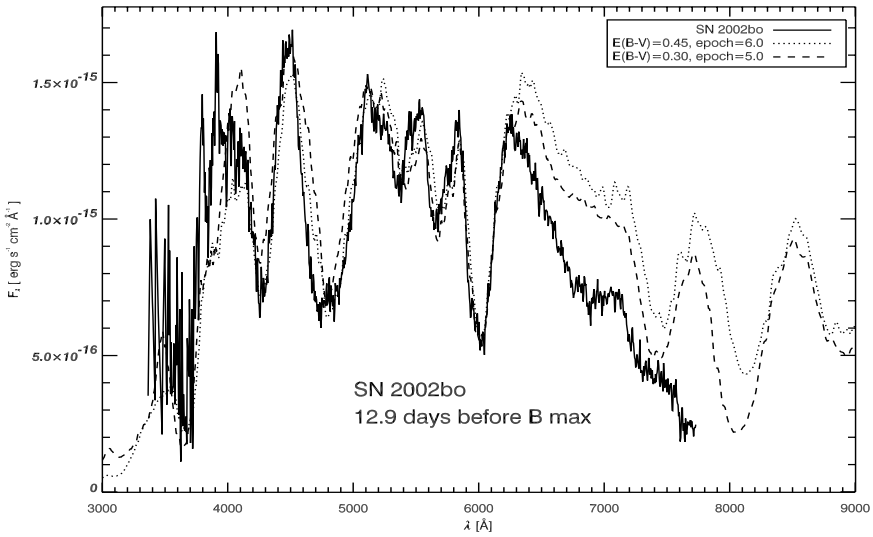

Fig. 1. Spectrum of SN 2002bo 12.9 days before maximum.

a photospheric radius of $v_{ph} = 15450$ km s^{-1} in the low-reddening (l-r) model. The high-reddening (h-r) model is computed with $log_{10}L = 42.13$ [erg s^{-1}] and $v_{ph} = 15100$ km s^{-1}. The luminosity is in good agreement with the observation, which predict $log_{10}L \approx 42.12$ [erg s^{-1}]. These luminosities lead to radiation temperatures at the photospheric radius of $T_R = 9710$ K (h-r) and $T_R = 9420$ K (l-r). T_R is the result of six iterations determining the temperature structure in the ejecta and is influenced by the "backwarming" effect, i.e. photons are scattered back into the photosphere and heat it up. This difference in temperature certainly affects the ionization structure and therefore the emergent spectra significantly. Ca is reduced to 1/10 of its initial value in the h-r model, whilst in the l-r one a reduction to 1/4 is sufficient. All abundances of the iron group elements are significantly lower ($\approx 10\%$ of the initial values), but here the h-r model needs larger amounts due to the higher temperature. The IME are changed only slightly. The overall reduction of most elements causes a increased O abundance ($\geq 70\%$).

Shortward of ∼6500 Å both models reproduce the main features of the data quite well. We examine some of the more prominent features, starting at the shortest wavelengths. We note first that a characteristic of the h-r model is that a higher temperature is required to reproduce the flux in the blue part of the spectrum. This, in turn, tends to increase the ratio of doubly- to singly-ionized species. To reproduce the deep MgII 4481 Å absorption at 4300 Å, a higher Mg abundance is required in the h-r higher temperature model to compensate for the smaller fraction of singly-ionized Mg. The deep, broad absorption feature at ∼4800 Å is produced mostly by FeII lines. In the h-r model this requires an Fe abundance of 0.02 in the outer parts of

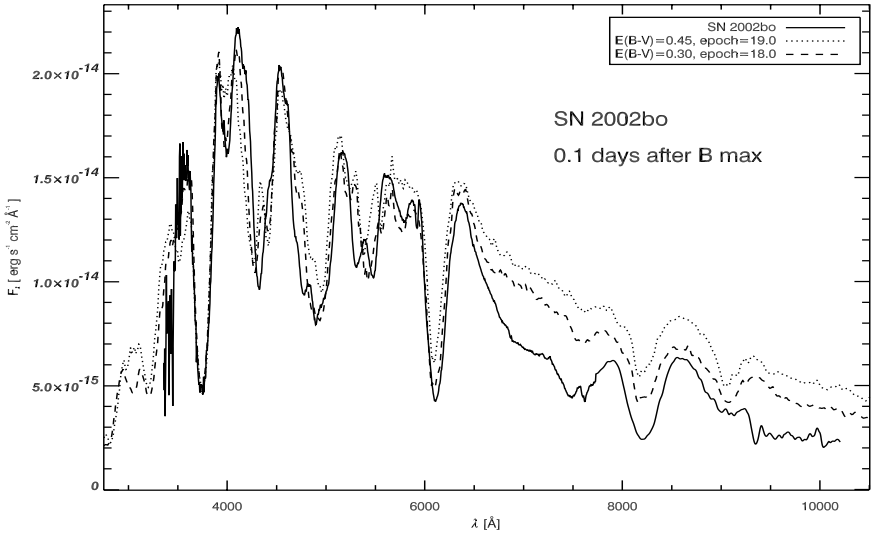

Fig. 2. Spectrum of SN 2002bo 0.1 days after B maximum.

the ejecta, but in the l-r model these drop to 0.015. Thus we see that higher abundances of Mg and Fe are required in the h-r model. In contrast, although the deep absorption feature at ∼5400 Å, attributed to SII 5640 Å, is equally well reproduced in both models, we need a somewhat higher S abundance in the l-r model (0.05 compared to 0.03). We ascribe this to the smaller fraction of ionized S at this lower temperature compared to the h-r model. However, when we consider Si, very serious difficulties for the h-r model become apparent. We find that in this model, most of the Si is ionized to SiIII, making it impossible to reproduce the depth of the SiII 5972 Å line. For the l-r model to reproduce the absorption features due to SiII 5972 Å, 6355 Å, a relative abundance of Si of 0.12 by mass at high velocities ($v \geq 15400$ km s^{-1}) is required. Since W7 predicts no Si at this velocity this supports the possible explanation of mixing, but the corresponding low-velocity O is not observed at later epochs. Alternatively, it may suggests that O was at least partially burned to Si even in the outer layers. At longer wavelengths, both models produce a large excess of flux. This is due to the limitation of the Schuster-Schwarzschild approximation which is used in the code. In the red part of the spectrum, where line opacity is low, the photosphere actually lies at a greater depth than is estimated in the code, and consequently the model overestimates the flux.

We turn now to the near-maximum spectrum (Fig. 2). The photospheric radius drops to 9750 km s^{-1} for the h-r model and to 9000 km s^{-1} for the l-r one. The photospheric luminosities are 43.27 [erg s^{-1}] and 43.03 [erg s^{-1}], respectively. Therefore again the h-r model has a higher temperature (T_R = 13420 K) compared to the l-r model (T_R = 12760 K). Both models have

problems fitting the region around 4300–4500 Å, which is mostly dominated by SiII lines. In both cases we need a high Si abundance (62.1% for the h-r model and 66.7% for the l-r one, respectively) indicating that the part of the ejecta with velocities near 10,000 km s^{-1} is dominated by IME. As with the earlier epoch, in the h-r model almost all Si is doubly ionized. While this results in the absorption of the 6355 Å line being slightly too shallow, the most dramatic difficulty is that the 5958 Å line is completely absent. Moreover, this model produces a rather strong SiIII 4567 Å absorption (near 4400 Å) which is not present in the data at all. These problems are much reduced in the l-r model although the persistence of a weak absorption due to SiIII 4567 Å in the model suggests that $E(B-V)$ could be even smaller than 0.30. As with the early-epoch spectrum, both models overproduce the flux longward of ∼6500 Å, with the h-r model being the most discrepant. The observed absorption at 7500 Å might be identified as OI 7771 Å. However, even with an unphysically high O abundance we cannot reproduce this feature since the high temperature ionizes all the neutral O. The CaII absorption at ∼3750 Å due to the 3933,68 Å H and K doublet matches the observation very well, whilst the absorption at ∼8200 Å due to the ∼8500 Å IR triplet has the correct strength, but it is superposed on a continuum that is too high. The match is somewhat better in the l-r model. In general, we find that the difficulties caused by the high reddening are even larger at this epoch.

We conclude that modeling of both epochs suggests a reddening value $\mathrm{E}(B-V) = 0.30$. This is significantly smaller than the value derived from the Lira relation [$\mathrm{E}(B-V)_L = 0.43$]. This is indicated by the line ratios, line depths, overall shape of the spectra and the model abundances. Apart from the reddening problem, the abundances and spectral features of the models confirm that SN 2002bo was a normal SN Ia. The model-derived explosion epoch of –18 ±1 days is consistent with the rise-time derived from our photometry using the Riess et al. procedure, and with the average value for SNe Ia given by Riess et al [7, 8]. It will be very interesting to see how the various elements are distributed throughout the ejecta. These aspects are being investigated and will be discussed in a separate analysis using an improved version of the MC code, including abundance stratification.

References

1. D.C. Abbott, L.B. Lucy: Astrophys. J. **288**, 679 (1985)
2. K. Iwamoto et al. : Astrophys. J. Suppl. **125**, 439 (1999)
3. L.B. Lucy: Astron. Astrophys. **345**, 211 (1999)
4. P.A. Mazzali, L.B. Lucy: Astron. Astrophys. **279**, 447 (1993)
5. P.A. Mazzali: Astron. Astrophys. **363**, 705 (2000)
6. K. Nomoto, F. Thielemann, K. Yokoi: Astrophys. J. **286**, 644 (1984)
7. A.G. Riess et al.: Astron. J. **116**, 1009 (1998)
8. A.G. Riess etal.: Astron. J. **118**, 2675 (1999)

Part II

Supernovae: Observations

Radio Supernovae

Richard A. Sramek[1], Kurt W. Weiler[2], and Nino Panagia[3]

[1] NRAO, Socorro, NM, USA;
dsramek@aoc.nrao.edu, mrupen@aoc.nrao.edu
[2] NRL, Washington, DC, USA;
Kurt.Weiler@nrl.navy.mil
[3] STScI, Baltimore, MD, USA and Astrophysics Division, Space Science Department of ESA;
panagia@stsci.edu

Summary. Detailed, multi-frequency radio observations of supernovae have shown that the radio emission can be understood as a blastwave interacting with a structured circumstellar medium (CSM) and modeling of the radio light curves allows estimation of the physical conditions in this medium. CSM structures, properties of the presupernova system, and the evolution of the system in the last stages before explosion can then be derived.

1 Introduction

Since 1970, the study of radio emission from extragalactic supernovae has resulted in the detection of thirty-four objects; 24 Type II of various subclasses, no Type Ia supernovae, 9 Type Ib and Ic, plus one object, SN1982aa for which there is no optical type established [10]. These detections were among the 155 supernovae studied by mid 2003. Almost all of these detections were made in the past 20 years using the *Very Large Array (VLA)*[1] radio telescope.

Out of this extensive study of the radio emission from supernovae, several general observations can be made:

* type Ia SNe are not radio emitters to the detection limit of the VLA;
* type Ib/c SNe are radio luminous with steep spectral indices (generally $\alpha < -1$; $S \propto \nu^{+\alpha}$) and a fast turn-on/turn-off, usually peaking at 6 cm near or before optical maximum;
* type II SNe show a range of radio luminosities with flatter spectral indices (generally $\alpha > -1$) and a relatively slow turn-on/turn-off, usually peaking at 6 cm significantly after optical maximum;
* type Ib/c may be fairly homogeneous in some of their radio properties while type II, as in the optical, are quite diverse.

[1] The *VLA* telescope of the National Radio Astronomy Observatory is operated by Associated Universities, Inc. under a cooperative agreement with the National Science Foundation.

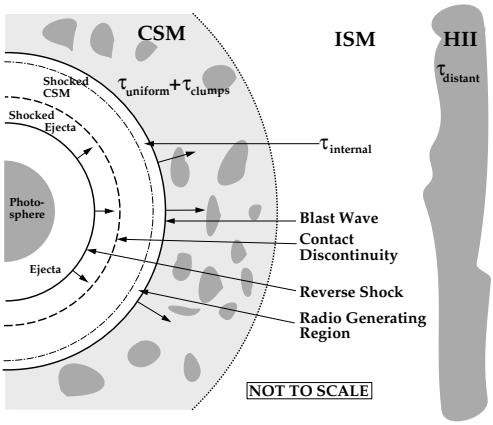

Fig. 1. Cartoon, not to scale, of the SN and its shocks, along with the stellar wind established circumstellar medium (CSM), the interstellar medium (ISM), and more distant ionized hydrogen (HII) absorbing gas. The radio emission is thought to arise near the blastwave front. The expected locations of the several absorbing terms in (1)–(10) are illustrated.

From the radio data it is possible to classify the properties of supernovae and to develop and test models for the radio emission which match the light curves. Among the results that come out of this work are estimates of the density and structure of the circumstellar material around supernovae, the density evolution of the presupernova stellar wind, and insight into the last stages of stellar evolution before the explosion.

2 Parameterized Light Curves for Radio Supernovae

The common characteristics that need to be incorporated in a radio supernova (RSN) model are:

* Nonthermal synchrotron emission with high brightness temperature;
* A decrease in absorption with time, resulting in a smooth, rapid turn-on first at shorter wavelengths and later at longer wavelengths;
* A power-law decline of the flux density with time at each wavelength after maximum flux density (optical depth ~ 1) is reached at that wavelength;
* A final, asymptotic approach of the spectral index α ($S \propto \nu^{+\alpha}$) to an optically thin, nonthermal, constant negative value [12, 13].

The characteristic RSN radio light curves (see, e.g., Fig. 2) arise from the competing effects of slowly declining non-thermal radio emission and more rapidly declining thermal or non-thermal absorption yielding a rapid turn-on and slower turn-off of the radio emission at any single frequency. Since

absorption processes are greater at lower frequencies, transition from optically thick to optically thin (turn-on) occurs first at higher frequencies and later at lower frequencies. After the radiation is completely optically thin and showing the ongoing decline of the underlying emission process (turn-off), the non-thermal spectrum causes lower frequencies to have higher flux density. These two effects cause the displacement in time and flux density of the light curves at different frequencies. Chevalier [1, 2] has proposed that the relativistic electrons and enhanced magnetic field necessary for synchrotron emission arise from the SN blastwave interacting with a relatively high density circumstellar medium which has been ionized and heated by the initial UV/X-ray flash.

Weiler et al. [12, 13] and Montes et al. [5] adopted a parameterized model which has been updated in Weiler et al. [17, 18] to the following form:

$$F_\nu(\mathrm{mJy}) = K_1 \left(\frac{\nu}{5\ \mathrm{GHz}}\right)^{\alpha} \left(\frac{t-t_0}{1\ \mathrm{day}}\right)^{\beta} e^{-\tau_{\mathrm{external}}} \left(\frac{1-e^{-\tau_{\mathrm{CSM_{clumps}}}}}{\tau_{\mathrm{CSM_{clumps}}}}\right) \times \left(\frac{1-e^{-\tau_{\mathrm{internal}}}}{\tau_{\mathrm{internal}}}\right) \tag{1}$$

with

$$\tau_{\mathrm{external}} = \tau_{\mathrm{CSM_{homog}}} + \tau_{\mathrm{distant}}, \tag{2}$$

where

$$\tau_{\mathrm{CSM_{homog}}} = K_2 \left(\frac{\nu}{5\ \mathrm{GHz}}\right)^{-2.1} \left(\frac{t-t_0}{1\ \mathrm{day}}\right)^{\delta} \tag{3}$$

$$\tau_{\mathrm{distant}} = K_4 \left(\frac{\nu}{5\ \mathrm{GHz}}\right)^{-2.1} \tag{4}$$

and

$$\tau_{\mathrm{CSM_{clumps}}} = K_3 \left(\frac{\nu}{5\ \mathrm{GHz}}\right)^{-2.1} \left(\frac{t-t_0}{1\ \mathrm{day}}\right)^{\delta'} \tag{5}$$

with K_1, K_2, K_3, and K_4 determined from fits to the data and corresponding, formally, to the flux density (K_1), homogeneous (K_2, K_4), and clumpy or filamentary (K_3) absorption at 5 GHz one day after the explosion date t_0. The terms $\tau_{\mathrm{CSM_{homog}}}$ and $\tau_{\mathrm{CSM_{clumps}}}$ describe the attenuation of local, homogeneous circumstellar medium (CSM) and clumpy CSM that are near enough to the SN progenitor that they are altered by the rapidly expanding SN blastwave. The $\tau_{\mathrm{CSM_{homog}}}$ absorption is produced by an ionized medium that completely covers the emitting source ("homogeneous external absorption"), and the $(1 - e^{-\tau_{\mathrm{CSM_{clumps}}}})\tau^{-1}_{\mathrm{CSM_{clumps}}}$ term describes the attenuation produced by an inhomogeneous medium ("clumpy absorption"; see [8] for a

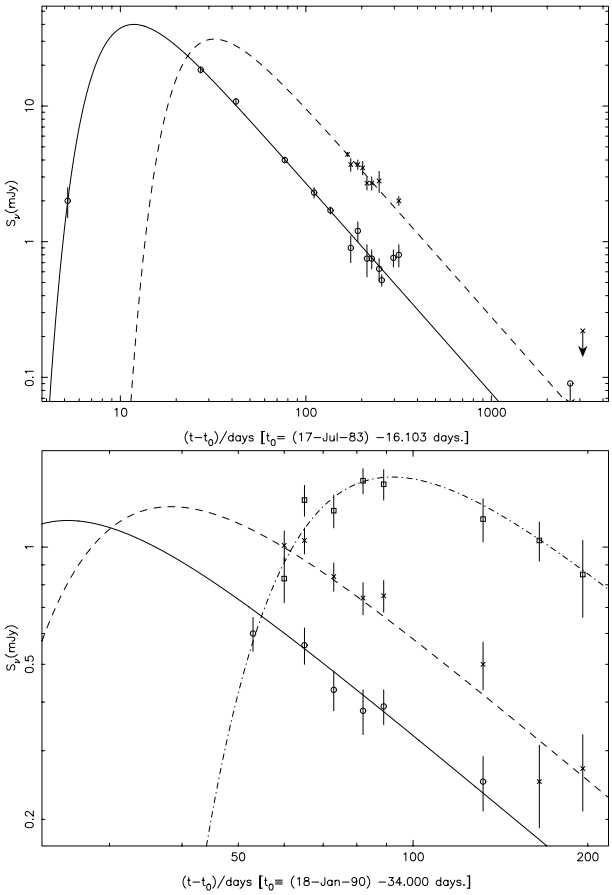

Fig. 2. Top (2a): type Ib SN1983N at 6 cm (4.9 GHz; *open circles, solid line*) and 20 cm (1.5 GHz; *stars, dashed line*). Bottom (2b): type Ic SN1990B. at 3.6 cm (8.4 GHz; *open circles, solid line*), 6 cm (4.9 GHz; *stars, dashed line*), and 20 cm (1.5 GHz; *open squares, dash-dot line*).

more detailed discussion of attenuation in inhomogeneous media). The $\tau_{\rm distant}$ term describes the attenuation produced by a homogeneous medium which completely covers the source but is so far from the SN progenitor that it is not affected by the expanding SN blastwave and is constant in time. All external and clumpy absorbing media are assumed to be purely thermal, singly ionized gas which absorbs via free-free (f-f) transitions with frequency dependence $\nu^{-2.1}$ in the radio. The parameters δ and δ' describe the time dependence of the optical depths for the local homogeneous and clumpy or filamentary media, respectively.

The f-f optical depth outside the emitting region is proportional to the integral of the square of the CSM density over the radius. Since in the simple Chevalier model the CSM density (constant mass-loss rate, constant wind velocity) decreases as r^{-2}, the external optical depth will be proportional to r^{-3}, and since the blastwave radius increases as a power of time, $r \propto t^m$ with $m \leq 1$ (i.e., m = 1 for undecelerated blastwave expansion), it follows that the deceleration parameter, m, is

$$m = -\delta/3. \tag{6}$$

The model by Chevalier [1, 2] relates β and δ to the energy spectrum of the relativistic particles γ ($\gamma = 2\alpha - 1$) by $\delta = \alpha - \beta - 3$ so that, for cases where $K_2 = 0$ and δ is, therefore, indeterminate, one can use

$$m = -(\alpha - \beta - 3)/3. \tag{7}$$

Since it is physically realistic and may be needed in some RSNe where radio observations have been obtained at early times and high frequencies, Eq. (1) also includes the possibility for an internal absorption term. This internal absorption ($\tau_{\rm internal}$) term may consist of two parts – synchrotron self-absorption (SSA; $\tau_{\rm internal_{SSA}}$), and mixed, thermal f-f absorption/non-thermal emission ($\tau_{\rm internal_{ff}}$).

$$\tau_{\rm internal} = \tau_{\rm internal_{SSA}} + \tau_{\rm internal_{ff}} \tag{8}$$

$$\tau_{\rm internal_{SSA}} = K_5 \left(\frac{\nu}{5\ {\rm GHz}}\right)^{\alpha-2.5} \left(\frac{t - t_0}{1\ {\rm day}}\right)^{\delta''} \tag{9}$$

$$\tau_{\rm internal_{ff}} = K_6 \left(\frac{\nu}{5\ {\rm GHz}}\right)^{-2.1} \left(\frac{t - t_0}{1\ {\rm day}}\right)^{\delta'''} \tag{10}$$

with K_5 corresponding, formally, to the internal, non-thermal ($\nu^{\alpha-2.5}$) SSA and K_6 corresponding formally to the internal thermal ($\nu^{-2.1}$) free-free absorption mixed with nonthermal emission, at 5 GHz one day after the explosion date t_0. The parameters δ'' and δ''' describe the time dependence of the optical depths for the SSA and f-f internal absorption components, respectively.

A cartoon of the expected structure of an SN and its surrounding media is presented in Fig. 1 (see also [4]). The radio emission is expected to arise near the blastwave [3].

3 Radio Supernova Light Curves

The success of the basic parameterization and modeling is shown in the good agreement between the model fits and the data for all subtypes of RSNe. The

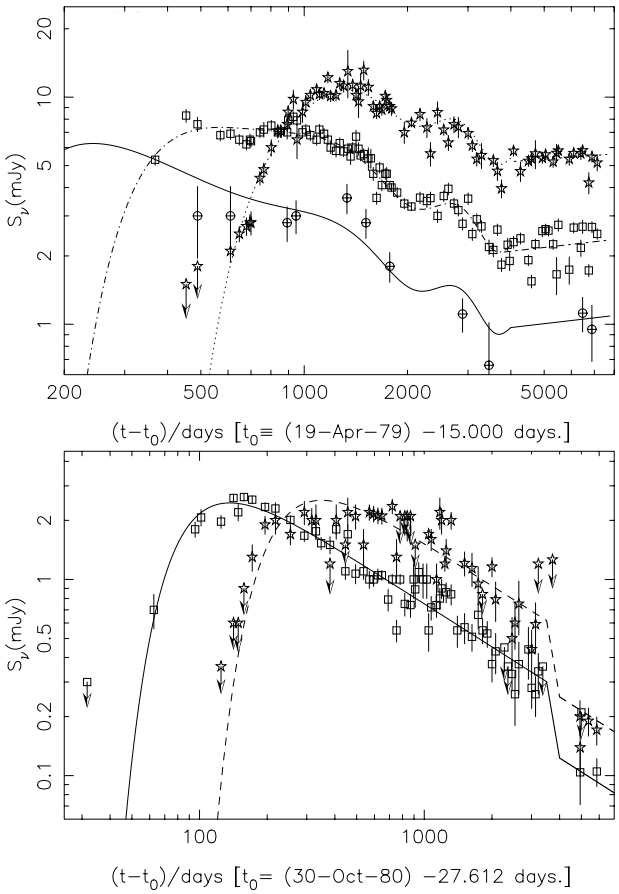

Fig. 3. Top (3a): type II SN1979C at 2 cm (14.9 GHz; *crossed circles, solid line*), 6 cm (4.9 GHz; *open squares, dash-dot line*), and 20 cm (1.5 GHz; *open stars, dotted line*) Bottom (3b): type II SN1980K at 6 cm (4.9 GHz; *open squares, solid line*), and 20 cm (1.5 GHz; *open stars, dashed line*).

observed data and the best fit model for the radio light curve of a Type Ib supernova, SN1983N [9] is shown in Fig. 2a; the radio light curve for a Type Ic supernova, SN1990B [11] is shown in Fig. 2b. For Type II supernovae, the data and model light curves are shown for SN1979C in Fig. 3a [7, 14, 15] and for SN1980K in Fig. 3b [6, 16]. Evidence for structure in the circumstellar medium can be seen in the optically thin, later portions of these latter two light curves. After day $\sim$ 4000, the radio emission from both SN1979C and SN1980K deviates from the simple model and SN1979C shows a sinusoidal modulation in its flux density prior to day $\sim$4000.

Thus, the radio emission from SNe appears to be relatively well understood in terms of blastwave interaction with a structured CSM as described by the Chevalier [1, 2] model and its extensions by [5, 12, 13, 18].

Acknowledgement. KWW wishes to thank the Office of Naval Research (ONR) for the 6.1 funding supporting this research. Additional information and data on radio supernovae can be found on *http://rsd-www.nrl.navy.mil/7213/weiler/* and linked pages.

References

1. R.A. Chevalier: Astrophys. J. **259**, 302 (1982)
2. R.A. Chevalier: Astrophys. J. Lett. **259**, L85 (1982)
3. R.A. Chevalier, C. Fransson: Astrophys. J. **420**, 268 (1994)
4. T.A. Lozinskaya: In: *Supernovae and Stellar Wind in the Interstellar Medium* (American Institute of Physics, New York 1992) p. 190
5. M.J. Montes, K.W. Weiler, N. Panagia: Astrophys. J. **488**, 792 (1997)
6. M.J. Montes, S.D. Van Dyk, K.W. Weiler, R.A. Sramek, N. Panagia: Astrophys. J. **506**, 874 (1998)
7. M.J. Montes, K.W. Weiler, S.D. Van Dyk, R.A. Sramek, N. Panagia, R. Park: Astrophys. J. **532**, 1124 (2000)
8. A. Natta N. Panagia: Astrophys. J. **287**, 228 (1984)
9. R.A. Sramek, N. Panagia, K.W. Weiler: Astrophys. J. Lett. **285**, L59 (1984)
10. R.A. Sramek, K.W. Weiler: Radio Supernovae. In: *Supernovae and Gamma-Ray Bursters*, ed by K.W. Weiler (Springer-Verlag, Berlin Heidelberg New York 2003) pp. 145–169
11. S.D. Van Dyk, R.A. Sramek, K.W. Weiler, N. Panagia: Astrophys. J. **409**, 162 (1993)
12. K. Weiler, R. Sramek, N. Panagia, J. van der Hulst, M. Salvati: Astrophys. J. **301**, 790 (1986)
13. K.W. Weiler, N. Panagia, R.A. Sramek: Astrophys. J. **364**, 611 (1990)
14. K. Weiler, S. Van Dyk, N. Panagia, R. Sramek, J. Discenna: Astrophys. J. **380**, 161 (1991)
15. K. Weiler, S. Van Dyk, J. Pringle, N. Panagia: Astrophys. J. **399**, 672 (1992)
16. K. Weiler, S. Van Dyk, N. Panagia, R. Sramek: Astrophys. J. **398**, 248 (1992)
17. K.W. Weiler, N. Panagia, M.J. Montes: Astrophys. J. **562**, 670 (2001)
18. K.W. Weiler, N. Panagia, M.J. Montes, R.A. Sramek: Ann. Rev. Astron. Astrophys. **40**, 387 (2002)

Low Frequency Radio and X-ray Properties of Core-Collapse Supernovae

A. Ray[1], P. Chandra[1,2], F. Sutaria[3], and S. Bhatnagar[4,5]

[1] Tata Institute of Fundamental Research, Mumbai, India;
akr@tifr.res.in
[2] Joint Astronomy Program, Indian Inst. Science, Bangalore, India;
poonam@tifr.res.in
[3] Physics Dept., Technical University Munich, Germany;
fsutaria@ph.tum.de
[4] National Centre for Radio Astrophysics, TIFR, Pune, India
[5] National Radio Astronomy Observatory, Socorro, USA;
sbhatnag@aoc.nrao.edu

Summary. Radio and X-ray studies of young supernovae probe the interaction between the supernova shock waves and the surrounding medium and give clues to the nature and past of the progenitor star. Here we discuss the early emission from type Ic SN 2002ap and argue that repeated Compton boosting of optical photons by hot electrons presents the most natural explanation of the prompt X-ray emission. We describe the radio spectrum of another type Ic SN 2003dh (GRB030329) obtained with combined GMRT and VLA data. We report on the low frequency radio monitoring of SN 1995N and our objectives of distinguishing between competing models of X-ray emission from this SN and the nature of its progenitor by X-ray spectroscopy. Radio studies on SN 2001gd, SN 2001ig and SN 2002hh are mentioned.

1 Introduction

The association of long duration gamma-ray bursts (GRBs) with core collapse supernovae is by now established with SN 2003dh (GRB030329) [7]. Observational evidence supports the viewpoint that GRBs are energetic explosions like supernovae occuring in star formation regions and a large fraction of their energy is directed in relativistic jets. Supernovae are known to be explosions of massive (and intermediate mass) stars, although the nature of the progenitor stars for varied supernova types remains an open subject.

A supernova explosion from the core collapse of a massive star drives a powerful shock wave into the circumstellar medium (CSM) of the progenitor. The shock wave with a speed approximately 1000 times larger than the speed of the progenitor star's wind quickly probes the circumstellar medium established by the wind lost over many thousands of years before the explosion. Relativistic electrons and magnetic fields in the interaction region give rise to nonthermal radio emission. The interaction of a supernova shock with its surrounding medium produces X-ray emission probing the environment.

Multi-waveband studies from radio and X-ray bands thus provide a handle on the past history of the parent star and the nature of the interaction region. Fingerprinting the exploded ejecta composition through X-ray spectroscopy [14] can give clues to the mass of the exploding star (e.g. in SN 1998S [11]).

In this paper, we discuss several supernovae: SN 2002ap – a "hypernova" of type Ic associated with GRBs that had no GRB counterpart; another type Ic "hypernova" SN 2003dh which was associated with GRB030329; and several other supernovae such as: SN 2001gd, SN 2001ig and SN 2002hh. We also mention how upcoming X-ray spectroscopic studies of SN 1995N will help discriminate between the sites of observed X-ray emission.

2 Hypernova SN 2002ap: Nature of its X-ray Emission

SN 2002ap showed early ("prompt") X-ray and radio emission. It was a nearby (7.3 Mpc) and optically bright ($V = 14.5$ upon discovery by Y. Hirose as in [10]) supernova. The broad spectral features in the optical (thus the name "hypernova") and a subsequent modeling of its spectroscopic and photometric data ([9]) suggested that it was energetic: $E_{\rm expl} \sim 4 - 10 \times 10^{51}$ erg.

XMM-Newton observed SN 2002ap with the EPIC X-ray cameras and the Optical Monitor for ~ 34 ks on Feb 2.0 – 2.4, 2002 UT, (day five after estimated explosion date Jan 28.0, 2002). A presupernova exposure of the field by Chandra X-ray Observatory on Oct. 19, 2001 revealed the presence of a nearby source about $14''.9$ away from the supernova, and the contribution of this source was taken into account in our measurement of the day 5 SN X-ray flux: $1.07^{+0.63}_{-0.31} \times 10^{-14}$ erg cm^{-2} s^{-1} (0.3 – 10 keV) (see [13] for details). Because the SN was very faint, both thermal bremsstrahlung model ($N_H = 4.9 \times 10^{21}$ cm^{-2}, $kT = 0.8$ keV) and a simple power law model ($N_H = 4.2 \times 10^{21}$ cm^{-2}, spectral index $\alpha = 2.6$) fit the sparse data equally well.

The earliest radio detection of SN 2002ap was 4.5 days after the explosion, in the VLA 8.46 MHz band, and the frequency of the peak radio flux declined from 8.46 GHz to 1.43 GHz over a period of 10 days from the explosion date [1]. SN 2002ap was observed with the GMRT at 610 MHz 8.96 days after explosion and yielded 2σ upper limit of 0.34 mJy on Feb 5, 2002 [13]. The wavelength dependence of the radio turn-on shifting to longer wavelengths can be due to either free-free absorption or synchrotron self-absorption in the expanding circumstellar matter overlying the interaction region. We have fitted the VLA and GMRT data on 2002 Feb. 5.96 (day 8.96) to a SSA model, with spectral index $\alpha = -0.8$ in the optically thin limit, implying that the radius of the radio photosphere on this day was $R_{\rm r} = 3.5 \times 10^{15}$ cm and the magnetic field in the shocked ejecta was $B = 0.29$ G. The SSA prediction of flux at 610 MHz band is consistent with the GMRT upper limit.

The measured flux density of the SN 2002ap on day 5 corrected for absorption: F_ν versus ν from the radio bands to the X-ray band is shown in Fig. 1.

A single power-law with the spectral index $\alpha = -0.9$ (from the radio spectrum) implies a flux density of only 58 picoJansky at 1 keV (corresponding to 5×10^{-16} ergs^{-1}cm^{-2} over the effective bandwidth) and fails to reproduce the observed X-ray flux. A synchrotron radiation spectrum from a single population of relativistic electrons produces a power law spectrum with a steepening beyond the cooling frequency. For the relevant parameters determined from radio frequency spectral fits, this break should occur in the optical region. A spectrum with such a break (Fig. 1) makes the observed radio and X-ray flux densities even more discrepant than that with a constant $\alpha = -0.9$.

The observed X-ray flux by XMM-Newton could have been accounted for by the thermal free-free emission (bremsstrahlung). However, with the reported high ejecta velocity ($v \geq 20,500$ km s^{-1} on day 3.5) the implied temperature of the shocked ejecta and the circumstellar matter a flat tail of high energy photons upto about 100 keV would have resulted [6] (only a limited cool absorbing shell may have been present at this stage). By contrast, the observed X-ray emission is quite soft (e.g. thermal bremsstrahlung temperature $T_B = 0.8$ keV). Even the reverse shock produced X-ray emission would be quite hard compared with observed colors unless the density gradient of the ejecta is extremely steep, normally not found for relevant progenitors.

The most natural explanation of the observed X-ray flux and spectral features is the (repeated) Compton scattering of hot electrons off optical photons from the photosphere at $T_{eff} \geq 10^4$ K. Detailed Monte Carlo simulations of the repeated Compton scattering have been performed by [12]. The Compton flux is approximately related to the optical flux by [3, 6]:

$$\mathcal{F}_\nu^{Compton} \sim \tau_e \mathcal{F}_\nu^{opt} (\nu_o/\nu)^\gamma \text{erg s}^{-1}\text{cm}^{-2}\text{Hz}^{-1}$$

where the optical depth and the energy index are:

$$\tau_e = \frac{\dot{M}\sigma_T}{4\pi m_p R_s u_w}\Big(1 - \frac{R_{opt}}{R_s}\Big); \;\; \gamma(\gamma+3) = -\frac{m_e c^2}{kT_e}\ln\Big[\frac{\tau_e}{2}(0.9228 - \ln\tau_e)\Big]$$

We note that on day 5 the unabsorbed X-ray and optical flux densities derived from XMM and ground based observations imply a multi-waveband power-law index $\gamma = 2.5 - 2.8$ (somewhat steeper than the XMM-band index $\gamma_{\rm XMM} \sim 1.6$) and a logarithm of the ratio of flux densities of ≈ 7.4. Typical electron temperature required of Comptonizing plasma is $T_e = 1.5 - 2 \times 10^9$ K for optical depths in the range $\tau_e = 4 - 25 \times 10^{-4}$ for progenitor scenarios such as Wolf-Rayet stars or interacting binaries involving Roche lobe overflow from a helium star. Such temperatures are well within the range of hot circumstellar gas even for the modest velocities of $16,000 - 20,000$ km s^{-1}.

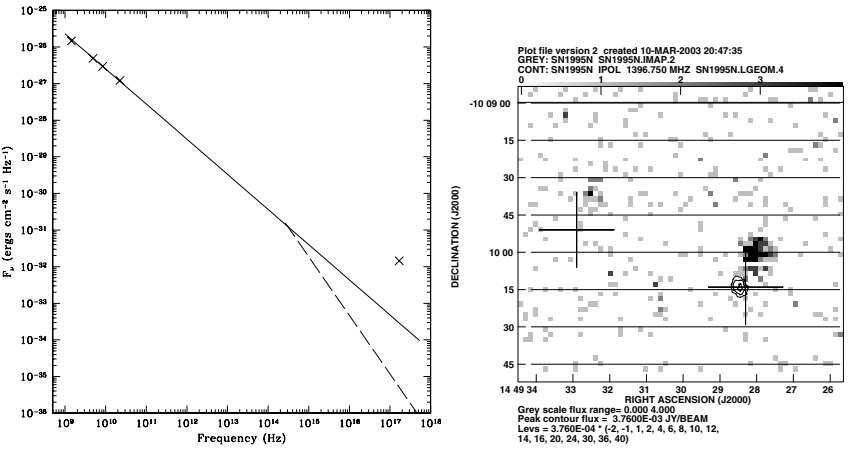

Fig. 1. Left: Multi-wave plot for 2002ap. Dashed line shows the cooling break. Right: SN1995N GMRT 1420MHz contour labels overlayed on ROSAT HRI grey image.

3 SN 1995N, SN 2003dh and Other Supernovae

SN 1995N was a type IIn supernova that exploded in the galaxy MCG-2-38-017. We have detected SN 1995N a number of times with the GMRT. Its low frequency radio flux is very slowly declining (1420 MHz band flux: 4.5 ± 0.75 mJy on 8 Nov 2000 and 4.2 ± 0.2 mJy on 21 Sep 2002; in 610 MHz band 3.3 ± 0.35 mJy on 16 Sep 2002). Of the 19 supernovae [8] that have been detected in the X-ray bands SN1995N appears at the high end of the X-ray luminosity ($\sim 1 \times 10^{41}$ ergs^{-1} [5]). There is indication of short term variations of its X-ray luminosity in the ROSAT and ASCA observations. The ROSAT HRI X-ray image is overlaid with the GMRT 1400 MHz band radio map of the region around SN 1995N in Fig. 1. Here the cross on the lower right is the position of the supernova while that on the left is the center of the host galaxy. The question of variation of its X-ray flux will be addressed by our Chandra/XMM observations in the current cycle. X-ray line-widths can also distinguish between the models of emission by 1) ejecta gas struck by the reverse shock [3] or 2) the radiative cooling of shocked dense clouds crushed by the strongly shocked circumstellar wind [4]. Nucleosynthetic fingerprinting through X-ray spectra will assist in determining the progenitor star mass.

In contrast, SN 2003dh was an energetic type Ic supernova (a hypernova, with an large expansion velocity $\sim 36,000 \pm 3000$ km s^{-1} and estimated total isotropic energy release $\sim 9 \times 10^{51}$ erg) that was spatially and temporally coincident with a GRB030329 at a redshift of $z = 0.1685$. We observed SN 2003dh with the GMRT in the 1280 MHz band and on June 17, 2003 in the 610 MHz band. The image of the region containing the SN is shown in Fig. 2. The flux of the SN was 2.1 ± 0.13 mJy in the 1280 MHz band on 13 Jun 2003.

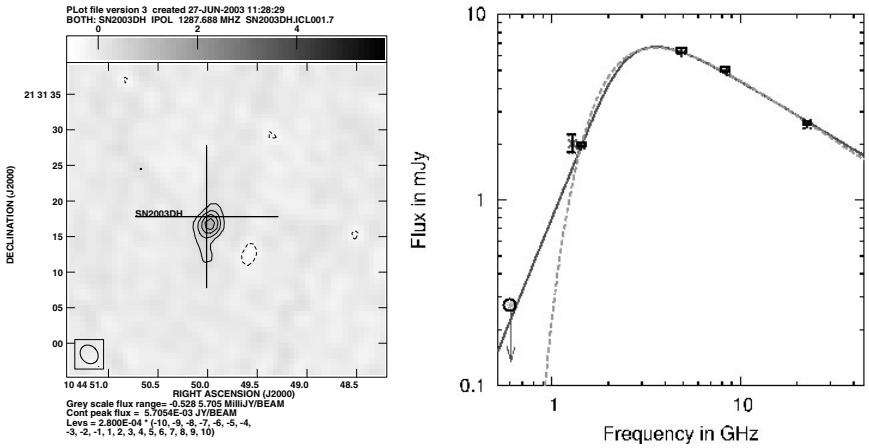

Fig. 2. Left: GMRT 1280MHz image of 2003dh & Right: SSA (solid) and FF (dash) fits to the VLA (rectangle)& GMRT (1280MHz: cross, 610 upper limit: circle).

The SN flux at 610 MHz in the Feb 2004 observation is 1.16 ± 0.29 mJy. We have combined our data with VLA measurements reported by Berger et al. [2] (June 4.01, 2003); the resultant spectrum is shown in Fig. 2. The spectrum is consistent with both free-free and synchrotron self-absorption (SSA) models. For the SSA model, the best fit parameters are: $R = 2.26 \times 10^{17}$ cm and $B = 0.13$ G. This is a relatively high field for the radio emission region since for other supernovae like SN 1998bw fields such as these are encountered much earlier.

In the GMRT 1420 MHz band observations, SN 2001gd (IIb) brightened marginally from 3.2 ± 0.3 mJy (22 Sep 2002) to 3.6 ± 0.2 mJy (15 Nov 2002) while SN 2001ig (also type IIb) dimmed between 14.5 ± 0.4 mJy (25 Sep 2002) to 9.5 ± 0.3 mJy (14 Nov 2002). The 1400 MHz flux of SN 2002hh (type II) on 27 Dec 2002 was 1.4 ± 0.24 mJy.

Acknowledgement. We thank the staff of XMM-Newton and GMRT (NCRA-TIFR) that made these observations possible.

References

1. E. Berger, S. Kulkarni, R.A. Chevalier: Astrophys. J. Lett. **577**, L5 (2002)
2. E. Berger et al. : astro-ph 0308187 (2003)
3. R.A. Chevalier, C. Fransson: Astrophys. J. **420**, 268 (1994)
4. N.N. Chugai: Astrophys. J. Lett. **414**, L101 (1993)
5. D.W. Fox et al. : Mon. Not. R. Astron. Soc. **319**, 1154 (2000)
6. C. Fransson: Astron. Astrophys. **111**, 140 (1982)
7. J. Hjorth et al. : Nature **423**, 847 (2003)
8. S. Immler, W.H.G. Lewin: In: *Supernovae and Gamma-Ray Bursters*, ed. K. Weiler (Springer: Berlin, 2002) pp. 91-112

9. P. Mazzali et al. : Astrophys. J. Lett. **572**, L61 (2002)
10. S. Nakano, R. Kushida, W. Li: IAUC **7810** (2002)
11. D. Pooley et al. : Astrophys. J. **572**, 932 (2002)
12. L. Pozdnyakov, I. Sobol, R. Sunyaev: Sov. Astron. **21**, 708 (1977)
13. F. Sutaria, P. Chandra, S. Bhatnagar, A. Ray: Astron. Astrophys. **397**, 1011 (2003)
14. H.-U. Zimmermann, B. Aschenbach: Astron. Astrophys. **406**, 969 (2003)

Supernova Spectra

Massimo Turatto

Osservatorio Astronomico di Padova, INAF, vicolo dell'Osservatorio 5, 35122 Padova, Italy;
turatto@pd.astro.it

Summary. In this paper are summarized the main advances of the last years in the field of SN spectra . The arguments against a monodimensional sequence for SNIa are discussed as well as the efforts to improve the temporal and spectral coverage of this kind of SNe, with the aim to understand the physics of the explosions for their use as cosmological distance indicators. Although variety is the main character of core-collapse SNe, we have been recently surprised by both exceptionally under- and over-energetic explosions. The main properties of these two extreme subclasses are here reviewed.

1 Introduction

Spectra provide most of the physical information on supernovae. Their early analysis has shown a variety of forms and evolutions. Indeed the identification of different spectral lines reveals the presence of several different ions in the layers above the photosphere, suggesting the existence of various progenitors and explosion models. Spectra also allow us the direct determination of the physical conditions of the emitting regions, while the line profiles provide the kinematics.

Supernova spectra evolve rapidly: the effective temperature and expansion velocity decrease, and the spectral lines change. Indeed, because of the expansion, the photosphere recedes into the ejecta and different layers are progressively exposed. In this way the analysis of SN spectra taken at different epochs allows us, at least in principle, to make the tomography of the exploding stars and to reconstruct their entire structures. A major limitation is that spectral features in SN spectra are generally blended due to the large expansion velocities and the full information can be extracted only with the use of complex spectral modeling which try to deal in a consistent way the luminosity, abundances, stratification, temperature, velocity and time evolution.

In general, the light from SNe is traveling for several megaparsecs before reaching the observers thus contains information on the circumstellar, interstellar and intergalactic matter it has passed through. In principle, high resolution spectroscopy might allow us to determine the distribution and physical conditions of the intervening medium and, in turn, the total reddening and extinction suffered by the light.

Finally, in the recent years spectral observations on faint, distant of SNIa have provided sufficiently accurate redshifts which, once coupled with the photometry, have inspired a new vision of the Universe we are living in.

This review discusses a number of hot topics concerning SN spectra while reference is given to other reviews for the detailed description of the properties and evolution of various spectral types [13, 57, 59].

2 A Spectral Sequence for SNIa ?

SNIa explode in all types of galaxies, in ellipticals as well as in spirals, but in the latter are not closely associated with the spiral arms as other SN types. The spectra are characterized by lines of intermediate mass elements such as Ca, O, Si and S during the peak phase, and by the absence of H at any time. With age the contribution of the Fe lines increases and several months past maximum the spectra are dominated by [Fe II] and [Fe III] lines. The overall homogeneous spectroscopic and photometric behavior has led to a general consensus that they are associated with the thermonuclear explosions of white dwarfs [5].

During the last decade a new scenario for the SNIa has been progressively developed. In particular, a correlation between the peak luminosity and the shape of the early light curve was found, with brighter objects having a rate of decline slower than dimmer ones [44, 45, 46, 47]. An analogous spectroscopic sequence has been found [41], according to which the absolute magnitude of SNIa and, in turn, the rate of decline, is correlated to $\mathcal{R}$(SiII), the ratio of the depths of two absorption features at 5800 and 6100 Å, usually attributed to Si II. Synthetic spectra modeling indicates that most of the spectral differences are caused by variations in the effective temperatures, likely due to different amounts of ^{56}Ni produced in the explosions. The finding that fainter SNe show slow expansion velocities both at early [4] and later epochs [54] is consistent with such scenario.

In first approximation all SNIa can be accommodated into such one-parameter sequence which can be regarded as a sequence of explosion strengths. Within such scheme fit the bright, slowly declining SN 1991T, which did not exhibit Si II or Ca II absorption lines in the premaximum spectra but had a normal behavior starting one month after maximum, and the faint, intrinsically red and fast declining SN 1991bg, which showed a slow expansion velocities and a deep trough around 4200 Å produced by Ti II.

In the last years, however, new findings have challenged such a monoparametric sequence. Hatano et al. [22] have shown that the $\mathcal{R}$(SiII) does not correlated with the photospheric velocity deduced from the Si II λ6355 absorption, as one would expect, and propose the existence of two or more explosion mechanisms as possible explanation for the lack of correlation. Also, a recent reanalysis [3] has shown that while the $\mathcal{R}$(SiII) vs. Δm_{15} relation

holds for $\Delta m_{15} \geq 1.2$, at smaller values it breaks down, thus questioning the correspondence between spectroscopic and photometric parameters.

A number of objects have now good sequences of spectra, some starting very early after the explosion, which make possible to study the temporal evolution of $\mathcal{R}$(SiII). It is found that before maximum $\mathcal{R}$(SiII) exhibits a dramatic evolution with opposite trends for various objects [3].

Moreover, objects with similar decline rates can show different spectral features, especially before maximum. In Fig. 2 the spectra of four objects taken about one week before B maximum are compared. The spectrum of SN 2000E ($\Delta m_{15} = 0.94$ mag $(100\mathrm{d})^{-1}$) shows noticeable differences with respect the two SNe at the bottom, having the same decline rates, but is very similar to that of SN 1990N ($\Delta m_{15} = 1.05$). Not only it differs from that of SN 1991T ($\Delta m_{15} = 0.94$) which is well known for not displaying at this epoch the characteristic Si II line but shows disturbing differences with the normal SN 1999ee ($\Delta m_{15} = 0.92$). In particular, the profile of the Si II 6355λ line is definitely broader in SN 1999ee indicating the presence of Si II at high velocity. Also the SiII 4130λ line, which can be used for classifying high redshift SNe as type Ia, is nearly washed out. Note also that the analysis of the Ca II IR triplet of SN 1999ee before maximum (Mazzali private communication) requires high velocity material in analogy to what found for 2001el [53].

Two other odd SNIa are 2000cx and 2002cx which do not fit into any photometric and spectroscopic sequence still showing the main characteristics of type Ia SNe [30, 31].

3 Trends in SNIa Spectroscopy

More and better data are required to clarify which parameters govern the SNIa explosions and to validate the proposed progenitor scenarios. To solve these questions large collaborations have born which have as immediate goal the intensive, multiwavelength monitoring of nearby SNIa.

Examples of such intensive monitoring are the studies of SNe 1999ee [19] and 2002bo [3], for which the rise to maximum has been sampled daily starting about two weeks before maximum. The analysis of these spectra has allowed the discovery of strong time evolutions of the ratio $\mathcal{R}$(SiII) with individual behaviors for each SNIa (cf. Fig. 9 of Benetti et al. [3]), as mentioned above.

These two objects have been extensively monitored spectroscopically also in the infrared. The comparative analysis with the IR spectra of SN 1994D [39] at about day -8.5, $+11.1$ and $+29.4$ confirms that the overall spectroscopic homogeneity among normal SNe Ia extends to the IR-domain, with small variations. Spectral synthesis on the spectra of SN 2002bo favors the MgII identification for the 10800Å line and that of SiII 16910Å and MgII 16760/800 Å(with the SiII dominant) for the broad P-Cygni profile observed

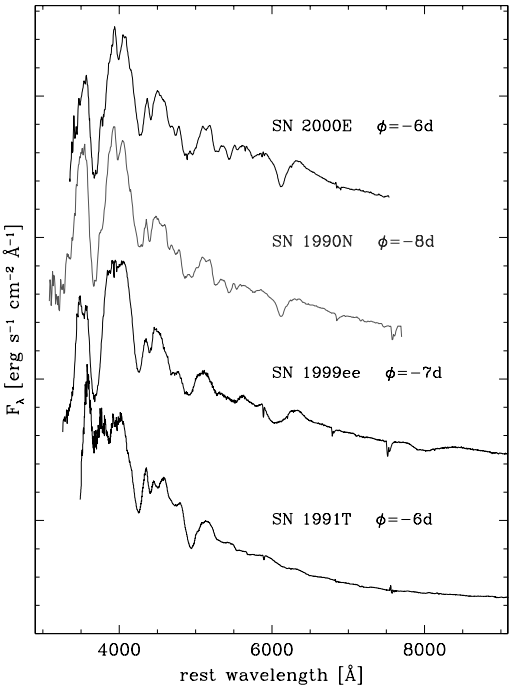

Fig. 1. Comparison of the spectra of SNe 2000E ($\Delta m_{15} = 0.94$ mag $(100\mathrm{d})^{-1}$), 1990N ($\Delta m_{15} = 1.05$), 1999ee ($\Delta m_{15} = 0.92$), 1991T ($\Delta m_{15} = 0.94$), taken about 1 week before maximum light. They have been corrected for extinction and reported to the parent galaxy rest frame.

at ∼16000Å. On the contrary, major differences are visible when the comparison is made with peculiar objects, e.g., the faint SN 1999by [23], especially because of the presence of strong C I and O I lines.

The optical and the IR spectra of SNIa [19] shows different behaviors: 1) while the optical spectrum before maximum is dominated by strong P Cygni profiles of intermediate-mass elements, such as Ca II, Si II, Mg II, S II, the IR is characterized by a smooth, almost featureless continuum; 2) the lines of iron group elements, such as Co II, Fe II and Ni II, emerge in the IR as soon as one week past maximum, definitely earlier than in the visual. This supports the suggestion [51] that the IR photosphere recedes rapidly to the center of the supernova, while at optical wavelengths the greater opacity arising from the higher spectral density of lines keeps the photosphere at higher velocities. At the longer wavelengths the overall emission increases after maximum light as a result of a shift in ionization to lower ionization species, which have greater emissivity in the near IR. It appears, therefore, that the J-band deficit is due to the relative absence of lines in the 12000 Å region, rather than increasing opacity, and that the secondary maxima

exhibited by the IR light curves are due to the increasing release of energy through lower optical depth IR transitions. The prominent postmaximum emission features displayed by SNe 1999ee and 2002bo in the H and K bands lend support to this scenario [19].

A new powerful tool for understanding the nature of SNIa is spectropolarimetry. SNIa polarization is usually very small, hence difficult to measure. In most cases only upper limits have been provided, in others polarization of the order of 0.2–0.3% (corresponding to an asphericity of ∼10%) has been detected before maximum light, likely due to a distorted photosphere or element distribution. Such asphericity may cause a directional dependence of the luminosity and a corresponding dispersion in the brightness-decline relation of SNe Ia. Although this may not jeopardize the use of SNIa as distance indicators, it might intrinsically limit the accuracy reachable via SNIa.

Very interesting spectropolarimetric data have been collected for special SNIa. High polarization (0.7%) was found in the subluminous SN 1999by [24], which may suggest a relation between the observed asymmetry and the mechanism that produces this kind of under energetic SNIa. The high velocity components (v∼ 25000 km s^{-1}) of the CaII IR triplet observed in SN 2001el have shown a polarization of about 0.7%, much higher than the continuum (0.2%) indicating that kinematically and geometrically distinct features can exist in SNIa [58]. High signal–to–noise data for more objects are definitely needed in order to understand if these asymmetries are the rule in SNIa, and to get insights on the geometry of the precursor systems.

A special case is that of SN 2002ic, the first SNIa for which H has been unequivocally detected [20]. Indeed both the light curve and the spectral line appearance points toward a strong interaction of the SN ejecta with a dense CSM. At the early phase the characteristic spectrum of a SNIa seemed veiled by a strong continuum. With time the spectrum evolved to resemble those of SNe 1997cy and 1999E, which are commonly considered as SNIIn [17, 48, 56]. Also the profile of the Hα emission requires at least two components with different widths to provide a reasonable fit. It has, therefore, been suggested that some SNIIn are the outcome of thermonuclear explosions rather than core collapses. Despite the early claim that these observations were a proof that the progenitor system of SN 2002ic was a binary consisting of a C/O WD and an AGB star [20], it may well be that it is the result of the merging of a WD with the core of an AGB star, and that the H we observe was previously ejected during a common envelope phase [32]. The rarity of such an event and the large amount of H required favors the latter hypothesis. A polarization of $p \geq 1\%$ [28] has been detected also in SN 2002ic.

4 Core Collapse Supernovae

Stars of initial mass larger than about 8 $M_{\odot}$ undergo the collapse of the core after burning H, He, C, Ne, O, Si. From such collapse a SN usually results.

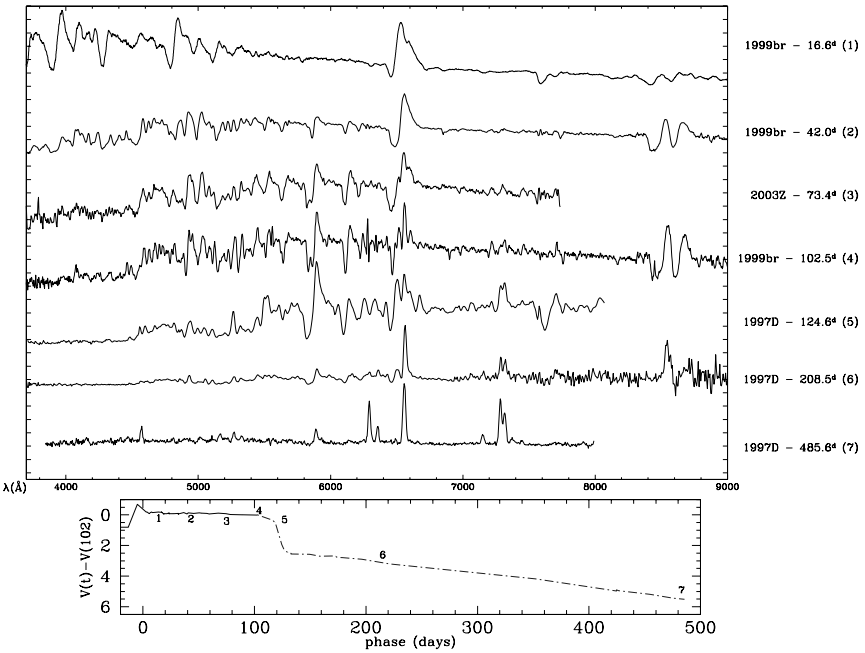

Fig. 2. Spectral evolution of low–luminosity SNII. The objects and the days after the estimated epochs of explosions are marked on the right. In the bottom panel are marked the corresponding epochs on a schematic light curve.

Core collapse SNe can vary considerably in luminosity, spectral lines and time evolution. The main parameter governing the observed diversity is the envelope mass [40]. Stars retaining H will display the lines of this element during their entire evolution and are called SNII. If the H mass is large (10−15 $M_\odot$) the release of the energy deposited by the shock in the envelope and by the recombination can sustain the luminosity for months, producing the so-called SNII Plateau. If the envelope is less massive ($1 - 2$ $M_\odot$), stripped by a companion or lost by stellar wind, the SN quickly fades producing the so–called SNII Linear.

In both cases the spectrum evolves from a very blue, featureless continuum short after the burst (color temperature higher than 10^4 K) to one dominated by H and He in a few days. Then, as the temperature continues to fall, other low excitation lines of Na I, Ca II, Fe II, Sc II appear, all with P–Cygni profiles. Subsequently, as the entire star becomes transparent and the light curve settles onto the radioactive tail, the spectrum enters the nebular phase, dominated by Hα and forbidden emission lines of [O I], [Ca II], [Fe II] and Mg I].

After SN 1987A, the best studied (but somehow atypical) object, whose detailed spectral observations provided evidences of clumps and mixing in the

ejecta [21, 50] as well as of dust formation [9], other SNII have been studied extensively. An interesting case is SN 1999em [1, 11, 18, 29]. The analysis of the Hα structure at photospheric epoch revealed non spherical ejection of ^{56}Ni, while the transformation of the [O I] 6300 λ line profile around day 500 showed that dust formed earlier and at lower velocity than in SN 1987A, probably because of the lower temperature due to a smaller amount of ^{56}Ni ejected. It appears, therefore, that these phenomena are common in core collapse SNe, though with distinctive characteristics for each object.

Core–collapse SNe which have lost most of their H and even most, or all, their He envelope, are called SNIb and Ic, respectively. Indeed the transition between SNII and SNIb, and between SNIb and SNIc is not sharp. SN1993J, celebrated with this Conference, is the best example (but not the only one) of a SN transforming with age from a type II to a type Ib SN, i.e. from one dominated by H to one dominated by He, with only residual H lines. For this reason it is called of type IIb [14].

At a deep scrutiny, H has been found in the spectra of other SNIb. SN 2000H is a remarkable case, but Branch et al. [7] have shown that tiny differences in the H mass can vary the optical depths of H lines and make the transition from type IIb to type Ib SNe. Similarly, an increasing number of SNIc show evidence of He, e.g., SN 1990B, SN 1987M and even the prototypical SN1994I [8, 12]. Again, it appears that moderate difference in the He mass can explain the spectroscopic difference between typical SNIb and SNIc [7]. Different is the case of SN 1999cq, in which He with expansion velocity much slower than other lines, points to the interaction of the ejecta with a dense shell of almost pure He originating from stellar wind or mass transfer to a companion [33].

4.1 News on Core Collapse SN Spectra

In the last years new light on the lower end of the luminosity function of SNII has been shed [42, 60]. SN1997D showed from discovery unprecedented properties. The expansion velocity deduced from the displacement of the absorption was extremely low and the continuum intrinsically red. Moreover, the luminosity was very low both at discovery and in the nebular stage, indicating the ejection of a very little amount of ^{56}Ni [55].

Four new objects with similar properties have been recently added [42]. Although the observations of individual objects are erratic and incomplete, because hampered by the faintness of the SNe, taken together these data show a common evolutionary path. Fig. 2 summarizes the spectroscopic evolution: during the first 50 days (spectra 1 and 2) the spectra change from a continuum dominated by Balmer lines to a more complex appearance with strong Na I, Ba II and Ca II. The expansion velocities, lower than in normal SNII, decrease from 5000 to 3000 km s^{-1}. During the second half of the plateau (spectra 3 and 4) these peculiarities strengthen significantly: the absorption troughs move to even lower velocities, down to $1000 - 1500$ km s^{-1}, the continuum

becomes redder and low excitation lines of Ba II, Sc II, Fe II, Sr II and Ti II appear. In particular, the Ba II lines become the strongest features of the entire spectrum, even stronger than Hα. During the post plateau decline (spectrum 5) the transition to the nebular phase begins and forbidden lines (e.g., [Ca II] 7291–7323 Å) emerge. The spectra of the latest epochs (6 and 7) resemble those of normal SNII, with the usual (though narrower) emissions of Hα, Na I, [O I], [Ca II], [Fe II], Mg I].

Pastorello et al. [42] conclude that low–luminosity CC–SNe are similar to typical CC–SNe in having a clear plateau, lasting for ∼100 days, followed by a late–time decline driven by the decay of ^{56}Co, and typical spectral lines at all phases. However, they keep distinctive characteristics in that: 1) during the plateau phase the luminosity is at least a factor 10 times less than in typical CC-SNe; 2) the expansion velocity is unusually low at all epochs; and 3) the mass of ^{56}Co which drives the late-time tail is at least a factor ∼10 lower than normal.

Important advances have been obtained also at the opposite extreme, i.e. for luminous and energetic SNe, often called hypernovae. In particular, large interest have received a number of SNe associated to GRBs. The first and best studied case is SN 1998bw which coincided in time and space with GRB980425 [15] and was a powerful radio and X-ray emitter. In the optical most of its peculiarity stayed in the unprecedented broadness of the spectral features corresponding to expansion velocities of the ejecta as high as 3×10^4 km s^{-1} at maximum light [43]. The high kinetic energy together with the high luminosity indicated an explosion energy of about 5×10^{52} erg, if spherical symmetry is assumed [25]. Detailed spectral modeling [6, 25, 27, 36] has shown that the apparent emissions, which at maximum peaked around 5000, 6300 and 8500 Å, were actually low opacity regions of the spectra from which photons could escape. Lines of Si II, O I, Ca II and FeII have been identified, as well as He I 10830 Å.

Only during the nebular phase SN 1998bw reentered into the conventional taxonomical scheme with [O I], Mg I], [Fe II], [Ca II] emissions which confirmed the early hypothesis that it was a peculiar case of SNIc. Also in the nebular phase the lines were unusually broad (9800 ± 500 km s^{-1} on day 201 [43]).

After SN 1998bw several other hypernovae have been recognized, some were SNIc bearing strong resemblance to SN 1998bw but with smaller KE (1997ef, 1997dq, 1999as, 2002ap [26, 27, 34, 37]), other were SNIIn (1997cy and 1999E [17, 48, 56]), which displayed narrow Hα on the top of broad wings and broad light curves, clear indications of ejecta-CSM interaction. For some of them the possible association with GRB has been claimed but no firm conclusion was reached. Other cases of possible SN-GRB association have been reported on the basis of 'bumps' detected in the light curves of GRB afterglows. The early spectroscopy of these bumps was intriguing but not conclusive [10, 16].

Excitement mounted when, short before this Conference, spectra of the rebrightening of the afterglow of the nearby GRB030329 (z=0.1685) were secured [35, 52]. Already one week after the burst a SN spectrum, with emissions at approximately 5000 and 4200 Å, was detected and it dominated over the power-law continuum few days later (day $\sim$ 11). This SN, named 2003dh, resembled, both as spectral evolution and light curve, SN 1998bw at the corresponding epoch from the associated GRB. A more accurate analysis and spectral modeling suggested that SN 2003dh was intermediate between SN 1998bw and SN 1997ef, as to kinetic energy and ^{56}Ni production [38] and pointed out the need for asymmetric explosions. Whatever the physics of the explosion, this new example provides solid evidence that at least some GRBs arise from core-collapse SNe and opens new frontiers in the SN research.

Acknowledgement. This research is supported in part by the European Community's Human Potential Programme under contract HPRN-CT-2002-00303, and grant Cofin 2001021149 of the Italian Ministry of Education, University and Research.

References

1. E. Baron et al. : Astrophys. J. **545**, 444 (2000)
2. S. Benetti et al. : Mon. Not. R. Astron. Soc. **322**, 361 (2001)
3. S. Benetti et al. : astro-ph 0309665 (2003)
4. D. Branch, S. Van Den Bergh: Astron. J. **105**, 2231 (1993)
5. D. Branch et al. : Pub. Astron. Soc. Pacific **107**, 1019 (1995)
6. D. Branch: In: *Supernovae and Gamma-Ray Bursts* eds. M. Livio, N. Panagia (Cambridge Univ. Press: Cambridge, 2001) p. 96
7. D. Branch et al. : Astrophys. J. **566**, 1005 (2002)
8. A. Clocchiatti et al. : Astrophys. J. **462**, 462 (1996)
9. I.J. Danziger et al. : In: *Supernova 1987A and Other Supernovae*, ed. I.J. Danziger, K. Kjar (ESO Conf. and Workshop Proc.) p. 217
10. M. Della Valle et al. : Astron. Astrophys. **406**, 33 (2003)
11. A. Elmhamdi et al. : Mon. Not. R. Astron. Soc. **338**, 939 (2003)
12. A.V. Filippenko et al. : Astrophys. J. Lett. **450**, L11 (1995)
13. A.V. Filippenko: Ann. Rev. Astron. Astrophys. **35**, 309 (1997)
14. A.V. Filippenko, T. Matheson: "Optical, Ultraviolet, and Infrared Observations of SN 1993J." In: this Proceedings
15. T.J. Galama et al. : Nature **395**, 670 (1998)
16. P.M. Garnavich et al. : Astrophys. J. **582**, 924 (2003)
17. L. Germany et al. : Astrophys. J. **533**, 320 (2000)
18. M. Hamuy et al. : Astrophys. J. **558**, 615 (2001)
19. M. Hamuy et al. : Astron. J. **124**, 417 (2002)
20. M. Hamuy et al. : Nature **424**, 651 (2003)
21. R.W. Hanuschik et al. : Mon. Not. R. Astron. Soc. **243**, 41 (1988)
22. K. Hatano et al. : Astrophys. J. Lett. **543**, L49 (2000)
23. P. Höflich et al. : Astrophys. J. **568**, 791 (2002)

24. D.A. Howell et al. : Astrophys. J. **556**, 302 (2001)
25. K. Iwamoto et al. : Nature **395**, 672 (1998)
26. K. Iwamoto et al. : Astrophys. J. **534**, 660 (2000)
27. K. Iwamoto et al. : "SN 1998bw and Hypernovae." In: *Supernovae and Gamma-Ray Bursters*, ed. K.W. Weiler (Springer: Berlin, 2003) pp. 243-281
28. K.S. Kawabata et al. : IAUC 8161 (2003)
29. D.C. Leonard et al. : Pub. Astron. Soc. Pacific **114**, 35 (2002)
30. W. Li, A.V. Filippenko et al. : Pub. Astron. Soc. Pacific **113**, 1178 (2001)
31. W. Li et al. : astro-ph 0301428 (2003)
32. M. Livio, A.G. Riess: Astrophys. J. Lett. **594**, L93 (2003)
33. T. Matheson et al. : Astron. J. **119**, 2303 (2000)
34. T. Matheson et al. : Astron. J. **121**, 1648 (2001)
35. T. Matheson et al. : astro-ph 0307435 (2003)
36. P. Mazzali et al. : Astrophys. J. **559**, 1047 (2001)
37. P. Mazzali et al. : Astrophys. J. Lett. **572**, L61 (2002)
38. P. Mazzali et al. : astro-ph 0309555 (2003)
39. W.P.S. Meikle et al. : Mon. Not. R. Astron. Soc. **281**, 263 (1996)
40. K. Nomoto, K. Iwamoto, T. Suzuki: Phys. Rep. **256**, 173 (1995)
41. P. Nugent et al. : Astrophys. J. Lett. **455**, L147 (1995)
42. A. Pastorello et al. : astro-ph 0309264 (2003)
43. F. Patat et al. : Astrophys. J. **555**, 917 (2001)
44. S. Perlmutter et al: Astrophys. J. **483**, 565 (1997)
45. M.M. Phillips: Astrophys. J. Lett. **413**, L105 (1993)
46. M.M. Phillips: Astron. J. **118**, 1766 (1999)
47. A,G. Riess et al. : Astron. J. **116**, 1009 (1998)
48. L. Rigon et al. : Mon. Not. R. Astron. Soc. **340**, 19 (2003)
49. B.P. Schmidt et al. : Astron. J. **107**, 1444 (1994)
50. J. Spyromilio et al. : Mon. Not. R. Astron. Soc. **263**, 530 (1993)
51. J. Spyromilio et al. : Mon. Not. R. Astron. Soc. **266**, L17 (1994)
52. K.Z. Stanek et al. : Astrophys. J. **591**, 17 (2003)
53. R.C. Thomas et al. : astro-ph 0302260 (2003)
54. M. Turatto, et al: Mon. Not. R. Astron. Soc. **283**, 1 (1996)
55. M. Turatto, et al: Astrophys. J. Lett. **498**, L129 (1998)
56. M. Turatto, et al: Astrophys. J. Lett. **534**, L57 (2000)
57. M. Turatto: "Classification of Supernovae." In: *Supernovae and Gamma-Ray Bursters*, ed. K.W. Weiler (Springer: Berlin, 2003) pp. 21-36
58. L. Wang et al. : Astrophys. J. **591**, 1110 (2003)
59. J.C. Wheeler, S. Benetti: In: *Allen's Astrophysical Quantities*, ed. A.N. Cox (Springer: New York, 2000) p. 451
60. L. Zampieri et al. : Mon. Not. R. Astron. Soc. **338**, 711 (2003)

Optical Spectroscopy of Type Ia Supernovae

Thomas Matheson

Harvard-Smithsonian Center for Astrophysics, 60 Garden Street, Cambridge, MA 02138, USA
tmatheson@cfa.harvard.edu

Summary. The supernova (SN) group at the Harvard-Smithsonian Center for Astrophysics has been using the facilities of the F. L. Whipple Observatory to gather optical photometric and spectroscopic data on nearby supernovae for several years. The collection of spectra of Type Ia SNe is now large enough to allow a comprehensive analysis. I will present preliminary results from a study of a subsample of the CfA Type Ia spectroscopic database, with over 200 spectra of 31 Type Ia SNe. The SNe selected all have well-calibrated light curves and cover a wide scope of luminosity classes. The epochs of observation range from fourteen days before maximum to fifty days past maximum. All of the spectra were obtained with the same instrument on the same telescope, and were reduced using the same techniques. With such a large, homogeneous data set, the spectroscopic similarities and differences among Type Ia SNe become readily apparent.

1 Introduction

Type Ia Supernovae (SNe) have long been viewed as a homogeneous class (see, e.g., [8]) for a review of Type Ia SNe). This perception began to change when SNe appeared that were still of Type Ia, yet showed peculiarities that clearly set them apart from the standard picture. The first dramatic examples were the overluminous SN 1991T (e.g., [3, 12]) and the underluminous SN 1991bg (e.g., [2, 7]). Some differences were already apparent from earlier SNe such as SN 1986G [11]. In recent years, it has become clear that peculiar Type Ia SNe are more common than previously thought (e.g., [9]).

While the diversity has been broadly characterized by light-curve shape [6, 13, 14, 15], there are also spectroscopic differences (see [4] for a general review of SN spectroscopy). For example, overluminous SNe lack strong silicon and calcium lines while higher-excitation lines of iron are present, as in SN 1991T [3, 10], although sometimes calcium is strong as in SN 1999aa [9]. Underluminous SNe are characterized by strong absorptions of titanium, whose strength increases with decreasing temperature (e.g., [5]). The once homogeneous class is now quite diverse (Fig. 1).

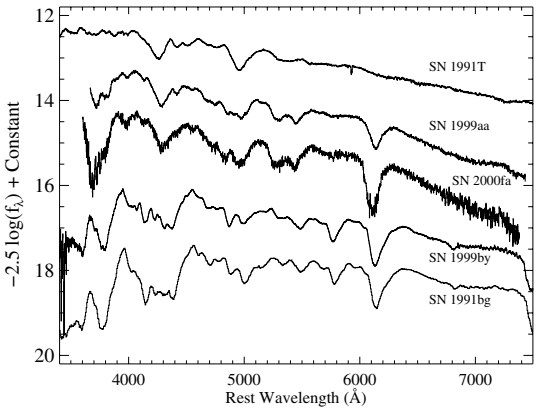

Fig. 1. Examples of Type Ia SNe with different Δm_{15} values and the spectroscopic differences that this implies.

2 Observations and Reduction

The SN group at the Harvard-Smithsonian Center for Astrophysics operates a long-term monitoring program for nearby SNe. We obtain low-dispersion spectra of two to three SNe per night with the FAST spectrograph [1] on the 1.5-m Tillinghast telescope at the F. L. Whipple Observatory (FLWO). The FAST spectrograph uses a 2688×512 Loral CCD with a spatial scale of 1.″1 per pixel in the binning mode used for these observations.

The data are reduced in the standard manner with IRAF[1] and our own routines. Wavelength calibration was accomplished with HeNeAr lamps taken immediately after each SN exposure. Small-scale adjustments derived from night-sky lines in the SN frames were also applied. All the data are from the same instrument/telescope combination and have been reduced in the same manner, ensuring consistency in the database.

For this sample, we selected Type Ia SNe for which we have well-sampled light curves from our complementary program of photometry with the FLWO 1.2-m telescope. With this data, the phase of each spectrum is known, as well as the value of Δm_{15}. The SNe chosen cover a wide range of Δm_{15} (0.85–1.93). In addition, all galaxy types are represented among the hosts. The current sample contains 387 spectra of 31 Type Ia SNe, with epochs from fourteen days before maximum to several months past maximum. There are 201 spectra within fourteen days of maximum (e.g., Fig. 2).

[1] IRAF is distributed by the National Optical Astronomy Observatories, which are operated by the Association of Universities for Research in Astronomy, Inc., under cooperative agreement with the National Science Foundation.

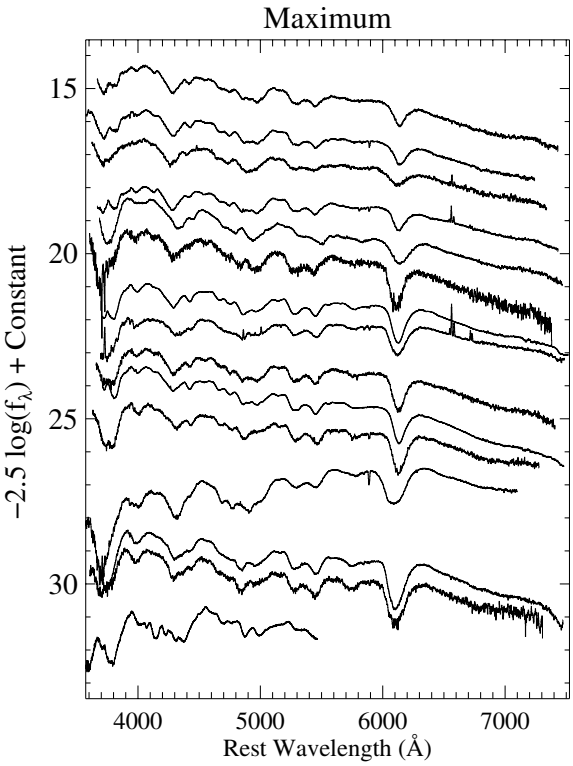

Fig. 2. Montage of Type Ia spectra at maximum. The value of Δm_{15} for each SN increases downward.

3 The CfA Type Ia Spectroscopic Database

We began our characterization of the Type Ia spectra in the database by selecting only those that were within fourteen days of maximum. The continuum was removed by selecting anchor points at regions of the spectrum that are not affected strongly by absorption lines. This removed some of the effects of reddening as well as issues related to differential light losses as a result of not observing at the same parallactic angle (which does affect some of our data). We then used a least-squares minimization technique to fit Gaussian profiles to the seventeen strongest lines in the spectrum. This was all done empirically, without any model of line formation. The result was a list of line depth, width, and position for each spectrum. Using plausible line identifications, we can then assign a velocity of expansion to each line.

One of the distinctive spectroscopic features of the peculiar Type Ia SNe, is the increase in strength of the titanium lines as Δm_{15} increases. The feature normally seen near 5800 Å is caused by silicon, but titanium begins to increase this absorption as the temperature decreases. This is shown in detail by [5],

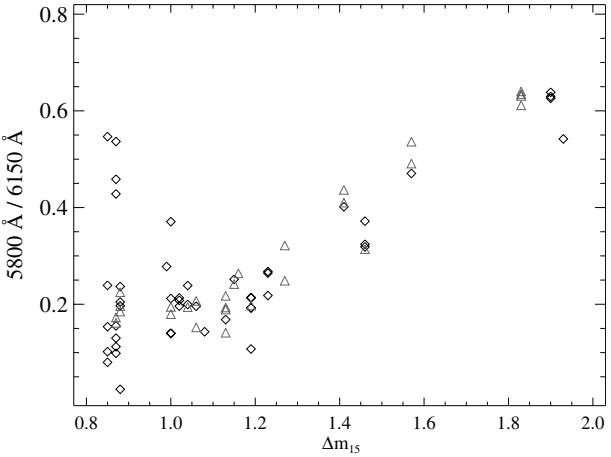

Fig. 3. Ratio of the depth of the 5800Å feature to the depth of the 6150 Å feature as a function of Δm_{15} for spectra taken within four days of maximum. The relative strength of the 5800 Å line increases as the SN becomes a faster decliner, and thus more underluminous. This has been attributed to a temperature sequence with the strength of a titanium absorption increasing as the temperature decreases.

and, using a different set of SNe, we can reproduce this effect (Fig. 3), with much more complete sampling for the underluminous SNe.

The velocity of expansion of the SN can be estimated from the minimum of the absorption lines. The Si II 6355 Å line that usually appears near 6150 Å is perhaps the most isolated feature in the spectral range that we observe. Using this line, we compared the velocity of expansion with Δm_{15}. As shown in Fig. 4, there is a large range in expansion velocity, but with a general

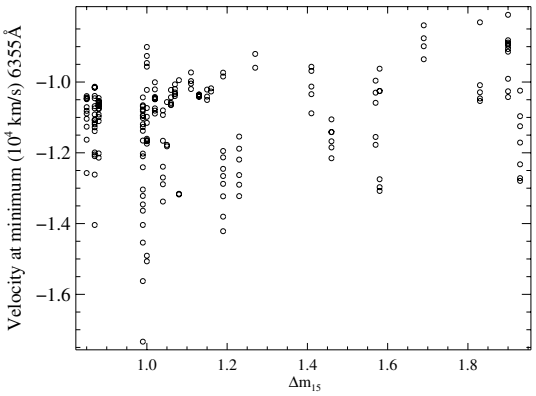

Fig. 4. Expansion velocity derived from the minimum of the 6150 Å feature as a function of Δm_{15}.

trend that the overluminous and normal SNe tend to have higher expansion velocities. The width of the line, though, does not follow this trend.

4 Final Remarks

We have just begun to explore the CfA spectroscopic database. It is clear from these initial surveys that the Type Ia SNe can show a large degree of heterogeneity. There are some trends with the defined light-curve characterizations that will help to constrain the explosion models. In addition, there is spectroscopic variation for SNe with identical Δm_{15} values, implying that there is not just a simple one-parameter sequence that can explain Type Ia SNe.

Acknowledgement. I wish to thank Robert Kirshner, Pete Challis, Saurabh Jha, and Peter Garnavich for their tremendous help in securing and analyzing the spectra described here. In addition, the two main observers at FLWO, Perry Berlind and Mike Calkins, have been invaluable to this project. Without their skill and dedication, this database would not exist.

References

1. D. Fabricant, P. Cheimets, N. Caldwell, J. Geary: Pub. Astron. Soc. Pacific **110**, 79 (1998)
2. A.V. Filippenko et al. : Astron. J. **104**, 1543 (1992)
3. A.V. Filippenko et al. : Astrophys. J. Lett. **384**, L15 (1992)
4. A.V. Filippenko: Ann. Rev. Astron. Astrophys. **35**, 309 (1997)
5. P.M. Garnavich et al. : Astrophys. J. in press
6. M. Hamuy, M.M. Phillips, N.B. Suntzeff, R.A. Schommer, J. Maza, R.C. Smith, P. Lira, R. Aviles: Astron. J. **112**, 2438 (1996)
7. B. Leibundgut et al. : Astron. J. **105**, 301 (1993)
8. B. Leibundgut: Astron. Astrophys. Rev. **10**, 179 (2000)
9. W. Li et al. : Astrophys. J. **546**, 734 (2001)
10. P.A. Mazzali, I.J. Danziger, M. Turatto: Astron. Astrophys. **297**, 509 (1995)
11. M.M. Phillips et al. : Pub. Astron. Soc. Pacific **99**, 592 (1987)
12. M.M. Phillips, L.A. Wells, N.B. Suntzeff, M. Hamuy, B. Leibundgut, R.P. Kirshner, C.B. Foltz: Astron. J. **103**, 1632 (1992)
13. M.M. Phillips: Astrophys. J. **413**, L105 (1993)
14. A.G. Riess, W.H. Press, R.P. Kirshner: Astrophys. J. **438**, L17 (1995)
15. A.G. Riess, W.H. Press, R.P. Kirshner: Astrophys. J. **473**, 88 (1996)

The Early Spectroscopy of Supernovae

Hitoshi Yamaoka[1], Kazuya Ayani[2] and Tetsuya Hashimoto[3]

[1] Department of Physics, Kyushu University, 812-8581 Japan;
yamaoka@rc.kyushu-u.ac.jp
[2] Bisei Astronomical Observatory
ayani@bao.go.jp
[3] Department of Physics, Kyushu University, 812-8581 Japan**;
bootes1129@yahoo.co.jp

Summary. The spectroscopy of a supernova (SN) just after its discovery is quite important not only for the spectral type classification but also for the planning further follow-up observations or the target-of-opportunity observations (ToOs). The early spectroscopy is needed also because the information from the outermost envelope of such exploding objects as SNe cannot be obtained in the later phase. In order to obtain the early spectrum, the quick circulation of the discovery information is important. We introduce our contributions with the public astronomical observatories in Japan, including the case of "hypernova" SN 2002ap discovered by a Japanese amateur astronomer. We summarize the time interval between the discoveries, the announcements, and the first spectral classifications of recent SNe, and discuss what would be required for the early spectroscopy.

1 Importance of the Early Spectroscopy

The early spectroscopic observation after the discovery of a SN is very important in many aspects. The early type determination is necessary to trigger the ToOs, and to plan the follow-up observations. For example, type Ia SNe are strong source of the line γ-ray. The maximum light in some line γ-ray is expected to be earlier than the optical one [14], so the prompt type determination and the early γ-ray observation is especially needed. The γ-ray from SN 1991T, a peculiarly luminous SN Ia, was successfully detected [13].

Type II, Ib, and Ic SNe are thought to be core-collapse events of the massive stars whose envelopes had been lost during the evolution, so the interaction of the SN ejecta with the circumstellar matter made up by the lost envelope will cause a strong X-ray and radio emission. When the discovered SN turns out to be of these types, radio telescopes and X-ray satellites are planned to observe them.

The early spectrum contains the information of the outermost part of the ejecta, which cannot be obtained from the later observation. The diversity of type Ia SNe has been reported in the pre-maximum spectra [4].

** Present address: National Astronomical Observatory, Japan

Furthermore, we professional astronomers must reward the amateur discoverers by getting the most fruitful output. The bright (nearby, important) SNe have been discovered mainly by the amateur astronomers.

2 Our Contribution

We have been taking early spectra of SNe in order to obtain type determination. In Japan, there are many observatories with 1-m class telescopes, a main part of which are funded by the local self-governing body, such as prefecture, city, town, or even a village whose population is only thousands.

In these five years, we determined the types of over twenty nearby SNe, with the Bisei Astronomical Observatory 1.01-m telescope and the Gunma Astronomical Observatory 0.60-m telescope. Among them, SN Ia 1998bu was at the Virgo distance. After our type determination, the COMPTEL instrument of the CGRO observed it. The line γ-ray could not be detected from it, which constrained the amount of produced ^{56}Ni and the explosion models [3].

SN 2002ap, a type Ic "hypernova", was observed by us on the night of the announcement of the discovery. It turned out to be a hypernova (Kyoku-Cho-Shinsei in Japanese) by us [6] and by the others [2, 12]. The determination of the SN classification led the follow-up observations in the all wavelengths, including by the Subaru telescopes in optical and IR [5], by the VLA in radio [1], by the XMM-Newton in X-UV regions [15], and so on. After the type determination, we continued to take spectra of this object, and revealed the rapid evolution of the spectra. The expansion velocity measured from the Si line was about 25000 km s^{-1} on the first epoch, which rapidly decreased, besides the other hypernovae evolved more slowly [7]. Probably it is because the ejecta mass was quite small [11].

3 Between the Discovery and the Spectroscopy

Typical progress from the discovery of a SN to its spectral type determination would be summarized as:

1. Discovery of the new object,
2. Confirmation of the existence and no proper motion, by the discoverer or his colleague,
3. Report to the Central Bureau of the Astronomical Telegrams (CBAT),
4. Announcement of the discovery on an IAU circular,
5. Following the discovery, the spectroscopic observation and the type determination.

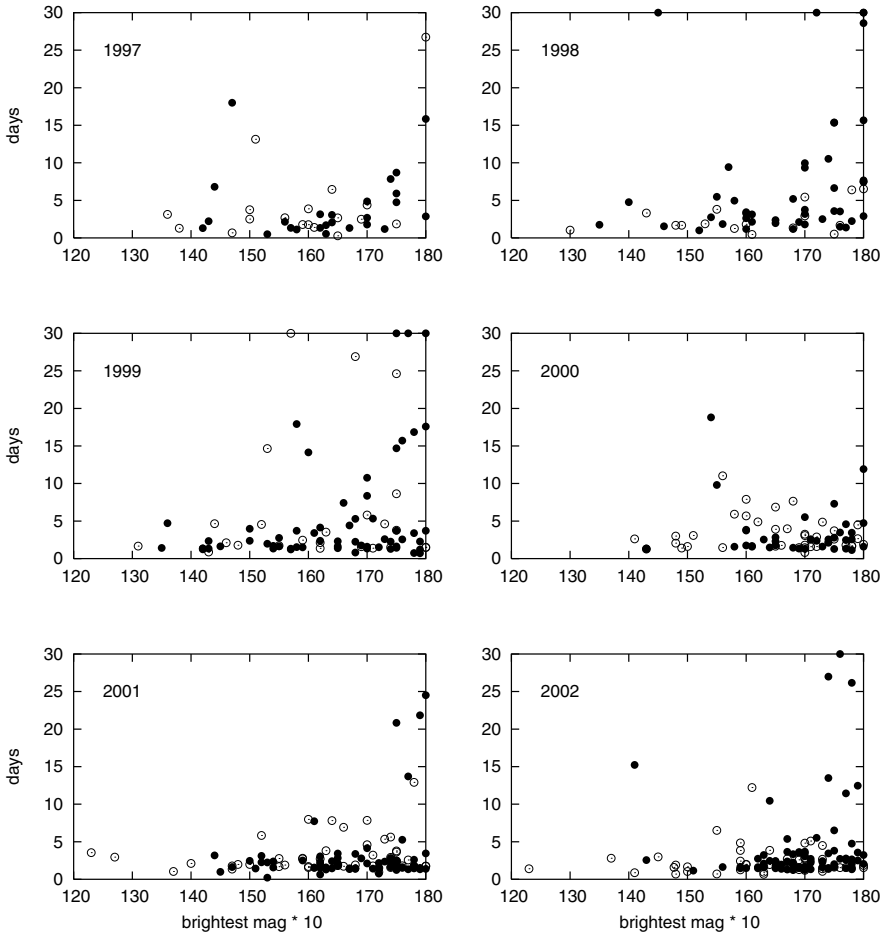

Fig. 1. Time intervals from the discovery of a SN and its announcement on the IAU Circular. The horizontal axis represents the observed brightest magnitude of the SN. Open circles represent the SNe discovered by the amateur astronomers, and filled circles are by the professionals (the KAIT, the NEAT and so on).

There are some bypasses on this course. If the CBAT thinks the confirmation by others is needed, it will be done within the closed members (skip Item 2). The discovery information is relayed also to the closed members to do spectroscopy (skip Item 3). Occasionally, the discovery information is posted to some mailing lists (skip Item 3 and/or Item 4). In such situations, the first spectroscopy is possibly reported on the same number of the IAU Circular as the discovery announcement.

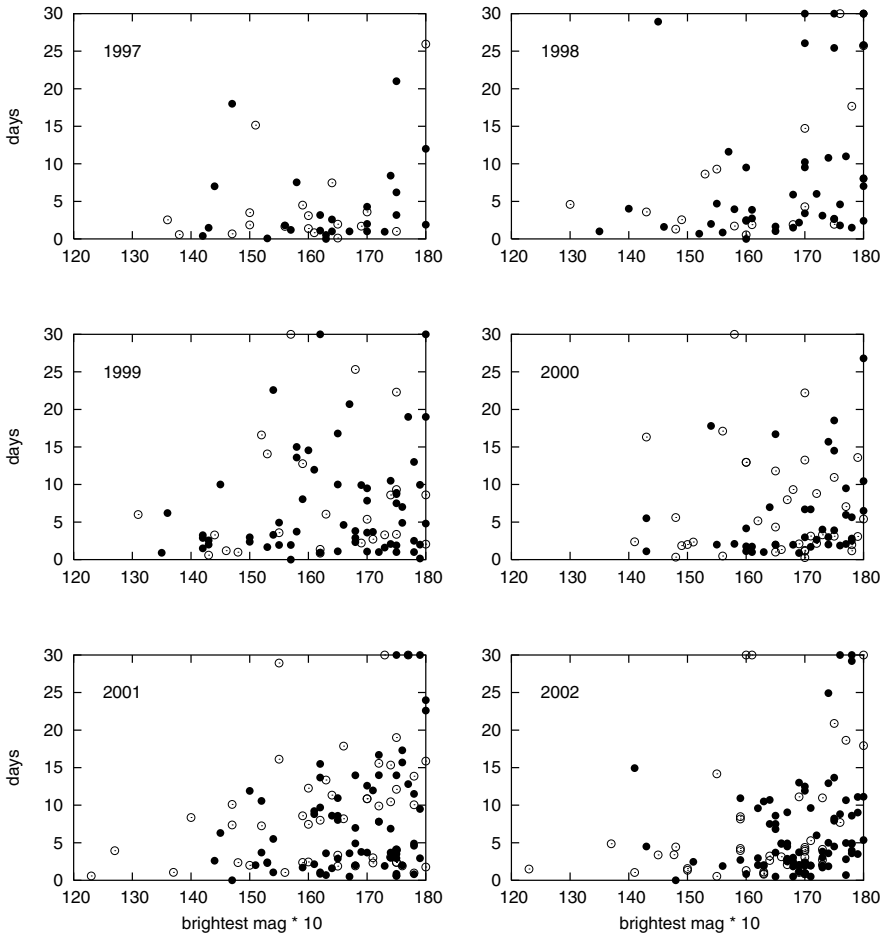

Fig. 2. Time intervals from the discovery of a SN and its spectroscopic type determination. The horizontal axis and the marks are same as Fig. 1.

4 Time Interval from the Discovery to the Announcement and the Spectroscopy

As shown in the previous section, there must be some time interval between the discovery of the new object and the announcement of it, or the spectroscopic observation. Fig. 1 shows the time duration from the discoveries to their announcement on the IAU circulars, year by year from 1997 to 2002. It is clearly shown that this interval has been much improved in recent years. There are, however, only small numbers of SNe being announced within one day after discovery. This "one day problem" is mainly caused by the CBAT

requirement for the discoverer to confirm the object on the second night before he/she reports it to the CBAT [8, 9, 10]. Indeed, SN 2002ap was left unobserved spectroscopically on the night of the discovery.

Figure 2 shows the time duration from the discovery to the first spectroscopy. This interval is slightly improved during recent years, but compared with Fig. 1, the improvement is rather slow.

5 Proposals and Most Recent Improvements

For the early spectroscopy, the "one day problem" should be avoided, at least for the nearby SNe. The SN hunter should report an SN discovery in the nearby galaxies, and it should be confirmed with the worldwide process. Open policy for the discovery information would help for the contribution by the potential observers. Such open policy can be seen on our web site[1].

On 2002 December, the CBAT began to issue the Central Bureau Electronic Telegram (CBET), which announces the discovery before the formal IAU Circular will be issued. And, as informed at the meeting of Commission 6 (Astronomical Telegrams) in the XXVth general assembly of the IAU at Sydney, the confirmation process is gradually opened. In the same assembly, the Division VIII (Galaxies and the Universe) established a working group on SNe, which will discuss the circulation of the information of SNe. We would like to be working together with these improvements.

References

1. E. Berger, S.R. Kulkarni, R.A. Chevalier: Astrophys. J. Lett. **577**, L5 (2002)
2. A. Gal-Yam, O. Shemmer, J. Dann: IAUC 7811 (2002)
3. R. Georgii et al. : Astron. Astrophys. **394**, 517 (2002)
4. D.J. Jeffery et al. : Astrophys. J. **397**, 304 (1992)
5. K.S. Kawabata et al. : Astrophys. J. Lett. **580**, L39 (2002)
6. K. Kinugasa et al. : IAUC 7811 (2002)
7. K. Kinugasa et al. : Astrophys. J. Lett. **577**, L97 (2002)
8. D.H. Levy: Sky & Tel. **95-2**, 69 (1998)
9. B.G. Marsden: IAUC 6737, 6739 (1997)
10. B.G. Marsden: IAUC 6739 (1997)
11. P.A. Mazzali et al. : Astrophys. J. Lett. **572**, L61 (2002)
12. P. Meikle, L. Lucy, S. Smartt et al: IAUC 7811 (2002)
13. D.J. Morris et al. : "Reassessment of the ^{56}Co emission from SN 1991T." In: *Proc. Fourth Compton Symposium*, eds. C.D. Dermer et al. (AIP Conf. Proc. **410**, 1997) pp. 1084-1088
14. T. Shigeyama et al. : Astron. Astrophys. Suppl. **97**, 223 (1993)
15. R. Soria, A.K.H. Kong: Astrophys. J. Lett. **572**, L33 (2002)

[1] `http://www.kusastro.kyoto-u.ac.jp/vsnet`

Optical Light Curves of Supernovae

Bruno Leibundgut

European Southern Observatory, Karl-Schwarzschild-Strasse 2, 85748 Garching, Germany;
bleibundgut@eso.org

Summary. Light curves are the most readily available and most frequently used astrophysical tools for variable phenomena. Supernovae are no exception to this. The information that can be extracted from detailed light and colors curves, together with the detailed study of the spectral evolution, tells us about the progenitor star, the various energy input sources, the explosion environment, material in the line of sight and cosmological effects. Over the past decade we have come to understand the power of detailed light curve studies and how they tie into the exploration of other astrophysical topics.

1 Introduction

This short review presents a general description of recent developments. More details can be found in the recent books edited by Weiler [58] and Hillebrandt and Leibundgut [29] and the reviews therein.

The importance of supernovae for cosmology has been stressed many times. After a long history of plans and predictions (e.g. [1, 9, 56]), the last decade has finally come through with large data sets confirming some of the foresights and added new surprises. Among the most interesting ones are the diversity of thermonuclear explosions (Type Ia Supernovae) and the richness in appearance of core-collapse supernovae. In addition, the emergence of GRBs as special core-collapse objects is enlarging the studies of supernovae.

Since light curves trace the temporal evolution of the supernova emission, they are most sensitive to the energy sources provided in the explosion, the radiation escape and modulations by external processes. The most important energy inputs are the supernova shock and the radioactivity from nucleosynthesis. These inputs are modulated by cooling due to the expansion and recombination, where shock energy is 'stored' for some time. The following sections will describe the energy source shaping the light curves and point towards important parameters which can be deduced from the light curves.

The importance of light curves also stems from the relative ease with which they can be acquired. With modern detectors and telescope technology it has become possible to obtain the essential photometry with robotic or semi-automatic telescopes. Hence, we are now faced with a wealth of light curves, many of them still unpublished, from several institutes (see [38] for

a list of references). The wavelength coverage has been extended into the near-infrared with new insights into the explosion physics, the homogeneity of the supernova subclasses and the emission mechanism. In each section will we point out the distinguishing features for the two main supernova mechanisms.

2 Energy Input

As mentioned above a supernova can draw from two major energy sources. While in core-collapse supernovae the energy comes from the gravitational energy freed in the collapse, the energy source of thermonuclear supernovae is the binding energy from fusion of intermediate-mass elements to the iron group. The collapse is converted to an explosion through mechanisms that are not fully understood (e.g. the role of the neutrino emission). However, once the shock is started, it propagates through the stellar envelope and ionizes the ejecta. The first electro-magnetic sign of the supernova explosion is when the shock breaks out of the stellar surface [17, 31]. This short phase (depending on the size of the progenitor star this is around a few hours) has never been observed. However, the rapid cooling due to the adiabatic expansion has been traced for SN 1987A [2], SN 1993J [42] and SN 1999ex [53]. The cooling and the expansion of the ejecta are balanced after a couple of days and the drop in the light curve is reversed into a brightening phase, during which the photosphere expands at roughly constant temperature. Depending on the size, mass and structure of the progenitor star and the explosion energy, the light curve peaks within a few days. When the temperature drops to about 5500K the hydrogen starts to recombine and the additional photons are added to the light curve [8, 50]. Again, depending on the mass and the explosion energy, the energy output is balanced into an extended plateau phase. This phase can reach up to 100 days in some cases. For explosions in stars that lack the hydrogen envelope this plateau phase is absent. This explains why Type Ib/c and some Type II supernovae have a rapid decline onto the radioactive tails.

During the implosion and the subsequent infall the material reaches densities and temperatures where explosive nucleosynthesis takes place. Some of the newly created elements are in radioactive isotopes and release nuclear energy on many different time scales. Since ^{56}Ni is close to the nuclear statistical equilibrium for these conditions, it becomes the major energy storage right after the explosion. Its radioactive decay produces $\gamma-$rays, which are converted in the debris to optical and infrared photons through down scattering. The half-life of ^{56}Ni of 6.1 days is swamped in the shock signatures, but the decay of the daughter nucleus ^{56}Co to stable ^{56}Fe has a half-life of 77.1 days and is the main power source after the recombination phase. The decline of the light curve after the plateau phase is tracing the ^{56}Co decay time extremely well. This has been observed for the classical SN 1999em [15, 26]

and SN 1987A [5] for several hundred days. For explosions with massive envelopes all energy produced in the radioactive decays is converted into optical and infrared radiation. In cases, where there are no massive envelopes, e.g. SNe Ib/c and SNe Ia, some of the $\gamma-$rays escape without leaving the energy behind. The decline rates then reflect the changes in the column densities and the $\gamma-$ray escape fraction. Eventually, even the massive envelopes thin out sufficiently so that some of the radioactive energy can escape.

One other energy source for supernovae is to tap into the kinetic energy available in the explosion. By converting kinetic energy of material into light (mostly through shocks and ionization) the supernovae can become significantly more luminous and also sustain the luminosity for a lot longer. Considering that for a typical core-collapse supernova about 100 times more kinetic energy is available than is emitted in light, this contribution can easily outshine the regular display.

For the thermonuclear supernovae the stars are incinerated from the inside out and no powerful shock is formed. In addition, the progenitor stars are very small, indeed tiny, if they really are white dwarfs, that a shock break out would last only for minutes and is unobservable. In this case, there is no preceding neutrino signal either. All energy is coming from the binding energy freed by burning material to the most densely bound nuclei in the iron group. The energy release is through the radioactive channel of ^{56}Ni through ^{56}Co to ^{56}Fe. The light curves show signatures of the Ni decay as well as the Co decay. No other energy input is expected in this case (for the only exception known so far see below).

3 Shaping Light Curves

The basic energy input for the supernova explosions are modified by the way the radiation escapes the ejecta and how the radiation interacts with material around the supernova. Through various different physical effects the light curves can take many different shapes. The two main types of supernovae can be treated separately, mostly because the thermonuclear supernovae display a much simpler behavior than the core-collapse variety.

3.1 Thermonuclear Supernovae

Type Ia Supernovae show less individuality among their light curve (and spectroscopic) behavior than the core-collapse explosions. This is a signature that they are coming from a more homogeneous parent population and also that their environment is less varied. The underlying physics of SN Ia explosions is probably also simpler than for core-collapse supernovae, although the calculations are extremely difficult involving physics at largely different scales [30]. The observational light curve can be summarized rather simply. Fig. 1 shows the main input sources, the radioactive decay chain of ^{56}Ni to

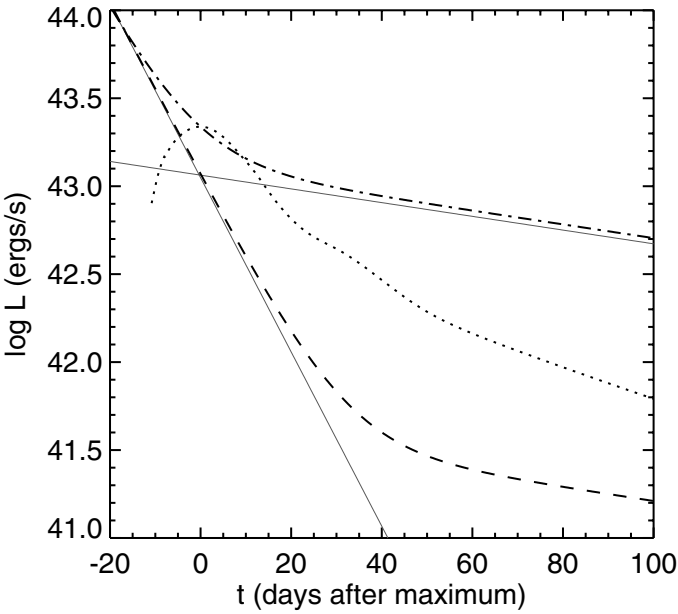

Fig. 1. Schematic of the energy input from radioactive ^{56}Ni and ^{56}Co to a thermonuclear supernova. The thin lines are for the pure ^{56}Ni (dashed) and ^{56}Co (dotted) decays. The dash-dotted line shows the total energy input from the decay chain, while the dashed line indicated the case when only the 5% of the ^{56}Co decay coming from electron capture is retained in the ejecta. The thick dotted line shows the observed bolometric light curve of SN 1992bc. Figure taken from [11].

^{56}Co and ^{56}Fe. The emission is modified by the fact that not all decay energy is released immediately at the surface. Right after explosion the surface expands at a nearly constant temperature of around 10000K and the brightness increase is mostly due to the increase in surface [51]. Before maximum most of the energy in fact is trapped within the dense ejecta and is released only slowly (e.g. [37]).

After about three weeks the emission reaches a maximum as the debris thins out and the mean free path of the photons increases to the size of the ejecta. Interestingly, this happens first in the near infrared [28, 32, 44, 48], where the light curves peak first. The optical light curves reach maximum about one week later. The color evolution around maximum is very fast with the supernova rapidly becoming redder within a couple of weeks. At this time the ejecta become progressively transparent to infrared and optical photons. Right after maximum the light curve slightly "overshoots" the energy input from the radioactive decays (as clearly seen in Fig. 1). These are photons that are produced from the previous radioactive decays and are escaping only now [49]. After the maximum phase the light curves are dominated by the continuous increase of the $\gamma-$ray escape and the reduction of the deposited energy

in the ejecta. There are quite some differences in the decline rates of the light curves in the various filters. Typically, the UV and blue light dims faster than the near-infrared. At wavelengths redder than R (about 650nm) the light curves display a re-brightening of the supernovae around two to three weeks after maximum [32, 44, 48]. The reason for this re-brightening is not completely clear. The main arguments are that the wavelength-dependent opacities allow redder photons to escape more easily and hence a re-distribution of the energy takes place.

Five weeks after explosion the thermonuclear supernovae decline towards oblivion. The ^{56}Co decay has a positron channel, where 19% of the energy is released. The positrons were assumed to deposit their energy within the ejecta and would not escape. In this case the light curves should follow the half-life of the cobalt decay. However, this is not observed and although the light curves do turn over [12, 36, 45], it appears that much of the energy from the positron channel still escapes [46]. This indicates that the magnetic fields in the explosion most likely have a radial form to allow the positrons to escape before annihilating.

The only real exception to the above picture is coming from the recent discovery of SN 2002ic. This object appears to have exploded within a very dense circumstellar environment and is displaying a very slow light curve [27]. The suspicion is that this explosion is interacting with this material and hence a lot of the kinetic energy of the explosion is converted to photons (cf. section 3.2).

3.2 Core-collapse Supernovae

The display of core-collapse supernovae is much more complex. This comes from the fact that many different physical processes play important roles here. The shock created in the explosion accelerates the material to velocities of about 10% of the speed of light. The progenitor stars are at different stages of their evolution, often influenced by companion stars, and depending on the amount of hydrogen still left in the envelope the appearances can be dramatically altered. As described above the early phases are dominated by emission coming from the shock and recombination. Type II supernovae can have quite a varied appearance at these phases, which indicates large differences in synthesized nickel mass, explosion energy and total mass [24]. The drop from the plateau onto the radioactive tail is a sensitive measure of the nickel mass as well [16]. Afterwards the energy from the radioactive decays powers the light curves for several hundred days. The decline rate at this stage gives a good indication of how massive the progenitor star was. If it tracks the half-life of ^{56}Co, then all energy is thermalized, while for faster declines less massive progenitors are indicated. SNe Ib/c typically have faster declines [13, 35]. The light curve of SN 1987A is a good example of a massive supernova [5] (see also Fig. 2).

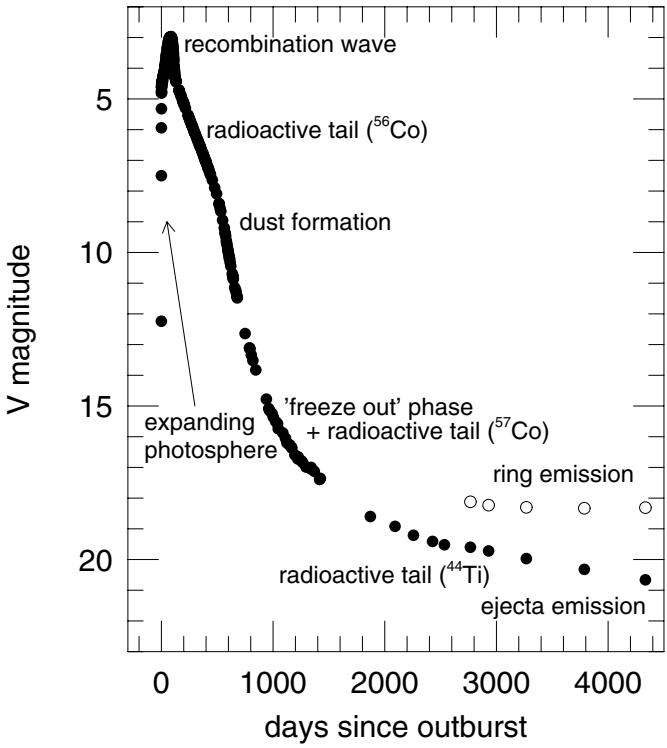

Fig. 2. The V light curve of SN 1987A as an example of the various phases core-collapse supernovae exhibit. Figure taken from [38].

For massive supernovae the absolute luminosity after about 120 days, together with the age of the supernova, gives a relatively accurate measure of the amount of ^{56}Co synthesized in the explosion [16, 24]. This measurement is now available for many core-collapse supernovae and is typically a factor 10 less than assumed in thermonuclear supernovae but spans almost a factor of 100 [47].

Only SN 1987A has been observed to late enough phases so that further changes in the light curves could be observed. Dust formation within the supernova lead to a dimming due to obscuration from the dust grains. Although precursor molecules for dust formation, mostly carbon monoxide, have been observed in many core-collapse supernovae [21, 22, 52], dust itself was only inferred from the observations of SN 1987A and recently possibly in SN 1999em [15, 41]. The SN 1987A light curve started to drop around 500 days when the dust formed.

Later SN 1987A started to show a flattening of the light curve. While the first explanations were pointing toward increased abundances of ^{44}Ti, which

would have been very difficult to explain within the nucleosynthesis picture, it turned out that the emission is coming from material that was ionized by the soft X-ray emission from the shock breakout and was recombining very slowly. This "freeze-out" was explained by Fransson and Kozma [19].

The light curve of SN 1987A has now declined further, although the decline in the near-infrared has slowed down to only a few tenths of magnitudes per year. The ejecta are now much fainter than the surrounding ring of dense pre-supernova material. The supernova shock has reached this ring after 15 years. The X-ray emission has already started to increase from this shock over the last few years [43] and also several dense intrusions have started to brighten [54].

Distances from Core-collapse Supernovae

The brilliance of core-collapse supernovae has enticed people to investigate their capabilities as distance indicators. Following early work by Baade [3], originally done for Cepheid stars, the expanding photosphere method (EPM, [14]) has been applied to several supernovae. The most comprehensive data sample has been assembled by Hamuy [23]. A critical test has become the distance to SN 1999em, which was determined through EPM [15, 26, 40] and which also has a Cepheid distance available [41]. The discrepancy is most likely attributable to the fact that the correction factor for the dilution of the black body flux in EPM are strongly model dependent and need to be calculated for each supernova individually.

Recently, Mario Hamuy has realized that the expansion velocity and the luminosity during the plateau phase correlate and that Type II SNe may be quite good distance indicators (see his article in these proceedings and [25]). The distance accuracy achieved this way can be better than 20%.

Supernovae with Circumstellar Interaction

Some supernovae explode in a dense environment. In this case, the shock breakout ionizes the material around the explosion. The ring around SN 1987A is only on example. In essence the supernova can create its own temporary HII region around itself. Within days, however, the material shock will start to interact with the dense circumstellar material [7]. The light curve in these cases are drowned in the photons from this interaction. The best studied cases so far are SN 1986J [39], SN 1988Z [57], SN 1995N [20] and SN 1998S [18]. The light curves of these objects evolve very slowly and they stay bright for a long time (typically over several years). Quite often these objects are also very luminous. Their spectral appearance is also markedly different from other supernovae. These objects are also detected as radio sources (see, e.g., [58]).

4 Conclusions

Light curve data of supernovae have reached a new quality in the past few years with increased temporal and wavelength coverage (e.g. [4, 6, 15, 25, 32, 33, 34, 53]). This will likely continue with more robotic telescopes and increased searches. Very importantly the amount of well-sampled infrared light curves is increasing rapidly. Although only little energy is radiated at these wavelengths during the first year or so of a supernova, it provides important information on the explosion physics. At late stages the supernovae have cooled down so much that most of the energy is actually emerging in the infrared and the predictions are that the light curves decay only very slowly as observed in SN 1987A, but also in SNe Ia.

The physics of supernovae can only be understood by combining as many observables as possible. The light curves, as the tracer of the temporal evolution of the luminosity, are essential and fundamental ingredients. The emission is shaped through various physical processes that can be identified and hence used for the interpretation of what is observed. One important tool, not discussed in this review, for such investigations are bolometric light curves, which combine all emerging flux. Such bolometric light curves are being assembled for some objects [10, 16]. They provide a convenient tool to investigate the physics behind the SNe Ia (e.g. [55]).

Supernovae are central to many astrophysical topics and the enhanced interest in them is creating a flood of data. The coming years will see the systematic exploration of these data for the physical interpretation of these brilliant events.

References

1. D. Arnett: Astrophys. J. **253**, 785 (1982)
2. D. Arnett, J.N. Bahcall, R.P. Kirshner, S.E. Woosley: Ann. Rev. Astron. Astrophys. **27**, 629 (1989)
3. W. Baade: Astronomische Nachrichten **228**, 359 (1926)
4. S. Benetti et al. : astro-ph 0309665 (2003)
5. P. Bouchet, M.M. Phillips, N.B. Suntzeff, C. Gouiffes. R. Hanuschik, D.H. Wooden: Astron. Astrophys. **245**, 490 (1991)
6. P. Candia et al. : Pub. Astron. Soc. Pacific **115**, 277 (2003)
7. R.A. Chevalier, C. Fransson: In: *Supernovae and Gamma−Ray Bursts*, ed. K. Weiler (Heidelberg: Springer, 2003)
8. N.N. Chugai: Sov. Astron. Lett. **16**, 457 (1990)
9. S.A. Colgate, A.G. Petschek, J.T. Kriese: Astrophys. J. Lett. **237**, L81 (1980)
10. G. Contardo, B. Leibundgut, W.D. Vacca: Astron. Astrophys. **359**, 876 (2000)
11. G. Contardo: *Bolometric light curves of Type Ia Supernovae*, PhD Thesis (Munich: Technical University, 2001)
12. J.B. Doggett, D. Branch: Astron. J. **90**, 2303 (1985)
13. V.T. Doroshenko, Yu.S. Efimov, N.M. Shakhovskoi: Astron. Lett. **21**, 580 (1995)

14. R.G. Eastman, B.P. Schmidt, R.P. Kirshner: Astrophys. J. **466**, 911 (1996)
15. A. Elmhamdi et al. : Mon. Not. R. Astron. Soc. **338**, 939 (2003)
16. A. Elmhamdi, N.N. Chugai, I.J. Danziger: Astron. Astrophys. **404**, 1077 (2003)
17. S.W. Falk, W.D. Arnett: Astrophys. J. Suppl. **33**, 515 (1977)
18. A. Fassia et al. : Mon. Not. R. Astron. Soc. **318**, 1093 (2000)
19. C. Fransson, C. Kozma: Astrophys. J. Lett. **408**, L25 (1993)
20. C. Fransson et al. : Astrophys. J. **572**, 350 (2002)
21. C.L. Gerardy, R.A. Fesen, P. Höflich, J.C. Wheeler: Astron. J. **119**, 2968 (2000)
22. C.L. Gerardy, R.A. Fesen, K. Nomoto, K. Maeda, P. Höflich, J.C. Wheeler: Pub. Astron. Soc. Pacific **54**, 905 (2002)
23. M. Hamuy: PhD Thesis (Tucson: University of Arizona, 2001)
24. M. Hamuy: Astrophys. J. **582**, 905 (2003)
25. M. Hamuy, P.A. Pinto: Astrophys. J. Lett. **566**, L63 (2002)
26. M. Hamuy et al. : Astron. J. **124**, 417 (2002)
27. M. Hamuy et al. : Nature **424**, 651 (2003)
28. M. Hernandez et al. : Mon. Not. R. Astron. Soc. **319**, 223 (2000)
29. W. Hillebrandt, B. Leibundgut (eds.): *From Twilight to Highlight: The Physics of Supernovae*, (Heidelberg: Springer, 2003)
30. W. Hillebrandt, J.C. Niemeyer: Ann. Rev. Astron. Astrophys. **38**, 191 (2000)
31. R.I. Klein, R.A. Chevalier: Astrophys. J. Lett. **223**, L109 (1978)
32. K. Krisciunas et al. : Astron. J. **125**, 166 (2003)
33. W. Li et al. : Pub. Astron. Soc. Pacific **113**, 1178 (2001)
34. W. Li et al. : Pub. Astron. Soc. Pacific **115**, 453 (2003)
35. B. Leibundgut: In: *The Lives of Neutron Stars*, eds. A. Alpar, Ü. Kiziloglu, J. van Paradijs (Dordrecht: Kluwer, 1995) p. 3
36. B. Leibundgut: Astron. Astrophys. Rev. **10**, 179 (2000)
37. B. Leibundgut, P.A. Pinto: Astrophys. J. **401**, 49 (1992)
38. B. Leibundgut, N.B. Suntzeff: In: *Supernovae and Gamma−Ray Bursts*, ed. K. Weiler (Heidelberg: Springer, 2003) p. 76
39. B. Leibundgut et al. : Astrophys. J. **372**, 531 (1991)
40. D.C. Leonard et al. : Pub. Astron. Soc. Pacific **114**, 35 (2001)
41. D.C. Leonard et al. : Astrophys. J. **594**, 247 (2003)
42. J.R. Lewis et al. : Mon. Not. R. Astron. Soc. **266**, L27 (1994)
43. R. McCray: In: *Supernovae and Gamma−Ray Bursts*, ed. K. Weiler (Heidelberg: Springer, 2003)
44. W.P.S, Meikle: Mon. Not. R. Astron. Soc. **314**, 782 (2000)
45. P.A. Milne, L.-S. The, M. Leising: Astrophys. J. Suppl. **124**, 503 (1999)
46. P.A. Milne, L.-S. The, M. Leising: Astrophys. J. **559**, 1019 (2001)
47. A. Pastorello et al. : astro-ph 0309264 (2003)
48. M.M. Phillips et al. : In: *From Twilight to Highlight: The Physics of Supernovae*, eds. W. Hillebrandt, B. Leibundgut (Heidelberg: Springer, 2003) p. 193
49. P.A. Pinto, R.G. Eastman: Astrophys. J. **530**, 757 (2000)
50. D.V. Popov: Astrophys. J. **414**, 712 (1993)
51. A.G. Riess, P. Nugent, A.V. Filippenko, R.P. Kirshner, S. Perlmutter: Astrophys. J. **504**, 935 (1998)
52. J. Spyromilio, B. Leibundgut, R. Gilmozzi: Astron. Astrophys. **376,**, 188 (2001)
53. M.D. Stritzinger et al. : Astron. J. **125**, 2100 (2002)
54. B.E.K. Sugerman, S.S. Lawrence, A.P.S. Crotts, P. Bouchet, S.R. Heathcote: Astrophys. J. **572**, 209 (2002)

55. N.B. Suntzeff: In: *From Twilight to Highlight: The Physics of Supernovae*, eds. W. Hillebrandt, B. Leibundgut (Heidelberg: Springer,2003) p. 183
56. G.A. Tammann: In: *Astronomical Uses of the Space Telescope,* eds. F. Macchetto, F. Pacini, M. Tarenghi (Garching: ESO Proceedings, 1978) p. 329
57. M. Turatto et al. : Mon. Not. R. Astron. Soc. **262**, 128 (1993) 329
58. K. Weiler (ed.): *Supernovae and Gamma−Ray Bursts*, (Heidelberg: Springer, 2003)

Late Light Curves of Type Ia SNe

Peter A. Milne[1] and G. Grant Williams[2]

[1] Steward Observatory, University of Arizona, Tucson, AZ, USA;
pmilne@as.arizona.edu
[2] MMTO, Tucson, AZ, USA;
ggwilli@mmto.org

Summary. At late times, the energy deposition in the ejecta of type Ia supernovae is dominated by the slowing of energetic positrons produced in $^{56}\mathrm{Co} \rightarrow {}^{56}\mathrm{Fe}$ decays. Through comparisons of simulations of energy deposition in SN Ia models with observed light curves from supernovae, we study the positron transport and thus the magnetic fields of SNe Ia. In this paper, we summarize the current status of these investigations, emphasizing the observations made of two recent SNe Ia, 1999by and 2000cx.

1 Introduction

The late light curves of Type Ia SNe afford a glimpse into how positrons produced in $^{56}\mathrm{Co} \rightarrow {}^{56}\mathrm{Fe}$ decays interact with the SN ejecta. As the trajectories of positrons are influenced by magnetic fields, studies of positron transport are equally studies of the magnetic fields in SN ejecta. The essential comparison is between some measure of the energy deposition rate for a SN Ia model and some measure of the luminosity of an observed SN Ia. Implicit in the comparison are the assumptions that the energy deposited in the ejecta is wholly converted into emission and that the observed emission is a reliable tracer of the bolometric luminosity. Whereas the coupling of energy deposition with 100% re-emission has never been seriously challenged, there is no consensus as to the correct way to estimate the bolometric luminosity.

The earliest works that attempted these comparisons utilized the observations that were available to them. Colgate, Petschek and Kriese [4] compared simulated energy deposition rates with the B and V band observations of SNe Ia and concluded that positron escape was in evidence. By contrast, Axelrod in his thesis [1] fit the 700+ day blue spectrum of SN 1972E with a model that trapped positron energy (he assumed instantaneous, in-situ deposition of 100% of the positron kinetic energy), but included an infrared catastrophe (IRC, where an increasing fraction of the emission is emitted in an unobservable portion of the IR wavelength range). Axelrod assumed color evolution (where no single band traces the bolometric luminosity) and arrived at one conclusion about positron transport, while Colgate, Petschek and Kriese assumed no color evolution and arrived at a different conclusion. Due to the limitations of our knowledge of the relevant interaction cross-sections, there remains no consensus as to which assumption is correct.

More recent investigations have attempted to broaden and deepen the comparisons. Ruiz-Lapuente and Spruit [9] emphasized comparisons with UVOIR bolometric light curves (i.e. based on multi-band photometry) and concluded that positron escape was suggested in some, but not all SN Ia light curves. That approach recognized the importance of including a wide wavelength range, but utilized UVOIR bolometric light curves that at late times include only observations made in the principal, BVRI photometric bands (and thus rely upon extrapolations of the UV and IR emission to approximate the bolometric light curve). Cappellaro et al. [3] assumed the V band is a reliable tracer of the bolometric luminosity (*a la* Colgate), and studied a larger number of SN Ia light curves. Their work tested the hypothesis that positron energy deposition drives the light curves at late times, and they concluded that varying degrees of positron escape were suggested by the light curves. Milne, The and Leising ([7], hereafter MTL99) looked at V and B band light curves of 10 SNe Ia and reported that all of the normally- and super-luminous SNe Ia light curves were consistent with positron escape. The general conclusion from those works was that positrons appear to escape from most SNe Ia if V and B band light curves accurately trace the bolometric luminosity.

2 BVRI Photometry of 22 SNe Ia

Milne, The and Leising then extended their first work to include B,V,R and I band photometry of 22 SNe Ia (Milne, The and Leising [8], hereafter MTL01). The efforts were intended to: 1) widen the wavelength range under investigation, and 2) recognize the heterogeneity that exists within the SNe Ia grouping and then to search for trends within sub-classes. The 22 SNe were classified as normally-, sub- or super-luminous based upon their $\Delta \mathrm{M}_B(15)$ values and then normalized to have the same luminosity at 65 days (thus studying the shape of the late light curves rather than the absolute magnitudes). They found that the normally-luminous (10) and super-luminous (6) SNe Ia have similar light curve shapes at late times while sub-luminous (6) SNe Ia have different light curve shapes. They further found that the SN color does evolve from 50-175 days. The V band does roughly trace the BVRI bolometric light curves during that epoch for the normally- and super-luminous SNe Ia (hereafter N/SP SNe), but this may be due to a coincidence as the ^{56}Co emission lines give way to ^{56}Fe emission lines. Beyond 175 days, the B,V,R and I band light curves are consistent with no color evolution that follows the energy deposition rate for positron escape.

The sub-luminous SNe Ia studied exhibited light curves with entirely different characteristics than the other two sub-classes. The V band light curves have more curvature than the energy deposition rates (either assuming positron trapping or positron escape), initially falling faster and later remaining flatter. For the sub-luminous SNe Ia, the B band appears to be a

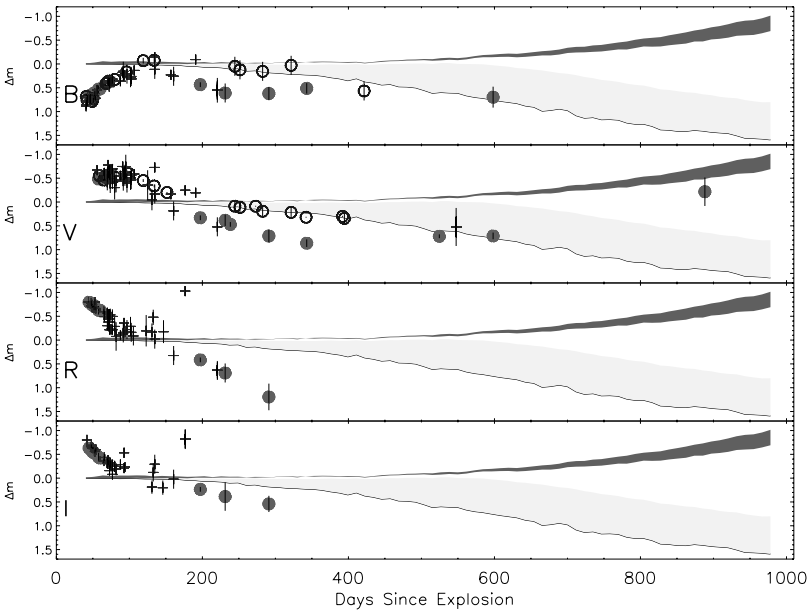

Fig. 1. B,V,R,I band photometry of SN 1999by (filled circles) compared with SN 1986G (open circles) and SN 1991bg (crosses). The data are shown as residuals relative to the energy deposition rates for the model,W7. The light shaded curves assume positron escape, the dark shaded curves assume positron trapping. All SNe were normalized to have the same magnitude at 65 days.

better fit to the energy deposition rates, while the R and I band light curves are similar in shape to the other two sub-classes. Derived bolometric corrections appear to be able to explain the color evolution in the light curves of the six SNe Ia, but the number and coverage of the existing spectral data-set are relatively poor and much more work needs to be done before definitive conclusions can be drawn.

3 Recent Developments

The previous sections are a review of investigations of the late light curves. The reader is referred to the above publications for details of those investigations. There have been three recent developments that have produced additional interest in this topic. First, the SN 1999by was extensively observed until very late times. Second, SN 2000cx occured with the necessary attributes to be detected two years post-explosion. Third, radiation transport simulations have been performed that include more physics and might provide an alternative explanation for the appearance of positron escape in SN Ia ejecta.

In MTL01, the SNe 1991bg and 1986G were grouped together as "sub-luminous" SNe Ia. This classification ignored the distinction that SN 1986G is considered to have been only slightly sub-luminous, while SN 1991bg is considered to have been very sub-luminous (on the low luminosity edge of SN Ia events). That appeared to be adequate considering the irregular sampling of the light curves of those two SNe. However, light curves derived from observations of SN 1999by have shed new light on the sub-luminous sub-class. SN 1999by has been determined to be a 1991bg-like based upon the peak emission, and when the late light curves of SN 1999by are compared with SN 1991bg and 1986G light curves, it is apparent that 1999by matches the former and not the latter (Fig. 1). The data for SN 1999by is from [5]. Whereas SN 1986G appears to transition to an epoch where the light curves can be explained by the energy deposition rates that feature positron escape (only B and V band light curves were published), the SNe 1991bg/1999by light curves do not follow the simulations at any epoch. Thus, it can be argued that SN 1986G (the transitional case between normal and fast declining SNe Ia in the luminosity-width relation) transitions at 150 days to light curves similar to the N/SP SNe Ia, while the very sub-luminous SNe Ia follow a different evolution at all epochs. Two SNe should not dictate a distinct sub-class, but the shapes of the light curves shown in Fig. 1 do motivate further study of late light curves of sub-luminous SN Ia.

SN 2000cx had peak light curves that challenged the luminosity-width relation by crossing the templates and defying categorization [6]. This fact, combined with the nearness and isolated nature of the SN, made it an ideal target for late-epoch observations. Although the light curves and spectra were unique, they exhibited characteristics spanned by N/SP SNe Ia. Based on that logic, we would expect SN 2000cx's light curves to match the light curves from the 16 N/SP SNe studied in MTL01. However, Candia et al. [2] list a SPF distance to NGC 524 (2000cx's host galaxy) that would make SN 2000cx a slightly sub-luminous SN Ia, thus the luminosity of SN 2000cx is currently debatable. Shown in Fig. 2 are BVRI light curves of SN 2000cx compared with the 16 N/SP SNe Ia. But for an anomaly in the B band from 50-150 days (see also [6]), the shape of the light curves are very similar to the other SNe. The data for SN 2000cx is from Li et al. [6] and Candia et al. [2]. The late data is from Sollerman et al. (these Proceedings), HST R and I band data (Li et al., unpublished), and unpublished data we collected at the Steward Observatory 2.3m Bok telescope.

The SN 2000cx observations are of additional interest in that Sollerman et al. were able to obtain late J,H, and K band photometry for that SN. In a poster shown at this meeting, they report a late flattening of those light curves, potentially due to an IRC. They performed radiation transport for the SN model, W7, and roughly reproduce the IRC while roughly fitting the V and R band light curve. Of particular interest is that this fit is accomplished while trapping positrons. Since Fig. 2 shows that the SN 2000cx B,V,R and I

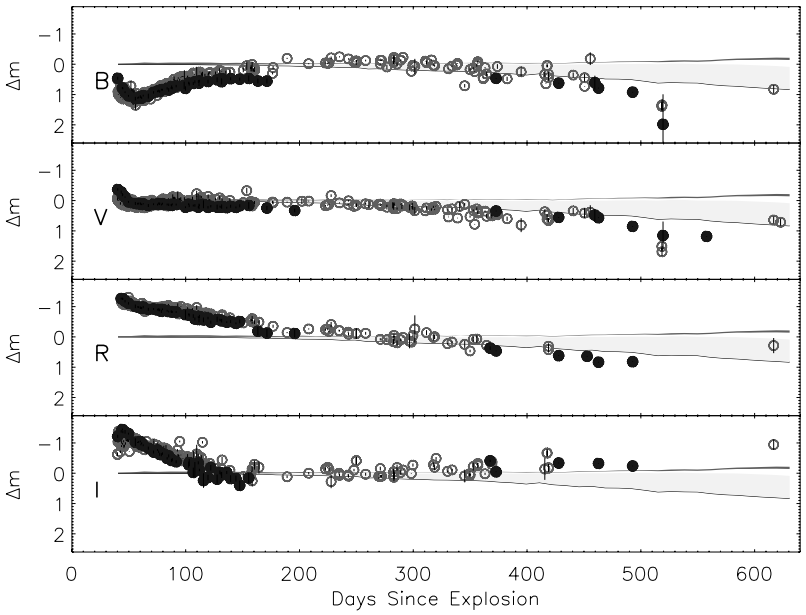

Fig. 2. B,V,R,I band photometry of SN 2000cx (filled circles) compared with 16 other normally- or super-luminous SNe Ia (open circles). The data are shown as residuals relative to the energy deposition rates for the model W7. The light shaded curves assume positron escape, the dark shaded curves assume positron trapping. All SNe were normalized to have the same magnitude at 65 days.

band light curves agree with other SNe Ia out to 500+ days, the suggestion is that color evolution in the B,V,R and I bands might exactly mimic the effects of positron escape. The simulations shown in the Sollerman et al. poster would not be able to explain the SNe that have been detected in the B,V,R and I bands after 600 days (1992A and 1990N for example), nor have they been shown to reproduce SN Ia light curves and spectra in detail. However, the work presents an alternative explanation for the late emission and represents an exciting development in this field.

4 Summary

Although challenging to detect, some SNe Ia have been observed until late epochs. From the collection of light curves derived from those observations, a picture is emerging. The late light curves of normally- and super-luminous SNe Ia appear quite similar from $50 - 500$ days, appearing as virtually a single set of shapes. By contrast, the sub-luminous SNe Ia have light curves that differ a great deal from the others, and amongst themselves. The two well-observed very sub-luminous SNe 1991bg and 1999by have similar light

curves whose B and V bands differ appreciably from the N/SP SNe at every epoch. By contrast, the slightly (or transitionally) sub-luminous SN 1986G appears to transition to having light curves that agree with the N/SP SNe Ia. The sub-luminous sub-class is severely under sampled, and it remains an open question whether the late light curves will continuously transition to the N/SP SNe.

SN 2000cx, whose near-peak light curves were unique, appears fairly typical of the N/SP sub-class with respect to the shape of the late light curves out to 400 days. Additional, very late, HST observations were performed, thus it is possible that yet more information can be obtained with regards to this interesting SN Ia.

Interpreting the light curves in terms of positron energy deposition remains an elusive goal. The N/SP SNe Ia are suitably fitted by energy deposition rates that feature positron escape. However, other simulations suggest that the luminosity deficit (relative to positron trapping) that results when positrons escape may instead be due to color evolution that coincidentally mimics the effects of positron escape.

References

1. T.S. Axelrod: *Ph.D. Thesis* (Univ. Calif.: Santa Cruz, 1980)
2. P. Candia et al. : Pub. Astron. Soc. Pacific **115**, 277 (2003)
3. E. Cappellaro et al. : Astron. Astrophys. **328**, 203 (1990)
4. S.A. Colgate, A.G. Petschek, J.T. Kriese: Astrophys. J. Lett. **237**, L81 (1980)
5. P. Garnavich et al. : astro-ph 0105490 (2001)
6. W. Li et al. : Pub. Astron. Soc. Pacific **115**, 453 (2003)
7. P.A. Milne, L.-S. The, M.D. Leising: Astrophys. J. Suppl. **124**, 503 (1999)
8. P.A. Milne, L.-S. The, M.D. Leising: Astrophys. J. **559**, 1019 (2001)
9. P. Ruiz-Lapuente, H. Spruit: Astrophys. J. **500**, 360 (1998)

Photometric Observations of Recent Supernovae

D.Yu. Tsvetkov

Sternberg Astronomical Institute, Universitetski pr.13, 119992, Moscow, Russia;
tsvetkov@sai.msu.su

Summary. Regular photometric observations of sufficiently bright northern supernovae are carried out at Sternberg Astronomical Institute's observatories. Since 1998 the observations of more than 60 supernovae were obtained on about 150 nights with different telescopes and detectors. We present the data of the observation program, the parameters of light curves for 18 SNe and the light curves for SNe 1999aa, 2001B, 2002bo.

1 Introduction

The light curves are among the major sources of information about the nature of supernovae. They are the main tool for the use of SNe as distance indicators, and can also be used for SN classification and for constraining theoretical models. The observational data have been substantially increased during last years. The modern observational programs contributed high-quality multicolor CCD photometry with good temporal sampling for many SNe. But the rate of SN discovery is so high, that for some sufficiently bright SNe only few photometric data points have been obtained. Often only the low-quality results of amateur groups are available. So, regular photometry of bright SNe remains an urgent observational task.

SN photometry has been carried out at Sternberg Astronomical Institute since the 1960s, and the most prominent results were obtained for SNe 1981B, 1984E, 1984L, and 1985F [7, 11, 12, 13]. Their light curves were derived from photographic and photoelectric observations. During the 1990s we had serious difficulties in accomplishing observations. Only since 1998 it was possible to revive the program, using CCD detectors.

2 Observations and Reductions

The observations were carried out with 125-, 60-, 50-, and 38-cm telescopes of Sternberg Institute Crimean observatory and also at 70- and 30-cm telescopes in Moscow. We used CCD cameras AP-7p, ST-8, ST-7 and ST-6 with different sets of filters, and occasionally obtained also photographic and photoelectric observations. The reductions were done in the usual manner. The

Table 1. Basic data for observation program

SN	T_1	T_n	N	SN	T_1	T_n	N	SN	T_1	T_n	N
1997cx	19	214	11	1999em	5	379	24	2001dn	2	82	17
1997dn	7	117	8	1999gi	4	354	21	2001dp	4	93	6
1997do	3	118	12	1999gn	103	29	5	2001ed	16	53	6
1997dq	5	116	10	1999gq	93	15	3	2001ef	11	52	4
1997ef	3	122	8	2000C	45	32	9	2001en	41	47	6
1997eg	79	8	5	2000E	13	79	13	2001fa	19	47	6
1997ei	62	6	4	2000cx	21	103	19	2001gd	94	41	6
1998D	21	11	7	2000db	19	100	5	2002an	52	51	8
1998S	29	366	15	2000dk	3	73	17	2002ap	3	307	23
1998aq	127	97	6	2000dx	13	67	12	2002bo	6	72	17
1998dh	31	95	5	2000ev	2	80	6	2002bu	3	57	10
1998ef	29	30	4	2000ew	1	156	7	2002cr	6	19	4
1998es	2	94	8	2001B	19	104	14	2002cs	2	19	4
1999D	4	96	10	2001C	18	98	8	2002es	11	76	5
1999X	20	49	13	2001G	16	71	5	2002hh	13	241	19
1999aa	2	72	17	2001V	9	84	14	2002ho	14	16	6
1999ac	16	43	6	2001X	17	76	11	2002hw	9	17	11
1999an	7	24	4	2001ai	6	33	3	2002ji	4	112	8
1999dk	7	82	4	2001ay	8	38	6	2003Z	29	57	4
1999dh	15	95	4	2001bf	3	133	10	2003as	9	72	8
1999ej	19	41	5	2001bg	2	13	3	2003cg	2	53	8
1999el	12	52	10								

magnitude differences between SNe and 1-2 comparison stars were derived by aperture photometry. When the galaxy background near SN was bright and non-uniform, we subtracted the image of the galaxy obtained after fading of SN from the image with SN. On photometric nights we calibrated the comparison stars and determined the transformation equations from instrumental system to the standard one by observing Landolt's [3] and Mermilliod's [6] standard stars, and also clusters M67 [1] and NGC7790 [9].

The brief review of the program is presented in Table 1, where for all SNe with more than 2 observations we report the following data: T_1 is the time in days from discovery until first observation; T_n is the time from first observation until last observation; N is the number of nights on which observations were obtained.

3 Results of Observations

Observations of 23 SNe have been already reduced. For 5 SNe the data were insufficient to determine the shape of the light curves. The main light curve parameters for 18 SNe are reported in Table 2, where m is magnitude at

Table 2. Parameters of light curves for SNe

SN	SN Type	m	Δm_{15}	μ	A_B	$E(B-V)$	M
1997cx	IIL	14.2R		32.0	0.10		-17.9R
1997do	Ia	14.2B	1.3	33.3	0.27		-19.4B
1997ef	IcPec	16.5		33.3	0.18		-17.1
1998D	Ia	15.5R	1.3	33.7	0.06	0.15	-18.6R
1998dh	Ia	13.9	1.0	32.6	0.29	0.1	-19.0
1998ef	Ia	15.0R	1.1	34.4	0.32	0.15	-19.7R
1998es	IaPec	13.8	0.9	33.1	0.14	0.16	-19.8
1999D	IIP	17.4		33.4	0.07		-16.1
1999X	Ia	16.3	1.0	35.0	0.14		-18.8
1999aa	IaPec	14.8	1.0	33.9	0.17		-19.2
1999gi	IIP	14.9		30.3	0.07	0.21	-16.1
1999el	IIL	14.9		31.9	1.58		-18.2
2000E	Ia	13.7	1.3	31.9	1.58	0.36	-19.3
2001B	Ib	15.0		32.0	0.54		-17.5
2001V	Ia	14.5	0.9	34.1	0.08		-19.5
2001X	IIP	15.3		32.0	0.17		-16.8
2002ap	IcPec	12.4		29.5	0.31	0.09	-17.4
2002bo	Ia	13.6	1.1	31.8	0.11	0.35	-19.2

plateau for SNe IIP and at maximum light for SNe of other types, in the V band unless followed by symbol denoting other band; Δm$_{15}$ is only a rough estimate, based on comparison with template SN Ia light curves; distance modulus μ is taken from [14] or estimated from radial velocity, corrected for Virgocentric infall, with $H_0 = 75$ km s^{-1} Mpc^{-1}; galactic absorption A_B is from [8], and $E(B-V)$ is estimated by comparing the color curves of SNe under study with those for which extinction is known to be negligible, for SNe 1999gi and 2002ap it is taken from [4, 5]; the absolute magnitude M, also in the V band unless another band is noted, is derived using the reported apparent magnitude, distance and extinction, for SNe with no data on $E(B-V)$ we assumed negligible reddening in parent galaxies and accounted only for galactic extinction.

The main conclusion is that all studied SNe are quite similar to the typical objects of their classes, as regarding shape of the light curves and absolute magnitudes. Among two peculiar SNe Ia (similar to SN 1991T) SN 1998es was slightly overluminous, while absolute magnitude of SN 1999aa was quite close to the average value for SNe Ia. The light curves for SNe 1999aa, 2001B and 2002bo are presented in Figs. 1-3.

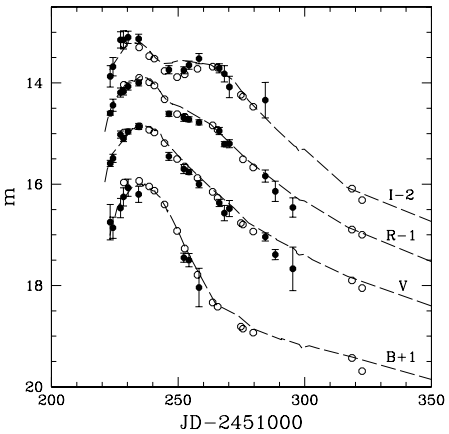

Fig. 1. Light curves of SN 1999aa in the B, V, R, I bands. Filled symbols show our results, open symbols are the data of [2]. The dashed lines are the light curves of SN IaPec 1991T.

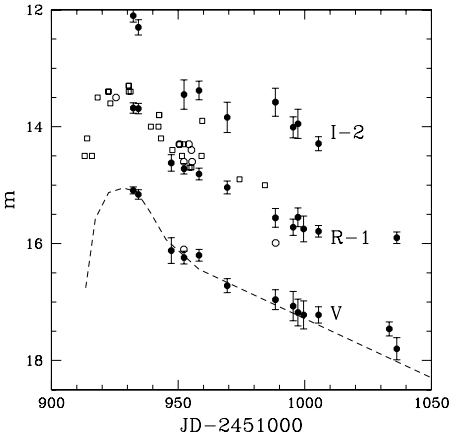

Fig. 2. Light curves of SN 2001B in the V, R, I bands. Filled symbols show our data, open symbols are the data from IAU Circulars and VSNET. The dashed line is V light curve of SN Ib 1984N.

References

1. C. Chevalier, S.A. Ilovaisky: Astrophys. J. Suppl. **90**, 225 (1991)
2. K. Krisciunas, A. Diercks, N.C. Hastings et al: Astrophys. J. **539**, 658 (2000)
3. A. Landolt: Astron. J. **97**, 337 (1992)
4. D.C. Leonard et al. : Astron. J. **124**, 2490 (2002)
5. P.A. Mazzali et al. : Astrophys. J. **572**, 61 (2002)

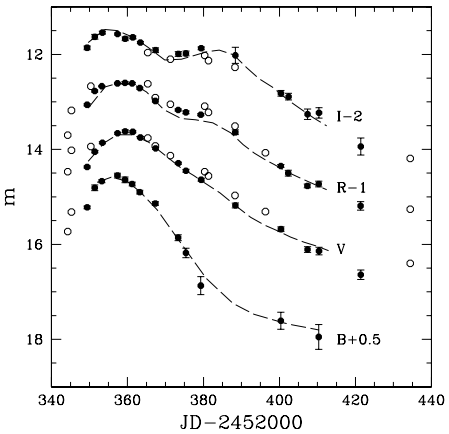

Fig. 3. Light curves of SN 2002bo in the B, V, R, I bands. Filled symbols represent our data, open symbols show the data of [10]. The dashed lines are the light curves of SN Ia 1998bu.

6. J.-C. Mermilliod: "The General Catalogue of Photometric Data" *obswww.unige.ch/gcpd*
7. N.V. Metlova, V.G. Metlov, D.Yu. Tsvetkov: Inform. Bull. Var. Stars **2780**, 1 (1985)
8. D.J. Schlegel, D.P. Finkbeiner, M. Davis: Astrophys. J. **500**, 525 (1998)
9. P.B. Stetson: Pub. Astron. Soc. Pacific **112**, 925 (2000)
10. G.M. Szabo et al. : astro-ph 0306606 (2003)
11. D.Yu. Tsvetkov: Astron. Zhurnal **8**, 219 (1982)
12. D.Yu. Tsvetkov: Astron. Zhurnal **12**, 784 (1986)
13. D.Yu. Tsvetkov: Astron. Zhurnal **13**, 894 (1987)
14. R.B. Tully: *Nearby Galaxies Catalog* (Cambridge University Press, Cambridge 1988)

Observational Properties of Type II Plateau Supernovae

A. Pastorello[1,2], M. Ramina[1,2], L. Zampieri[2], H. Navasardyan[2], M. Salvo[3], M. Fiaschi[1]

[1] Dipartimento di Astronomia, Università di Padova, Vicolo dell' Osservatorio 2, 35122 Padova, Italy;
pastorello@pd.astro.it
[2] INAF - Osservatorio Astronomico di Padova, Vicolo dell' Osservatorio 5, 35122 Padova, Italy
[3] Australian National University - Mount Stromlo Observatory, Cotter Road, Weston ACT 2611, Australia

Summary. We present spectroscopic and photometric data of a sample of Type II plateau Supernovae, covering a wide range of properties from the ^{56}Ni rich, high luminosity events (e.g. SN 1992am) to the low-luminosity, ^{56}Ni poor SNe (e.g. SN 1997D). We provide an observational framework to analyze correlations among observational data, physical parameters and progenitors characteristics of Type II supernovae.

1 The Sample of SNe II-P

Type II plateau Supernovae (SNe II-P) are considered a heterogeneous group of core-collapse events sharing a very wide range of physical properties. Despite their variety of observational parameters (e.g. early- and late-time luminosity, expansion velocity, continuum temperature), recent studies highlight tight correlations among their physical parameters [6, 10]. However, in these works the low-luminosity tail of the SNe II-P distribution was poorly sampled. Zampieri et al. [these Proceedings] have recently investigated such correlations, including also low-luminosity events. Our sample was selected in such a way to cover a large range in luminosity and line velocity, preferably among SNe II-P discovered at very early stages. We selected a few well studied SNe from literature and unpublished data from the Padova-Asiago SN Archive. Most of them have long-duration plateaux, but also events with relatively short plateaux (SNe 1992H and 1995ad) and spectroscopic evolution of a normal SN II-P, were considered. SNe from our archive have been observed either in spectroscopy and photometry from a few days after their discovery to the nebular phase, when the main output of energy comes from the radioactive decays. The sample includes 6 Ni poor ($< 10^{-2} M_{\odot}$) SNe, 5 intermediate Ni mass ($1 - 5 \times 10^{-2} M_{\odot}$) SNe and five Ni rich ($> 7 \times 10^{-2} M_{\odot}$) events.

In Table 1 we list the main data about the selected SNe (see also Ramina, Laurea Thesis, 2003, unpublished and references therein). When the distance

Table 1. Main data of the selected SNe II-P

SN	μ	A_V	t_0 (JD)	ref.($\star$)	SN	μ	A_V	t_0 (JD)	ref.($\star$)
1969L	29.84	0.20	2440550.5	[2]	1996an	31.50	0.16	2450222	[9]
1987A	18.49	0.60	2446849.82	SAAO	1997D	31.29	0.07	2450361	[13, 1]
1992H	32.48	0.33	2448661	[3]	1999br	31.19	0.08	2451278	[5, 8]
1992am	36.74	0.44	2448799	[12]	1999em	29.47	0.31	2451476	[4, 7]
1992ba	30.91	0.19	2448883.2	[5, 9]	1999eu	31.08	0.09	2451394	[8]
1994N	33.34	0.13	2449451	[8]	2001dc	32.85	1.28	2452056	[8]
1995ad	32.02	0.11	2449981	[9]	2002gd	33.09	0.22	2452552	[9]
1996W	31.95	0.70	2450180	[9]	2003Z	31.93	0.13	2452665	[9]

($\star$) Reference for spectro-photometric data

modulus μ is obtained from the host galaxy recession velocity, H_0 has been assumed to be equal to 65 km s^{-1} Mpc^{-1}. The total extinction reported in Table 1 is the sum of the host galaxy reddening and the Galactic contribution, from [11]. More details on the estimated distances and interstellar extinction are in Ramina [Laurea Thesis, 2003, unpublished].

1.1 Faint SNe II-P

SN 1997D [13, 1] is the prototype of a homogeneous group of CC-SNe with unique observational properties. The light curves, showing flat plateaux lasting $\sim 90-110$ days, are underluminous at all epochs, and their spectra, redder than "typical" SNe II-P, show strong and narrow P-Cygni features indicating very small expansion velocities (~ 1000 km s^{-1} at the end of the plateau phase, see Fig. 1). In [8, 14] other similar SNe were discussed (SNe 1994N, 1999br, 1999eu and 2001dc). The database has been recently enriched by the discovery of a well representative event, SN 2003Z, extensively monitored at TNG[1]. This SN provides a very good example of the spectro-photometric evolution of low-luminosity SNe (see Fig. 2). The SN was observed both in spectroscopy and photometry during the photospheric phase, and observations during the nebular phase, useful to estimate the ^{56}Ni mass, are still in progress. Preliminary late-time photometry suggests that SN 2003Z ejected 0.006 $M_\odot$ of ^{56}Ni. We suggest that low-luminosity events may occur with relatively high frequency.

The observed properties of the faint CC-SNe are consistent with very small ejected ^{56}Ni mass ($< 10^{-3}$ $M_\odot$) and low explosion energy ($\ll 10^{51}$ erg, [14]). This suggests high-mass progenitors ($M_{MS} > 20 - 25 M_\odot$) for which significant fall-back might have occurred ([14] and Zampieri et al., these Proceedings).

[1] program TAC 48

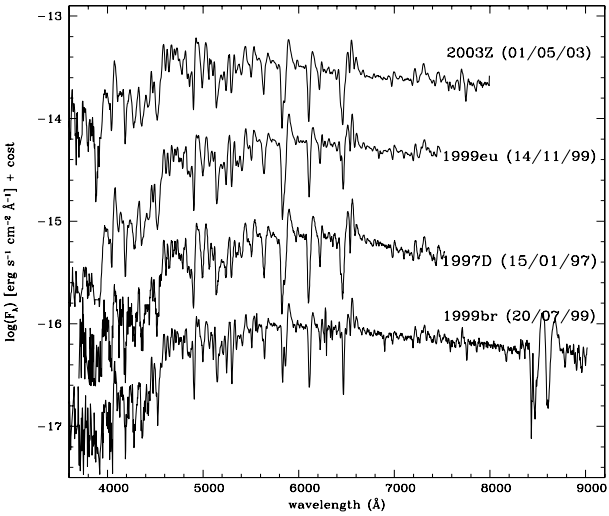

Fig. 1. Spectra of low-luminosity SNe II-P at ~ 100 days after the explosion.

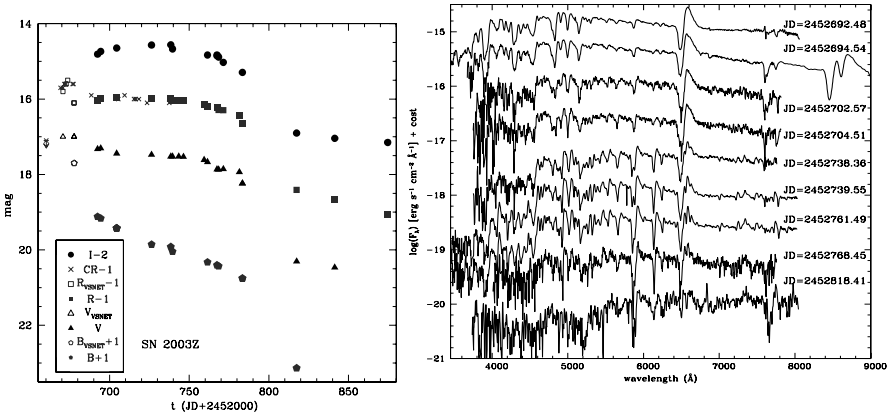

Fig. 2. Photometric and spectroscopic evolution of the low-luminosity SN 2003Z. Unfiltered measurements and VSNET (*http://vsnet.kusastro.kyoto-u.ac.jp/vsnet/*) data are also reported.

1.2 Normal SNe II-P

The sample contains also a number of "normal" and high luminosity events covering a large range of physical properties (e.g. Ni mass, explosion energy, ejected mass). Even if we observe a large spread both in luminosity ($2 - 20 \times 10^{42}$ erg s^{-1}) and in expansion velocity ($3000 - 5000$ km s^{-1} at the beginning of recombination), these SNe never show the extreme properties of SN 1997D and other faint events. Zampieri et al. (these Proceedings) suggest that the

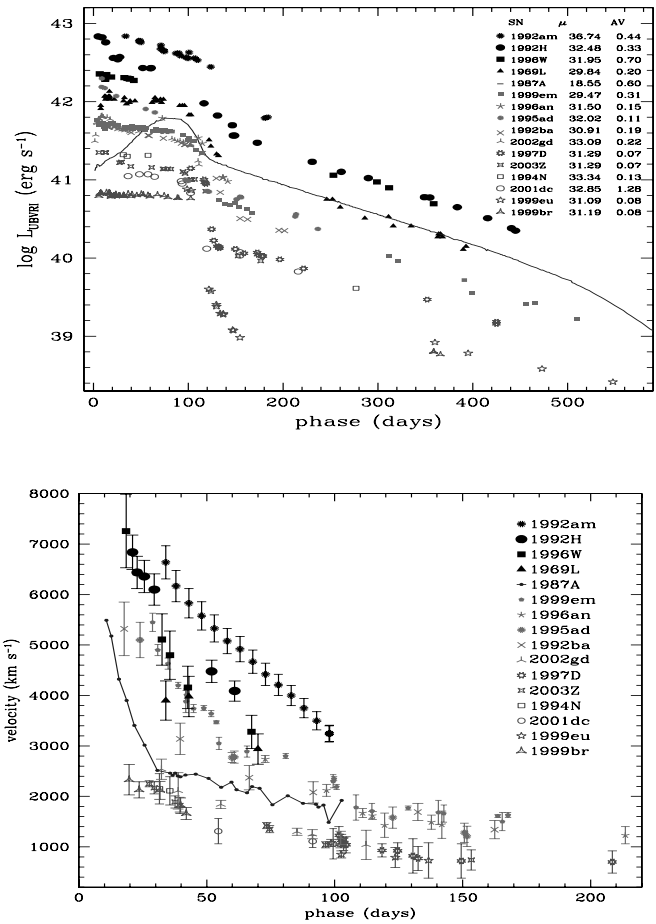

Fig. 3. Top: Luminosity evolution of our selected sample of SNe II-P. Bottom: expansion velocities obtained from the blueshift of the minimum of Sc II lines. Adopted colors are: red for faint 1997D-like SNe, magenta for intermediate-luminosity SNe, black for normal and high luminosity events; blue (solid line) is SN 1987A.

ejected envelope mass is in the range $12 - 26$ $M_{\odot}$, with no definite tendency to vary with the other SN parameters.

Peculiar is the case of SN 2002gd, well observed during the plateau, then lost behind the sun. The plateau luminosity is relatively high, but the expansion velocity deduced from the P-Cygni minima of spectral lines is small, close to that of faintest SNe II-P. This SN was recently observed and our preliminary photometry suggests an unusually strong post-plateau luminosity decrease. We may explain it with a very low amount of ejected ^{56}Ni

($< 10^{-3} M_{\odot}$). Or, alternatively, dust formation into the ejecta might absorb the light at optical wavelengths, leading us to underestimate the ^{56}Ni mass. Because of its peculiar behavior, more late-time observations are required to better understand this event before any systematic analysis of its properties can be performed.

2 The Heterogeneous Family of SNe II-P

A comparison among the pseudo-bolometric light curves for the SNe II-P of our sample is shown in Fig. 3. The light curves appear to be heterogeneous in shape and luminosity at all epochs. In particular the exponential tails are powered by very different amounts of ^{56}Ni ($0.002 - 0.3$ $M_{\odot}$). It is remarkable that the low-luminosity SNe are fainter at all stages than all other SNe shown in Fig. 3.

Also the evolution of the expansion velocity, obtained measuring the blueshift of the minimum of the Sc II lines (see Fig. 3) shows a large spread at all epochs, ranging from 3300 km s^{-1} for SN 1992am [12] to about 1000 km s^{-1} for SN 1999br at $\sim$100 days after explosion. A similar spread is present also in the evolution of the continuum temperature. This suggests, in accordance with [6], that plateau luminosity, Ni mass, continuum temperature, expansion velocity and explosion energy are correlated, from the high values of physical parameters of the luminous SNe 1992H and 1992am to the exceptionally small ones for the faint SNe (see discussion in Zampieri et al., these Proceedings).

References

1. S. Benetti et al. : Mon. Not. R. Astron. Soc. **322**, 361 (2001)
2. F. Ciatti, L. Rosino, F. Bertola: Mem. Soc. Astron. It. **42**, 163 (1971)
3. A. Clocchiatti, M. M. Phillips, J. Spyromilio, B. Leibundgut: Astron. J. **111**, 1286 (1996)
4. A. Elmhamdi et al. : Mon. Not. R. Astron. Soc. **338**, 939 (2003)
5. M. Hamuy: *Type II Supernovae as Distance Indicators.* (PhD Thesis, University of Arizona, 2001)
6. M. Hamuy: Astrophys. J. **534**, 905 (2003)
7. D.C. Leonard et al. : Pub. Astron. Soc. Pacific **114**, 35 (2002)
8. A. Pastorelloet al. : Mon. Not. R. Astron. Soc. **347**, 74 (2004)
9. A. Pastorello: *Hydrogen Rich Core–Collapse Supernovae.* (PhD Thesis, University of Padova, 2003)
10. D.K. Nadyozhin: Mon. Not. R. Astron. Soc. **346**, 97 (2003)
11. D.J. Schlegel et al. : Astrophys. J. **500**, 525 (1998)
12. B. Schmidt et al. : Astron. J. **107**, 1444 (1994)
13. M. Turatto et al. : Astrophys. J. **498**, 129 (1998)
14. L. Zampieri et al. : Mon. Not. R. Astron. Soc. **338**, 711 (2003)

X-ray Spectra of Young Supernovae

David Pooley

MIT Center for Space Research, 70 Vassar St., Cambridge, MA 02139, USA;
dave@mit.edu

Summary. X-ray spectra of young supernovae (SNe) can provide information on the progenitor star and the interaction of the supernova ejecta and the circumstellar material. I will discuss some examples, with particular emphasis on SN 1998S, whose X-ray spectrum revealed for the first time in a young supernova a wealth of heavy element emission features (Ne, Al, Si, S, Ar, and Fe). By comparison with detailed calculations of supernova explosion elemental yields, these data can be used to constrain the progenitor mass. With increasingly sophisticated models and additional high quality data, application of this technique could result in many more reliable progenitor mass determinations. In addition, high resolution X-ray spectra allow us to measure the temperature evolution of a supernova and can give us a detailed picture of the progenitor's pre-supernova evolution. As we build up additional examples from the great diversity of core collapse supernovae, we hope to come to a better understanding of the last stages of massive star evolution.

1 The Utility of X-ray Spectra

In this talk, I will focus on two particular uses of X-ray spectra, both of which rely on emission lines. The first use is simply to measure the velocity-broadened width of an emission line. This would unambiguously determine whether the X-ray emission originated from the reverse shock region (with a characteristic speed of $\sim$10,000 km s^{-1}, see [1]) or from a shocked, clumpy wind (with a characteristic speed of $\sim$9,000 km s^{-1}, see [2]). The second use requires multiple emission lines in the spectrum. The observed elemental abundance ratios are compared with those calculated from numerical simulations of supernova explosions with a range of progenitor masses. This comparison will constrain the progenitor mass.

2 Observed Spectra with Emission Lines

To date, 20 core-collapse supernovae have been observed in X-rays, and nine of these have been observed just in the last four years since the launch of the *Chandra X-ray Observatory* and *XMM-Newton*. An online list of all the observations is maintained by Stefan Immler and available at *http://lheawww.gsfc.nasa.gov/users/immler/supernovae_list.html*. Of these 20

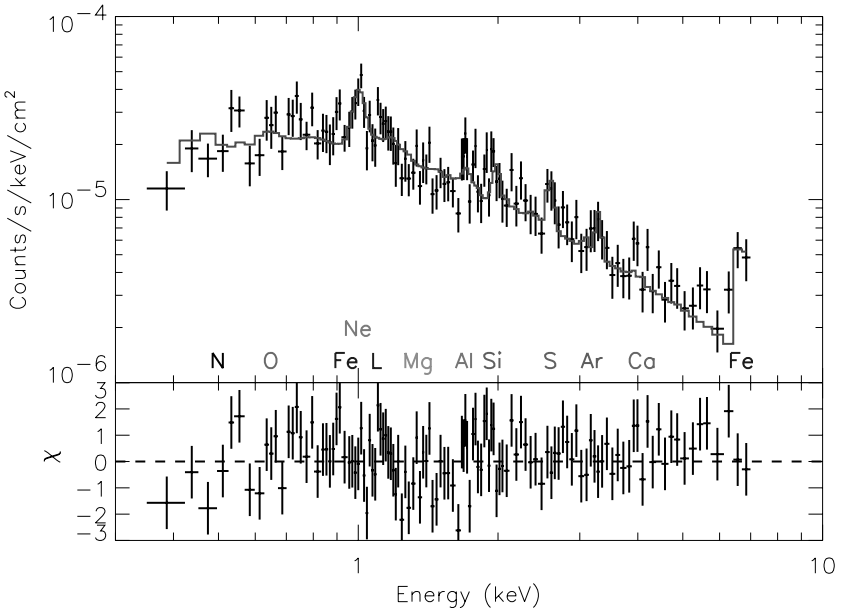

Fig. 1. MEKAL fit (solid line) to the summed spectrum (crosses) of SN 1998S. Labels indicate approximately where emissions lines for each element would be observed.

supernovae, only a handful have shown emission features in their X-ray spectra. I will now briefly review these.

2.1 SN 1986J – *ASCA* Reveals an Fe Line

The type IIn SN 1986J was observed twice with the *ASCA* satellite, once in 1994 and again in 1996. Houck et al. [4] reported the detection of an Fe K line at 6.7 keV. SN 1986J was relatively near ($d = 9.6$ Mpc) and luminous ($L_{\rm x} = 2 \times 10^{40}$ erg s^{-1}), but the low collecting area of *ASCA* resulted in only about 6200 counts in the 1994 observation and about 6000 counts in the 1996 observation. The authors were only able to constrain the width of the Fe line on the upper end, with a 90% confidence limit that the width is less than 20,000 km s^{-1}.

2.2 SN 1993J – *ASCA* Reveals an Fe Line

This nearby ($d = 3.6$ Mpc) type IIb supernova was observed many times with *ASCA* in the year following the explosion. These early observations are described by [6]. The first observation was eight days after explosion, when the X-ray luminosity was $L_{\rm x} = 1.5 \times 10^{40}$ erg s^{-1}. An Fe K line at 6.7 keV

Table 1. Observed and Calculated Elemental Abundance Ratios

Ratio	SN 1998S	13 $M_\odot$	15 $M_\odot$	18 $M_\odot$	20 $M_\odot$	25 $M_\odot$	40 $M_\odot$
Ne/Si	0.6–14	0.14	0.17	*0.86*	*1.1*	*2.2*	0.56
Mg/Si	0–0.7	*0.18*	*0.49*	*0.58*	1.1	2.1	1.1
O/Si	0–1.2	*0.20*	*0.43*	*0.80*	1.4	2.4	1.6

was detected, but again the width could not be constrained on the lower end. The 90% upper limit on the width is 27,000 km s^{-1}.

2.3 SN 1995N – A Possible Si Line

This type IIn supernova at 24 Mpc was still quite luminous ($L_x = 15 \times 10^{40}$ erg s^{-1}) when an *ASCA* observation was made in 1998. Although there were no clear line detections in the 3200-count spectrum, Fox et al. [3] point out a "hint in the fit residuals" near the Si K line.

2.4 SN 1998S – *Chandra* Reveals a Wealth of Emission Lines

This type IIn supernova at 17 Mpc was observed with *Chandra* five times from early 2000 to late 2001. Pooley et al. [8] reported there was little evolution of the spectral shape, and the X-ray luminosity decreased steadily from 9.3×10^{39} erg s^{-1} in the first observation to 5.3×10^{39} erg s^{-1} in the last. The individual spectra were summed to produce a 2600-count spectrum in which emission lines were seen from Ne, Al, Si, S, Ar, and Fe (see Fig. 1). Unfortunately, none of the emission lines was strong enough to have a well-constrained width. However, given the plethora of emission lines, Pooley et al. compared the observed abundance ratios (derived from MEKAL fits in XSPEC) to those calculated from the numerical simulations of [7] in the hopes of constraining the progenitor mass. This was the first time such an analysis had been done with X-ray data. Although there were large uncertainties, Table 1 shows that the observed abundance ratios are compatible with a progenitor mass in the range 15–20 $M_\odot$.

This progenitor mass determination comes with some caveats, however. First, it assumes the ejecta are well mixed, but such mixing has been observed, for example in the Cas A supernova remnant [5]. Another caveat is that the observed abundance ratios are model-dependent, in this case the MEKAL model. In addition, there are uncertainties in not only the data but also the model calculations. However, as our understanding of the explosion grows and as we continue to obtain high-quality X-ray data and develop increasingly sophisticated models, this method could yield many progenitor mass determinations of future supernovae.

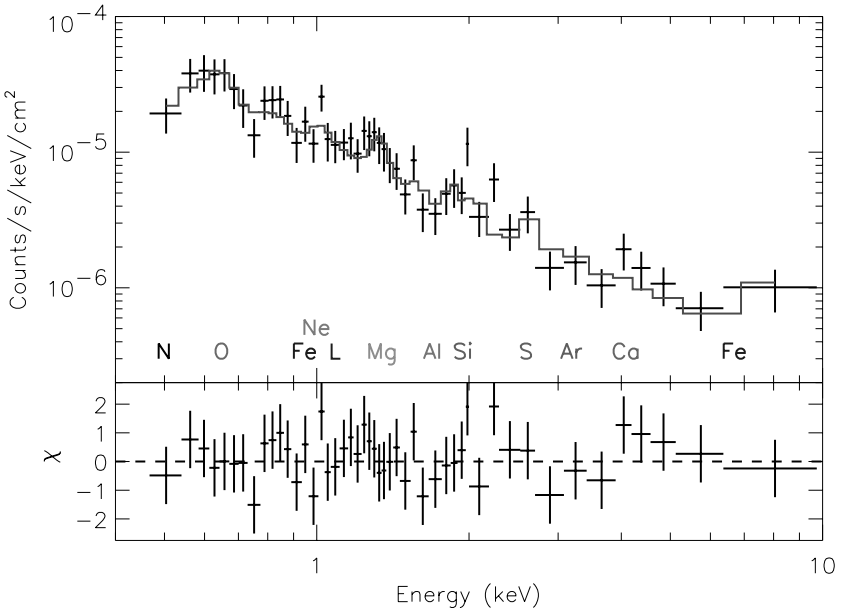

Fig. 2. MEKAL fit (solid line) to the spectrum (crosses) of SN 2003bg. Labels indicate approximately where emissions lines for each element would be observed.

2.5 SN 2003bg – *Chandra* Reveals a Wealth of Emission Lines Again

This type Ic/pec supernova at 19 Mpc was observed with *Chandra* about a month after discovery. A preliminary analysis of the data [9] indicates an X-ray luminosity of 4×10^{39} erg s^{-1}, and MEKAL fits in XSPEC indicate emission features from O, Mg, Si, S, Fe, and possibly Ne (see Fig. 2). In comparison to SN 1998S, there is much stronger O emission and much weaker Ne emission in SN 2003bg. An analysis of the abundance ratios is in preparation, as is the analysis of a follow-up *Chandra* observation taken a few months after the first one (Pooley et al., in prep.).

3 Summary and Future Prospects

The X-ray spectra of young supernovae can be a powerful tool to determine the X-ray emitting regions and to constrain the progenitor mass. The ability to accurately measure the width of an X-ray emission line is hampered by the relatively low X-ray flux of all but the closest supernovae; the situation should improve as the collecting area of satellites grows. The current generation of X-ray satellites (*Chandra* and *XMM-Newton*) is ushering in a new

era in the study of young supernovae. Future satellites (such as *Astro-E* and *Constellation-X*) will feature larger collecting areas and will have exquisite energy resolution (by using calorimeter instruments). With future instruments, we will be able to resolve emission line complexes and perform detailed plasma diagnostics to determine elemental abundances with less dependence on specific models.

References

1. R.A. Chevalier, C. Fransson: Astrophys. J. **420**, 268 (1994)
2. N.N. Chugai: Astrophys. J. Lett. **414**, L101 (1993)
3. D.W. Fox et al. : Mon. Not. R. Astron. Soc. **319**, 1154 (2000)
4. J.C. Houck, J.N. Bregman, R.A. Chevalier, K. Tomisaka: Astrophys. J. **493**, 431 (1998)
5. J.P. Hughes, C.E. Rakowski, D.N. Burrows, P.O. Slane: Astrophys. J. Lett. **528**, L109 (2000)
6. Y. Kohmura et al. : Pub. Astron. Soc. Japan **46**, L157 (1994)
7. K. Nomoto et al. : Nuc. Phys. **616**, 79 (1997)
8. D. Pooley et al. : Astrophys. J. **572**, 932 (2002)
9. D. Pooley, W.H.G. Lewin: IAUC 8110 (2003)

Part III

Supernovae: Progenitors/Remnants

Pre-Supernova Evolution of Rotating Massive Stars

Raphael Hirschi[1], Georges Meynet[1], André Maeder[1], and Stéphane Goriely[2]

[1] Observatoire de Genève, 1290 Sauverny, Switzerland;
raphael.hirschi@obs.unige.ch
[2] Université Libre de Bruxelles, Bruxelles, Belgique

Summary. The Geneva evolutionary code has been modified to study the advanced stages (Ne, O, Si burnings) of rotating massive stars. Here we present the results of four 20 $M_\odot$ stars at solar metallicity with initial rotational velocities, $\upsilon_{\rm ini}$, of 0, 100, 200 and 300 km/s in order to show the crucial role of rotation in stellar evolution. As already known, rotation increases mass loss and core masses [4]. A fast rotating 20 $M_\odot$ star has the same central evolution as a non-rotating 26 $M_\odot$. Rotation also increases strongly net total metal yields. Furthermore, rotation changes the SN type so that more SNIb are predicted (see [5] and [6]). Finally, SN1987A-like supernovae progenitor colors can be explained in a single rotating star scenario.

1 Computer Model

The computer model used is the Geneva evolutionary code (see [5]). Convective stability is determined by the Schwarzschild criterion. The overshooting parameter, $\alpha_{\rm over} = d_{\rm over}/H_{\rm P}$ is equal to 0.1 for hydrogen- and helium-burning cores and equal to 0 afterwards. Modifications have been made to study the advanced stages of the evolution of rotating massive stars. Dynamical shear has been included using $Ri_c = 1/4$ [2]. Note that the computer model still includes secular shear and meridional circulation. The structure equations have been stabilized using Sugimoto's prescription [7]. Furthermore, convection is treated as diffusion from the Oxygen (O) burning stage because convection is no longer instantaneous. The algorithm developed for rotational mixing is used for this purpose. Finally, the nuclear reaction network has been extended and contains all the multiple-α elements up to ^{56}Ni except ^{8}Be. The reaction rates are taken from the NACRE compilation or Hauser-Feschbach code calculations (ULB, Belgium).

2 Evolution

The early evolutionary stages are presented in [5]. Here we concentrate on solar metallicity 20 $M_\odot$ stars and study the effect of rotation by examining four models with initial rotational velocities of 0, 100, 200 and 300 km/s. Calculations have been followed until end of central O-burning for the $\upsilon_{\rm ini}$ =

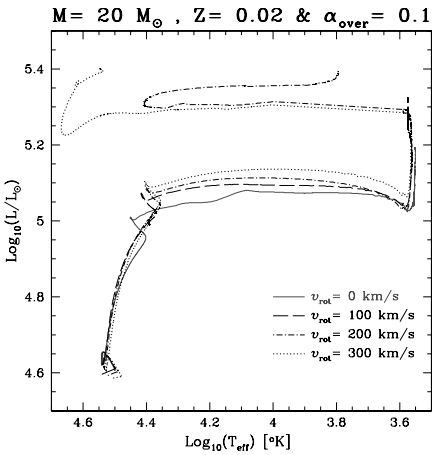

Fig. 1. HR diagram for the solar metallicity $20\,M_\odot$ stars with initial rotational velocities of 0, 100, 200 and 300 km/s.

100 and 200 km/s models, end of central Si-burning for the $v_{\rm ini} = 300$ km/s model and end of first shell Si-burning for the non-rotating model.

2.1 Hertzsprung-Russell (HR) Diagram

Figure 1 shows the evolutionary tracks of the four different $20\,M_\odot$ stars in the HR diagram. The non-rotating model ends up as a red supergiant (RSG) like other group models (see, e.g., [1] or [3]). However, the rotating models show very interesting features. Although the 100 km/s model remains a RSG, the 200 km s^{-1} model undergoes a blue loop to finish as a yellow-red supergiant whereas the 300 km s^{-1} model ends up as a blue supergiant (BSG). Thus rotation may strongly affect the shock wave travel time through the envelope when the star explodes in a supernova event, since this time is proportional to the radius of the star (RSG radii are about hundred times BSG ones). Moreover, the behavior of the models with $v_{\rm ini}$ between 200 and 300 km s^{-1} is reminiscent of the evolution of the progenitor of 1987A indicating that rotation may play a role in similar cases.

2.2 Central Evolution

The central evolution is best seen in the central temperature, T_c, versus central density, ρ_c, diagram (Fig. 2). We can see that rotation makes the cores slightly less degenerate (higher T_c and smaller ρ_c). This is explained by the bigger core masses. We also see that the "C-bump" due to the convective central C-burning fades away when rotation increases (see also Fig. 3). This is again a consequence of more massive cores in rotating models which implies

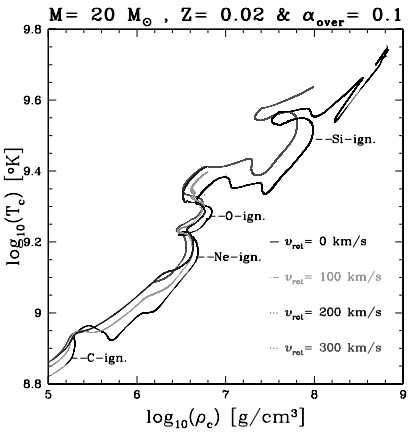

Fig. 2. T_c versus ρ_c diagram.

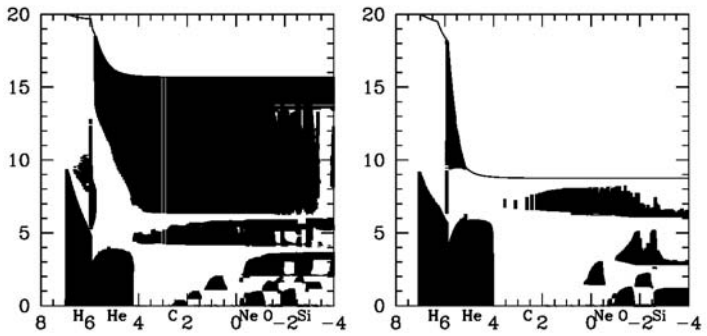

Fig. 3. Kippenhahn diagrams: mass ($M_\odot$) versus $\log_{10}(\sim$ time left until core collapse) (yr). *Left* non-rotating $20\,M_\odot$ model. *Right* $\upsilon_{\rm ini} = 300\,$km/s $20\,M_\odot$ model. Colored zones show convective zones. Letters indicate burning stages.

higher neutrino loss rates and smaller central carbon abundance at the end of He-burning phase.

3 "Pre-SN" Models

3.1 Mass Loss and Core Masses

We can see in Fig. 4 that both mass loss and helium (He) core masses, M_α, increase with rotation as already known. There is a saturation effect at high rotation when the star is left with hardly any hydrogen (H) envelope. As can be seen in [5], rotation noticeably increases the number of Wolf-Rayet stars (WR). Here we see that there is a smooth transition between SN type from

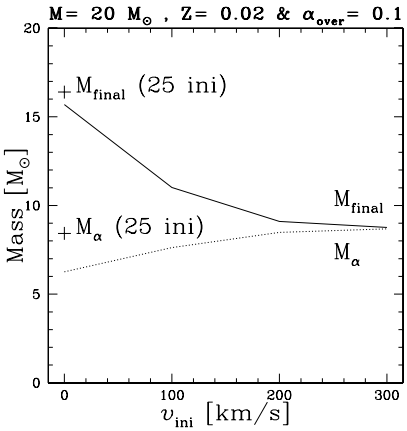

Fig. 4. Final total mass, M_{final}, and helium core mass, M_α, as a function of υ_{ini}. Non-rotating 25 $M_\odot$ model masses are also shown for comparison.

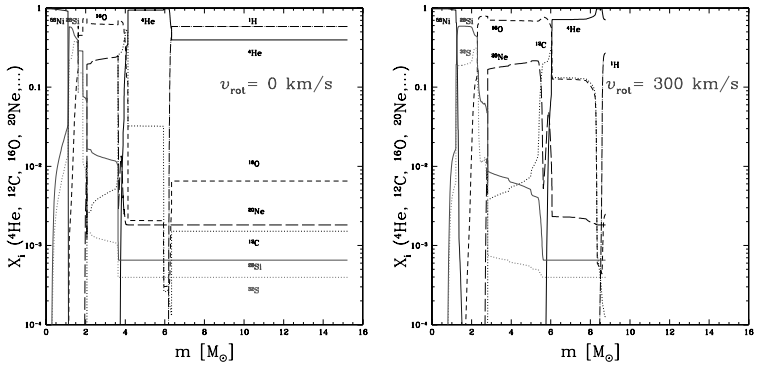

Fig. 5. Abundances profile for main elements at the end of central Si-burning. *Left* non-rotating 20 $M_\odot$ model. *Right* υ_{ini} = 300 km/s 20 $M_\odot$ model.

IIP → IIL → IIb (→ Ib). We also note that the υ_{ini} = 300 km s^{-1} 20 $M_\odot$ model has a bigger He core than the non-rotating 25 $M_\odot$ model (it would correspond to the core of a non-rotating 26 $M_\odot$ model). The carbon-oxygen core mass, M_{CO}, increases with rotation in a similar way as M_α. The Silicon (Si) core mass at the end of central O-burning only slightly increases with rotation.

3.2 Abundances Profile and Net Yields

In Fig. 5 we notice the smoother profiles due to rotational mixing and also the very small quantity of remaining H. The "pre-SN" net yields calculated at this stage show that rotation increases the total metal yield and ^{16}O yield.

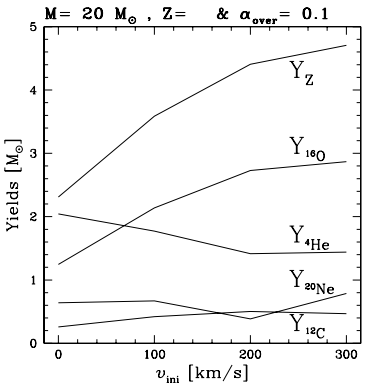

Fig. 6. Net yields of the sum of all metals, Y_Z, and individual elements as a function of $v_{\rm ini}$.

Typically, the total metal yield of the $v_{\rm ini} = 300$ km s^{-1}model is twice the one of the non-rotating model. On the other hand, rotation decreases H-burning products yields (notably ^{4}He) as can be seen in Fig. 6.

References

1. A. Heger, N. Langer: Astrophys. J. **544**, 1016 (2000)
2. R. Hirschi et al. : astro-ph 0301357 (2003)
3. M. Limongi, O. Straniero, A. Chieffi: Astrophys. J. Suppl. **129**, 625 (2000)
4. G. Meynet, A. Maeder: Astron. Astrophys. **361**, 101 (2000)
5. G. Meynet, A. Maeder: Astron. Astrophys. **404**, 975 (2003)
6. N. Prantzos, S. Boissier: Astron. Astrophys. **406**, 259 (2003)
7. D. Sugimoto: Astrophys. J. **159**, 619 (1970)

Radiation Bursts from a Presupernova Collapsar

Volodymyr Kryvdyk

Kyiv National University, av. Glushkova 6, Kyiv 03022, Ukraine;
kryvdyk@mail.univ.kiev.ua

Summary. The radiation from the magnetic presupernova star is calculated. This radiation will generate when the magnetosphere of presupernova star compresses during collapse and its magnetic field increases considerably. The variable magnetic field will accelerate the charged particle, which generate radiation when moving in the magnetic field. The particles dynamics and their non-thermal emission in the magnetospheres of presupernova collapsing star with initial dipole magnetic fields and a certain initial energy distribution of charged particles in a magnetosphere are considered. The radiation flux depend on the distance to the star, its magnetic field, and the particle spectrum in the magnetosphere. This flux can be observed by means of modern instruments in broad band (from radio waves to gamma rays). The radiation flux grows with decreasing stellar radius and frequency and can be observed in the form of radiation bursts with duration equal to the stellar collapse time.

1 Introduction

Collapsing stars have investigated first Chandrasekhar and Oppenheimer-Volkoff in papers [1, 13]. Collapse begins when the mass of stellar core exceeds the Chandrasekhar Limit, and the star become dynamically unstable. The star compress and its radius decrease. The stellar magnetic field grows during the collapse [2]. The stars must emit electromagnetic and the gravitational waves under the collapse [3, 4, 5, 6, 11]. Today we can not detected these waves near Earth over the very low frequencies these waves [3, 4, 5, 11], and maybe it is the main problem in the observation of stellar collapse. Therefore the collapsing stars are so far only the theoretical objects and not detected directly by astronomical observations. Of course, we can detected such phenomenon as the explosion of supernova stars and their emission [10, 12]. But the explosion takes place after collapse and this phenomenon is a consequence of the gravitational collapse.

In our paper we propose a test for search of the presupernova stars on the stage of gravitational collapse using the non-thermal emission from the magnetospheres of presupernova collapsing stars.

2 Presupernova Collapsar Magnetosphere

When the star magnetosphere compresses under the collapse, its magnetic field considerably increases. The cyclic electric field thus produced, accelerate charged particles that generate radiation when moving in the magnetic field. The field structure and particles dynamics in the magnetosphere are influenced by three factors: particles pressure, collisions, and star rotation. As follow with the detail analysis [7], these effects can be neglected during the collapse. To investigate particle dynamics in magnetosphere the method of adiabatic invariant have used as since the magnetospheric plasmas is frozen in magnetic field and collision-free. In this case there are two mechanisms of the particle interaction with the magnetic fields. First is betatron acceleration in the variable magnetic field, second is bremsstrahlung energy losses in this field.

The external electromagnetic field of a collapsing star is given by [7] $B(r,\theta,t) = (1/2)F_o R r^{-3}\left(1+3\cos^2\theta\right)^{1/2}$. Here $F_o = B_o R_o^2$ is the initial magnetic flux of star with the radius R having the initial radius R_o and the initial magnetic field B_o.

The particles spectrum for such magnetosphere [7] is $N_p(E,R) = K_p E^{-\gamma} R_*^{-\beta_1} N_M(E,R) = K_M E^2 R_*^{-\beta_2}\exp(-E/kT)$, $N_B(E,R) = K_B R_*^{-\beta_3}\exp(-E/\ kT)$, respectively for the initial a power -law, relativistic Maxwell and Boltzmann distributions of charged particles in the magnetosphere. Here K_C, K_M, K_B are the spectral coefficients; k is the Boltzmann constant; E is the particle energy and T is the temperature in the magnetosphere; γ is the power spectrum, $R_* = R_0/R$, $\beta_1 = a_1(\gamma-1)$; $\beta_2 = a_1(E/kT\ln E - 3)$; $\beta_3 = a_1(E/kT\ln E - 1)$, $a_1 = (5k_1/3)(3\cos^4\theta + 1.2\cos^2\theta - 1)(1+3\cos^2\theta)^{-2}$; $k_1 = 1$ and $k_1 = 2$ for relativistic and non-relativistic particles, respectively.

3 Non-thermal Radiation from Presupernova Collapsar

The ratio between the radiation flux from the presupernova collapsing stars on the any stage of collapse (when the stellar radius decrease to the value R) and its initial radiation flux (when the radius is R_0), respectively for the power-law, relativistic Maxwell, and Boltzmann distributions are [8]

$$I_{\nu P}/I_{\nu P0} = (\nu/\nu_0)^{(1-\gamma)/2} R_*^{\gamma-2}(I_{\nu P2}/I_{\nu P20})\ , \tag{1}$$

$$I_{\nu M}/I_{\nu M0} = R_*^{-3}(\nu/\nu_0)(1/kT)\int_0^\infty\int_0^{\pi/2} R_*^{-\beta_2}\exp(-E/kT)\sin\theta dE d\theta, \tag{2}$$

$$I_{\nu B}/I_{\nu B0} = R_*^{-3}(kT)(\nu/\nu_0)\int_0^{\infty}\int_0^{\pi/2} R_*^{-\beta_3}E^{-2}\exp(-E/kT)\sin\theta dEd\theta \tag{3}$$

Using equations (1)-(3) the radiation flux from presupernova collapsar can be calculated. The ratio between the radiation flux from collapsing stars and its initial flux by $\nu/\nu_0 = 1$ are in the ranges:

$1 \leq I_{\nu P}/I_{\nu P0} \leq 1.34 \times 10^{10}$ for $2.4 \leq \gamma \leq 3.4$, $10 \leq R_* \leq 1000$;

$1 \leq J_{\nu M}/J_{\nu M0} \leq 4.86 \times 10^{5}$ for $1\ eV \leq kT \leq 9\ eV$, $145 \leq R_* \leq 850$;

$1 \leq J_{\nu B}/J_{\nu B0} \leq 2.23 \times 10^{11}$ for $1\ eV \leq kT \leq 9\ eV$, $145 \leq R_* \leq 850$;

These values obtained by the numerical integration of the equations for the ratio between the radiation flux in the range $2\ eV \leq E \leq 10^9\ eV$, $0 \leq \theta \leq \pi/2$ for the different radius R_* , temperature kT and index γ.

4 Conclusions

We can see that the presupernova stars on the stage of gravitational collapse can be the powerful sources of the non-thermal radiation impulses. Then collapsing star can lose the part their mass and flare up as supernova with a expanding shell. But before the explosion supernova star must precede the stage of gravitational collapse when the star compress under the influence of gravitation. On this stage a star is the powerful source of the non-thermal radiation. The impulse of the non-thermal radiation can observed also before explosion of nova. The powerful sources of the non-thermal radiation can be also the white dwarfs in double systems on the stage accretion induced collapse [9]. Periodic impulses of non-thermal radiation can be generated also by pulsation of the stars with magnetic field, since in this case the charged particles can accelerate and the non-thermal emission generate.

What problems can arise by the astrophysical observation of the non-thermal radiation from the collapsing presupernova stars? First the theory of the stellar evolution does not enable us today to point to the location of presupernova stars before their explosion. This fact is principal problem in the astrophysical observation for the search of presupernova collapsing stars. Second problems is that the stellar collapse pass very rapidly. But this problem can be solved since the modern instruments enable to observe the very short impulse. Next problems is how to choose the impulse from presupernova collapsing stars from the great numbers of bursts with the unknown origin. These questions require additional investigations.

References

1. S. Chandrasekhar: Mon. Not. R. Astron. Soc. **95**, 207 (1935)

2. V.L. Ginzburg, L.M. Ozernoy: J. Theor. & Experiment. Phys. **47**, 1030 (1964)
3. C.T. Gunningham, R.H. Price, V. Moncrief: Astrophys. J. **224**, 643 (1978)
4. C.T. Gunningham, R.H. Price, V. Moncrief: Astrophys. J. **230**, 870 (1979)
5. C.T. Gunningham, R.H. Price, V. Moncrief: Astrophys. J. **236**, 674 (1980)
6. R.N. Henriksen, W.Y. Chau, K.L.Chau: Astrophys. J. **227**, 1013 (1979)
7. V. Kryvdyk: Mon. Not. R. Astron. Soc. **309**, 593 (1999)
8. V. Kryvdyk: Adv. Space Res. **28**, 463 (2001)
9. V. Kryvdyk: NATO ASIB Proc. **10**, 205 (2003)
10. A.I. MacFadyen, S.E. Woosley: Astrophys. J. **524**, 262 (1999)
11. V. Moncrief: Astrophys. J. **238**, 333 (1980)
12. M. Milgrom, V.V. Usov: Astrophys. J. Lett. **531**, L127 (2000)
13. I.R. Oppenheimer, G. Volkoff : Phys. Rev. **55**, 374 (1939)

Radio Observations of Supernova Remnants in the M82 Starburst

Alan Pedlar, Tom Muxlow and Jon Riley

Jodrell Bank Observatory, University of Manchester, Cheshire SK11 9DL, UK;
ap@jb.man.ac.uk

Summary. We report on recent MERLIN, VLA and VLBI observations of the compact radio sources in the nearby starburst M82, with angular resolutions ranging from arcseconds to milliarcseconds. The spectral properties of the compact sources have been investigated by 15 GHz VLA-Pie Town observations which show that 16 of the less luminous compact sources are, in fact, HII regions. However the steep non-thermal spectrum, parsec size and small variability of the remaining sources is consistent with their being supernova remnants. Several show clear shell structures at MERLIN resolution (∼50 mas) and 5 have been resolved further using VLBI. Measurements of the most compact source (41.95+575) shows an expansion velocity of $\sim$ 2000 km s^{-1}, and one of the best defined SNR shells (43.31+592) shows an expansion velocity of $\sim 10^4$ km s^{-1}. Recent VLBI and MERLIN measurements confirm this expansion velocity and show little evidence for deceleration. We comment on the discrepancy between this measured expansion velocity and the low expansion velocities predicted theoretically for remnants in M82.

1 Introduction

Although studies of extragalactic supernova remnants (SNR) are currently limited by sensitivity, and to some extent angular resolution, such studies provide unique insights into the early evolution of radio supernovae and supernova remnants. Whilst the extensive studies of remnants in our own galaxy are particularly valuable for testing details of the physical processes occurring in individual remnants, they are limited by the fact that the youngest known galactic supernova remnant is over 300 years old. In addition the distances of many galactic remnants are quite uncertain, which has resulted in studies involving surface brightness-diameter plots being highly suspect. Furthermore because of the large differences in distance, statistical inferences based on observations with constant angular resolution and sensitivity are severely affected by selection effects.

Studies of extragalactic SNR in starburst galaxies have a number of advantages. Firstly the high star formation rate results in a relatively large number of young supernova remnants with ages measured in decades, rather than centuries. Secondly as the starburst region is typically a kiloparsec in extent, and as distances to even the nearest starburst galaxies are a few Mpc, the relative distances to each SNR will only vary by ∼0.1%. Finally

radio synthesis techniques ensure that all the SNR are observed with same angular resolution and sensitivity. Hence as all the SNR are essentially at the same distance this corresponds to a constant linear resolution and surface luminosity limit.

2 The Compact Sources in Messier 82

Although radio supernova remnant studies have been carried out on several nearby starburst galaxies, by far the most extensive have been carried out in the Messier 82 starburst. Compact sources were first noted in M82 by Kronberg & Wilkinson [5], but it was not until the advent of MERLIN [13] and the VLA [6] that ∼50 compact radio sources were separated from the extended background. Although initially it was thought that some of these may be radio supernovae, the relatively low star formation rate inferred from FIR observations (see below), together with the lack of significant variability of most sources, implied that the more luminous compact sources were supernova remnants. This was subsequently confirmed by 5 GHz MERLIN observations [10] in which all the sources were shown to be extended with sizes of typically a few parsecs and many had the shell or partial shell structures typical of remnants.

2.1 Distinguishing Between Supernova Remnants and HII Regions

The majority of the more luminous compact sources in M82 showed a steep spectrum, consistent with synchrotron emission from supernova remnants (e.g., [1]). Although from these initial spectral studies it appeared that only one compact source had a spectrum consistent with thermal emission, the sample only included about half (∼26) of the known compact sources and as they were selected at relatively low frequencies hence had a bias towards non-thermal sources.

However recent work [9] determined the two point (5 and 15 GHz) spectra of 46 the compact sources in M82 by using the extended VLA (i.e., including the Pie-Town Antenna) at 15 GHz which resulted in an angular resolution of 80 mas (=1.2 pc) which can be directly compared to MERLIN 5 GHz observations with 50 mas resolution. Fig. 1 shows a plot of spectral index against average brightness temperature of the compact sources, from which it can be seen that 16 had inverted spectra and brightness temperatures consistent with optically thick compact HII regions with emission measures of $\sim 10^7$ pc cm^{-6} implying relatively high thermal pressures.

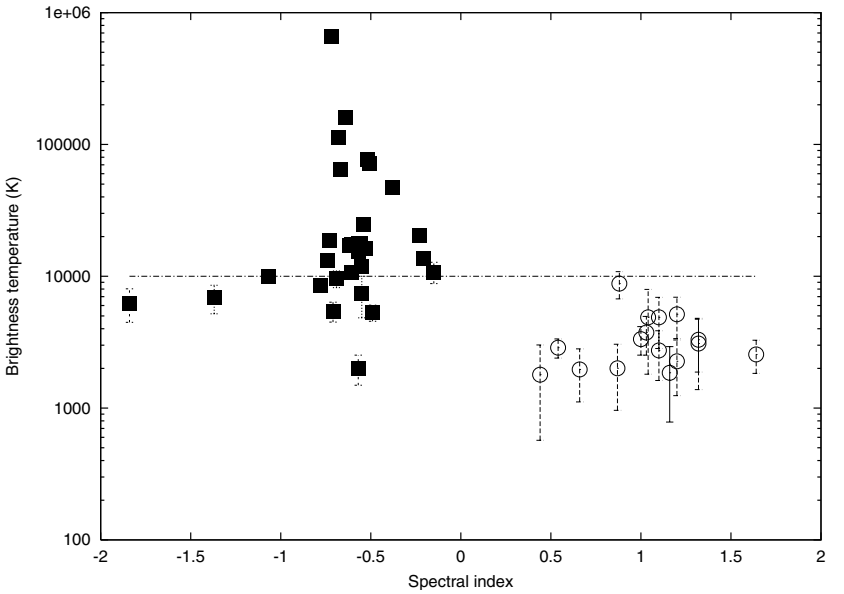

Fig. 1. The 5/15 GHz spectral index plotted against the average brightness temperature of 46 of the compact sources in Messier 82. The filled squares are consistent with supernova remnants, and the open circles with compact HII regions (adapted from [9]).

3 Star Formation and Supernova Rates in M82

The global star formation rate (SFR) of a galaxy can be estimated using a measurements in the ultra-violet, optical, infra-red and radio [4]. However as starburst galaxies usually contain large quantities of dust, the estimates of SFR from ultraviolet and optical data are uncertain due to dust extinction. M82 is no exception with A_v typically 20-30 magnitudes. Fortunately the radio method [4] is not affected by dust extinction and hence the star formation rate can be estimated from the equation

$$SFR(M \geq 5\ M_{\odot}) = \frac{L_{1.4}}{4.0 \times 10^{21}}\ \mathrm{M_{\odot} yr^{-1}} \qquad (1)$$

where $L_{1.4}$ is the total 1.4 GHz luminosity of the galaxy [4]. Note that to avoid complications with the initial mass function (IMF) of low mass stars, this relation gives the star formation rate for stars with mass $> 5\ M_{\odot}$. Hence as the total flux density of M82 at 1.4 GHz is $\sim$8.5 Jy and using a distance of 3.2 Mpc, then SFR($M \geq 5\ M_{\odot}$) for M82 can be estimated to be $\sim 2.5\ \mathrm{M_{\odot}\ yr^{-1}}$. Also the radio thermal free-free contribution is reasonably well defined in M82 [2] and can be used to estimate a star formation rate [12] consistent

with the above value. Finally the star formation rate derived from the total FIR luminosity also gives a value of SFR($M \geq 5\ M_{\odot}$) close to 2 $M_{\odot}$ yr^{-1}.

If the SFR is constant over $\sim 10^7$ years, then in principle the type II supernova rate can be derived directly from the star formation rate and the initial mass function, on the assumption that all stars with masses $> 8\ M_{\odot}$ become supernovae. Hence assuming a Miller-Scalo IMF the supernova rate ν_{sn} is related to the star formation rate via

$$SFR(M \geq 5\ M_{\odot}) = 25\nu_{sn}\ \mathrm{M_{\odot}yr^{-1}}. \quad (2)$$

Thus, if $SFR(M \geq 5\ M_{\odot})$ is $\sim 2 - 2.5$ M$_{\odot}$yr^{-1} this implies a supernova rate of $\sim 0.08 - 0.1$ yr^{-1} in M82.

Several methods can be used to estimate the supernova rate directly from the radio parameters of the M82 supernova remnants [10, 12]. The simplest method is to assume that all the M82 remnants which are brighter and smaller than the Cassiopeia A remnant in our galaxy are younger than 330 years. Alternatively if a constant expansion velocity is assumed (e.g., 5000-10000 km s^{-1}) this gives the ages of the remnants and hence the supernova rate [10]. Finally van Buren & Greenhouse [14] estimated the supernova rates from remnant luminosities. These methods give supernova rates ranging from 0.05 to 0.1 yr^{-1} - consistent with the star formation rates derived above. It is possible that not all supernovae produce radio emitting remnants, and if so this would imply an even larger supernova rates.

However some doubts have been raised concerning the evolution of the remnants in M82. Kronberg et al [7], in a study of the variability of 24 remnants, claim, using statistical arguments, that in a large fraction of the remnants the radio luminosity is decaying at less than 0.1% per year. If true this could suggest that the remnants are over a thousand years old. Also recent theoretical studies [3] have suggested that the high pressure of the interstellar medium in M82 would result in the supernova remnants expanding at only 500 km s^{-1}, hence as the observed sizes are typically a few parsecs, this again would imply ages of thousands of years. Both these results appear to be inconsistent with the supernova rates of $\sim$0.1 yr^{-1} derived above, which require that the ages of typical remnants are a few hundred years.

4 Interstellar Medium Pressures in M82

Chevalier & Fransson [3] assume that the pressure in the starburst region of M82 is 10^7 cm^{-3}K and from this derive the low (500 km s^{-1}) SNR expansion velocities. While there is no doubt that part of the starburst must be at this pressure (e.g., the compact HII regions [9]), it seems likely that much of the starburst is not in static pressure equilibrium and that a range of pressures are present.

As the photoionized component in M82 has a temperature of $\sim 10^4$ K, the pressure assumed by Chevalier & Fransson would require that the density

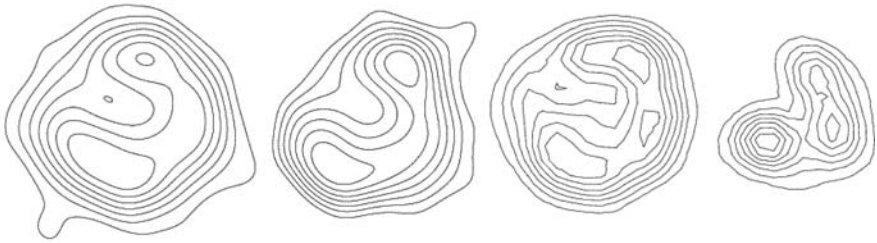

Fig. 2. Four VLBI images ([11] and Riley et al. , this meeting) of the supernova remnant 43.31+59 taken in 2001.1, 1998.9, 1997.5, and 1986.9 convolved to a common angular resolution of 15 mas. The contours levels are at 12.5% of the peak flux density of each image.

of this gas be $\sim 10^3$ cm^{-3}. However the free-free absorption measurements taken against the individual remnants show emission measures of $\sim 5 \times 10^5$ pc cm^{-6} [16], and hence densities of $\sim 10^3$ cm^{-3} would imply ionized gas path lengths of only ∼0.5 pc. Given that the extent of the starburst region is at least 500 pc, unless the ionized gas is contrived to occupy the 0.1% of the volume of the starburst in the immediate vicinity of each remnant, it is difficult to see how the ionized component can provide sufficient pressure to slow the SNR expansion to 500 km s^{-1}.

Chevalier& Fransson suggest that the SNR may be confined by the interclump medium of molecular clouds in M82 and note that many of the remnants are in the line of sight to regions of strong CO emission. This is, however, not conclusive evidence that the remnants are embedded within the clouds, and often the H1 absorption spectra measured directly against the remnants [17] do not support this interpretation (see discussion of 43.31+592 below). Furthermore studies by Weiss et al [15] have shown that the molecular gas in the star forming regions of M82 has a kinetic temperatures of ~ 150 K and densities of $\sim 10^3$ cm^{-3} which corresponds to a pressure two orders of magnitude less than that assumed by Chevalier & Fransson.

Clearly the ISM of M82 is complex, and to assign a single pressure to the starburst region may be unrealistic. Hence it is likely that many of the SNR in M82 are embedded in regions with pressures significantly lower than 10^7 cm^{-3} K and hence have expansion velocities $>>$ 500 km s^{-1}.

4.1 Measuring Expansion Velocities

Now that we can resolve the compact sources in M82 [10], in principle it is a relatively simple matter to measure their expansion velocities by measuring their size over a period of time, although such studies are limited by current instrumental sensitivity to the brightest sources. The first expansion measurements were made by Pedlar et al [11] on the compact sources 41.95+575 & 43.31+592. The brightest, most compact source (41.95+575) was shown to

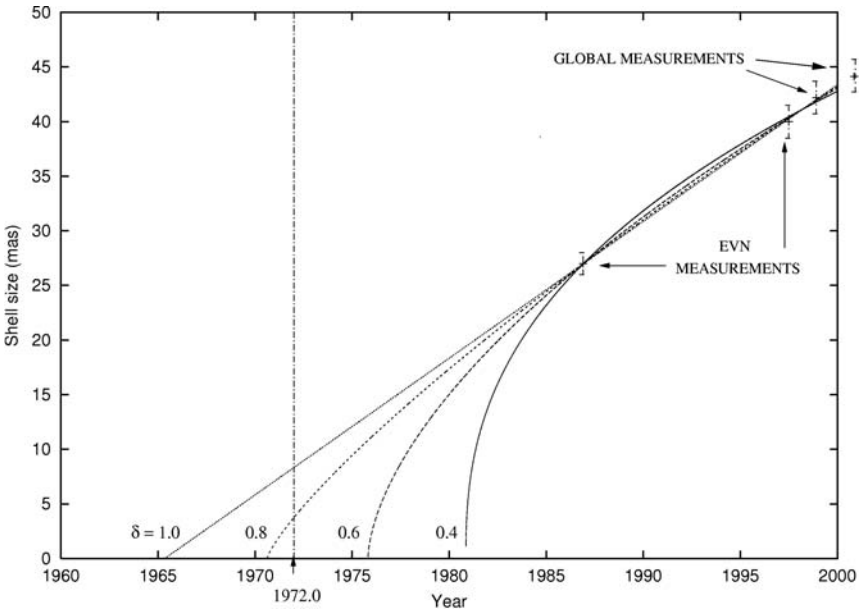

Fig. 3. The size of 43.31+592 plotted as a function of age including the 2001.1 measurement. The Figure also shows different expansion models. Adapted from McDonald et al [8].

have an elongated structure and the expansion velocity along the major axis was constrained to < 4000 km s^{-1}. Subsequent global VLBI measurements [8] showed it to have an expansion velocity of ~ 2000 km s^{-1}. This source is, however, rather anomalous on account of its high radio luminosity and its rapid decay. Also the global VLBI structure is highly elongated and more like a bipolar structure than a shell – unlike a typical SNR [8].

The source 43.31+592 is much more typical an SNR of shows a well-defined shell structure (Fig. 2). By comparing data observed in 1986 and 1997, Pedlar et al [11] deduced an expansion velocity of $\sim$ 10000km s^{-1}. Subsequent Global VLBI measurements ([8] and Riley et al. , this meeting) have confirmed this result and shown its expansion to be consistent with no deceleration (Fig. 3), implying an age of about 35 years. As the SNR seems to be in free expansion we can set a simple constraint of < 2000 atoms cm^{-3} to the external density by assuming that the mass of gas swept up is less than the mass ejected. The expansion velocity of this source clearly exceeds the 500 km s^{-1} predicted by Chevalier & Fransson, which may be accounted for if it is in a region with relatively low external pressure. This assertion is supported by the lack of a low frequency turnover at 73 cm [16] in the spectrum of 43.31+592 even though it is in the line of sight to regions with strong free-free emission. This shows that the remnant is in front of, and

not embedded in, the relatively dense ionized gas in the central region of M82. Even though relatively strong H1 absorption (5×10^{21} atoms cm^{-2}) is seen against this remnant [17], its narrow width and systemic velocity is consistent with absorption by a disk of H1 external to the central region of M82. Hence this is further evidence that this SNR is not embedded in neutral gas the center of the starburst. Thus if this SNR is in a relatively low pressure region, it may be possibly reconcile the difference between the 500 km s^{-1} predicted by Chevalier & Fransson and the measured ∼10000 km s^{-1} expansion velocity.

Recent MERLIN observations (Muxlow et al. , this meeting) have independently confirmed the above expansion velocities and also measured the expansion velocities of 2 more remnants. One of the remnants has a velocity close to 10000 km s^{-1}, whereas the other is relatively low at 2000 km s^{-1}. We now have 4 expansion measurements and find little evidence for 500 km s^{-1} expansion velocities. Hence we see no reason to revise the supernova rates or remnant ages that we have inferred previously. Higher sensitivity observations using e-MERLIN, combined with an increasing time baseline, will enable the expansion velocities of many more remnants in M82 to be determined and hence constrain both the supernova rate and the parameters of the interstellar medium in M82.

References

1. M.L. Allen, P.P. Kronberg: Astrophys. J. **502**, 218 (1998)
2. J.E. Carlstrom, P.P. Kronberg: Astrophys. J. **366**, 422 (1991)
3. R.A. Chevalier, C. Fransson: Astrophys. J. **558**, 27 (2001)
4. L. Cram et al. : Astrophys. J. **507**, 155 (1998)
5. P.P. Kronberg, P.N. Wilkinson: Astrophys. J. **200**, 430 (1975)
6. P.P. Kronberg, P. Biermann, F.R. Schwab: Astrophys. J. **291**, 693 (1985)
7. P.P. Kronberg et al. : Astrophys. J. **535**, 706 (2000)
8. A.R. McDonald et al. : Mon. Not. R. Astron. Soc. **322**, 100 (2001)
9. A.R. McDonald et al. : Mon. Not. R. Astron. Soc. **334**, 912 (2002)
10. T.W.B. Muxlow et al. : Mon. Not. R. Astron. Soc. **266**, 455 (1994)
11. A. Pedlar et al. : Mon. Not. R. Astron. Soc. **307**, 761 (1999)
12. A.Pedlar: "Extragalactic supernovae and the starformation rate." In: *Proc. IAU symposium 205*, ed. by R. Schilizzi (ASP 2001) p. 366
13. S.W. Unger et al. : Mon. Not. R. Astron. Soc. **211**, 783 (1984)
14. D. van Buren, M.A. Greenhouse: Astrophys. J. **431**, 640 (1994)
15. A. Weiss et al. : Astron. Astrophys. **365**, 571 (2001)
16. K.A. Wills et al. : Mon. Not. R. Astron. Soc. **291**, 517 (1997)
17. K.A. Wills, A. Pedlar, T.W.B. Muxlow: Mon. Not. R. Astron. Soc. **298**, 347 (1998)

Deep Radio Imaging with MERLIN of the Supernova Remnants in M82

T.W.B. Muxlow[1], A. Pedlar[1], J.D. Riley[1], A.R. McDonald[1], R.J. Beswick[1], and K.A. Wills[2]

[1] Jodrell Bank Observatory, University of Manchester, Macclesfield, Cheshire SK11 9DL; UK;
twbm@jb.man.ac.uk
[2] Department of Physics and Astronomy, University of Sheffield, Sheffield S3 7RH. UK

Summary. An 8 day MERLIN deep integration at 5GHz of the central region of the starburst galaxy M82 has been used to investigate the radio structure of a number of supernova remnants in unprecedented detail revealing new shells and partial shell structures for the first time. In addition, by comparing the new deep 2002 image with an astrometrically aligned image from 36 hours of data taken in 1992, it has been possible to directly measure the expansion velocities of 4 of the most compact remnants in M82. For the two most compact remnants, 41.95+575 and 43.31+592, expansion velocities of $2800 \pm 300\,\mathrm{km\,s^{-1}}$ and $8750 \pm 400\,\mathrm{km\,s^{-1}}$ have been derived. These confirm and refine the measured expansion velocities which have been derived from VLBI multi-epoch studies. For remnants 43.18+583 and 44.01+596, expansion velocities of $10500 \pm 750\,\mathrm{km\,s^{-1}}$ and $2400 \pm 250\,\mathrm{km\,s^{-1}}$ have been measured for the first time. In addition, the peak of the radio emission for SNR 45.17+612 has moved between the two epochs implying velocities around $7500\mathrm{km\,s^{-1}}$. The relatively compact remnants in M82 are thus found to be expanding over a wide range of velocities which appear unrelated to their size. The new 2002 map is the most sensitive high-resolution image yet made of M82, achieving an rms noise level of $17\mu\mathrm{Jy\ beam^{-1}}$. This establishes a first epoch for subsequent deep studies of expansion velocities for many SNR within M82.

1 Introduction

M82 is a well known nearby (3.2Mpc) starburst galaxy. The central 1 kpc region contains at least 30 compact supernova remnants (SNR) with ages less than around 1000 years which have been imaged at high angular resolution by MERLIN [3] for over a decade. The most compact SNR have also been studied at very high angular resolution with VLBI [2, 4, 5]. All the SNR are resolved by MERLIN; however detailed expansion studies have been limited by the relatively poor signal-to-noise ratios of the earlier epoch images of many of the more resolved SNR. The 2002 epoch deep 8 day integration establishes the first MERLIN 5GHz image with high signal-to-noise ratios on the majority of well-resolved SNRs seen in M82. Subsequent deep images planned for later epochs will utilize the resurfaced Lovell antenna and new

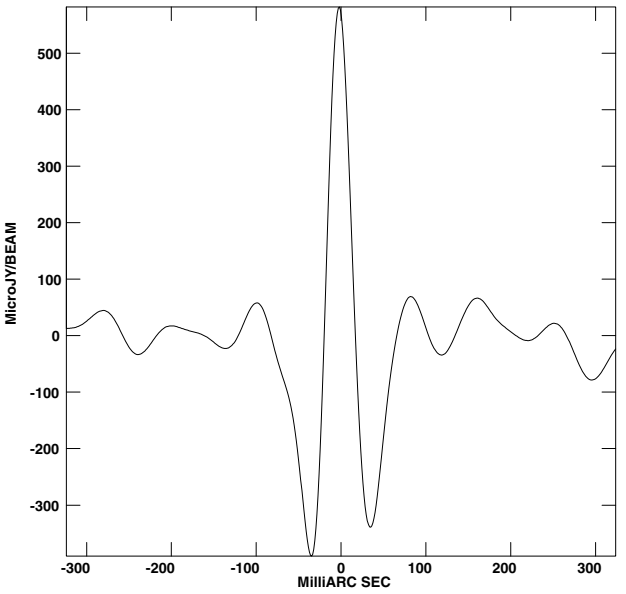

Fig. 1. Profile through the residual image of SNR 43.31+592 after subtraction of the 2002 image from the 1992 map. The positive central and negative outer regions are indicative of expansion between the epochs.

more sensitive 5GHz receiver systems and optical-fiber wide-band links which are being developed for *e*-MERLIN. This will allow the detailed study of the evolution of the expanding shells to be made for the majority of SNR in M82.

2 The MERLIN Observations

Observations of M82 and the phase calibration source 0955+697 lasting around 36 hours were made on 2 – 3 July 1992 at 4994GHz with the 6 element MERLIN array. The deep 8 day MERLIN integration was observed between the 1 and 28 April 2002 at the same frequency. The flux density scale was calibrated from observations of the point source OQ208 and 3C286.

The 2002 dataset were processed directly in J2000 coordinates with an updated position for the phase calibration source 0955+697 which has been measured to better than 1 mas [1]. In order to astrometrically align the 1992 data, they were first precessed to J2000 and corrections made to the nominal pointing center in order to account for the error in the original assumed position for 0955+697 (several tens of mas). Finally, the peak of the most compact source in M82 (41.95+575) as measured in the 1992 image was aligned under the peak as seen in the deep 2002 image; involving a positional translation of less than 2 mas. After alignment on 41.95+575, the peaks

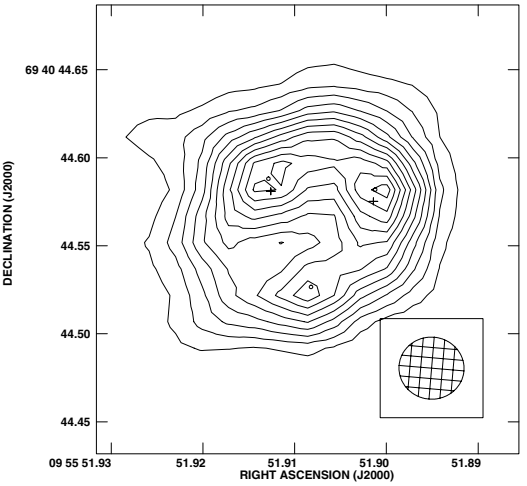

Fig. 2. Map of SNR 43.18+585 from the deep 2002 epoch MERLIN dataset convolved with a 35 mas circular beam, with contours at $(1, 2, 3, ...12) \times 50\,\mu$Jy beam^{-1}. Fitted positions for the 2002 epoch are shown as circles. Fitted positions for the 1992 epoch are shown as crosses.

of emission for the next two most compact SNR in M82 (43.31+592 and 44.01+596) were found to align between the two epochs to better than 1 mas. Since SNR 44.01+596 lies 16.5 arcseconds from 41.95+575 this implies than any relative stretch errors between the two epochs are at levels of 0.001% or better.

3 Structural Evolution Between 1992 and 2002 for Compact SNR in M82

In this section we summarize the structural evolution found between the images taken in epochs 1992.504 and 2002.249. The two most compact sources (41.95+575 and 43.31+592) have been studied for a number of years at mas angular resolution with Global VLBI. For these sources MERLIN provides an independent measure of the expansion velocities.

41.95+575 is the only source in M82 to show long-term systematic flux density variation with time and has been found to monotonically decrease in flux density at a rate of 8.5% year^{-1} over many years. Between 1992 and 2002 the source was found to have decreased in flux density from ~ 40 mJy to ~ 17 mJy and the major axis of the source to have increased in size by 3.6 mas from 21.12 ± 0.05 to 24.71 ± 0.07 mas implying an expansion velocity of 2800 ± 300 km s^{-1}. This is in good agreement with global VLBI results and if the source is in free expansion, suggests a birth date around 1945.

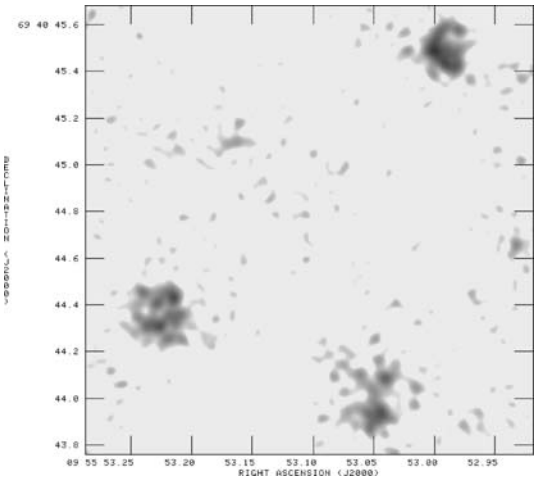

Fig. 3. SNR shell and partial shell structures in M82 revealed for the first time by the deep 2002 MERLIN image.

Between 1992 and 2002 this SNR 43.31+592 was found to have grown in size. The formal fit to the major axis is for an increase from 39.03 ± 0.04 to 49.52 ± 0.02 mas and for the minor axis an increase from 28.69 ± 0.04 to 40.43 ± 0.02 mas. Taking an average value, this implies an expansion speed of 8750 ± 400 km s^{-1}, again in good agreement with global VLBI results (J.D. Riley et al. , these proceedings). There is also some evidence to suggest that the flux density of this SNR may have increased from $\sim$8.5 to $\sim$10.2 mJy between the two epochs. If the SNR is in free expansion this high velocity makes it the youngest SNR in M82 with a birth date around 1963.

SNR 43.18+585 is substantially resolved by MERLIN and positional fits to the peaks of emission as seen in the 1992 and 2002 epochs (See Fig. 2) together with integrated annular profiles, have shown that these peaks have moved outward by 7.05 ± 0.15 mas in the 9.75 years between the epochs of the images implying an expansion velocity of $10,500 \pm 750$ km s^{-1}. If the SNR is in free expansion, with a measured mean radius of 37.7 mas in 2002, the source has a birth date around 1949. This is the first time that a reliable expansion velocity has been found for this SNR.

SNR 44.01+596 has a somewhat disrupted shell-like radio structure. However, a comparison between the images from the two epochs shows that the major axis has increased by 3.40 ± 0.05 mas, and the minor axis by 2.70 ± 0.05 mas. This yields a relatively low expansion velocity of 2400 ± 250 km s^{-1}. Assuming free expansion gives an age in excess of 160 years. Again, this is the first time that an expansion velocity has been found for this SNR.

SNR 45.17+612 shows only a partial shell structure. The peak of emission in the deep 2002 epoch image is found to be significantly displaced from that of the 1992 image by $\sim$ 9.5 mas. This implies velocities $\sim$ 7500 km s^{-1}.

However, the direction of displacement does not appear to be radial (so far as this can be discerned from a partial shell structure). The interpretation of the measured motion is therefore unclear in this object.

The 2002 epoch image has revealed the detailed radio structures of many other SNR in M82 for the first time. However the poor signal-to-noise ratio of the original 1992 maps prevents reliable expansion measurements from being achieved. For these weaker SNR, later epoch deep images will be required before expansions velocities can be derived. These are planned, and with the advent of *e*-MERLIN, we expect to make such measurements for the majority of SNR in the central region of M82 over the next decade.

4 Conclusions

We have successfully measured the expansion velocities of the four most compact SNR in the central nuclear region of M82 over a 9.75 year period between 1992 and 2002. The velocities found range from around 2500 kms^{-1} to in excess of 10000 kms^{-1} and do not appear to be related directly to the size or implied age of the remnant. We confirm the velocities found by VLBI for the two most compact remnants and report new results on two additional sources. The deep 2002 epoch MERLIN image will be used as the first epoch of a long-term study which should reveal the expansion velocities for the majority of established SNR in M82

References

1. A.J. Beasley: Private communication
2. A.R. McDonald et al. : Mon. Not. R. Astron. Soc. **322**, 100 (2001)
3. T.W.B. Muxlow et al. : Mon. Not. R. Astron. Soc. **266**, 455 (1994)
4. A. Pedlar et al. : Mon. Not. R. Astron. Soc. **307**, 761 (1999)
5. J.D. Riley et al. : "Second epoch global VLBI observations of compact radio sources in the M82 starburst." In: *These Proceedings.*

Thermonuclear Supernova Explosions and Their Remnants: The Case of Tycho

Carles Badenes[1], Eduardo Bravo[1], and Kazimierz J. Borkowski[2]

[1] Institut d'Estudis Espacials de Catalunya, Gran Capitá 2-4, 08034 Barcelona, Spain ; and Departament de Física i Enginyeria Nuclear, Universitat Politécnica de Catalunya, Av. Diagonal 647, 08028 Barcelona, Spain
badenes@ieec.fcr.es, eduardo.bravo@upc.es

[2] Department of Physics, North Carolina State University, Raleigh NC 27695
kborkow@unity.ncsu.edu

Summary. We propose to use the thermal X-ray emission from young supernova remnants (SNRs) originated in Type Ia supernovae (SNe) to extract relevant information concerning the explosion mechanism. We focus on the differences between numerical 1D and 3D explosion calculations, and the impact that these differences could have on the modeling of young SNRs. We use the remnant of the Tycho supernova (SN 1572) as a test case to compare with our predictions, discussing the observational features that allow to accept or discard a given model.

1 From Supernova to Supernova Remnant

Thermonuclear supernovae play a key role in our understanding of the origin of elements, the chemical evolution of galaxies and the large scale structure of the universe. Yet, the many attempts to constrain their progenitor systems and elucidate the detailed physics of the explosion mechanism have been unsuccessful so far (see [3, 9] for reviews). In [1] we established a connection between the thermal X-ray emission from shocked ejecta in the young supernova remnants originated by Type Ia explosions and a grid of 1D theoretical supernova models, including examples from all the explosion mechanisms currently under debate: pure deflagrations, delayed detonations, pulsating delayed detonations and sub-Chandrasekhar explosions. We showed that the different density and chemical composition profiles for the ejecta predicted by the explosion models have a profound impact on the dynamics of the young SNRs and result in different ionization states and electron temperatures for the shocked plasma, and therefore different emitted thermal X-ray spectra for each model. Significant conclusions about the explosion models can be drawn using this technique; in particular, the differences between 1D and 3D explosion models are large enough to have a noticeable impact on the spectrum of the shocked ejecta several hundred years after the explosion itself.

2 Discussion of the Analysis Technique

In [1] an adiabatic 1D hydrodynamic code was used to follow the evolution of the SNR models. The use of an adiabatic code is justified by the absence of optical emission from radiatively cooled knots in the well known Type Ia SNRs Tycho and SN1006, in contrast to some core-collapse SNRs like Cas A, which do have such emission. We have calculated the order of magnitude of the radiative and ionization losses in the ejecta, and found that, except for a few extreme cases, their impact on the dynamics was negligible up to several thousand years after the explosion. Other factors that could compromise this simple modeling technique, like thermal conduction, would require even longer timescales, of the order of 10,000 yr, to have an impact on the overall evolution. Deviations from 1D dynamics, either produced during the formation of the remnant or already present in the ejecta or ambient medium (AM), are difficult to quantify [15]. Type Ia SNRs seem to be more spherically symmetric than core-collapse SNRs, with significantly less turbulent dynamics, but the amount of clumping present in Type Ia SN ejecta is not known, even if observations seem to imply that it is not very large (see Bravo & García-Senz, these proceedings, and references therein). The presence of clumps in the shocked ejecta will not affect our conclusions unless their density contrast is very large. It is worth noting that analysis of some of the bright ejecta knots in Cas A seems to suggest that they have a low density contrast [11], but this remains an open question, and needs to be addressed with 3D models and high resolution X-ray observations.

3 Explosion Models: 3D vs 1D

Numerical calculations of thermonuclear supernova explosions in one dimension have become a commonplace benchmark for the analysis of Type Ia SNe, but their validity is questionable because the subsonic combustion fronts (deflagrations) that play a fundamental role in all of them are subject to instabilities, and therefore cannot be simulated with 1D codes in a self-consistent way.

In recent times, the first three dimensional (3D) calculations of Type Ia explosions have begun to appear in the literature: see [7, 14] and the paper by Bravo & García-Senz in these proceedings. A common feature of all these calculations, and the most remarkable difference between 1D and 3D models, is the uniform mixing of unburned C and O material with ^{56}Ni and other elements throughout the ejecta. This mixing should have an impact on the optical spectra of the supernovae and on the thermal X-ray spectra from the shocked ejecta in the SNRs, but neither of these signatures has been confirmed so far. [7] pointed out that no evidence for low-velocity C and O was found in optical spectra of Type Ia SNe, but this assertion is being revised [2]. Spatially resolved spectroscopy of Type Ia SNRs also provides

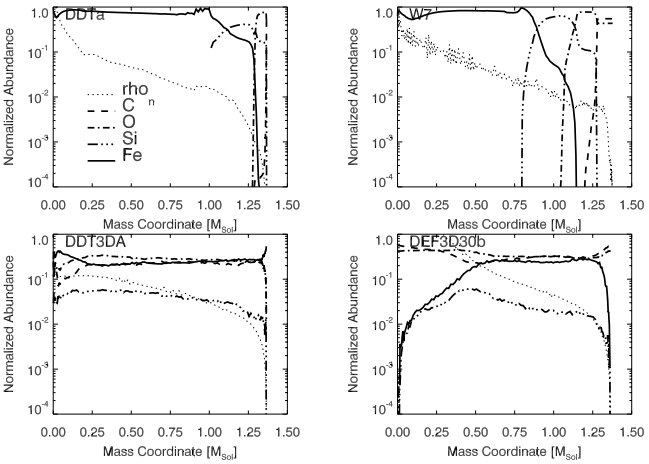

Fig. 1. Composition and normalized density profiles of the four Type Ia models discussed in this paper: DDTa, W7, DDT3DA and DEF3D30b. For clarity, only C, O, Si and Fe are represented. The thin dotted line is the normalized density profile.

indirect evidence for some kind of composition stratification in the shocked ejecta [4, 10, 12]. The absorbed UV spectrum of the Schweizer-Middleditch star, which is placed behind the remnant of SN1006, poses an alternative observational constraint for the presence of mixing in Type Ia SN ejecta. No evidence has been found for C or O absorption lines in HST observations of this star [8], implying that these elements, if present, would have to be in ionization states very different from those of the observed Si and Fe.

4 Spectral Signatures of C and O Mixing in the Ejecta of Young SNRs

In Fig. 1 we present the composition and density profiles of four Type Ia explosion models. DDTa is a 1D delayed detonation [1]; W7 is a 1D "fast" deflagration [13]; DDT3DA and DEF3D30b are 1D mappings of 3D models described by Bravo & García-Senz elsewhere in these proceedings: DDT3DA is the delayed detonation with the transition where D>2.5 and DEF3D30b is the deflagration with 30 equal size bubbles. The mixing of unburned C and O with ^{56}Ni (which we have represented as Fe, the product of its decay) is apparent in the two 3D models, in contrast with the layered structure of the 1D models.

One of the main conclusions of [1] was that the density enhancement effect towards the contact discontinuity between ejecta and ISM, first pointed out in [5] and confirmed by 2D simulations in [6], dominates the integrated thermal X-ray emission from the shocked ejecta. Self-consistent calculation of electron

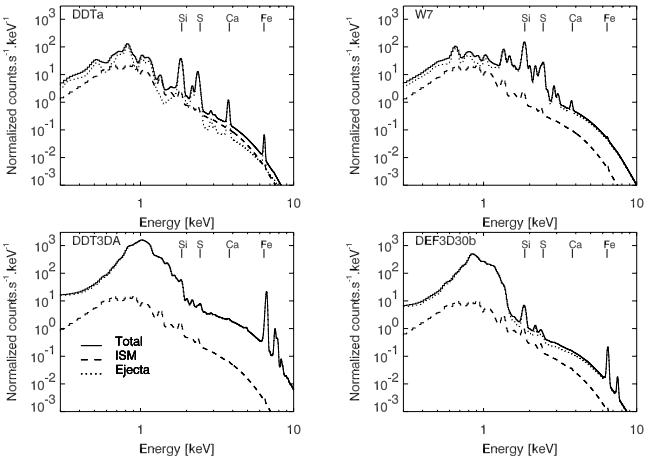

Fig. 2. Synthetic spectra at the age of Tycho for the four models. The contributions from shocked ejecta and ISM are shown with dotted and dashed lines, respectively.

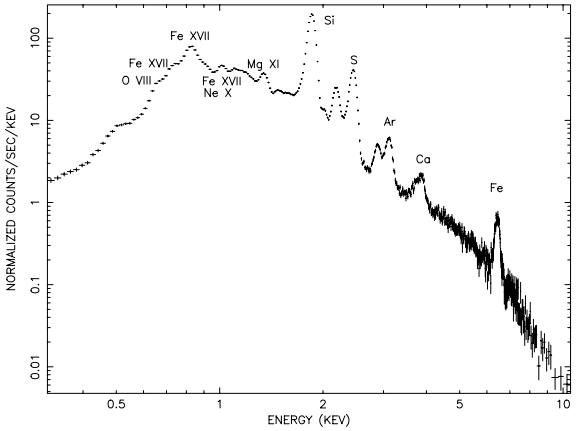

Fig. 3. XMM-EPIC MOS1 spectrum of the Tycho SNR, from [4].

heating reveals that this is also the hottest region. This leads to important contributions to the spectrum from elements that were not synthesized in large quantities in the explosion, but are located in hot, high density regions in the young SNR (X-ray emissivity scales as ρ^2). The relative smoothness of the chemical composition profile for the 3D explosion models, however, tends to assuage this effect, and the relative contribution from each element to the emitted spectrum will be more closely related to the total amount of the element synthesized in the explosion.

In Fig. 2 the total integrated spectrum for the four models at the age of the Tycho SNR is shown, calculated following the scheme described in [1] and

convolved with the instrumental response of the XMM-Newton Epic-MOS1 camera to facilitate comparison with the observed spectrum from the Tycho SNR, which is given in Fig. 3. No Ar data are present in our atomic code, but there is enough information in the Kα lines of Si, S, Ca and Fe, marked in Fig. 2, and in the overall spectral shape, to extract significant conclusions. The large amount of Fe in the outer layers of the 3D models, which turn out to be the densest and hottest regions in the shocked ejecta throughout the evolution of the SNR (see [1]), dominates their emitted spectrum. The strength of the Fe L complex around 1 keV and the Fe Kα line at 6.4 keV are incompatible with the observed spectrum of Tycho. The Fe emission is so strong, in fact, that the Fe continuum masks the contribution from Si, S and Ca, which are clearly seen in the observed spectrum. Another interesting feature of the 3D models is the presence of the Ni Kα line at 7.5 keV. This line comes from stable Ni, whose parent nuclei are synthesized in small amounts together with ^{56}Ni, and it has not been observed so far in any young Type Ia SNR. The large amount of C and O in the ejecta does not have a clear imprint on the spectrum because lines of these elements are located at low photon energies where the interstellar absorption and the poor spectral resolution of the XMM-Newton EPIC makes their detection difficult. The 1D models, on the other hand, show important contributions from Si, S and Ca, albeit the overall spectral shape is reproduced much better (but not perfectly!) by the DDTa model than by the W7 model. The absence of the Fe Kα line in the W7 model is due to the fact that the Fe is at smaller radii, and therefore at a lower density and in a lower ionization state.

We conclude that the X-ray spectrum of the Tycho SNR cannot be explained with the current 3D explosion models for Type Ia SNe using the simulation scheme described in [1]. The mixing of burnt and unburned material throughout the supernova ejecta seems to contradict a number of independent observations, casting a doubt on the validity of the current 3D explosion models, at least in their present state. This is a preliminary conclusion; a final resolution of this issue should be based on more sophisticated hydrodynamical simulations of Type Ia SNRs.

References

1. C. Badenes, E. Bravo, K. Borkowski I. Domínguez: Astrophys. J. **593**, 358 (2003)
2. E. Baron, E. Lentz, P. Hauschildt: Astrophys. J. Lett. **588**, L29
3. D. Branch, A. Khokhlov: Phys. Rep. **256**, 53 (1995)
4. A. Decourchelle et al. : Astron. Astrophys. **365**, L218 (2001)
5. V. Dwarkadas, R. Chevalier: Astrophys. J. **497**, 807 (1998)
6. V. Dwarkadas: Astrophys. J. **541**, 418 (2000)
7. V. Gamezo, A. Khokhlov, E. Oran, A.Ctchelkanova: Science **299**, 77 (2003)
8. A. Hamilton, R. Fesen, C. Wu, D. Crenshaw, C. Sarazin: Astrophys. J. **482**, 838 (1997)

9. W. Hillebrandt, J. Niemeyer: Ann. Rev. Astron. Astrophys. **38**, 191 (2000)
10. U. Hwang, E. Gotthelf: Astrophys. J. **475**, 665 (1997)
11. M. Laming, U. Hwang: In press
12. K. Lewis et al. : Astrophys. J. **582**, 770 (2003)
13. K. Nomoto, F.-K. Thielemann, K. Yokoi: Astrophys. J. **286**, 644 (2003)
14. M. Reinecke, W. Hillebrandt, J. Niemeyer: Astron. Astrophys. **391**, 1167 (2002)
15. C.-Y. Wang R. Chevalier: Astrophys. J. **549**, 1119 (2001)

Part IV

Supernovae: Models

Models of Supernova Explosions: Where Do We Stand?

Wolfgang Hillebrandt

Max-Planck-Institut für Astrophysik, 85748 Garching, Germany;
wfh@mpa-garching.mpg.de

Summary. The present status of our understanding of core-collapse and of thermonuclear supernovae is reviewed. It will be argued that the failure of numerical simulations of the collapse of massive stars to produce explosions is probably caused by our incomplete knowledge of the (micro-) physics involved. In contrast, for thermonuclear (type Ia) supernovae the basic physics seems to be well under control and, therefore, it is not surprising that model predictions and observations are in good agreement.

1 Introduction

The modeling of both core-collapse and thermonuclear supernovae is still a major a challenge in astrophysics. In the case of core collapse models, which utilize gravitational binding for the explosion, the problem is not so much an energy but rather a momentum problem. There is plenty of energy available and only a small fraction of it has to be converted into outward momentum of the stellar envelope, but this is a non-trivial problem. It is somewhat embarrassing that despite all the effort that went into the construction of core-collapse supernova models until now none of them yielded the desired explosions.

Thermonuclear explosion models, on the other hand, suffer from the fact that once nuclear burning is ignited the progenitor star, presumably a white dwarf, tends to expand and cool. It is known since many years that an explosion can only result if the thermonuclear burning front propagates with a velocity much larger than the laminar speed of nuclear flames in degenerate matter. But only very recently it has been shown that models taking advantage of small scale turbulent velocity fluctuations lead indeed to the desired results.

In this review, recent developments in theoretical model-calculations for supernovae explosions are reviewed, including both core-collapse and thermonuclear supernovae, but with more emphasis on the (successful) thermonuclear (type Ia) models. A review concentrating on the recent progress of core-collapse supernovae is given by H.-Th. Janka in these Proceedings.

2 Core-collapse Supernovae

Supernovae of type II, i.e. explosions of stars which show strong Balmer lines of hydrogen in their spectra, and also type Ib and Ic events, are thought to originate from the collapse of massive stars, $M \gtrsim 8\ M_{\odot}$, at the end of their quiet hydrostatic nuclear burning, and the final outcome is believed to be the birth event of (most) neutron stars, and sometimes of black holes and γ-ray bursts. If this picture is correct the energy observed in the explosion ultimately must come from the binding energy of the newly born neutron star or black hole. However, although various mechanisms have been proposed which are potentially able to transform a small fraction of the gravitational energy into outward momentum of the stellar envelope, the cause of the explosion is still subject considerable discussions (see [8] for a recent review). Here we will concentrate on some micro-physics aspects of the problem and on "neutrino driven" explosions.

2.1 Basic Input Physics

In constructing a (core-collapse) supernova model one has to solve the hydrodynamic equations, some field equations describing gravity, rate equations for composition changes, and transport equations for particle numbers and energy for a given set of initial conditions (densities, entropies, velocities, composition variables, etc.) and material functions (equation of state, reaction rates, interaction cross-sections, etc.). It is obvious that this set of equations cannot be solved in full generality and that many approximations are necessary in order to make the problem tractable.

Concerning numerical methods for solving the hydro-equations great progress has been made during the last couple of years, provided Newtonian mechanics and gravity is a valid prescription [10]. However, in stellar collapse peak velocities approach several tenths of the velocity of light and general relativistic effects are not negligibly small, in particular at core bounce and during the early cooling and deleptonization phase of the newly born neutron star. The use of the Newtonian approximation, therefore, is questionable. For general relativistic hydrodynamics, on the other hand, the numerical techniques are much less advanced, in particular for multidimensional simulations which seem to be necessary [3, 4]. One has to keep this situation in mind when discussing uncertainties in and implications from micro-physics input data.

The Nuclear Equation of State

One of the most important ingredients is the equation of state (EOS) and, consequently, also a major fraction of the uncertainties result from our incomplete knowledge of it. Also, there is little hope that we can learn much about the EOS from laboratory experiments, such as heavy ion collisions,

because they test the nuclear EOS under rather different conditions. Therefore we have to rely on theoretical models or, possibly, on interpretations of astrophysical observations.

At rather low densities ($\varrho \lesssim 10^{-2}\varrho_0$; $\varrho_0 \sim 3 \times 10^{14}$ g cm^{-3}) the EOS can in principle be calculated from a Boltzmann-gas approximation for nucleons and nuclei, provided nuclear binding energies and partition functions are known. However, most nuclei present in the interior of a collapsing stellar core or in the outer layers of a neutron star would be very short-lived under laboratory conditions, and most of them have not even been synthesized yet by experiments. Therefore one has to rely on extrapolations from the properties of stable and "mildly" unstable nuclei.

At higher densities the Boltzmann-gas approach to the nuclear part of the EOS is no longer valid. This happens because the nuclear radius becomes comparable to the Coulomb interaction radius. Therefore, at those densities (above about 10^{12} g cm^{-3}) self-consistent models have to be used, and at even higher densities, $\varrho \gtrsim 0.1\varrho_0$, similar arguments show that also nucleon-nucleon interactions have to be included in such a self-consistent model. The most advanced method which has been applied to the supernova problem so far is the temperature dependent Hartree-Fock method but very little progress has been made in the past years.

Even more problematic is the EOS beyond nuclear saturation density. In the deep interior of a newly born neutron star "nuclei" dissolve into a homogeneous fluid of free neutrons and protons once the density exceeds ϱ_0. Consequently now nucleon-nucleon interactions in a dense Fermi fluid dominate the EOS. Phenomenologically determined nucleon-nucleon forces gradually lose reliability with increasing density and it is therefore not surprising that up to now the EOS at densities above, say, twice nuclear saturation density is still subject to considerable dispute, but it might be crucial for the neutrino luminosity during the first second past core-bounce, thought to trigger the ejection of the stellar envelope.

Most EOS in use in core-collapse simulations are simple, and include only part of the important physics. They are either phenomenologically motivated (e.g., [22]) or are based on mean field approaches (e.g., [21]).

Weak Interaction Rates

Next we want to mention briefly some of the uncertainties entering through our incomplete knowledge of weak interaction rates. It is well known that during most of core collapse and during the early cooling phase of newly born neutron stars typical weak interaction timescales are of the same order as the dynamic or evolution time scale of the stellar core or star, respectively. So in contrast to strong and electromagnetic interactions weak rates have to be known explicitly. Moreover, because in some cases neutrino energy distributions are not in equilibrium, it is not even sufficient to calculate energy-averaged rates. Fortunately, in this field considerable progress has

been made recently. The best rates available to date are based on shell model wave functions or use the quasiparticle random phase approximation, but from the sensitivity of those results to details of the nuclear model one may still conclude that the calculated rates are uncertain to within a factor of two on the average, and possibly by an order of magnitude in some particular cases [11, 12].

Other important week interaction processes include neutrino-absorption by free neutrons, neutrino-electron scattering, neutrino-nucleus coherent scattering and neutrino-neutron scattering. These cross sections and reaction rates can, in principle, be computed numerically exactly but in most numerical studies only approximate values are used.

Neutrino Transport

During collapse and after core-bounce we will always find regions in the star where neutrinos are either streaming freely or diffusing outward. So, in principle, we have to solve the Boltzmann transport equation. This transport equation, however, is a set of complicated partial integro-differential equations and, therefore, has only recently been used in core-collapse computations, but most models still use approximations to it.

Generally speaking, neutrino transport calculations for supernovae face two major problems. Firstly, at densities below 10^{12} g cm^{-3} neutrinos are not in thermal equilibrium and, secondly, the diffusion approximation to the Boltzmann equation breaks down at the neutrino-sphere, where the mean free path $\bar{\lambda}$ becomes comparable to the stellar radius. The second problem is usually circumvented by introducing a so-called flux-limiter which guarantees that for $\bar{\lambda} \gg \Delta r$ the free streaming limit is obtained. The first problem can only be solved by non-equilibrium transport models such as "two-fluid models", "multi-group flux-limited" diffusion, "variable Eddington-factor" methods, Monte-Carlo transport, or even direct integrations of the Boltzmann equation [2, 9, 13, 16].

2.2 Recent Models of Core-collapse Supernovae

Since most of the recent numerical simulations are reviewed by Janka in these Proceedings we will not go into details but rather summarize some of the main problems.

As far as numerical simulations of stellar collapse and the subsequent supernova explosion are concerned, the most crucial phase seems to be when the newly born neutron star looses its leptons and thermal energy by neutrinos of all flavors. During this phase, both the proto-neutron star itself and the matter behind the stalled shock in the mantle are found to be unstable to entropy and/or lepton number driven buoyancy instabilities which can increase the neutrino luminosity considerably. It is commonly believed that

this increase in luminosity is required in order to revive the stalled shock by neutrino heating [8].

Although none of the recent simulations give the desired results, namely an envelope ejection with a typical energy of about 10^{51}erg, leaving behind a neutron of about 1.4 $M_\odot$, "hope is left in Pandora's box". In fact, the simulations are close to explosions, and minor changes in the input physics and/or the numerical treatment might change the outcome. An obvious example is the neutrino luminosity of the newly-born neutron star which seems to be a bit too low for success, but can be changed during the contraction and cooling phase by different EOS's or neutrino-transport properties of hot and dense nuclear matter. A second example are hydrodynamic instabilities of the neutrino-heated convectively unstable matter behind the stalled shock which, again, can change the energy (and momentum) transport. Finally, general relativistic effects have not yet been studied in great detail in models based on realistic micro-physics input [2, 10].

3 Thermonuclear Supernovae

A strong motivation for studying thermonuclear (type Ia) supernovae comes from their use for cosmology because at present they are the most accurate cosmological distance indicators and supernovae at different redshifts are the only way to determine the nature of the suspected "dark energy" that causes the Universe to accelerate its expansion.

The most popular progenitor model for the average type Ia supernova is a massive white dwarf, consisting of carbon and oxygen, which approaches the Chandrasekhar mass ($M_{Ch} \simeq 1.4\,M_\odot$) by a yet unknown mechanism, presumably accretion from a companion star, and is disrupted by a thermonuclear explosion (see [7] for a recent review). At high densities explosive carbon burning mostly leads to radioactive ^{56}Ni. At lower densities intermediate-mass nuclei, like ^{28}Si, are produced. These elements give rise to the typical observed spectra of SNe Ia, which are dominated by lines of Fe, Si and S.

The general picture of such an explosion is that first carbon burns rather quietly in the core of the contracting white dwarf. Because this core is convectively unstable temperature fluctuations will be present and they may locally reach run-away values. After ignition, the flame is thought to propagate through the star as a sub-sonic turbulent deflagration wave which may or may not change into a detonation at low densities (around 10^7 g cm^{-3}), disrupting the star in the end in both cases.

3.1 The Physics of Turbulent Thermonuclear Combustion

Due to the strong temperature dependence of the carbon-fusion reaction rates nuclear burning during the explosion is confined to microscopically thin layers that propagate either conductively as subsonic deflagrations ("flames")

or by shock compression as supersonic detonations. Both modes are hydrodynamically unstable to spatial perturbations. The best studied and probably most important hydrodynamical effect for modeling SN Ia explosions is the Rayleigh-Taylor (RT) instability resulting from the buoyancy of hot, burned fluid with respect to the dense, unburned material [14]. Subject to the RT instability, small surface perturbations grow until they form bubbles (or "mushrooms") that begin to float upward while spikes of dense fluid fall down. In the nonlinear regime, bubbles of various sizes interact and create a foamy RT mixing layer whose vertical extent grows with time. Secondary instabilities related to the velocity shear along the bubble surfaces [14] quickly lead to the production of turbulent velocity fluctuations that cascade from the size of the largest bubbles ($\approx 10^7$ cm) down to the microscopic Kolmogorov scale, $l_{\rm k} \approx 10^{-4}$ cm, where they are dissipated. Since no computer is capable of resolving this range of scales, one has to resort to statistical or scaling approximations of those length scales that are not properly resolved. The most prominent scaling relation in turbulence research is Kolmogorov's law for the cascade of velocity fluctuations, stating that in the case of isotropy and statistical stationarity, the mean velocity v of turbulent eddies with size l scales as $v \sim l^{1/3}$.

Given the velocity of large eddies, e.g. from computer simulations, one can use this relation to extrapolate the eddy velocity distribution down to smaller scales under the assumption of isotropic, fully developed turbulence. Turbulence wrinkles and deforms the flame. These wrinkles increase the flame surface area and therefore the total energy generation rate of the turbulent front. In other words, the turbulent flame speed, defined as the mean overall propagation velocity of the turbulent flame front, becomes larger than the laminar speed. If the turbulence is sufficiently strong the turbulent flame speed becomes independent of the laminar speed, and therefore of the microphysics of burning and diffusion, and scales only with the velocity of the largest turbulent eddy [1].

As the density of the white dwarf material declines and the laminar flamelets become slower and thicker, it is plausible that at some point turbulence significantly alters the thermal flame structure [15]. So far, modeling this so-called distributed burning regime in exploding white dwarfs has not been attempted explicitely since neither nuclear burning and diffusion nor turbulent mixing can be properly described by simplified prescriptions. However, it is this regime where the transition from deflagration to detonation is assumed to happen in certain phenomenological models.

3.2 A Numerical Model for Turbulent Combustion

It is straight forward to convert the ideas presented in the previous section into a numerical scheme. The basic ingredients are a finite-volume method to solve the fluid-dynamics equation, a front-tracking algorithm which allows us to propagate the thermonuclear flame (assumed to be in the flamelet regime),

and a model to determine the turbulent velocity fluctuations on unresolved sub-grid scales. Since the details of the method have been published elsewhere [17, 18, 19] we only repeat the basic ideas here.

The central aspect of our code is a front tracking method based on a level set function G which is determined in such a way that the zero level set of G behaves exactly as the flame. This can be obtained from the consideration that the total velocity of the front consists of two independent contributions: it is advected by the fluid motions at a speed $\boldsymbol{v}$ and it propagates normal to itself with a burning speed s.

This front tracking algorithm is implemented as an additional module for the hydrodynamics code PROMETHEUS [5]. In all simulations presented here a simple implementation was used which, however, describes the basic physics quite well [17, 18]. It assumes that the G-function is advected by the fluid motions and by burning and is only used to determine the source terms for the reactive Euler equations. Nuclear burning can now be computed provided the normal velocity of the burning front is known everywhere and at all times. In computations discussed in the following it is determined according to a flame-brush model of [14].

3.3 Some Results of Supernova Simulations

We have carried out numerical simulations in 2D and 3D, for a variety of different initial conditions, and for different numerical resolution. In most of our simulations the white dwarf, constructed in hydrostatic equilibrium for a realistic equation of state, has a central density of 2.9×10^9 g cm^{-3}, a radius of 1.5×10^8 cm, and a mass of 2.8×10^{33} g, identical to the one used in [14]. The initial mass fractions of C and O are chosen to be equal, and the total binding energy is 5.4×10^{50} erg. At low densities ($\rho \leq 10^7$ g cm^{-3}), the burning velocity of the front is set equal to zero because the flame enters the distributed regime and our physical model is no longer valid. However, since in reality some matter may still burn the energy release obtained in the simulations is probably somewhat too low. An extended parameter study, varying the chemical composition as well as the ignition density, is presently under way and will be published elsewhere.

A first and important result is that we do find numerically converged solutions. Although an increase in spatial resolution gives more structured burning fronts with larger surface area, the corresponding increase of fuel consumption is compensated by the lower values of the turbulent velocity fluctuations on smaller length scales. So the net effect is that, for identical initial conditions, the explosion energies are independent of the numerical resolution, demonstrating that the level-set prescription allows one to resolve the structure of the burning front down almost to the grid scale, thus avoiding artificial smearing of the front, which is an inherent problem of front-capturing schemes.

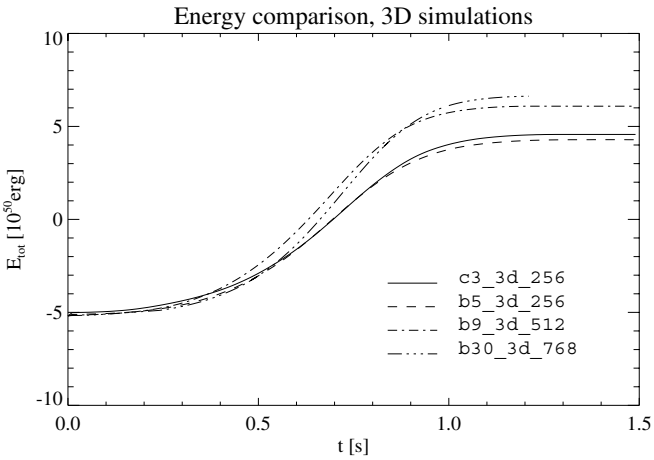

Fig. 1. Energy evolution of several three-dimensional (3d) explosion models (dashed and dashed-dotted). For comparison we also show a centrally ignited ("three fingers") model of [18] (solid line). The other labels give the number of initial "bubbles" (bn) and the number of grid points per dimension (ijk).

In our approach, the initial white dwarf model (composition, central density, and velocity structure), as well as assumptions about the location, size and shape of the flame surface as it first forms, fully determine the simulation results. A plausible ignition scenario suggested by [6] is the simultaneous runaway at several different spots in the central region of the progenitor star. Therefore, in the following we will concentrate on such initial conditions. Fig. 1 shows the energy generated for a series of models including, for comparison, one centrally ignited model (3c_3d_256).

During the first 0.5 seconds, all models are nearly indistinguishable as far as the total energy is concerned, which at first glance appears somewhat surprising, given the quite different initial conditions. A closer look at the energy generation rate actually reveals noticeable differences in the intensity of thermonuclear burning for the simulations, but since the total flame surface is initially very small, these differences have no visible impact on the integrated curve in the early stages.

However, after about 0.5 seconds, when fast energy generation sets in, the models with more ignition spots burn more vigorously due to their larger surface and therefore they reach higher final energy levels. Fig. 1 also shows that the centrally ignited model (c3_3d_256) is almost identical to the off-center model b5_3d_256 with regard to the explosion energetics. But, obviously, the scatter in the final energies due to different initial conditions appears to be small. Moreover, all models explode with an explosion energy in the range of what is observed.

Table 1. Overview over element production and energy release of typical supernova simulations

model	$m_{\text{“Mg”}}$ $[M_\odot]$	$m_{\text{“Ni”}}$ $[M_\odot]$	E_{nuc} $[10^{50}\,\text{erg}]$
c3_3d_256	0.177	0.526	9.76
b5_3d_256	0.180	0.506	9.47
b9_3d_512	0.190	0.616	11.26

3.4 Predictions for Observable Quantities

In this section we present a few results for various quantities which can, in principle, be observed and which therefore can serve as tests for the models.

The most direct test of explosion models is provided by observed light curves and spectra. According to “Arnett’s Law” light curves measure mostly the amount and spatial distribution of radioactive ^{56}Ni in type Ia supernovae, and spectra measure the chemical composition in real and velocity space.

In [20] the results of one of our centrally ignited 3D-models have been used, averaged over spherical shells, to compute color light curves in the UBVI-bands. Their code assumes LTE radiation transport and loses reliability at later times (about 4 weeks past maximum) when the supernova enters the nebular phase. Also, this assumption and the fact that the opacity is not well determined at longer wavelength make I-light curves less accurate. Keeping this in mind, they produce the light curves of typical SNe Ia very well. The main reason for the good agreement between the model and, e.g., SN 1994D is the presence of high-velocity radioactive Ni in outer layers of the supernova model which is not be predicted by spherical models.

A summary of the gross abundances obtained for some of our 3D models is given in Table 1. Here “Mg” stands for intermediate-mass nuclei, and “Ni” for the iron-group. In addition, the total energy liberated by nuclear burning is given. Since the binding energy of the white dwarf was about 5×10^{50} erg, all models do explode. Typically one expects that around 80% of iron-group nuclei are originally present as ^{56}Ni bringing our results well into the range of observed Ni-masses. This success of the models was obtained without introducing any non-physical parameters, but just on the basis of a physical and numerical model of subsonic turbulent combustion. We also stress that our models give clear evidence that the often postulated deflagration-detonation transition is not needed to produce sufficiently powerful explosions.

Finally, we have “post-processed” several of our models in order to see whether or not also reasonable isotopic abundances are obtained. The results, shown in Fig. 2, are preliminary and should be considered with care. However, it is obvious that, with a few exceptions, also isotopic abundances are within the expected range. Exceptions include the high abundance of (unburned) C and O, and the overproduction of ^{48,50}Ti, ^{54}Fe, and ^{58}Ni. We think that this reflects a deficiency of some of our models which burn to little C and O at

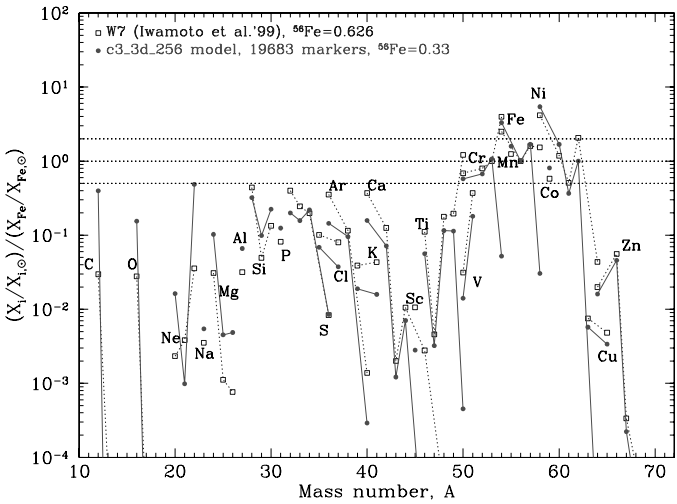

Fig. 2. Isotopic abundances obtained for the centrally ignited 3D model 3c_3d_256 in comparison to W7 predictions (Travaglio et al., in preparation).

densities too high and temperatures too low, and which also, because of the low ^{56}Ni, would not give a good light curve.

4 Summary and Conclusions

The physics of supernovae as well as the present status of numerical simulations of the explosion process have been discussed. It was demonstrated that multi-dimensional models are needed for both types and that, to a certain extent, they have been carried out in 2D with moderately good physics input for core-collapse supernovae, and in 3D with just sufficient numerical resolution for thermonuclear ones. The bad news is that these calculations have not solved the core-collapse supernova problem yet, and the limiting factor does not seem to be the numerical resolution of the simulations but rather still existing uncertainties in the (micro-) physics. This is in contrast to thermonuclear explosion models where the physics is reasonably well under control, but the numerical resolution is barely sufficient.

In case of core collapse supernovae it is likely that with the next generation of supercomputers one will be able to carry out fully resolved simulations in 3D, but most of the work has to go into improving the micro-physics and the neutrino transport. In contrast, for thermonuclear explosions one will never be able to resolve all relevant scales numerically and, therefore, developing new and clever tools to overcome this difficulty is a must. However, even the recent (admittedly still limited) type Ia models do predict explosion energies,

light curves, spectra, and nuclear abundances that are well within the range of their observed counterparts.

References

1. P. Clavin: Ann. Rev. Fluid Mech. **26**, 321 (1994)
2. R. Buras et al. : Phys. Rev. Lett. **90**, 1101 (2003)
3. H. Dimmelmeier, J.A. Font, E. Müller: Astron. Astrophys. **388**, 917 (2003)
4. H. Dimmelmeier, J.A. Font, E. Müller: Astron. Astrophys. **393**, 523 (2003)
5. B.A. Fryxell, E. Müller, W.D. Arnett: MPA Preprint **449** (1989)
6. D. Garcia-Senz, S.E. Woosley: Astrophys. J. **454**, 895 (1995)
7. W. Hillebrandt, J.C. Niemeyer: Ann. Rev. Astron. Astrophys. **38**, 191 (2000)
8. H.-Th. Janka et al. : Core Collapse and Then? The Route to Massive Star Explosions. In: *From Twilight to Highlight: The Physics of Supernovae*, ed by W. Hillebrandt, B. Leibundgut (Springer, Berlin Heidelberg New York 2003) p. 39
9. M.Th. Keil, G.G. Raffelt, H.-Th. Janka: Astrophys. J. **590**, 971 (2003)
10. K. Kifonidis et al. : Astron. Astrophys. **408**, 621 (2003)
11. K. Langanke, G. Martinez-Pinedo: Rev. Mod. Phys. **75**, 819 (2003)
12. K. Langanke et al. : Phys. Rev. Lett. **90**, 1102 (2003)
13. M. Liebendörfer et al. : Nuc. Phys. **A719**, 144 (2003)
14. J.C. Niemeyer, W. Hillebrandt: Astrophys. J. **452**, 769 (1995)
15. J.C. Niemeyer, S.E. Woosley: Astrophys. J. **475**, 740 (1997)
16. M. Rampp, H.-Th. Janka: Astron. Astrophys. **396**, 361 (2002)
17. M. Reinecke, W. Hillebrandt, J.C. Niemeyer: Astron. Astrophys. **347**, 739 (1999)
18. M. Reinecke, W. Hillebrandt, J.C. Niemeyer: Astron. Astrophys. **386**, 936 (2002)
19. M. Reinecke, W. Hillebrandt, J.C. Niemeyer: Astron. Astrophys. **391**, 1167 (2002)
20. E. Sorokina, S. Blinnikov: Light Curves of Type Ia Supernovae as a Probe for an Explosion Model. In: *From Twilight to Highlight: The Physics of Supernovae*, ed by W. Hillebrandt, B. Leibundgut (Springer, Berlin Heidelberg New York 2003) p. 268
21. K. Sumiyoshi, H. Toki: Astrophys. J. **422**, 700 1994
22. F.D. Swesty, J.M. Lattimer, E.S. Myra: Astrophys. J. **425**, 195 (1994)

Core-Collapse Supernovae at the Threshold

H.-Th. Janka, R. Buras, K. Kifonidis, A. Marek, and M. Rampp

Max-Planck-Institut für Astrophysik, Postfach 1317, 85741 Garching, Germany;
thj@mpa-garching.mpg.de

Summary. Recent progress in modeling core-collapse supernovae is summarized and set in perspective. Two-dimensional simulations with state-of-the-art treatment of neutrino transport still fail to produce powerful explosions, but evidence is presented that they are very close to a success.

1 Aiming High

Despite of still bothering uncertainties and ongoing controversy, the convectively supported neutrino-heating mechanism [10] must be considered as a promising way to explain supernova explosions of massive stars. Neutrinos drive the evolution of the collapsing stellar core and of the forming neutron star and dominate the event energetically by carrying away about 99% of the gravitational binding energy of the compact remnant. A detailed description of their processes in models which couple (relativistic) hydrodynamics and accurate neutrino transport is therefore indispensable for making progress towards an understanding of the remnant-progenitor connection, supernova energetics, explosion asymmetries, pulsar kicks, nucleosynthesis, and observable neutrino and gravitational-wave signals. It is a necessary ingredient in any calculation which claims a higher degree of realism.

2 Stepping Forward

Successful simulations of neutrino-driven supernova explosions have so far either employed special, usually controversial, assumptions about the physics at neutron star conditions or have made use of crude approximations in the neutrino transport. They are contrasted by simulations with widely accepted microphysics and an increasing sophistication of the transport treatment, which have not been able to produce explosions.

It must be stressed, however, that these simulations do not conflict with each other. They were performed with largely different numerical descriptions and the discrepant results simply demonstrate the sensitivity of the delayed explosion mechanism to variations at the level of the different approaches.

2.1 Successful Explosions on the One Hand

Wilson and collaborators [27, 28, 29] found explosions in one-dimensional simulations by assuming that neutron finger convection below the neutrino sphere boosts the neutrino emission from the nascent neutron star and thus increases the neutrino heating behind the stalled supernova shock. Neutron finger convection, however, requires a faster exchange of energy than lepton number between fluid elements, an assumption that could not be confirmed by detailed analysis of the multi-flavor neutrino transport [3]. Another ingredient to the energetic explosions of Wilson's group is a nuclear equation of state (EoS) which yields high neutron star temperatures and ν_e luminosities because of the formation of a pion condensate at rather low densities [19]. The adopted dispersion relation of the pions in dense matter, however, is not supported by accepted nuclear physics.

In the early 1990's it was recognized that violent convective overturn between the neutrino sphere and the supernova shock is helpful for the neutrino-heating mechanism and a possible origin of the anisotropies and large-scale mixing observed in SN 1987A [10]. Two-dimensional hydrodynamic models [5, 6, 7, 11] and, more recently, 3D simulations [8] that take this effect into account produced explosions, but used grey (i.e., spectrally averaged), flux-limited diffusion for describing the neutrino transport, an approximation which fell much behind the elaborate multi-group diffusion that had been applied by Bruenn in spherical symmetry [1].

2.2 Failures on the Other Hand

Bruenn, using standard microphysics and a sophisticated multi-group flux-limited diffusion treatment of neutrino transport, could never confirm explosions in one-dimensional simulations [2]. But there was hope that an even better description of the transport might bring success.

A new level of accuracy has indeed been reached with the use of solvers for the Boltzmann transport equation. Employing different numerical techniques, they were only recently applied in time-dependent hydrodynamic simulations of spherical stellar core collapse with Newtonian gravity [21, 22, 26], approximate treatment of relativistic effects [23], and general relativity [17]. These simulations, all performed with the EoS of Lattimer and Swesty [16], agree that neither prompt explosions by the hydrodynamic bounce-shock mechanism, nor delayed, neutrino-driven explosions could be obtained without the help of convection, not even with the best available treatment of the neutrino physics and general relativity.

Mezzacappa et al. [20] also expressed concerns that the success of multi-dimensional calculations [5, 6, 7, 8, 11] might disappear once the neutrino transport is improved to the sophistication reached in 1D models. They demonstrated this by mapping transport results from 1D supernova models

to 2D hydrodynamics. The lacking self-consistency of this approach, however, was an obvious weakness of the argument.

3 Pushing the Limits

In this situation the core-collapse group at Garching has advanced to the next level of improvements in supernova modeling. To this end we have generalized our 1D neutrino-hydrodynamics code (VERTEX [23]) for performing multi-dimensional supernova simulations with a state-of-the-art treatment of neutrino transport and neutrino-matter interactions, calling the extended code version MuDBaTH [14].

3.1 A New Tool

The hydrodynamics part of the program is based on the PROMETHEUS code, which is an Eulerian finite-volume method for second-order, time-explicit integration of the hydrodynamics equations. It employs a Riemann solver for high-resolution shock capturing, a consistent multi-fluid advection scheme, and general relativistic corrections to the gravitational potential. "Odd-even decoupling" at strong shocks is avoided by an HLLE solver. More details about technical aspects and corresponding references can be found in Refs. [14, 23].

The hydro routine is linked to a code which solves the multi-frequency transport problem for neutrinos and antineutrinos of all flavors by closing the set of moment equations for particle number, energy and momentum with a variable Eddington factor that is computed from a model Boltzmann equation. The transport is done in a time-implicit way and takes into account moving medium effects and general relativistic redshift and time dilation. Transport and hydro components are joined by operator-splitting. The multi-dimensional version of the code assumes that the neutrino flux is radial and the neutrino pressure tensor can be taken as diagonal, thus ignoring effects due to neutrino viscosity. While the variable Eddington factor is determined as an average value at all radii by solving the transport equations on an angularly averaged stellar background, the multi-dimensionality of the problem is retained on the level of the moment equations, which are radially integrated within every angular zone of the spherical coordinate grid. In addition, lateral gradients that correspond to neutrino pressure and advection of neutrinos with the moving stellar fluid are included in the moment equations ("ray-by-ray plus"). Note that neutrino pressure cannot be ignored in the protoneutron star interior and advective transport of neutrinos is faster than diffusion below the neutrino sphere.

Electron neutrinos and antineutrinos are produced by e^- captures on nuclei and protons and e^+ captures on neutrons, respectively. Nucleon-nucleon bremsstrahlung and e^+e^- annihilation are considered for the creation of $\nu\bar{\nu}$

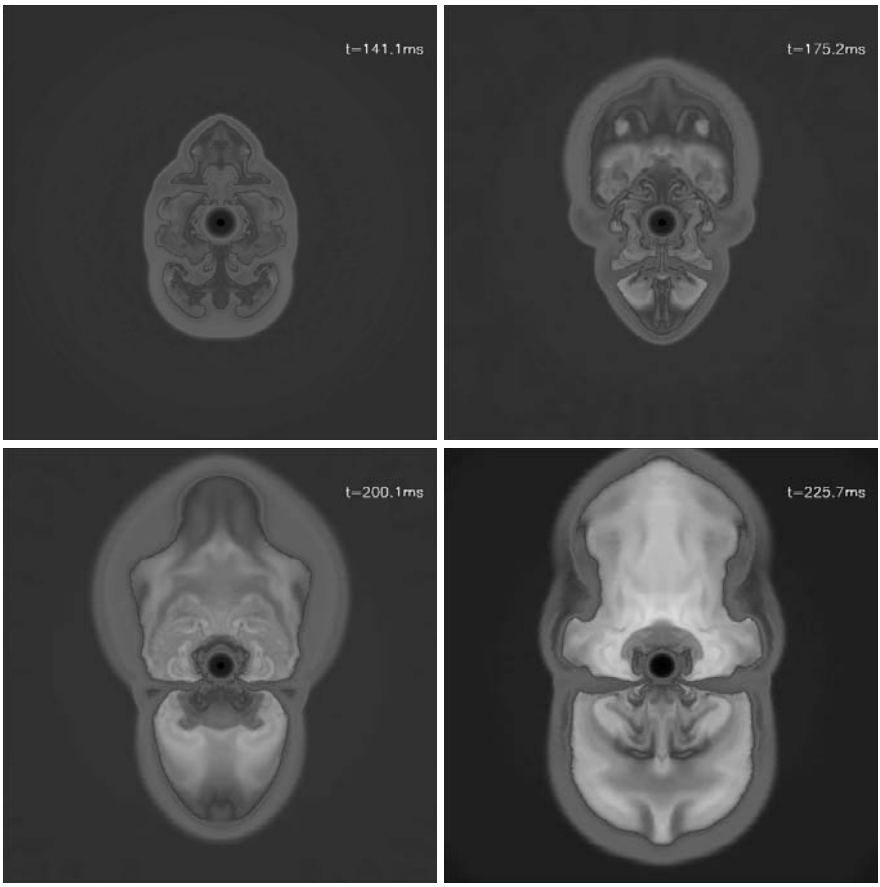

Fig. 1. Sequence of snapshots showing the large-scale convective overturn in the neutrino-heated post shock layer at four post-bounce times ($t_{\rm pb}$ = 141.1 ms, 175.2 ms, 200.1 ms, and 225.7 ms, from top left to bottom right) during the evolution of a (non-rotating) 11.2 $M_\odot$ progenitor model from Woosley et al. [30]. The entropy is grey scale coded. The dense neutron star is visible as low-entropy circle at the center. The convective layer interior of the neutrino sphere cannot be visualized with the employed color scale because the entropy contrast there is small. Convection in this region is driven by a negative gradient of the lepton number. The computation was performed with spherical coordinates, assuming axial symmetry, and employing the "ray-by-ray plus" variable Eddington factor technique developed by Rampp & Janka [23] and Buras et al. [4] for treating neutrino transport in multi-dimensional supernova simulations. Equatorial symmetry is broken on large scales soon after bounce, and low-mode convection begins to dominate the flow between the neutron star and the strongly deformed supernova shock. The "face" on the top right does not need to look so sad, because the model continues to develop a weak explosion. The scale of the plots is 1200 km in both directions.

pairs of all flavors. Muon and tau neutrino-antineutrino pairs are also made by $\nu_e\bar{\nu}_e$ annihilation. Neutrino scattering off n, p, $e^{\pm}$, and nuclei is included, for muon and tau neutrinos also off ν_e and $\bar{\nu}_e$. The charged-current reactions of neutrinos with nucleons take into account nucleon thermal motions, recoil and phase-space blocking, weak magnetism corrections, the reduction of the effective nucleon mass and the quenching of the axial-vector coupling in nuclear matter, and nucleon correlations at high densities.

Recently, the treatment of electron captures on heavy nuclei has been improved in collaboration with K. Langanke and coworkers [15]. Details were reported at this meeting by G. Martínez-Pinedo. Previously these reactions were described rather schematically [1] and were switched off above a few $10^{10}\,\mathrm{g\,cm^{-3}}$. Therefore e^- captures on p determined the subsequent evolution. In the new models, in contrast, nuclei dominate the ν_e production by far. This leads to a significant shrinking of the homologously collapsing inner core and shock formation at a smaller mass coordinate [15]. Despite of this conceptually and quantitatively important change the subsequent shock propagation and expansion remains astonishingly similar because of differential changes of the core structure and cancelations of effects [13].

3.2 A New Generation of Multi-dimensional Models

Running simulations for progenitors with different main sequence masses (Woosley et al.'s 11.2, 15, and $20\,\mathrm{M}_\odot$ models [30]) in 1D and 2D, we could confirm the finding of previous multi-dimensional models with simpler neutrino transport, namely that two spatially separated regions exist in the supernova core where convection sets in on a timescale of some ten milliseconds after bounce [4].

The one region is characterized by a negative entropy gradient which is left behind by the weakening shock and enhanced by the onset of neutrino heating between gain radius and shock. Despite of a positive gradient of the electron fraction, this region is Ledoux unstable and Rayleigh-Taylor mushrooms start to grow between 40 ms and 80 ms post bounce (slower for higher-mass progenitors). The violent convective overturn that develops in this region supports the shock expansion and allows for larger shock radii. Two effects seem to be mainly responsible for this helpful influence on the neutrino-heating mechanism. On the one hand bubbles of neutrino-heated matter can rise, which pushes the shock farther out and reduces the energy loss by the re-emission of neutrinos. On the other hand, cold, lower-entropy matter is carried by narrow down flows from the shock to near the gain radius, where it is heated by neutrinos at very high rates. This enhances the efficiency of neutrino energy transfer. Fully developed, the convective overturn can become so violent that down flows penetrate with supersonic velocities through the electron neutrino sphere, thereby increasing the luminosity of ν_e and $\bar{\nu}_e$.

The second region of convective activity lies beneath the neutrino sphere. Convection there is driven by a negative lepton gradient and sets in between

about 20 ms post bounce and about 60 ms post bounce (again later for the more massive progenitors). Despite of the transport of energy and lepton number and the corresponding change of the outer layers of the protoneutron star, the effect on the luminosities of ν_e and $\bar{\nu}_e$ is rather small. The neutrino sphere of heavy-lepton neutrinos, however, is located within the convective layer and an enhancement of muon- and tau neutrino luminosities (10–20%) is visible at times somewhat later than 100 ms. The influence on the shock propagation and the explosion mechanism is marginal and mostly indirect by modifying the neutron star structure and ν_μ and ν_τ emission.

Although convective overturn behind the shock strongly affects the post-bounce evolution, we were disappointed by not obtaining explosions in a recently published first set of simulations [4]. These results seem to confirm the suspicion [20] that a more accurate treatment of neutrino transport might not allow one to reproduce the convectively supported neutrino-driven explosions seen previously.

3.3 Ultimate Success?

But there is light at the end of the long tunnel and the situation is more favorable than it looks at first glance. There are reasons to believe that our models are very close to explosions, in fact graze the threshold of conditions which are required to drive mass ejection by the outward acceleration of the supernova shock.

One of our models (a $15\,M_\odot$ star) included rotation at a rate that is consistent with pre-collapse core rotation of magnetized stars [9]. The assumed initial angular velocity was chosen to be slightly faster ($\Omega = 0.5\,\mathrm{rad\,s^{-1}}$) than predicted by Heger et al. [9]. It would lead to a neutron star spinning with a period of 1–2 ms if the angular momentum in the protoneutron star is conserved after the end of our simulations. We intentionally did not consider more extreme rotation rates which are expected for collapsars and needed for gamma-ray burst models, but which are probably not generic for supernovae.

Rotation makes a big difference! Centrifugal forces reduce the infall velocity near the equatorial plane and help to support the shock at a larger radius. Enhanced by rotationally induced vortex motion extremely violent convective overturn develops behind the shock. Powerful non-radial oscillations are initiated and drive the shock temporarily to distances near 300 km along the rotation axis where the more rapidly decreasing density favors strong shock expansion.

Huge global deformation was also observed in case of the (non-rotating) $11.2\,M_\odot$ star when we increased the angular grid from a $\sim 90^\mathrm{o}$ wedge ($\pm 46.8^\mathrm{o}$ around the equatorial plane of the coordinate grid with periodic boundary conditions) to full 180^o. The $11.2\,M_\odot$ model is characterized by a small iron core ($\sim 1.25\,M_\odot$) and an abrupt entropy jump at the edge of the Si shell (at $\sim 1.3\,M_\odot$). A strong dipolar expansion occurs and the shock is slowly pushed outward by the pulsational expansion of two huge bubbles which are

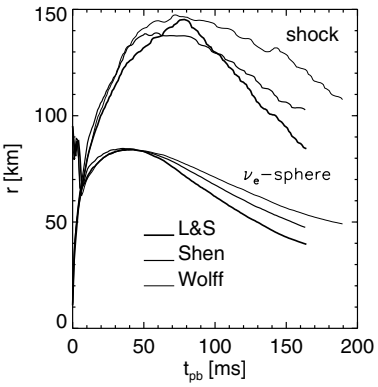

Fig. 2. Shock radii and electron neutrino spheres for simulations of a 15 $M_\odot$ star in spherical symmetry with three different nuclear EoSs [18], namely those of Lattimer and Swesty ([16]; bold lines), which is the widely used standard for supernova simulations these days, Shen et al. ([24, 25]; medium lines), and Wolff and Hillebrandt ([12]; thin lines). Times are synchronized at the moment of core bounce.

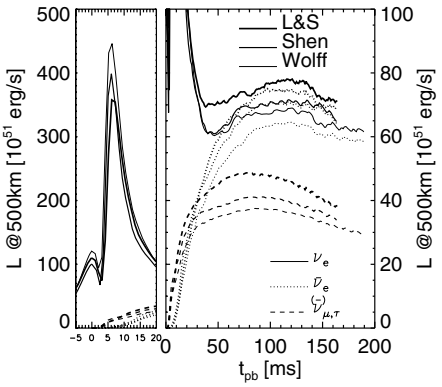

Fig. 3. Luminosities for ν_e, $\bar{\nu}_e$, and heavy-lepton neutrinos (ν_μ, ν_τ, $\bar{\nu}_\mu$ or $\bar{\nu}_\tau$ individually), measured by an observer comoving with the infalling stellar plasma at a radius of 500 km, for the three spherically symmetric simulations shown in Fig. 2 [18]. The left panel displays a time interval around the prompt ν_e burst, the right panel a longer period of the post-bounce evolution. Note the different scales on the vertical axes of both frames.

alternately fed by neutrino heated matter that comes from a single (due to the assumed symmetry, toroidal), waving down flow near the equatorial plane of the coordinate grid (Fig. 1). The shock has reached a maximum radius of more than 600 km with no sign of return until we had to stop the simulation 226 ms after bounce.

We consider it as very likely that a weak explosion develops in this model. It is exciting to imagine how the evolution might have proceeded with the

additional help from rotation. Patience, however, is necessary when results for longer post-bounce periods or other progenitors are desired. The computations require far more than 10^{17} floating point operations and take several months on machines available to us.

We actually have hints of how an explosion can emerge in a $15\,M_\odot$ star which was computed with omitted velocity-dependent terms in the neutrino momentum equation. The resulting 20–30% change of the neutrino density between neutrino sphere and shock was sufficient to initiate an explosion, thus demonstrating that not much was missing for the convectively supported neutrino-heating mechanism to work. The explosion had an energy of about 6×10^{50} erg and left behind a neutron star with an initial baryonic mass of $\sim 1.4\,M_\odot$. The neutrino-heated ejecta did not show the dramatic overproduction of $N = 50$ closed neutron shell nuclei which signaled a problem with the neutrino transport approximations used in previous models.

These results suggest that we are on the right track. Once the critical threshold for explosions can be overcome, the subsequent evolution seems to proceed very favorably with respect to observable facts.

4 Longing for More

What can provide or support the ultimate kick beyond the explosion threshold? Is it three-dimensional effects? Very fast rotation? Truly multi-dimensional transport that accounts for lateral neutrino flow and neutrino shear? Full general relativity instead of approximations? Or yet to be improved microphysics, e.g. reactions of neutrinos with nuclei? Or the uncertain high-density equation of state which has not been extensively varied up to now but can cause sizable differences (Figs. 2 and 3)? Or so far ignored or unresolved modes of instability that could boost the neutrino luminosity or drive accretion shock instability? Or magnetohydrodynamic effects? Or is it the combination of all?

Much work still needs to be done for completing the supernova codes and testing these possibilities. A number of groups around the world have set out to meet this challenge!

Acknowledgement. Support by the Sonderforschungsbereich SFB-375 "Astro-Teil--chenphysik" of the Deutsche Forschungsgemeinschaft is acknowledged. The simulations were done on the IBM "Regatta" supercomputer of the Rechenzentrum Garching.

References

1. S.W. Bruenn: Astrophys. J. Suppl. **58**, 771 (1985)

2. S.W. Bruenn: "Numerical simulations of core collapse supernovae." In: *Nuclear Physics in the Universe*, ed. M.W. Guidry, M.R. Strayer (IOP: Bristol, 1993) pp. 31-50
3. S.W. Bruenn, T. Dineva: Astrophys. J. Lett. **458**, L71 (1996)
4. R. Buras, M. Rampp, H.-Th. Janka, K. Kifonidis: Phys. Rev. Lett. **90**, 241101 (2003)
5. A. Burrows, J. Hayes, B.A. Fryxell: Astrophys. J. **450**, 830 (1995)
6. C.L. Fryer: Astrophys. J. **522**, 413 (1999)
7. C.L. Fryer, A. Heger: Astrophys. J. **541**, 1033 (2000)
8. C.L. Fryer, M.S. Warren: Astrophys. J. Lett. **574**, L65 (2002)
9. A. Heger, S.E. Woosley, N. Langer, H. Spruit: astro-ph 0301374 (2003)
10. M. Herant, W. Benz, S.A. Colgate: Astrophys. J. **395**, 642 (1992)
11. M. Herant et al. : Astrophys. J. **435**, 339 (1994)
12. W. Hillebrandt, R.G. Wolff: "Models of type II supernova explosions." In: *Nucleosynthesis: Challenges and New Developments*, eds. D. Arnett, J.W. Truran (Univ. of Chicago Press: Chicago, 1985) pp. 131-150
13. W.R. Hix et al. : Phys. Rev. Lett. **91**, 201102 (2003)
14. H.-Th. Janka et al. :astro-ph 0212314 (2002)
15. K. Langanke et al. : Phys. Rev. Lett. **90**, 241102 (2003)
16. J.M. Lattimer, F.D. Swesty: Nuc. Phys. **535**, 331 (1991)
17. M. Liebendörfer et al. : Phys. Rev. D **63**, 3004 (2001)
18. A. Marek: In: *The effects of the nuclear equation of state on stellar core collapse and supernova evolution.* Diploma Thesis, Technical University Munich (2003)
19. R.W. Mayle, M. Tavani, J.R. Wilson: Astrophys. J. **418**, 398 (1993)
20. A. Mezzacappa et al. : Astrophys. J. **495**, 911 (1998)
21. A. Mezzacappa et al. : Phys. Rev. Lett. **86**, 1935 (2001)
22. M. Rampp, H.-Th. Janka: Astrophys. J. Lett. **539**, L33 (2000)
23. M. Rampp, H.-Th. Janka: Astron. Astrophys. **396**, 361 (2002)
24. H. Shen, H. Toki, K. Oyamatsu, K. Sumiyoshi: Nuc. Phys. **637**, 435 (1998)
25. H. Shen, H. Toki, K. Oyamatsu, K. Sumiyoshi: Prog. Theor. Phys. **100**, 1013 (1998)
26. T.A. Thompson, A. Burrows, P.A. Pinto: Astrophys. J. **592**, 434 (2003)
27. T. Totani, K. Sato, H.E. Dalhed, J.R. Wilson: Astrophys. J. **496**, 216 (1998)
28. J.R. Wilson, R. Mayle: Phys. Rep. **163**, 63 (1988)
29. J.R. Wilson, R. Mayle: Phys. Rep. **227**, 97 (1993)
30. S.E. Woosley, A. Heger, T.A. Weaver: Rev. Mod. Phys. **74**, 1015 (2002)

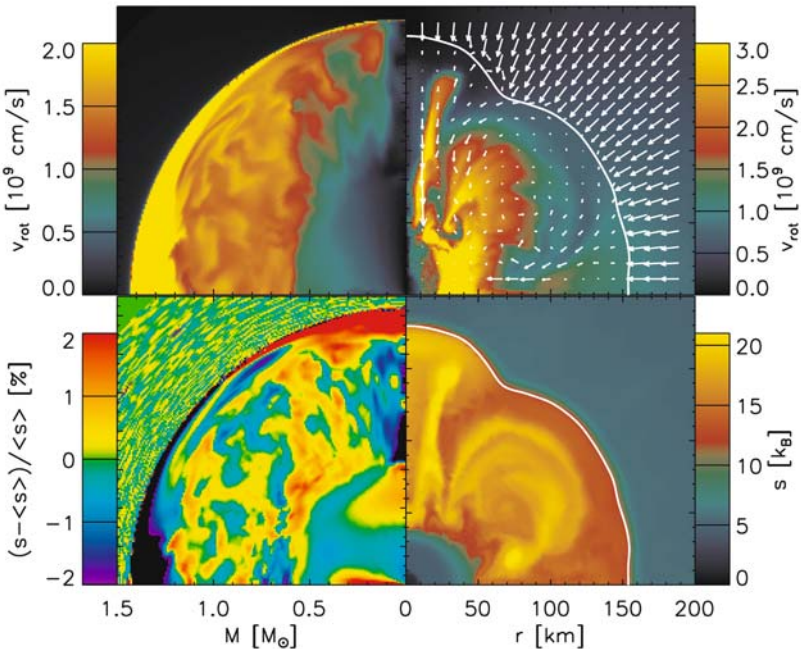

Structure of the collapsing core of a rotating 15 $M_\odot$ star at about 200 ms after bounce. The left two panels show rotational velocity (top) and entropy fluctuations versus enclosed mass, and and zoom in mainly on conditions inside the nascent neutron star. The right panels give rotational velocity (top; the white arrows indicate the velocity component in a meridional plane) and entropy of the supernova shock. The latter is marked with a white line.
(From Buras et al. PRL 90 (2003) 241101)

Plate (Janka et al.)

Plate 3.

Two New Possible Mechanisms of Supernova-Like Explosions

V.V. Tikhomirov and S.E. Yuralevich

Institute for Nuclear Problems, Belarus State University, Bobrujskaya str. 11, Minsk 220050, Belarus;
tikh@inp.minsk.by, svetaju@inp.minsk.by

Summary. Primordial black holes (PBHs) of microscopical size can completely absorb neutron stars (NSs) and white dwarfs (WDs) for less than the Hubble time. NS absorption is accompanied by inverse URCA process giving rise to emission of antineutrino. However considerable part of these antineutrino fails to escape NS being drawn into the growing black hole by accreting NS matter. The final stage of dense WD absorption is accompanied by 10^{51}erg neutrino burst able to ignite nuclear burning giving rise to supernova-like WD explosion.

1 Introduction

Primordial black holes (PHBs) [5, 11] could form from primordial inhomogeneities, topological defects and phase transitions in the early Universe. Either PBH detection or proof of their nonexistence could give invaluable information about the earliest stages of cosmological expansion. Till present various methods of PBH search have been based on their Hawking radiation. These methods, however, have not led to detection of neither PBHs nor any consequence of their existence in the past, though stringent restrictions on their abundance have been established. That is why we would like to draw attention to an alternative way of PBHs search, namely to that based on PBHs interaction with cosmic objects, first of all with such dense ones as white dwarfs (WDs) and neutron stars (NSs). We will discuss the mechanisms of neutrino (antineutrino) emission by WD (NS) matter accreting onto a PBH, which can give rise to supernova like explosions. The neutrino burst accompanying WD absorption and igniting its nuclear burning is discussed in more detail.

2 WD Absorption and Accompanying Neutrino Burst

It is really possible to describe the process of WD matter accretion onto a PBH due to both the simplicity of degenerate electron gas equation of state and conservation of its adiabaticity under compression [7]. Right up to a growing PBH mass of about a hundredth of the WD's mass the equations [8] of spherical adiabatic collapse reduce to that of stationary spherical adiabatic accretion [10]. The latter allow to evaluate the WD matter density and

velocity distributions, and to get the rate of WD matter accretion onto BH growing from a PBH and the time

$$T_{WD} = \frac{27 \times 10^9 yr}{(M_{bh}/10^{15}g)(x_0 + \sqrt{1+x_0^2})^{3/2}}, \qquad x_0 = \left(\frac{\rho_0}{\rho_{rel}}\right)^{1/3} \tag{1}$$

of complete WD absorption by a PBH with initial mass M_{bh}. Here ρ_0 is central WD density in PBH absence and $\rho_{rel} = 1.95 \times 10^6 g/cm^3$ is the density of carbon-oxygen WD separating nonrelativistic and ultrarelativistic ones. One can see that a WD of any density is absorbed by a PBH of mass $M \gg M_*$ for less than the Hubble time and that the most dense WDs with $1 \ll x_0 \leq 10$ have enough time to be absorbed also by PBHs with $M \simeq M_*$. $M_* = 5 \times 10^{14} g$ is the Hawking mass, PBHs of such mass have to complete their evaporation at present epoch.

WD absorption by PBH proves to be a really observable phenomenon due to accompanying neutrino emission. Indeed, the theory [10] allows to evaluate the maximum WD density reached at the growing BH surface $\rho_{max} \simeq 1.44 \times 10^{11}(x_0 + \sqrt{1+x_0^2})^{1/2} g/cm^3$. The electron Fermi energy amounts to 20-100 MeV at such a density, thus, not only exceeding the threshold energies Δ =13.88 MeV and 12.17 MeV of the neutronization reactions

$$^{12}_{6}C + e^- \rightarrow ^{12}_{5}B + \nu, \qquad ^{12}_{5}B + e^- \rightarrow ^{12}_{4}Be + \nu \tag{2}$$

of carbon WD matter but also being sufficient to supply up to $\varepsilon_{\rm F} - \Delta \sim 10 - 100$ MeV to neutrino produced in these reactions. This way neutrino emission can provide a significant energy release on which a new approach of PBH search can be based.

Neutrino emission intensity grows with the accretion rate up to the moment of absorption of several tenth of WD mass, when the stationary accretion approximation is essentially violated and free fall of WD matter onto BH occurs. To describe the neutrino emission maximum one should use the adiabatic collapse theory [8] supplemented with the evolution equations

$$\begin{aligned} \dot{n} &= -nu' - \frac{2nu}{r} - n_{\rm C}\Gamma_{\rm C} - n_{\rm B}\Gamma_{\rm B}, \\ \dot{n}_{\rm C} &= -n_{\rm C}u' - \frac{2n_{\rm C}u}{r} - n_{\rm C}\Gamma_{\rm C}, \\ \dot{n}_{\rm B} &= -n_{\rm B}u' - \frac{2n_{\rm B}u}{r} + n_{\rm C}\Gamma_{\rm C} - n_{\rm B}\Gamma_{\rm B} \end{aligned} \tag{3}$$

of electron (n), carbon ($n_{\rm C}$) and boron ($n_{\rm B}$) nuclei number densities at distance r from the BH center. The nuclei neutronization probabilities $\Gamma_{\rm C,B} = \Gamma_{\rm C,B}(n)$ are evaluated in the same way as that of proton [10]. Let us consider a case of absorption of a WD with central density $\rho_0 = 10^9 g/cm^3$ and mass $M_{WD} = 2.68 \times 10^{33} g$ as an example. Its accretion density distributions at the moments of absorption of 0.01, 0.04, 0.16, 0.32, 0.64 and 0.96 of M_{WD}

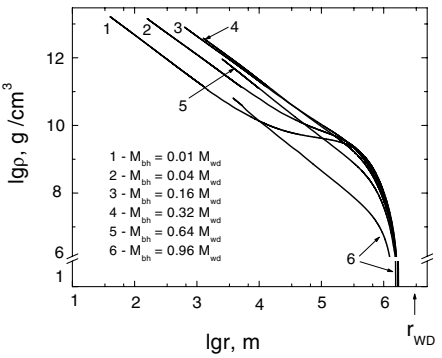

Fig. 1. Radial distributions of accreting WD matter density at the moments when BH mass reaches indicated parts of WD mass.

are given in Fig. 1. The neutrino emission intensity I_ν was evaluated taking into consideration the neutronization neutrino spectrum modified by both gravitational and kinematical Doppler effects as well as by neutrino capture by a growing BH. Given in Fig. 2, time dependence of I_ν demonstrates that it reaches $(1-2)\times 10^{52} erg/s$ for about 0.1 second, taking away more then $10^{51} erg$. The average neutrino energy exceeds 16 MeV in this case. Note that the Doppler effects and neutrino capture lower together the total and average neutrino energy 3.5 and 1.65 times, respectively.

Such a neutrino burst can be detected by modern neutrino telescopes. In particular, SuperKamiokande will register about $300(kpc/r)^2$ neutrino events from such a burst at distance r, allowing to detect it if $r \leq 10 kpc$. A HyperKamiokande-scale telescope will be able to detect it in all the Galaxy.

It is quite possible that the WD absorption by a PBH can be observed, like a supernova explosions, at much greater distances. Though unable to simulate it in detail in the meanwhile, we can prove for sure that the described neutrino burst can ignite the nuclear burning. Indeed, the WD matter degeneracy, first, $Z+1$ times (Z is the nuclear charge) lowers its specific heat capacity and, second, nearly one order increases the $\nu - e$ cross-section [4]. Due to both of these factors the neutrino burst will be able to heat the massive WD layers up to 10^{10}K and more, quite enough [4] to ignite nuclear burning leading to a supernova-like explosion observable from other galaxies.

The absorption of more dense WDs with $\rho_0 > 10^9 g/cm^3$ will naturally be accompanied by even more intense neutrino emission and nuclear burning. However less dense absorbed WDs will emit much weaker. A WD with $\rho_0 = 10^8 g/cm^3$ will emit only 1.4×10^{49}erg in the form of neutrino with average energy of only 4.6 MeV. It will be difficult to observe such a burst and it will hardly ignite nuclear burning. To find a threshold WD density of thermonuclear ignition and simulate the nuclear burning will be our next step.

3 NS Absorption

One can foresee that as more dense objects NSs will be absorbed by PBHs much faster than WDs. In fact, Hawking predicted that as in early as his paper [5]. Our estimates show that a PBH of Hawking mass will be absorbed for a few million years and that the absorption time is inversely proportional to PBH initial mass. Thus there is no doubt that a NS will have enough time to be absorbed by a PBH and the possibility to observe this phenomenon is entirely determined by the existence and efficiency of a mechanism of energy release by accreting NS matter.

Using various equations of state of NS matter [9, 10] we have elucidated that the degree of compression of accreting NS matter will hardly exceed ten and, thus, will not give rise to the results of [3]. The actual mechanism of energy release by compressed NS matter will be modified URCA process driven at zero temperature by the neutron energy increase which accompanies compression. A spectrum of antineutrino specific emission capacity can be evaluated following [10]

$$\frac{dN_{\tilde{\nu}}}{d\varepsilon_{\tilde{\nu}}dt} = \frac{m_n^3 m_p^{3/2}\varepsilon_{\tilde{\nu}}^2}{2^{12}c^6\hbar^4}\int_{\varepsilon_{Fp}}^{\varepsilon_{Fn}-\varepsilon_{Fe}+q-\varepsilon_{\tilde{\nu}}}\int_{\varepsilon_{Fe}}^{\varepsilon_{Fn}+q-\varepsilon_p-\varepsilon_{\tilde{\nu}}}\int_{\varepsilon_e+\varepsilon_p+\varepsilon_{\tilde{\nu}}-q}^{\varepsilon_{Fn}}$$
$$\int_{\varepsilon_{Fn}-q-\varepsilon_{n1}+\varepsilon_p+\varepsilon_e+\varepsilon_{\tilde{\nu}}}^{\varepsilon_{Fn}}\sum_{spins}|H_{fi}|^2\sqrt{\varepsilon_p}\varepsilon_e^2 d\varepsilon_p d\varepsilon_e d\varepsilon_{n1} d\varepsilon_{n2} \qquad (4)$$

where $\sum_{spins}|H_{fi}|^2$ is the squared matrix element of the reaction

$$n + n \rightarrow n + p + e^- + \tilde{\nu}, \qquad (5)$$

sum over final and averaged over initial particle spins, $q = (m_n - m_p)c^2$, m_n and m_p are the neutron and proton masses, $\varepsilon_{\tilde{\nu}}$, ε_{n1}, ε_{n2}, ε_p and ε_e are antineutrino, two neutron, proton and electron energies respectively. According to Eq. 4 the average antineutrino energy amounts to few tens MeV. Similarly to the WD case, the most part of antineutrino energy will be released at the stage of free fall of NS matter onto a BH having the mass comparable with that of NS. Since the free fall time does not exceed the time of antineutrino diffusion to the neutrinosphere, a considerable, if not the most part of emitted antineutrino will be drawn into the BH with accreting matter. This circumstance allows to argue that NS absorption will not be accompanied by such large energy release as that of a WD. It should be also mensioned that both WD and NS absorption by PBHs will give rise to formation of BHs which are essentially lighter than that forming in usual star collapse.

4 PBH Caption

The best condition for an efficient gravitational PBH capture existed at the epoch preceding the galaxy formation when the first astrophysical objects

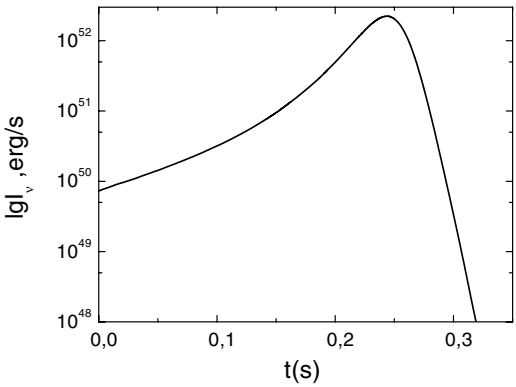

Fig. 2. Time dependence of a neutrino emission intensity measured from the moment when $M_{bh} = 0.01 M_{WD}$.

with masses of the order $10^5 - 10^6 M_\odot$ were forming [2]. A PBH capture by first solitary stars [1] looks the most promising. However except for the formation process, further evolution of such stars has not been investigated and does not allow to estimate the number of WDs and NSs formed. Globular clusters (GCs) will also abundantly capture PBHs. Both the high concentration and low velocity of stars as well as the high concentration of captured PBHs in GCs predetermine a high probability of PBH capture by stars in triple PBH-star-star collisions. Further process of star binary hardening in collisions and companion exchange with other stars lead to significant PBH orbit shrinking and penetration of considerable PBH fraction into stars, some of which turn later into WDs and NSs. Our investigation of these processes is in progress.

5 Conclusions

In conclusion, complete WD absorption by a PBH can give rise to a supernova like neutrino burst which is able to ignite WD matter nuclear burning and opens up a new way of PBH detection.

References

1. T. Abel, G.L. Bryan, M.L. Norman: Science **295**, 93 (2002)
2. E.V. Derishev, A.A. Belyanin: Astrophys. Space Sci. **343**, 1 (1999)
3. E.V. Derishev, V.V. Kocharovsky, Vl.V. Kocharovsky: Pisma v Zh. Eksp. Teor. Fiz. **70**, 652 (1999)
4. S.S. Gershtein et al. : Zh. Eksp. Teor. Fiz. **69**, 1473 (1975)
5. S.W. Hawking: Mon. Not. R. Astron. Soc. **152**, 75 (1972)
6. D.C. Heggie: Mon. Not. R. Astron. Soc. **173**, 729 (1975)

7. S.E. Juralevich, V.V. Tikhomirov: astro-ph 0202445
8. C.W. Misner, D.H. Sharp: Astrophys. Space Sci. **136**, 571 (1964)
9. G.S. Sahakian: In: *Physics of Neutron Stars*, (JINR, Dubna 1995) pp. 45-56
10. S. Shapiro, S. Teukolsky: In: *Black Holes, White Dwarfs and Neutron Stars*, (Wiley, New York 1986) p. 176
11. J.B. Zel'dovich, I.D. Novikov: Astron. Zhurnal **43**, 758 (1966)

Tests for Supernova Explosion Models: from Light Curves to X-ray Emission of Supernova Remnants

Elena Sorokina[1] and Sergey Blinnikov[2]

[1] SAI, Universitetskij pr. 13, 119992 Moscow, Russia;
sorokina@sai.msu.su
[2] ITEP, B. Cheremushkinskaya 25, 117218 Moscow, Russia;
blinn@sai.msu.su

Summary. The successful theoretical supernova explosion models should be able to explain any features of the emission from supernovae at any evolutionary stage. We check several models from two different points of view. With the multi-frequency radiation hydro code STELLA we calculate gamma-ray, bolometric and broad-band UBVI light curves. Then we use the same models to calculate the emission from young supernova remnants. Here we present new plots for gamma-ray luminosity from several SN Ia models and recomputations of bolometric and UBVRI light curves of model 13C for SN 1993J.

1 Introduction

So far, there exist many explosion models proposed by theorists for different types of supernovae, but still there are no definite criteria to decide which of the models are realized in nature. Only a few parameters, such as kinetic energy and total ^{56}Ni production, can be derived directly from the modeling of the explosion and compared with the observational values. The subsequent evolution of the exploded star gives us much more possibilities to compare models and to decide which one fits observations better.

The first possibility is modeling of gamma-ray luminosity of supernovae. The comparison with the observational values allows to define the total mass of radioactive isotopes, to judge on the composition of the outer layers where gamma-rays are absorbed and thermalized, and also to check the approximations of gamma-ray opacity. During the first months after an explosion one can examine a theoretical model by calculating bolometric and monochromatic light curves and spectra, and comparing them with observations. Later on, gas in the ejecta cools down and becomes almost unobservable. The next opportunity to analyze the ejecta is on the stage of a young supernova remnant (SNR), when noticeable amount of circumstellar gas is swept up. Then a reverse shock forms, goes inwards the ejecta and illuminates them once again.

The successful theoretical supernova explosion models should be able to explain any feature of the emission from supernovae at any evolutionary

Table 1. Parameters of SN Ia models

Model	DD4	W7	LA4	WD065	MR
$M_{\rm WD}$ [a]	1.3861	1.3775	0.8678	0.6500	1.4
$M_{^{56}\rm Ni}$ [a]	0.63	0.60	0.47	0.05	0.42
E_{51} [b]	1.23	1.20	1.15	0.56	0.46

[a] in $M_\odot$
[b] in 10^{51} ergs $\rm s^{-1}$

stage. Different combinations of codes we have in our group allows us to compute the evolution of models, and therefore test them, on several stages. For calculations of broad-band optical and bolometric light curves we use the multi-frequency radiation hydro code STELLA. At the young remnant stage, while gas is transparent, we calculate the evolution and X-ray emission by combination of hydro part of STELLA with the non-equilibrium ionization code which is based on the original algorithm by Peter Lundqvist.

2 SN Ia Models

We choose five models of Type Ia supernovae which are shown in Table 1. W7 [8] and DD4 [14] are more or less similar classical 1D Chandrasekhar mass models. LA4 [7] and WD065 [11] are sub-Chandrasekhar mass ones. (See original works for details.) The last model was computed a couple of years ago in Garching, in the Max-Planck-Institute group [9]. It is originally 3D. We average it over 4π for our calculation, since we use only 1D codes at the moment. The main feature of the model is that it is very well mixed, while energetics and the amount of $\rm Ni^{56}$ are lower than in other Chandrasekhar mass models. In our calculations we compare two versions of the model with the same hydro part, but different element distributions.

3 Results

3.1 SNe Ia

Now there appears more and more possibilities to obtain gamma-ray light curves using modern gamma-ray space observatories, like COMPTEL [5]. Here we just compare what one would observe after the explosion of the models we have discussed.

In Fig. 1 we compare the light curves in gamma-rays produced by different models. We have chosen W7 as a representative case of Chandrasekhar-mass models. The light curves in gamma-rays are more or less similar for all of them. The luminosity of the MR model is lower due to smaller amount of

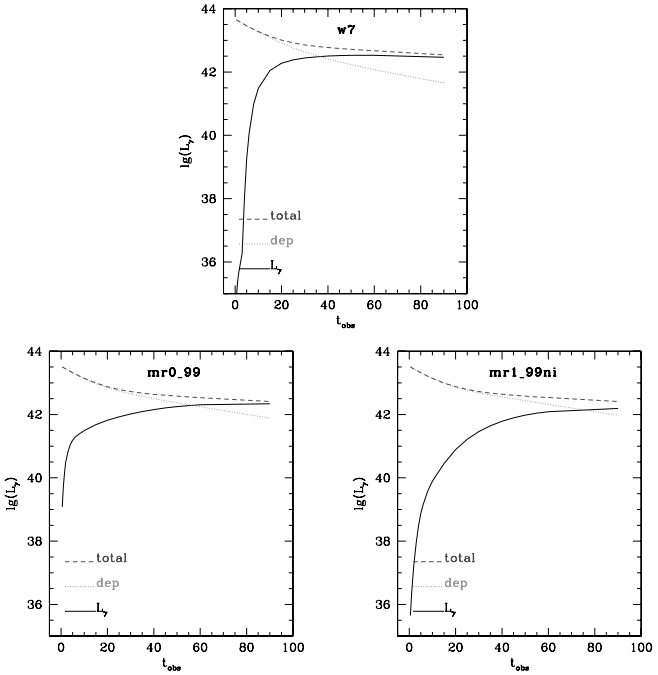

Fig. 1. Gamma-ray production by Ni and Co decays (*dashes*), gamma-ray power deposited into heating (*dots*), and total gamma-ray luminosity of SN (*solid*) versus time in days for different explosion models: W7 (*top panel*), MR model averaged over 4π (*bottom left*), and MR model averaged over an opening angle of 14° with the same mass of ^{56}Ni, which is situated mostly near the center (*bottom right*).

^{56}Ni, and it rises slower since it is less energetic, so γ-photons are locked inside the ejecta for longer time. One can see even smaller number of γ-photons during the first weeks after the explosion in the model similar to MR but less mixed, with ^{56}Ni residing mostly near the center. The maximum luminosity in gamma-rays is still the same as in original MR, since we preserve the total amount of ^{56}Ni.

Therefore, the light curve in gamma-rays during the first months can be divided into two epochs, that represent different physical parameters of the explosion: the first $40-60$ days and the following evolution. From the observations during the first period one can judge on the combination of explosion energy and the distribution of radioactive stuff over the ejecta, while the second period tells us mostly about total production of radioactive elements at the explosion. Since currently the observations can only provide us with fluxes integrated over several days (or even weeks), it seems expedient to make two different sets of observations: during the first two months after the

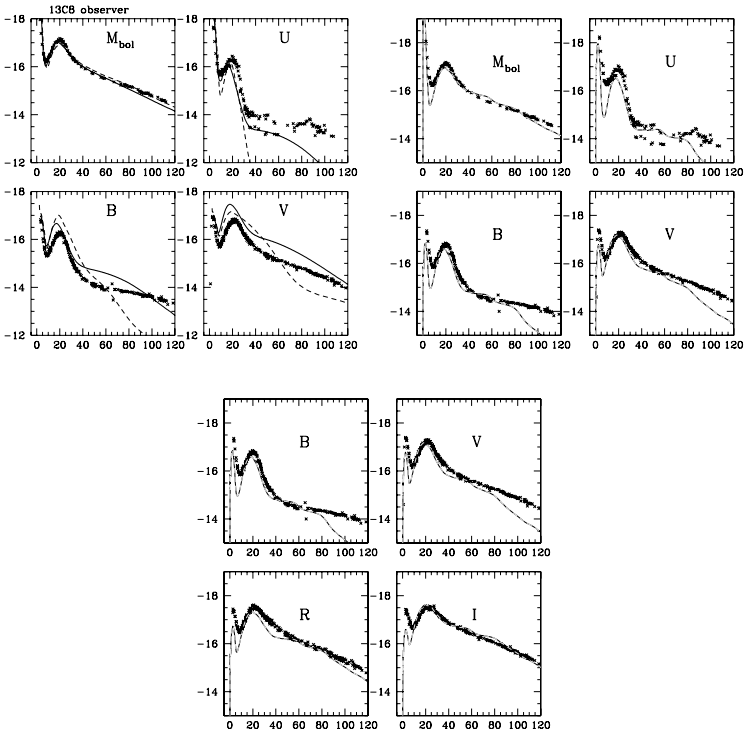

Fig. 2. Bolometric and UBVRI light curves for SN 1993J. *Top left panel*: The best model 13C8 from [2] (*solid line* – calculations with STELLA, *dashes* – with EDDINGTON). *Top right and bottom panels:* Our recalculation of the same model with a new version of STELLA. Observational data are taken from [10] and shown by crosses. The value of reddening is taken to be $E(B-V) = 0.08$.

explosion, and after that, in order to distinguish between different parameters of explosion, and to test explosion models.

We have described our modeling of bolometric and UBVRI light curves and calculations of X-ray emission of young SNRs in previous work. For details one can see, e.g., [3, 4, 6]. We just mention here that a bit less energetic and more mixed models, like MR, seem to us more preferable both for SN light curve and for SNR X-ray emission. At the latter point, our results seem to contradict the conclusions by [1], that iron lines from well mixed models at the SNR stage are too strong, while less mixed models give a better agreement with observations of Tycho. Still we trust in our results more, since we take into account the ionization energy in the equation of state, which is comparable to the thermal energy. Electron thermal conductivity is also included into our calculations, and it smoothes very much the temperature profile between forward and reverse shocks. Both these effects are neglected

in the code by [1], though they are able to change the emitted spectrum appreciably. The code by [1] takes into account possible difference between electron and ion temperature using the standard Coulomb collision equation, while we treat this effect parametrically. This can also lead to differences in our results. The work on improving physics and making our code more self-consistent is in progress.

3.2 SN 1993J

In order to pay attention to the SN entitling this conference, we have recalculated its light curve. We use the same model 13C from [13] which was investigated a few years ago in [2]. It is one of the best models for SN 1993J, and we just wanted to check if the new version of our code STELLA, with improved and renovated physics, still produces the light curve that fits observations well.

The results of previous and current calculations are compared in Fig. 2. The main improvement in the code is a new approach for expansion opacities [12]. They become much more complicated, and, most probably, the bumps on the new light curves are the results of this improvement. But sometimes (for instance, in the U band) these bumps seem to fit the observations even better than it was in the old version. R and I bands are calculated with STELLA for the first time, and they look perfect.

There is a discussion in the literature on the estimates of the reddening to SN 1993J ([10] and references therein). In the plots in Fig. 2 we assume $E(B-V) = 0.08$. With larger value, the observational curves become higher than the modeled ones. So the new version of STELLA confirms that the model 13C corresponds to the explosion of SN 1993J very well, but in the case of low reddening.

Acknowledgement. ES is grateful to the organizers of the meeting for their warm hospitality and support. The work is supported by RFBR through grants 02–02–16500, 03–02–06770, and 03–02–26598.

References

1. C. Badenes, E. Bravo, K.J. Borkowski, I. Domínguez: Astrophys. J. **593**, 358 (2003)
2. S.I. Blinnikov et al. : Astrophys. J. **496**, 454 (1998)
3. S. Blinnikov, E. Sorokina: Astron. Astrophys. **356**, L30 (2000)
4. S. Blinnikov, E. Sorokina: "Type Ia Supernova Models: Latest Developments." In: *Hunting the Cosmological Parameters*, ed. D. Barbossa et al. (Kluwer: Dordrecht, 2003)
5. R. Georgii, S. Plüschke, R. Diehl et al: Astron. Astrophys. **394**, 517 (2002)

6. D.I. Kosenko, E.I.Sorokina, S.I. Blinnikov, P. Lundqvist: "X-ray Emission of Young SN Ia Remnants as a Probe for an Explosion Model." In: *Proc. of 34th Scientific Assembly of COSPAR*, (ASR: 2003)
7. E. Livne, D. Arnett: Astrophys. J. **452**, 62 (1995)
8. K. Nomoto, F.-K. Thielemann, K. Yokoi: Astrophys. J. **286**, 644 (1984)
9. M. Reinecke, W. Hillebrandt, J.C. Niemeyer: Astron. Astrophys. **386**, 936 (2002)
10. M.W. Richmond et al. : Astron. J. **107**, 1022 (1994)
11. P. Ruiz-Lapuente et al. : Nature **365**, 728 (1993)
12. E.I. Sorokina, S.I. Blinnikov: "Energy exchange inside SN ejecta and light curves of SNe Ia." In: *Nuclear Astrophysics, MPA/P13*, ed. W. Hillebrandt, E. Müller (Garching: 2002) pp. 57-62
13. S.E. Woosley, R.G. Eastman, T.A. Weaver, P.A. Pinto: Astrophys. J. **429**, 300 (1994)
14. S.E. Woosley, T.A. Weaver: "Massive Stars, Supernovae, and Nucleosynthesis." In: *Supernovae*, ed. R. Bludman et al. (Elsevier Sci. Pub.: Amsterdam, 1994) pp. 63-154

Understanding Type II Supernovae

L. Zampieri[1], M. Ramina[1,2] and A. Pastorello[1,2]

[1] INAF-Osservatorio Astronomico di Padova, Vicolo dell'Osservatorio 5, 35122 Padova, Italy;
zampieri@pd.astro.it
[2] Dipartimento di Astronomia, Università di Padova, Vicolo dell'Osservatorio 2, 35122 Padova, Italy

Summary. We present the results of a systematic analysis of a group of Type II plateau supernovae that span a large range in luminosities, from faint objects like SN 1997D and 1999br to very luminous events like SN 1992am. The physical properties of the supernovae appear to be related to the plateau luminosity or the expansion velocity. The simultaneous analysis of the observed light curves, line velocities and continuum temperatures leads us to robust estimates of the physical parameters of the ejected envelope. We find strong correlations among several parameters. The implications of these results regarding the nature of the progenitor, the central remnant and the Ni yield are also addressed.

1 Introduction

Type II supernovae (SNe) are believed to be core-collapse SNe originating from massive (> 8 $M_\odot$) red supergiants that retain their hydrogen (H) envelopes. The overall phenomenological appearance of these SNe is rather well understood (see, e.g., [1]). However, although lightcurve and spectral modeling have provided important information on the physical properties of single objects (see, e.g., [7]), comparatively little effort has been devoted to study the correlations between the basic properties of Type II SNe and to understand to what extent the variety of their observational properties can be explained in terms of continuous changes of some fundamental physical variables. This is especially interesting after the recent discovery of a group of low luminosity (LL), ^{56}Ni poor SNe [5, 8], whose relation with the "normal" and more luminous Type II events is still under debate. The work in this area has certainly been hampered also by the very heterogeneous behavior of Type II SNe. However, a recent investigation has shown that significant correlations exist among the plateau luminosity, the expansion velocity measured at 50 days after the explosion and the ejected ^{56}Ni mass [2]. Here we present the results of a systematic analysis of a group of Type II plateau supernovae that extends, especially at very low luminosity, the sample previously considered. While we confirm the results of Hamuy [2], we do not find evidence of a definite correlation between the ejected envelope mass and the other parameters.

2 Selected Sample of Type II Plateau SNe

The data were taken from literature and/or extracted from the large database of lightcurves and spectra of the Padova-Asiago Supernova Archive. A description of the selection process is outlined in Pastorello et al. (these Proceedings). Observations of SN 2003Z[1], the first LL event extensively monitored from explosion up to the nebular stage, are also included in the Pastorello et al. work. SNe with uncertain estimates of the distance and interstellar absorption and/or with signs of significant interaction with the circumstellar material were not considered. The main selection criterion was to choose objects that cover a big range in luminosity, including LL, 97D-like events [5, 8] and luminous 92am-like objects [6]. The selected objects are reported in Table 1. Most of them have a good photometric coverage until $300 - 400$ days after the explosion and at least $4 - 5$ spectra in the photospheric phase (up to $\sim 100 - 120$ days). The best available estimates of the explosion epoch, the distance modulus and interstellar absorption (Galactic and internal) for these objects are reported in Pastorello et al. (these Proceedings) and Ramina (Laurea Thesis, unpublished). SN 1987A is included for comparison.

3 Modeling Core-collapse SNe

In the present analysis the physical parameters of the selected sample of SNe are derived comparing the observational data to model calculations. The adopted model is a semi-analytic code that solves the energy balance equation for a spherically symmetric, homologously expanding envelope at constant density [8]. The initial conditions are rather idealized and provide an approximate description of the ejected material after shock (and possible reverse shock) passage, as derived from hydrodynamical calculations. In particular, elements are assumed to be completely mixed throughout the envelope and their distribution depends only on the coordinate mass. Hydrogen, helium, carbon and oxygen are assumed to be uniformly distributed, whereas ^{56}Ni is more centrally peaked. The evolution of the expanding envelope is computed including all the relevant energy sources powering the SN and is schematically divided in 3 phases from the photospheric up to the late nebular stages (for more details see Zampieri et al. [8] and Ramina [Laurea Thesis, unpublished]). The most important quantities computed by the code are the light curve and the evolution of the line velocity and continuum temperature at the photosphere. The physical properties of the envelope are derived by performing a simultaneous fit of these three observables with model calculations.

[1] Made in part at the Telescopio Nazionale Galileo (TNG) under program TAC_48.

Table 1. Physical parameters from the semi-analytic model

	R_0 (10^{12} cm)	M_{env} ($M_\odot$)	M_{Ni} ($M_\odot$)	V_0 (10^8 cm s^{-1})	E (10^{51} erg)	$t_{rec,0}$ (days)	T_{eff} (K)	$\log L_p$
1992am	41^{+6}_{-5}	26^{+8}_{-3}	$0.41^{+0.04}_{-0.04}$	$5.1^{+0.5}_{-0.4}$	$8.1^{+4.1}_{-2.0}$	53	4400^{+400}_{-300}	42.55
1992H	38^{+3}_{-2}	23^{+7}_{-3}	$0.18^{+0.01}_{-0.01}$	$4.9^{+0.2}_{-0.4}$	$6.6^{+2.7}_{-1.8}$	50	4300^{+200}_{-200}	42.4
1996W	37^{+5}_{-3}	16^{+4}_{-2}	$0.17^{+0.02}_{-0.02}$	$4.1^{+0.3}_{-0.3}$	$3.2^{+1.3}_{-0.8}$	48	4500^{+400}_{-300}	42.25
1995ad	17^{+3}_{-2}	12^{+2}_{-2}	$0.029^{+0.003}_{-0.004}$	$4.0^{+0.4}_{-0.4}$	$2.3^{+0.9}_{-0.7}$	30	4700^{+300}_{-200}	41.9
1969L	25^{+3}_{-2}	16^{+2}_{-1}	$0.067^{+0.006}_{-0.005}$	$3.6^{+0.2}_{-0.2}$	$2.5^{+0.6}_{-0.4}$	50	4300^{+200}_{-10}	42.0
1987A	$6^{+0.9}_{-0.7}$	18^{+4}_{-2}	$0.075^{+0.006}_{-0.006}$	$2.8^{+0.2}_{-0.2}$	$1.7^{+0.6}_{-0.4}$	26	4300^{+100}_{-200}	41.35
1996an	19^{+2}_{-3}	13^{+2}_{-1}	$0.050^{+0.005}_{-0.005}$	$3.3^{+0.1}_{-0.2}$	$1.7^{+0.3}_{-0.3}$	46	4200^{+200}_{-100}	41.8
1999em	14^{+3}_{-2}	14^{+2}_{-1}	$0.022^{+0.002}_{-0.003}$	$3.2^{+0.1}_{-0.2}$	$1.7^{+0.4}_{-0.3}$	48	3800^{+100}_{-200}	41.6
1992ba	13^{+2}_{-1}	17^{+2}_{-2}	$0.016^{+0.003}_{-0.002}$	$3.2^{+0.2}_{-0.4}$	$2.1^{+0.5}_{-0.7}$	42	3500^{+200}_{-300}	41.5
2003Z	13^{+2}_{-1}	19^{+2}_{-2}	$0.006^{+0.001}_{-0.002}$	$2.2^{+0.2}_{-0.1}$	$1.1^{+0.3}_{-0.2}$	28	4000^{+200}_{-200}	41.25
1997D	$10^{+0.5}_{-0.5}$	17^{+3}_{-2}	$0.008^{+0.001}_{-0.002}$	$2.1^{+0.2}_{-0.2}$	$0.9^{+0.3}_{-0.2}$	32	3900^{+200}_{-200}	41.15
1994N	16^{+1}_{-3}	15^{+2}_{-2}	$0.0068^{+0.0003}_{-0.0003}$	$2.1^{+0.2}_{-0.2}$	$0.8^{+0.3}_{-0.2}$	38	4200^{+300}_{-200}	41.4
2001dc	10^{+1}_{-1}	12^{+2}_{-2}	$0.0058^{+0.0005}_{-0.0007}$	$1.9^{+0.3}_{-0.2}$	$0.5^{+0.3}_{-0.1}$	27	4000^{+200}_{-200}	41.1
1999eu	$8^{+0.4}_{-0.6}$	12^{+2}_{-1}	$0.003^{+0.0005}_{-0.0004}$	$1.8^{+0.3}_{-0.1}$	$0.5^{+0.3}_{-0.1}$	38	3600^{+200}_{-100}	40.9
1999br	$7^{+0.4}_{-0.6}$	15^{+2}_{-2}	$0.0021^{+0.0002}_{-0.0002}$	$1.8^{+0.1}_{-0.2}$	$0.6^{+0.1}_{-0.2}$	33	3400^{+100}_{-200}	40.85

R_0 is the initial radius of the ejected envelope at the onset of expansion
M_{env} is the ejected envelope mass
M_{Ni} is the ejected ^{56}Ni mass
V_0 is the velocity of the homologously expanding envelope at the outer shell
E is the initial thermal+kinetic energy of the ejected envelope
$t_{rec,0}$ is the time when the envelope starts to recombine
T_{eff} is the effective temperature during recombination
L_p Luminosity (BVRI bands) at $t_{rec,0}$

4 Correlations Among Physical Parameters

The physical parameters of the post-shock, ejected envelope are listed in Table 1. Only some of them are input parameters (R_0, M_{env}, V_0, T_{eff}), while the others are computed by the code or fixed by the observations. Two other input physical constants are the fraction of the initial energy that goes into kinetic energy, f_0, and the gas opacity, κ. In this calculation we adopt $f_0 = 0.5$ (initial equipartition between thermal and kinetic energies) and $\kappa = 0.2$ cm^2 g^{-1} (appropriate for an envelope comprised of He and iron-group elements). The color correction factor $f_c = T_c/T_{eff}$, that measures the deviation of the continuum radiation temperature T_c from the blackbody effective temperature T_{eff}, was kept fixed and equal to 1.2.

As shown in Fig. 1 (left panel), the inferred physical parameters of the ejected envelope are strongly correlated. All quantities appear to vary continuously with the plateau luminosity L_p or, alternatively, with the expansion velocity of the envelope at the outer shell V_0, which coincides with the photospheric velocity measured at the onset of recombination. In particular, the ^{56}Ni mass increases with V_0 over several orders of magnitude. The sole

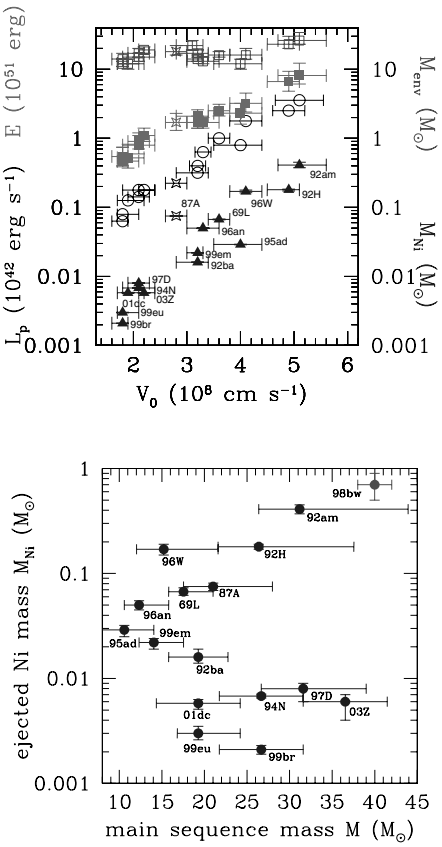

Fig. 1. *Left*: Luminosity L_p (*circles*), energy E (*filled squares*), envelope mass M_{env} (*open squares*) and ^{56}Ni mass M_{Ni} (*triangles*) vs expansion velocity V_0 for the SNe of our sample. The asterisks denote SN 1987A. *Right*: Ejected ^{56}Ni mass M_{Ni} vs inferred progenitor main sequence mass M. SN 1998bw is shown for comparison.

exception is the ejected envelope mass M_{env} that, within the estimated errors, does not show any definite tendency to vary with the other parameters. Only at high velocities (and luminosities) does M_{env} increase slightly with V_0.

Correlations between the observed luminosity and photospheric velocity at 50 days after the explosion, and between the observed luminosity and inferred ejected ^{56}Ni mass have recently been reported by Hamuy [2]. Our results confirm his findings and clarify that the physical variable associated with the photospheric velocity at 50 days after the explosion is the expansion velocity V_0. It is worth noting also that LL, Ni-poor SNe, such as SN 1997D

and SN 1999br, do not appear to occupy a separate area of the diagram but, instead, populate the low energy tail of the correlation.

The very weak dependence of M_{env} on the other parameters has important consequences for the nature of the progenitor and the compact remnant. We derived a rough estimate of the progenitor main sequence mass M assuming no mass loss and a simple but physically plausible "mixing recipe", that is, the fraction of carbon-oxygen-helium mass M_{mix} mixed into the hydrogen layer and ejected increases with increasing ^{56}Ni yield or expansion velocity ($f_{mix} = M_{mix}/M_{env} = 0.15$ for the LL events, $f_{mix} = 0.4$ for the "normal" Type II SNe, $f_{mix} = 0.45$ for the high luminosity objects). The results are not strongly dependent on the specific prescription for mixing, as long as it is taken to increase with M_{Ni} or V_0. From this, assuming no rotation, we then estimate the hydrogen mass from $M_H = M_{env} - M_{mix} = (1 - f_{mix})M_{env}$ and the main sequence mass from the approximate expression $M = 2.9(1 - f_{mix})M_{env} - 10.3$ (see, e.g., [1]). Including mass loss would result in larger values of M, especially for $M \geq 20$ M$_\odot$, with a significant dependence on metallicity. We find that both high and LL SNe have massive progenitors with $M \geq 20 - 25$ M$_\odot$. This follows, for the first, from the large inferred value of M_{env} while, for the second, from the fact that f_{mix} is small. Because "normal" and LL events have similar ejected envelope masses M_{env} but rather different mixing fractions, the first have comparatively less massive progenitors ($12 \leq M \leq 20$ M$_\odot$). For the "normal" and high luminosity SNe a large fraction of the ejected envelope mass comes from the carbon-oxygen-helium layer that was successfully ejected, while in the LL events M_{env} essentially measures the ejected hydrogen mass. Despite the large errors, we find that only LL SNe appear to have progenitors with masses significantly in excess of M_{env}. Thus, they may have undergone significant fallback, as suggested by Zampieri et al. [8], and harbor black hole remnants.

In Fig. 1 (right panel) we show the plot of the ejected ^{56}Ni mass versus the inferred progenitor main sequence mass. Again, albeit the errors are very large, it is possible to recognize that Type II SNe populate different regions in this diagram. In particular, as originally suggested by Iwamoto et al. [3], there appears to be a bimodal behavior above ≈ 20 M$_\odot$, with high luminosity events populating the high ^{56}Ni tail (close to the area occupied by hypernovae as SN 1998bw) and LL objects filling the low ^{56}Ni yield region. The reason for the large spread in ejected ^{56}Ni and the non monotonic behavior of the $M - M_{Ni}$ relation is not clear. Perhaps, as suggested by Maeda and Nomoto [4], in luminous events a large amount of angular momentum is retained by the post-shock envelope causing the formation of jets and an enhanced energy release along the jet axes, whereas "normal" and LL events may have more spherical shapes. It could also be that different metallicities and mass loss histories prior to explosion play an important role, with high luminosity events having more powerful winds while LL ones retain almost all their hydrogen envelope until explosion.

References

1. W.D. Arnett: In: *Supernovae and Nucleosynthesis*, (Princeton Univ. Press: Princeton, 1996)
2. M. Hamuy: Astrophys. J. **582**, 905 (2003)
3. K. Iwamoto et al. : Astrophys. J. **534**, 660 (2000)
4. K. Maeda, K. Nomoto: Astrophys. J. **598**, 1163 (2003)
5. A. Pastorello et al. : Mon. Not. R. Astron. Soc. **347**, 74 (2003)
6. B. Schmidt et al. : Astron. J. **107**, 1444 (1994)
7. S.E. Woosley: Astrophys. J. **330**, 218 (1988)
8. L. Zampieri et al. : Mon. Not. R. Astron. Soc. **338**, 711 (2003)

Magnetorotational Mechanism of Supernova Type II Explosion

S.G. Moiseenko[1], G.S. Bisnovatyi-Kogan[1], and N.V. Ardeljan[2]

[1] Space Research Institute, Profsoyuznaya str. 84/32 Moscow 117997, Russia;
moiseenko@iki.rssi.ru, gkogan@iki.rssi.ru
[2] Department of Computational Mathematics and Cybernetics, Moscow State University, Vorobjevy Gory, Moscow B-234 Russia;
ardel@cs.msu.su

Summary. Results of 2D simulations of the magnetorotational mechanism of supernova type II are presented. Amplification of toroidal magnetic field of the star due to differential rotation of the star leads to the transformation of the rotational (gravitational) energy to the energy of the supernova explosion. In our simulation the energy of the explosion is 1.12×10^{51} erg. The explosion ejects about 0.11 $M_\odot$.

1 Magnetorotational Mechanism

The magnotorotational supernova (MRS) explosion model was suggested in [5]. The idea of MRS consists of getting explosion energy from the rotational (gravitational) energy of the collapsed magnetized massive star. 1D numerical simulation of the MRS mechanism has been made in [1, 6]. We have made 2D numerical simulation of the MRS using specially developed implicit conservative Lagrangian scheme on triangular grid with grid reconstruction. Our results show that MRS leads to the energy output of the 1.12×10^{51} erg and ejection of 0.11 $M_\odot$.

Core collapse of a star leads to formation of the rapidly (almost rigidly) rotating neutron core and a differentially rotating large envelope. The explosion energy for the supernova is taken from the rotational (gravitational) energy of the magnetized star. The magnetic field plays the role of the "transmission belt" for the rotational (gravitational) energy to the energy of the supernova explosion. Toroidal component of the magnetic field is amplifying with time due to the differential rotation of the star. When the force produced by magnetic pressure substantially changes the local balance of forces a compression MHD wave appears and goes through the star's envelope outwards. Moving along a steeply decreasing density profile this wave transforms to the MHD shock which produces supernova explosion.

2 Formulation of the Problem

2.1 Basic Equations

Consider a set of magnetohydrodynamical equations with self gravitation and with infinite conductivity:

$$\frac{\mathrm{d}\mathbf{x}}{\mathrm{d}t} = \mathbf{u}, \quad \frac{\mathrm{d}\rho}{\mathrm{d}t} + \rho\nabla\cdot\mathbf{u} = 0,$$

$$\rho\frac{\mathrm{d}\mathbf{u}}{\mathrm{d}t} = -\nabla\left(p + \frac{\mathbf{H}\cdot\mathbf{H}}{8\pi}\right) + \frac{\nabla\cdot(\mathbf{H}\otimes\mathbf{H})}{4\pi} - \rho\nabla\Phi,$$

$$\rho\frac{\mathrm{d}}{\mathrm{d}t}\left(\frac{\mathbf{H}}{\rho}\right) = \mathbf{H}\cdot\nabla\mathbf{u}, \quad \Delta\Phi = 4\pi G\rho,$$

$$\rho\frac{\mathrm{d}\varepsilon}{\mathrm{d}t} + p\nabla\cdot\mathbf{u} + \rho F(\rho, T) = 0,$$

where $\frac{\mathrm{d}}{\mathrm{d}t} = \frac{\partial}{\partial t} + \mathbf{u}\cdot\nabla$ is the total time derivative, $\mathbf{x} = (r, \varphi, z)$, $\mathbf{u}$ is velocity vector, ρ is density, p is pressure, $\mathbf{H} = (H_r, H_\varphi, H_z)$ is magnetic field vector, Φ is gravitational potential, ε is internal energy, G is gravitational constant, $\mathbf{H}\otimes\mathbf{H}$ is tensor of rank 2, $F(\rho, T)$ is the rate of neutrino losses, other notations are standard..

Axial symmetry ($\frac{\partial}{\partial\varphi} = 0$) and symmetry to the equatorial plane ($z = 0$) are assumed.

2.2 Equations of State

The equations of state $P(\rho, T)$ [2]. includes approximation of the tables from [4, 8] for the cold degenerate matter $P_0(\rho)$: $P \equiv P(\rho, T) = P_0(\rho) + \rho\Re T + \frac{\sigma T^4}{3}$,

$$P_0(\rho) = \begin{cases} P_0^{(1)} = b_1\rho^{1/3}/(1 + c_1\rho^{1/3}), & at\ \rho \le \rho_1, \\ P_0^{(k)} = a\cdot 10^{b_k(\lg\rho - 8.419)^{c_k}} & at\ \rho_{k-1} \le \rho \le \rho_k,\ k = \overline{2,6} \end{cases} \tag{1}$$

$b_1 = 10.1240483$, $c_1 = 10^{-2.257}$, $\rho_1 = 10^{9.419}$, $b_2 = 1.0$, $c_2 = 1.1598$, $\rho_2 = 10^{11.5519}$, $b_3 = 2.5032$, $c_3 = 0.356293$, $\rho_3 = 10^{12.26939}$, $b_4 = 0.70401515$, $c_4 = 2.117802$, $\rho_4 = 10^{14.302}$, $b_5 = 0.16445926$, $c_5 = 1.237985$, $\rho_5 = 10^{15.0388}$, $b_6 = 0.86746415$, $c_6 = 1.237985$, $\rho_6 \gg \rho_5$, $a = 10^{26.1673.}$

Here ρ is a total mass-energy. The energy of the unit mass is defined as: $\varepsilon = \varepsilon_0(\rho) + \frac{3}{2}\Re T + \frac{\sigma T^4}{\rho}$, where $\Re$ - gas constant, σ - constant radiation density, and $\varepsilon_0(\rho) = \int\limits_0^\rho \frac{P_0(\tilde\rho)}{\tilde\rho^2}\mathrm{d}\tilde\rho$.

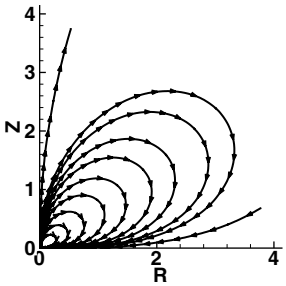

Fig. 1. Initial poloidal magnetic field.

The neutrino losses from Urca processes are defined by relation [7]:

$$f(\rho,T)=\frac{1.3\cdot 10^9 æ(\overline{T})\overline{T}^6}{1+(7.1\cdot 10^{-5}\rho\overline{T})^{\frac{2}{5}}}\quad \mathrm{erg}\cdot \mathrm{g}^{-1}\cdot \mathrm{c}^{-1}, \tag{2}$$

$$æ(\mathrm{T})=\begin{cases} 1, & \overline{T}<7,\\ 664.31+51.024(\overline{T}-20), & 7\le\overline{T}\le 20,\\ 664.31, & \overline{T}>20,\ \overline{T}=T\cdot 10^{-9}. \end{cases} \tag{3}$$

Neutrino losses from pair annihilation, photo-production and plasma were also taken into account. These type of the neutrino losses have been approximated by the interpolation formulae from [9]: $Q_{tot}=Q_{pair}+Q_{photo}+Q_{plasm}$ These three terms can be written in the following general form:

$$Q_d=K(\rho,\alpha)e^{-c\xi}\frac{a_0+a_1\xi+a_2\xi^2}{\xi^3+b_1\alpha+b_2\alpha^2+b_3\alpha^3}. \tag{4}$$

For $d=pair$, $K(\rho,\alpha)=g(\alpha)e^{-2\alpha}$, $g(\alpha)=1-\frac{13.04}{\alpha^2}+\frac{133.5}{\alpha^4}+\frac{1534}{\alpha^6}+\frac{918.6}{\alpha^8}$; For $d=photo$, $K(\rho,\alpha)=(\rho/\mu_Z)\alpha^{-5}$; For $d=plasm$, $K(\rho,\alpha)=(\rho/\mu_Z)^3$; $\xi=\left(\frac{\rho/\mu_Z}{10^9}\right)^{1/3}\alpha$. Here $\mu_Z=2$ is number of nucleons per electron. Coefficients c, a_i, b_i for different d are given in [9].

The general formula for neutrino losses in non-transparent star has been written in the following form: $F(\rho,T)=(f(\rho,T)+Q_{tot})e^{-\frac{\tau_\nu}{10}}$. The multiplier $e^{-\frac{\tau_\nu}{10}}$, where $\tau_\nu=S_\nu n l_\nu$ restricts neutrino flux for non zero depth to neutrino interaction with matter τ_ν. The cross-section for this interaction S_ν was represented in the form $S_\nu=\frac{10^{-44}T^2}{(0.5965\cdot 10^{10})^2}$, the nucleons concentration is: $n=\frac{\rho}{m_p}$, $m_p=1.67\cdot 10^{-24}$g. The characteristic length scale l_ν which defines the depth for the neutrino absorption, was taken to be equal to the characteristic length of the density variation, as $l_\nu=\frac{\rho}{|\nabla\rho|}=\frac{\rho}{((\partial\rho/\partial r)^2+(\partial\rho/\partial z)^2)^{1/2}}$. This value monotonically decreases when moving to the outward boundary, from a maximum in the center. It approximately determines to the depth of the neutrino absorbing matter. The multiplier 1/10 was applied because in the degenerate matter of the hot neutron star only part of the nucleons

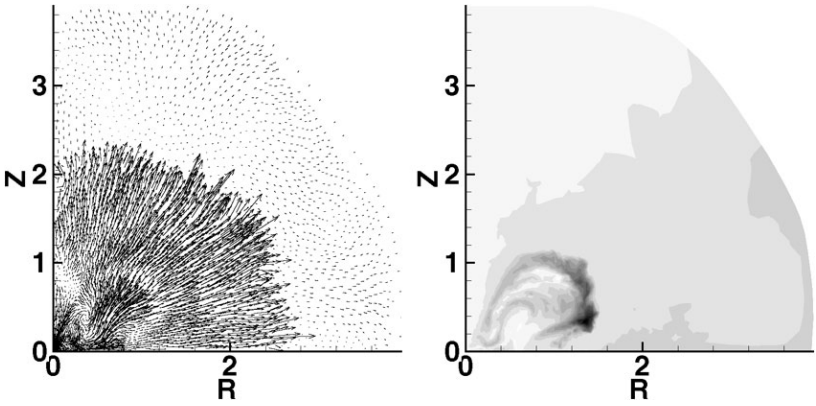

Fig. 2. Velocity field (left plot) and specific angular momentum $v_\varphi r$ (right plot) at $t = 0.191$s after turning on the magnetic field. The darker parts at the right plot correspond to the larger angular momentum.

with the energy near Fermi energy (it was taken $\approx 1/10$) takes part in the neutrino interaction processes.

3 Results

For the numerical simulations we have used implicit Lagrangian difference scheme on triangular grid with grid reconstruction. For the description of the applied numerical method see, for example, [3] and references therein. The number of knots of the triangular grid was about 5000.

As a first stage of the MRS mechanism we have calculated a collapse of rotating star, leading to differentially rotating configuration. After the collapse the star (core of evolved massive star) consists of an almost rigidly rotating neutron star with radius $\sim$ 10 km which rotates with the period ~ 0.001 sec, and large, differentially rotating envelope.

After formation of the differentially rotating configuration the initial poloidal magnetic field was switched on (Fig. 1).

The energy of the initial magnetic field was $E_{mag0} = 10^{-6} E_{grav}$. Where E_{mag0} - is the energy of the initial magnetic field, E_{grav} - is the gravitational energy of the collapsed star.

Due to the differential rotation the toroidal component of the magnetic field is increasing with time. The magnetic pressure grows and produces a compression MHD wave, which moves through the envelope with steeply decreasing density. Soon after appearing this wave transforms into the MHD shock, which throws away part of the matter of the envelope. The MHD shock front is clearly seen at the velocity field plot (Fig. 2 - left plot). The magnetic

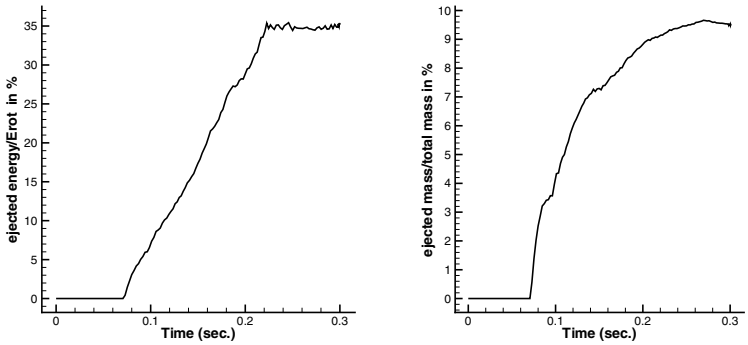

Fig. 3. Time evolution of the (ejected energy)/(rotational energy) in percent (left plot) and (ejected mass)/(total mass) in percent (right plot).

field transmits angular momentum of the neutron star outwards (Fig. 2 - right plot).

Results of our simulations show that the energy of the supernova explosion is about 1.12×10^{51} erg (35% of the rotational energy of the star). The explosion ejects about 0.11 $M_\odot$ ($\sim$ 9.7% of the mass of the star). At the Fig. 3 the time evolution of the ejected mass and ejected energy are presented.

Detailed description of the results of the simulations of the MRS will be published elsewhere.

Acknowledgement. This work was partially supported by the grant RFBR 02-02-16900. The authors would like to thank the Organizing Committee for support and hospitality.

References

1. N.V. Ardeljan, G.S. Bisnovatyi-Kogan, Yu.P. Popov: Astron. Zhurnal **56**, 1244 (1979)
2. N.V. Ardeljan, G.S. Bisnovatyi-Kogan, Yu.P. Popov, S.V. Chernigovsky: Sov. Astron. **64**, 761 (1987)
3. N.V. Ardeljan, K.V. Kosmachevskii: Comput. Math. and Model. **6**, 209 (1995)
4. G. Baum, C. Pethick, P. Sutherland: Astrophys. J. **170**, 197 (1971)
5. G.S. Bisnovatyi-Kogan: Astron. Zhurnal **47**, 813 (1970)
6. G.S. Bisnovatyi-Kogan, Yu.P. Popov, A.A. Samokhin: Astrophys. Space Sci. **41**, 287 (1976)
7. L.N. Ivanova, V.S. Imshennik, D.K. Nadyozhin: In: *Nauch. Inf. Astr. Sov. AN SSSR (Sci. Inf. of the Astr. Council of the Acad. Sci. USSR)* **13**, 3 (1969)
8. R. Malone, M.B. Johnson, H.A. Bethe: Astrophys. J. **199**, 741 (1975)
9. P. Schindler et al. : Astrophys. J. **313**, 531 (1987)

Nucleosynthesis in Black-Hole-Forming Supernovae

K. Nomoto[1], K. Maeda[1], H. Umeda[1], N. Tominaga[1], T. Ohkubo[1], J. Deng[1], P. A. Mazzali[1,2]

[1] Department of Astronomy & Research Center for the Early Universe, University of Tokyo, Tokyo, Japan;
nomoto@astron.s.u-tokyo.ac.jp
[2] Osservatorio Astronomico, Via Tiepolo, 11, 34131 Trieste, Italy

Summary. Stars more massive than $\sim 20 - 25$ $M_\odot$ form a black hole at the end of their evolution. Stars with non-rotating black holes are likely to collapse "quietly" ejecting a small amount of heavy elements (faint supernovae). In contrast, stars with rotating black holes are likely to give rise to very energetic supernovae (hypernovae). We present distinct nucleosynthesis features of these two types of "black-hole-forming" supernovae. Nucleosynthesis in hypernovae is characterized by larger abundance ratios (Zn,Co,V,Ti)/Fe and smaller (Mn,Cr)/Fe than normal supernovae, which can explain the observed trend of these ratios in extremely metal-poor stars. Nucleosynthesis in faint supernovae is characterized by a large amount of fall-back. We show that the abundance pattern of the recently discovered most Fe-poor star, HE0107-5240, and other extremely metal-poor carbon-rich stars are in good accord with those of black-hole-forming supernovae, but not pair-instability supernovae. This suggests that black-hole-forming supernovae made important contributions to the early Galactic (and cosmic) chemical evolution. Finally we discuss the nature of first (Pop III) Stars.

1 Hypernovae and Faint Supernovae

Among the important developments in recent studies of core-collapse supernovae are the discoveries of two distinct types of supernovae (SNe) (Fig. 1) [16, 23]: 1) very energetic SNe (hypernovae), whose kinetic energy (KE) exceeds 10^{52} erg, about 10 times the KE of normal core-collapse SNe (hereafter $E_{51} = E/10^{51}$ erg), and 2) very faint and low energy SNe ($E_{51} \lesssim 0.5$; faint supernovae). These two types of supernovae are likely to be black-hole-forming supernovae with rotating or non-rotating black holes. We compare their nucleosynthesis yields with the abundances of extremely metal-poor (EMP) stars to identify the Pop III (or first) supernovae. We show that the EMP stars, especially the C-rich class, are likely to be enriched by black-hole-forming supernovae.

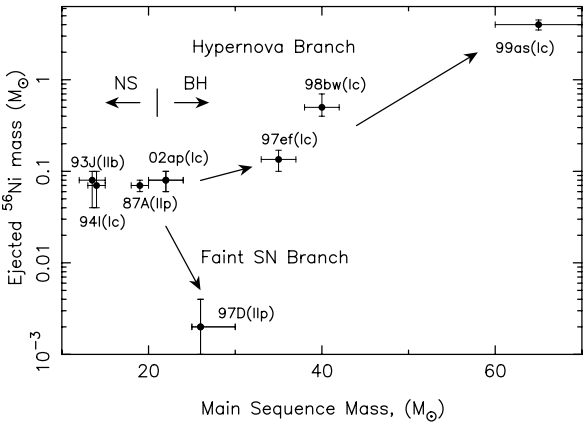

Fig. 1. The ejected ^{56}Ni mass as a function of the main sequence mass of the progenitors for several supernovae/hypernovae [16, 22, 23].

2 Nucleosynthesis in Hypernova Explosions

In core-collapse supernovae/hypernovae, stellar material undergoes shock heating and subsequent explosive nucleosynthesis. Iron-peak elements are produced in two distinct regions, which are characterized by the peak temperature, $T_{\rm peak}$, of the shocked material. For $T_{\rm peak} > 5 \times 10^9$ K, material undergoes complete Si burning whose products include Co, Zn, V, and some Cr after radioactive decays. For 4×10^9 K $< T_{\rm peak} < 5 \times 10^9$ K, incomplete Si burning takes place and its after decay products include Cr and Mn [9, 32].

2.1 Supernovae vs. Hypernovae

The right panel of Fig. 2 shows the composition in the ejecta of a 25 $M_\odot$ hypernova model ($E_{51} = 10$). The nucleosynthesis in a normal 25 $M_\odot$ SN model ($E_{51} = 1$) is also shown for comparison in the left panel of Fig. 2 [33].

We note the following characteristics of nucleosynthesis with very large explosion energies [19, 20, 21, 25]:

1. Both complete and incomplete Si-burning regions shift outward in mass compared with normal supernovae, so that the mass ratio between the complete and incomplete Si-burning regions becomes larger. As a result, higher energy explosions tend to produce larger [(Zn, Co, V)/Fe] and smaller [(Mn, Cr)/Fe], which can explain the trend observed in very metal-poor stars [36].
2. In the complete Si-burning region of hypernovae, elements produced by α-rich freeze out are enhanced. Hence, elements synthesized through capturing of α-particles, such as ^{44}Ti, ^{48}Cr, and ^{64}Ge (decaying into ^{44}Ca, ^{48}Ti, and ^{64}Zn, respectively) are more abundant.

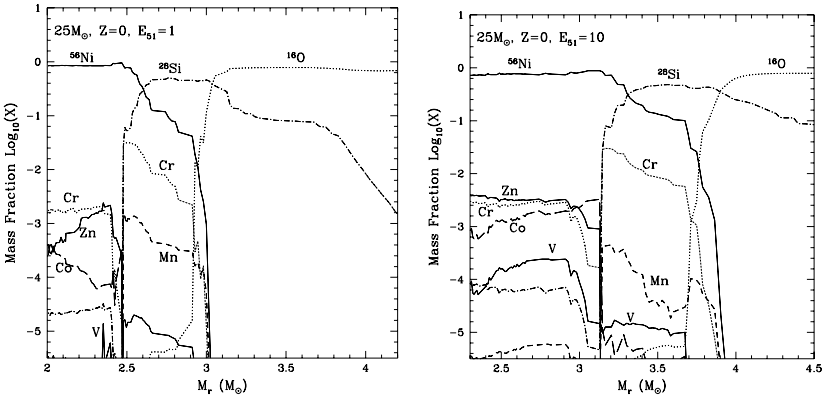

Fig. 2. Abundance distribution plotted against the enclosed mass M_r after the explosion of Pop III 25 $M_\odot$ stars with $E_{51} = 1$ (left) and $E_{51} = 10$ (right) [33].

3. Oxygen burning takes place in more extended regions for the larger KE. Then more O, C, Al are burned to produce a larger amount of burning products such as Si, S, and Ar. Therefore, hypernova nucleosynthesis is characterized by large abundance ratios of [Si,S/O], which can explain the abundance feature of M82 [34].

2.2 Hypernovae and Zn, Co, Mn, Cr

Hypernova nucleosynthesis may have made an important contribution to Galactic chemical evolution. In the early Galactic epoch when the Galaxy was not yet chemically well-mixed, [Fe/H] may well be determined by mostly a single SN event [3]. The formation of metal-poor stars is supposed to be driven by a supernova shock, so that [Fe/H] is determined by the ejected Fe mass and the amount of circumstellar hydrogen swept-up by the shock wave [27]. Then, hypernovae with larger E are likely to induce the formation of stars with smaller [Fe/H], because the mass of interstellar hydrogen swept up by a hypernova is roughly proportional to E [27, 30] and the ratio of the ejected iron mass to E is smaller for hypernovae than for normal supernovae.

In the observed abundances of halo stars, there are significant differences between the abundance patterns in the iron-peak elements below and above [Fe/H]$\sim -2.5 - -3$.

1. For [Fe/H] $\lesssim -2.5$, the mean values of [Cr/Fe] and [Mn/Fe] decrease toward smaller metallicity, while [Co/Fe] increases [17, 27].
2. [Zn/Fe]~ 0 for [Fe/H] $\simeq -3$ to 0 [31], while at [Fe/H] < -3.3, [Zn/Fe] increases toward smaller metallicity [4, 26].

The larger [(Zn, Co)/Fe] and smaller [(Mn, Cr)/Fe] in the supernova ejecta can be realized if the mass ratio between the complete Si burning region and

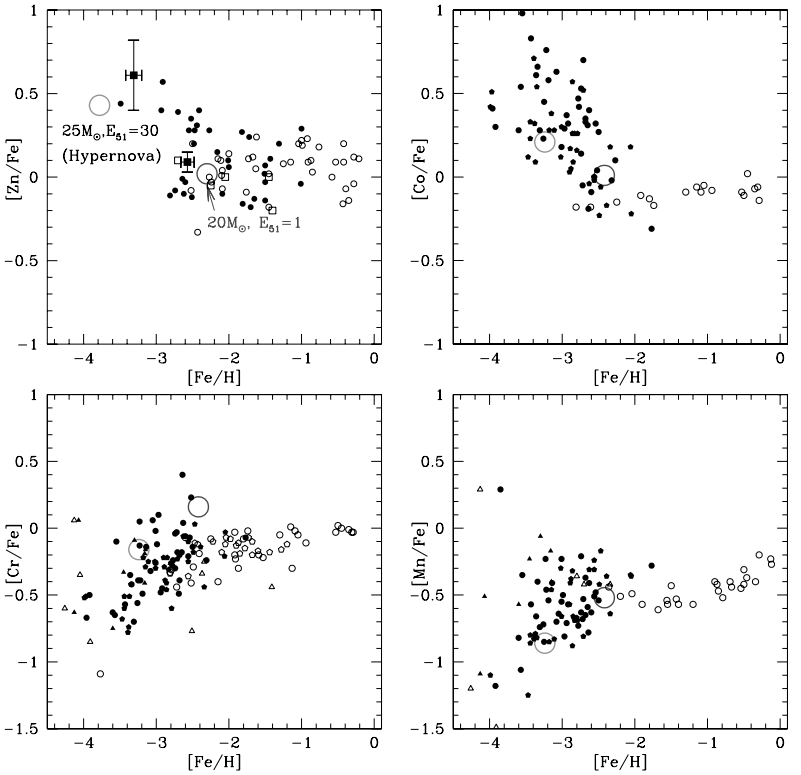

Fig. 3. Observed abundance ratios of [Zn, Co, Cr, Mn/Fe] vs [Fe/H] compared with (20M, $E_{51} = 1$) and (25M, E_{51}=30) models (large open circles) [36].

the incomplete Si burning region is larger, or equivalently if deep material from the complete Si-burning region is ejected by mixing or aspherical effects. This can be realized if:

1. The mass cut between the ejecta and the compact remnant is located at smaller M_r [18];
2. E is larger to move the outer edge of the complete Si burning region to larger M_r [19]; or
3. Asphericity in the explosion is larger [14].

Among these possibilities, a large explosion energy E enhances α-rich freeze out, which results in an increase of the local mass fractions of Zn and Co, while Cr and Mn are not enhanced [25, 33]. Models with $E_{51} = 1$ do not produce sufficiently large [Zn/Fe]. To be compatible with the observations of [Zn/Fe] ~ 0.5, the explosion energy must be much larger, i.e., $E_{51} \gtrsim 20$ for $M \gtrsim 20$ M$_\odot$, i.e., hypernova-like explosions of massive stars are responsible for the production of Zn.

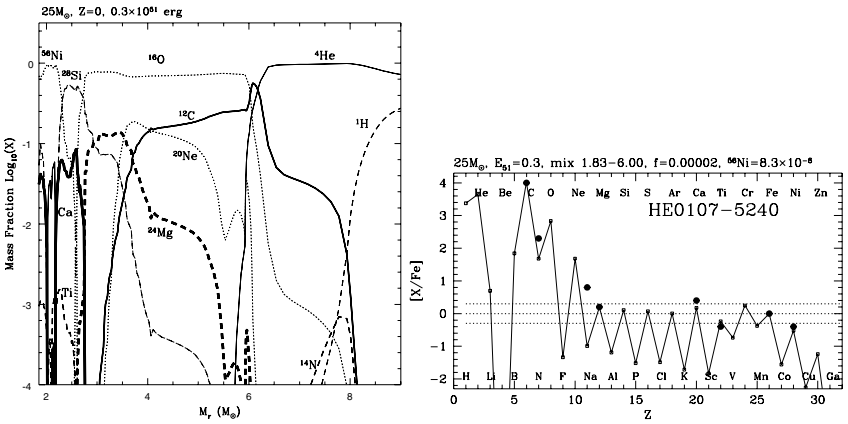

Fig. 4. (left) The post-explosion abundance distributions for the 25 $M_\odot$ model with the explosion energy $E_{51} = 0.3$ [35]. (right) Elemental abundances of the C-rich most Fe deficient star HE0107-5240 (filled circles), compared with a theoretical supernova yield [35].

In the hypernova models, the overproduction of Ni, as found in the simple "deep" mass-cut model, can be avoided [25]. Therefore, if hypernovae made significant contributions to the early Galactic chemical evolution, it could explain the large Zn and Co abundances and the small Mn and Cr abundances observed in very metal-poor stars (Fig. 3) [36].

3 Extremely Metal-Poor (EMP) Stars and Faint Supernovae

Recently the most Fe deficient and C-rich low mass star, HE0107-5240, was discovered [6]. This star has [Fe/H] = −5.3 but its mass is as low as 0.8 $M_\odot$. This would challenge the recent theoretical arguments that the formation of low mass stars, which should survive until today, is suppressed below [Fe/H] = −4 [29].

The important clue to this problem is the observed abundance pattern of this star. This star is characterized by a very large ratios of [C/Fe] = 4.0 and [N/Fe] = 2.3, while the abundances of elements heavier than Mg are as low as Fe [6]. Interestingly, this is not the only extremely metal poor (EMP) stars that have the large C/Fe and N/Fe ratios, but several other such stars have been discovered [28]. Therefore the reasonable explanation of the abundance pattern should explain other EMP stars as well. We show that the abundance pattern of C-rich EMP stars can be reasonably explained by the nucleosynthesis of $20 - 130$ $M_\odot$ supernovae with various explosion energies and the degree of mixing and fallback of the ejecta.

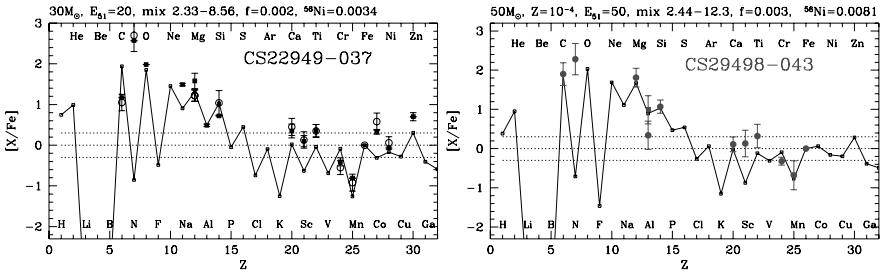

Fig. 5. (left) Elemental abundances of CS 22949-037 (open circles for Norris et al. 2001 [24], and solid squares for Depagne et al. 2002 [7]), compared with a theoretical supernova yield [35, 36]. (right) Same as the left panel but for CS 29498-043 [2].

3.1 The Most Fe-poor Star HE0107-5240

We consider a model that C-rich EMP stars are produced in the ejecta of (almost) metal-free supernova mixed with extremely metal-poor interstellar matter. We use Pop III pre-supernova progenitor models, simulate the supernova explosion and calculate detailed nucleosynthesis [35].

In Fig. 4 (right) we show that the elemental abundances of one of our models are in good agreement with HE0107-5240, where the progenitor mass is 25 $M_\odot$ and the explosion energy $E_{51} = 0.3$ [35].

In this model, explosive nucleosynthesis takes place behind the shock wave that is generated at $M_r = 1.8$ $M_\odot$ and propagates outward. The resultant abundance distribution is seen in Fig. 4 (left), where M_r denotes the Lagrangian mass coordinate measured from the center of the pre-supernova model [35]. The processed material is assumed to mix uniformly in the region from $M_r = 1.8$ $M_\odot$ and 6.0 $M_\odot$. Such a large scale mixing was found to take place in SN1987A and various explosion models [8, 11]. Almost all materials below $M_r = 6.0$ $M_\odot$ fall back to the central remnant and only a small fraction ($f = 2\times 10^{-5}$) is ejected from this region. The ejected Fe mass is 8×10^{-6} $M_\odot$.

The CNO elements in the ejecta were produced by pre-collapse He shell burning in the He-layer, which contains 0.2 $M_\odot$ ^{12}C. Mixing of H into the He shell-burning region produces 4×10^{-4} $M_\odot$ ^{14}N. On the other hand, only a small amount of heavier elements (Mg, Ca, and Fe-peak elements) are ejected and their abundance ratios are the average in the region of $M_r = 1.8 - 6.0$ $M_\odot$. The sub-solar ratios of [Ti/Fe] $= -0.4$ and [Ni/Fe] $= -0.4$ are the results of the relatively small explosion energy ($E_{51} = 0.3$). With this "mixing and fallback", the large C/Fe and C/Mg ratios observed in HE0107-5240 are well reproduced [35].

In this model, N/Fe appears to be under produced. However, N can be produced inside the EMP stars through the C-N cycle, and brought up to the surface during the first dredge up stage while becoming a red-giant star [5].

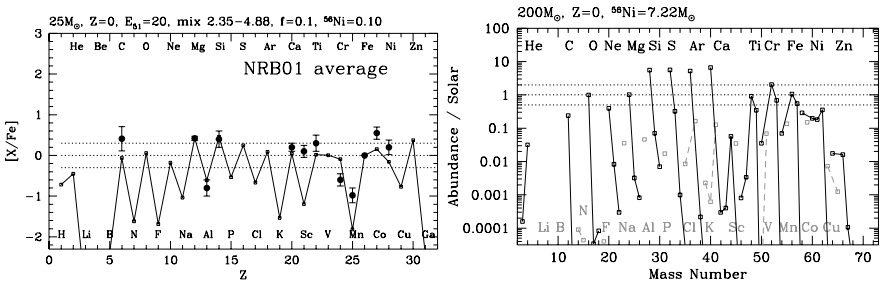

Fig. 6. (left) Averaged elemental abundances of stars with [Fe/H] = −3.7 [24] compared with a theoretical supernova yield [36]. (right) Yields of a pair-instability supernova from the 200 $M_\odot$ star [33].

3.2 Carbon-rich EMP Stars: CS 22949-037 and CS 29498-043

The mixing and fallback is commonly required to reproduce the abundance pattern of typical EMP stars. In Fig. 5 (left) we show a model, which is in good agreement with CS22949-037 [35]. This star has [Fe/H] = −4.0 and also C, N-rich [7, 24], though C/Fe and N/Fe ratios are smaller than HE0107-5240. The model is the explosion of a 30 $M_\odot$ star with $E_{51} = 20$. In this model, the mixing region (M_r = 2.33 - 8.56 $M_\odot$) is chosen to be smaller than the entire He core (M_r = 13.1 $M_\odot$) in order to reproduce relatively large Mg/Fe and Si/Fe ratios.

Similar degree of the mixing, but for a more massive progenitor, would also reproduce the abundances of CS29498-043 [2], which shows similar abundance pattern (Fig. 5: right).

We assume a larger fraction of ejection than HE0107-5240, 0.2%, from the mixed region for CS22949-037, because the C/Fe and N/Fe ratios are smaller. The ejected Fe mass is 0.003 $M_\odot$. The larger explosion energy model is favored for explaining the large Zn/Fe, Co/Fe and Ti/Fe ratios [33].

Without mixing, elements produced in the deep explosive burning regions, such as Zn, Co, and Ti, would be under produced. Without fallback the abundance ratios of heavy elements to lighter elements, such as Fe/C, Fe/O, and Mg/C would be too large. In this model, Ti, Co, Zn and Sc are still under produced. However, these elements may be enhanced efficiently in the aspherical explosions [12, 13, 14].

3.3 EMP Stars with a Typical Abundance Pattern

Similarly, the "mixing and fall back" process can reproduce the abundance pattern of the typical EMP stars without enhancement of C and N. Fig. 6 (left) shows that the averaged abundances of [Fe/H] = −3.7 stars in Norris et al. [24] can be fitted well with the model of 25 $M_\odot$ and $E_{51} = 20$ but larger fraction ($\sim$ 10%) of the processed materials in the ejecta. This yield [36] is

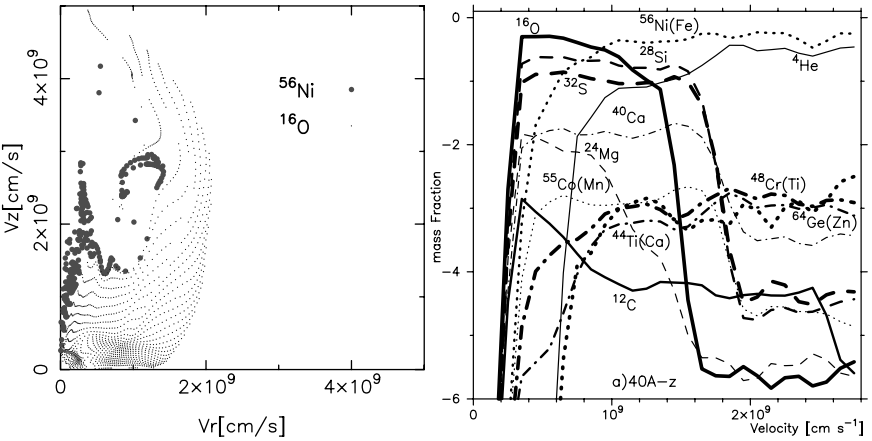

Fig. 7. Left: Distributions of ^{56}Ni (which decays into ^{56}Fe: filled circles) and ^{16}O (dots). The mass elements in which the mass fraction of each isotope exceeds 0.1 are plotted. Right: Mass fractions of selected isotopes in the velocity space along the z-axis [13, 14].

recommendable as averaged core-collapse SN yields for the use of chemical evolution models.

3.4 Aspherical Explosions

Some observations have indicated that hypernovae ever studied show asphericity to some extent (e.g., [15]). The "mixing and fall-back" effect may also be effectively realized in non-spherical explosions accompanying energetic jets (e.g., [12, 13, 14]). Compared with the spherical model with the same $M_{\rm cut}(i)$ and E, the shock is stronger (weaker) and thus temperatures are higher (lower) in the jet (equatorial) direction. As a result, a larger amount of complete Si-burning products are ejected in the jet direction, while only incomplete Si-burning products are ejected in the equatorial direction (Fig. 7). In total, complete Si-burning elements can be enhanced [13, 14].

The jet-induced explosion results in angle-dependent distribution of nucleosynthetic products as shown in Fig. 7. The distribution of ^{56}Ni (which decays into ^{56}Fe) is elongated in the jet direction, while that of ^{16}O is concentrated in the central region.

Zn and Co are ejected at higher velocities than Mn and Cr, so that the latter accrete onto the central remnant more easily. As a consequence, [Zn/Fe] and [Co/Fe] are enhanced, while [Mn/Fe] and [Cr/Fe] are suppressed.

4 The First Stars

It is of vital importance in current astronomy to identify the first generation stars in the Universe, i.e., totally metal-free, Pop III stars. The impact of the formation of Pop III stars on the evolution of the Universe depends on their typical masses. Recent numerical models have shown that, the first stars are as massive as ~ 100 $M_\odot$ [1]. The formation of long-lived low mass Pop III stars may be inefficient because of slow cooling of metal free gas cloud, which is consistent with the failure of attempts to find Pop III stars.

If the most Fe deficient star, HE0107-5240, is a Pop III low mass star that has gained its metal from a companion star or interstellar matter [37], would it mean that the above theoretical arguments are incorrect and that such low mass Pop III stars have not been discovered only because of the difficulty in the observations?

Based on the results in the earlier section, we propose that the first generation supernovae were the explosion of $\sim 20-130$ $M_\odot$ stars and some of them produced C-rich, Fe-poor ejecta. Then the low mass star with even [Fe/H] < -5 can form from the gases of mixture of such a supernova ejecta and the (almost) metal-free interstellar matter, because the gases can be efficiently cooled by enhanced C and O ([C/H] ~ -1).

We have shown that the ejecta of core-collapse supernova explosions of $20-130$ $M_\odot$ stars can well account for the abundance pattern of EMP stars. In contrast, the observed abundance patterns cannot be explained by the explosions of more massive, $130-300$ $M_\odot$ stars. These stars undergo pair-instability supernovae (PISNe) and are disrupted completely (e.g., [10, 33]), which cannot be consistent with the large C/Fe observed in HE0107-5240 and other C-rich EMP stars. The abundance ratios of iron-peak elements ([Zn/Fe] < -0.8 and [Co/Fe] < -0.2) in the PISN ejecta (Fig. 6, [10, 33]) cannot explain the large Zn/Fe and Co/Fe in the typical EMP stars [17, 24, 26] and CS22949-037 either. Therefore the supernova progenitors that are responsible for the formation of EMP stars are most likely in the range of $M \sim 20-130$ $M_\odot$, but not more massive than 130 $M_\odot$. This upper limit depends on the stability of massive stars.

Acknowledgement. Detailed yields are seen at http://supernova.astron.s.u-tokyo.ac.jp/∼umeda/data.html. This work has been supported in part by the grant-in-Aid for COE Scientific Research (14047206, 14540223, 15204010, 16042201, 16540229) of the Ministry of Education, Science, Culture, Sports, and Technology in Japan.

References

1. T. Abel, G.L. Bryan, M.L. Norman: Science **295**, 93 (2002)
2. W. Aoki, S.G. Ryan, T.C. Beers, H. Ando: Astrophys. J. **567**, 1166 (2002)
3. J. Audouze, J. Silk: Astrophys. J. Lett. **451**, L49 (1995)

4. L.A.J. Blake, S.G. Ryan, J.E. Norris, T.C. Beers: Nuc. Phys. **688**, 502 (2001)
5. A.I. Boothroyd, I.-J. Sackmann: Astrophys. J. **510**, 217 (1999)
6. N. Christlieb et al. : Nature **419**, 904 (2002)
7. E. Depagne et al. : Astron. Astrophys. **390**, 187 (2002)
8. I. Hachisu, T. Matsuda, K. Nomoto, T. Shigeyama: Astrophys. J. Lett. **358**, L57 (1990)
9. M. Hashimoto, K. Nomoto, T. Shigeyama: Astron. Astrophys. **210**, L5 (1989)
10. A. Heger, S.E. Woosley: Astrophys. J. **567**, 532 (2002)
11. K. Kifonidis, T. Plewa, H.-Th. Janka, E. Muller: Astrophys. J. Lett. **531**, L123 (2000)
12. K. Maeda, T. Nakamura, K. Nomoto, P.A. Mazzali, F. Patat, I. Hachisu: Astrophys. J. **565**, 405 (2002)
13. K. Maeda, K. Nomoto: Nuc. Phys. **A718**, 167 (2003)
14. K. Maeda, K. Nomoto: Astrophys. J. **598**, 1163 (2003)
15. K. Maeda, P.A. Mazzali, J. Deng, K. Nomoto, Y. Yoshii, H. Tomita, Y. Kobayashi: Astrophys. J. **593**, 931(2003)
16. P.A. Mazzali, K. Nomoto, J. Deng, K. Maeda, K. Iwamoto, A.V. Filippenko, R.T. Foley: In: these Proceedings
17. A. McWilliam, G.W. Preston, C. Sneden, L. Searle: Astron. J. **109**, 2757 (1995)
18. T. Nakamura, H. Umeda, K. Nomoto, F.-K. Thielemann, A. Burrows: Astrophys. J. **517**, 193 (1999)
19. T. Nakamura, H. Umeda, K. Iwamoto, K. Nomoto, M. Hashimoto, R.W. Hix, F.-K. Thielemann: Astrophys. J. **555**, 880 (2001)
20. K. Nomoto et al. : In: *Supernovae and Gamma Ray Bursts*, eds. M. Livio et al. (Cambridge Univ. Press: Cambridge, 2001) p. 144
21. K. Nomoto, K. Maeda, H. Umeda, T. Nakamura: In: *The Influence of Binaries on Stellar Populations Studies*, ed. D. Vanbeveren (Kluwer: Dordrecht, 2001) p. 507
22. K. Nomoto, K. Maeda, H. Umeda, T. Ohkubo, J. Deng, P.A. Mazzali: In: *IAU Symp 212, A Massive Star Odyssey, from Main Sequence to Supernova*, eds. V.D. Hucht, A. Herrero, C. Esteban (ASP: San Francisco, 2003) p. 395
23. K. Nomoto, K. Maeda, P.A. Mazzali, H. Umeda, J. Deng, K. Iwamoto: astro-ph 0308136 (2003)
24. J.E. Norris, S.G. Ryan, T.C. Beers: Astrophys. J. **561**, 1034 (2001)
25. T. Ohkubo, H. Umeda, K. Nomoto: Nuc. Phys. **A718**, 632 (2003)
26. F. Primas et al. : In: *The First Stars*, eds. A. Weiss, et al. (Springer: Berlin, 2000) p. 51
27. S.G. Ryan, J.E. Norris, T.C. Beers: Astrophys. J. **471**, 254 (1996)
28. S.G. Ryan: astro-ph 0211608 (2002)
29. R. Schneider, A. Ferrara, P. Natarajan, K. Omukai: Astrophys. J. **571**, 30 (2002)
30. T. Shigeyama, T. Tsujimoto: Astrophys. J. Lett. **507**, L135 (1998)
31. C. Sneden, R.G. Gratton, D.A. Crocker: Astron. Astrophys. **246**, 354 (1991)
32. F.-K. Thielemann, K. Nomoto, M. Hashimoto: Astrophys. J. **460**, 408 (1996)
33. H. Umeda, K. Nomoto: Astrophys. J. **565**, 385 (2002)
34. H. Umeda, K. Nomoto, T. Tsuru, H. Matsumoto: Astrophys. J. **578**, 855 (2002)
35. H. Umeda, K. Nomoto: Nature **422**, 871 (2003)
36. H. Umeda, K. Nomoto: astro-ph 0308029 (2003)
37. Y. Yoshii: Astron. Astrophys. **97**, 280 (1981)

Nucleosynthesis in Multi-Dimensional Simulations of SNII

C. Travaglio[1,2], K. Kifonidis[1] and E. Müller[1]

[1] Max-Planck Institut für Astrophysik, Karl-Schwarzschild Str. 1, 85741 Garching bei München, Germany
[2] INAF-Osservatorio Astronomico di Pino Torinese, Strada Osservatorio 20, 10025 Torino, Italy;
travaglio@to.astro.it

Summary. We investigate explosive nuclear burning in core collapse supernovae by coupling a tracer particle method to one- and two-dimensional Eulerian hydrodynamic calculations. Adopting the most recent experimental and theoretical nuclear data, we compute the nucleosynthetic yields for 15 $M_{\odot}$ stars with solar metallicity, by post-processing the temperature and density history of advected tracer particles. We compare our results to 1D calculations published in the literature.

1 Introduction

The pre- and post-explosive nucleosynthesis of massive stars has been studied extensively by several groups over the last years (see [6, 10, 12, 13], and the references therein). Although a lot of work has been performed in this field, computed nucleosynthetic yields are still affected by numerous uncertainties. The impact of multidimensional hydrodynamics has not been investigated in detail so far. In addition, among the isotopes whose yields are known to depend sensitively on the explosion mechanism, and thus cannot be predicted accurately at present, are key nuclei, like ^{56}Ni and ^{44}Ti, that are of crucial importance for the evolution of supernova remnants and for the chemical evolution of galaxies.

2 Hydrodynamic Models and Marker Particle Method

The nucleosynthesis calculations presented in this work are based on one and two-dimensional hydrodynamic models of SNe which follow the revival of the stalling shock, which forms after iron core collapse, and its propagation through the star from 20 ms up to a few seconds after core bounce (when the explosion energy has saturated and all important nuclear reactions have frozen out). The simulations are started from post-collapse models of Rampp & Janka (private communication), who followed core-collapse and bounce in the 15 $M_{\odot}$, $Z = Z_{\odot}$ progenitors of [13] and [6]. We employ the HERAKLES code, which solves the hydrodynamic equations in 1, 2 or 3 spatial dimensions

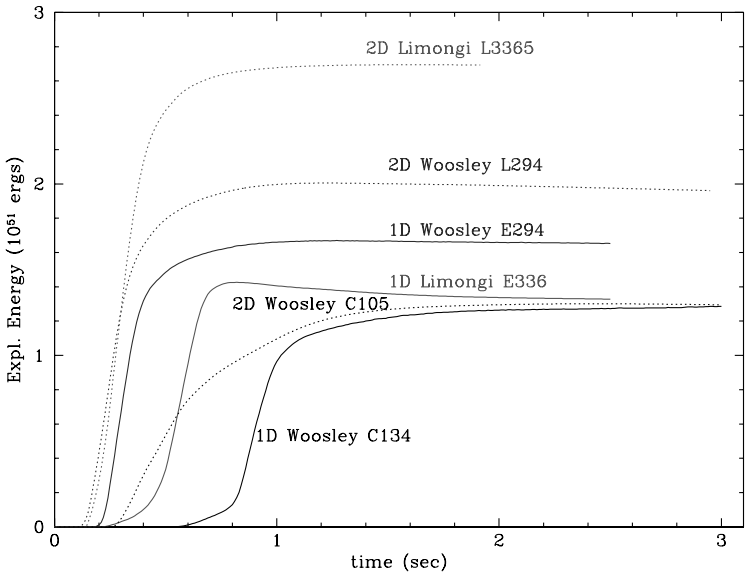

Fig. 1. Explosion energies for the different models discussed in the text.

with the direct Eulerian version of the Piecewise Parabolic Method [2], and which incorporates the light-bulb neutrino treatment and the equation of state of [3] (for more details see [5], and the references therein). The main advantages of our approach are that we drive the shock by accounting for neutrino-matter interactions in the layers outside the newly born neutron star, instead of using a piston (see, e.g., [13]) or a "thermal bomb," and the possibility to perform calculations from one up to three spatial dimensions.

Choosing a hydrodynamic scheme for computing multi-dimensional hydrodynamic models that include the nucleosynthesis, one faces the dilemma of using either a Lagrangian or an Eulerian method. Since nuclear networks with hundreds of isotopes are prohibitively expensive in terms of CPU time and memory for multi-dimensional calculations, such networks can only be solved in a post-processing step (the energy source term due to nuclear burning can usually be calculated with a small network online with the hydrodynamics, and may even be neglected completely in some cases, depending on the structure of the progenitor). Using an Eulerian scheme (where the grid is fixed in space) or even adaptive schemes (in which the grid automatically adapts to resolve steep gradients in the solution) the problem arises how one should obtain the necessary data for the post-processing calculations. We do this by adding a "Lagrangian component" to our Eulerian scheme in the form of marker particles that we passively advect with the flow in the course of the Eulerian calculation, recording their T and ρ history by interpolating the corresponding quantities from the underlying Eulerian grid. A similar method has been adopted in a previous study of multi-dimensional nucleosynthesis

Table 1. Parameters of models, using the [13](WW95) and [6](LSC00) progenitors.

Model	Zones	$N_{markers}$	$L^0_{\nu_e,52}$	$E_{exp,51}$	t_{exp} (ms)	^{56}Ni ($M_\odot$)
E294	2000	1024	2.940	1.46	230	0.192
L294	400×180	8000	2.940	1.99	125	0.120
E336	2000	1024	3.365	1.33	260	0.234
L3365	400×180	8000	3.365	2.69	150	0.146
C134	2000	1024	1.344	1.28	600	0.085
C105	400×180	8000	1.050	1.29	280	0.064

in core collapse SNe by [8], in very massive stars [7], and in Type Ia SNe [9]. For our 1D and 2D calculations we have used 1024 and 8000 marker particles, respectively. They are distributed homogeneously in mass throughout the progenitor's Fe core, Si, O, and C shells assuming the composition of the progenitor at the corresponding mass coordinate as the initial composition of the respective tracer particle.

3 Nucleosynthesis: Results and Perspectives

Given the temperature and density history of individual marker particles we can calculate their nucleosynthetic evolution and compute the total yields (including the decays of unstable isotopes) as a sum over all particles. The reaction network employed for our nucleosynthesis calculations contains 296 nuclear species, from neutrons, protons, and α-particles to ^{78}Ge (F.-K. Thielemann, private communication). The reaction rates include experimental and theoretical nuclear data as well as weak interaction rates.

So far we have investigated six explosion models for their nucleosynthetic yields: a one-dimensional (E294) and a corresponding two-dimensional (L294) model that made use of model s15s7b of [13], with high energy of the explosion. A second pair of a one (E336) and two-dimensional (E3365) simulation for the 15 $M_\odot$ [6] progenitor. Also in this second case the explosion energy obtained is high. Finally, a third pair of a one (C134) and two-dimensional (C105) simulation for the 15 $M_\odot$ s15s7b of [13], but with a much lower explosion energy. The properties of these models are given in Table 1, where $L^0_{\nu_e,52}$ is the electron neutrino luminosity (in units of 10^{52} erg/s), $E_{exp,51}$ is the explosion energy (in units of 10^{51} erg), and t_{exp} is the explosion time scale (in ms) defined as the time after the start of the simulation when the explosion energy exceeds 10^{49} erg (for a detailed explanation of the neutrino parameters see [3, 5]). In the last column of Table 1 we also added the ^{56}Ni mass obtained using these hydrodynamic models and the nucleosynthesis calculations described above.

Figure 1 shows the evolution of the explosion energy for the six models, using the same neutrino luminosity for the 1D and 2D model of the same

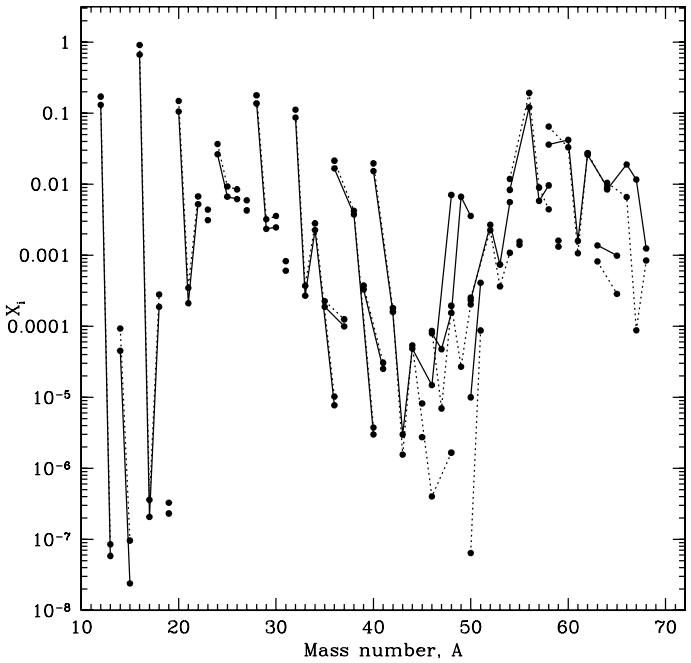

Fig. 2. Final mass fractions obtained for the 1D (*dotted line*) and 2D simulation (*solid line*) as a function of the atomic number, for the cases E294 and L294.

progenitor. The [6] progenitor needs higher neutrino luminosity to explode, mainly due to the fact that it has a more compact core. The C134 and C105 models evolve much slower in time (as an effect of a lower explosion energy). Our goal is to investigate the consequences on nucleosynthesis (in particular mixing can play a major role under these conditions).

In Fig. 2 we compare the yields of the 1D and 2D simulations (E294 and L294, respectively) for the [13] progenitor. The differences, which are apparently negligible in case of the lighter nuclei and small for the heavier ones, are mainly due to the on average higher temperatures in the 2D simulation, i.e. more free neutrons are available in the innermost layers of the 2D simulation. This results in higher production factors for isotopes very sensitive to neutron captures, like e.g. ^{46,48}Ca, ^{49,50}Ti, ^{50,51}V, ^{54}Cr, and ^{67}Zn. A more detailed discussion on nucleosynthesis calculation in multidimensional simulations of SNII is included in Travaglio et al. (2004, in preparation), where also a network extended to heavier isotopes has been considered.

For the cases with high energy of the explosion, the reason for the rather small differences in the yields between the 1D and 2D simulations are the high initial neutrino luminosities, that we adopted for our calculations, and their rapid exponential decline. This leads to very rapid (and energetic) explosions. The short explosion time scale prevents the convective bubbles,

which form due to the negative entropy gradient in the neutrino-heated region, to merge to large-scale structures that can lead to global anisotropies, and hence to significant differences compared to the 1D case. Lowering the neutrino luminosities (and the explosion energies), as in the cases C134 and C105, we obtain stronger convection that strongly distorts the shock wave by developing large bubbles of neutrino-heated material (see [3, 4] for examples). Adopting constant core luminosities instead of an exponential law, we can produce models where the phase of convective overturn lasts for several turn-over times and which exhibit the vigorous boiling behavior reported by [1]. Such cases can finally develop global anisotropies, showing a dominance of the $m = 0$, $l = 1$ mode of convection (see [11]). As a consequence, convection can lead to large deviations from spherical symmetry, and thus to larger differences in the final yields than those visible in Fig. 2. We are currently investigating such models in more detail.

References

1. A. Burrows, J. Hayes, B.A. Fryxell: Astrophys. J. **450**, 830 (1995)
2. P. Colella, P.R. Woodward: J. Comput. Phys. **54**, 174 (1984)
3. H.-Th. Janka, E. Müller: Astron. Astrophys. **306**, 167 (1996)
4. K. Kifonidis, T. Plewa, H.-Th. Janka, E. Müller: Astrophys. J. Lett. **531**, L123 (2000)
5. K. Kifonidis, T. Plewa, H.-Th. Janka, E. Müller: Astron. Astrophys. **408**, 621 (2003)
6. M. Limongi, O. Straniero, S. Chieffi: Astrophys. J. Suppl. **129**, 625 (2000)
7. K. Maeda, T. Nakamura, K. Nomoto, P. Mazzali, F. Patat, I. Hachisu: Astrophys. J. **565**, 405 (1992)
8. S. Nagataki, M.-A. Hashimoto, K. Sato, S. Yamada: Astrophys. J. **486**, 1026 (1997)
9. J. Niemeyer, M. Reinecke, C. Travaglio, W. Hillebrandt 2002: In Workshop *From Twilight to Highlight: The Physics of Supernovae*, p. 151
10. T. Rauscher, A. Heger, R.D. Hoffman, S.E. Woosley: Astrophys. J. **576**, 323 (2002)
11. L. Scheck, T. Plewa, H.-Th. Janka, K. Kifonidis, E. Müller: astro-ph 0307352
12. F.-K. Thielemann, K. Nomoto, M.-A. Hashimoto: Astrophys. J. **460**, 408 (1996)
13. S.E. Woosley, T.A. Weaver: Astrophys. J. Suppl. **101**, 181 (1995)

^{56}Ni Mass in Type IIP SNe: Light Curves and Hα Luminosity Diagnostics

A. Elmhamdi[1], N.N. Chugai[2], and I.J. Danziger[3]

[1] SISSA / ISAS , via Beirut 4, 34014 Trieste, Italy
elmhamdi@sissa.it
[2] Institute of Astronomy RAS, Pyatnitskaya 48, 109017 Moscow, Russia
[3] Osservatorio Astronomico di Trieste, Via G.B.Tiepolo 11, 34131 Trieste, Italy

Summary. We analyze late-time observations, available photometry and spectra, of a sample of type II plateau supernovae (SNe IIP). The possibility of using Hα luminosity at the nebular epoch as a tracer of ^{56}Ni mass in this class of objects is investigated, yielding a consistency with the photometry-based estimates within 20%. Interesting correlations are found and their impacts on our present understanding of the physics of core collapse SNe are discussed.

1 Results and Discussion

The study of SNe IIP (i.e., optical properties, asymmetry, clumping, nucleosynthesis and yields) provides constraints on the explosion models and pre-supernova parameters. In particular, the ^{56}Ni mass is one of the crucial parameters since it presumably depends on the presupernova structure and the explosion model [1].

We select a sample of type IIP SNe on the basis of available photometry and spectra, especially at latter epochs. In Fig. 1(left) we display the absolute $V-$light curves of the SNe sample together with that of SN 1987A. We adopt unique distance determination methodology, namely using the recession velocity of the host galaxy corrected for Local Group in fall onto the Virgo Cluster and assuming a Hubble constant H_0=70 km s^{-1}Mpc^{-1}. Galactic extinction is removed using the map of galactic dust extinction by Schlegel et al. [7], while the host galaxy reddening is estimated from the "$B-V$" and "$V-R$" color excess compared to the intrinsic color curves of SN 1987A. This is based on the fact that at the late photospheric phase, through the end of the recombination phase, SNe IIP seem to follow color evolution similar to SN 1987A [8].

The computed late time decline slopes, in the $150-400$ d time range, are consistent with the radioactive decay of ^{56}Co and consequent trapping of the gamma-rays. Indeed a mean value of about $<\gamma^V> \simeq 0.99$ ($\pm$0.13) for the sample SNe is measured.

Once we fix the points related to the extinction and distance, which are crucial when dealing with a SN-sample study, we proceed with computing the amounts of ejected ^{56}Ni using the absolute $V-$light curve of SN 1987A

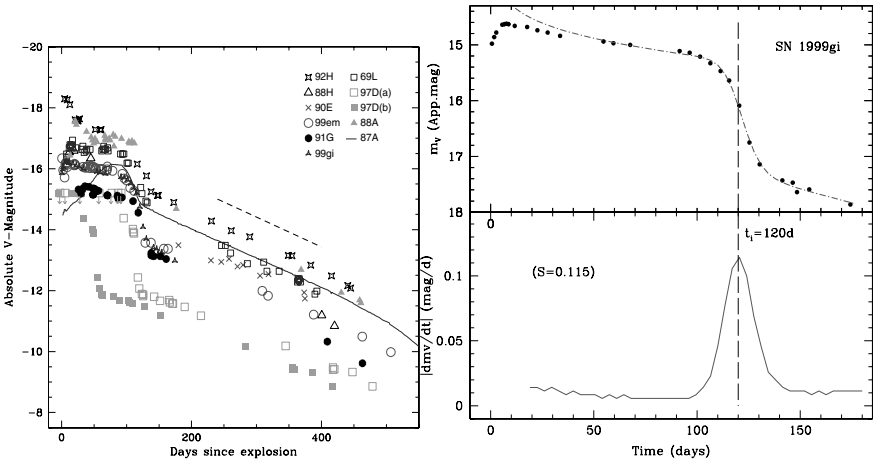

Fig. 1. Left: M_V light curves of the SNe sample. The dashed line shows the slope for ^{56}Co decay. Right: determination of the steepness and inflection time for the case of SN 1999gi (data from Leonard et al. [6]).

as template (in the 120−400 days time range). We found a range from lower values for SN 1999eu and SN 1997D to a higher one for SN 1992H ($[0.003 - 0.13]$ $M_\odot$), with an average of about 0.05 $M_\odot$. These results combined with the emergence of the extremely faint and bright events (see also the chapters by Pastorello and by Hamuy in these Proceedings) tend to change the general belief about the ^{56}Ni production in type II SNe (i.e. all eject $\sim$ 0.07 $M_\odot$). The above facts are extremely important for modeling the chemical evolution of galaxies since they impose constraints on the iron production.

Analyzing the absolute light curves of the sample events, we introduce a new parameter, called "*steepness*" and defined as $S = -dM_V/dt$, which describes the shape of the light curves and provides a way to measure the decay rate at the inflection point. The light curves in the transition period from plateau to radioactive tail are approximated by a sum of plateau and radioactive terms:

$$F = A\frac{(t/t_0)^p}{1+(t/t_0)^q} + B\exp(-t/111.26), \tag{1}$$

where A, B, t_0, p and q are parameters derived by the χ^2 minimization technique in the sensitive interval $t_\mathrm{i} \pm 50$ days. Fig. 1(right) demonstrates the behavior of S and determination of the inflection time t_i for the case of SN 1999gi.

The correlation between the ^{56}Ni mass and plateau M_V found by Hamuy [5] is confirmed (Fig. 2, left), and the linear fit is described by the equation:

$$\log\, M(^{56}\mathrm{Ni}) = -0.438 M_V(t_\mathrm{i} - 35) - 8.46. \tag{2}$$

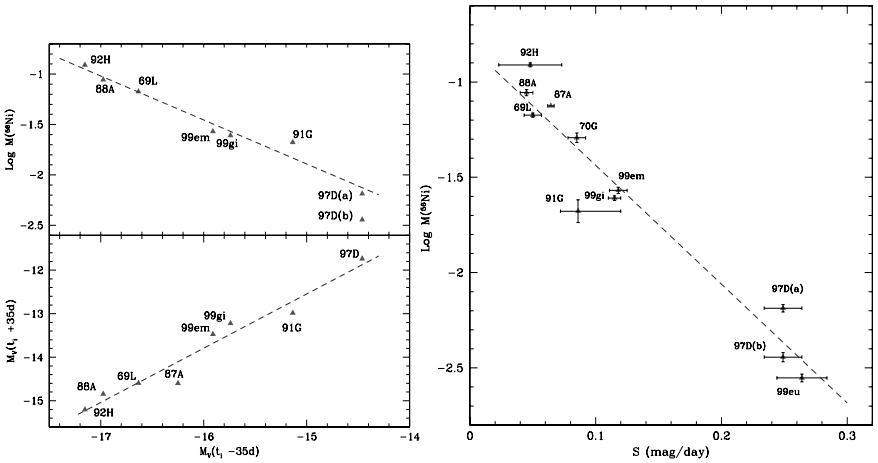

Fig. 2. Left: the correlation between M_V magnitudes of plateau and of radioactive tail. Upper panel shows the correlation between M_V at the moment $(t_\mathrm{i} - 35\mathrm{d})$ and ^{56}Ni mass derived from the tail magnitudes. Lower panel shows directly the correlation of plateau magnitude $M_V(t_\mathrm{i} - 35\mathrm{d})$ and tail magnitude $M_V(t_\mathrm{i} + 35\mathrm{d})$. Right: the correlation between ^{56}Ni mass and steepness S. Case "a" of SN 1997D is adopted for the fits (dashed lines).

Furthermore an interesting by-product of the sample photometry analysis is the correlation found between ^{56}Ni mass and the steepness parameter S. The correlation is quantified on the basis of the available data (Fig. 2, right), and the best linear fit reads:

$$\log M(^{56}\mathrm{Ni}) = -6.2295\, S - 0.8147 \qquad (3)$$

The correlation is such that the steeper the decline at the inflection point the lower is the mass of ^{56}Ni. Although the interpretation of this correlation requires hydrodynamical modeling with different amounts of ^{56}Ni and degrees of mixing, it may well be that somehow the increase of the ^{56}Ni mass in SNe IIP ejecta favors the larger radiative diffusion times at the end of the plateau and, therefore, a less steep transition from plateau to the radioactive tail, or that the increase of the ^{56}Ni mass is accompanied by the growth of the degree of mixing which favors a less steep decline. This correlation is interesting in the sense that, if confirmed, it will provide distance and extinction independent estimates of the ^{56}Ni mass in SNe IIP.

We construct then a "*two−zone*" model of the Hα luminosity in SN IIP to explore the sensitivity of the Hα behavior to variation of model parameters. The primary purpose of the upgraded model is to specify better the early nebular phase compared to the previous version [2]. We found that if mass, energy and mixing conditions do not vary strongly among SNe IIP (less than factor 1.4) then with an accuracy better than 10% Hα luminosity is

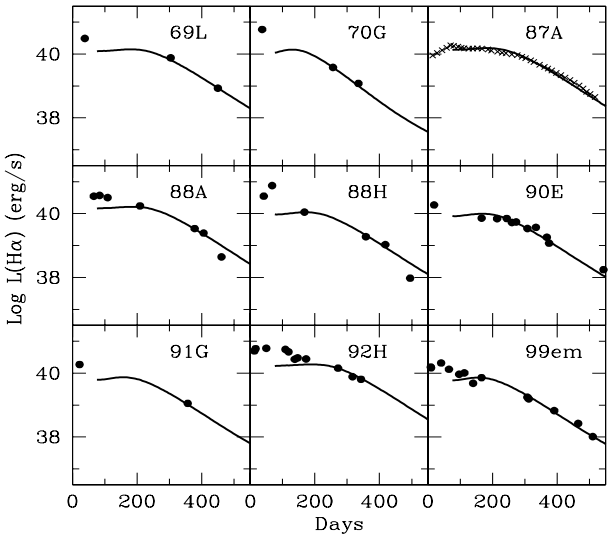

Fig. 3. The Hα luminosity evolution in different SN IIP. Models (*solid lines*) are over plotted on the observational data *dots*.

proportional to ^{56}Ni mass during the $200-400$ days after explosion (for more details see Elmhamdi et al. [4]). Hα luminosities are then used to derive ^{56}Ni masses of the SNe sample. This is done employing two approaches: first, using the Hα light curve in SN 1987A as template and, second, applying the model fitting (Fig. 3). Both approaches agree within 15% unless we are dealing with extreme cases such as SN 1970G (type IIP/L) and the underluminous SN 1997D. In both these cases we should possess additional information about ejecta mass and energy to derive the ^{56}Ni mass from Hα modeling. SN 1997D is indeed a special case for which two scenarios have been argued, namely: a small age scenario with a low ejecta mass (case "b" [3]) and a large age option with high mass of the ejecta (case "a" [9]).

Worth noting is the simple approach of using Hα light curve of SN 1987A as a template to estimate the ^{56}Ni mass. The ^{56}Ni mass values derived using this method agree within 20% with those from the photometry, which thus gives us confidence that Hα is a good indicator of the amount of ^{56}Ni in SNe IIP (Fig. 4). Simultaneously, this consistency suggests that parameters of SNe IIP (mass, energy and mixing) are not very different. In fact this is consistent with the uniformity of plateau luminosities and plateau lengths of SNe IIP.

This simple approach is applied then for three SNe for which we have late spectra but no photometry (SNe 1995ad, 1995V and 1995W), giving reasonable values, and thus demonstrating the usefulness of the method [4]. Generally, the approach based upon Hα may be indispensable in cases, when the photometry at the nebular epoch is absent, or when there is a problem

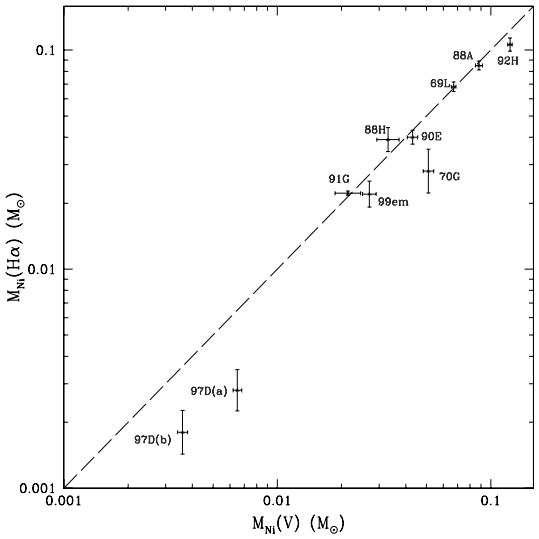

Fig. 4. The correlation between the ^{56}Ni mass derived from the Hα luminosity, $M_{\rm Ni}$(Hα), and that derived from the tail M_V magnitude, $M_{\rm Ni}(V)$. The dashed line has a slope of unity. Clear deviation is seen for SN 1970G(SNP/L) and for the faint event SN 1997D.

with subtraction of stellar background (SN IIP in the bulge, or in high redshift galaxies).

On the one hand, the clustering of the points around two values of ^{56}Ni mass viz. 0.005 and 0.05 $M_\odot$ in Fig. 4 may result from poor statistical sampling, or it may be a hint that a mechanism such as fall-back is an important one in the evolution of the low-mass group.

The interesting correlations demonstrated in this class of objects point to a high degree of homogeneity and this is encouraging for the use of type IIP SNe as cosmological probes. Improved statistical samples and better sampled data are however needed to have a firmer confirmation of these correlations.

These kinds of analyses demonstrate how large sample analyses in SNe studies can provide robust results and correlations with their consequent impact for our understanding of SNe physics.

References

1. M.B. Aufderheide, E. Baron, F.K. Thielemann: Astrophys. J. **370**, 630 (1991)
2. N.N. Chugai: Sov. Astron. Lett. **16**, 457 (1990)
3. N.N. Chugai, V.P. Utrobin: Astron. Astrophys. **354**, 557 (2000)
4. A. Elmhamdi, N.N. Chugai, I.J. Danziger: Astron. Astrophys. **404**, 1077 (2003)

5. M. Hamuy: Astrophys. J. **582**, 905 (2003)
6. D.C. Leonard et al. : Astron. J. **124**, 2490 (2002)
7. D.J. Schlegel, D.P. Finkbeiner, M. Davis: Astrophys. J. **500**, 525 (1998)
8. B.P. Schmidt, R.P. Kirshner, R.G. Eastman: Astrophys. J. **395**, 366 (1992)
9. L. Zampieri et al. : Mon. Not. R. Astron. Soc. **338**, 711 (2002)

Effects of Small-Scale Fluctuations of Neutrino Flux in Supernova Explosions

Hideki Madokoro, Tetsuya Shimizu, and Yuko Motizuki

RIKEN, Hirosawa 2-1, Wako 351-0198, Japan;
madokoro@postman.riken.go.jp

Summary. We examine effects of small-scale fluctuations with angle in the neutrino radiation in core-collapse supernova explosions. As the mode number of fluctuations increases, the results approach those of spherical explosion. We conclude that global anisotropy of the neutrino radiation is the most effective mechanism of increasing the explosion energy when the total neutrino luminosity is given.

1 Introduction

It has turned out that most simulations of core-collapse supernova explosions with spherical symmetry fail to produce a successful explosion [10]. In addition, observations suggest that the ejecta of core-collapse supernova explosions are aspherical(e.g., [17]). These facts lead us to multidimensional simulations. In 2-D and 3-D simulations [1, 2, 3, 4, 7, 9, 12, 13, 16], it has been shown that multidimensional effects, such as convection inside the proto-neutron star and convective overturn around the neutrino-heated region, increase the explosion energy and can trigger a successful explosion [4, 7, 8].

When a proto-neutron star rotates, the neutrino flux is expected to be enhanced along the rotational (polar) axis. Janka and Mönchmeyer [5, 6] first discussed the possibility of aspherical neutrino emission from a rapidly rotating inner core. They argued that a neutrino flux along the polar axis might become three times greater than that on the equatorial plane.

Shimizu et al. [14, 16] proposed that the anisotropic neutrino radiation should play a crucial role in the explosion mechanism itself. They carefully investigated the effects of anisotropic neutrino radiation on the explosion energy. They found that only a few percent enhancement in the neutrino emission along the pole is sufficient to increase the explosion energy by a large factor, and leads to a successful explosion. They also found that this effect saturates around a certain degree of anisotropy. It should be noted here that the assumed rotational velocity of the inner core is very different between Janka et al. [5, 6] and Shimizu et al. [14, 16].

In the work of Shimizu et al. [16], they considered only a form of global anisotropy; the maximum peak in the neutrino flux distribution was located at the pole and the minimum at the equatorial plane. On the other hand, Burrows et al. [1] have suggested that the neutrino flux can fluctuate with

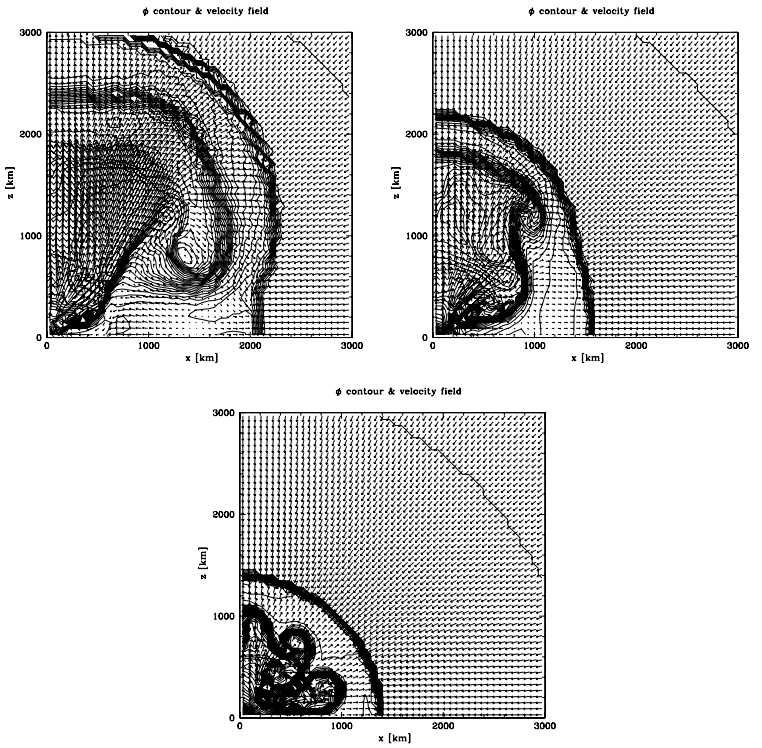

Fig. 1. Contour maps of the dimensionless entropy distribution and the velocity fields for the three models; top left: $n_\theta = 1$ (model A1-T470) at $t = 244$ms, top right: $n_\theta = 3$ (model A3-T470) at $t = 254$ms, bottom: $n_\theta = 5$ (model A5-T470) at $t = 252$ms.

angle and time due to gravitational oscillation on the surface of the proto-neutron star. In this work, we introduce such small-scale fluctuations in the neutrino flux in our numerical code by modifying the angular distribution of the neutrino flux. We aim to study the effects of these small-scale fluctuations on the shock position, the explosion energy, and the asymmetric explosion. Details are found in [11].

2 Numerical Code

We perform 2-D simulations by solving hydrodynamic equations in spherical coordinates. A generalized Roe's method is employed to solve the hydrodynamic equations with general equations of state (EOSs). The details of our numerical technique, together with the EOS and the initial condition used, are described in the previous article [16]. In our study, we have improved

Table 1. Simulated models

Model	n_θ	c_2
A1-T470	1	0.100
A3-T470	3	0.051
A5-T470	5	0.035

the numerical code of Shimizu et al. [16]; the cells in the θ-direction were shifted by half of the cell size [15] in order to avoid a numerical error near the pole, although the error was not serious for the investigation of the explosion energy.

In the present work, the local neutrino flux is assumed to be [11]

$$l_\nu(r,\theta) = \frac{7}{16}\sigma T_\nu^4 c_1 \left(1 + c_2 \cos^2(n_\theta \theta)\right) \frac{1}{r^2}, \tag{1}$$

where σ is the Boltzmann constant, and T_ν is the temperature on the neutrino sphere. In Eq. (1), n_θ represents the number of waves in the θ-direction. The case of $n_\theta = 1$ corresponds to the global anisotropy, namely, no fluctuation. c_2 is a parameter which is related to the degree of anisotropy in the neutrino radiation. We see in Eq. (1) that the neutrino fluxes in the x (equatorial) and z (polar) directions become $l_x \equiv l_\nu(r, \theta = 90^\circ) \propto c_1$ and $l_z \equiv l_\nu(r, \theta = 0^\circ) \propto c_1(1 + c_2)$, respectively. The degree of anisotropy l_z/l_x is then represented as

$$\frac{l_z}{l_x} = 1 + c_2. \tag{2}$$

The value of c_1 is calculated from c_2 and n_θ so as to adjust the total neutrino luminosity to that in the spherical model at the same T_ν.

It should be noted here that the amplitude of fluctuations in the neutrino flux distribution for an observer far from the neutrino sphere and that on the neutrino-emitting surface are different. When we observe the neutrino flux far from the neutrino sphere, the local neutrino flux is seen as Eq. (1). On the other hand, the neutrino flux on the neutrino-emitting surface has a profile similar to Eq. (1) but the amplitude is different. In the latter, c_2 is replaced by a where a is a parameter which represents the degree of anisotropy of the neutrino flux on the neutrino sphere. It is preferable that we compare the results for the same value of a, since a is more directly related to explosion dynamics. The value of c_2, therefore, is calculated from a given a, depending on n_θ. Although it is difficult to calculate the exact relationship between c_2 and a, we can estimate it by assuming that the strength of the neutrino flux on the neutrino sphere is approximated by a profile of step function. This makes it possible to relate the value of c_2 to the value of a for each n_θ. For detail, see Madokoro et al. [11].

We set $a = 0.31$ in this work. This value of a is chosen in such a way that the value of l_z/l_x for the global model ($n_\theta = 1$) becomes 1.10. The

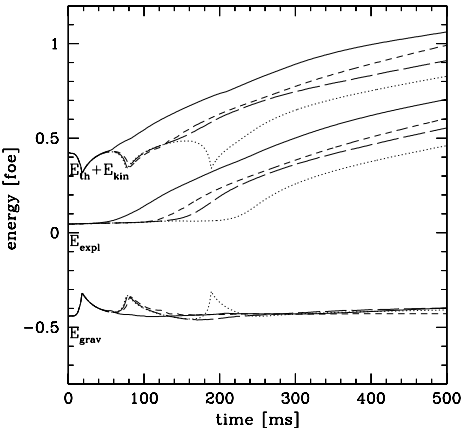

Fig. 2. Evolution of thermal and kinetic energy ($E_{\rm th} + E_{\rm kin}$), gravitational energy ($E_{\rm grav}$) and explosion energy ($E_{\rm expl}$) for the three models; solid line: $n_\theta = 1$, short-dashed line: $n_\theta = 3$, long-dashed line: $n_\theta = 5$. For comparison, the result of the spherical explosion at the same T_ν is also plotted (dotted line).

values of c_2 for each fluctuation model ($n_\theta = 3, 5$) are accordingly calculated. These are summarized in Table 1. The neutrino temperature on the neutrino-emitting surface T_ν is assumed to be 4.70 MeV. In our simulation, we have 500 nonuniform radial zones which cover from 50 to 10000 km in radius. For θ, we have 62 uniform angular zones from $\theta = 0°$ to $\theta = 90°$ with equatorial symmetry for $n_\theta = 1$ and 3. Note that we use a double value of the angular zones for $n_\theta = 5$, which is different from that used in [11].

3 Results

Fig. 1 depicts the contour maps of the dimensionless entropy [16] distribution with the velocity fields for the three models at $t \sim 250$ ms after the shock stall. The shock front is represented by the crowded contour lines at $r \sim 2000-3000$ km for the model A1-T470, $r \sim 1600-2200$ km for the model A3-T470, and $r \sim 1400$ km for the model A5-T470. We see in Fig. 1 that the shock front is largely distorted in a prolate form for the model A1-T470. This is because the neutrino heating along the pole is more intensive than that on the equatorial plane. Due to increased pressure in the locally heated matter near the polar axis, the shock front along the pole is pushed up, resulting in a prolate deformation. We find that the shock position becomes less extended than that of the global anisotropy, and the shock front approaches the spherical shape when the mode number of fluctuation increases. This trend is especially remarkable for the model A5-T470 in which the shock front is almost spherical.

Figure 2 shows the evolution of the explosion energy, as well as the thermal, kinetic, and gravitational energies for the three models. The energy gain for the case of $n_\theta = 1$ is the highest among others at all stages of the explosion. It is also seen in Fig. 2 that the explosion energy decreases as the mode number of fluctuations in the neutrino flux increases and finally approaches that of the spherical explosion.

Thus, we found that there are remarkable differences in the explosion energy depending on the mode number of the fluctuations. We also found that larger number of modes in the fluctuations makes the result closer to that of the spherical explosion. This is because any small-scale fluctuations on the neutrino sphere are greatly averaged out when the neutrino emission is observed far enough from the neutrino-emitting surface. Moreover, we found that a certain broad space is needed to be heated by neutrinos to revive the stalled shock wave rigorously and hence the global anisotropy ($n_\theta = 1$) is the most effective to increase the explosion energy. These results support the claim by Shimizu et al. [16].

4 Conclusion

We have investigated the effects of small-scale fluctuations in the neutrino flux on the core-collapse supernova explosion. The profile of the neutrino radiation field was specified taking its geometric effects into account. Since the small-scale fluctuations are averaged out for radiative and hydrodynamic reasons, the results of the fluctuation models become closer to that of the spherical explosion. Consequently, the global anisotropy is the most effective mechanism in increasing the explosion energy when L_ν is given. This supports the claim made by Shimizu et al. [16].

References

1. A. Burrows, J. Hayes, B.A. Fryxell: Astrophys. J. **450**, 830 (1995)
2. C.L. Fryer, A. Heger: Astrophys. J. **541**, 1033 (2000)
3. C.L. Fryer, M.S. Warren: Astrophys. J. Lett. **574**, L65 (2002)
4. M. Herant, W. Benz, W.R. Hix, C.L. Fryer, S.A. Colgate: Astrophys. J. **435**, 339 (1994)
5. H.-T. Janka, R. Mönchmeyer: Astron. Astrophys. **209**, L5 (1989)
6. H.-T. Janka, R. Mönchmeyer: Astron. Astrophys. **226**, 69 (1989)
7. H.-T. Janka, E. Müller: Astron. Astrophys. **306**, 167 (1996)
8. W. Keil, H.-T. Janka, E. Müller: Astrophys. J. Lett. **473**, L111 (1996)
9. K. Kifonidis, T. Plewa, H.-T. Janka, E. Müller: astro-ph 0302239 (2003)
10. M. Liebendoerfer, A. Mezzacappa, F.-K. Thielemann, O.E.B. Messer, W.R. Hix, S.W. Bruenn: Phys. Rev. D **63**, 103004 (2001)
11. H. Madokoro, T. Shimizu, Y. Motizuki: Astrophys. J. **592**, 1035 (2003)

12. A. Mezzacappa, A.C. Calder, S.W. Bruenn, J.M. Blondin, M.W. Guidry, M.R. Strayer, A.S. Umar: Astrophys. J. **495**, 911 (1998)
13. D.S. Miller, J.R. Wilson, R.W. Mayle: Astrophys. J. **415**, 278 (1993)
14. T. Shimizu, S. Yamada, K. Sato: Astrophys. J. Lett. **432**, L119 (1994)
15. T.M. Shimizu: *Ph.D. Thesis*, (Univ. Tokyo, 1995)
16. T.M. Shimizu, T. Ebisuzaki, K. Sato, S. Yamada: Astrophys. J. **552**, 756 (2001)
17. L. Wang et al. : Astrophys. J. **579**, 671 (2002)

Neutrino Gas in Equilibrium with Self-Interaction

M. Sirera[1] and A. Perez[2]

[1] Departamento de Astronomia y Astrofísica, Universidad de Valencia, 46100 Burjassot (Valencia) Spain;
Miguel.Sirera@uv.es
[2] Departamento de Física Teórica, Universidad de Valencia, 46100 Burjassot (Valencia) Spain;
Armando.Perez@uv.es

Summary. We study a neutrino gas in equilibrium both at $T = 0$ and at finite temperature. The neutrinos are assumed to be massive Dirac particles with two generations interacting with each other via neutral currents and with a background of matter. We analyze the main properties of the neutrino eigenmodes in the medium, such as effective masses and mixing angle.

1 Introduction

The neutrino behavior in matter is important in several astrophysical scenarios, especially is the case of supernova explosions, where neutrino interactions and oscillations can change the shock dynamics [4, 11, 14, 15, 16, 17, 18]. A crucial ingredient in this scenario is the neutrino self- interaction [1, 3, 12, 20]. As it has been remarked, such interactions are non-diagonal in flavor space, and give raise to new phenomena in the oscillatory behavior [5, 9, 10]. Here we analyze in detail the equilibrium of a neutrino gas both at $T = 0$ and at finite temperature. The neutrinos are supposed to be massive Dirac particles with two generations, namely electron-neutrinos ν_e and muon-neutrinos ν_μ, which are assumed to interact among them via neutral currents and with a background of matter. This might be the situation for neutrinos in a supernova inside the neutrino sphere, if self-interactions are effective enough to reach the equilibrium, where we assume that the equilibrium is not only thermal but also chemical between the two generations [2, 5]. To this end, we use a method based on Wigner functions, which has been shown to be appropriate to describe both the equilibrium and kinematics of many-particle neutrino systems with mixing [19].

In this work neutrinos are treated as extremely relativistic particles of positive helicity (antineutrinos of negative helicity), whose states of defined momentum $\overrightarrow{p}$ are also of defined energy (or effective masses different of their vacuum masses) i.e. what is called the "quasi-particle approximation." We make the assumption that the background of matter is electrically neutral and consisting only of nucleons and electrons ($n_e = n_p$).

2 Hartree Approximation

First we treat the gas in the so-called "Hartree approximation," i.e., without taking into account the effects of the statistical correlations. At first, let us suppose that we have only neutrinos which are interacting among them (without a background of matter). In this case, starting from the general equation of motion and imposing proper conditions, we obtain that the equation of motion for the Wigner Function of neutrinos in equilibrium is [19]

$$(\gamma p - M)F(p) = \frac{G_F}{2\sqrt{2}} \int d^4k Tr[\gamma_\mu(1-\gamma^5)F(k)]\gamma^\mu(1-\gamma^5)F(p), \quad (1)$$

where G_F is the Fermi constant, M^{ab} is the mass matrix and $F^{ab}(p)$ the Wigner Function for the neutrinos. Both of them have flavor indices in the generation space, such that $a, b = e, \mu$.

From this equation, and assuming that neutrinos basically consist on their left-chirality projections, we can obtain a specific equation for neutrinos (with negative helicity), where $n_\nu = n_1 + n_2 = n_{\widetilde{\nu}_1} + \ n_{\widetilde{\nu}_2} - n_{\widetilde{\overline{\nu}}_1} - n_{\widetilde{\overline{\nu}}_2}$ is the total density of neutrinos (with $p^0 \simeq |\overrightarrow{p}|$) minus the corresponding antineutrino density (with $p^0 \simeq -|\overrightarrow{p}|$)

Let us now assume that, in addition to the self-interaction among the neutrinos, we have an electrically neutral background of matter composed by electrons and nucleons. In this case, the effective masses of neutrinos are [6, 7, 19]

$$M^2_{1,2} = 1/2(A_c + \Sigma) \mp 1/2(A_c^2 + \Delta^2)^{1/2} + A_n, \quad (2)$$

where

$$\begin{aligned} \Sigma &= m_1^2 + m_2^2 \\ \Delta &= m_1^2 - m_2^2 \\ A_c &= 2\sqrt{2}G_F|\overrightarrow{p}|n_e \\ A_n &= 2\sqrt{2}G_F|\overrightarrow{p}|n_\nu - \sqrt{2}G_F|\overrightarrow{p}|n_n \end{aligned} \quad (3)$$

being n_e the number density of electrons (minus antielectrons) and n_n the number density of neutrons (minus antineutrons).

3 Corrections to the Hartree Approximation

The collective effects in the neutrino gas are brought in by means the statistical correlations, which modify the equation of motion of the Wigner Function (or the left-quirality part $F_L(x)$), which now becomes

$$[\gamma p - \sqrt{2}G_F\gamma a + \sqrt{2}G_F \int d^4q\gamma F_L(q)\gamma - M]F_L(p) = 0. \tag{4}$$

where the four-vector a is defined as

$$a_\mu = \int d^4kTr\gamma_\mu F_L(k). \tag{5}$$

Obviously, the third term of this equation provides us with an additional correction to the corresponding equation in the Hartree approximation. After some algebra, we arrive to the following expression for the effective masses in the medium:

$$M^{*2}_{1,2}\left(p^0\right) = \frac{1}{2}\left[\Sigma + 2\sqrt{2}G_F\left(3n_\nu + n_e - n_n\right)p^0\right] \mp \frac{1}{2}\Delta^*, \tag{6}$$

where

$$\Delta^* = \left[\left(2\sqrt{2}G_F p^0\left(n_e + \delta\right) - \Delta\cos 2\theta_0\right)^2 + \left(4\sqrt{2}G_F p^0 n_{12} - \Delta\sin 2\theta_0\right)^2\right]^{1/2} \tag{7}$$

is the effective mass difference. In Eq. (6) the upper (lower) sign corresponds to M_1^* (M_2^*) ,where Σ and Δ have been defined in Eq. (3). The mixing angle is now given by

$$\sin 2\theta = \frac{\Delta\sin 2\theta_0 - 4\sqrt{2}G_F p^0 n_{12}}{\Delta^*}. \tag{8}$$

The quantities that appear in these equations are defined in the following manner:

$$\begin{aligned} n_{\nu_e} &= \tfrac{1}{2\pi^2}\textstyle\int_0^\infty d|\boldsymbol{q}||\boldsymbol{q}|^2[c^2 f_1(q) + s^2 f_2(q)], \\ n_{\nu\mu} &= \tfrac{1}{2\pi^2}\textstyle\int_0^\infty d|\boldsymbol{q}||\boldsymbol{q}|^2[s^2 f_1(q) + c^2 f_2(q)], \\ n_{\nu_{12}} &= \tfrac{1}{2\pi^2}\textstyle\int_0^\infty d|\boldsymbol{q}||\boldsymbol{q}|^2 cs[f_1(q) - f_2(q)], \end{aligned} \tag{9}$$

where $f_1(q)$ and $f_2(q)$ are the Fermi statistical distribution functions for each generation, corresponding to quasi-particles with well-defined effective masses, and s and c are the *sin* and *cos* of the rotation angle θ which relates the eigenstates of effective masses to flavor eigenstates. In this way, n_{ν_e} (n_{ν_μ}) is the number density of electron (muon) neutrinos and $n_{\nu_{12}}$ contains interference effects. Analogously, we can define the number densities for antineutrinos, so we have that $n(e) = n_{\nu_e} - \bar{n}_{\nu_e}$ is the net electron neutrino number density, $n(\mu) = n_{\nu_\mu} - \bar{n}_{\nu_\mu}$ is the net muon neutrino number density, $n_\nu = n(e) + n(\mu)$ is the total number neutrino density, $n_{12} = n_{\nu_{12}} - \bar{n}_{\nu_{12}}$, and $\delta = n(e) - n(\mu)$ is a statistical parameter of asymmetry between the two flavors.

The dispersion relation for neutrinos and antineutrino mass eigenstates, can be written as:

$$p^2 - M_{1,2}^{*2}\left(p^0\right) = 0 \tag{10}$$

and provides (as an implicit equation) the energy p^0 as a function of the momentum $|\boldsymbol{p}|$. As a first approximation, one can use the fact that, under most situations of interest, neutrinos are extremely relativistic particles. Thus, for neutrinos one can replace p^0 by $|\boldsymbol{p}|$. In this way, the above dispersion equation can be approximately solved as:

$$p_0 = \sqrt{|\boldsymbol{p}|^2 + M_{1,2}^{*2}\left(|\boldsymbol{p}|\right)} \tag{11}$$

To obtain the corresponding formulae for antineutrinos we only have to change $|\boldsymbol{p}|$ to $-|\boldsymbol{p}|$ in the two previous equations.

An interesting consequence of Eq. (8) is that the condition for the MSW resonance is modified with respect to the situation where there is not a neutrino background. In fact, the condition for the resonance is now:

$$p^0 = \frac{\Delta\left[\left(\delta + n_e\right)\cos 2\theta_0 + 2n_{12}\sin 2\theta_0\right]}{2\sqrt{2}G_F\left[\left(\delta + n_e\right)^2 + 4n_{12}^2\right]} \tag{12}$$

This new condition can be of interest if $\sin 2\theta_0 \simeq 1$, as suggested for both solar and atmospheric neutrino oscillation values (for a review, see [8]). In this case, the MSW resonance might be dominated by the neutrino background.

4 Low-Temperature Limit

Since the gas is in total equilibrium, the state is characterized by a single chemical potential μ of the neutrinos, and the temperature T of the gas. Here we treat, for the sake of simplicity, the low-temperature case ($T/\mu \ll 1$). In this case, we can apply the "Sommerfeld expansion" in order to carry out the Fermi integrals and calculate the thermodynamical variables of the system. In this type of calculation, we have a series expansion in T/μ. Using this, we can calculate the total neutrino density to the lowest order in T. In this calculation we can neglect the antiparticles. The total density turns out to be

$$n_\nu = n_{\nu_e} + n_{\nu_\mu} = \tfrac{1}{2\pi^2}\int_0^\infty d|\boldsymbol{p}||\boldsymbol{p}|^2[(f_1(p) + f_2(p)] \simeq \frac{2\mu^3 - 3\sqrt{2}G_F\mu^2(n_e - n_n) + 2\pi^2\mu T^2 - \sqrt{2}\pi^2 G_F(n_e - n_n)T^2}{6\pi^2 + 9\sqrt{2}G_F\mu^2}, \tag{13}$$

where we are using the high density approximation, in which the neutrino vacuum masses are negligible as compared to the self-energies of the interaction.

We can now calculate the variable δ of asymmetry starting from its definition. We restrict ourselves to the value $\theta_0 = \pi/4$ and since we are in the high-density limit, then one finds $\theta \simeq 90^o$ for the in-medium mixing angle, and thus $\cos 2\theta \simeq -1$. This implies that ν_e can be approximately identified with ν_2 (the heaviest eigenstate, according to our convention) and, similarly, ν_μ corresponds to ν_1. This identification can also be seen from the corresponding distribution functions, Eq. (9). Since the mass difference is usually very small (as compared to the chemical potential and temperature), we have

$$f_1(p) \simeq f_2(p) \tag{14}$$

which implies that

$$n_{\nu_{12}} \ll n_{\nu_e} \simeq n_{\nu_\mu} \tag{15}$$

To illustrate this assertion, let us calculate the asymmetry parameter δ for a low-temperature neutrino gas

$$\begin{aligned} \delta = n_{\nu_e} - n_{\nu_\mu} &\simeq -\tfrac{1}{2\pi^2} \int_0^\infty d|\boldsymbol{p}||\boldsymbol{p}|^2[(f_1(p) - f_2(p)] \\ &= -\tfrac{3\sqrt{2}\mu^2 G_F n_e + \sqrt{2}\pi^2 G_F n_e T^2}{6\pi^2} \end{aligned} \tag{16}$$

Consider, for example, the core of a protoneutron star (see, for example, [13]). For a density equal to the saturation density and an electron-to-baryon fraction $Y_e = 0.3$ one has $n_e = 1.1 \times 10^8$ MeV^3. If the neutrino chemical potential is $\mu = 100$ MeV then the asymmetry density over the neutrino number density is

$$\delta/n_\nu \sim -\frac{G_F n_e}{\mu} \sim -2.6 \times 10^{-5} \tag{17}$$

in accordance with the above discussion.

5 Conclusions

In conclusion, we can say that to obtain more accurate results when treating the neutrino gas, we have to consider the collective effects by including the correlations, which, under the conditions assumed above, give a non-diagonal term in the effective mass matrix. Therefore, in addition to a modification in the effective masses of eigenstates, there is a change in the in-medium mixing angle, as compared to the Hartree result. Also, the condition for the MSW resonance (when a matter background is included) differs from the usual MSW condition.

On the other hand, and considering the high-density case, the effective mass difference is much larger than the vacuum difference, and one finds $\theta \simeq$

90^o for the in-medium mixing angle. Under these circumstances, the flavor states can be approximately identified with mass eigenstates. Since both $f_1(p)$ and $f_2(p)$ share the same chemical potential and the vacuum masses are negligible one finds, in practice, that in equilibrium the two neutrino flavors are mixed in the same proportion. In fact, the estimations we have presented for typical values inside a supernova show that the flavor asymmetry δ is very small.

References

1. K.N. Abazajian, J.F. Beacom, N.F. Bell: Phys. Rev. D **66**, 013008 (2002)
2. N.F. Bell, A.A. Rawlinson, R.F. Sawyer: hep-ph 0304082 (2003)
3. A.D. Dolgov, S.H. Hansen, S. Pastor, S.T. Petcov, G.G. Raffelt, D.V. Semikoz: Nuc. Phys. **632**, 363 (2002)
4. G.L. Fogli, E. Lisi, D. Montanino, A. Palazzo: Phys. Rev. D **65**, 073008 (2002)
5. A. Friedland, C. Lunardini: hep-ph 0304055 (2003)
6. C.W. Kim, A. Pevsner: In: *Neutrinos in Physics and Astrophysics,* ed. Harwood (Academic Pub., 1993)
7. D. Nötzold, G. Raffelt: Nuc. Phys. **307**, 924 (1988)
8. S. Pakvasa, J.W.F. Valle: hep-ph 0301061 (2003)
9. J. Pantaleone: Phys. Lett. B **287**, 128 (1992)
10. J. Pantaleone: astro-ph 9405008 (1994)
11. S. Pastor, G. Raffelt: Phys. Rev. Lett. **89**, 191101 (2002)
12. S. Pastor, G. Raffelt, D.V. Semikoz: Phys. Rev. D **65**, 053011 (2002)
13. Mad. Prakash, I. Bombaci, Man. Prakash, P.J. Ellis, J.M. Latimer, R. Knorren: Phys. Rep. **280**, 1 (1997)
14. Y.-Z. Qian, G.M. Fuller, G.J. Mathews, R.W. Mayle, J.R. Wilson, S.E. Woosley: Phys. Rev. Lett. **71**, 1965 (1993)
15. Y.-Z. Qian, G.M. Fuller: Phys. Rev. D **51**, 1479 (1995)
16. G. Raffelt: Nuc. Phys. **95**, 183 (2001)
17. G. Raffelt: New Astron. Rev. **46**, 699 (2002)
18. G. Sigl: Phys. Rev. D **51**, 4035 (1995)
19. M. Sirera, A. Pérez: Phys. Rev. D **59**, 125011 (1999)
20. Y.Y.Y. Wong: Phys. Rev. D **66**, 025015 (2002)

Weak Interaction Processes in Core-Collapse Supernovae

G. Martínez-Pinedo[1,2], K. Langanke[3], J.M. Sampaio[3], D.J. Dean[4], W.R. Hix[4,5,6], O.E.B. Messer[4,5,6], A. Mezzacappa[4], M. Liebendorfer[7,4,5], H.-Th. Janka[8], and M. Rampp[8]

[1] Institut d'Estudis Espacials de Catalunya, Barcelona, Spain; martinez@ieec.fcr.es
[2] Institució Catalana de Recerca i Estudis Avançats, Barcelona, Spain
[3] Institute for Physics and Astronomy, University of Århus, Denmark
[4] Physics Division, Oak Ridge National Laboratory, Tennessee, USA
[5] Department of Physics and Astronomy, University of Tennessee, USA
[6] Joint Institute for Heavy Ion research, Oak Ridge, Tennessee, USA
[7] Canadian Institute for Theoretical Astrophysics, Toronto, Ontario, Canada
[8] Max-Planck-Institut fur Astrophysik, Garching, Germany

Summary. Supernova simulations to date have assumed that during core collapse electron captures (EC) occur dominantly on free protons, while captures on heavy nuclei are Pauli-blocked and are ignored. Using microscopic calculations we show that the EC rates on heavy nuclei are large enough that, in contrast to previous assumptions, electron capture on nuclei dominates over capture on free protons. This leads to significant changes in core collapse simulations.

1 Introduction

Stars with masses exceeding roughly 10 $M_\odot$ reach a moment in their evolution when their iron core provides no further source of nuclear energy generation. At this time, the evolution in the core is determined by the competition of gravity, that produces the collapse of the core, and the weak interaction, that determines the rate at which electrons are captured and the rate at which neutrinos are trapped during the collapse. As the density of the star's center increases electrons become more degenerate and their chemical potential grows. For sufficiently high values of the chemical potential electrons are captured by nuclei producing neutrinos, which for densities $\lesssim 10^{11}$ g cm^{-3}, freely escape from the star, removing energy and entropy from the core. Thus entropy stays low during the collapse ensuring that nuclei dominate in the composition over free nucleons.

Before the collapse sets in, during the presupernova stage, i.e. at core densities $\lesssim 10^{10}$ g cm^{-3}, and proton-to-neutron ratios $Y_e \gtrsim 0.42$, nuclei with $A = 55 - 65$ dominate in the composition. The relevant rates for weak interaction processes were initially determined by Fuller, Fowler and Newman [4]. The rates have been recently improved based on modern data and state-of-

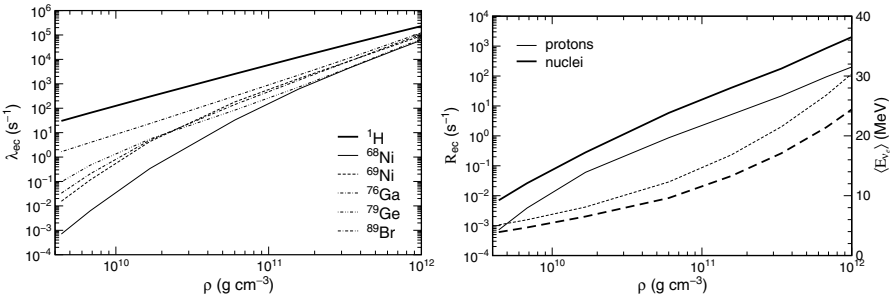

Fig. 1. (left panel) Comparison of the electron capture rates on free protons and selected nuclei as function of the electron chemical potential along a stellar collapse trajectory. (right panel) The reaction rates for electron capture on protons (thin line) and nuclei (thick line) are compared as a function of density along a stellar collapse trajectory. The dashed lines (right scale) show the related average energy of the neutrinos emitted by capture on nuclei and protons.

the-art shell-model calculations [13, 14]. Presupernova models utilizing these improved weak rates are presented in [9, 10].

During collapse, i.e., at densities $\gtrsim 10^{10}$ g cm^{-3}, temperatures and densities are high enough to ensure that nuclear statistical equilibrium is achieved. Then, for sufficiently low entropies, the matter composition is dominated by the nuclei with the largest binding energy for a given Y_e. In current collapse simulations a very simple description of electron capture on nuclei is used. The rates are estimated using an independent particle model (IPM) that assumes pure Gamow-Teller (GT) transitions [2]. In this model GT transitions are Pauli-blocked for nuclei with $N \geq 40$ and $Z \leq 40$ [5, 6]. These nuclei dominate the composition for densities larger than a few 10^{10} g cm^{-3}. As a result, electron capture on nuclei ceases at these densities and the capture is entirely due to free protons. In the next section we will show that the employed model for electron capture on nuclei is incorrect, as Pauli-blocking of the GT transitions is overcome once correlations [15] and temperature effects are taken in account [3, 5, 6].

2 Electron Capture During Core Collapse

The residual nuclear interaction, beyond the IPM, mixes the pf shell with the levels of the sdg shell, in particular, with the lowest orbital, $g_{9/2}$. The presence of configurations were more than a neutron is promoted from the pf shell into the $g_{9/2}$ orbit unblocks the GT transitions for nuclei with $N \geq 40$. In addition, during core collapse electron capture occurs at temperatures $T \gtrsim 0.8$ MeV. A model that is a able to describe both correlations and finite temperature is then necessary for the calculation of the relevant rates. This model is the

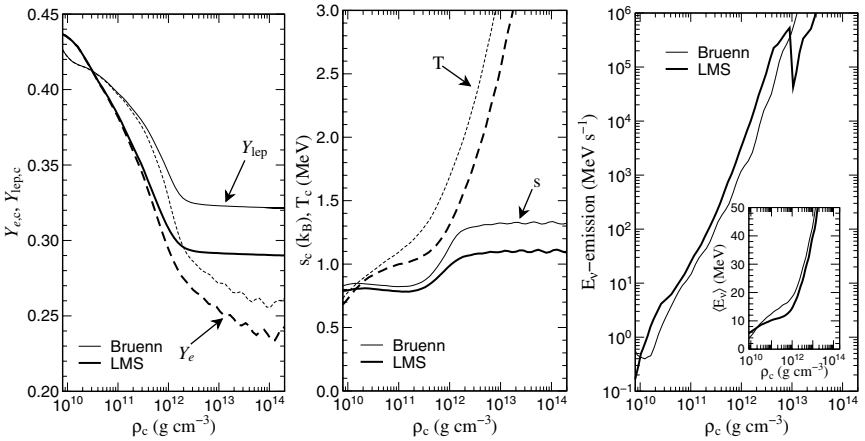

Fig. 2. Comparison of the evolution of several quantities at the center of a 15 $M_\odot$. The initial presupernova model was taken from [9, 10]. The thin line is a simulation using the Bruenn parameterization [2] while the thick line uses the LMS rate set (see text). Both models were calculated using a General Relativistic treatment of gravity by the Garching collaboration.

shell model Monte Carlo (SMMC) [12] supplemented with calculations based in the random phase approximation for the transition operators [16].

The left panel of Fig. 1 shows the electron capture rates for protons and selected nuclei along a stellar trajectory taken from [18]. The electron chemical potential, μ_e, and the reaction Q value are the two important energy scales of the capture process. For the lowest densities the electron chemical potential ($\mu_e \approx 6$ MeV for $\rho = 5 \times 10^9$ g cm^{-3}) is of the same order than the typical nuclear Q value. Then, the electron capture rates on nuclei are very sensitive to the Q-value and smaller than the rate on protons. For higher densities the chemical potential grows much faster than the Q-value and the rate becomes independent of the heavy nucleus. Due to the much smaller Q-value, the electron capture rate on free protons is larger than the rates on the abundant nuclei during the collapse. However, this is misleading as the low entropy keeps the protons significantly less abundant than heavy nuclei. The right panel of Fig. 1 shows that the reaction rate for electron capture on heavy nuclei ($R_h = \sum_i Y_i \lambda_i$, where the sum runs over all the nuclei present and Y_i denotes the number abundance of species i) dominates over the one of protons ($R_p = Y_p \lambda_p$) by roughly an order of magnitude throughout the collapse, when the composition is considered.

Electron capture on nuclei and on free protons differ quite noticeably in the neutrino spectra they generate. The right panel of Fig. 1 shows that neutrinos produced by captures on nuclei have a mean energy 40–60% smaller than those produced by captures on protons (mainly due to the larger Q-value for capture on nuclei). Despite that, the total neutrino energy loss rate

is larger when electron capture on nuclei is considered, caused by the increase in the total (nuclei plus protons) electron capture rate.

3 Consequences for the Collapse

Simulations of core collapse require reaction rates for the electron capture on protons, R_p, and heavy nuclei, R_h. While R_p is readily derived from [2], the calculation of R_h requires knowledge of the nuclear composition, in addition to the electron capture rates described earlier. In order to compute the needed abundances a Saha-like nuclear statistical equilibrium (NSE) is used to calculate the needed abundances of individual isotopes, including coulomb corrections to the nuclear binding energy [1, 11]. Coulomb corrections to the electron capture rates themselves impose a reduction of a factor ~ 2, that doesn't produce appreciable differences with the results obtained using unscreened rates that are discussed below [17]. The combination of NSE abundances with electron capture rates for around 200 nuclei with $A = 45$–112 was used [16] to compute the rate of electron capture on nuclei and the emitted neutrino spectra as a function of temperature, density, and electron fraction, adequately covering the range until weak equilibrium during the collapse is achieved. The range of validity is estimated to be $\rho \lesssim 2 \times 10^{12}$ g cm^{-3} and $T \lesssim 2$ MeV. This rate set will be denoted LMS (Langanke, Martínez-Pinedo, and Sampaio) in the following. The rates for the inverse neutrino absorption process are determined by detailed balance.

The consequences of this more realistic implementation of electron capture rates on heavy nuclei have been evaluated in independent self-consistent neutrino radiation hydrodynamics simulations by the Oak Ridge and Garching Collaborations. The basis of these models is described in detail in [18, 19]. The results obtained by the Garching collaboration for the evolution of several quantities at the center of a 15 $M_\odot$ star using the standard treatment of Bruenn [2] and the new LMS rates for heavy nuclei are compared in Fig. 2. With the improved treatment of electron capture rate on heavy nuclei the total electron capture rate (heavy nuclei plus protons) is bigger than in the Bruenn treatment resulting in a smaller Y_e value and $Y_{\rm lepton}$. The right panel shows that the energy emission rate by neutrinos is higher in the LMS treatment resulting in a reduction of the central temperature and entropy (middle panel). Notice however, that the average energy of the emitted neutrinos is smaller in the LMS treatment due to the higher Q-values for electron capture on nuclei (inset of the right panel).

Figure 3 shows the star profiles for several quantities obtained in collapse simulations carried out by the Oak Ridge collaboration (similar results are obtained by the Garching collaboration) at the moment when the central density reaches 10^{14} g cm^{-3}. In the inner regions of the star, the additional electron capture on heavy nuclei results in more electron capture in the LMS models that produce a reduction in Y_e and a smaller central temperature.

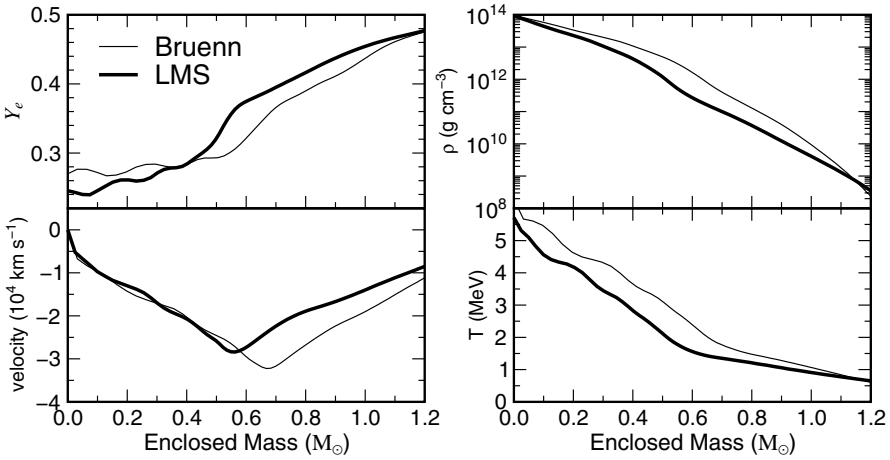

Fig. 3. The electron fraction, velocity, density and temperature as functions of the enclosed mass at the moment when the center reaches nuclear matter densities for the same 15 $M_\odot$ star as Fig. 2. The thin line is a simulation using the Bruenn parameterization [2] while the thick line uses the LMS rate set (see text). Both models were calculated using Newtonian gravity by the Oak Ridge collaboration.

In outer regions, where $A < 65$ nuclei dominate, the LMS models predict less electron capture. This is so, because for these mass ranges the electron capture rates of ref. [13, 14] are smaller than the ones used in the Bruenn parameterization [2]. Due to the smaller electron capture rates, these regions collapse more slowly so that the density and temperature are smaller in the new models. The velocity distribution shows a displacement in the minimum, which marks the eventual location of shock formation, by 0.1 $M_\odot$.

Acknowledgement. GMP acknowledges financial support of the Spanish MCyT under contracts AYA2002-04094-C03-02 and AYA2003-06128

References

1. E. Bravo, D. García-Senz: Mon. Not. R. Astron. Soc. **307**, 984 (1999)
2. S.W. Bruenn: Astrophys. J. Suppl. **58**, 771 (1985)
3. J. Cooperstein, J. Wambach: Nuc. Phys. **420**, 591 (1984)
4. G.M. Fuller, W.A. Fowler, M.J. Newman: Astrophys. J. Suppl. **42**, 447 (1980)
5. G.M. Fuller, W.A. Fowler, M.J. Newman: Astrophys. J. Suppl. **48**, 279 (1982)
6. G.M. Fuller, W.A. Fowler, M.J. Newman: Astrophys. J. **252**, 715 (1982)
7. G.M. Fuller: Astrophys. J. **252**, 741 (1982)
8. G.M. Fuller, W.A. Fowler, M.J. Newman: Astrophys. J. **293**, 1 (1985)
9. A. Heger, K. Langanke, G. Martínez-Pinedo, S.E. Woosley: Phys. Rev. Lett. **86**, 1678 (2001)

10. A. Heger, K. Langanke, G. Martínez-Pinedo, S.E. Woosley: Astrophys. J. **560**, 307 (2001)
11. W.R. Hix: Ph.D. Thesis (Harvard Univ.: 1995)
12. S.E. Koonin, D.J. Dean, K. Langanke: Phys. Rep. **278**, 2 (1997)
13. K. Langanke, G. Martínez-Pinedo: Nuc. Phys. **673**, 481 (2000)
14. K. Langanke, G. Martínez-Pinedo: At. Data. Nucl. Data Tables **79**, 1 (2001)
15. K. Langanke, E. Kolbe, D.J. Dean: Phys. Rev. C **63**, 032801 (2001)
16. K. Langanke etal.: Phys. Rev. Lett. **90**, 241102 (2003)
17. G. Martínez-Pinedo, K. Langanke, H.-T. Janka, M. Rampp: in preparation
18. A. Mezzacappa etal.: Phys. Rev. Lett. **86**, 1935 (2001)
19. M. Rampp, H.-T. Janka: Astron. Astrophys. **396**, 361 (2002)

Synthetic Spectra for Type Ia Supernovae at Early Epochs

D.N. Sauer[1], A.W.A. Pauldrach[2], T. Hoffmann[2], and W. Hillebrandt[1]

[1] Max-Planck-Institut für Astrophysik, Garching, Germany;
dsauer@mpa-garching.mpg.de, wfh@mpa-garching.mpg.de
[2] Institut für Astronomie und Astrophysik der Universität München, Germany;
uh10107@usm.uni-muenchen.de, hoffmann@usm.uni-muenchen.de

Summary. We present the current status of our construction of synthetic spectra for type Ia supernovae. These properly take into account the effects of NLTE and an adequate representation of line blocking and blanketing. The models are based on a sophisticated atomic database. We show that the synthetic spectrum reproduces the observed spectrum of 'normal' SN-Ia near maximum light from the UV to the near-IR. However, further improvements are necessary before truly quantitative analyses of observed SN-Ia spectra can be performed. In particular, the inner boundary condition has to be fundamentally modified. This is due to the dominance of electron scattering over true absorption processes coupled with the flat density structure in these objects.

1 Introduction

A detailed understanding of the physics and the explosion mechanism of type Ia supernovae (SNe Ia) is essential to minimizing systematic errors of cosmological parameters derived from the interpretation of SNe Ia observations. A key role in this context play realistic models of the expanding atmospheres of SNe Ia which are based on the full non-equilibrium physics involved, which link the results of current hydrodynamic explosion models (see, e.g., [1, 9]) to the comprehensive observational data.

The spectra of SNe Ia contain useful information about the energetics of the explosion – luminosity and velocity – and the nucleosynthesis, especially in shells above the pseudo-photosphere, which are primarily observable in early epochs. To gain access to this information several groups have started to compute synthetic optical spectra for SNe Ia in the photospheric epoch [2, 3, 5, 6]. So far, however, all use simplifying assumptions with uncertain influence on the resulting spectrum. Realistic models for quantitative analysis are still missing.

The main reason we still do not have realistic models is that the physical conditions in expanding SN Ia-atmospheres – high radiation energy density in a low matter density environment – make this modeling especially difficult. Simplifying assumptions such as local thermodynamic equilibrium (LTE) are invalid because radiative processes dominate over local collisional processes. Thus, a realistic model requires at minimum a solution of the full non-LTE

problem. Other difficulties arise because the ejecta do not contain significant amounts of hydrogen or helium, elements that form the main contribution to continuous opacity in other stellar objects. This causes a strong dominance of line opacity over continuous opacity, which is further complicated by the high expansion velocities of the ejecta (up to ~ 30000 km s^{-1}). Thus, thousands of Doppler-shifted and -broadened spectral lines of low-ionized metal atoms overlap and form a non-thermal "pseudo-continuum" with strong line-blocking and line-blanketing effects.

Furthermore, the entire light emission is powered by γ-photons (and in later times also positrons) originating from the decay of $^{56}\mathrm{Ni} \rightarrow {}^{56}\mathrm{Co} \rightarrow {}^{56}\mathrm{Fe}$. These γ-photons are redistributed to lower energies by scattering and ionization events. They are unlikely to be thermalized – in best case only partially – even within the pseudo-photosphere and the outer-most parts of the atmosphere because the density increases only moderately toward the center. Recent explosion models predict that ^{56}Ni can be present even at high velocities [9]. This indicates the need for a consistent treatment of the energy input within the atmosphere, which may significantly influence the emergent spectrum. Also, the observed changes in the spectra with time as the photosphere recedes into the ejecta show that the abundance of the elements varies strongly with radius.

All these factors have to be taken into consideration to develop a realistic radiative transfer model that allows a reliable quantitative analysis of SNe Ia.

In this paper, we describe the computation of synthetic spectra for SNe Ia based on a consistent treatment of the full NLTE radiative transfer (see [10]). This method will be used to test hydrodynamic explosion models against the observations and will eventually provide a powerful tool for spectral diagnostics of SNe Ia.

2 The Method

The basic approach for modeling supernova spectra is analogous to the treatment of O-stars with expanding atmospheres because the physics involved is similar in many respects. Our code development is based on a program package which has proven to be very successful for the quantitative spectral analysis of hot stars with radiation-driven winds [7, 8].

The models treat the expanding atmosphere as stationary and spherically symmetric. The underlying density structure, velocity field, and composition of the ejecta (averaged over angles) are provided by the explosion model.

The code provides a consistent solution of the radiative transfer and the NLTE rate equations for the occupation numbers of the atomic levels. A proper treatment of line blocking and blanketing effects is included. All significant contributions to opacity and emissivity from bound-bound, bound-free, and free-free transitions, as well as Thomson-scattering, are taken into account – for this purpose we have compiled and computed a comprehensive

atomic database involving accurate radiative and collisional ionization and excitation cross-sections and atomic level energies of all important ions.

After each iteration cycle, the temperature for each radius point is determined by balancing all energy gains and losses to the gas – implementation of the γ-photon deposition is currently under development; thus far, it is only considered with the assumption that all deposition takes place below the photosphere. Together with the use of the diffusion approximation at the lower boundary this implies the assumption of a complete thermalization of the γ-photons. The total luminosity (given by the amount of synthesized ^{56}Ni and the γ-deposition efficiency) is a parameter that is used to fit the shape of an observed spectrum.

Finally, the emergent spectrum is given by the computed radiation field at the outer boundary of the converged model.

3 First Results

Figure 1 (see [10]) compares the synthetic spectrum of a NLTE-model based on the W7 explosion model [4] to the observed spectrum of SN 1992A. At first glance the spectra seem to agree quite well. However, a closer look reveals a few discrepancies: the model reproduces the UV and blue part of the observed spectrum fairly well, but it fails to match the relatively steep decline toward infrared bands. Additionally, the absorption features of the model that are deeper than the observed may suggest that the peak fluxes are too large.

Thus, we cannot yet consider the models to be sufficient for quantitative spectroscopy of SNe Ia. Relevant SN Ia physics, in particular the treatment of the γ-deposition and a better analytical approach to the boundary condition at the photosphere (see next section) still have to be included into the model.

4 Discussion and Conclusions

The enhanced fluxes of the model to the red of ~ 4000 Å shown in Fig. 1 result from the invalid assumption of a photosphere analogous to the atmospheres of hot stars.

Various conditions in the ejecta contribute to the breakdown of the diffusion-approximation at the lower boundary. For stellar atmospheres, the diffusion limit for radiation is an excellent approximation as the conditions deep in the photosphere are very close to LTE. This is because the opacities at all wavelengths are dominated by true processes: H and He provide a strong bound-free continuum and free-free processes are supported by the exponential density increase at the photosphere (see Fig. 2).

In SNe Ia, however, the opacity is dominated by electron scattering over a large wavelength range, between the optical red and the radio band (see Fig. 2) – the sources of true continuous opacity (free-free and bound-free) are

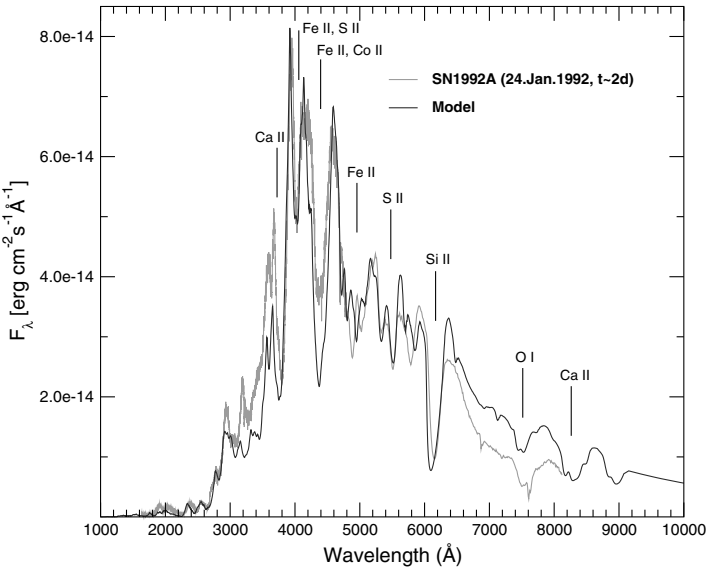

Fig. 1. Synthetic spectrum for a SN Ia around maximum light based on the W7 explosion model with homogenized composition. For comparison, the observed spectrum of SN1992A is also plotted.

orders of magnitude smaller because the composition does not contain hydrogen and helium, and the density distribution is flat. The electron scattering opacity, in contrast to true opacities, does not couple the radiation field to the local temperature. As the flux at the inner boundary from the diffusion approximation is determined by the temperature gradient which is constrained only by the true processes and does not consider scattering dominance. The input flux at these wavelengths is overestimated. We note these conditions do not change at larger optical depths. Moreover, the situation already occurs at early epochs where the assumption of a photosphere is generally considered to be a valid approximation.

These results show that the commonly used lower boundary condition (i.e., analytical expressions based on the diffusion-approximation) is highly problematic for SNe Ia. An inner boundary that correctly accounts for the physical conditions is required in order to correctly solve for the radiation field in SNe Ia.

Overall, the first results obtained with our method are encouraging. The main spectral features of SN Ia spectra are well reproduced, indicating that the underlying physics is correctly described. However, the results also show that even at early epochs the SNe Ia envelopes are comparable neither to the atmospheres of hot stars nor to gaseous nebula. Thus, the assumptions usually made for these cases cannot be applied to the expanding envelopes of

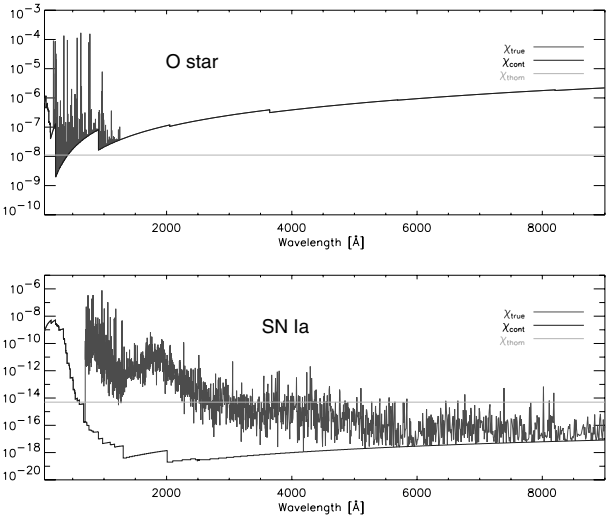

Fig. 2. The contributions to the opacity in a stellar atmosphere (upper panel) and a supernova (lower panel). Shown are the in both cases the Thomson-opacity $\chi_{\rm Thom}$ (the grey straight line) and the true continuum opacity $\chi_{\rm cont}$ (the dark solid line). $\chi_{\rm true}$ denotes the sum of the continuum opacity and the line opacity.

SNe Ia. In particular, a valid analytic approach to the boundary condition at the inner radius of a scattering-dominated atmosphere has to be formulated.

Acknowledgement. We thank our collaborators in the MPA Hydro-Group and the USM Hot-Star group for helpful discussions. This work was supported by the "Sonderforschungsbereich 375-95 für Astro-Teilchenphysik" der Deutschen Forschungsgemeinschaft. Attendance at the meeting was made possible by an EU CORDIS grant provided by the conference organizers.

References

1. V.N. Gamezo, A.M. Khokhlov, E.S. Oran, A.Y. Chtchelkanova, R.O. Rosenberg: Science **299**, 77 (2003)
2. P. Höflich, C.L. Gerardy, R.A. Fesen, S. Sakai: Astrophys. J. **568**, 791 (2002)
3. E.J. Lentz, E. Baron, D. Branch, P. Hauschildt: Astrophys. J. **557**, 266 (2001)
4. K. Nomoto, F. Thielemann, K. Yokoi: Astrophys. J. **286**, 644 (1984)
5. P. Nugent, E. Baron, D. Branch, A. Fisher, P.H. Hauschildt: Astrophys. J. **485**, 812 (1997)
6. A.W.A. Pauldrach, M. Duschinger, P.A. Mazzali, J. Puls, M. Lennon, D. Miller: Astron. Astrophys. **312**, 525 (1996)
7. A.W.A. Pauldrach, T.L. Hoffmann, M. Lennon: Astron. Astrophys. **375**, 161 (2001)

8. A.W.A. Pauldrach: astro-ph 0202226 (2003)
9. M. Reinecke, W. Hillebrandt, J.C. Niemeyer: Astron. Astrophys. **391**, 1167 (2002)
10. D. Sauer, A.W.A. Pauldrach: "Model atmospheres for type Ia supernovae: basic steps towards realistic synthetic spectra." In: *Nuclear Astrophysics,* ed. W. Hillebrandt, E. Müller (MPA Proc., 2002) p. 48

On the Stability of Thermonuclear Burning Fronts in Type Ia Supernovae

F.K. Röpke[1] and W. Hillebrandt[2]

Max-Planck-Institut für Astrophysik, Karl-Schwarzschild-Str. 1, 85741 Garching, Germany;
fritz@mpa-garching.mpg.de, wfh@mpa-garching.mpg.de

Summary. The propagation of cellularly stabilized thermonuclear flames is investigated by means of numerical simulations. In Type Ia supernova explosions the corresponding burning regime establishes at scales below the Gibson length. The cellular flame stabilization – which is a result of an interplay between the Landau-Darrieus instability and a nonlinear stabilization mechanism – is studied for the case of propagation into quiescent fuel as well as interaction with vortical fuel flows. Our simulations indicate that in thermonuclear supernova explosions stable cellular flames develop around the Gibson scale and that a deflagration-to-detonation transition is unlikely to be triggered from flame evolution effects here.

1 Introduction

The standard model of Type Ia supernovae (SNe Ia) describes these astrophysical events as thermonuclear explosions of white dwarf (WD) stars [7]. In our study, we refer to the specific scenario (for a review on SN Ia explosion models see [6]), where the WD consists of carbon and oxygen and the thermonuclear reaction propagates in form of a flame that starts out in the so-called "deflagration mode." That is, the flame is mediated by microphysical transport processes and its burning velocity is subsonic. One key ingredient in such a SN Ia model is the determination of the effective propagation velocity of the deflagration flame. The so-called "laminar burning speed," s_l, i.e. the propagation velocity of a planar deflagration flame, is much too low (a few percent of the sound speed in the unburned material) to explain powerful SN Ia explosions. The solution to this problem is provided by the concept of turbulent combustion. Instabilities on large scales result in the formation of a turbulent cascade, where large-scale eddies decay into smaller ones thereby transporting kinetic energy from large to small scales. Interaction of the flame with those eddies wrinkles the flame front and enlarges its surface. This is equivalent to an increase in the net fuel consumption rate and hence causes an acceleration of the flame.

Recent SN Ia explosion models on scales of the WD could show that in this way enough energy can be released to gravitationally unbind the star [3, 12]. However, these models cannot resolve all relevant length scales down to the flame width and therefore have to rely on assumptions on the physics

on unresolved small scales. The goal of our small-scale simulations of the propagation of the thermonuclear flame is to test those assumptions and eventually to reveal new physics that additionally needs to be included in the SN Ia models. The most significant assumptions of the large scale models by Reinecke et al. (e.g., [12]) are that the energy input into the turbulent cascade originate solely from large scales and the flame be stable on unresolved scales.

A fundamental feature of the turbulent cascade is that in a certain intermediate scale range, the turbulent velocity fluctuations decrease monotonically with smaller length scales of the eddies. This is captured by the corresponding scaling law. From that effect it is obvious, that there must exist a cutoff scale, below which flame propagation is not affected by the turbulent cascade anymore. Below this Gibson scale, the velocity fluctuations are so small, that the flame burns faster through the eddies than they can deform it. Thus the flame here propagates through "frozen turbulence." Our simulations aim on the study of effects around and below the Gibson scale. Except for the very late stages of the SN Ia explosion, the Gibson scale is well-separated from the width of the flame and the flame may safely be regarded as a discontinuity between burnt and unburned material.

2 Theoretical Background

What are the effects that dominate flame propagation below the Gibson scale? Here, two counteracting effects become important. The first is the Landau-Darrieus (LD) instability [2, 9]. It is based on a hydrodynamical effect and would completely prevent flame stability on the scales under consideration. This would have drastic impact on SN Ia models. However, there exists a second effect of purely geometrical origin [17], which balances the LD instability. Once the perturbations have grown to a critical size, former recesses of the flame front will develop into cusps, which possess propagation velocities slightly exceeding the burning speed of the rest of the front. This effect gives rise to a stable cellular shape of the flame. Therefore, the regime of flame propagation that will be studied in the present contribution is termed "cellular burning regime."

In connection with SN Ia explosions, this burning regime was studied by [1, 10] and [13] demonstrated its existence by means of a full hydrodynamical simulation. The questions that arise here are: Can the cellular flame stabilization break down under certain conditions (e.g., low fuel densities or interaction with turbulent velocity fields)? If so, could the flame itself generate turbulence on small scales (in contradiction to the assumption of large-scale SN Ia models) and thereby actively accelerate? This conjecture was put forward under the name active turbulent combustion by [11] on the basis of [8]. The questions are closely connected to the search for a mechanism providing a deflagration-to-detonation transition (DDT) of the flame propagation mode

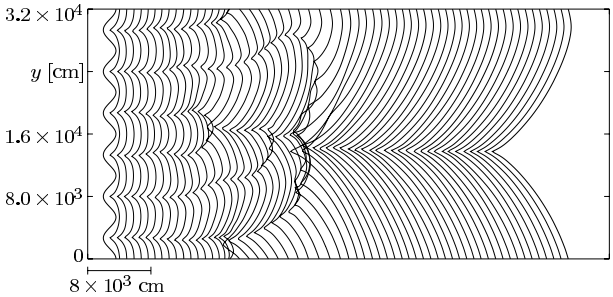

Fig. 1. Flame propagation into quiescent fuel of a density of $5 \times 10^7\,\mathrm{g\,cm^{-3}}$. Each contour marks a time step of $3.3 \times 10^{-3}\,\mathrm{s}$. The contours are shifted for better visibility and the spacing between them does not reflect the flame velocity.

in the context of the delayed detonation model of SNe Ia. A detonation wave is mediated by shocks and propagates with supersonic velocities.

3 Results of Numerical Simulations

In order to find answers to the above questions, we performed numerical simulations of the flame propagation in two dimensions. For a description and tests of the numerical implementation we refer the reader to [13, 16]. Our simulations addressed the flame propagation into quiescent fuel as well as flame interaction with a vortical flow field. The simulations were performed on an equidistant Cartesian grid. The flame was initialized in the computational domain and perturbed in a sinusoidal way from its planar shape. To follow the long-term flame evolution, we performed the simulations in a frame of reference comoving with the flame. This was implemented by imposing an inflow boundary condition ahead of the flame front and an outflow boundary on the opposite side of the domain. Transverse to the direction of flame propagation we applied periodic boundary conditions.

3.1 Flame Propagation into Quiescent Fuel

The first part of our investigations addressed the flame propagation into quiescent fuel. Here two stages of flame evolution are revealed. In the beginning, the small sinusoidal perturbation imposed on the flame front increases due to the LD instability. This part of flame evolution was studied in [13], were it was shown that the growth rates observed in our simulations agree well with the expectations from Landau's linear stability analysis [9]. In the second, nonlinear stage the flame stabilizes in a cellular pattern. The propagation of a flame with an initial perturbation of 6 periods fitting into the domain is plotted in Fig. 1.

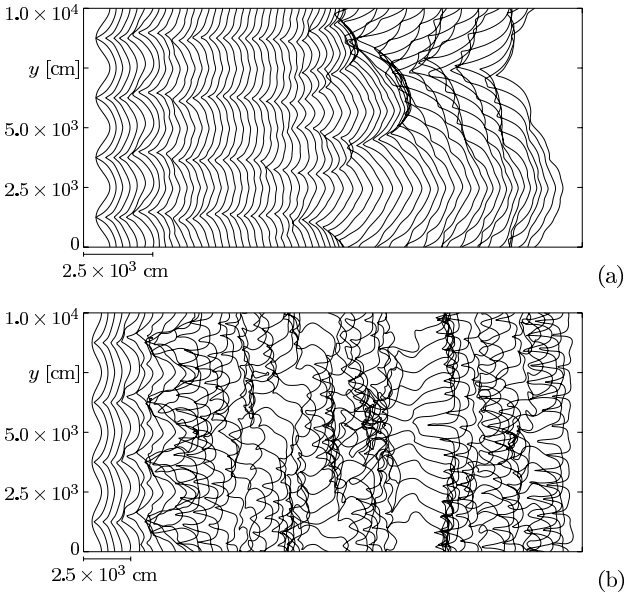

Fig. 2. Flame propagation into vortical fuel of a density of $5 \times 10^7\,\mathrm{g\,cm^{-3}}$. **(a)** $v'/s_l = 0.7$; **(b)** $v'/s_l = 2.5$. Each contour represents a time step of 8.0×10^{-4} s (a), and 2.4×10^{-3} s (b). Again, the contours are artificially shifted for better visibility.

The tendency of the small cells to merge in the nonlinear regime finally stabilizing in a single domain-filling cusp-like structure is apparent here. This result is consistent with semi-analytical studies of flame evolution [4].

3.2 Flame Propagation into Vortical Fuel

In SN Ia explosions, turbulent velocity fluctuations around the Gibson scale can be expected and also relics from pre-ignition convection may contribute to turbulent flows. In order to explore the effects of flame interaction with such velocity fluctuations, we modified the inflow boundary condition to a so-called "oscillating inflow condition," which generates vortices by imposing the following velocities at the boundary

$$v_x = s_l \left\{-1 + v' \sin 2k\pi y \cos 2k\pi(x - ts_l)\right\}$$
$$v_y = s_l\, v' \cos 2k\pi y \sin 2k\pi(x - ts_l).$$

Here, the parameter v' characterizes the strength of the imprinted velocity fluctuations and k denotes the wavenumber of the oscillation. This produces what is termed "square vortices" by [5].

The results of two of such simulations for different strengths of the square vortices are plotted in Fig. 2.

Although in case of weak vortices in the incoming flow there is some interaction with the flame, the flame still shows the tendency to align in a large-wavelength cellular structure (cf. Fig. 2a). This is similar to the case of flame propagation into quiescent fuel. On the other hand, if the vortices are strong enough, they can completely break up the cellular stabilization and prevent the flame from evolving into a single domain-filling structure (cf. Fig. 2b). However, we do not observe a drastic increase in flame surface and thus flame propagation speed. The flame structure rather adapts to the vortices imprinted on the fuel flow.

4 Conclusions

The presented simulations of flame propagation into quiescent fuel are in good agreement with theoretical expectations. The linear stage of flame evolution is consistent with Landau's dispersion relation [9, 13] and in the nonlinear regime the flame stabilizes in a cellular pattern. Thus, our hydrodynamical model of flame evolution shows that the cellular burning regime exists for SN Ia explosions.

Interaction of the flame with vortical flow fields may lead to a break-down of cellular stabilization if the velocity fluctuations are sufficiently large. In this case, however, the flame shows the tendency to adapt to the imprinted flow field. Thus, we observe a moderate increase in the effective flame propagation velocity but no drastic effects. No indication of active turbulent combustion could be found. Therefore, it seems unlikely that effects around the Gibson scale account for a DDT at late stages of the SN Ia explosion as has been anticipated by [11]. More detailed discussions of flame propagation into quiescent fuel at different fuel densities and interaction with vortical flow fields of varying strengths are currently in preparation [14, 15].

References

1. S.I. Blinnikov, P.V. Sasorov: Phys. Rev. E **53**, 4827 (1996)
2. G. Darrieus: In: "Propagation d'un front de flame." Presented at: *La Technique Moderne*, unpublished (1938)
3. V.N. Gamezo, A.M. Khokhlov, E.S. Oran, A.Y. Chtchelkanova, R.O. Rosenberg: Science **299**, 77 (2003)
4. S. Gutman, G.I. Sivashinsky: Physica D **43**, 129 (1990)
5. B.T. Helenbrook, C.K. Law: Combustion and Flame **117**, 155 (1999)
6. W. Hillebrandt, J.C. Niemeyer: Ann. Rev. Astron. Astrophys. **38**, 191 (2000)
7. F. Hoyle, W.A. Fowler: Astrophys. J. **132**, 565 (1960)
8. A.R. Kerstein: Combust. Sci. Technol. **118**, 189 (1996)
9. L.D. Landau: Acta Physicochim URSS **19**, 77 (1944)
10. J.C. Niemeyer, W. Hillebrandt: Astrophys. J. **452**, 779 (1995)
11. J.C. Niemeyer, S.E. Woosley: Astrophys. J. **475**, 740 (1997)

12. M. Reinecke, W. Hillebrandt, J.C. Niemeyer: Astron. Astrophys. **391**, 1167 (2002)
13. F.K. Röpke, J.C. Niemeyer, W. Hillebrandt: Astrophys. J. **588**, 952 (2003)
14. F.K. Röpke, W. Hillebrandt, J.C. Niemeyer: In: "The Cellular Burning Regime in Type Ia Supernova explosions: I. Flame Propagation into Quiescent Fuel." Astron. Astrophys. , inpress (2004)
15. F.K. Röpke, W. Hillebrandt, J.C. Niemeyer: In: "The Cellular Burning Regime in Type Ia Supernova explosions: II. Flame Propagation into Vortical Fuel." Astron. Astrophys. , inpress (2004)
16. F.K. Röpke: In: "On the Stability of Thermonuclear Flames in Type Ia Supernova Explosions." Ph.D. Thesis (Technical University of Munich: 2003)
17. Ya.B. Zel'dovich: J. Appl. Mech. and Tech. Phys. **1**, 68 (1966)

Explosion Models for Thermonuclear Supernovae Resulting from Different Ignition Conditions

Eduardo Bravo[1,2] and Domingo García-Senz[1,2]

[1] Departament de Física i Enginyeria Nuclear, Universitat Politècnica de Catalunya, Av. Diagonal 647, Barcelona, Spain
eduardo.bravo@upc.es domingo.garcia@upc.es
[2] Institut d'Estudis Espacials de Catalunya

Summary. We have explored in three dimensions the fate of a white dwarf of mass of 1.38 $M_\odot$ as a function of different initial locations of carbon ignition, with the aid of a SPH code. The calculated models cover a variety of possibilities ranging from the simultaneous ignition of the central volume of the star to the off-center ignition in multiple scattered spots. In the former case, the possibility of a transition to a detonation when the mean density of the nuclear flame decreases to $\rho \simeq 2 \times 10^7$ g cm^{-3} and its consequences are discussed. In the last case, the dependence of the results as a function of the number of initial igniting spots and the chance of some of these models to evolve to the pulsating delayed detonation scenario are also outlined.

1 Statement of the Problem

The analysis of light curves of many Type Ia Supernovae (SNIa) indicates that these events are not as homogeneous as one would desire to use them as perfect standard candles. In fact, the inferred mass of Nickel ejected in the explosion, estimated from the bolometric light curves [9], could range within a factor of ten. From a theoretical point of view, there remain a number of fundamental issues to be solved before we can rely on the predictions of SNIa modeling: pre-supernova evolution (progenitor systems, path of the white dwarf up to the Chandrasekhar mass, ignition conditions), physics of the explosion (subgrid-scale physics vs. large-scale combustion, flame behavior at low densities, deflagration–detonation transition), role of rotation and magnetic fields, etc.

Although one–dimensional (spherical) models of SNIa have succeeded to explain a wide range of observational properties, these kind of models unavoidably rely on phenomenological descriptions of inherently multidimensional processes. Among them, flame acceleration due to hydrodynamic instabilities is of particular importance. Recent multi-dimensional (3D) simulations of deflagrations in Chandrasekhar mass white dwarfs have shown that the subsonic propagation of the burning front can release enough energy to unbind the whole star and, maybe, can produce SNIa-like explosions [2, 8].

Although the final test of these models will have to be done by comparing self-consistent calculations of light curves and spectra (computed in three dimensions) with observations, one can already wonder if there is any significant observational evidence of departure from spherical symmetry in SNIa. In this respect, we note that: 1) Light curves are well described by a one-parameter family of curves (e.g. [7]), 2) spectral absorption features by SiII show quite homogeneous profiles from event to event [10], and 3) polarization has not been detected in most SNIa, although there are a few exceptions [6]. Supernova remnants (SNR) provide another means to constrain the geometry of the explosions, although it depends also on the presence of interstellar medium inhomogeneities and on the development of further hydrodynamic instabilities. Still, some SNRs do not show large departures from spherical symmetry (e.g. the blast wave of Tycho's SNR), which implies that both the supernova ejecta and the interstellar medium possessed a high degree of symmetry in these cases (see also the paper by Badenes et al. in these proceedings). All these data point to approximately spherical explosions in which the chemical inhomogeneities are constrained to small-size clumps (a quantitative criterion, proposed in [10], is that the area of the individual clumps present at the photosphere has to be lower than $1 - 10\%$ of the photospheric area).

Our aim here is to address the following questions:

- Are 3D simulations of thermonuclear supernovae able to cover the full range of light curve variations (up to a $10\times$ factor in ^{56}Ni production)?
- How much the ejecta structure obtained in these simulations deviates from spherical symmetry (overall shape, small-scale clumping)?

We present the results from 3D hydrodynamic simulations starting from different initial conditions. We have explored as well the possible outcomes from deflagration–detonation transitions in 3D. It has to be stressed that all calculations were carried out consistently, i.e. using the same hydrocode [4], with the same numerical resolution, the same physics, and simulating the whole white dwarf volume to avoid the introduction of artificial and unrealistic symmetry conditions.

2 Computed 3D Models, ^{56}Ni Productivity and Asymmetry

We have started from several ignition configurations, in which the carbon runaway took place either in a central volume, slightly perturbed from spherical symmetry, or in multiple scattered spots or "bubbles" [3]. In the second case, we have explored the sensitivity of the results to questions like: How many bubbles ignite simultaneously? Which are the sizes of the hot bubbles? Both theoretical analysis [1] and 2D simulations [5] do not seem to favor the

Table 1. List of 3D simulations performed

Model category	Ignition configuration	$E_{\rm kin}$ (10^{51} erg)	$M(^{56}{\rm Ni})$ ($M_\odot$)	$M({\rm C+O})$ ($M_\odot$)
Deflagration	Central volume	0.26	0.27	0.65
Deflagration	6 equal size bubbles	-	0.21	-
Deflagration	7 equal size bubbles	-	0.21	-
Deflagration	10 equal size bubbles	0.05	0.24	0.88
Deflagration	30 equal size bubbles	0.44	0.56	0.58
Deflagration	90 random size bubbles	0.45	0.58	0.58
Delayed detonation	Transition where $D > 2.5$	0.75	0.54	0.39
Delayed detonation	Transition in central layers	0.48	0.40	0.55
Delayed detonation	Transition in medium layers	0.51	0.43	0.51
Delayed detonation	Transition in external layers	0.33	0.32	0.65
Pulsating reverse detonation	6 bubbles	0.89	0.35	0.22

formation of a large number of bubbles igniting in phase (i.e. of the same size).

As for the deflagration–detonation transition, up to now there is no convincing mechanism that could account for the acceleration of the burning front up to supersonic velocities, so we have computed delayed detonation models making use of several different algorithms for the initiation of the detonation. In one case, we started the detonation in those points in which the fractal dimension of the flame was larger than 2.5, while in the other cases, the condition for detonation ignition was that the density were lower than 2×10^7 g cm^{-3} and the particles to be detonated were selected according to their radius. The initial deflagration phase of all the delayed detonation models was coincident with the deflagration model given in the first row of Table 1.

In Table 1, there are listed the models computed and the main results of the simulations. In all cases, the ignition started when the white dwarf central density reached 1.8×10^9 g cm^{-3}, and the simulations used 250,000 identical mass particles (each particle was about the same mass as the Earth). The third column in Table 1 gives the final kinetic energy, the fourth column gives the ejected mass of ^{56}Ni, and the fifth column gives the ejected mass of unburned C and O.

As can be seen from Table 1, all the deflagration models gave a kinetic energy too low to account for SNIa properties, with the exception of the two simulations starting from a large number (> 30) of bubbles. It is a remarkable result that the explosion properties resulting from these two models were almost the same, even though they started from very different initial conditions (in terms of number and sizes of hot bubbles). The results of these two simulations were as well close to the ones given in [8], for comparable

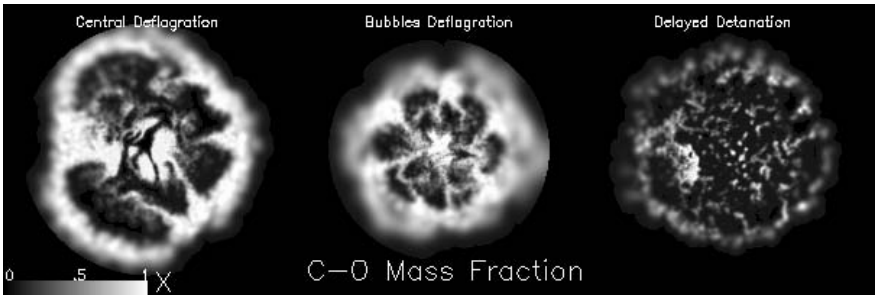

Fig. 1. Final distribution of unburned C-O in selected models. From left to right: deflagration starting from a central volume, deflagration starting from 30 bubbles, and delayed detonation initiated where the flame fractal dimension was $D > 2.5$.

initial conditions, which reinforces the reliability of the outcome we obtained. However, in the deflagration scenario there always remains a large mass of unburned C and O, which would undoubtedly have to be detectable in the optical spectra of SNIa.

All our delayed detonation models gave healthy explosions with reasonable kinetic energies and a wide range of ^{56}Ni masses. If nature provided a range of conditions for transition to detonation as wide as we have explored, the delayed detonation scenario would help to explain the diversity of SNIa explosions observed. However, our 3D simulations have shown that the delayed detonations are relatively inefficient in converting C and O to intermediate mass elements or to iron peak elements (which is in sharp contrast with 1D models of delayed detonations), which results in a lower velocity range than expected. The ultimate reason for this behavior is the geometry of the distribution of fuel resulting from the previous deflagration stage. Due to the unavoidable distortion of the flame front caused by hydrodynamic instabilities during subsonic burning, the initial conditions for delayed detonation formation consist on large plumes of ashes coexisting at the same radii with deep tongues of fuel (see Fig. 1). These plumes of ashes act as true barriers obstructing the propagation of the detonation waves and, in fact, decoupling large volumes occupied by C and O from other regions which can hold propagating detonations.

To discuss the geometrical properties of the explosions, we will refer to Fig. 1, in which we show the distributions of the ejected C–O in YZ slices. None of the models displays an overall shape that departs largely from spherical symmetry, although the distribution of chemical species presents irregularities of different sizes. However, the deflagration model starting from a central volume (left image in Fig. 1) is the most asymmetric. This is due to Rayleigh–Taylor instabilities during flame propagation, which favor the formation of large–scale structures that stand out in the final geometry of the ejecta. This configuration is in clear disagreement with the limits to the size

of clumps given in [10]. In the case of deflagrations starting from hot bubbles, the geometrical appearance of the ejecta retains a larger degree of spherical symmetry, but still the chemical inhomogeneities represent a large fraction of the radius of the star. We have estimated that, in the model starting from 30 bubbles (center image in Fig. 1), a typical clump size is $\sim 10\%$ of the ejecta radius, still too large.

Delayed detonations (right image in Fig. 1) are approximately spherical in shape, and show only small clumps. We have estimated a typical clump size of $\sim 4\%$ of the ejecta radius in these kind of models. This could seem a striking result, as the delayed detonations were computed starting from the final configuration of the deflagration shown in the left image in Fig. 1. The reason for this apparent contradiction is that the detonations were able to destroy the large structures built up during the deflagration phase, thus allowing the formation of only small-sized chemically differentiated clumps.

3 Discussion and a New SNIa Paradigm

To summarize, deflagrations computed in 3D produce large clumps, ejecta with low kinetic energy, reasonable quantities of ^{56}Ni, and too much unburned C–O ($> 0.58\ M_{\odot}$). On the other hand, multidimensional delayed detonations produce smaller clumps, although they are not as efficient as their 1D counterparts at rising the kinetic energy ($< 0.75 \times 10^{51}$ erg) nor at burning C and O ($M(C-O) > 0.39\ M_{\odot}$). In addition, we have seen that deflagrations starting from a reasonable number of bubbles ($< 6-10$) fail to unbind the white dwarf, which brings us to the following question: What is the fate of the white dwarf following explosion failure?

We have followed the evolution of the star during the first pulsation with the 3D SPH code. What came out from this multidimensional calculation was in fact quite different from what is obtained in 1D pulsating models. Due to the ability of bubbles to float to large radii in 3D, most of the thermal and kinetic energy resided in the outer parts of the structure, which resulted in an early stabilization of the central region (mostly made of C and O, i.e. fuel) while the outer layers were still in expansion. Few seconds later, an accretion shock formed at the border of the central nearly hydrostatic core (whose mass was about $0.9\ M_{\odot}$). Therefore, the temperature at the border of the core increased to nearly 10^9 K, on a material composed mainly by fuel but with a non-negligible amount of hot ashes, thus giving rise to a highly explosive scenario. If a detonation were ignited at this point, it would probably propagate all the way inwards through the core, burning most of it and producing an energetic explosion. We have called this new paradigm of SNIa explosion mechanism the Pulsating Reverse Detonation. Currently, we are in the process of completing the 3D calculation of its detonating phase. As a first evaluation of what one can expect from this new scenario, we have computed a 1D model (last row in Table 1), which ended with the largest

kinetic energy, and the lowest mass of C and O from all the set of models we have computed in 3D up to now. It turns out that it is worth following the evolution of this scenario in 3D to see if it can derive in a new reliable and competitive model of SNIa.

References

1. E. Bravo, D. García-Senz: "Thermonuclear supernovae: Is deflagration triggered by floating bubbles?" In: *From Twilight to Highlight: The Physics of Supernovae*, ed by W. Hillebrandt, B. Leibundgut (Springer, Berlin 2003) pp. 165-168
2. V.N. Gamezo et al. : Science **299**, 77 (2003)
3. D. García-Senz, S.E. Woosley: Astrophys. J. **454**, 895 (1995)
4. D. García-Senz, E. Bravo, N. Serichol: Astrophys. J. Suppl. **115**, 119 (1998)
5. P. Höflich, J. Stein: Astrophys. J. **568**, 779 (2002)
6. D. Kasen et al. : Astrophys. J. **593**, 788 (2003)
7. M.M. Phillips et al. : Astron. J. **118**, 1766 (1999)
8. M. Reinecke, W. Hillebrandt, J.C. Niemeyer: Astron. Astrophys. **391**, 1167 (2002)
9. N.B. Suntzeff: "Optical, infrared, and bolometric light curves of Type Ia supernovae." In: *From Twilight to Highlight: The Physics of Supernovae*, ed by W. Hillebrandt, B. Leibundgut (Springer, Berlin 2003) pp. 183-192
10. R.C. Thomas, D. Kasen, D. Branch, D., E. Baron: Astrophys. J. **567**, 1037 (2002)

Snapshotplate 1. (*Top*) Students relax between sessions; (*Middle*) Museo de las Ciencias Príncipe Felipe; (*Bottom; left to right*) C. Pollas, J. Maza, R. Evans, D. Tsvetkov, B. Schmidt, A. Filippenko, W. Li.

Snapshotplate 2. (*Top; left to right*) J. Marcaide, R. Evans, F. García; (*Middle; left to right*) R. Evans, J. Marcaide, M. Rees; (*Bottom; left to right*) M. Rees, I. Marchite.

Snapshotplate 3. (*Top*) A session in progress; (*Middle; left to right*) M. Bietenholz, A. Alberdi; (*Bottom; left to right*) R. Chevalier, A. Filippenko.

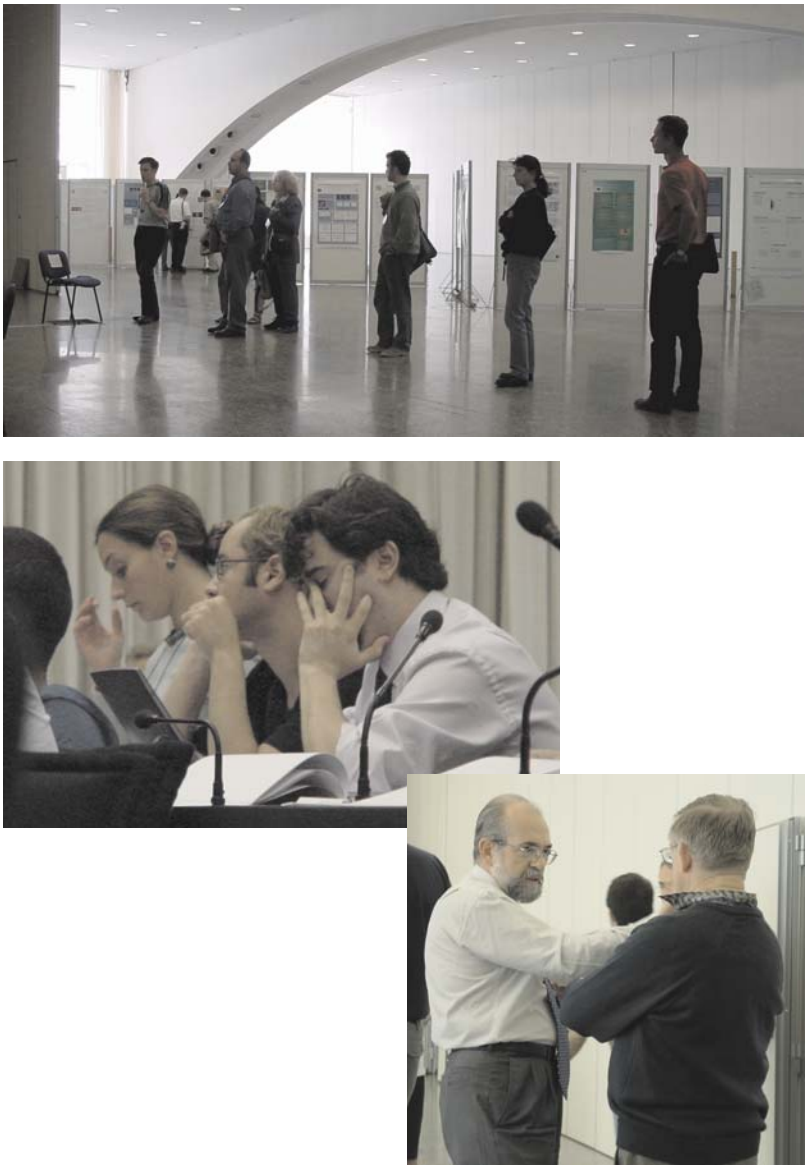

Snapshotplate 4. (*Top*) Poster viewing; (*Middle*) Concentration is needed!; (*Bottom; left to right*) J. Maza, R. Evans.

Snapshotplate 5. (*Top; left to right*) M. Pérez-Torrez, A. Alberdi, J. Guirado, E. Ros; (*Middle; left to right*) E. Berger, A. Soderberg; (*Bottom*) W. Hillebrandt.

Snapshotplate 6. (*Middle; left to right*) R. McCray, M. Rees, R. Chevalier, B. Schmidt, K. Weiler, J. Marcaide; (*Middle; left to right*) K. Weiler, J. Marcaide, R. Chevalier, M. Rees, R. McCray, B. Schmidt, J. Guirado; (*Bottom; left to right*) R. Chevalier, K. Weiler, R. McCray, B. Schmidt, M. Rees, J. Marcaide.

Snapshotplate 7. (*Middle; left to right*) Students from Valencia; (*Middle; left to right*) M. Hamuy, M. Pérez-Torres; (*Bottom; left to right*) J. Marcaide, K. Weiler.

Part V

Supernovae: Searches/Statistics

Supernova Statistics

Enrico Cappellaro[1], Roberto Barbon[2], and Massimo Turatto[3]

[1] INAF - Osservatorio Astronomico di Capodimonte, via Moiariello 16, 80181 Napoli, Italy;
cappellaro@na.astro.it
[2] Dipartimento di Astronomia, Università di Padova, vicolo dell'Osservatorio 2, 35132 Padova (Italy)
barbon@pd.astro.it
[3] INAF - Osservatorio Astronomico di Padova, vicolo dell'osservatorio 5, 35132 Padova (Italy)
turatto@pd.astro.it

Summary. The statistics of SN discoveries is used to reveal selection biases of past and current SN searches and to gain insight on the progenitor scenarios for the different SN types. We also report estimates of the SN rate per unit mass in galaxies of different types and on the first attempts to study the evolution of the supernova rate with redshift.

1 Counting Supernovae

Event statistics is an invaluable tool to link the different supernova types to their parent stellar populations and in turn to assess the consistency of the possible progenitor scenarios. Since the early days of SN research, the simple observation that type Ia SNe are found in all type of galaxies, including ellipticals where star formation ceased long time ago, is used to deduce that their progenitors must be low mass, long lived stars. Today the standard scenario for type Ia calls for an accreting white dwarf in a close binary system which explodes when it reaches the Chandrasekhar mass. However, the real nature of the progenitor system has not yet been identified and the different candidates, e.g., double degenerate or single degenerate, have still to pass the basic test of the occurrence statistics [14].

Type II and Ib/c SNe are believed to be the outcomes of the core collapse of stars with mass larger than $8-9$ $M_{\odot}$. Different sub-types have been related to progenitors with different initial masses and/or metallicities [10]. Since only for a few events it has been possible to collect direct informations on the progenitors [19], one of the basic tool of investigation remains the event statistics in systems with different stellar populations.

It is fair to say that the new interest for SNe in the last few years has been driven not just by the wish to understand their physical properties but mainly by their role as cosmological probes, in particular the use of type Ia to measure the geometry of the Universe. In addition, we believe that measurements of the SN rates as a function of redshift is an attractive tool to recover the history of the star formation rate with the cosmic age [1, 18].

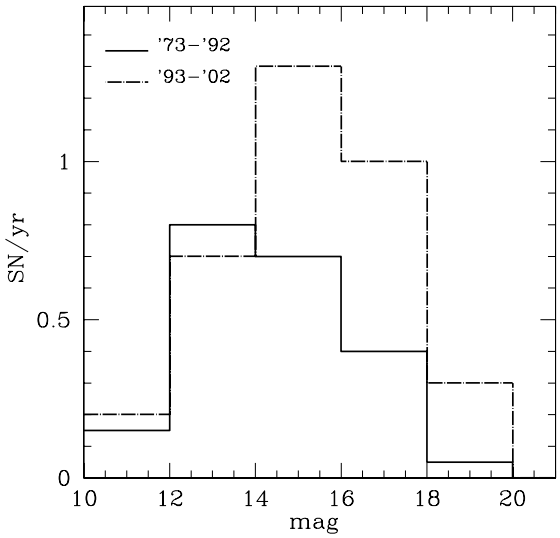

Fig. 1. Distribution of the apparent magnitude for the nearby SNe (recession velocity $v_{hel} < 1200\,\mathrm{km\,s^{-1}}$) discovered in two periods: the last decade (1993–2002) and the preceding twenty years (1973–1992).

2 SN Searches

At a rate of a few hundred new SNe discovered each year, the number of known SNe doubled in the last 5 years for a total count of over 2500 events[1]. Yet, the discovery rate of bright events, those < 15 mag at discovery, remains more or less constant, at about 10 SN/year. This may appear to confirm the common assumption that in modern time, say after 1970, all the SNe which exploded in the local Universe were discovered [21]. However, although most of the faint SNe discovered in the last decade are distant events, there is also a significant contribution for nearby SNe. This can be seen in Fig. 1 where we compare the apparent magnitude distribution of the SNe discovered in the local Universe ($v_{hel} < 1200\,\mathrm{km\,s^{-1}}$) in two different periods, the last decade and the twenty years before. It turns out that the discovery rate in nearby galaxies is today almost a factor 2 larger than in the past and that the average apparent magnitude at discovery is about 1 mag fainter.

It is important to stress that among the faint, nearby events there are not only those SNe that, due to seasonal observational limitations, were discovered long after maximum, but also highly extinguished events (e.g., SN 2002cv [6]) and intrinsically faint SNe (e.g., SN 1997D [22]).

The presence of such bias explains why the absolute value of the SN rate cannot be derived from the general list of SNe but instead through a detailed

[1] See http://www.pd.astro.it/supern/snean.txt for an up-to-date version of *The Asiago SN Catalogue*.[2]

analysis of the data of an individual SN search, for which actual limits and biases can be carefully accounted for.

The main problem, when considering the data of an individual SN search, is that the statistics is not very large, especially when considering less frequent SN types. Therefore the analysis of the relative SN rates from the general list can still be of interest. In Fig. 2 we report, in a separate panel for each of the three main SN type (Ia, II and Ib/c), the SN counts as a function of galaxy type. It results that the discovery rate of type Ia SN appears more or less independent on galaxy type, while the core collapse SN rate rapidly increases from early to late type spirals. The latter gives a very close match of the current estimates of the star formation rate in galaxies of different type (cf. Fig.3 in [11]) and directly reflects the fact that SN II derive from massive, short lived progenitors. An intriguing feature which is seen in Fig. 2 is the spike for type Ib/c SNe in Sc galaxies which, because of a similar peak in the star formation rate, suggests that, in the average, their progenitors are more massive than those of normal type II SNe. We should note that this effect seems to be washed-out when using, instead of the RC3 galaxy classification system as in the Asiago SN catalogue, the DDO system [23].

Because of the peak of the SFR, the ratio of the events in Sc galaxies compared to the total counts for a given SN type can be used to rank the SN types according to their progenitor masses. This ratio results $12 \pm 1\%$ for type Ia, $19 \pm 2\%$ for type II and $34 \pm 6\%$ for type Ib/c which gives the same indication of Fig. 2 in a different form and can be used as reference to derive some hints for less frequent SN sub-types. For instance, we found that the same ratio for type IIn is $24 \pm 6\%$ which suggests that these SNe have in average the same progenitor mass, or maybe even somewhat higher, than normal type II. This has become interesting after the discovery of SN 2002ic [9], a SN Ia showing evidence of interaction with a dense H envelope and, at late time, developing a spectrum very similar to that of some type IIn like SN 1997cy. That this is the most common channel for type IIn is not consistent with the fact that their progenitors, in the average, seems to be massive (cf. [23]).

Another example is that of faint type II SNe [22]. These low energy explosions delivering one order of magnitude less Ni that normal type II have been related to the formation of a black hole rather than to a neutron star. This is attributed to their progenitors being more massive than those of normal SNII [16, 24] and it is consistent with the fact that out of 10 events, 5 occurred in Sc galaxies.

3 SN Rates

As we mentioned before, the absolute value of the SN rates requires that the detection efficiency and selection biases of individual SN searches are accurately estimated. At the same time, it is important to maintain a sufficient

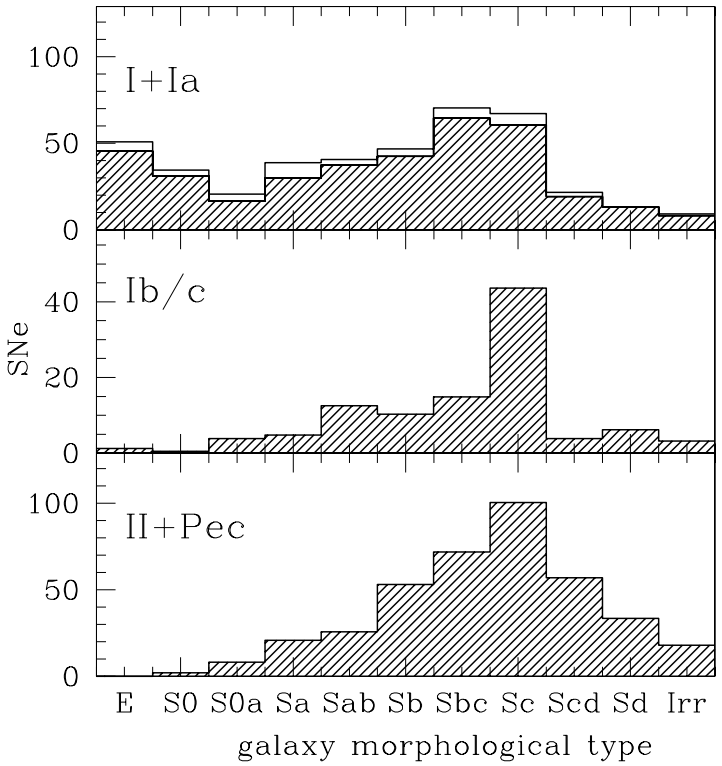

Fig. 2. SN counts for galaxies of different morphological type for the three main SN types, normalized to the fraction of galaxy of the given type as derived from the RC3 galaxy catalog [5]. Only SNe at redshift $z < 0.05$ have been included. In the upper panel the shaded area are type Ia SNe only.

statistics for SN events which, especially in the past, was not achievable using one search alone. An obvious solution is to pool the data from a few systematic SN searches as in [4]. Somewhat surprisingly, these most significant results still rely on photographic and/or visual SN searches, while the modern, systematic CCD SN searches have still to be exploited.

One of the main uncertainties on the current estimate of the SN rates is the bias against SN detection in spiral galaxies which are not seen face-on. Likely, this is due to the fact that the larger optical depth trough the dust, and hence the higher extinction, makes the average SN in inclined spirals fainter that in face-on ones. It is often claimed that the effect was only important for photographic surveys whereas modern CCD searches, due to the better spectral sensitivity in the red, are less affected. Although this is certainly true, the inclination effect does remain important. This is shown in Fig.3, where the SN discovery counts in spiral galaxies of different inclination are compared for different grouping of galaxy and SN types. Only SNe discovered

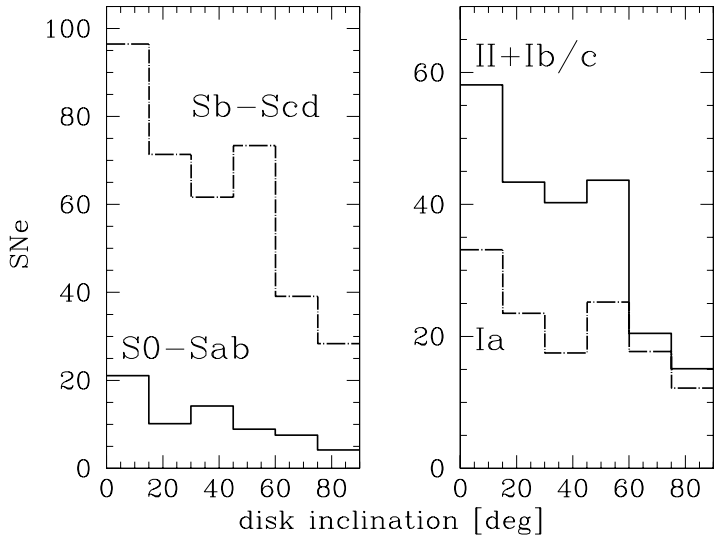

Fig. 3. SN counts in spiral galaxies of different inclinations (0 deg is for face-on galaxies) normalized to the fraction of galaxies in each bin of inclination as given in the RC3. In the left panel we show separately early and late type spirals, whereas in the right panel we distinguish core collapse (II+Ib/c) from thermonuclear (Ia) Supernovae. Only the SNe discovered after 1998 have been included.

in the last 5 years, hence mainly in systematic CCD searches, have been included. It turns out that taking as reference the discovery rate in face-on spirals ($i < 30°$), even in the present day SN searches we are missing half of the type Ia and 2/3 of the core collapse SNe occuring in edge-on spirals ($i > 60°$). We stress that although it may occur that in some SN searches face-on galaxies are monitored more frequently, it is not expected that this depends on galaxy or SN type.

After Tammann [20], the rate of SNe is usually normalized to the galaxy blue luminosity (SNu = SN $10^{-10} L_{\odot}^{B}$ 10^{-2}yr). This is convenient because *a*) the luminosity can easily be measured for large galaxy samples and *b*) the SN rate has been found to be proportional to the galaxy luminosity. However, while interpreting the results, it has to be taken into account that there are different contributors to a galaxy blue luminosity depending on its stellar population mixture. Indeed it is well know that the mass to light ratio (M/L) changes by one order of magnitude along the Hubble galaxy sequence. We can convert SN rate per unit luminosity to SN rate per unit mass assuming an average M/L for each galaxy type [7]. The results are reported in Table 1.

It is known been that for SN Ia the rate per unit luminosity remains almost constant moving from ellipticals to spirals. On the other side as it can be seen from Table 1, because M/L is lower, the rate of SNIa per unit mass in late spirals is almost 3 times higher than in ellipticals. This implies that

Table 1. SN rate per unit mass $[10^{-11}\mathrm{M}_\odot\, 10^{-2}\mathrm{yr} \times (\mathrm{H}/75)^2]$.

galaxy type	SN rate			
	Ia	Ib/c	II	All
E-S0	0.16 ± 0.03	< 0.01		0.16 ± 0.03
S0a-Sb	0.29 ± 0.07	0.16 ± 0.07	0.69 ± 0.17	1.14 ± 0.20
Sbc-Sd	0.46 ± 0.10	0.30 ± 0.11	1.89 ± 0.34	2.65 ± 0.37
All	0.27 ± 0.03	0.11 ± 0.03	0.53 ± 0.07	0.91 ± 0.08

a fraction of SN Ia in spirals must be related to a relatively young stellar population.

Because of the short time scale of evolution of massive stars, the core collapse (II+Ib/c) SN rate can be translated in the present time star formation rate if we know the initial mass function and the mass range of core collapse progenitors. Assuming a Saltpeter mass function (with index 1.35) and choosing 8 and 40 M$\odot$ for the lower and upper limits of core collapse progenitor masses, from the measured core-collapse SN rates we derive than in a $10^{11}\,\mathrm{M}_\odot$ Sbc-Sd galaxy of the local Universe the star formation rate is $1.8\,\mathrm{M}_\odot\,\mathrm{yr}^{-1}$, in S0a-Sb is $0.7\,\mathrm{M}_\odot\,\mathrm{yr}^{-1}$, whereas for E-S0 we derive an upper limit of $0.01\,\mathrm{M}_\odot\,\mathrm{yr}^{-1}$. These numbers strongly depend on the lower mass limit for core collapse progenitors which is not well known. For instance if we take for the latter 10 $\mathrm{M}_\odot$ the estimate of the star formation rates increases by $\sim 40\%$.

4 Evolution of the SN Rate with Redshift

Estimates of the supernova rate, in particular that of core collapse SNe at different redshifts can be used to recover the history of star formation with cosmic age. Conversely, if the latter is known, it is possible to constrain the SN progenitor scenario which is especially important for type Ia which has not yet been firmly established. Despite of these prospectives, very few observational estimates have been published to date and all rely on the major efforts devoted to the search of type Ia to be used as cosmological distance indicators. This means that *a*) only type Ia rate have been measured and *b*) the search strategy introduces severe biases. In particular, to allow for accurate photometry, the candidates found in the galaxy inner regions and/or in bright galaxies are usually rejected.

A further concern is that little is known about the properties of the galaxy sample. Among other things, this makes impossible to verify the presence of a spiral inclination effect such as in the local Universe. We stress that although high redshift SN searches are usually performed in the red (R or I band), the host galaxy extinction occurs in the SN rest frame wavelength (ie. B or V for

$z \sim 0.5$). Therefore if in galaxies at $z \sim 0.5$ the dust content and properties are the same as in the local Universe, we expect similar biases.

The few available estimates seem to indicate an evolution of the type Ia SN rate with redshift. At $z = 0.55$ the measured value is $0.33^{+0.06}_{-0.05}(H/75)^2$ SNu [15] to be compared with the local estimate (not corrected for host galaxy inclination) of $0.14 \pm 0.04(H/75)^2$ [4]. Taken as a face value, this indicates a very rapid increase of the SN Ia rate. However, due to the large uncertainty, this is still consistent with the current scenario of galaxy and SN Ia progenitor system evolution [12].

In the last few years we started a long term project which is especially designed to measure SN rates and to overcome some of the previous limitations. In particular we try to:

1. reduce as much as possible the candidate selection biases. Indeed we do count candidates in the galaxy nuclear region (but we try to reduce the contamination from variable AGN using the long term variability history of the source).
2. count both type Ia and core collapse SNe. Core collapse SN rate can be used to constraints the star formation rate at the given redshift. Besides, relative SN rates have smaller systematic errors than absolute values.
3. use photometric redshift to characterize the galaxy sample

The first results of this program are now becoming available [1] and indicate that the rate of core collapse SNe is increasing at a faster pace than SN Ia. In particular we found evidence that the star formation rate a $z = 0.30$ is a factor 3 higher than in the local Universe. Although this is a preliminary result it confirms similar finding based on the measurements of the Hα emission from galaxies at the same redshift [8]. The coming in operation of new wide field telescopes (e.g., VST+OmegaCAM [3, 13] and LBT+LBC [17] will give the chance to strongly improve the statistics and to probe different redshifts.

References

1. G. Altavilla et al. : In: These proceedings
2. R. Barbon, V. Buondí, E. Cappellaro, M. Turatto: Astron. Astrophys. Suppl. **139**, 531 (1999)
3. M. Capaccioli, D. Mancini, G. Sedmak: Mem. Soc. Astron. It. **74**, 450 (2003)
4. E. Cappellaro, R. Evans, M. Turatto: Astron. Astrophys. **351**, 459 (1999)
5. G. de Vaucouleurs, A. de Vaucouleurs, H.G. Corwin, R.J. Buta, G. Paturel, P. Fouque: *Third Reference Catalogue of Bright Galaxies.* Vol. 1-3, XII (Springer-Verlag, Berlin, 1991)
6. A. Di Paola et al. : Astron. Astrophys. **393**, L21 (2002)
7. S.M. Faber, J.S. Gallagher: Ann. Rev. Astron. Astrophys. **17**, 135 (1979)
8. S.S. Fujita et al. : Astrophys. J. Lett. **586**, L115 (2003)

9. M. Hamuy et al. : Nature **424**, 651 (2003)
10. A. Heger, C.L. Fryer, S.E. Woosley, N. Langer, D.H. Hartmann: Astrophys. J. **591**, 288 (2003)
11. R.C. Kennicutt: Ann. Rev. Astron. Astrophys. **36**, 189 (1998)
12. C. Kobayashi, T. Tsujimoto, K. Nomoto: Astrophys. J. **539**, 26 (2000)
13. K. Kuijken et al. : The Messenger **110**, 15 (2002)
14. R. Napiwotzki et al. : In: *From Twilight to Highlight: The Physics of Supernovae.* (Proc. ESO/MPA/MPE Workshop, 2003) p. 134
15. R. Pain et al. : Astrophys. J. **577**, 120 2002
16. A. Pastorello et al. : Mon. Not. R. Astron. Soc. **347**, 74 (2004)
17. R. Ragazzoni et al. : SPIE **4008**, 439 (2000)
18. R. Sadat et al. : In: These proceedings
19. S.J. Smartt, J.R. Maund, G.F. Gilmore, C.A. Tout, D. Kilkenny, S.D. Benetti: Mon. Not. R. Astron. Soc. **343**, 735 (2003)
20. G.A. Tammann: Astron. Astrophys. **8**, 458 1970
21. G.A. Tammann, W. Loeffler, A. Schroeder: Astrophys. J. Suppl. **92**, 487 (1994)
22. M. Turatto et al. : Astrophys. J. Lett. **498**, L129 (1998)
23. S. van den Bergh, W. Li, A.V. Filippenko: astro-ph 0308195 (2003)
24. L. Zampieri et al. : Mon. Not. R. Astron. Soc. **338**, 711 (2003)

The Infrared Supernova Rate

F. Mannucci[1] G. Cresci[2] R. Maiolino[3] and M. Della Valle[4]

[1] IRA-CNR, Largo E. Fermi 5, 50125 Firenze, Italy;
filippo@arcetri.astro.it
[2] Dip. di Astronomia, Universitá di Firenze, Largo E. Fermi 5, 50125 Firenze Italy;
gcresci@arcetri.astro.it
[3] INAF-Osservatorio Astrofisico di Arcetri, Largo E. Fermi 5, 50125 Firenze Italy;
maiolino@arcetri.astro.it
[4] INAF-Osservatorio Astrofisico di Arcetri, Largo E. Fermi 5, 50125 Firenze Italy;
massimo@arcetri.astro.it

Summary. Optical searches can detect supernovae (SNe) only if they suffer of a limited amount of dust extinction. This is a severe limitation as most of the core-collapse SNe could explode inside dusty regions. We describe a few ongoing projects aimed at detecting dusty SNe at near-IR wavelengths both in ground-based and HST images and to study their properties.

1 The Problem

Supernovae (SNe) exploding inside dusty regions could dominate, even by a large amount, the number of core-collapse events in the universe, as most of the star-forming activity is hidden by dust. Nevertheless, centuries of optical searches have discovered only very few SNe in dusty regions and no very obscured event.

This is clearly a selection effect, and infrared or radio observations are needed to reveal highly obscured SNe. Events detected at these long wavelengths can be used to study the properties of the SNe in dusty galaxies, and to obtain a complete estimate of the total SN rate in the local universe, important to calibrate the SN rate at high redshift now under study. In principle the number of events could also be used to derive information on the main energy source (starburst vs. AGN) of the galaxies when they are dominated by a hidden central source, as for the Luminous Infrared Galaxies (LIRGS).

2 Optical vs. Near-Infrared

The observed rates of the core-collapse SNe, when derived from optical observations and normalized to the B luminosity of the galaxy, don't show any significant dependence on the galaxy type. Normal galaxies between Sa and Sm [1], starburst galaxies [8], galaxies with an active nuclei [1], and interacting galaxies [7], all show the same SN rate of about 1 in SN units SNu (number of SNe per century per 10^{10} solar luminosities in the B band).

This is a puzzling result. When a new episode of star formation starts in an old galaxy, both the B luminosity and the SN rate increase (if the obscuration by the dust is neglected) but the SN rate expressed in SNu is not expected to remain constant. The SN rate, barely contaminated by the underlying old population, is expected to show a sharper increase and evolve on different time scales. As a result the constancy of the SN rate cannot be explained by dust-free models of galaxy evolution.

Large amount of dust are always present in starburst galaxies, effecting both the B luminosity and the SN rate. Extinctions of $A_V \sim 10$ are often found, preventing the detection of SNe by optical observations. It is therefore crucial to use radio or infrared observation to derived a more complete view of the SN events. Already in the near-infrared, at 2 μm of wavelength, dust extinction is much reduced, being about 1/10 of that in V.

When dealing with dusty active galaxies, the normalization based on the B luminosity has no clear meaning as this band is produced by both the old and new populations and is absorbed by the dust. In this case we prefer to use the "far infrared SN unit" SNuIR, define as the number of SNe per century per 10^{10} solar luminosities in the Far Infrared (FIR). This normalization is more meaningful as the FIR luminosity is proportional to the current Star-Formation Rate (SFR). It is actually possible to predict the number of expect SN from the FIR luminosity [5, 6]. This prediction depends on several factors, as the radio properties of the SN (used to estimate the intrinsic SN rate in nearby galaxies), the relation between SFR and FIR luminosity, the Initial Mass function (IMF), the presence of an AGN. The number of detected SN can also be used to constrain these parameters.

3 The Ground-based Observations

Several groups have completed or started near-IR SN searches (see [2, 6, 9] and the *SWIRT* project web site[1]), but these works produced only two detections and no spectroscopic follow-up. The reason of these negative results are probably due to a combination of low spatial resolution, limited field-of-view, low sensitivity and small number of expected events.

Our campaign started in 1999. Observations up to 2001 are described in [5], while in this contribution we present the updated results up to summer 2003. The galaxies were selected to have large FIR luminosities, between $2 \times 10^{11} L_{\odot}$ and $2 \times 10^{12} L_{\odot}$, corresponding to about 0.3−3 expected SNe per year per galaxy. Such high expected rates were chosen to assure significant statistical results even in a short period of time. The distances are below 200 Mpc, assuring enough sensitivity and resolution to detect point sources over the bright galaxy background. We monitored 47 starburst galaxies in the K band (2.2μm) mainly by using 4m class telescope in sites of good seeing,

[1] *http://www.te.astro.it/attivitascientifica/telescopi/azt24/swirt_eng.html*

the TNG in La Palma and the NTT at La Silla. Some observations were also obtained by the University of Arizona 61 inch telescope. In 2002 and 2003 we obtained 50 new images, mainly with the NTT. The total number of observations is now 304, with an average number of 6.5 observations per galaxy. A sample of less distant, less luminous galaxies were also monitored with the TIRGO 1.5m telescope. The results will be discussed in a different paper (Cresci et al., in preparation).

The various images of the same galaxy were carefully aligned, scaled to the same flux, reduced to the same PSF and subtracted. Typical limiting magnitudes were K$\sim$17 on the nucleus and K$\sim$19 at distances larger that about 1 arcsec.

These observations produced the detection of 4 events, the first significant sample of events detected in the near-infrared. For one event, SN2001db [3], we also obtain a spectroscopic follow-up: this event is a type II SN discovered after maximum light. The extinction, measured by the Hβ/Hα and Brα/Hα line ratios [4] is $A_V \sim 5.6$. As expected, this one was the SN with the highest extinction known at that time.

Obtaining an infrared SN rate from the data is not straightforward and is subject to large uncertainties: this is due to the small number of detected events, to the variability of the properties of core-collapse SNe in the near-IR and to the dependence of the detection limit on the distance from the galaxy nucleus. Using the same hypothesis of [5] we derive an expected number of 55 SNe if they are all out of the nucleus and 16 if they are in the central arcsec. Reducing these numbers to the observed 4 events imply extinctions of $A_V = 33$ and $A_V = 10$, respectively. The measured SN rate SN_r^{NIR}, assuming that 80% of the SNe explode in the nucleus (see [5]), is 0.40 SNuIR.

These limits are already quite high and are based on 4 years of (sparse) observations. To do better it is necessary to use instruments with higher sensitivity to point sources, as the HST.

4 Archive HST Observations

The NICMOS camera on the HST is an ideal instrument to look for SNe in the near-infrared. Its resolution is a few times higher than from the ground under average seeing, and the PSF is much more stable allowing for a better subtraction even near the bright galactic nucleus.

Most nearby starburst galaxies were already observed with this camera. Unfortunately, the HST target selection policy does not usually allow for duplicate observations of the same object with the same instrument setting. As a consequence, only very few archive data can be used to look for variability.

In a pilot study, we have searched the NICMOS archive for repeated observations of starburst galaxies with a long time span. We found 4 objects: NGC34, NGC5256, Arp200 and NGC6240. For NGC34 and Arp220 a narrow-band filter image was acquired a few months after the corresponding

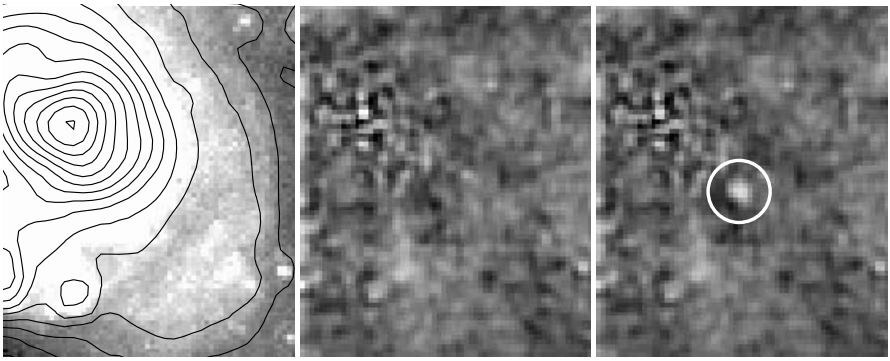

Fig. 1. *Left panel:* NICMOS image of the nucleus of NGC3690 in the F160W filter taken in Aug 2003; *center panel:* residuals with an image taken in 1997 with the same instrument setting; a fraction of less then 0.3% of the flux in the central arcsec (H$\sim$ 13.6) remains in the residual image. *Right panel:* a simulated SN with magnitude H = 19.5 is added to show the residual noise level and the NICMOS detection power. The circle is 1 arcsec of diameter.

broad-band one. In this case each pixel of the broad-band image can be "scaled" to the other bandpass by interpolation over the observed broad-band colors. NGC5356 was observed twice with the same F160W filter but with a different camera. NGC6240 was observed twice in the same broad-band filter and camera, probably because of problems with the PSF of the first observation. All the images have short exposure times, up to 4 minutes: nevertheless the resulting limit magnitudes are between H = 18.8 and 21.0. The nuclear region where the residuals of the subtraction are large is confined in the central 0.3 arcsec, but we expect to reduce it when the same instrument setting is used.

Despite the limited sample of only 4 objects, the small number of observations and the far than ideal instrument settings, the galaxies should produce about 5 observable SNe given their FIR luminosities, the time span of the observations and limit magnitudes. Despite of these expectations, no SN was detected. Also in this case we attribute this lack of detection to the presence of high extinctions, but the limits are less stringent.

5 Incoming HST and VLA Observations

In order to obtain more useful data, recently an HST proposal by our group was approved for cycle 12. The aim of the proposal is to obtain second epoch images of a sample of 37 nearby starburst galaxies already observed by NICMOS in the F160W filter. This "snapshot" program is already active and at the moment of writing the first galaxy was already observed (see Fig. 1). If

all the galaxies will be observed, we expect to detect up to 50 SNe, value corresponding to no extinction. Even if all SNe suffer an extinction of $A_V = 30$ we would still expect to detect 8 SNe. Therefore we are looking forward to these observations.

All the detected objects will be observed spectroscopically. Any event detected in galaxies within 100 Mpc will be observed by VLA: in these starburst galaxies we expect to find SNe with peculiar radio properties, as the emission of the core-collapse SN at these wavelength is dominated by the interaction of the ejecta with the circumstellar medium. The radio properties of these SNe can be used to derive the density and the structure of the circumstellar medium and the details of the late stages of the presupernova stellar evolution. Comparison with the existing radio SN models will also test their validity in a wider range of physical conditions than previously available.

References

1. E. Cappellaro, R. Evans, M. Turatto: Astron. Astrophys. **351**, 459 (1999)
2. B. Grossan, E. Spillar, R. Tripp, N, Pirzkal, B.M. Sutin, P. Johnson, D. Barnaby: Astron. J. **118**, 705 (1999)
3. R. Maiolino, M. Della Valle, L. Vanzi, F. Mannucci: IAUC 7661 (2001)
4. R. Maiolino, L. Vanzi, F. Mannucci, G. Cresci, F. Ghinassi, M. Della Valle: Astron. Astrophys. **389**, 84 (2002)
5. F. Mannucci et al. : Astron. Astrophys. **401**, 519 (2003)
6. S. Mattila, W.P.S. Meikle: Mon. Not. R. Astron. Soc. **324**, 325 (2001)
7. H. Navasardyan, A.R. Petrosian, M. Turatto, E. Cappellaro, J. Boulesteix: Mon. Not. R. Astron. Soc. **328**, 1181 (2001)
8. M.W. Richmond, A.V. Filippenko, J. Galisky: Pub. Astron. Soc. Pacific **110**, 553 (1998)
9. D. van Buren, T. Jarrett, S. Terebey, C. Beichman, M. Shure, C. Kaminski: IAUC 5960 (1994)

The Rate and the Origin of Type Ia SNe in Radio Galaxies

M. Della Valle[1], N. Panagia[2,3], E. Cappellaro[4], P. Padovani[2,3], M. Turatto[5]

[1] INAF-Arcetri Astrophysical Observatory, Largo E. Fermi 5, 50125, Firenze, Italy;
massimo@arcetri.astro.it
[2] Space Telescope Science Institute, 3700 San Martin Drive, Baltimore, MD 21218, USA;
panagia@stsci.edu; padovani@stsci.edu
[3] Affiliated with the Space Telescope Division of the European Space Agency, ESTEC, Noordwijk, Netherlands
[4] INAF-Napoli, Salita Moiariello, 16, 80131, Napoli, Italy;
cappellaro@na.astro.it
[5] INAF-Padova, Vicolo dell'Osservatorio 5; 35122, Padova, Italy;
turatto@pd.astro.it

Summary. An analysis of type Ia supernova (SNIa) events in early type galaxies from the Cappellaro et al. [6] database provides strong evidence that the rate of type Ia supernovae (SNe) in radio-loud galaxies is about 4 times higher than the rate measured in radio-quiet galaxies, i.e. SNIa-rate(radio-loud)=$0.41^{+0.13}_{-0.14}$ h^2_{75} SNe per century and per $10^{10}\mathrm{L}^B_\odot$ (SNU) as compared to SNIa-rate(radio-quiet)= 0.11 ± 0.03 h^2_{75} SNU. The exact value of the enhancement is still rather uncertain, but is likely to be in the range $\sim 2-7$. We discuss the possible causes of this result and we conclude that the enhancement of the SNIa explosion rate in radio-loud galaxies has the same common origin as their being strong radio sources, but that there is no causality link between the two phenomena. We argue that repeated episodes of interaction and/or mergers of early type galaxies with dwarf companions are responsible for inducing both strong radio activity in ∼14% of early type galaxies, and the ∼ 1 Gyr old stellar population needed to supply an adequate number SNIa progenitors.

1 Introduction

The knowledge of the supernova rate is essential for constraining the mechanisms of galaxy formation and for understanding galaxy evolution. Particularly the chemical evolution of systems that at the present epoch have a reduced or totally exhausted star formation activity, such as the elliptical galaxies, dramatically depends on the rate of type Ia events (e.g. [18]). Thus, any mechanism capable of producing an enhancement of SNIa rate in this type of galaxies should be regarded with the highest interest. Two recent works [4, 12] deal with this possibility. Capetti [4] finds a close association between the position of 6 type Ia SNe discovered in radio galaxies and their jets, while [12] claim the detection of an enhancement of the nova rate in

M87 in the regions near its jet. The former result would indicate that type Ia SNe in radio galaxies show a statistically significant preference (at the level of $\sim 95\%$) to occur close to their jets. The latter result may suggest that the presence of jets could increase the accretion rate from the interstellar medium onto the white dwarfs by 1-2 orders of magnitude, up to $\sim 10^{-8} - 10^{-9} M_{\odot}$ yr^{-1}, which is the rate necessary to trigger classical nova explosions [17]. By combining the two results, one would infer that the presence of the jets may increase the efficiency of accretion rate from the ISM and drive an accreting white dwarf to approach the Chandrasekhar mass and ignite, according to the standard single-degenerate model, a SNIa explosion ([12], and references therein). In this scenario it is the jet itself that alters the physical conditions of its environment and thus it is the direct cause of a local enhancement of nova and type Ia SN explosions.

Since jets are outstanding signatures of radio galaxies (e.g. [3]), it is important to extend the investigation to all galaxies with strong radio emission and to study the SNIa rate as a function of the radio activity. In this paper we use a larger SN databases to extend the study of [8] to investigate if, and to which extent radio galaxies exhibit an over-production of type Ia SNe with respect to quiescent galaxies of the same luminosity class, and to clarify what is the dominant mechanism that drives this process. In the following, we will denote as radio-loud sources, or radio galaxies, all galaxies which have radio luminosities at 1.4GHz higher than 10^{29} erg s^{-1} Hz^{-1}, and $M_R < -20.5$ (e.g. [11, 19]) and radio-quiet all galaxies with radio luminosities below that threshold. The threshold value of $\sim 10^{29}$ erg s^{-1} Hz^{-1} is the faint limit of the luminosity function for the radio-galaxies (see also [20]), and, therefore, it represents the most natural threshold to identify "radio-loud" galaxies.

2 Statistics of SNIa Explosions in Early Type Galaxies

Among the several databases on supernovae currently available, we have used the one compiled by Cappellaro, Evans and Turatto [6] which has the advantage of being defined *a priori*, i.e. the galaxies to be monitored were selected before the SN explosions. As a consequence our statistical analysis does not suffer of any kind of *a posteriori* selection criteria, which actually may affect the statistical analysis carried out on compilations of parent galaxies of SNe. An inspection to Table 1 reveals the following facts:

1. The fraction of radio galaxies in our sample is 0.12 of the whole sample of galaxies. Such fraction is marginally smaller than ~ 0.14 reported by [11] for radio galaxies having the same radio luminosities ($> 10^{29}$ erg s^{-1} Hz^{-1} at 1.4 GHz). This indicates that the frequency of radio galaxies in our sample is not affected by biases related to their radio properties.
2. Separating radio-loud from radio-quiet galaxies, we have 9 SNIa events in radio-loud galaxies and 10 in radio-quiet galaxies. Therefore, we can

Table 1. Number of Galaxies, Surveillance time $T(\mathrm{yr}\times \mathrm{L}^B/10^{10}\mathrm{L}^B_\odot)$ and Number of SNIa events

Galaxies	N	T	SNe
radio-quiet	2216	8894	10
radio-loud	274	2220	9
total	2490	11114	19

confidently estimate the rate of type Ia SNe for radio-loud galaxies to be $0.41^{+0.13}_{-0.14}\ h^2_{75}$ SNU (the errors are estimated from a direct application of Poisson statistics), whereas the rate of type Ia SNe in radio-quiet systems turn out to be $0.11 \pm 0.03\ h^2_{75}$ SNU.

3 Discussion and Conclusions

An analysis of [6] database provides strong evidence that the rate of type Ia SNe in radio galaxies is about 4 times higher than the rate measured in quiescent galaxies. The actual value of the enhancement is still rather uncertain, due to the uncertainties involved in the SN rate measurements (see [5]) but is likely to be in the range $\sim 2 - 7$. This confirms the result recently obtained by [8] on the basis of a smaller statistical sample. The observed enhancement of the rate of SNIa events in radio galaxies can be explained in basically two different ways:

1. **The enhanced SNIa explosion rate in radio-loud galaxies is a direct consequence of their being strong radio sources.** This is the scenario suggested by [4] and [12]. In radio galaxies the accretion rate from the interstellar medium onto white dwarfs could be enhanced by the action of the jets. This process could also account for the high rate of novae observed in M87 in the regions nearby the jets. The association between type Ia SNe and jets requires a further step, i.e. that the progenitors of these SNeIa are cataclysmic-type systems, according to the single degenerate scenario. In this hypothesis, the enhancement of SNIa in radio galaxies is expected to be spatially confined to the regions immediately adjacent to radio jets and/or the bulk of radio activity. While this may be true for Virgo A (M87), it appears not to be the case for Fornax A (NGC 1316), in which the two SNIa (SN 1980N and SN 1981D) are located quite far from strong radio lobes ([9]), nor for Centaurus A (NGC 5128), in which SN 1986G is deeply embedded in the equatorial lane of gas and dust. At any rate, if the dominant phenomenon is accretion from the ISM rather than from a binary companion, an extreme consequence would be that single WDs will contribute to Nova and perhaps SNIa production, and not only binary systems with suitable parameters.

Actually, since the fraction of binary systems that may give rise to a SNIa is only 5-10% of the total number of systems with masses above 3 solar masses [13], one should expect a very dramatic increase of the SNIa rate in jet dominated radio-galaxies, by factors as high as 20 or higher if direct accretion from ISM becomes the dominant accretion process.

2. **The enhancement of SNIa explosion rate in radio-loud galaxies has the same common origin as their being strong radio sources, but there is no causality link between the two phenomena.** We favor this alternative. Indeed, the radio activity of a galaxy is most likely triggered by interaction and/or mergers (e.g. [1, 2, 10]). Also, the SNIa rate can be enhanced by the formation or the capture of relatively young stellar populations in which SNIa occur at much higher rates than in genuinely old populations. SNIa progenitors are stars with original masses above ∼3 solar masses, having nuclear-burning lifetimes shorter than ∼400 Myrs. After that time, the star becomes a white dwarf and may explode as a SNIa only after an additional time as needed for either accreting mass from a companion or merging with it. Such a time is essentially unconstrained by theory, but measurements of SNIa rates at different redshifts suggest that it should be shorter than ∼1 Gyrs (e.g. [13, 15]). As a consequence, in order to sustain a substantial rate of SNIa explosion, a galaxy has to have a steady supply of young stellar populations, at least over a time-scale of 1-2 Gyrs. In late type galaxies, the active star formation provides the needed input for a steady production of SNIa events. Such a supply in early type galaxies is naturally provided by repeated episodes of interaction or mergers that induces either formation of young stellar populations (galaxy interaction; e.g. the Antennae galaxies [21]) or capture of young stars from dwarf companions. Well known examples of interacting and/or merging early type galaxies are Centaurus A (NGC 5128) and Fornax A (NGC 1316), which are strong radio sources and indeed have produced 1+2 SNIa in the last century. Moreover, the Virgo Cluster radio galaxy NGC 4753, had given birth to another SNIa (SN1965I) less than two decades before, thus confirming its high SNIa rate.

Also in favor of this hypothesis is the fact that the observed SNIa rates are higher in late type galaxies than in early type galaxies (about a factor of 10 between Ellipticals and Sd galaxies) once the rates are normalized to the galaxy H or K band luminosities, and, therefore, to their masses in stars, rather than to their B-band magnitudes [7, 14, 16]. This fact confirms the connection between recent stellar populations and type Ia supernovae, and provides a natural explanation of why among early type galaxies are SNIa rates higher in radio galaxies, without requiring the concurrence of any new and/or additional process to enhance the SNIa rates.

Finally, we note that in our scenario the occurrence of a few type II-Ib/c SNe in early type galaxies is expected at the early stages of the same

star formation burst that provides a steady supply of SNIa events. Since core collapse SNe are produced by progenitors more massive than $8M_{\odot}$, whose lifetime is shorter than about 30 Myrs, only for a small fraction of the time between subsequent interaction/capture episodes (approximately 30Myrs/1Gyr=3%) would one expect to see such SNe in early type galaxies. Since in galaxies with active star formation the rate of core collapse SNe is about 4 times higher than that of SNIa, we estimate that one should expect to detect core collapse SNe at an average rate of about $0.03\times4 \simeq 12\%$ that of SNIa events. Since 9 SNIa were discovered in E/S0 galaxies during time-controlled surveys ([5]), one would expect the occurrence of about 1 ± 1 core collapse event in those galaxies, but none has been detected so far. It is then clear that, while missing one event is statistically acceptable within the currently available statistics, our prediction will be observationally testable when the SNIa statistics will have increased appreciably.

References

1. W. Baade, R. Minkowski: Astrophys. J. **119**, 206 (1954)
2. B. Balick, T.M. Heckman: Ann. Rev. Astron. Astrophys. **20**, 431 (1982)
3. G.V. Bicknell: New Astron. Rev. **46**, 365 (2002)
4. A. Capetti: Astrophys. J. Lett. **574**, L25 (2002)
5. E. Cappellaro, M. Turatto, S. Benetti, D.Yu. Tsvetkov, O.S. Bartunov, I.N. Makarova: Astron. Astrophys. **268**, 472 (1993)
6. E. Cappellaro, R. Evans, M. Turatto: Astron. Astrophys. **351**, 459 (1999)
7. M. Della Valle, M. Livio: Astrophys. J. Lett. **423**, L31 (1994)
8. M. Della Valle, N. Panagia: Astrophys. J. Lett. **587**, L71 (2003)
9. B.J. Geldzahler, E.B. Fomalont: Astron. J. **89**, 1650 (1984)
10. T.M. Heckman et al. : Astrophys. J. **311**, 526 (1986)
11. M.J. Ledlow, F.N. Owen: Astron. J. **112**, 9 (1996)
12. M. Livio, A. Riess, W. Sparks: Astrophys. J. Lett. **571**, L99 (2002)
13. P. Madau, M. Della Valle, N. Panagia: Mon. Not. R. Astron. Soc. **297**, L17 (1998)
14. F. Mannucci, R. Maiolino, G. Cresci, M. Della Valle, L. Vanzi, F. Ghinassi, V.D. Ivanov, N.M. Nagar, A. Alonso-Herrero: Astron. Astrophys. **401**, 519 (2003)
15. R. Pain et al. : Astrophys. J. **577**, 120 (2002)
16. N. Panagia: In: *Experimental Physics of Gravitational Waves.* eds. G. Calamai, M. Mazzoni, R. Stanga, F. Vetrano (World Scientific: Singapore, 2002) pp. 107-119
17. T. Prialnik, A. Kovetz: Astrophys. J. **445**, 789 (1995)
18. A. Renzini, L. Ciotti, A. D'Ercole, S. Pellegrini: Astrophys. J. **419**, 52 (1993)
19. E.M. Sadler, C.R. Jenkins, C.G. Kotanyi: Mon. Not. R. Astron. Soc. **240**, 591 (1989)
20. C.M. Urry, P. Padovani: Pub. Astron. Soc. Pacific **107**, 803 (1995)
21. B.C. Whitmore, Q. Zhang, C. Leitherer, S.M. Fall, F. Schweizer, B.W. Miller: Astron. J. **118**, 1551 (1999)

Supernovae in Galaxy Clusters

A. Gal-Yam, D. Maoz, K. Sharon[1], F. Prada[2], P. Guhathakurta[3], A.V. Filippenko[4]

[1] School of Physics and Astronomy, Tel Aviv University, Tel Aviv, Israel; avishay@wise.tau.ac.il
[2] Instituto de AstrofÃ-sica de Canarias and The Isaac Newton Group, Spain
[3] Herzberg Institute of Astrophysics, National Research Council, Canada
[4] Department of Astronomy, University of California, Berkeley, CA, USA

Summary. We present the results of several surveys for supernovae (SNe) in galaxy clusters. SNe discovered in deep, archival *HST* images were used to measure the cluster SN Ia rate to $z = 1$. A search for SNe in nearby ($0.06 \leq z \leq 0.2$) Abell galaxy clusters yielded 15 SNe, 12 of which were spectroscopically confirmed. Of these, 7 are cluster SNe Ia, which we will use to measure the SN Ia rate in nearby clusters. This search has also discovered the first convincing examples of intergalactic SNe. We conclude with a brief description of ongoing and future cluster SN surveys.

1 Introduction

This contribution describes our observational studies of SNe in galaxy clusters. The motivation to search for SNe in the fields of rich galaxy clusters is discussed in a contribution by Maoz et al. (this volume), and more fully by Gal-Yam, Maoz & Sharon [1] and Maoz & Gal-Yam [5].

Observationally, SN searches in galaxy clusters were pioneered in the late 1980's by Norgaard-Nielsen et al. [6], resulting in the first detection of a $z = 0.31$ SN in the galaxy cluster AC118. More recently, low-redshift clusters have been monitored for SNe by the Mount Stromlo Abell Cluster SN Search [7]).

We present below the results from several surveys for SNe in galaxy clusters we have carried out using both ground-based telescopes and the Hubble Space Telescope (*HST*).

2 The SN Rate in High-z Clusters from HST

We have conducted a survey for high redshift SNe in deep *Hubble Space Telescope* archival images of nine galaxy clusters. Six apparent SNe are detected (Fig. 1), with $21.6 \leq I_{814} \leq 28.4$ mag. Two SNe are associated with cluster galaxies (at redshifts $z = 0.18$ and $z = 0.83$), three are probably in galaxies not in the clusters (at $z = 0.49$, $z = 0.60$, and $z = 0.98$), and one is at unknown z. After accounting for observational efficiencies and

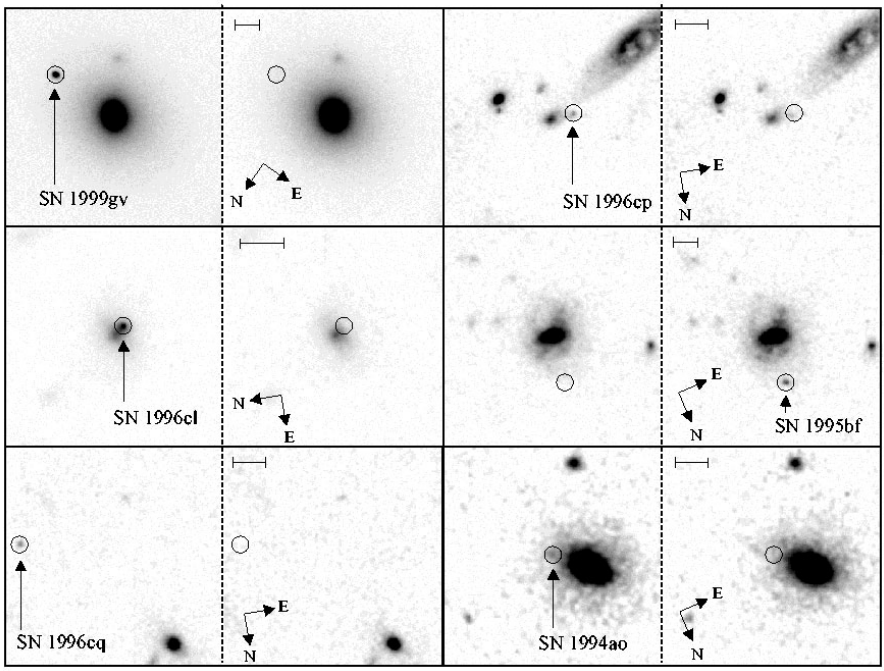

Fig. 1. Sections of the images, at two epochs, for each of the six apparent SNe discovered in our *HST* cluster survey. The scales shown in the upper-left-hand corners correspond to $1''$.

uncertainties (statistical and systematic) we derive the rate of type-Ia SNe within the projected central $500h_{50}^{-1}$ kpc of rich clusters: $R = 0.20^{+0.84}_{-0.19}h_{50}^2$ SNu in $0.18 \leq z \leq 0.37$ clusters, and $R = 0.41^{+1.23}_{-0.39}h_{50}^2$ SNu in clusters at $0.83 \leq z \leq 1.27$ (95 per cent confidence interval; 1 SNu $\equiv$ 1 SN century^{-1} per $10^{10}L_{B\odot}$). Combining the two redshift bins, the mean rate is $R_{\bar{z}=0.41} = 0.30^{+0.58}_{-0.28}h_{50}^2$ SNu.

We also compare our observed counts of field SNe (i.e., non-cluster SNe of all types) to recent model predictions. The observed field count is $N \leq 1$ SN with $I_{814} \leq 26$ mag, and $1 \leq N \leq 3$ SNe with $I_{814} \leq 27$ mag. These counts are about two times lower than some of the predictions. Since the counts at these magnitudes are likely dominated by type-II SNe, our observations may suggest obscuration of distant SNe II, or a SN II luminosity distribution devoid of a large high-luminosity tail. Further details are presented by Gal-Yam, Maoz & Sharon [1]. Additional archival SNe from *HST*, providing significantly stronger constraints on the properties of high-z SNe, are discussed in a contribution by Sharon, Gal-Yam & Maoz (these proceedings).

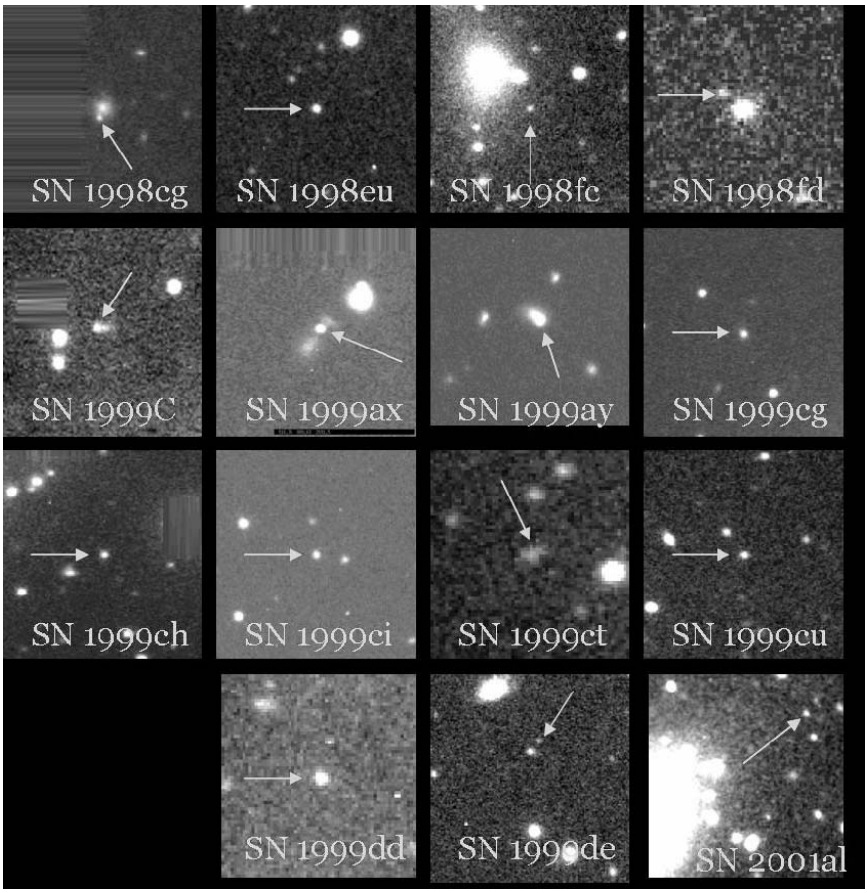

Fig. 2. Images of the 15 supernovae discovered by WOOTS.

3 WOOTS: A Survey for SNe in $0.06 < z < 0.2$ Clusters

3.1 Cluster SN Rates

The Wise Observatory Optical Transient Search (WOOTS) is a survey for SNe in the fields of $0.06 \leq z \leq 0.2$, rich Abell galaxy clusters using the Wise 1 m telescope. 15 SNe were discovered (Fig. 2), and for 12 of these we obtained follow-up spectroscopy. Seven SNe turned out to have occurred in cluster galaxies, while five are field events. 11 of the events (including all cluster SNe) are apparently SNe Ia, and many were discovered near maximum light. The cluster SN sample is suitable for the calculation of the SN rate in clusters (Gal-Yam & Maoz, in preparation).

3.2 Intergalactic SNe

Of the seven cluster SNe Ia discovered in the course of WOOTS, two SNe, 1998fc in Abell 403 ($z = 0.10$) and 2001al in Abell 2122/4 ($z = 0.066$), have no obvious hosts. Both events appear projected on the halos of the central cD galaxies, but have velocity offsets of 750-2000 km s^{-1} relative to those galaxies, suggesting they are not bound to them. Deep Keck imaging of the locations of the two SNe are used to put upper limits on the luminosities of possible dwarf hosts, $M_R > -14$ mag for SN 1998fc and $M_R > -11.8$ mag for SN 2001al. The fractions of the cluster luminosities in dwarf galaxies fainter than these limits are $< 3 \times 10^{-3}$ and $< 3 \times 10^{-4}$, respectively. Thus, 2/7 of the SNe would be associated with $\leq 3 \times 10^{-3}$ of the luminosity attributed to galaxies. It is argued, instead, that the progenitors of both events were probably members of a diffuse population of intergalactic stars, recently detected in local clusters via planetary nebulae and red giants. Considering the higher detectability of host-less SNe compared to normal SNe, we estimate that 20^{+12}_{-15} percent of the SN Ia parent stellar population in clusters is intergalactic. This fraction is consistent with other measurements of the intergalactic stellar population, and implies that the process that produces intergalactic stars (e.g., tidal disruption of cluster dwarfs) does not disrupt or enhance significantly the SN Ia formation mechanism. Host-less SNe are potentially powerful tracers of the formation of the intergalactic stellar population out to high redshift. Further details can be found in Gal-Yam, Maoz, Guhathakurta, & Filippenko [2].

4 Future Prospects

Measurements of SN rates in clusters out to $z = 1$ provide a powerful and unique tool to probe cluster metal enrichment and the progenitors of SNe Ia (see contribution by Maoz et al., this volume). The results are currently limited by large errors due to small number statistics. It is therefore desirable to obtain additional measurements of SN rates in clusters. The WOOTS cluster SN sample will provide another measured point at $z \sim 0.15$. We have also begun a ground-based survey for SNe in rich, lensing clusters at $z \sim 0.3$, using the 2.5 m NOT telescope at La Palma, Spain. This survey aims to enlarge the number of SNe used to calculate the cluster SN rate in the $z \sim 0.3$ bin (1 SN) by an order of magnitude, and thus to significantly decrease the statistical error. The first results of this survey include the discovery of several cluster SNe (e.g., Fig. 3; Gal-Yam, Maoz, Prada & Guhathakurta [3]) as well as new strong lensing clusters. A similar survey for SNe in high redshift clusters ($z \sim 0.8$) using 4 m class (or larger) telescopes is being planned. With such data, it will be possible to set strong constraints on the origin of iron in the ICM and the characteristic delay time of SNe Ia.

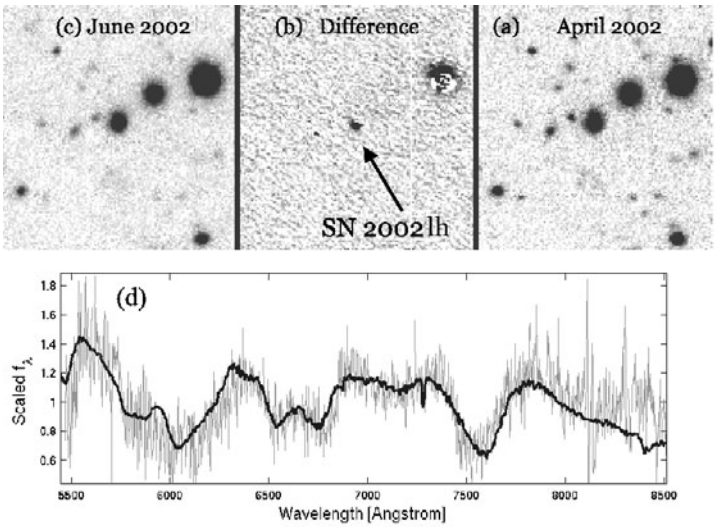

Fig. 3. Subtraction of a NOT image of Abell 1961 (z=0.232) obtained in April 2002 (a) from a similar image obtained in June 2002 (c) reveals SN 2002lh (b). In panel (d) the comparison of the Keck spectrum of this event (light) with a redshifted spectrum of the nearby SN 1999ee near peak magnitude (bold, from Hamuy et al. [4]), reveals this is a SN Ia at z=0.236, i.e., in one of the cluster galaxies.

References

1. A. Gal-Yam, D. Maoz, K. Sharon: Mon. Not. R. Astron. Soc. **332**, 37 (2002)
2. A. Gal-Yam, D. Maoz, P. Guhathakurta, A.V. Filippenko: Astron. J. **125**, 1087 (2003)
3. A. Gal-Yam, D. Maoz, F. Prada, P. Guhathakurta: IAUC 8169 (2003)
4. M. Hamuy et al. : Astron. J. **124**, 417 (2002)
5. D. Maoz, A. Gal-Yam: Mon. Not. R. Astron. Soc. **347**, 951 (2004)
6. H.U. Norgaard-Nielsen et al. : Nature **339**, 523 (1989)
7. D. Reiss et al. : Astron. J. **115**, 26 (1998)

Using Multi-Band Photometry to Classify Supernovae

Dovi Poznanski, Avishay Gal-Yam, Dan Maoz[1], Alexei V. Filippenko[2], Douglas C. Leonard[3], and Thomas Matheson[4]

[1] School of Physics & Astronomy, Tel-Aviv University, Tel-Aviv 69978, Israel; (dovip, avishay, dani)@wise.tau.ac.il
[2] Department of Astronomy, 601 Campbell Hall, University of California, Berkeley, CA 94720-3411, USA; alex@astro.berkeley.edu
[3] Five College Astronomy Department, University of Massachusetts, Amherst, MA 01003-9305, USA; leonard@corelli.astro.umass.edu
[4] Harvard-Smithsonian Center for Astrophysics, 60 Garden Street, Cambridge, MA 02138, USA; tmatheson@cfa.harvard.edu

Summary. Large numbers of supernovae (SNe) have been discovered in recent years, and many more will be found in the near future. Once discovered, further study of a SN and its possible use as an astronomical tool (e.g., as a distance estimator) require knowledge of the SN type. Current classification methods rely almost solely on the analysis of SN spectra to determine their type. However, spectroscopy may not be possible or practical. We present a classification method for SNe based on the comparison of their observed colors with synthetic ones, calculated from a large database of multi-epoch optical spectra of nearby events. Broadband photometry at optical wavelengths allows classification of SNe up to $z = 0.75$, and the use of infrared bands extends it further to $z = 2.5$. We demonstrate the applicability of this method, outline the observational data required to further improve the usefulness of the method, and discuss prospects for its use on future SN samples. Community access to the tools developed is provided by a dedicated website.[1]

1 Introduction

Once discovered, the study of a particular supernova (SN), and its use as a tool for any application, is almost always based on spectroscopic verification and classification, but this follow-up may not always be a viable option. First, the interesting population of very distant ($z > 1$) supernovae (SNe), where the mark of cosmic deceleration should be detected, is usually fainter than 25 mag, the practical limit for spectroscopy. Second, the fast evolution of astronomical archives, toward the realization of the "virtual observatory" concept, is expected to produce a large number of SNe discovered in retrospective studies, for which any follow up is, of course, impossible. And last,

[1] See http://wise-obs.tau.ac.il/∼dovip/typing

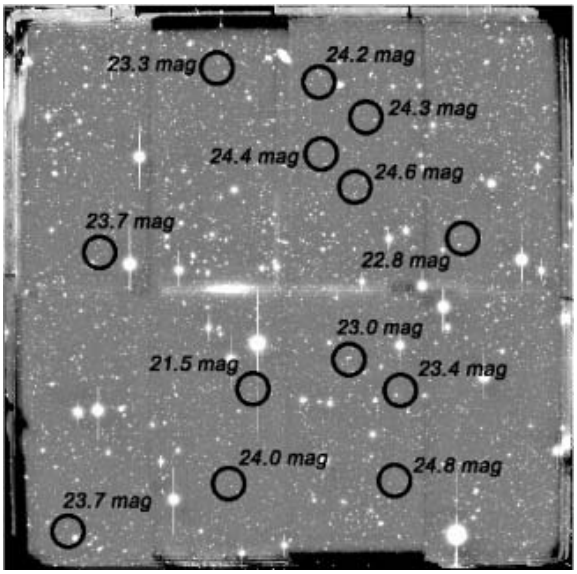

Fig. 1. Complete field ($36' \times 36'$) taken with the wide field mosaic camera on the KPNO 4m telescope. Candidate SNe with their approximate brightnesses are marked. There are tens of still uncertain, and dimmer, candidates not marked here.

spectroscopy is impossible if large numbers (hundreds or thousands) of SNe are detected within a relatively short time.

In an example of such occurrence, we have acquired with B. Jannuzi, deep (limiting mag $\sim$26) and wide ($36' \times 36'$) images with the mosaic camera mounted on the KPNO 4m telescope, on two epochs. The difference image of these two frames, reveals dozens of candidate SNe of which only the brightest, which can be seen in Fig. 1, can be observed spectroscopically. We have confirmation for two of these objects, which are indeed SNe Ia at redshifts of 0.21 and 0.67 [5]. Since these SNe are in a well studied field, we have redshifts for most of the galaxies, and hence for the candidate SNe, and can compute the SN redshift distribution in addition to the faint SN counts. As we will show below, a similar dataset with photometry in more than one band would allow a separation of such an analysis to the different SN types.

The next alternative to spectroscopy is the use of multi-color broadband photometry to classify SNe. In a recent paper [4] we have shown that in the absence of spectral information, much can be gleaned from the broad band colors of the SN. First, most SNe discovered are associated with host galaxies, so their redshift is either known, or can be measured long after the SN has faded (using spectroscopy or photometric redshifts). Second, by comparing the colors of the SN in question to those expected for SNe of various types, at various ages, and at the known redshift, one can determine, or at least constrain, its age and type.

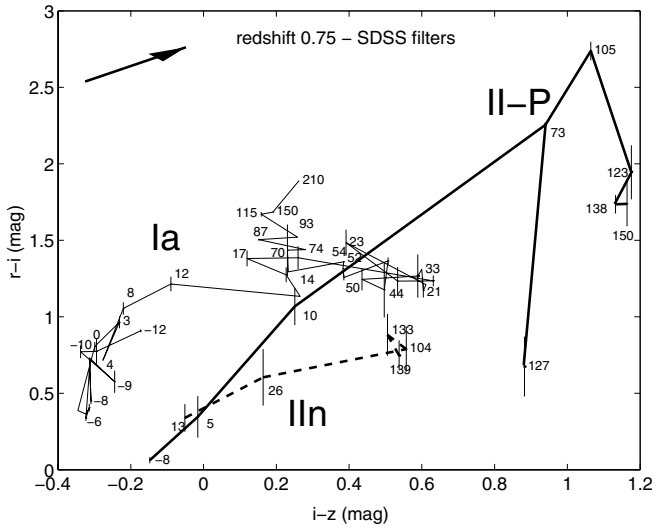

Fig. 2. $r-i$ vs. $i-z$ for SNe of type Ia (line), II-P (thick line), and IIn (thick-dashed line), at $z = 0.75$. The time evolution of each SN type is illustrated by linearly connecting, in temporal order, the locations occupied by such events. The marked ages are in days relative to B-band maximum. For clarity, we have sometimes omitted the age labels of data points with similar ages and colors. The arrow shows the reddening effect of $A_V = 1$ mag (in rest frame V) extinction by dust in the host galaxy.

2 Method

In order to compute the expected colors of SNe of all types at a chosen z, we have compiled a large database of high signal-to-noise spectra of nearby SNe, mostly from Lick Observatory. We can then derive synthetic photometry from these spectra at any given redshift. The use of synthetic colors is the key that allows the tracing of the color behavior, i.e., the time evolution of the colors, of the various SN types, at arbitrary redshift. Using color-color diagrams one can then look for areas that are either populated by one type of SNe or not populated by others. Our method allows the classification of SNe up to a redshift of 0.75 using optical bands, while the use of infrared bands increases the range up to $z = 2.5$.

2.1 Example Diagram and Application

Figure 2 shows an example of the color paths of SNe of type Ia, II-P, and IIn (other types are omitted for clarity), at $z = 0.75$ in the Sloan colors $r - i$ versus $i - z$. The numbers along the curves represent the time in days relative to maximum B-band brightness. One sees that most SNe before maximum

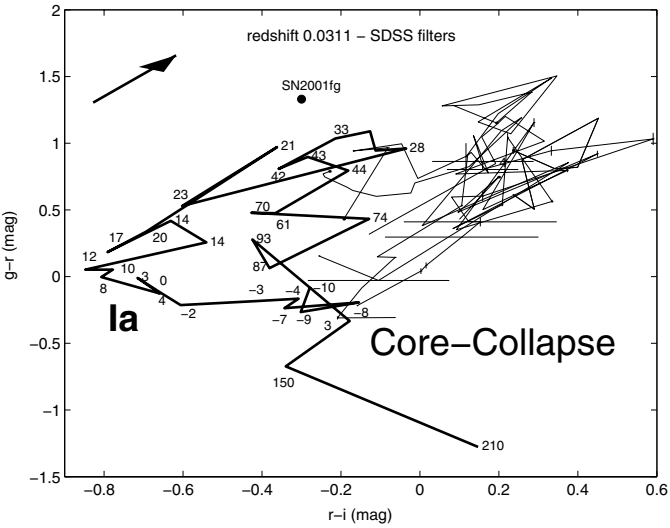

Fig. 3. $g - r$ vs. $r - i$ for SNe of all types at $z = 0.0311$. SNe Ia tracks are thick lines, and core-collapse SNe tracks are thin lines. The observed colors of SN 2001fg are indicated by the filled circle. The colors suggest a SN Ia about 1 month past maximum brightness, as confirmed by spectra of this event.

light are blue, with $i - z < 0$ mag, but Ia SNe are significantly bluer with $i-z \sim -0.25$ mag, while being redder in $r-i$. Older SNe II-P have the reddest colors of all SNe with $i-z > 1$ mag, and IIn SNe have consistently lower $r-i$ colors than Ia SNe. The arrow shows the reddening effect corresponding to $A_V = 1$ mag of extinction in the host galaxy, assuming the Galactic reddening curve of Cardelli et al. (1989). One can see that the unique colors of young ($t < 12$ days) and very old ($t > 100$ days) SNe Ia cannot be masked even by significant reddening in their host, so that some candidates with appropriate observed colors can be uniquely determined to be SNe Ia. Even when the type of a SN cannot be uniquely determined, it may still be deduced by supplementing the color information with other available data on the SN, such as constraints on its brightness, and information (even if very limited) on its variability (e.g., whether its flux is rising or declining).

Since the classification of a particular SN at a given redshift and with specific observed colors requires the generation of custom diagrams, we have built a dedicated web site[2] that allows the astronomical community access to the tool have we developed.

An example of such an application is shown in Fig. 3. SN 2001fg was one of the first SNe reported from SDSS data. This event was discovered on 15 October 2001 UT [6] with $g = 19.20$, $r = 17.87$, and $i = 18.17$ mag. Inspecting

[2] *http://wise-obs.tau.ac.il/∼dovip/typing/*

the color-color diagram calculated for the appropriate redshift ($z = 0.0311$, see below), one can see (Fig. 3) that the type and approximate age of the SN candidate can be deduced. The diagram clearly indicates this is a SN Ia, about one month old. Followup spectra [1] using the Keck II 10-m telescope reveal that the object is indeed a SN Ia, at $z = 0.0311$. The spectrum is similar to those of SNe Ia about two months past maximum brightness. This age, at the time of the spectral observation (18 November UT), implies an age around one month past maximum brightness at discovery, confirming our diagnosis. A fully "blind" application would have, of course, required an independent photometric or spectroscopic redshift for the SN host galaxy.

3 Conclusions and Future Prospects

We have shown that SNe can be classified using broad band colors, so that spectroscopy is not a prerequisite. Such an approach will enable the analysis of larger number of SNe, as expected to be discovered in the coming years, but with limited information. This is important especially at high z where spectroscopy becomes almost impossible.

In order to better sample the evolution of the covered SN types, we plan to enrich the spectral database used. This will smooth the current scatter seen, e.g., in Fig. 2, which is largely due to variations between individual objects. We also intend to incorporate spectra of SN 1998bw-like Ic SNe, also called hypernovae [2], associated with gamma-ray bursts. Finally, in order to enable classification of higher redshift SNe observed in optical bands, UV spectra, of which only a handful exist [3], will be added to the database.

References

1. A.V. Filippenko, R. Chornock: IAUC 7754 (2001)
2. M. Hamuy: Astrophys. J. **582**, 905 (2003)
3. N. Panagia: In: "Supernovae and Gamma-Ray Bursters," ed. K.W. Weiler (Springer: Berlin, 2003) pp. 113-144
4. D. Poznanski, A. Gal-Yam, D. Maoz, A.V. Filippenko, D.C. Leonard, T. Matheson: Pub. Astron. Soc. Pacific **114**, 833 (2002)
5. D. Poznanski, A. Gal-Yam, K. Sharon, D. Maoz, B.T. Jannuzi: IAUC 8058 (2003)
6. D. Vanden Berk, B. Wilhite, A. Miceli, C. Stubbs, B. Lawton: IAUC 7744 (2001)

Part VI

Supernova and Gamma-Ray Burst Connections

Optical and Near-IR Observations of SN 1998bw

Ferdinando Patat

European Southern Observatory, Garching, Germany;
fpatat@eso.org

> *Thus, the observation of gamma-ray line emission from a young supernova seems very promising in the near future. The observation, or even a null observation at a low threshold, will give significance in the fields of nuclear astrophysics and supernova theory. The scientific importance of a positive measurement would be analogous with and comparable to the importance of successful detection of neutrinos from the Sun.*
>
> Clayton, Colgate, and Fishman [2].

Summary. SN 1998bw, especially after the discovery of GRB 030329/SN 2003dh, seems to be the equivalent of the Rosetta stone for the SN/GRB connection. In this paper I review optical and near IR observations that have been carried out for this uncanny object, which has probably confirmed suspicions and ideas originally formulated in the early seventies of last century.

1 Introduction

This story probably begins in 1969, with what I like to call a "prophecy," and it is right that I wish to start this review on the optical and near-IR observations of SN 1998bw[1].

As J. Sollerman said in one of his papers on this striking object, SN 1998bw was born famous. And it was doomed to become even more famous as time went by, so famous that it was sometimes named "the supernova of the century." And this is indeed interesting, since it was born in the same century of SN 1987A, one of the most studied and referenced objects in the sky.

Just from the optical and near-IR observations point of view, this is witnessed by the large number of papers which have been published in the first four years. Starting with the *Nature* papers by Galama et al. [7] and Iwamoto et al. [11], a number of authors have presented the results of their observational campaigns [5, 8, 16, 18, 21, 22, 23].

[1] This talk was given in Valencia on 25 April 2003. For some cabalistic reason, this coincided exactly with the fifth anniversary of GRB 980425/SN1998bw.

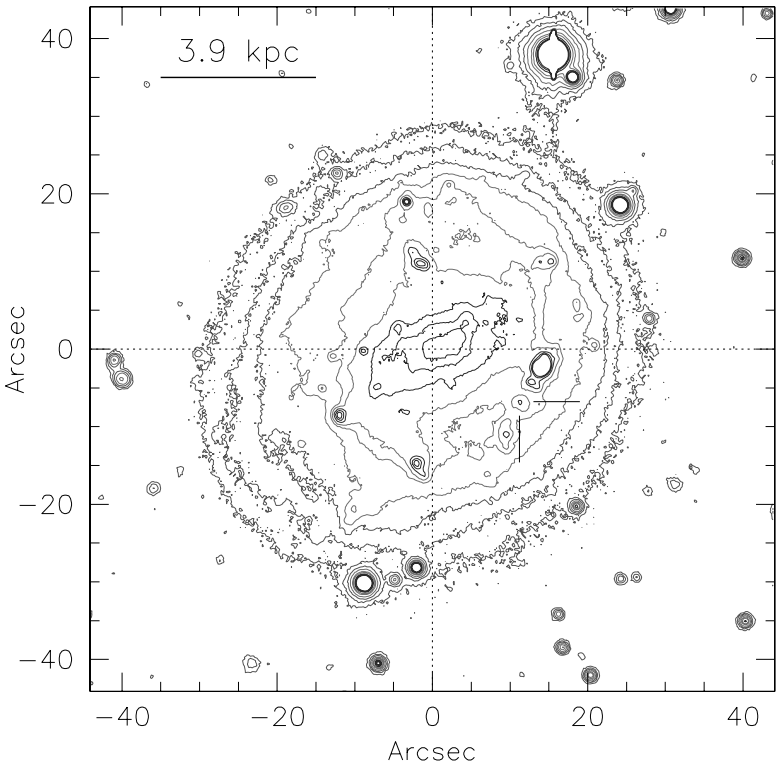

Fig. 1. Contour plot of ESO-184-G82. The original image stack was obtained at VLT+FORS1 at about 900 days after the explosion. Spatial scale was computed for a distance of 40 Mpc. The SN position is marked.

The reader is referred to these papers for a detailed account on the observations, while here I will try to give only a general view of the SN 1998bw phenomenon.

SN 1998bw was discovered by Galama et al. [6] in the BeppoSAX Wide Field Camera error box of GRB 980425 [19, 20] close to a spiral arm of the barred galaxy ESO 184-G82 (see Fig. 1), by comparing two frames taken at the ESO New Technology Telescope on Apr 28.4 and May 1.3 UT. Spectroscopic and photometric observations, both in the optical and in the near IR, started at ESO–La Silla immediately after the discovery, and showed that this object was profoundly different from all then known SNe [14].

Its peculiar spectroscopic appearance, its unusually high radio luminosity at early phases [13], its optical luminosity ($M_V \sim -19.2 + 5 \log h_{65}$) and, in particular, the probable association with GRB 980425 through positional and temporal coincidence [6, 19] placed SN 1998bw at the center of discussion concerning the nature of gamma-ray bursts (GRBs). The object was tentatively classified as a peculiar Ic [4, 17], I would say "by definition" more

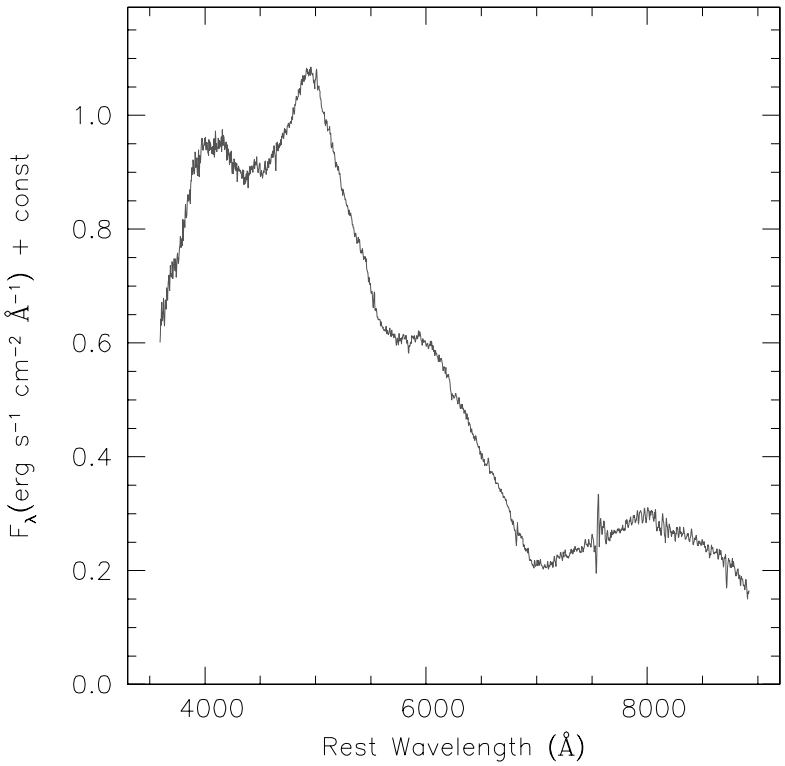

Fig. 2. Spectrum of SN 1998bw taken at ESO-La Silla on May 5, 1998.

than anything else, due to the complete absence of H lines, the weakness of the Si II 6355 Å line and no clear He I detection in the optical spectra (see Fig. 2). Main spectral features were identified as O I, Ca II, Si II and Fe II [11]. The estimated expansion velocities were exceptionally high ($\sim 30,000$ km s^{-1}) and this caused a severe line blending. The evolution during the first months was unusually slow compared to known Ic, with the nebular spectra still retaining many of the features present during the photospheric phase [18, 23].

The late onset of the fully nebular phase has been interpreted as an indication for a large ejected mass [23] as it was predicted by the early light curve models. During the intermediate phase, the emission lines were definitely broader than in known Type Ib/c SNe and the simultaneous presence of iron–peak and α-elements indicated unusual relative abundances or physical conditions in the SN ejecta [18]. The late spectroscopy presented by [21] showed that the tentative morphological classification of SN 1998bw as a Type Ic event was indeed appropriate. The main features have been identified as [O I], Ca II, Mg I and Na I D, the latter possibly contaminated by He I 5876 Å.

As far as the gamma-ray burst is concerned, GRB 980425 was pretty weak, since the implied energy for a 40 Mpc distance was $8.1 \pm 1.0 \times 10^{47}$ erg [19], which is definitely smaller than the usual 10^{53} erg value typical for the so-called cosmological GRBs. This has led the community to believe that GRB 980425 is a member of an unusual class of GRBs/SNe (see, e.g., [5]).

The galaxy which hosted GRB 980425/SN 1998bw, ESO 184–G82, is an SBc galaxy with a recession velocity $v_r = 2532$ km s^{-1} [18]. Its luminosity is $L \sim 0.5-1.2\ L_{LMC}$, it is currently undergoing strong star formation, it shows a bar and rather clear indications of morphological disturbances [5]. This is clearly visible in the late VLT images, which show a possibly double nucleus, isophotal twisting and asymmetry (see Fig. 1). All this suggests that the observed star formation is related to galaxy interaction/merging.

The HST images have shown that SN 1998bw exploded in a star-forming region [5], containing several bright and young stars within a projected distance of 100 pc. This is consistent with the progenitor of SN 1998bw being a young and massive star

Due to its relatively high apparent brightness, Kay et al. [12] and Patat et al. [18] have attempted to perform some polarimetric measurements at different epochs. After correcting for the interstellar polarization in the direction of the host galaxy, the estimated optical linear polarization was 0.6% (day −7), 0.4% (day +10) and 0.5% (day +42). The fluctuations in these values seem to suggest that the observed polarization is intrinsic to the SN, although a dusty medium in the parent galaxy cannot be ruled out.

The small degree of polarization at optical wavelengths can be explained in terms of a moderate departure from sphericity (axial ratio less than 2:1 [10]), either in the photosphere or in the outer scattering envelope when the line of sight is not coincident with an axis of symmetry.

Interestingly, no polarization, either circular or linear, was detected in the radio, and this has been interpreted as the signature of a spherically symmetric blast wave [13]. This apparent discrepancy might suggest that the radio and the optical radiation were generated in regions of different geometry.

2 Photometric and Spectroscopic Evolution

The early light curve of SN 1998bw has shown that the object was unusually bright when compared to known SNe of type Ib/c [7] and, in this respect, it was much more similar to a type Ia. The broad-band photometric observations by [16] taken during the intermediate phases revealed that the object settled on an exponential decay similar to that observed in other type Ic SNe. McKenzie and Schaefer first suggested that even in this case the light curve was powered by the radioactive decay of ^{56}Co with some leakage of γ-rays. Photometry covering later phases was then presented by [18, 21, 22],

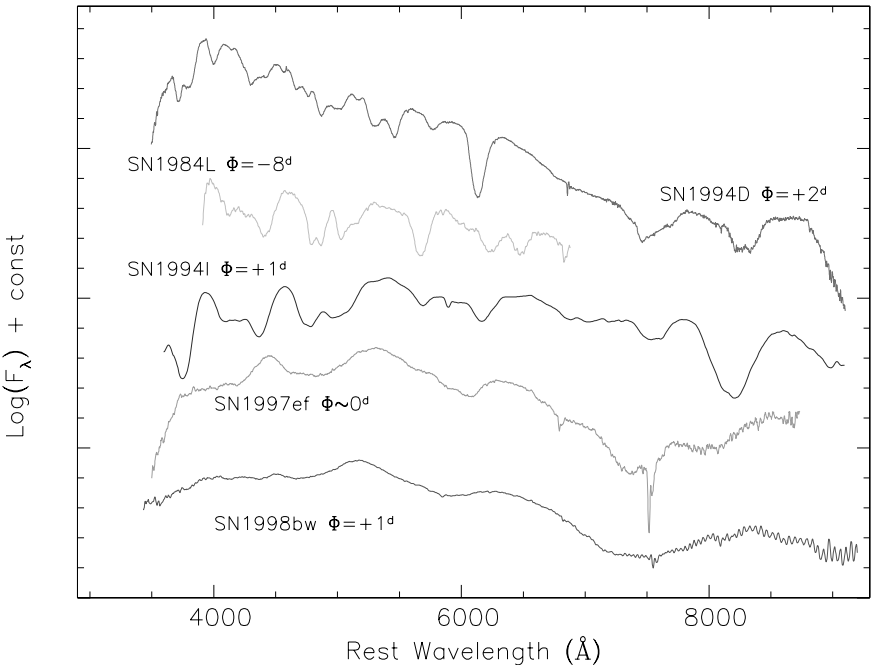

Fig. 3. Comparison between SN 1998bw and other SNe at maximum light.

the latter extending to ∼1000 days after the explosion by means of HST observations.

The late light curve continues to fall significantly steeper that the decay rate of ^{56}Co up to more than 500 days. There is no sign of the so-called positron phase, in which the fully deposited kinetic energy from the positrons would dominate the light curve.

Another interesting feature is the light curve flattening observed at about 800 days past explosion. For a detailed discussion on the possible explanations, we refer the reader to the original paper by [22] and here we just mention them: onset of more long-lived isotopes radioactive decay (e.g., ^{57}Co), freeze-out, interaction with CSM, black-hole powering and faint light echoes.

Using a simple radioactive model, Sollerman et al. [22] could fit the data with ∼0.3 $M_\odot$ of ejected ^{56}Ni, which can be regarded as a lower limit to the amount of ejected nickel in SN 1998bw. In this respect we note that the early light curve modeling (see [11]) required ∼0.7 $M_\odot$ in order to reproduce the observed high peak luminosity.

Extensive spectroscopic data sets were presented by [18, 23]. The general appearance of the spectrum at maximum light is quite unique among SNe, even though it is somewhat reminiscent of SN 1997ef (see Fig. 3), which has been modeled as a massive SN Ic [15]. At these early epochs, when the velocity is high, line blending is particularly severe; the modeling presented

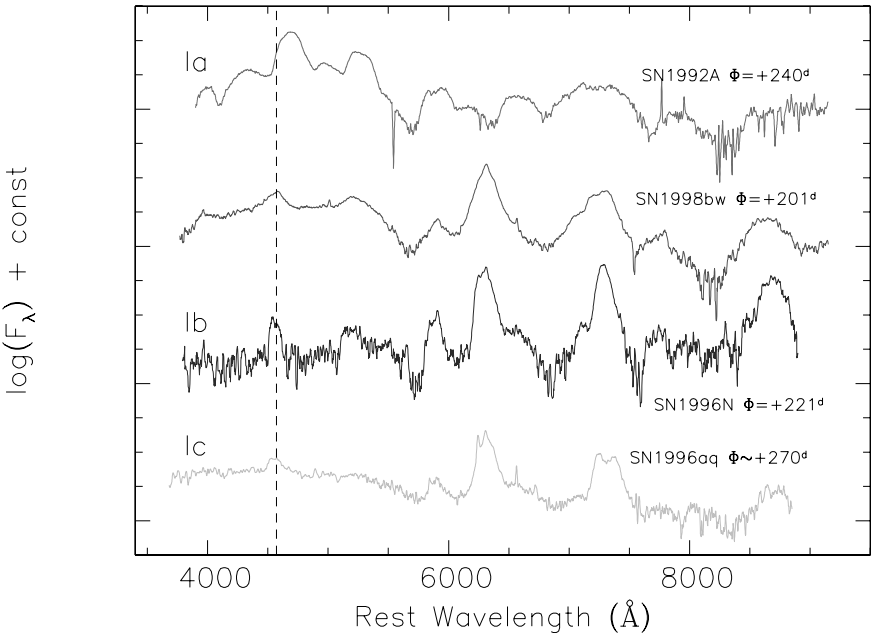

Fig. 4. Comparison between SNe 1992A (Ia), 1998bw, 1991N (Ib) and 1996aq (Ic) at late phases. The vertical dashed line is placed at the rest-frame wavelength of MgI]λ4571.

by [11] suggests that the main features are due to lines of Si II, O I, Ca II and Fe II. The velocity, deduced from the Si II λ6355 line is about 30,000 km s^{-1} at day -7 and decreases to about 18,000 km s^{-1} at day +22. These value are exceptionally high, for any SN.

Starting at about one month after maximum light, the SN enters its nebular phase. The transition from an absorption to an emission spectrum is slow and subtle. While the evolution of SN 1998bw in the range $5500 - 9000$ Å is similar to that of SN Ic events, the expansion velocities are larger, and the region between 4000 and 5500 Å is dominated (at least until about day +200) by a wide bump to which Fe II transitions probably contribute significantly (see Fig. 4). In general, the spectral appearance supports the idea that this object is related to SNe Ib/c. It might be regarded as an extreme case among these objects, having large kinetic energy, ejecta mass and ejected mass of synthesized ^{56}Ni, while SN 1997ef could represent a less extreme case closer in properties to the known SNe Ic.

At one year, despite its early marked peculiarity, SN 1998bw is practically indistinguishable from known type Ib (see Fig. 5). Even the high expansion velocities measured during the first 6 months have slowed down to the values that are typical for other type Ib SNe ($\sim$ 5000 km s^{-1}). But, the much higher ejected mass estimated by the models and the high luminosity, which persists

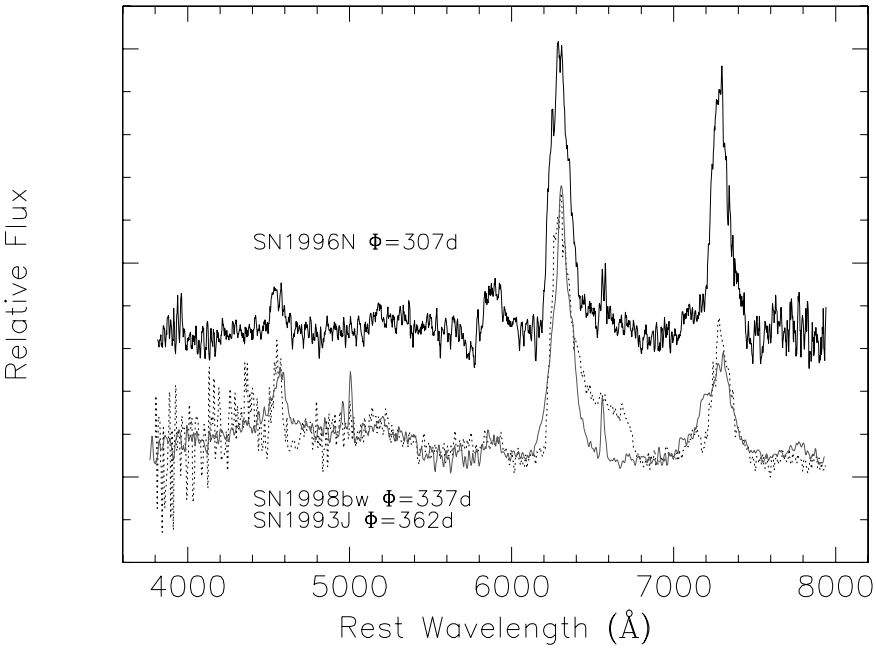

Fig. 5. Comparison between Type IIb SN 1993J (dotted line), Type Ib 1996N and SN 1998bw at about 1 year after maximum light. Spectra have been normalized to the [OI] $\lambda\lambda$6300,6364 peak and arbitrarily shifted for presentation.

also at these advanced phases (SN 1998bw is 3 mag brighter than SN 1996N at late phases), tend to support the idea of a hyper-energetic event.

An important aspect, which may give some hints about the progenitor's nature is the presence/absence of helium. The optical spectra have shown no traces of this element (see Fig. 6) and this is why the SN was classified as a Ic. On the other hand, near-IR spectroscopy (1.0−2.5 μm) during the early phases has shown the presence of a strong emission accompanied by a P-Cyg profile, which might be He I 1.08 μm. This identification is somewhat supported by the detection of another He I line at 2.06 μm. However, alternative identifications are possible (see the discussion in [18]) and, therefore, the detection of helium in the spectra of SN 1998bw is not so firm.

3 A New Beginning

After finishing the work on SN 1998bw I had the impression that the show was over and we had met just another peculiar object with no future. And, more depressing, we were left with more questions than answers. But nature is subtle and a very recent GRB, named 030329, has shown clear traces of an underlying SN spectrum, indeed similar to that of SN 1998bw (see [9]

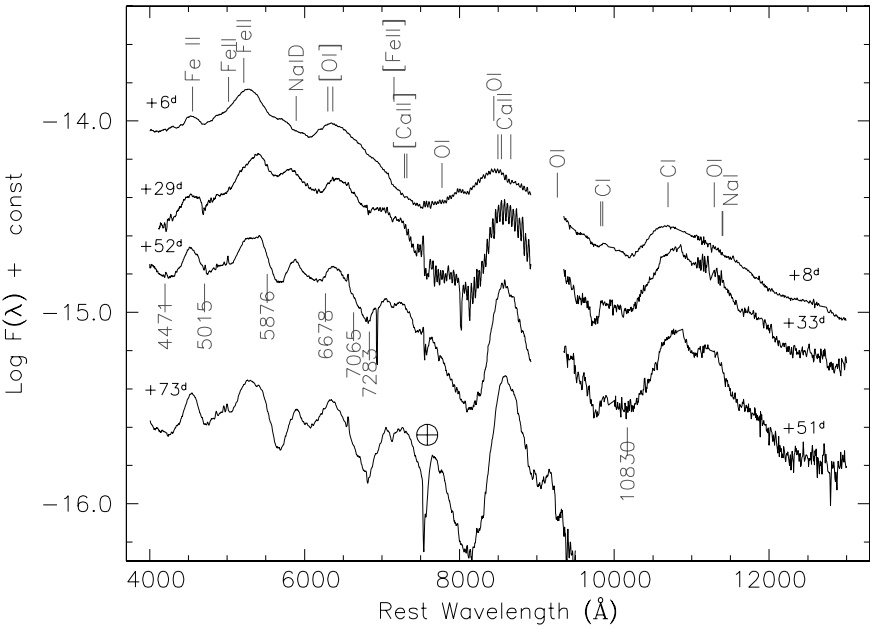

Fig. 6. Optical and IR spectra of SN 1998bw at comparable phases. Line identifications from spectral modeling are plotted for the most prominent emission features (top) and for the He I lines (bottom). The He marks are placed at the expected absorption positions for an expansion velocity of 18,300 km s^{-1}.

and the contribution by T. Matheson in these Proceedings). Even though GRB 030329 was among the brightest ever recorded (while GRB 980425 was extremely weak), the spectral resemblance to SN 1998bw is really astonishing.

This clearly indicates that, at least some GRB events are linked to core-collapse SNe and it confirms the ideas that were born with the discovery of GRB 980425/SN 1998bw and which have their original seed in the pioneering work by [1].

I have started this review quoting the paper by Clayton, Colgate and Fishman [2]. Actually, a few years later, in 1974, S. Colgate advanced the idea that γ-ray pulses of cosmic origin observed from the Vela spacecraft could be originated by the core-collapse of massive stars in distant galaxies [3].

Thirty years after, this prophecy seems to come true[2].

[2] The first idea actually dates back to 1959, when S. Colgate gave a talk to the Russian delegation of the conference for the cessation of nuclear testing in space, suggesting that "SNe or something like them might trigger our treaty detectors in orbit, causing us to lob nuclear weapons at each other" (private communication).

Fig. 7. Stirling Colgate at Aiguablava (Spain) in 1995. Photo by the author.

References

1. J.S. Bloom et al. : Nature **401**, 453 (1999)
2. D.D. Clayton, S.A. Colgate, G.J. Fishman: Astrophys. J. **155**, 75 (1969)
3. S.A. Colgate: Astrophys. J. **187**, 333 (1974)
4. A.V. Filippenko: IAUC 6969 (1998)
5. J.U. Fynbo et al.: Astrophys. J. Lett. **542**, L89 (2000)
6. T.J. Galama, P.M. Vreeswijk, E. Pian, F. Frontera, V. Doublier, J.F.Gonzalez: IAUC 6895 (1998)
7. T.J. Galama et al. : Nature **1395**, 670 (1998)
8. T.J. Galama et al. : Astron. Astrophys. Suppl. **138**, 465 (1999)
9. P. Garnavich, T. Matheson, E. W. Olszewski, P. Harding, K. Z. Stanek: IAUC 8108 (2003)
10. P. Höflich, J.C. Wheeler, L. Wang: Astrophys. J. **521**, 179 (1999)
11. K. Iwamoto et al. : Nature **395**, 672 (1998)
12. L.E. Kay, J.P. Halpern, K.M. Leighly, S. Heathcote, A.M. Magalhaes: IAUC 6969 (1998)
13. S.R. Kulkarni et al. : Nature **395**, 663 (1998)
14. C. Lidman, V. Doublier, J.F. Gonzalez, T. Augusteijn, O. Hainaut, H. Boehnhardt, F. Patat, B. Leibundgut: IAUC 6895 (1998)
15. P.A. Mazzali, K. Iwamoto, K. Nomoto: Astrophys. J. **545**, 407 (2000)
16. E.H. McKenzie, B.E. Schaefer: Pub. Astron. Soc. Pacific **111**, 964 (1999)
17. F. Patat, A. Piemonte: IAUC 6918 (1998)
18. F. Patat et al. : Astrophys. J. **555**, 900 (2001)
19. E. Pian et al. : Astron. Astrophys. Suppl. **138**, 463 (1999)
20. P. Soffita et al. : IAUC 6884 91998)

21. J. Sollerman, C. Kozma, C., C. Fransson, B. Leibundgut, P. Lundqvist, F. Ryde, P. Woudt: Astrophys. J. Lett. **537**, L127 (2000)
22. J. Sollerman et al. : Astron. Astrophys. **386**, 944 (2002)
23. R.A. Stathakis et al. : Mon. Not. R. Astron. Soc. **314**, 807 (2000)

SN 1998bw and Other Hyperenergetic Type Ic Supernovae

Paolo A. Mazzali[1,2], Ken'ichi Nomoto[2], Jinsong Deng[2], Keiichi Maeda[2], Koichi Iwamoto[3], Alexei V. Filippenko[4], and Ryan T. Foley[4]

[1] INAF - Osservatorio Astronomico di Trieste, Via Tiepolo, 11, Trieste, Italy
mazzali@ts.astro.it
[2] Department of Astronomy and Research Center for the Early Universe, School of Science, The University of Tokyo, Tokyo 113-0033, Japan
[3] Department of Physics, College of Science and Technology, Nihon University, Tokyo 101-8308, Japan
[4] Astronomy Department, Univ. of California, Berkeley, CA 94720-3411

Summary. The properties of the best-observed peculiar, SN 1998bw-like Type Ic supernovae (sometimes called "hypernovae") are reviewed, starting from SN 1998bw itself and including SNe 1997ef and 2002ap. Analysis of the light curves and the spectra shows that, while these SNe display a range of properties (kinetic energy, mass of the ejecta, mass of ^{56}Ni synthesized in the explosion), they have in common a larger-than-normal explosion kinetic energy, giving rise to the characteristic broad-lined spectra. Also, they all come from the collapse of bare CO cores of massive ($\gtrsim 20 M_\odot$) progenitor stars. Some of the properties of these SNe, such as kinetic energy and mass of ^{56}Ni, are probably correlated with the mass of the progenitor. Evidence that these powerful events are intrinsically asymmetric, suggesting that a correlation with at least some gamma-ray bursts can be expected, is also discussed.

1 Introduction

One of the most interesting recent developments in the study of supernovae (SNe) is the discovery of objects with a kinetic energy ($E_{\rm kin}$) on the order of 10^{52} erg, about 10 times more than normal core-collapse SNe (hereafter $E_{51} = E/10^{51}$ erg). The most luminous and powerful of these objects, the Type Ic supernova (SN Ic) 1998bw, was probably linked to the gamma-ray burst GRB 980425 [6]. Moreover, SN 1998bw was exceptional for a SN Ic: it was as luminous at peak as a SN Ia, indicating that it synthesized ~ 0.5 $M_\odot$ of ^{56}Ni, and it showed very broad absorption lines, reaching velocities of $\sim 30,000$ km s^{-1}. This was interpreted as due to a very powerful explosion, with $E_{51} \sim 30$ in spherical symmetry [11, 44].

Subsequently, other unusually energetic SNe Ic have been discovered or recognized, such as SN 1997ef [12, 23], SN 1997dq [21], possibly SN 1999as [17], and SN 2002ap [26]. These objects did not appear to be associated with GRBs. Fig. 1 shows the near-maximum spectra and the absolute V-band light curves of these so-called "hypernovae" and of the normal SN Ic 1994I; they span a wide range of properties. Not all of them are extremely luminous,

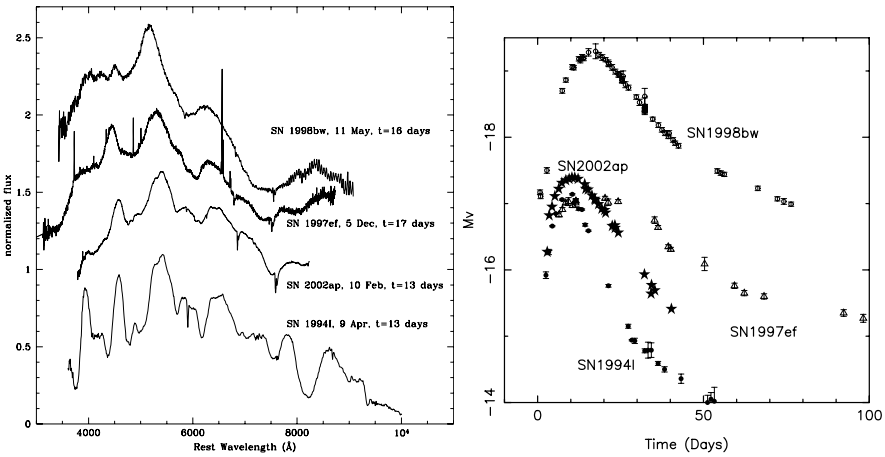

Fig. 1. (a) The near-maximum spectra and (b) the absolute V-band light curves of SN Ic 1994I and a few hyperenergetic Type Ic SNe [26].

yet they are spectrally similar to SN 1998bw, so they have also been dubbed "SN 1998bw-like SNe."

In this paper, we examine the properties of SN 1998bw-like SNe as derived from optical light curves and spectra, and we discuss what may be the discriminating factor for their birth or the connection with a GRB.

2 SN 1998bw and GRB 980425

The discovery of SN 1998bw immediately generated a great deal of interest, since the SN was detected in the error box of GRB 980425, and was very possibly linked to it. The object was identified as a supernova from its light curve, which was different from those of typical optical transients of GRBs. Extensive data were collected at ESO [6, 36] and other observatories.

Early-time spectra were rather blue and featureless, quite unlike those of other known SNe. More careful inspection showed clear similarities with the spectra of SNe Ic, but with one major difference: the absorption lines were so broad in SN 1998bw that they blended together, giving rise to what could even be confused with an emission spectrum. Very large expansion velocities ($\sim 30,000\,\mathrm{km\ s^{-1}}$) were measured in the ejecta. Also, SN 1998bw was very bright for a SN Ic: for a redshift distance of 39 Mpc ($z = 0.0085$ and $H_0 = 65\ \mathrm{km\ s^{-1}\ Mpc^{-1}}$), the SN reached a maximum $V = -19.4$ mag, which is luminous even for a SN Ia, while a typical SN Ic like SN 1994 I was almost 2 mag dimmer [33, 37].

Modeling of the early data ([11], hereafter IMN98) led to several striking conclusions. First, the SN produced about $0.7\mathrm{M}_\odot$ of ^{56}Ni, as much as a SN Ia.

This was necessary to power the light curve via the deposition of the γ-rays emitted in the decay of ^{56}Ni into ^{56}Co and ^{56}Fe.

IMN98 discuss that the light curves are degenerate: different combinations of ejecta mass $M_{\rm ej}$ and kinetic energy $E_{\rm kin}$ can reproduce the data equally well. Spectra came to the rescue: spectral synthesis showed that the only way to reproduce the observed extensive line blending was to have significant amounts of material moving at very large velocities. Since models with different $E_{\rm kin}$ give different degrees of blending, it was possible to select as the best model one with $M_{\rm ej} = 10.9{\rm M}_\odot$ and $E_{51} = 30$. This had an exploding core mass of $13.8{\rm M}_\odot$ and was designated CO138 accordingly. A typical SN Ic has $M_{\rm ej} = 1{\rm M}_\odot$, and the typical kinetic energy of most SNe of all types is only about $E_{51} = 1$. An even larger value, $E_{51} = 50$ [30], gives a better fit to the declining part of the light curve and to the spectra. A comparable value was obtained from an analysis of the early-time spectra [2]. Because of its exceptionally large $E_{\rm kin}$, SN 1998bw was called a "hypernova" by some authors [13].

The progenitor must have been a massive star, with a main-sequence mass of about $40{\rm M}_\odot$. Also, the remnant mass, which is computed by allowing only as much of the ^{56}Ni produced by core Si burning to be ejected as is necessary to power the SN light curve, turned out to be $\sim 3{\rm M}_\odot$ [30, 31]. This probably exceeds the maximum mass of a neutron star, suggesting that the explosion that was observed as SN 1998bw resulted in the creation of a black hole.

Since SN 1998bw was probably connected to a highly non-spherical event like a GRB, departure from spherical symmetry could be expected. Early polarization measurements confirmed this. Polarization of $\sim 0.5\%$, possibly decreasing with time, was detected [11, 15, 36]. This was interpreted as an axis ratio of about 2:1 in the expanding ejecta [10]. Models of the collapse of a rotating stripped core of a massive star confirmed that the explosion should be asymmetric, thus establishing a possible link with the GRB [19].

The transition to the nebular phase occurred ~ 100 days after the outburst, which is assumed to coincide with GRB 980425. Nebular spectra probe the deepest parts of the ejecta. Early in the nebular epoch the spectra show the properties of a typical SN Ic, with strong lines of [O I], Ca II, [Ca II], and Mg I], and weaker lines of [Fe II]. However, the [Fe II] lines are unusually strong for a SN Ic. Also, lines of different elements have different widths, indicating different expansion velocities. In particular, iron appears to expand more rapidly than oxygen. Furthermore, the [O I] lines decline more slowly than the [Fe II] ones, signaling deposition of γ-rays in a slowly moving O-dominated region. These facts suggest that the explosion was aspherical. The absence of [Fe III] lines can be understood if the ejecta are significantly clumped.

The properties of aspherical hypernova explosions were computed by Maeda et al. [20]. In such explosions Fe is mostly ejected at high velocity in a jet along the polar direction, while nearer the equatorial plane burning

is less effective and low-velocity O is mostly ejected. The unusual ratio of the width of the O and Fe nebular lines in SN 1998bw can be explained with a strongly aspherical explosion model viewed from a near-jet direction. Also, in this case the O line has a very sharp peak, in agreement with the observations. The value of $E_{\rm kin}$ in these models goes down to $E_{51} \approx 10$.

3 SNe 1997ef and 1997dq

SN 1997ef was a SN Ic whose $E_{\rm kin}$ was determined to be large by both Branch [2], who found $E_{51} \approx 30$ from spectral fits, and Iwamoto et al. [12], who derived from a simultaneous study of the light curve and spectra the values $E_{51} = 8$, $M_{\rm ej}$= 8M$_\odot$, and M(^{56}Ni)= 0.15M$_\odot$, and suggested that it was the result of the collapse of the stripped CO core of a massive star (ZAMS $\approx 25 - 30$M$_\odot$). Following the association between SN 1998bw and GRB 980425, Wang et al. [42] looked for other possible associations between SNe and GRBs, and suggested that GRB 971115 may be compatible with SN 1997ef in position and time of occurrence, although the correlation is much weaker than for SN 1998bw and GRB 980425.

Mazzali et al. [23] analyzed a series of early-time spectra of SN 1997ef. Using spectroscopic dating of the 1997 Nov. 29 spectrum they estimated that the explosion occurred on Nov. 20 $\pm$1 day. They derived the density and abundance distributions in the ejecta, and found that typical hypernova abundances describe SN 1997ef very well. However, their results differed from the explosion model in two ways: (1) the outer density structure turned out to be rather flat (a power law with index $n = -4$), as required by the very broad absorption features, extending to $v \approx 25,000$ km s^{-1}; and (2) matter was found to be present at low velocities ($\sim 2,000$ km s^{-1}), well below the low-velocity cutoff of a spherically symmetric explosion model (5,000 km s^{-1}). They found that a model with $E_{51} = 20$, $M_{\rm ej}$= 10M$_\odot$, and M(^{56}Ni)= 0.13M$_\odot$ (model CO100) gives a good representation of the light curve and spectra.

A synthetic light curve obtained with this modified density structure fits the observations near the peak quite nicely. Mazzali et al. [23] suggested that if an additional 0.05M$_\odot$ of ^{56}Ni is contained at low velocities and high density, then the observed slowing down of the light curve between days 60 and 160 might be explained by the ensuing additional deposition of γ-rays. They also suggested that the distribution of ^{56}Ni may be aspherical.

Matheson et al. [21] showed a set of spectra of the Type Ic SN 1997dq, and suggested that it is similar to SN 1997ef (cf. their Figures 17 and 18). Unlike SN 1997ef, a nebular spectrum is available for SN 1997dq. This can be used to determine the mass of ^{56}Ni ejected by this SN and, by analogy, by SN 1997ef. We modeled this spectrum with our NLTE nebular code (e.g., [25]). Given the relative distance modulus of SN 1997dq with respect to SN 1997ef (-1.8 mag), the best fit required M(^{56}Ni)= 0.16M$_\odot$, and a total mass of 2.3M$_\odot$,

of which only about $0.8 M_\odot$ consists of O; the rest is mostly Si, C, and S [28]. The masses of Ca and Mg are rather small by comparison, even though they do give rise to rather strong emission features. The outer velocity of the nebula is only 5,000 km s^{-1}, which is similar to the velocity of the nebular component in earlier spectra of SN 1997ef. The density of the outer regions is too low at these advanced epochs to contribute significantly to the nebular spectrum, and the deposition of γ-rays and positrons is also probably quite small, because ^{56}Ni is not expected to be mostly located there. The fact that the velocities of the regions that form the nebular spectrum are low confirms the finding that significant amounts of mass are present at velocities lower than the cutoff imposed by one-dimensional explosion models [23].

Indeed, Mazzali et al. [23] estimated that the mass between 3,000 and 5,000 km s^{-1} in SN 1997ef is $1.65 M_\odot$, in good agreement with the result for SN 1997dq, which refers to all regions with $v < 5000$ km s^{-1}. The estimate of the ^{56}Ni mass for SN 1997dq is also in good agreement with the results obtained for SN 1997ef. Although the nebular spectrum of SN 1997dq is not of exceptionally high signal-to-noise ratio, the line profiles do not seem to show signs of an asymmetric explosion, such as the multiple components (narrow and broad) observed in the nebular spectra of SN 1998bw [25].

4 SN 2002ap

SN Ic 2002ap was discovered in M74 on 2002 January 30 [9]. The SN was immediately recognized as SN 1998bw-like from its broad spectral features [5, 7, 16, 29]. Luckily, the SN was discovered very soon after it exploded: the discovery date was Jan. 29, while the SN was not detected on Jan. 25 [32]. This is among the earliest any SN has been observed.

SN 2002ap reached V maximum on about Feb. 8 at $V = 12.3$ mag. It peaked earlier than both SNe 1998bw and 1997ef, but later than the normal SN 1994I, suggesting an intermediate value of the ejecta mass $M_{\rm ej}$. Using a distance to M74 of 8 Mpc ($\mu = 29.5$ mag; [38]), and a combined Galaxy and M74 reddening of $E(B-V) = 0.09$ mag [40], the peak absolute magnitude was $M_V = -17.4$. This is comparable to SN 1997ef and fainter than SN 1998bw by almost 2 mag. Since peak brightness depends on the ejected ^{56}Ni mass, SNe 2002ap, 1997ef, and 1994I appear to have synthesized similar amounts of it. Estimates were ~ 0.07 $M_\odot$ for SN 1994I [33] and 0.13 $M_\odot$ for SN 1997ef [23]. The ^{56}Ni mass for SN 2002ap is estimated to be ~ 0.07 $M_\odot$, which is similar to that of normal core-collapse SNe such as SNe 1987A and 1994I.

If line width is the distinguishing feature of a "hypernova," then clearly SN 2002ap belongs to this group, as its spectrum resembles that of SN 1997ef much more than that of SN 1994I (Fig. 1a). Line blending in SN 2002ap and SN 1997ef is comparable. However, individual features that are clearly visible in SN 1994I but completely blended in SN 1997ef can at least be discerned in SN 2002ap (e.g., the Na I–Si II blend near 6000 Å and the Fe II lines

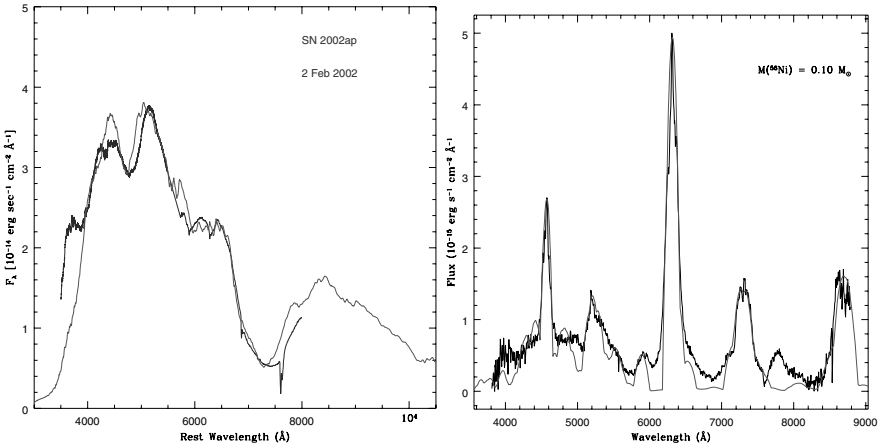

Fig. 2. a. A spectrum of SN 2002ap observed on Feb. 2, 2002, compared to a synthetic spectrum obtained with our Monte Carlo code [24, 22].
b. A spectrum of SN 2002ap observed at Lick Observatory on October 1, 2002, compared to a synthetic NLTE spectrum computed for a ^{56}Ni mass of 0.09 $M_\odot$ and a total mass of ≈ 1.3 $M_\odot$below 5600 km s^{-1} [27].

near 5000 Å). Therefore, spectroscopically SN 2002ap appears to be located just below SN 1997ef in a "velocity scale," but considerably above SN 1994I, confirming the evidence from the light curve.

The spectral evolution of SN 2002ap follows closely that of SN 1997ef, at a rate about 1.5 times faster. The spectra and the light curve of SN 2002ap can be reproduced by a model with $M_{\rm ej}$= 2.5–5 $M_\odot$ and E_{51} = 4–10 (see Fig. 2a). Both $M_{\rm ej}$ and $E_{\rm kin}$ are much smaller than those of SNe 1998bw and 1997ef (the higher limits quoted may apply if a significant amount of He is present).

For these values of $E_{\rm kin}$, $M_{\rm ej}$, and $M(^{56}{\rm Ni})$, we can constrain the progenitor's main-sequence mass $M_{\rm ms}$ and the remnant mass $M_{\rm rem}$. Modeling the explosions of C+O stars yields $M(^{56}{\rm Ni})$ as a function of the parameter set ($E_{\rm kin}$, $M_{\rm CO}$, $M_{\rm rem}$ =$M_{\rm ej}$−$M_{\rm CO}$). The model which is most consistent with our estimates of ($M_{\rm ej}$, E) is one with $M_{\rm CO} \approx 5\,M_\odot$, $M_{\rm rem} \approx 2.5\,M_\odot$, and E_{51} = 4.2. The 5 $M_\odot$ C+O core forms in a He core of mass M_α = 7 $M_\odot$, corresponding to a main-sequence mass $M_{\rm ms} \approx$ 20–25 $M_\odot$. The $M_{\rm ms} - M_\alpha$ relation depends on convection and metallicity (e.g., [34, 41]).

SN 2002ap was not apparently associated with a GRB. This may be a consequence of the fact that the explosion energy of SN 2002ap is about a factor of 5–10 smaller than that of SN 1998bw, as also indicated by the weak radio signature [1]. The present data show no clear signature of asymmetry, except perhaps for some polarization [14, 18, 43], which is smaller than that of SN 1998bw. This suggests that the degree of asphericity is smaller in SN 2002ap and that the possible "jet" may have been weaker, which makes

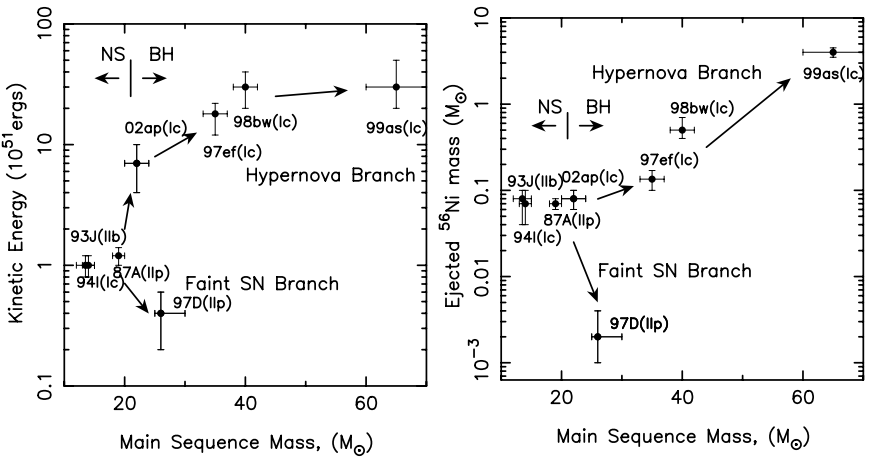

Fig. 3. a. Explosion energies and b. ejected ^{56}Ni mass against main sequence mass of the progenitors for several core collapse supernovae/hypernovae [35].

GRB generation more difficult. It is also possible that a GRB did occur, but that it was not observed because of an unfavorable inclination with respect to the line-of-sight. Asymmetric models indeed show more "normal" properties away from the jet axis.

Nebular spectra, which developed at an epoch of about 4 months, do not show the peculiar narrow [O I] 6300Å line as in SN 1998bw, but they do show a narrow core in both [O I] and Mg I] 4571Å, which may be interpreted as a signature of asymmetry. The mass of ^{56}Ni estimated from modeling these spectra with a 1D NLTE code (Fig. 2b) is $\approx 0.1\,M_\odot$.

5 Properties of Hypernovae

Based on the observed objects and their interpretation, it is possible to make some generalization regarding the properties of hyperenergetic type Ic SNe and their relation to the progenitor stars.

5.1 The Kinetic Energy

All hypernovae are highly energetic. Fig. 3 shows $E_{\rm kin}$ as a function of the main-sequence mass $M_{\rm ms}$ of the progenitor star as derived from fitting the optical light curves and spectra of normal and highly energetic SNe. In a "hypernova branch" $E_{\rm kin}$ appears to increase with $M_{\rm ms}$, reaching values much larger than the canonical 10^{51} erg. The faint Type II-P SNe 1997D and 1999br, on the contrary, have very small values of $E_{\rm kin}$.

This trend might be interpreted as follows. Stars with $M_{\rm ms} \lesssim$ 20-25 $M_\odot$ form neutron stars and become normal supernovae, their type depending on

their envelope properties. (SN 1987A may be a borderline case between neutron star and black hole formation.) Stars with $M_{\rm ms} \gtrsim$ 20-25 $M_\odot$ form black holes (e.g., [4]); whether they become hypernovae or faint SNe may depend on the angular momentum in the collapsing core, which in turn depends on the stellar winds, metallicity, magnetic fields, and binarity.

Hypernova progenitors may have rapidly rotating cores owing possibly to the spiraling-in of a companion star in a binary system. The cores of faint SNe II-P might not have a large angular momentum, because the progenitor's massive H-rich envelope may have been able to transport the angular momentum of the core out to the envelope possibly via a magnetic-field effect.

Between these two branches, there may be a variety of SNe. A dispersion in the properties of SNe II-P has been reported [8], but whether the region of normal explosion energy and large progenitor mass is actually populated remains an open issue awaiting observational verification.

5.2 The Mass of Ejected ^{56}Ni

A similar relation is observed between the mass of ^{56}Ni, $M(^{56}\mathrm{Ni})$, synthesized in core-collapse supernovae and $M_{\rm ms}$ in Fig. 3a. This is important for the study of the chemical evolution of galaxies. Stars with $M_{\rm ms} \lesssim$ 20-25 $M_\odot$, forming a neutron star, produce $\sim 0.08 \pm 0.03$ $M_\odot$ ^{56}Ni as in SNe 1993J, 1994I, and 1987A. For stars with $M_{\rm ms} \gtrsim$ 20-25 $M_\odot$, which form black holes, $M(^{56}\mathrm{Ni})$ appears to increase with $M_{\rm ms}$ in the "hypernova branch," while SNe in the "faint SN branch" produce only very little ^{56}Ni. For faint SNe the explosion energy is so small, probably because of the large gravitational potential, that most ^{56}Ni falls back onto the compact remnant.

5.3 Asymmetry

All hyperenergetic SNe Ic show some signatures of asymmetry, or at least of a departure from purely 1-dimensional spherically symmetric models. This may support the case for their connection with at least some GRBs.

Only for SN 1998bw and the recent SN 2003dh/GRB 030329 is the connection with a GRB well established. In the other cases, either a GRB was not generated or, if it was, it was weak and/or not pointing toward us. The issue of directionality is very important. If hypernovae are aspherical, objects with the same ^{56}Ni mass should show a range of properties, reflecting different orientations. These objects may look very different at early phases, displaying different light curves, velocities, and abundances. At late times, these effects should disappear. So far, however, this evidence is missing. Further observations of supernovae in GRBs are obviously essential (e.g., [3, 39]).

References

1. E. Berger, S.R. Kulkarni, D.A. Frail: IAUC 7817 (2002)

2. D. Branch: Supernovae and Gamma-Ray Bursts (Proc. of the STScI Symp., Baltimore), eds. M. Livio, N. Panagia, K. Sahu (Cambridge, 2001), pp. 96-109
3. M. Della Valle et al. : Astron. Astrophys. **406**, L33 (2003)
4. E. Ergma, E.P.J. van den Heuvel: Astron. Astrophys. **331**, L29 (1998)
5. A.V. Filippenko, R. Chornock: IAUC 7825 (2002)
6. T. Galama et al. : Nature **395**, 670 (1998)
7. A. Gal-Yam, E.O. Ofek, O. Shemmer: Mon. Not. R. Astron. Soc. **332**, L73 (2002)
8. M. Hamuy: Astrophys. J. **582**, 905 (2003)
9. Y. Hirose: IAUC 7810 (2002)
10. P. Höflich, J.C. Wheeler, L. Wang: Astrophys. J. **521**, 179 (1999)
11. K. Iwamoto et al. : Nature **395**, 672 (1998)
12. K. Iwamoto et al. : Astrophys. J. **534**, 660 (2000)
13. K. Iwamoto et al. : SN 1998bw and Hypernovae. In: *Supernovae and Gamma-Ray Bursters*, LNP 598, ed by K. Weiler (Springer, Berlin, Heidelberg, New York, 2003) pp. 243-282
14. K.S. Kawabata et al. : Astrophys. J. Lett. **580**, L39 (2002)
15. L.E. Kay, J.P. Halpern, K.M. Leighly, S. Heathcote, A.M. Magalhaes, A.V. Filippenko: IAUC 6969 (1998)
16. K. Kinugasa et al. : IAUC 7811 (2002)
17. R. Knop et al. : IAUC 7128 (1999)
18. D. Leonard, A.V. Filippenko, R. Chornock, R. Foley: Pub. Astron. Soc. Pacific **114**, 1333 (2002)
19. A.I. MacFadyen, S.E. Woosley: Astrophys. J. **524**, 262 (1999)
20. K. Maeda, T. Nakamura, K. Nomoto, P.A. Mazzali, F. Patat, I. Hachisu: Astrophys. J. **565**, 405 (2002)
21. T. Matheson, A.V. Filippenko, W. Li, D.C. Leonard, & J.C. Shields: Astron. J. **121**, 1648 (2001)
22. P.A. Mazzali: Astron. Astrophys. **363**, 705 (2000)
23. P.A. Mazzali, K. Iwamoto, K. Nomoto: Astrophys. J. **545**, 407 (2000)
24. P.A. Mazzali, L.B. Lucy: Astron. Astrophys. **279**, 447 (1993)
25. P.A. Mazzali, K. Nomoto, F. Patat, K. Maeda: Astrophys. J. **559**, 1047 (2001)
26. P.A. Mazzali et al. : Astrophys. J. Lett. **572**, L61 (2002)
27. P.A. Mazzali, K. Nomoto, J. Deng, K. Maeda, Y. Qiu: From Highlight to Twilight: the Physics of Supernovae (ESO, Garching, 2003), p. 246
28. P.A. Mazzali et al. : in preparation
29. P. Meikle et al. : IAUC 7811 (2002)
30. T. Nakamura, P.A. Mazzali, K. Nomoto, K. Iwamoto: Astrophys. J. **550**, 991 (2001)
31. T. Nakamura, H. Umeda, K. Iwamoto, K. Nomoto, M. Hashimoto, W.R. Hix, F.-K. Thielemann: Astrophys. J. **555**, 880 (2001)
32. S. Nakano, R. Kushida, W. Li: IAUC 7810 (2002)
33. K. Nomoto et al. : Nature **371**, 227 (1994)
34. K. Nomoto, M. Hashimoto: Phys. Rep. **256**, 173 (1988)
35. K. Nomoto et al. : Supernovae and Gamma-Ray Bursts (Baltimore), eds. M. Livio, N. Panagia, K. Sahu (Cambridge, 2001), pp. 144-170
36. F. Patat et al. : Astrophys. J. **555**, 917 (2001)
37. M.W. Richmond et al. : Astron. J. **111**, 327 (1996)
38. M.E. Sharina, I.D. Karachentsev, N.A. Tikhonov: Astron. Astrophys. Suppl. **119**, 499 (1996)

39. K.Z. Stanek et al. : Astrophys. J. Lett. **591**, L17 (2003)
40. M. Takada-Hidai, W. Aoki, G. Zhao: Pub. Astron. Soc. Japan **54**, 899 (2002)
41. H. Umeda, K. Nomoto: Astrophys. J. **565**, 385 (2002)
42. L. Wang, J.C. Wheeler: Astrophys. J. Lett. **504**, L87 (1998)
43. L. Wang et al. : Astrophys. J. **592**, 457 (2003)
44. S. Woosley, R. Eastman, B. Schmidt: Astrophys. J. **516**, 788 (1999)

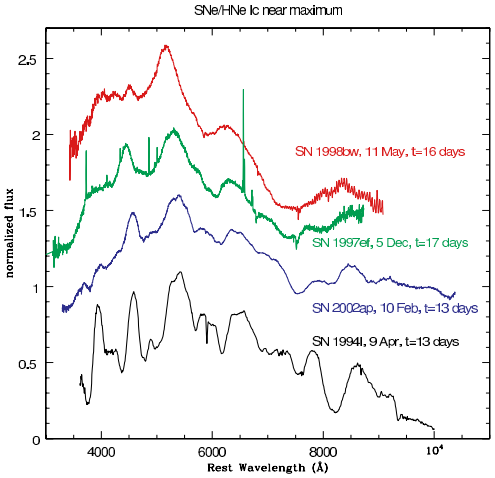

a) Spectra of four Type Ic supernovae near maximum: The increasing width of the absorption feature indicates progressively larger explosion kinetic energies.

b) Spectra of two GRB–hosting Type Ic supernovae ("Hypernovae"); SN 1998bw and SN 2003dh (blue). (From Tom Matheson)

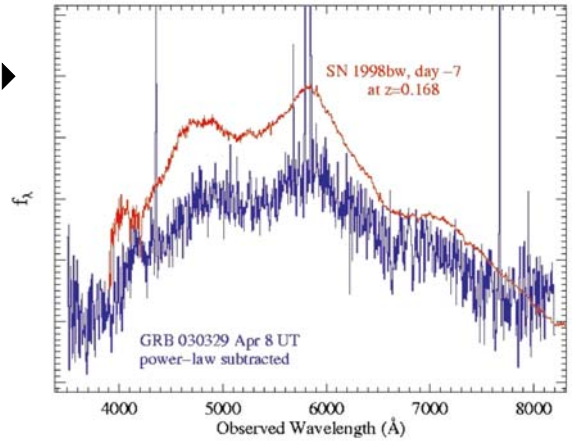

Plate (Mazzali et al.)

Plate 4.

The Supernova/GRB Connection

P. Höflich[1], D. Baade[2], A. Khokhlov[3], L. Wang[4], and J.C. Wheeler[1]

[1] Dept. of Astronomy, University of Texas, Austin, TX 78681, USA;
pah@astro.as.utexas.edu & wheel@hej3.as.utexas.edu
[2] ESO, Karl-Schwarzschild-Str. 2, 85748 Garching, Germany;
pdbaade@eso.org
[3] Naval Research Lab, Washington DC, USA;
ajk@lcp.nrl.navy.mil
[4] Lawrence Berkeley Lab, CA 94720, USA;
lifan@panisse.lbl.gov

Summary. We discuss the possible connection between supernova explosions (SN) and gamma-ray bursters (GRB) from the perspective of our current understanding of SN physics. Core collapse supernovae (SN) are the final stages of stellar evolution in massive stars during which the central region collapses, forms a neutron star (NS) or black hole, and the outer layers are ejected. Recent explosion scenarios assumed that the ejection is due to energy deposition by neutrinos into the envelope but detailed models do not produce powerful explosions. There is new and mounting evidence for an asphericity and, in particular, for axial symmetry in several supernovae which may be hard to reconcile within the spherical picture. The 3-D signatures are a key to understand core collapse supernovae and the GRB/SN connection. In this paper we study the effects and observational consequences of asymmetric explosions.

1 Introduction

Recently, the connection between supernovae (SN) and gamma-ray bursters (GRB) has been established with the observations of GRB 030329 and the identification of the underlying SN2003dh [25]. Further evidence is found in observations of the circumstellar surrounding in GRB 021004, the coincidence between SN1998bw and GRB 980425 [24], possible identification of the Fe K line in the X-rays, and some evidence that GRBs are related to star forming regions. There is a general agreement that the explosion of a massive star is caused by the collapse of its central parts into a neutron star or, for massive progenitors, into a black hole. The mechanism of the energy deposition into the envelope is still debated. For an overview, see [11]. In particular, the direct collapse of the central region a very massive star to a black hole and the connection with the newly found hypernovae is a very attractive option [34].

In recent years, there has been a mounting evidence that the explosions of massive stars (core collapse supernovae) are highly aspherical.

1. The spectra of core-collapse supernovae (e.g., SN1987A, SN1993J, SN1994I, SN1999em, SN2002ap) are significantly polarized at a level of 0.5 to 3 %

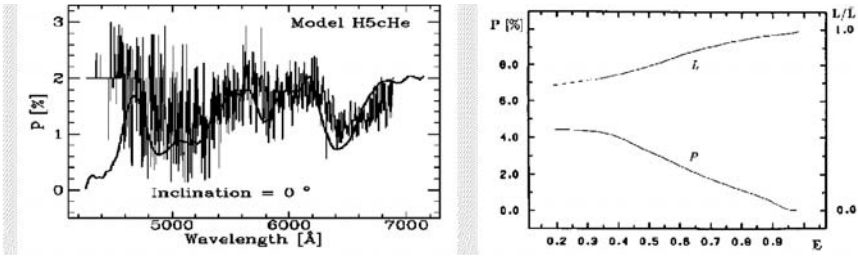

Fig. 1. Polarization spectrum for SN1993J for an axis ratio of 1/2 for an oblate ellipsoid in comparison with observations by Trammell et al. [29] (left plot). On the right, the dependence of the continuum polarization (right) and directional dependence of the luminosity is shown as a function axis ratios for oblate ellipsoids seen from the equator (from [8, 10]).

(e.g., Fig. 1 and [4, 8, 14, 22, 30]) indicating aspherical envelopes by factors of up to 2 (Fig. 2). The degree of polarization tends to vary inversely with the mass of the hydrogen envelope, being maximum for Type Ib/c events with no hydrogen [31]. For SNeII, Leonard et al. [19] and Wang et al. [32] showed that the polarization and, thus, the asphericity increase with time. Both trends suggest a connection of the asymmetries with the central engine. For supernovae with a good time and wavelength coverage, the orientation of the polarization vector tends to stay constant both in time and with wavelength. This implies that there is a global symmetry axis in the ejecta.

2. Observations of SN 1987A showed that radioactive material was brought to the hydrogen rich layers of the ejecta very quickly during the explosion (e.g., [19]).
3. The remnant of the Cas A supernova shows rapidly moving oxygen-rich matter outside the nominal boundary of the remnant and evidence for two oppositely directed jets of high-velocity material [5].
4. Recent X-ray observations with the CHANDRA satellite have shown an unusual distribution of iron and silicon group elements with large scale asymmetries in Cas A [13].
5. After the explosion, neutron stars are observed with high velocities, up to 1000 km/s [27].
6. Direct HST-images from 11 June 2000, are able to resolve the inner debris of SN1987A showing its prolate geometry with an axis ratio of ~ 2 [11, 32].

2 Jet-Induced Supernovae and Observations

In SNe, electron scattering is the main mechanism to polarize the light. It can be caused by asymmetries in the density, abundances or excitation structure

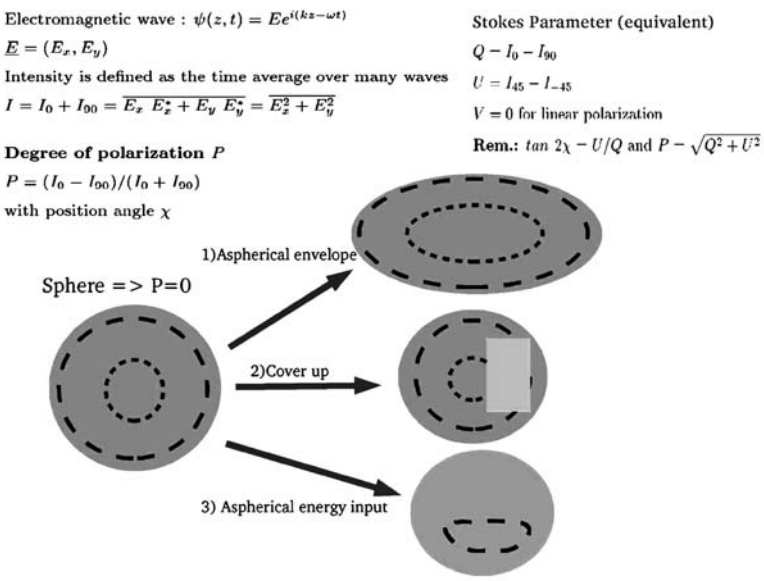

Fig. 2. Definition of the polarization and schematic diagram for its production. The dotted lines give the main orientation of the electrical vectors. For an unresolved sphere, the components cancel out. Three main mechanisms can be distinguished. $\bar{P}$ can be caused by 1) an aspherical envelope, 2) shading parts of the disk, or by 3) an aspherical excitation/ionization (from [9]).

of an envelope. In general, the supernovae ejecta cannot be spatially resolved. Although the light from different parts of a spherical disk is polarized, the resulting polarization $\bar{P}$ is zero for the integrated light (Fig. 2). To produce $\bar{P}$, three basic configurations must be considered. The envelope is aspherical, parts of the disk are shaded, and the envelope may be illuminated by an "off-center" source. In case 2, the shading may be either by a broad-band absorber such as dust or a specific line opacity. In the latter case, this would produce a change of $\bar{P}$ in a narrow line range (Fig. 4). In reality, a combination of all cases is realized (see below). Quantitative analyses are need to take into account that the continua and lines are formed in the same layers (e.g., Fig. 1).

We have numerically studied the explosion of core collapse supernovae caused by supersonic jets generated in the center of the star to ask for the jet-properties needed to reproduce observations. The initial stellar structures are based on stellar evolution calculations [26]. The explosion and jet propagation are calculated by a full 3-D code within a cubic domain. The Euler equations are integrated using an explicit, second-order accurate, Godunov type (PPM, [3]), adaptive-mesh-refinement, massively parallel, Fully-

Threaded Tree (FTT) program, ALLA [16]. The subsequent evolution, LCs and spectra are calculated by using modules of our hydrodynamical radiation transport code for spherical and full 3-D (HYDRA) [12]. This code includes modules for hydrodynamics using PPM (without mesh refinement), detailed networks for nuclear processes and for atomic, non-LTE level populations, and radiation transport (with mesh-refinement). Its components have been used to carry out many of the previous calculations to analyze light curves, flux and polarization spectra of thermonuclear and supernovae ([7] ... [12]).

2.1 General Results

We simulated the process of the jet propagation through the star, the redistribution of elements, and radiation transport effects. Qualitatively, the jet-induced picture allows to reproduce the polarization observed in core collapse supernovae. Both asymmetric ionization and density/chemical distributions are crucial for the production of P. Even within the picture of jet-induced explosion, the latter effect alone cannot (!) account for the large P produced in the intermediate H-rich layers of core-collapse SN with a massive H-rich envelopes (e.g., SN1987A and SN1999em).

A strong explosion and a high efficiency for the conversion of the jet energy requires low jet velocities or a low, initial collimation of the jet. With increasing extension of the envelope, the conversion factor increases. Typically, we would expect higher kinetic energies in SNe II compared to SNe Ib/c if a significant amount of explosion energy is carried away by jets. Within the framework of jet-induced SN, the lack of this evidence suggests low jet-velocities. The He, C, O and Si rich layers of the progenitor show characteristic, butterfly-shape structures, and jets bring heavy elements (e.g., ^{56}Ni into the outer layers). Due to the high entropies of the jet material close to the center, this may be a possible site for r-process elements. Moreover, aspherical explosion models show a significantly increased fall-back of material on the central object, e.g., a neutron star, on time scales of minutes to hours which may trigger the delayed formation of a black hole. Fallback and the low velocity material may alter the escape probability for γ-rays produced by radioactive decay of ^{56}Ni which is critical for mass estimates of ^{56}Ni which are based on late time observations (e.g., SN1998bw). For more details, see [11, 17].

2.2 SN1987A and SN1999em

In our models for these SNe II, the jet material stalls within the expanding envelope corresponding to a velocity of $\sim$ 4500 km s^{-1}during the phase of homologous expansion. In SN1987A, a bump in spectral lines of various elements has been interpreted by material excited by a clump of radioactive ^{56}Ni (Lucy 1988). Within our framework, this bump may be a measure of

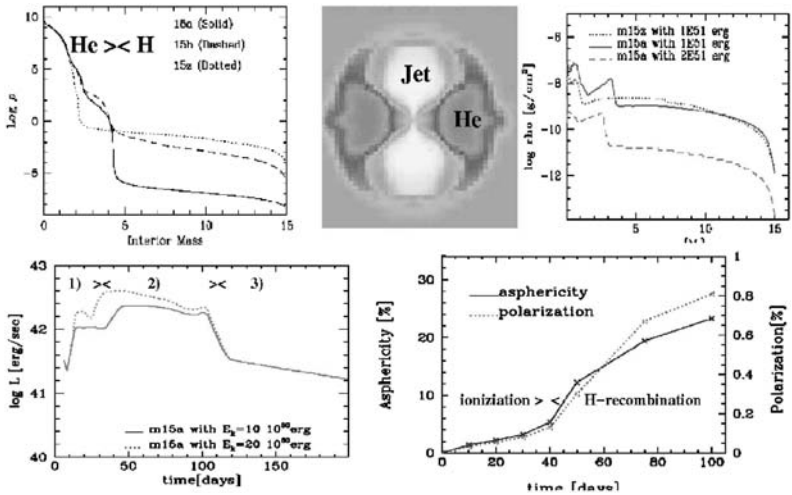

Fig. 3. Polarization produced by an aspherical, chemical distribution for an extreme SN IIP model such as SN1999em (see text).

the region where the jet stalled. This could also explain the early appearance of X-rays in SN1987A which requires strong mixing of radioactive material into the hydrogen-rich layers, and the overall distribution of elements in the resolved HST images of the inner debris of SN 1987A. For both SN1987A and SN1999em, aspherical excitation by hard radiation is found to be crucial to explain the size and presence of the polarization observed early on (Fig. 4). For the extreme SN IIP 1999em (Fig. 3), our model is based on a star with 15 solar masses and an explosion energy of 2×10^{51} erg. The initial density profile is given for a star at the final stage of stellar evolution for metallicities Z of 0.02, 0.001 and 0 (models 15a, 15b, 15z, upper left panel). For the explosion, we use model 15a. In the upper, middle panel, the chemical distribution of He is given at 250 sec for the He-rich layers after the jet material has stalled. The several curves correspond to He mass fractions of 0.0, 0.18, 0.36, 0.72, and 1.0, respectively. The subsequent explosion has been followed in 1-D up to the phase of homologous expansion. In the upper, right panel, the density distribution is given at about 5 days after the explosion. The steep gradients in the density in the upper right and left panels are located at the interface between the He-core and the H-mantel. In the lower, left panel, the resulting bolometric LCs are given for explosion energies of 2×10^{51} erg (dotted line) and 1×10^{51} erg, respectively. Based on full 3-D calculations for the radiation and γ-ray transport, we have calculated the location of the recombination front (in NLTE) as a function of time. The resulting shape of the photosphere is always prolate. The corresponding axis ratio and the polarization seen from the equator are shown (lower, right panel). Note the

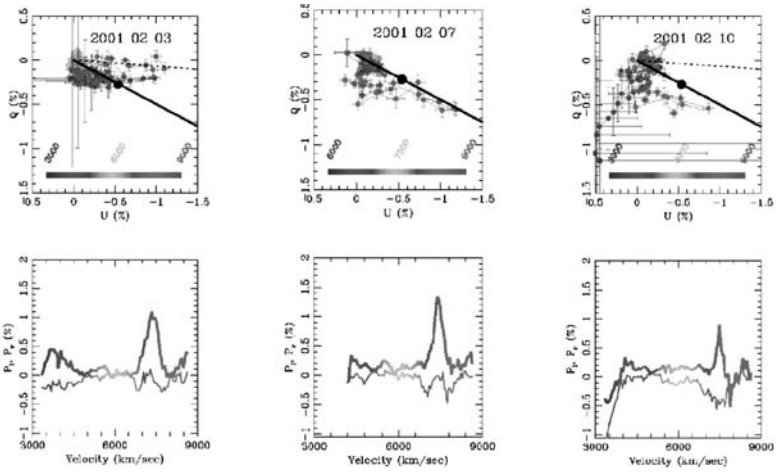

Fig. 4. Spectropolarimetry of SN2002ap at about -6d, -2d and +1 relative to maximum light in V. An intrinsic polarization component (shown as a solid dot) is subtracted from the observed Stokes Parameters so that the data points present the intrinsic polarization of the SN. The dashed line illustrates the dominant axis of the polarization. There has been a distinct shift and, perhaps, a small rotation of the axis in the Q-U plane during the early epochs, and the spectra are dominated by FeII, NaI D and OI. In the spectrum at about 1d after maximum, the original, dominant axis has shifted further in the Q-U plane, and a new axis starts to appear at an angle of about 110^o defined by Ca II H &K and Ca II IR triplet.

strong increase of the asphericity after the onset of the recombination phase between day 30 to 40 [11]. For the polarization in a massive, H-rich envelope, P is linked to the recombination process and asymmetric excitation.

2.3 SN 2002ap

SN 2002ap has attracted much attention because early spectra showed a lack of hydrogen and helium characteristic of SN Ic and broad velocity components [6, 15, 21], which have been taken as one characteristic of "hypernovae." The nature, existence of, and importance of hypernovae remains to be clarified, and the study of SN 2002ap presents an important opportunity to shed light on the general category of hypernovae. and their relation to typical SNe Ic such as SN1994I. High-quality spectropolarimetry (range 417-860 nm; spectral resolution 1.27 nm) of SN 2002ap was obtained with the ESO Very Large Telescope Melipal (+ FORS1) at 3 epochs that correspond to -6, -2, and +1 days for a V maximum of 9 Feb 2002. The polarization spectra show three distinct broad ($\sim$ 100 nm) features at $\sim$ 400, 550, and 750 nm that evolve in shape, amplitude and orientation in the Q-U plane. The continuum polarization grows from nearly zero to $\sim$ 0.2 percent. The 750 nm feature is

polarized at a level ≥ 1 percent. We identify the 550 and 750 nm features as Na I D and OI λ 777.4 moving at about 20,000 km s^{-1}. The blue feature may be Fe II. We interpret the polarization evolution in terms of the impact of a bipolar flow from the core that is stopped within the outer envelope of a carbon/oxygen core and, consequently, the Ca features show up only at about maximum light. The interpretation of a stalled jet is also supported by IR-spectra taken by C. Gerardy and M. Meikle (2002, private communication) which show strong CI lines (940.5 and 1070. nm) at expansion velocities of $\sim 15,000$ to $25,000$ km s^{-1}but not, as in SNe Ia, the strong 1600 to 1900 nm feature due to Fe/Co/Ni. Although the symmetry axis remains fixed, the photosphere retreats by different amounts in different directions due to the asymmetric velocity flow and density distribution geometrical blocking effects leading to a continuous shift with time of the main axis of polarization. At about maximum light, the appearance of an additional axis in a Q-U plane due to Ca and processed material indicates a second axis of symmetry. Qualitatively and within the picture of jet-induced supernovae this may be explained by bipolar-jets which are not perfectly aligned and, thus, produce a kick of the central region (e.g., neutron star and processed material). Detailed radiation-hydro calculations are under way. We conclude that the features that characterize SN 2002ap, specifically its high velocity, can be accounted for in an asymmetric model with a larger ejecta mass than SN 1994I such that the photosphere remains longer in higher velocity material. The characteristics of hypernovae may be the result of orientation effects in a mildly inhomogeneous set of progenitors, rather than requiring an excessive total energy or luminosity. In the analysis of asymmetric events with spherically symmetric models, it is probably advisable to refer to "isotropic equivalent" energy, luminosity, ejected mass, and nickel mass. This aspect may also be relevant for the interpretation of the hypernova SN1998bw.

Acknowledgement. The authors are grateful to the European Southern Observatory for the generous allocation of observing time. They especially thank the staff of the Paranal Observatory for their competent and un-tiring support. This work was supported in part by NASA Grant NAG5-7937.

References

1. G.S. Bisnovatyi-Kogan: Sov. Astron. **14**, 652 (1971)
2. R.L. Bowers R.L., J.R. Wilson: J.R. Astrophys. J. Suppl. **50**, 115 (1982)
3. P. Colella, P.R. Woodward: J. Comput. Phys. **54**, 174 (1984)
4. M. Cropper et al. : Mon. Not. R. Astron. Soc. **231**, 685 (1988)
5. R.A. Fesen, K.S. Gunderson: Astrophys. J. **470**, 967 (1996)
6. A. Gal-Yam, O. Shemmer, J. Dann: IAUC 7811 (2002)
7. P. Höflich: Pub. Astron. Soc. Pacific **7**, 434 (1988)
8. P. Höflich: Astron. Astrophys. **246**, 481 (1991)

9. P. Höflich: Astrophys. J. **443**, 89 (1995)
10. P. Höflich, J.C. Wheeler, D. Hines, S. Trammell: Astrophys. J. **459**, 307 (1995)
11. P. Höflich, A. Khokhlov, L. Wang: In: 20^{th} *Texas Conf. on Rel. Astro.* (AIP Conf. Proc. **586**, 2001), p. 459
12. P. Höflich: astro-ph 0207103 (2002)
13. J.P. Hughes, C.E. Rakowski, D.N. Burrows, P.O. Slane: Astrophys. J. Lett. **528**, L109 (2000)
14. D.J. Jeffrey: Astrophys. J. **375**, 264 (1991)
15. K. Kinugasa et al. : IAUC 7811 (2002)
16. A.M. Khokhlov: J. Comput. Phys. **143**, 519 (1998)
17. A. Khokhlov, P. Höflich, E. Oran, C. Wheeler, L. Wang: Astrophys. J. Lett. **524**, L107 (1999)
18. J.M. LeBlanc, J.R. Wilson: Astrophys. J. **161**, 541 (1970)
19. D.C. Leonard, A.V. Filippenko, A.J. Barth, T. Matheson: Astrophys. J. **536**, 239 (2000)
20. L.B. Lucy: In: 4^{th} *Mason Conference,* ed. M. Kafatos (Cambridge Univ. Press: Cambridge 1998) p. 323
21. P. Meikle et al. : IAUC 7811 (2002)
22. R.H. Mendez et al. : Astrophys. J. **334**, 295 (1998)
23. R. Mönchmeyer, G. Schäfer, E. Müller, R.E. Kates: Astron. Astrophys. **246**, 417 (1991)
24. B.E. Schaefer et al. : Astrophys. J. **588**, 387 (2003)
25. K.Z. Stanek et al. : Astrophys. J. Lett. **591**, L17 (2003)
26. O. Straniero, A. Chieffi, M. Limongi: Astrophys. J. **490**, 425 (1997)
27. R. Strom, H.M. Johnston, F. Verbunt, B. Aschenbach: Nature **373**, 587 (1995)
28. E.M.D. Symbalisty: Astrophys. J. **285**, 729 (1984)
29. S. Trammell, D. Hines, J.C. Wheeler: Astrophys. J. **414**, 21 (1993)
30. L. Wang, J.C. Wheeler, Z. Li, A. Clocchiatti: Astrophys. J. **467**, 435 (1996)
31. L. Wang, A. Howell, P. Höflich, J.C. Wheeler: Astrophys. J. **550**, 1030 (2001)
32. L. Wang, D. Baade, P. Höflich, J.C. Wheeler: Astrophys. J. **592**, 457 (2003)
33. L. Wang et al. : Astrophys. J. **591**, 1100 (2003)
34. S.E. Woosley, A.I. MacFadyen: Astron. Astrophys. Suppl. **138**, 499 (1999)

Optical Bumps in Cosmological GRBs as Supernovae

J.S. Bloom[1,2]

[1] Harvard-Smithsonian Center for Astrophysics, MC 20, 60 Garden Street, Cambridge, MA 02138, USA;
jbloom@cfa.harvard.edu
[2] Harvard Society of Fellows, 78 Mount Auburn Street, Cambridge, MA 02138, USA

Summary. From both photometric and broadband spectral monitoring of γ-ray burst (GRB) lightcurve "bumps," particularly in GRB 011121, a strong case grew for a supernova (SN) origin. The GRB-SN connection was finally solidified beyond a reasonable doubt with the discovery that the bump in GRB 030329 was spectroscopically similar to a bright Type Ic SN. In light of this result, I re-assess the previous SN bump claims and conclude that: 1) the distribution of GRB-SN bump peak magnitudes is consistent with the local Type Ib/c SNe peak distribution and 2) the late-time bumps in all long-duration GRBs are likely supernovae.

1 Introduction

The connection of GRBs to supernovae (SNe) – and hence the death of massive stars – was explored theoretically [7] even before the discovery of GRBs. In the subsequent discovery paper, Klebesadel, Strong, & Olson [15] reported on a catalog search for SNe coincident in time and position with the first 13 GRBs known. In retrospect, the lack of a clear association is easy to explain: not only were SNe sparsely discovered, but the highest redshift SN discovered by 1973 (SN 1968P; $z = 0.11$) was less than the redshift of all $\sim$35 classic GRBs redshifts known today. With the development of a model for the production of a GRB from a collapsing massive star [23], came renewed interest in the possibility of a GRB–supernova connection. The modern form of, and new spins on, Woosley's collapsar was presented in great detail by Andrew MacFadyen (this meeting).

The discovery of the low redshift SN 1988bw, a bright type Ic associated with GRB 980425 [9] implied that massive stars were capable of producing at least some incarnation of a GRB; the low energy release of GRB 980425 compared with all other known cosmological GRB energies suggests it may be only a sub-class of GRBs [1]. Attempts to theoretically unify GRB 980425 with the majority of the long-duration cosmological ($z > 0.1$) bursts fall short of explaining all the observational differences (see papers by Iwamoto and by Patat at this meeting).

Our discovery of a faint red light curve "bump" superimposed on the afterglow of GRB 980326 [2] was the first suggestion of a SN associated with

a cosmological GRB. Supernovae-like features were later found photometrically in a number of bursts, some more plausible than others; the principal difficulty is that SNe peak at a brightnesses comparable to their respective host galaxies (see Fig. 1; [4, 5]). Our multicycle effort on HST was designed to search for late-time afterglow features and discriminate between other physical models for such emission. While a few bursts showed no evidence for a SN (e.g., [20]), the late-time multicolor HST light curve and broadband spectra of GRB 011121 was reliably modeled by a bright Type Ic supernova that occurred nearly contemporaneously with the GRB [3]. Moreover, this was the first burst for which the data were of high enough quality to statistically demonstrate that the afterglow propagated in a wind-stratified medium rather than a constant-density ISM [19]. I recently reviewed the pre-2003 evidence for the GRB-SN connection in [5].

2 GRB 030329 and Beyond

While the case was rather strong for late-time emission bumps as being due to underlying supernovae [5], the definitive direct spectroscopic evidence was found only recently with the low-redshift ($z = 0.17$; [11]) GRB 030329. For this burst, a number of groups [8, 12, 14, 22] found a bump with supernova absorption features indicative of very high velocity ejecta. The close evolutionary track of this apparent supernova (2003dh; [10]) with SN 1998bw should quell any remaining doubt that long-duration GRBs are produced in the death of massive stars.

The rare proximity of this event allowed for high-precision coverage from the ground around the SN peak (e.g., [16, 17]). Using optical/IR imaging at the CTIO 1.3m to infer the line–of–sight dust extinction, we inferred that the SN was roughly 0.3 mag brighter at peak than the bright Type Ic 1998bw [6]. Since the precise peak SN magnitude depends on the line–of–sight extinction toward the GRB, it is imperative to infer extinction from the early afterglow in future events. With new dedicated robotic IR systems and space-based UV imaging, the broadband spectral coverage (from 0.1 to 2 μm) of *Swift* afterglows should routinely be used to infer line-of-sight extinction.

The peak brightness and early evolution of SN 2003dh, when compared to 1998bw, enabled estimates of the total mass of the ejecta (8 $M_\odot$), synthesized ^{56}Ni mass (0.35 $M_\odot$), and mass of the progenitor ($\sim$35 $M_\odot$) [18]. At this meeting, I suggested that a great deal more could be learned with a concerted long-term effort on HST to resolve and follow the evolution of the SN as it faded below the integrated brightness of the host galaxy. A measurement of the polarization of the light curve during the decay phase would constrain the asphericity of the emission region [13, 24]. If the late-time evolution of SN 2003dh was indeed powered by radioactive decay of ^{56}Co to ^{56}Fe, then the time history of the integrated luminosity would also determine the amount of synthesized ^{56}Ni (now only inferred by scaling 1998bw). To be sure, leakage

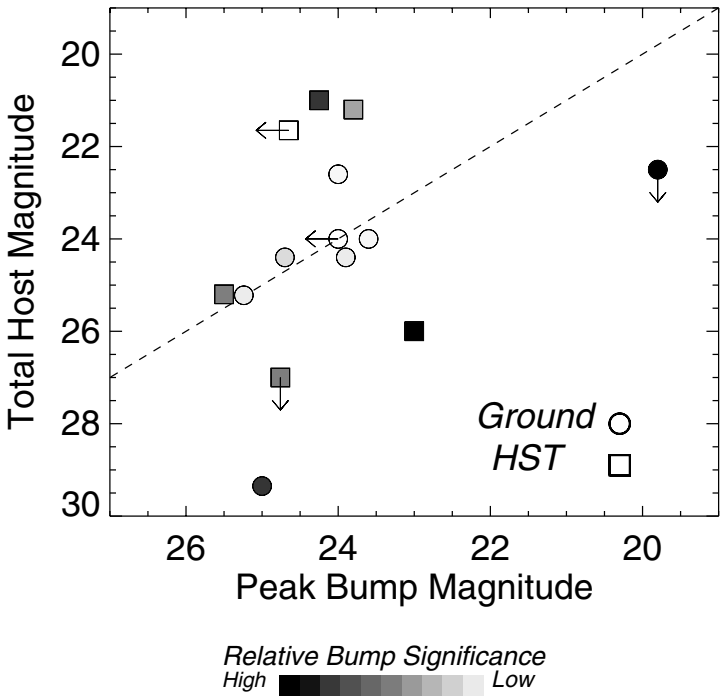

Fig. 1. The difficulty of detecting supernovae associated with GRBs: the magnitude of the host galaxy versus the peak magnitude of the putative bump (in whichever optical filter the peak bump magnitude was reported). Above the dashed line, bump magnitudes are fainter than the integrated light of the host galaxy. The circles are measurements where only ground-based imaging was used and squares are measurements derived also using *Hubble Space Telescope* (HST) imaging. Relative significances of the reliability of the bump detection were assigned by the author based roughly on the number of detections of the bump above the host light and the photometric error reported on the bump peak. Updated (from [5]) with new bumps in GRB 030329 and GRB 021211, reported at this meeting.

of γ-rays produced by radioactivity from the expanding nebula would make the late-time decay steeper than a pure ^{56}Co exponential.

Though some of the details of SN 2003dh have not been flushed out observationally, it seems clear that a bright core-collapse supernova and GRB 030329 occurred nearly simultaneously (to less than 1 week) [16, 17]. A pressing question is now whether a supernova accompanies all long-duration GRBs. On this point, a brief caution: while bumps have been claimed in more than 10 events, a number of these may be spurious due to improper subtraction of the host light. Fig. 1 shows a compilation of the peak brightnesses of all late-time bumps reported to-date in comparison with the total magnitude of the respective host galaxy. Five bumps have been found to peak within

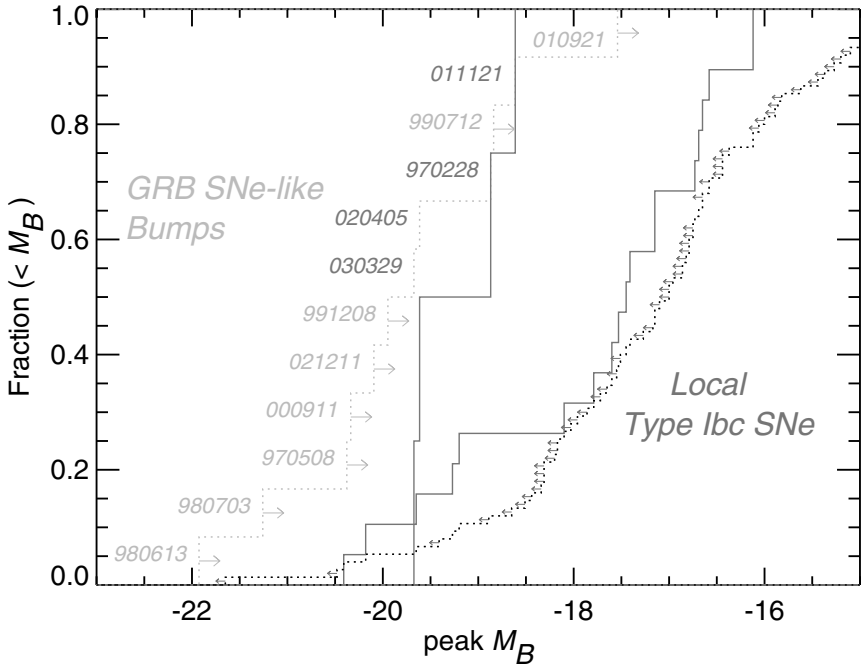

Fig. 2. Comparison of the peak magnitudes of GRB-SNe with those of local Type Ib/Ic SNe. The solid cumulative histogram to the left is for those GRBs with a believable detection of a SN bump; the brightnesses of all other claimed GRB-SN peaks or reported upper-limits are shown as a dotted histogram. The solid histogram to the right is for those local Ib/c SNe for which the SN was observed before peak; all others were discovered after peak. The faintest GRB-SN non-detection (GRB 010921) only probes the top ∼40th-percentile of local Type Ib/Ic SNe. It is clear that current GRB-SNe population may have only revealed the tip of the iceberg; plausibly, then, SNe could accompany all long-duration GRBs. Compilation of local Ib/c SNe from [21].

0.3 magnitudes of hosts at ∼24–26 mag, uncomfortably close for photometric differencing at such faint levels.

Of the bursts with redshift, I believe that only GRBs 030329, 020405, 970228, and 011121 can be legitimately claimed as true detections of SN-like bumps related to a GRB. This statement is not intended to imply that SNe do not accompany long-duration GRBs. Instead, the SN peaks may simply have fallen below the detection threshold of the instrument and/or the brightness of the host galaxy. How do these non-detections compare with the expected brightnesses of GRB-SNe? Even if all GRB-SNe are of type Ib/c, it is important to note that there is no *a priori* theoretical reason to require that all GRB-SNe should be identical: observed local Type Ib/c SNe show rather diverse light curves, peak brightnesses and spectral evolution.

Thus, the simplest assumption is that the peak magnitude distribution of GRB-SNe should follow the distribution of local Type Ib/c SNe.

Figure 2 shows a comparison of the distribution of absolute B-band peak magnitudes GRB-SNe (with known redshift) and local Ib/c SNe. After correcting for the extinction due to dust in our Galaxy, I have (simplistically) k-corrected the observed (or lower-limit) peak magnitude to the rest frame B-band using the observed redshift and assuming a blackbody spectrum peaked in the rest frame V-band. The uncertainty introduced by this approximation on an individual M_B is likely less than 0.5 mag. From the figure, it is clear that most GRB-SNe detections (or limits) only probe the bright end of the local Ib/c population. In fact, the deepest non-detection of a GRB-SN (GRB 010921) only probes the brightest 40th percentile of local Ib/c SNe. From Fig. 2, it is reasonable to conclude that the observed supernovae related to GRBs have only probed the tip of the iceberg of a plausible brightness distribution. A systematic survey of late-time bumps from nearby ($z \lesssim 0.5$) *Swift* bursts will test this hypothesis.

References

1. J.S. Bloom et al. : Astrophys. J. Lett. **506**, L105 (1998)
2. J.S. Bloom et al. : Nature **401**, 453 (1999)
3. J.S. Bloom et al. : Astrophys. J. Lett. **572**, L45 (2002)
4. J.S. Bloom: astro-ph 0301028
5. J.S. Bloom: astro-ph 0303478
6. J.S. Bloom et al. : Astron. J. **127**, 252 (2004)
7. S.A. Colgate: Canadian J. Phys. **46**, 476 (1968)
8. R. Chornock et al. : IAUC 8114 (2003)
9. T.J. Galama et al. : Nature **395**, 670 (1998)
10. P. Garnavich, T. Matheson, E.W. Olszewski, P. Harding, K.Z. Stanek: IAUC 8114 (2003)
11. J. Greiner et al. : GCN 2020
12. J. Hjorth et al. : Nature **423**, 847 (2003)
13. K. Iwamoto et al. : Nature **395**, 672 (1998)
14. K.S. Kawabata et al. : Astrophys. J. Lett. **593**, L19 (2003)
15. R.W. Klebesadel, I.B. Strong, R.A. Olson: Astrophys. J. Lett. **182**, L85 (1973)
16. Y.M. Lipkin et al. : in preparation
17. T. Matheson et al. : in press
18. P.A. Mazzali et al. : astro-ph 0309555
19. P.A. Price et al. : Astrophys. J. Lett. **572**, L51 (2002)
20. P.A. Price et al. : Astrophys. J. **584**, 931 (2003)
21. D. Richardson et al. : Astron. J. **123**, 745 (2002)
22. K.Z. Stanek et al. : Astrophys. J. Lett. **591**, L17 (2003)
23. S.E. Woosley: Astrophys. J. **405**, 273 (1993)
24. S.E. Woosley, R.G. Eastman, B.P. Schmidt: Astrophys. J. **516**, 788 (1999)

Long GRBs and Supernovae from Collapsars

A.I. MacFadyen

Theoretical Astrophysics, California Institute of Technology, MC 130-33,
Pasadena, CA 91125, USA;
andrew@tapir.caltech.edu

Summary. Long duration gamma-ray bursts are associated with the death of massive stars as earlier observations and theoretical arguments had suggested. Supernova 2003dh observed with GRB030329 confirms this picture. Current progress in developing numerical special relativistic hydrodynamics codes with adaptive mesh refinement is allowing for high-resolution simulations of relativistic flow relevant for simulations of GRBs.

Long Gamma-Ray Bursts

Gamma ray bursts (GRBs) are the most luminous explosions in the universe, briefly out shining all other sources in the sky. As is well known, GRBs were discovered by military satellites in the late 1960s and have fascinated scientists ever since. We now believe that the common long variety of these bursts mark the death of stars many times more massive than our Sun (M $\gtrsim$20 $M_\odot$) and are the birth cries of rotating stellar mass black holes (or highly magnetized rapidly rotating neutron stars). The energetic supernova 2003dh, discovered on March 29, 2003 underneath the fading glare of a long GRB and widely discussed at this meeting, confirms this picture.

GRBs are defined as short ($\tau \sim 10$s) non-thermal bursts of $\gtrsim$100 keV gamma rays. They exhibit diverse light curves but fall into two general classes defined by total durations above and below ~ 2 s. Long GRBs have mean detected durations of 35 seconds, comprise roughly 2/3 of all the total GRB population and have softer spectra than their shorter duration cousins. Some vary on millisecond timescales, others shut off completely for a few seconds and then turn back on, some last over 2000 seconds. The rapid detected variability ($< 1\ \mu s$) and the large energy ($\approx 10^{52}$ erg) point to a stellar mass compact object as the "central engine" powering the GRB explosion. However, the duration of long GRBs is millions of dynamical times for such a dense object. Theoretical models must explain the discrepant timescales.

Among the many early theories attempting to explain GRBs was the emergence of a shockwave from a star during a supernova explosion. According to the collapsar model [4] some stars manage to produce asymmetric outflows traveling at 99.999% the speed of light. Such ultra-relativistic outflows are required to produce the non-thermal spectrum and rapid variability.

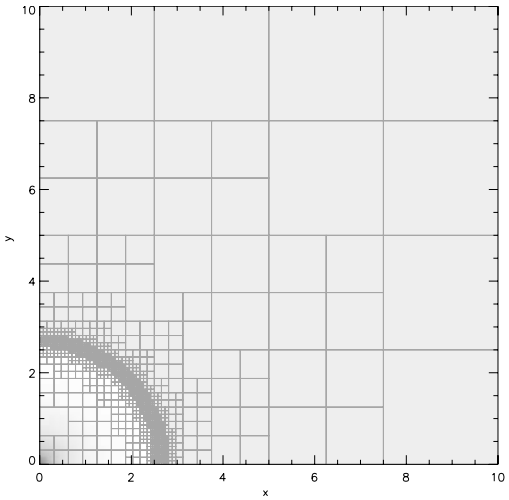

Fig. 1. Relativistic Blast Wave: Planar slice through a three-dimensional simulation of a spherical relativistic blast wave. Nine levels of adaptive mesh refinement were used to resolve the thin relativistically expanding spherical shell at radius 2.75. Each box is a block of $8 \times 8 \times 8$ zones. The Lorentz factor of the shell at this time is 120. The effective resolution of the simulation is 4096^3. It was run on 256 processors of the IBM SP Seaborg supercomputer at NERSC for twelve hours.

GRBs are now thought to be roughly ten times as energetic as supernovae in terms of the kinetic energy of the explosive outflow. A key question is why the explosion energy is concentrated in so little mass (10^{-5} solar masses) in a GRB instead of several solar masses in an "ordinary" supernova. In both cases much more energy (10^{53} ergs) may be released as neutrinos and yet more in gravitational waves. Understanding the total energetics of GRB explosions and the partitioning between the various channels (photon energies from gamma-rays to radio, neutrinos, gravitational waves) is critical to fully understanding GRBs.

Observable GRBs occur roughly once every 10 million years per galaxy. X-ray observations indicate that GRBs are beamed to about 1% of the sky so the true rate is higher: one per 100,000 years per galaxy. Since the supernova rate is about one per 100 years per galaxy, roughly 1/1000 supernova make a GRB. A key question is what special circumstances cause the star to make a GRB. It may be the formation of a black hole, a highly magnetized neutron star (magnetar) or a supermassive spinning neutron star.

Collapsars

The collapsar model proposes [4] that some rotating massive stars, more than about 25 times the mass of the Sun, fail to explode in the ordinary

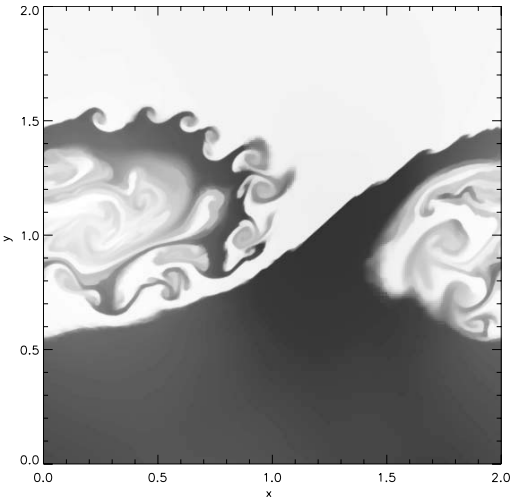

Fig. 2. Relativistic Kelvin–Helmholtz Instability: A mildly relativistic shearing layer with velocity 0.25 c and density 1 above and velocity -0.25 c and density of 5 below and a sinusoidal vertical velocity perturbation.

way thought to produce normal neutron stars. Instead the core of the star collapses to form a black hole. If the star is spinning sufficiently rapidly when it collapses, the gas in the star swirls into the new black hole by forming an accretion disk. The release of gravitational energy is thought to power a jet-like outflow along the rotational axis of the star. In addition the disk may sustain magnetic fields capable of extracting rotational energy directly from the black hole. Since gas falls immediately along the rotation axis where there is no centrifugal barrier, the polar regions of the star drain quickly into the black hole. As accretion disk energy is deposited in this low density channel by magnetic processes, perhaps aided by neutrino annihilation, a fast beamed outflow forms. The stellar gas remaining along the poles is shock heated and much of it is pushed sideways. Eventually the jet breaks out of the star and accelerates to ultra-relativistic speeds (See Fig. 1). Much of the gas attempting to accrete is expelled from the accretion disk since it can not cool. This outflowing gas and shockwaves from the jet explode the star. The collapsar model predicts an exploding star with every long GRB. Since hot gas flowing out in the star can form ^{56}Ni, some of these stellar explosion should be observable as supernovae beneath the glare of the fading optical counterpart of the GRB. Furthermore the star must have been small in radius when it died so that the relativistic jet can escape the star while it is still being powered by the accretion disk. Such a star should appear as a Type Ib/c supernova. SN2003dh was indeed of this type.

It is also possible that an highly magnetized rapidly spinning neutron is formed. This magnetar may act like a supercharged pulsar that accelerates a

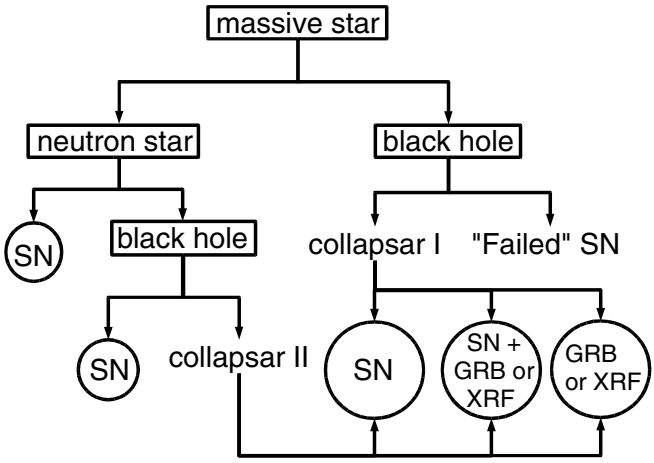

Fig. 3. Flowchart: Evolutionary paths leading to stellar explosions. SN = supernova explosion. GRB = Gamma-ray burst and XRF = X-ray flash.

magnetically dominated flow. In both scenarios, the jet may be composed of extremely relativistic particles which manage to escape the star and travel far away before internal collisions dissipate energy and emit the gamma-rays we observe. Alternatively, the outflow may be magnetically dominated plasma with few particles that dissipates energy through plasma instabilities. A combinations of particles and magnetic fields is also possible. A key question is the degree to which instabilities can mix material into the jet.

Ni Production

It is important to note that models for long GRBs must explain the large amount of ^{56}Ni observed in the explosion. The Type Ibc supernovae observed so far shine principally because of radioactive decay of the Ni. In the collapsar models this Ni is though to be produced from gas that is ejected from an accretion disk [4]. The jet itself is not hot enough to synthesize the Ni and does not contain very much mass.

Relativistic Blastwaves

Recent fundamental progress in understanding the physics of GRBs and their environment has resulted from detailed comparison between observed light curves and theoretical models for relativistic blast waves e.g., [3]. The data to be obtained by the SWIFT satellite requires accurate theoretical models of GRB jet dynamics to address fundamental questions:

How do relativistic jets spread as they decelerate? What is the lateral dynamics of the post shock material? How do multi-dimensional dynamical effects alter a structured jet? How do multi-dimensional jets interact with various external mass distributions: stellar wind, constant density, clumpy medium? How does late-time or slower ejecta interact with the decelerated blast wave when it catches up? What is the structure of refreshed shocks when they occur? Are relativistic blast waves stable to small perturbations? Can they disrupt on an outflow timescale?

All of these questions are critical for accurate modeling of SWIFT GRB data.

Code Development

Recent progress has been made developing high-order special relativistic hydrodynamics code using adaptive mesh refinement (AMR) to allow high resolution simulation of GRB jets in two and three dimensions [1, 7]. With sufficient development we will be capable of fully resolving relativistic blast waves relevant for GRBs in multi-dimensional computer simulations. With the code, we perform fully resolved multi-dimensional simulations of a jetted relativistic blast wave from the ultra-relativistic phase, described by the Blandford-McKee solution [2], to the trans-relativistic spreading phase as swept up ambient medium decelerates the flow (Figure 1). Comparison of synchrotron emission to be calculated from our simulations with afterglow light curves from SWIFT GRBs will constrain jet structures and test analytic treatments of relativistic fluid dynamics.

Preliminary tests have shown that we have sufficient resolution (effective resolution of 4096^3 and higher) in three dimensions using Cartesian coordinates (avoiding coordinate singularities). AMR is ideally suited to this problem because relativistic blast waves form extremely thin structures requiring resolution of $\delta r/r \lesssim 1/4\Gamma^2$ but are not volume filling. We fully resolve the thin shells (sometimes referred to as pancakes in the GRB community) as they propagate, but use coarser resolution in the smooth regions in front of and behind the blast wave.

Previous studies have treated the jet evolution with various one-dimensional simplifications to the dynamics. There has been some work done in 3D but it is with diffusive hydro schemes and were very far from the resolution required to resolve the jet structure. This problem requires the resolution achievable with high order algorithms with adaptive mesh refinement on massively parallel super-computers.

The code already runs in three-dimensions and runs on massively parallel computers at NERSC. Our project is at a critical juncture because so much has been accomplished in a short time of collaborative work. Our project will benefit enormously from several sustained visits where the team can work collaboratively.

Relativistic blast waves are ideally suited for AMR because they form extremely thin structures which do not necessarily fill the computational volume. To correctly solve for the dynamics of a relativistic blast waves it is necessary to resolve characteristic scales of $\frac{\delta r}{r} \lesssim \frac{1}{16\Gamma^2}$. For $\Gamma \sim 100$ this requires that zones of width $\delta r \lesssim 6.25^{-6} r$. To grid the entire volume with sufficient resolution would require $(1.6 \times 10^5)^n$ zones where n is the number of spatial dimensions.

Fig. 1 shows a thin spherical shell formed as a fireball deposited at the center expands. Most of the volume is smooth and well resolved with low refinement (large blocks).

Our simulations will be of sufficient quality that comparison with SWIFT light curves may allow for confirmation of the dynamics of relativistic shock waves. Preliminary tests on 512 processors of a parallel supercomputer (Seaborg at NERSC) confirm that we have more than sufficient resolution to resolve 3D.

Mixing

Compactness arguments require that GRB jets be ultra-relativistic during the gamma-ray emitting phase. This requires that they maintain an extremely large energy to mass ratio ($\eta \equiv \frac{E}{m} \gtrsim 100$) as they are born and propagate. A key unanswered question is whether or not GRB outflows can remain sufficiently clean or whether baryons will be mixed in to the flow lowering the maximum asymptotic Lorentz factor below the values required by observations. This problem is especially relevant for collapsars in which the jet must propagate through a star. Do shear instabilities and microscopic mixing processes load unacceptably large numbers of baryons into the jet? What is he the timescale for the mixing? Can pressure gradients and centrifugal barriers repel material from the jet core along the rotation axis? Some aspects of these questions are addressable with numerical simulation. AMR can be helpful for initial phases of evolution before inhomogeneities fill the simulation volume. Even then, our code is capable of simulating high resolution throughout the volume when run on massively parallel machines. Fig 2, shows a calculation of the relativistic Kelvin-Helmholtz instability. Such shear instabilities can be suppressed for ultra-relativistic flows. We can track mixing in these flows by adding multiple fluids to our calculations.

An important advance in the study of GRB physics is the development of new high resolution special relativistic hydrodynamics code using adaptive mesh refinement (AMR) [7]. These are the first codes capable of fully resolving relativistic blast waves relevant for ultra-relativistic GRB blastwaves in multidimensional computer simulations. It is now possible to perform the first fully resolved multidimensional simulations of a jetted relativistic blast wave from the ultra-relativistic phase, described by the Blandford-McKee solution, to the trans-relativistic spreading phase as swept up ambient medium

decelerates the flow. Comparison of synchrotron emission to be calculated from these simulations with afterglow light curves from SWIFT GRBs will constrain jet structures and test analytic treatments of relativistic fluid dynamics.

Future simulations will be of sufficient quality that comparison with SWIFT lightcurves may allow for confirmation of the dynamics of relativistic shockwaves. Preliminary tests on 512 processors of a parallel supercomputer (Seaborg at NERSC) confirm that we have more than sufficient resolution to resolve 3D. Such calculations are critical for interpreting the detailed lightcurves of GRBs to be discovered by SWIFT.

Future Prospects

The present and future is bright for GRB research. The HETE-II satellite is currently in orbit contributing valuable localizations of GRBs including GRB030329. The SWIFT satellite is scheduled for launch this Spring (2004). The principle problem for observing GRBs has been the very fact that they release energy on rapid timescales. In order to the take full measure of the photon output of GRBs integrated over all wavelengths, it is necessary to observe the GRB rapidly with instruments tuned to a wide range of wavelengths. In addition to their gamma-ray emission much energy is released in the X-ray through radio bands. We need to detect GRBs from space (gamma-rays are absorbed by the atmosphere and don't reach Earth) and quickly determine accurate positions on the sky so that other satellites (HST Chandra) and Earth-based telescopes (Keck, VLT) can search for their emission. HETE is doing this now and SWIFT will soon. We can look forward to exciting new discoveries.

References

1. M.A. Aloy, J.M. Ibáñez, J.M. Martí, E. Müller: Astrophys. J. Suppl. **122**, 151 (1999)
2. R.D. Blandford, C.F. McKee: Phys. Fluids **19**, 1130 (1976)
3. P. Kumar, J. Granot: Astrophys. J. **591**, 1075 (2003)
4. A.I. MacFadyen, S.E. Woosley: Astrophys. J. **524**, 262 (1999)
5. A.I. MacFadyen, S.E. Woosley, A. Heger: Astrophys. J. **550**, 410 (2001)
6. W. Zhang, S.E. Woosley, A.I. MacFadyen: Astrophys. J. **586**, 356 (2003)
7. W. Zhang, A.I. MacFadyen: In preparation

How Common are Engines in Ib/c Supernovae?

Edo Berger

Division of Physics, Mathematics and Astronomy, 105-24, California Institute of Technology, Pasadena, CA 91125
ejb@astro.caltech.edu

Summary. The association of γ-ray bursts (GRBs) and core-collapse supernovae (SNe) of Type Ib and Ic was motivated by the detection of SN 1998bw in the error box of GRB 980425 and the now-secure identification of a SN 1998bw-like event in the cosmological GRB 030329. The bright radio emission from SN 1998bw indicated that it possessed some of the unique attributes expected of GRBs, namely a large reservoir of energy in (mildly) relativistic ejecta and variable energy input. Here we discuss the results of a systematic program of radio observations of most reported Type Ib/c SNe accessible to the Very Large Array, designed to determine the fraction of Type Ib/c SNe driven by an engine. We conclude that: (i) the incidence of such events is low, $< 3\%$, and (ii) there appears to be a clear dichotomy between the majority of hydrodynamic explosions (SNe) and engine-driven explosions (GRBs).

1 Hydrodynamic vs. Engine Driven Explosions

Stellar explosions can be characterized by their kinetic energy, E_K, and the mass of the ejecta, $M_{\rm ej}$. Equivalently one may consider E_K and the mean initial speed of ejecta, v_0, or the Lorentz factor, $\Gamma_0 = [1 - \beta_0^2]^{-1/2}$, where $\beta_0 = v_0/c$. In this context, supernovae (SNe) and γ-ray bursts (GRBs), are distinguished by their ejecta velocities: $v_0 \sim 10^4$ km s^{-1} as inferred from optical absorption features (e.g. [9]), and $\Gamma_0 > 100$, inferred from the non-thermal prompt emission [14, 20], respectively.

In the conventional interpretation, $M_{\rm ej}$ for SNe is large because E_K is derived from the (essentially) symmetrical collapse of the core and the energy thus couples to all the mass left after the formation of the compact object.

GRB models, on the other hand, appeal to an engine — a stellar mass black hole, which accretes matter on many dynamical timescales and powers relativistic jets (the so-called collapsar model; [24]). Observationally, this model is supported by the complex temporal profiles and long duration of GRBs, their high Lorentz factors, a high degree of asymmetry [12], and episodes of energy injection.

2 SN 1998bw: An Engine Driven Supernova

The unusual SN 1998bw shares some of the unique attributes expected of GRBs. This Type Ic SN coincided in time and position with GRB 980425 [13], for which the inferred isotropic energy in γ-rays was only 8×10^{47} erg [22], three to six orders of magnitude fainter than typical GRBs. More importantly, SN 1998bw exhibited unusually bright radio emission indicating about 10^{50} erg of mildly relativistic ejecta as well as variable energy input [16]. To date these features have not been seen in any other nearby SN. Thus, the empirical data strongly favor an engine in SN 1998bw.

Two scenarios for the origin of SN 1998bw and its relation to GRBs have been proposed: (i) GRB 980425 may have been a typical burst but viewed well away from the jet axis (hereafter, the off-axis model), and (ii) SN 1998bw represents a different class of SNe.

A powerful discriminant between these two scenarios is the expected rate of SN 1998bw-like events. In the off-axis model, the fraction of Type Ib/c SNe that are powered by a central engine is linked to the mean beaming factor of GRBs, f_b (e.g. [12]); a recent estimate is $\langle f_b^{-1} \rangle \sim 500$ [12]. Coupled with an estimated local GRB rate of ~ 0.5 Gpc^{-3} yr^{-1} [23] compared to a Type Ib/c SN rate of $\sim 4.8 \times 10^4$ Gpc^{-3} yr^{-1} [6, 10, 17], we expect that $\sim 0.5\%$ of Type Ib/c SNe will be similar to SN 1998bw.

On the other hand, if SN 1998bw is not an off-axis burst, then the rate of similar events has to be assessed independent of the GRB rate. In this context, Norris (2002) [19] has argued that of the 1429 long-duration BATSE bursts, about 90 events possess similar high-energy attributes as that of GRB 980425. This number corresponds to about 25% of Type Ib/c SNe within 100 Mpc.

3 A VLA Survey of Type Ib/c Supernovae

Our basic hypothesis is that (mildly) relativistic ejecta are best probed by radio observations, as was demonstrated in the case of SN 1998bw. To this end we began a program of observing most reported Type Ib/c SNe with the Very Large Array in late 1999 [3].

Figure 1 provides a succinct summary of the radio lightcurves and upper limits. Three strong conclusions can be drawn from this Figure. First, SNe as bright as SN 1998bw are rare; we find a limit of $< 3\%$ from our survey. Second, there is significant dispersion in the luminosities of Type Ib/c SNe. Finally, the radio emission from SNe (including SN 1998bw) is orders of magnitude dimmer than that of GRB afterglows.

3.1 Expansion Velocities and Energetics

In the framework of synchrotron self-absorption, the peak time and peak luminosity directly measure the mean expansion speed of the fastest ejecta

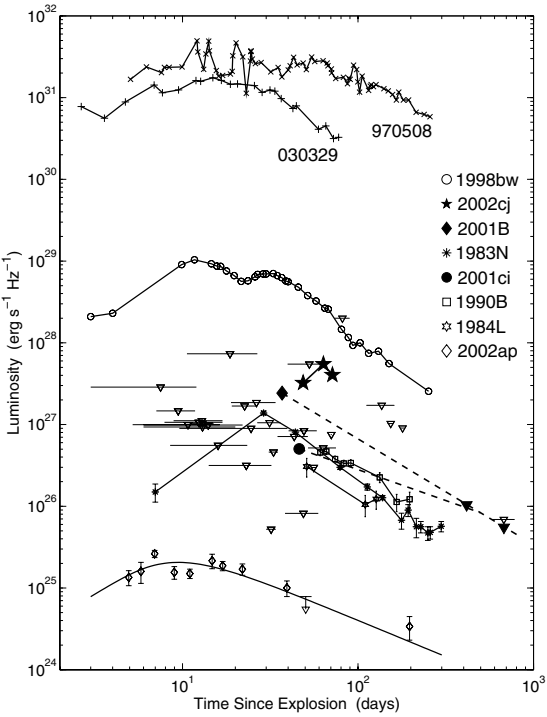

Fig. 1. Radio lightcurves of Type Ib/c SNe detected in this survey and from the literature, as well as upper limits for the non-detections (Ref. [3] and references therein). We also include the radio lightcurves of GRB 970508 [11] and GRB 030329 [4]. The uncertainty in time for the non-detections represents the uncertain time of explosion.

[8]. We infer velocities ranging from $v \sim 10^4$ to 10^5 km s^{-1} based on our detections and upper limits [3].

We also find that the ejecta giving rise to the radio emission from SNe for which detailed information is available (SN 1984L and SN 2002ap) can be produced by a hydrodynamic explosion [1, 3]. In fact, the estimated energies from the hydrodynamic models [7, 15, 18] exceed those inferred from the radio observations by up to two orders of magnitude. This may indicate that the total kinetic energies have been over-estimated, possibly as a result of neglecting a mild asymmetry.

We therefore conclude that none of the SNe observed in our survey and in the past clearly exhibits the unique characteristics of SN 1998bw: a significant excess of energy in mildly relativistic ejecta.

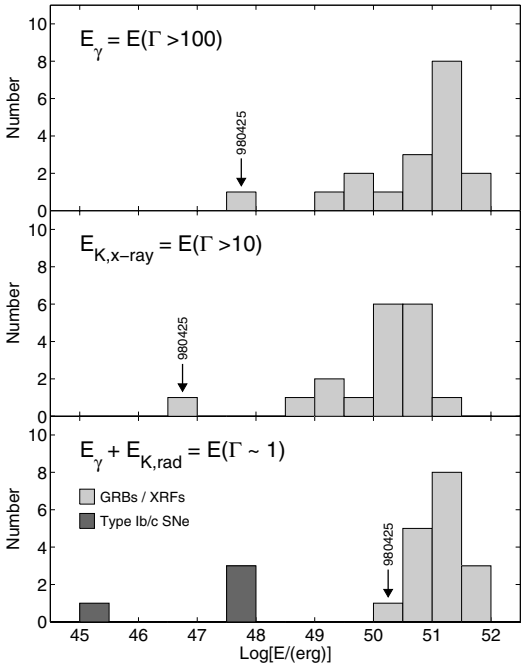

Fig. 2. Histograms of the beaming-corrected γ-ray energy [5], E_γ, the kinetic energy inferred from X-rays at $t = 10$ hr [2], $E_{K,X}$, and total relativistic energy, $E_\gamma + E_K$, where E_K is the beaming-corrected kinetic energy inferred from the broad-band afterglows of GRBs [16, 21] and radio observations of SNe. The wider dispersion in E_γ and $E_{K,X}$ compared to the total energy indicates that engines in cosmic explosions produce approximately the same quantity of energy, thus pointing to a common origin, but the ultra-relativistic output of these engines varies widely. In Type Ib/c SNe, on the other hand, the total explosive yield in fast ejecta (typically $\sim 0.3c$) is significantly lower.

4 A Comparison to γ-Ray Burst Afterglows

From Figs. 1 and 2 it is clear that the radio lightcurves of GRB afterglows and SNe are dramatically different. This has significant implications, namely *none* of the Type Ib/c SNe presented in Fig. 1 could have given rise to a typical γ-ray burst. However, SN 1998bw is unique in both samples: it is fainter than typical radio afterglows of GRBs but much brighter than Type Ib/c SNe (Fig. 2).

4.1 Hypernovae

The discovery of broad optical lines and large explosive energy release (greater than a few FOE) in SN 1998bw prompted some astronomers to use the

designation "hypernovae" for SN 1998bw-like SNe. Unfortunately, this designation is not well defined, and has been applied liberally in recent years.

In our framework the critical distinction between an ordinary supernova and a GRB explosion is relativistic ejecta carrying a considerable amount of energy. Such ejecta are simply not traced by optical spectroscopy. This reasoning is best supported by the fact that the energy carried by the fast ejecta in SN 1998bw and SN 2002ap [1] differ by four orders of magnitude even though both exhibit broad spectral features at early times and both have been called hypernovae.

5 Conclusions

First, radio observations provide a robust way of measuring the quantity of energy associated with high velocity ejecta. This allows us to clearly discriminate between engine-driven SNe such as SN 1998bw and ordinary SNe, powered by a hydrodynamic explosion, such as SN 2002ap [1]. Second, at least 97% of local Type Ib/c SNe are not powered by engines and furthermore have a total explosive yield of only 10^{48} erg in fast ejecta. As summarized in Fig. 2, this indicates that there is a clear dichotomy between Type Ib/c SNe and cosmic, engine-driven explosions.

References

1. E. Berger, S.R. Kulkarni, R.A. Chevalier: Astrophys. J. Lett. **577**, L5 (2002)
2. E. Berger, S.R. Kulkarni, D.A. Frail: Astrophys. J. **590**, 379 (2003)
3. E. Berger et al. : Astrophys. J. **599**, 408 (2003)
4. E. Berger et al. : Nature **426**, 154 (2003)
5. J.S. Bloom, D.A. Frail, S.R. Kulkarni: Astrophys. J. **594**, 674 (2003)
6. E. Cappellaro, R. Evans, M. Turatto: Astron. Astrophys. **351**, 459 (1999)
7. R.A. Chevalier: Astrophys. J. **258**, 790 (1982)
8. R.A. Chevalier: Astrophys. J. **499**, 810 (1998)
9. A.V. Filippenko: Ann. Rev. Astron. Astrophys. **35**, 309 (1997)
10. S. Folkes et al. : Mon. Not. R. Astron. Soc. **308**, 459 (1999)
11. D.A. Frail, E. Waxman, S.R. Kulkarni: Astrophys. J. **537**, 191 (2000)
12. D.A. Frail et al. : Astrophys. J. Lett. **562**, L55 (2001)
13. T.J.Galama et al. : Nature **395**, 670 (1998)
14. J. Goodman: Astrophys. J. Lett. **308**, L47 (1986)
15. K. Iwamoto et al. : Astrophys. J. **534**, 660 (2000)
16. Z. Li, R.A. Chevalier: Astrophys. J. **526**, 716 (1999)
17. R.O. Marzke et al. : Astrophys. J. **503**, 617 (1998)
18. C.D. Matzner, C.F. McKee: Astrophys. J. **510**, 379 (1999)
19. J.P. Norris: Astrophys. J. **579**, 386 (2002)
20. B. Paczynski: Astrophys. J. Lett. **308**, L43 (1986)
21. A. Panaitescu, P. Kumar: Astrophys. J. **571**, 779 (2002)
22. E. Pian et al. : Astrophys. J. **536**, 778 (2000)
23. M. Schmidt: Astrophys. J. **552**, 36 (2001)
24. S.E. Woosley: Astrophys. J. **405**, 273 (1993)

Part VII

Gamma-Ray Bursters

Cosmic Gamma-Ray Bursts: The Big Picture

Kevin Hurley

University of California Space Sciences Laboratory, Berkeley, CA, 94720-7450, USA;
khurley@sunspot.ssl.berkeley.edu

Summary. A "typical" GRB occurs in a star-forming region of a galaxy at a redshift z∼1. In currently popular models, it is caused by the collapse of a massive star which has exhausted its nuclear fuel supply. The star collapses to a black hole threaded by a strong magnetic field, and possibly fed by an accretion torus. Through a variety of processes, electrons are accelerated and gamma-rays, X-rays, optical light, and radio emission ensue, with durations from seconds to years. In this talk, I will review the general observational properties of bursts, their afterglows and host galaxies, and some of the open questions about them.

1 Introduction

Cosmic gamma-ray bursts are the brightest, if not the most energetic, explosions in the universe. They are observed at cosmological distances, out to redshifts of 4.5. This places them at somewhat smaller distances than those of the most distant quasars, but there is no reason why they could not be observed to much greater distances, if indeed they are generated there. Their practical uses are wide-ranging, including such diverse topics as tracing star formation rates in distant galaxies and probing the reionization epoch, as well as the study of quantum gravity and relativistic shocks, to name just a few. For the first 25 years after the announcement of their discovery [23] it was not at all obvious that gamma-ray bursts were anything but a relatively weak Galactic phenomenon, possibly involving single neutron stars. A paradigm shift came in 1997, with the discovery of the first X-ray [9], optical [31], and radio [12] counterparts to bursts. In the 6 years that have followed, gamma-ray bursts have evolved from a curiosity into a subject of mainstream astrophysical research. The story of how this happened has been told in two recent books [22, 28], so it will not be summarized here. This review will concentrate on the observational properties of bursts, and what appear today to be the most promising theoretical explanations of these properties.

2 Observational Properties of the Prompt Emission

A gamma-ray burst (GRB) may last between 10 ms and 1000 s or so, with a typical value being around 10 s (Fig. 1). During that time, it may be the

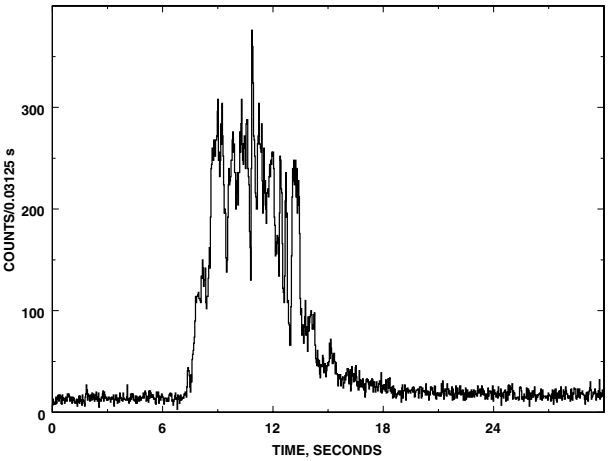

Fig. 1. The gamma-ray burst of December 6 2002. The data are from the Ulysses GRB experiment, in the 25 - 150 keV energy range.

brightest object in the gamma-ray sky. Most of its electromagnetic energy comes out in gamma-rays with energies greater than around 25 keV. A striking feature of the GRB duration distribution is that it is bimodal, with one group having durations of a few hundred milliseconds, and the other, about 20 seconds. Virtually everything that we know about bursts and their counterparts comes from observations of the "long" class. No counterpart to a short burst has yet been observed.

The spatial distribution of burst sources is completely isotropic, and the number-intensity distribution is consistent with a non-Euclidean population [26], as would be expected from cosmological sources. No convincing evidence has been found to date which would imply that a single source has ever emitted more than one burst [17].

GRB energy spectra are diverse, but at their hardest they are perhaps *the* hardest of all known astrophysical objects. They have been measured from $\sim$ 2 keV to 18 GeV. The latter is only an instrumental limit, and there is no indication that spectra are falling off at the highest energies. At the soft end of the GRB spectra, there are events which display almost no emission above several 10's of keV. These are referred to as "X-ray flashes" or "X-ray rich GRB's" [18]. They are identical to GRBs in all other properties. Fig. 2 compares the general shape of GRB energy spectra with those of other well-known astrophysical X- and gamma-ray emitters.

Very recently, polarization has been detected in the gamma-radiation from a burst [7]. The burst was GRB021206 (whose time history appears in Fig. 1), and the level of polarization was 80%, which suggests the presence of an ordered magnetic field.

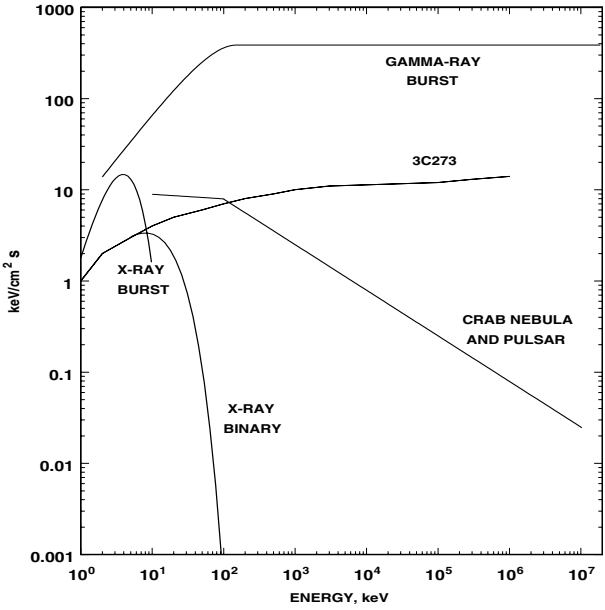

Fig. 2. GRB energy spectra compared to the spectra of X-ray burst sources (blackbody), X-ray binaries (optically thin thermal bremsstrahlung), 3C273 [30], and the Crab Nebula and pulsar (broken power law). Although the latter spectrum has been observed at energies well above those of GRBs, it tends to be softer. The GRB spectrum shown here uses the function of Band et al. [2]. Short GRBs tend to have harder spectra than long ones.

3 Gamma-ray Burst Afterglows and Host Galaxies

As the gamma-ray emission ends, afterglows begin at various times, depending on their wavelengths, and fade at different rates. In some very intense bursts, a gamma-ray afterglow is clearly observed, which remains detectable for ∼1000 s [6]. There is evidence that this is in fact a common feature of all bursts [8], although it is harder to detect in weak events. The emission fades as a power law with various indices, but a rough average might be ∼ -1. Soft X-ray (1-10 keV) afterglows commence as the gamma-ray burst progresses or ends [15], and fade as a power law with index ∼ -1.5. They remain detectable for several weeks with sensitive instruments such as *Chandra* and XMM-*Newton* . Optical afterglows are observed for roughly half of all the long duration bursts. In one case, intense (9th magnitude) optical emission has been observed which was simultaneous with the burst [1]. However, although many searches have been carried out, this remains the only example of simultaneous optical emission [32]. More commonly, weaker (∼ 17th magnitude) optical emission is discovered in the hours following the burst, and it fades as a power law (index ∼ -1.3), or a broken power law, with time, but

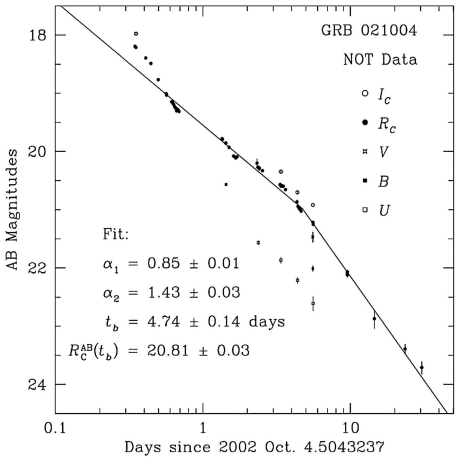

Fig. 3. The afterglow light curve of GRB021004, fit by a broken power law. Note the bump at the start of the curve. The data were taken at the Nordic Optical Telescope [19], and are reproduced by permission of the AAS.

often with significant fluctuations. An example is shown in Fig. 3. It is not unusual for the optical afterglow to initially outshine the host galaxy in which it originates. It is possible to track the afterglow for weeks or even months with the most sensitive telescopes. Finally, radio afterglows are similarly observed for about half of the long bursts, and they become detectable with telescopes such as the VLA several days after the burst, at levels of several tenths of a milliJansky. In some cases, they can be observed for a year or more [13].

In almost all cases where an optical or radio counterpart to a GRB is found, a host galaxy is identified, and in most of those cases, a redshift can be measured. A typical magnitude is m_R=25. The closest burst comes from a redshift of 0.1055 (with one possible exception, discussed below), and the farthest, 4.5. The distribution of GRB redshifts is shown in Fig. 4. The host galaxies are normal, which is to say that they are not active galaxies, and that it would be difficult, perhaps impossible, to identify them in a random sample of galaxies at similar redshifts. The gamma-ray burst sources are found within the host galaxies, sometimes within regions which can be identified as undergoing star formation. Reviews of host galaxy properties have appeared [5, 20].

4 The Short Explanation

The following picture is based on observations of the long GRB's, their afterglows, and their host galaxies. A GRB occurs in the star-forming region

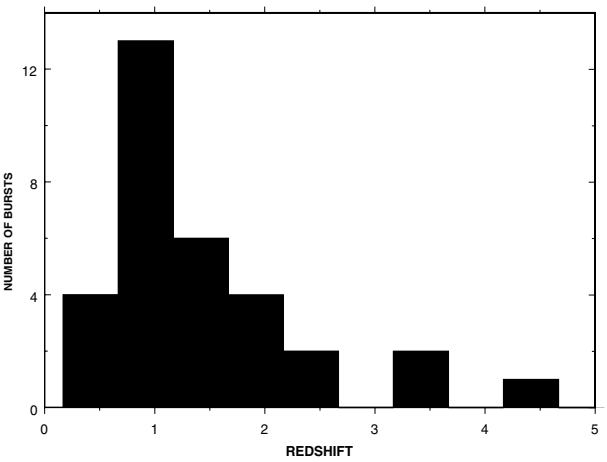

Fig. 4. The redshift distribution of gamma-ray burst sources.

of a galaxy at redshift around 1. In currently popular models, it is caused by the collapse of a massive star ($\approx$ 30 solar masses) to a black hole threaded by a strong magnetic field, and energy is extracted through the Blandford-Znajek [3] mechanism. This energy goes into accelerating shells of matter to ultra-relativistic velocities (Lorentz factors of several hundred). These shells collide with one another as they move outward, producing "internal" shocks. The shocks accelerate electrons, which emit synchrotron radiation. In the observer's frame, this radiation appears in gamma-rays. The fact that the gamma-rays are polarized is most easily explained by the presence of a large-scale, ordered magnetic field, roughly at equipartition strength [7].

The break which is observed in the optical light curves is evidence of beaming; it signals the expansion of a jet whose opening angle is initially only several degrees [14]. The total energy emitted in this stage is $\sim 5 \times 10^{50}$ erg. As the shells continue to move outward, they eventually reach a region of enhanced density. This could be either the interstellar medium, or a region which originated due to a wind from the massive star in its final stages of evolution. As the shells impinge on this region, they produce "external" shocks, which give rise to long-wavelength afterglows. There is about an order of magnitude less energy in the afterglow than in the burst itself. Depending on their specific properties, irregularities, or "bumps" in the optical light curve can be interpreted as being caused by regions of enhanced density, a supernova-like component in the explosion, or as the result of microlensing.

The model described above is known as the "standard fireball model" [25]. To be sure, there are competing models [10] as well as variations on this theme. In those cases where afterglows are not detected, the host galaxies cannot be identified, and it is almost impossible to demonstrate that the

GRB is due to the collapse of a massive star, as opposed to the merger of two neutron stars, for example.

Because the gamma-rays are beamed, we detect only a small fraction of them. This implies that the Universe-wide GRB rate is at least 1000/day.

5 Loose Ends

The discovery of long-wavelength counterparts and the measurement of host galaxy redshifts solved a long-standing GRB mystery. But other questions have now arisen. Some of the new mysteries are listed below.

1. What is the nature of the short bursts? No counterparts to them have yet been identified [21]. One possibility is that they arise from the merger of two compact objects, rather than the collapse of a massive star [27].

2. Why have no radio and/or optical counterparts been found for approximately one-half of the long GRBs? One fact which has emerged from studies of bursts localized in near real-time by the HETE spacecraft is that some afterglows fade very quickly and/or are intrinsically weak to begin with [11, 24], but this is probably not the whole story.

3. What distinguishes X-ray flashes from hard-spectrum GRB's? They appear to be identical to GRBs in all respects, except for the lack of gamma-rays. About 30% of all GRBs fall into this category [18].

4. What is the relation between GRBs and supernovae? The first experimental evidence that the two phenomena were related came from GRB980425, which was roughly spatially and temporally coincident with SN1998bw [16]. The very low redshift of the host galaxy ($z = 0.008$) would have suggested that any GRB from it would be extremely intense; in fact, GRB980425 was quite weak. But further evidence for an association comes from features in the optical light curves of GRB afterglows [4]. The best evidence to date, however, is from the study of GRB030329, a GRB discovered by the HETE spacecraft and studied extensively in the optical. The optical spectrum of the afterglow [29] bears a striking resemblance to that of SN1998bw.

6 Conclusions

Multi-wavelength measurements are the key to understanding cosmic gamma-ray bursts. Ideally, they should commence as the burst starts, and continue throughout the afterglow phase, from radio to gamma-ray wavelengths. The HETE mission has made it possible for the first time to obtain near real-time, precise GRB positions, and significant advances have followed as a result. INTEGRAL is now doing the same. The Swift mission will be launched in 2004. Swift should detect over 100 bursts/year, localize them in near real-time, and conduct X-ray and optical observations of the counterparts within

minutes. These observations should resolve many of the outstanding issues, and usher in a new era in GRB astrophysics.

References

1. C. Akerloff et al. : Nature **398**, 400 (1999)
2. D. Band et al. : Astrophys. J. **413**, 281 (1999)
3. R. Blandford, R. Znajek: Mon. Not. R. Astron. Soc. **179**, 433 (1977)
4. J. Bloom et al. : Nature **401**, 453 (1999)
5. J. Bloom: astro-ph 0301028 (2002)
6. R. Burenin et al. : Astron. Astrophys. **344**, L53 (1999)
7. W. Coburn, S. Boggs: Nature **423**, 415 (2003)
8. V. Connaughton: Astrophys. J. **567**, 1028 (2002)
9. E. Costa et al. : Nature **387**, 783 (1997)
10. S. Dado, A. Dar, A. De Rújula: Astrophys. J. Lett. **585**, L15 (2003)
11. D. Fox et al. : Astrophys. J. Lett. **586**, L5 (2003)
12. D. Frail, S. Kulkarni, L. Nicastro, M. Feroci, G. Taylor: Nature **389**, 261 (1997)
13. D. Frail, E. Waxman, S. Kulkarni: Astrophys. J. **537**, 191 (2000)
14. D.A. Frail et al. : Astrophys. J. Lett. **562**, L55 (2001)
15. F. Frontera et al. : Astrophys. J. Suppl. **127**, 59 (2000)
16. T. Galama et al. : Nature **395**, 670 (1998)
17. J. Hakkila et al. : "GRB repetition limits from current BATSE observations." In: *Gamma-Ray Bursts AIP Conference Proc. **428***, ed. by C. Meegan, R. Preece, T. Koshut (AIP: New York, 1998) pp. 236-240
18. J. Heise et al. : "X-ray flashes and X-ray rich gamma-ray bursts." In: *Gamma-Ray Bursts in the Afterglow Era*, eds. E. Costa, F. Frontera, J. Hjorth (Springer: Berlin, Heidelberg, New York, 2000) pp. 16-21
19. S. Holland et al. : Astron. J. **125**, 2291 (2003)
20. K. Hurley, R. Sari, S. Djorgovski: astro-ph 0211620 (2002)
21. K. Hurley et al. : Astrophys. J. **567**, 447 (2002)
22. J. Katz: In: *The Biggest Bangs*, (Oxford University Press: Oxford 2002)
23. R. Klebesadel, I. Strong, R. Olson: Astrophys. J. Lett. **182**, L85 (1973)
24. W. Li, A. Filippenko, R. Chornock, S. Jha: Astrophys. J. Lett. **586**, L9 (2003)
25. P. Meszaros: Ann. Rev. Astron. Astrophys. **40**, 137 (2002)
26. W. Paciesas et al. : Astrophys. J. Suppl. **122**, 465 (1999)
27. R. Perna, K. Belczynski: Astrophys. J. **570**, 252 (2002)
28. G. Schilling: In: *Flash! The Hunt for the Biggest Explosions in the Universe* (Cambridge Univ. Press: Cambridge, 2002)
29. K. Stanek et al. : Astrophys. J. Lett. **591**, L17 (2003)
30. M. Turler et al. : Astron. Astrophys. Suppl. **135**, 89 (1999)
31. J. van Paradijs et al. : Nature **386**, 686 (1997)
32. G. Williams et al. : Astrophys. J. Lett. **519**, L25 (1999)

The Surroundings of Gamma-Ray Bursts: Constraints on Progenitors

Roger A. Chevalier

Department of Astronomy, University of Virginia, P.O. Box 3818, Charlottesville, VA 22903, USA
rac5x@virginia.edu

Summary. The association of a supernova with a gamma-ray burst (GRB 030329) implies a massive star progenitor, which is expected to have an environment formed by pre-burst stellar winds. Although some sources are consistent with the expected wind environment, many are not, being better fit by a uniform density environment. One possibility is that this is a shocked wind, close to the burst because of a high interstellar pressure and a low mass loss density. Alternatively, there is more than one kind of burst progenitor, some of which interact directly with the interstellar medium. Another proposed environment is a pulsar wind bubble that has expanded inside a supernova, which requires that the supernova precede the burst.

1 Introduction

Some of the best evidence for nature of gamma-ray burst (GRB) progenitors has come from the identification of the Type Ic supernovae SN 1998bw with GRB 980425 [18] and of the recent SN 2003dh with GRB 030329 [49]. The finding of these events supports models of long-duration GRBs originating from stripped massive stars [35]. The surroundings of massive stars are expected to be shaped by the winds emanating from the progenitor stars. Clear evidence for the signature of a wind has been difficult to establish, and the possibility remains that there is more than one type of progenitor for the long-duration bursts. Direct interaction with the interstellar medium might be expected if the progenitor involves a compact binary system.

Another possibility is that the GRB occurs in a massive star weeks to years after it has become a supernova [51]. The progenitor of the GRB may be a rapidly spinning neutron star that spins down and eventually collapses, leading to a burst. This can create a pulsar wind nebula immediately surrounding the burst progenitor, which has possible advantages for producing a GRB [28].

2 Afterglows

2.1 Afterglows and the Circumburst Medium

The afterglows of GRBs provide a probe of the immediate surroundings of GRBs. The evidence that we have from bursts related to supernovae is that

the progenitors are Type Ic supernovae. In addition to SN 1998bw and SN 2003dh, the burst GRB 021211 has possibly been identified with a Type Ic supernova like SN 1994I [12]. These supernovae are thought to have massive star progenitors that have been stripped of their hydrogen envelopes, i.e. Wolf-Rayet stars. This type of massive star progenitor is also suggested by the argument that the collimated flow from a burst be able to pass through the star in a time that is not significantly longer that the duration of the GRB. Even for the long duration bursts, this implies a relatively compact stellar progenitor like the Wolf-Rayet stars [35, 37].

Wolf-Rayet stars are found to have winds with typical mass loss rate $\dot{M} = 10^{-5}\mathrm{M}_\odot$ yr^{-1} and wind velocity $v_w = 1000$ km s^{-1}ending in a termination shock where the wind runs into the surrounding medium [5]. A steady wind produces a density distribution $\rho = Ar^{-2}$; the value of the density can be scaled to the corresponding value for the standard wind parameters, $A_* = A/(5 \times 10^{11}$ gm cm$^{-1})$. For a surrounding medium of pressure p, the wind termination shock occurs at a radius

$$R_t = 5.7 \times 10^{19} \left(\frac{v_w}{1000 \text{ km s}^{-1}}\right) \left(\frac{p/k}{10^4 \text{ cm}^{-3} \text{ K}}\right)^{-1/2} A_*^{1/2} \text{ cm} \qquad (1)$$

where k is Boltzmann's constant. The pressure is normalized to a typical value in the interstellar medium of our Galaxy. A higher pressure can occur as a result of the wind bubble evolution, or as the result of an especially high pressure interstellar medium.

For a spherical explosion with energy E, the blast wave in the free wind reaches the radius R_t after a time

$$t_t = 1.35 \times 10^4 \left(\frac{v_w}{1000 \text{ km s}^{-1}}\right)^2 \left(\frac{p/k}{10^4 \text{ cm}^{-3} \text{ K}}\right)^{-1} \left(\frac{E}{10^{53} \text{ ergs}}\right)^{-1} A_*^2 \text{ days}. \qquad (2)$$

This shows that over typical times of observation, the blast wave may be expanding into the free wind for standard parameters. In view of this, interaction with a wind has become one of the models that is investigated in modeling the afterglows of GRBs [6]. This model is compared to results for a constant density medium, which was initially taken in afterglow modeling as the simplest assumption. Taking the surrounding density of the form $\rho \propto r^{-s}$, these cases can be designated $s = 0$ (uniform) and $s = 2$ (wind). In afterglow models, both wind and constant density models provide adequate fits to the data in some cases, although the constant density model is usually favored [41, 42].

At first sight, this ambiguity is surprising. In the context of models with constant efficiencies evolving before a jet break sets in, the two cases have distinctive behavior: the synchrotron self-absorption frequency, ν_a, evolves to higher frequency with $s = 2$, but remains constant for $s = 0$; the peak flux

drops with time for $s = 2$, but remains constant for $s = 0$; the synchrotron cooling frequency, ν_c, evolves to higher frequency for $s = 2$, but evolves to lower frequency for $s = 0$. There are various reasons why these differences have not provided clear tests of the models. The evolution of ν_c requires good light curve information at optical/IR and X-ray wavelengths, which is usually lacking. The evolution of ν_a requires early radio data; these data are usually sparse and are affected by interstellar scintillation. Another problem is that jet breaks are observed in light curves and the evolution in the post-break regime can mimic some of the features of evolution in an $s = 2$ medium: the peak flux drops with time and ν_a evolves to higher frequency [46].

Another possibility for distinguishing between the models is to go to very early times, within about a minute of the GRB burst. In addition to the older case of GRB 990123, this has recently been achieved for GRB 021004 [13] and GRB 021211 [32, 43, 53]. The advantage of these early times is that jet effects do not play a role in the evolution. Li & Chevalier [34] suggested that the early flat optical light curve of GRB 021004 could be interpreted in terms of wind interaction, in which the critical frequency ν_m had not yet moved down through optical wavelengths. Although this model has some promise, the case remains ambiguous in that the relatively flat evolution might also be produced by a combination of emission from the reverse shock wave and the later forward shock emission in the case of interaction with a $s = 0$ medium [27]. To distinguish between these possibilities, both good light curve data and color information are needed.

An additional problem with GRB 021004 is that the optical light curve showed variability superposed on the overall trend [25]. This makes it difficult to clearly specify characteristic times in the evolution of the afterglow. The variability, which is not seen in all afterglows, may be due to density inhomogeneities in the circumburst medium and may thus provide additional diagnostics for that medium [24]. The winds of Wolf-Rayet stars are known to be inhomogeneous, with clumps filling $\sim 1/4$ of the volume [22]. However, the observed degree of inhomogeneity refers to a region close to the stellar surface and the inhomogeneity may decrease in the outer parts of the wind where the afterglow occurs.

2.2 Jets

Jet breaks themselves provide a possible diagnostic for the medium. The usual assumption has been that an afterglow light curve steepens due to geometric and spreading effects when its Lorentz factor is about 1/(opening angle) to the form t^{-p} [46]. Kumar & Panaitescu [29] find that the transition to the asymptotic jet evolution requires a factor $\gtrsim 10$ in time for expansion in a uniform medium, but expansion by $\sim 10^4$ in time for expansion in a wind medium. However, they used a simplified treatment of jet evolution. Numerical simulations indicate that sharp jet breaks do occur in a uniform medium, but that most of the emission remains within the initial opening

angle of the jet [19]. Granot & Kumar [20] have recently considered structured jets in uniform and declining density media, and again found that jets in an $s = 2$ medium cannot give sharp jet breaks.

The recent burst GRB 030329, which was clearly associated with a supernova, showed a sharp break in the light curve at $t \sim 0.5$ day, which has been interpreted as a jet break [3]. However, it has become clear that there is considerable structure in the light curve of GRB 030329 over the first 10 days [36, 50] and the identification of an early jet break cannot be made with certainty.

2.3 Afterglow Parameters

There are uncertainties in the basic assumptions involved in standard afterglow modeling, which include constant values of electron energy efficiency, ϵ_e, magnetic energy efficiency, ϵ_B, and particle spectral index, p, in the evolution of one source (e.g., [45]). If these parameters remain constant during the evolution of one source, the expectation would be that they tend toward "universal" values that apply to various sources. Standard models developed for observed afterglows do not show this. As an example, I take the results of Panaitescu & Kumar [42], who treat a set of the 10 best observed afterglows with the standard assumptions. The values of spectral index, p, cover the range $1.36 - 2.78$. The presence of values $p < 2$ is noteworthy because most of the particle energy is at high energy for this case, although the number of particles is dominated by the low energy particles. The values of ϵ_B and ϵ_e cover the ranges of $4 \times 10^{-5} - 0.07$ and $0.01 - 0.4$, respectively.

The theoretical values of these parameters are poorly known. The production of the magnetic field requires some mechanism at the forward shock front to build up the magnetic field. The mechanism remains uncertain, although the Weibel instability has been suggested [38], and recent simulations show some promise for this mechanism [16, 40]. Studies of Fermi-type particle acceleration in ultrarelativistic shocks have yielded a preferred value of $p = 2.2 - 2.3$ in the test particle limit [1]. The way electrons are injected into the acceleration process remains uncertain, and there are indications that the acceleration may differ from the Fermi process [16, 40].

The fact that a range of parameters is needed to explain the various afterglows suggests that the parameters depend on the physical conditions. It might be expected that the shock velocity and preshock density are important determinants of the physical conditions, so that the model parameters should vary during the evolution of a burst. Yost et al. [54] have recently considered models in which ϵ_B is allowed to vary as a power law of the shock Lorentz factor and in which the value of the preshock density parameter s is allowed to cover a large range. Their modeling of 4 sources shows that a wide variety of models are potentially possible, including ones in which the density increases steeply with radius. It appears that more extensive observations, including spectral information over a wide time range, are needed to further constrain

the models. One possibility is to follow the evolution of the characteristic frequency, ν_m, from optical to radio wavelengths. This frequency is typically observed at radio wavelengths on a timescale ~ 10 days. Its passage at optical wavelengths requires very early observations; as noted above, this may have been observed in GRB 021004. The typical frequency is not sensitive to the density, but it is sensitive to the efficiency factors, so that constraints on their evolution may be obtainable.

2.4 A Shocked Wind Environment

In view of the evidence for the association of GRBs with massive stars and the evidence from afterglows for interaction with a constant density medium, consideration must be given as to how a massive star might produce a uniform density surrounding. The most plausible way to do this is the approximately constant density region expected downstream from the wind termination shock [52]. Wijers [52] suggested two ways for creating a smaller value of t_t (Eq. 2): reducing the mass loss rate from the progenitor to 10^{-6} $M_\odot$ yr^{-1}because of the low metallicity of the progenitor star and increasing the pressure by interacting with dense molecular gas, especially if the progenitor star is moving. However, the metallicity dependence of the mass loss from Wolf-Rayet stars is uncertain: WN type stars in the lower metallicity Large Magellanic Cloud [23] and the Small Magellanic Cloud [9] have similar mass loss rates to those in the Galaxy, although WC stars do seem to show a metallicity effect [10]. Also, photoionizing radiation during the life of a massive star tends to clear a region around the star to a moderately low density. Another way of increasing p is by having the burst occur in a high pressure starburst region [15], where the pressure can reach values of $p/k \gtrsim 10^8$ cm^{-3} K [7]. In this case, there should be a relation between the properties of the afterglow (relatively dense surroundings) and the position of the burst relative to a region of very active star formation.

One expectation of the models with a termination shock is that some bursts should be observed to make a transition from an $s = 2$ to an $s = 0$ medium, with a density jump between them. There has been little evidence for such a transition. The expectation for such a transition is that the light curve should evolve to a flatter asymptotic decline after a jump in flux. Wijers [52] mentioned GRB 970508 because it had a bump in the optical light curve at an age of 1 day. However, it did not show the expected flattening of the light curve. A burst that showed a steepening with a possible bump is GRB 030226. Dai & Wu [11] suggested that the transition was due to the interaction with a large density jump, which might occur at the contact discontinuity between the shocked progenitor wind and the dense red supergiant wind from a previous evolutionary phase. In this picture, the steepening of the light curve is due to the sideways expansion of the jet in the dense medium. However, the data on GRB 030226 are not of sufficient quality to clearly show the expected features at the time of transition with the density jump.

In the case of interaction with the termination shock of the stellar wind, the density jump is such that the effects of the reverse shock are not expected to be important, as opposed to the high density jump case.

3 Optical/Ultraviolet Absorption Lines

A recent development relevant to the surroundings of GRBs is the observation of strong optical/ultraviolet absorption lines in a few cases. The best case is GRB 021004, which has a redshift $z = 2.32$ so that strong ultraviolet lines in the rest frame are redshifted to optical wavelengths [39, 47]. Strong lines of Lyα, Lyβ, C IV, and Si IV are found blueshifted relative to the host velocity by -450, -990, and -3155 km s^{-1}[39]. The lines have not been observed to vary, so they cannot be directly tied to the immediate circumburst environment, but both Mirabal et al. [39] and Schaefer et al. [47] argue that they are likely to be formed in the nearby environment. One argument for this is that the strong lines are unusual for intervening systems observed in the spectra of quasars. The lines may be formed close to the host galaxy if the burst occurred in a starburst region with a strong galactic superwind. However, the maximum velocity shift is higher than has been observed in galactic superwinds. In addition, the high velocity would require a high initial temperature for the gas if the wind is thermally driven. The gas would be completely ionized and it is unlikely that it would be able to cool to allow the observed ions.

For a circumstellar origin, there are two possibilities: the high velocities are related to the wind velocities of the progenitor system, or the velocities are due to radiative acceleration by the GRB light; combinations of these models are also possible. Schaefer et al. [47] argue that the high blueshifted velocity can be naturally produced by the Wolf-Rayet star wind velocity and the lower velocity components can be identified with denser shells swept-up by the fast wind. Mirabal et al. [39] argue that the abundances deduced from the lines disfavor the wind model. Hydrogen is present in the observed lines, but it is also observed in the spectra of some WN stars [48]; however, the absence of N V lines in the observed spectra indicates that N is not overabundant. In the radiatively accelerated model, the accelerated clumps must be at an initial distance of several 0.1's pc from the progenitor star. The acceleration, primarily by bound-free transitions, must occur early in order to avoid the observation of time variability.

The problem with both of these scenarios is that the strong radiation field from the GRB and its afterglow is able to completely photoionize the gas out to a distance $\gtrsim 10^{18}$ cm [31]. At a sufficiently high density ($\gtrsim 10^7$ cm^{-3}), the recombination time becomes shorter than the age of the burst. This density might be present in clumps of the swept-up red supergiant wind, especially if the progenitor is in a high pressure region, but further exploration of this topic is needed.

GRB 021004 is not alone in showing these line features. High excitation, high velocity absorption features have been found in GRB 020813 [2] and GRB 030226 [8, 21, 44]. The absorption lines of CIV in GRB 020813 are at 0 km $s^{-1}$and -4320 km s^{-1}relative to the host. In this case, the blueshifted absorption is also present in a number of lower ionization species (Si II, Al II, Fe II, Mg II, and Mg I); there is no coverage of Lyα. In the case of GRB 030226, strong absorption line systems are present at a velocity separation of 2300 km s^{-1}, with C IV and Si IV present, as well as numerous lower ionization species and Lyα. The velocity separation seen in these sources is consistent with expectations for the velocity of a Wolf-Rayet star wind. However, the presence of H does not support this origin for the lines.

4 Pulsar Wind Bubble Environment

An interesting possibility for a GRB environment is that created by a pulsar wind nebula. This possibility was proposed in the context of the supranova model in which the supernova precedes the GRB [28, 51]. In this scenario, the supernova core contracts to a massive, rapidly rotating neutron star which spins down and collapses to a black hole after a period of weeks, months, or years. If the neutron star has a magnetic field similar to that of radio pulsars, it can create a shocked bubble of relativistic electron/positron fluid and magnetic field before it collapses. The bubble accelerates the supernova ejecta, so that the ejecta can play a role in producing the X-ray lines that have possibly been observed in some bursts.

One issue is how effectively the pulsar nebula can accelerate the supernova gas, because the situation is subject to Rayleigh-Taylor instabilities [26, 28]. The X-ray line features are typically blueshifted by $\sim 0.1c$, which is higher than the velocities of the heavy element ejecta that would be expected from the supernova itself. A supernova energy of 10^{51} ergs in an ejecta mass of 10 $M_\odot$ leads to a typical velocity of $0.01c$. Königl & Granot [28] suggest that the rotational energy of a rapidly rotating neutron star, 10^{53} ergs, is transferred to the ejecta, giving the observed velocity. Although a pulsar nebula can certainly shock and compress the ejecta gas, the ability to further accelerate the ejecta is less certain. However, if the supernova explosion energy is high ($> 10^{52}$ ergs as inferred for some supernovae) and the ejecta mass is low, a typical velocity of $0.1c$ can be attained.

Another issue is the fact that the observation of X-ray line features at an age of ~ 1 day requires dense gas at $r \sim 10^{16}$ cm, but observations of afterglow emission at an age of a week or more imply a radial scale $\gtrsim 3 \times 10^{17}$ cm. Königl & Granot [28] suggest that pulsar nebula and supernova may be highly elongated along the axis along which the GRB flow propagates.

Although the observational evidence for X-ray lines remains controversial, there are other reasons for considering a pulsar wind nebula environment, as

articulated by Königl & Granot [28]. One is that the pulsar nebula is composed of just the ingredients that are necessary for the synchrotron emission from a GRB afterglow. There is no problem with the efficiencies for production of the synchrotron emission. In addition, the bubble density can be constant with radius, or drop with radius. The first case can occur in the same way that a constant density occurs downstream from an ordinary stellar wind. The decreasing density occurs in regions where the magnetic field pressure becomes important, although the structure of such regions in pulsar nebulae remains uncertain.

Although the pulsar bubble model has some appeal, it does not apply to cases where the GRB occurs close in time to the supernova, as apparently was the case with GRB 030329 and SN 2003dh (e.g., [36]).

5 Discussion and Conclusions

Despite several years of effort, the study of GRB environments from their interaction has not clearly pointed to the progenitor objects. Reasons for this include the uncertainties in the basic model parameters, the fact that the GRB ejecta appear to be collimated and the similarity in the surrounding densities expected in different scenarios. The clearest progenitor information we have comes from the association of SN 2003dh with GRB 030329. The similarity of the supernova to SN 1998bw suggests that the progenitor object is a similar massive star. Analysis of the radio emission from SN 1998bw showed compatibility with expectations of a wind-like surrounding medium [33]. The radio observations of GRB 030329 are slightly better fit by a uniform medium than a wind-like medium, although the difference between the fits is not large [3]. The host galaxy of GRB 030329 appears to be a starburst dwarf galaxy [36] and the burst is positioned near the edge of the star forming region [17], so it is not clear whether a high pressure surroundings is expected. Detailed modeling will be needed to determine whether the afterglow features can be explained by a complex explosion, or whether the surroundings need special properties.

An outstanding question is whether there is any need for a progenitor of long-duration bursts other than massive stars. Since massive stars are expected to modify their surroundings through winds, this evidence would be an incompatibility with the wind effects expected around a massive star. Frail et al. [14] and Yost et al. [54] have noted that a number of afterglows that can best be modeled as expanding into a uniform density medium with $n \sim 10-30$ cm^{-3}, and that this density is typical of Galactic interstellar clouds or the interclump medium of molecular clouds. However, such a medium would be modified by the winds from a massive star progenitor and a significant fraction of GRBs probably occur in starburst regions where clouds are denser than in Galactic case. One possibility is that the uniform medium is created by a shocked stellar wind in a high pressure medium.

A possible problem for massive star models is the low density inferred around some GRBs. Even if a shocked wind is present, it has higher density at a given radius than the corresponding free wind, so strong limits on the wind density can be set. Two afterglows with low densities are GRB 990123 [42] and GRB 021211 [30], which require $A_* \lesssim 10^{-3} - 10^{-2}$. Such low densities have not been observed around Wolf-Rayet stars. GRB 021211 shows evidence for a supernova [12], but the evidence is not conclusive. The low densities are not a problem for a burst that interacts directly with the hot interstellar medium in a galaxy. Another problem with the massive star models is the lack of evidence for bursts crossing the interface between a free wind and a shocked wind.

If direct interaction with the interstellar medium is required, a plausible progenitor object is a binary of compact objects. This requires that two different progenitor objects can give GRBs that appear similar, presumably from the formation of black holes. The application of the pulsar wind nebula model to some bursts requires both that different progenitor objects give rise to similar bursts, but also that the expansion of the burst into a different kind of medium (pair plasma and magnetic field) can give rise to similar afterglows. The finding of a supernova (SN 2003dh) occurring at approximately the same time as a GRB (GRB 030329) mitigates against the pulsar wind nebula picture for this case.

Acknowledgement. I am grateful to Jon Marcaide and the other conference organizers for their hospitality in Valencia, and to Zhi-Yun Li and Claes Fransson for continuing collaboration on these topics. This work was supported in part by NASA grant NAG5-13272 and NSF grant AST-0307366.

References

1. A. Achterberg, Y.A. Gallant, J.G. Kirk, A.W. Guthmann: Mon. Not. R. Astron. Soc. **328**, 393 (2001)
2. A.J. Barth et al. : Astrophys. J. Lett. **584**, L47
3. E. Berger et al. : astro-ph 0308187 (2003)
4. R.A. Chevalier, J.N. Imamura: Astrophys. J. **270**, 554 (1983)
5. R.A. Chevalier, Z.-Y. Li: Astrophys. J. Lett. **520**, L29 (1999)
6. R.A. Chevalier, Z.-Y. Li: Astrophys. J. **536**, 195 (2000)
7. R.A. Chevalier, C. Fransson: Astrophys. J. Lett. **558**, L27 (2001)
8. R. Chornock, A.V. Filippenko: GCN 1897 (2003)
9. P.A. Crowther: Astron. Astrophys. **356**, 191 (2000)
10. P.A. Crowther, L. Dessart, D.J. Hillier, J.B. Abbott, A.W. Fullerton: Astron. Astrophys. **392**, 653 (2002)
11. Z.G. Dai, X.F. Wu: Astrophys. J. Lett. **591**, L21 (2003)
12. M. Della Valle et al. : Astron. Astrophys. **406**, L33 (2003)
13. D.W. Fox et al. : Nature **422**, 284 (2003)
14. D.A. Frail et al. : Astrophys. J. **590**, 992 (2003)

15. C. Fransson: In: These proceedings
16. J.T. Frederikson, C.B. Hededal, T. Haugboelle, A. Nordlund: astro-ph 0308104 (2003)
17. A. Fruchter et al. : GCN 2243 (2003)
18. T.J. Galama et al. : Nature **395**, 670 (1998)
19. J. Granot, M. Miller, T. Piran, W.-M. Suen, P.A. Hughes: In: *Gamma-Ray Bursts in the Afterglow Era.* ed. by E. Costa, F. Frontera, J. Hjorth (Springer: Berlin, 2001) p. 312
20. J. Granot, P. Kumar: Astrophys. J. **591**, 1086 (2003)
21. J. Greiner, E. Guenther, S. Klose, R. Schwarz: GCN 1886 (2003)
22. W.-R. Hamann, L. Koesterke: Astron. Astrophys. **335**, 1003 (1998)
23. W.-R. Hamann, L. Koesterke: Astron. Astrophys. **360**, 647 (2000)
24. J.S. Heyl, R. Perna: Astrophys. J. Lett. **586**, L13 (2003)
25. S.T. Holland et al. : Astron. J. **125**, 2291 (2003)
26. S. Inoue, D. Guetta, F. Pacini: Astrophys. J. **583**, 379 (2003)
27. S. Kobayashi, B. Zhang: Astrophys. J. Lett. **582**, L75 (2003)
28. A. Königl, J. Granot: Astrophys. J. **574**, 134 (2002)
29. P. Kumar, A. Panaitescu: Astrophys. J. Lett. **541**, L9 (2000)
30. P. Kumar, A. Panaitescu: Mon. Not. R. Astron. Soc. **346**, 905 (2003)
31. D. Lazzati, E. Rossi, S. Covino, G. Ghisellini, D. Malesani: Astron. Astrophys. **396**, L5 (2002)
32. W. Li, A.V. Filippenko, R. Chornock, S. Jha: Astrophys. J. Lett. **586**, L9 (2003)
33. Z.-Y. Li, R.A. Chevalier: Astrophys. J. **526**, 716 (1999)
34. Z.-Y. Li, R.A. Chevalier: Astrophys. J. Lett. **589**, L69 (2003)
35. A.I. MacFadyen, S.E. Woosley, A. Heger: Astrophys. J. **550**, 410 (2001)
36. T. Matheson et al. : Astrophys. J. **599**, 394 (2003)
37. C.D. Matzner: Mon. Not. R. Astron. Soc. **345**, 575 (2003)
38. M.V. Medvedev, A. Loeb: Astrophys. J. **526**, 697 (1999)
39. N. Mirabal et al. : Astrophys. J. **595**, 935 (2003)
40. K.-I. Nishikawa, P. Hardee, G. Richardson, R. Preece, H. Sol, G.J. Fishman: Astrophys. J. **595**, 555 (2003)
41. A. Panaitescu, P. Kumar: Astrophys. J. **554**, 667 (2001)
42. A. Panaitescu, P. Kumar: Astrophys. J. **571**, 779 (2002)
43. H.S. Park, G. Williams, S. Barthelmy: GCN 1736 (2002)
44. P.A. Price, D.W. Fox, S.G. Djorgovski, P. Cote, A. Jordan: GCN 1889 (2003)
45. R. Sari, T. Piran, R. Narayan: Astrophys. J. Lett. **497**, L17 (1998)
46. R. Sari, T. Piran, J.P. Halpern: Astrophys. J. Lett. **519**, L17 (1999)
47. B.E. Schaefer et al. : Astrophys. J. **588**, 387 (2003)
48. L.F. Smith, M.M. Shara, A.F.J. Moffat: Mon. Not. R. Astron. Soc. **281**, 163 (1996)
49. K.Z. Stanek et al. : Astrophys. J. Lett. **591**, L17 (2003)
50. M. Uemura et al. : Nature **423**, 843 (2003)
51. M. Vietri, L. Stella: Astrophys. J. Lett. **507**, L45 (1998)
52. R.A.M.J. Wijers: In: *Gamma-Ray Bursts in the Afterglow Era.* ed. by E. Costa, F. Frontera, J. Hjorth (Springer: Berlin, 2001) p. 306
53. P. Wozniak et al. : GCN 1757 (2002)
54. S.A. Yost, F.A. Harrison, R. Sari, D.A. Frail: Astrophys. J. **597**, 459 (2003)

The Radio Afterglows of Gamma-Ray Bursts

Dale A. Frail

National Radio Astronomy Observatory, Socorro, NM 87801 USA;
dfrail@nrao.edu

Summary. Radio afterglow observations continue to provide complementary and sometimes unique diagnostics on gamma-ray burst explosions, their progenitors and their environments. In this review we will first describe current search strategies and the observational properties of the detected sample. In the second part of this review we will follow the evolution of a typical radio afterglow, describe the diverse phenomenology that is observed, and interpret these observations within the framework of the fireball model.

1 Introduction

Our understanding of the gamma-ray bursts (GRBs) has advanced rapidly since the discovery of long-lived "afterglow" emission from these events. Radio afterglow studies have become an integral part of this field, providing complementary and sometimes unique diagnostics on GRB explosions, their progenitors, and their environments. The reason for this is that the radio part of the spectrum is phenomenologically rich. This can be illustrated simply by calculating the brightness temperature ($T_b \propto \mathrm{F}_\nu/(\theta_s\,\nu)^2$) for a 1 mJy centimeter wavelength source at cosmological distances ($\sim 10^{28}$ cm), expanding with $V_{exp} \leq c$ one week after the burst. Since the derived $T_b \sim 10^{13}$ K is well in excess of the $T_{IC} \sim 10^{11} - 10^{12}$ K limit imposed by inverse Compton cooling, it follows, independent of any specific afterglow model, that the radio emission must originate from a compact, synchrotron-emitting source that is expanding superluminally (i.e. $T_b \sim \Gamma \times T_{IC}$, $\Gamma >> 1$). Likewise, since the brightness temperature cannot exceed the mean kinetic energy of the electrons, the emission is expected to be self-absorbed at longer wavelengths [31]. Finally, strong modulation of the centimeter signal is expected on timescales of hours and days because the angular size θ_s of this superluminal source is comparable to the Fresnel angle of the turbulent ionized gas in our Galaxy [25]. Synchrotron self-absorption, interstellar scintillation, forward shocks, reverse shocks, jet-breaks, non-relativistic transitions and obscured star formation are among the phenomena routinely observed.

This short review is divided into two parts. The first section (§2) is a summary of the current search strategies and the main observational properties of radio afterglows. In the second section (§3) we highlight the key

scientific contributions made by radio observations, either alone or as part of panchromatic studies. By necessity we will restrict this brief review to long-duration GRBs, although radio afterglows have also been detected toward the newly classified X-ray flashes, and searches have been carried out toward short bursts [30].

2 Detection Statistics and Observational Properties

The search for a radio afterglow is initiated either by a satellite localization of the burst, or by the detection of the X-ray or optical afterglow. The current search strategy has been to use the Very Large Array (VLA)[1] or the Australia Telescope Compact Array (ATCA; for declinations, $\delta < -40^{\circ}$)[2] at 5 GHz or 8.5 GHz. These frequencies were chosen as a compromise between the need to image the typical error box size of 30-100 arcmin^2, while having the requisite sensitivity to detect afterglows at sub-milliJansky levels. At lower frequencies the afterglow is attenuated by synchrotron self-absorption ($f_\nu \propto \nu^2$), while at higher frequencies the field-of-view is proportionally smaller (FOV$\propto \nu^2$). For typical integration times (10 min at the VLA, and 240 min at the ATCA) the *rms* (receiver) noise is 30-50 μJy. Follow-up observations of detected afterglows were carried out by a network of radio facilities at centimeter, millimeter and submillimeter wavelengths [19].

In the five year period beginning in 1997 and ending in 2001 approximately 1500 radio flux density measurements (or upper limits) were made toward 75 bursts [23]. From these 75 GRBs, there are a total of 32/36 successful X-ray searches, 27/70 successful optical searches, and 25/75 successful searches. These afterglow search statistics illustrate a well-known result, namely that the detection probability for X-ray afterglows is near unity, while for optical afterglows and radio afterglows it is 40% and 33%, respectively. The origin of these optically "dark bursts" could either be due to intrinsic effects (i.e. inadequate search due to rapid evolution of the afterglow and/or an under-energetic GRB) [5, 24], or an extrinsic effect (i.e. extinction of the optical flux caused by circumburst dust or by the intergalactic medium) [14, 38].

To accurately derive the fraction of "radio quiet" bursts it is necessary to incorporate both detections and upper limits in a statistically sound manner. This has been done in Fig. 1 where flux density distribution at 8.5 GHz is shown for a sample of 44 GRBs, toward which measurements or upper limits have been made between 5 and 10 days after a burst. The time since the burst is an important variable since radio light curves do not exhibit the simple power-law decays seen in X-ray and optical afterglows, but rise to a

[1] The NRAO is a facility of the National Science Foundation operated under cooperative agreement by Associated Universities, Inc.

[2] The Australia Telescope is funded by the Commonwealth of Australia for operation as a National Facility managed by CSIRO.

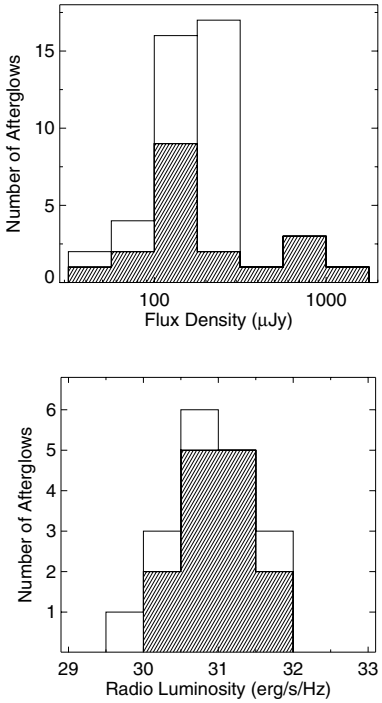

Fig. 1. (*Left*) Histogram distribution of flux densities (or upper limits) at 8.5 GHz for a complete sample of bursts. The hatched histogram shows the distribution for the detections only. (*Right*) Histograms of radio luminosity from the same sample but restricted to the subset of bursts with known redshifts. The hatched histogram shows the distribution for bursts with detected radio afterglows only.

peak on average about one week after the burst and decay on timescales of a month. The mean of the 19 *detections* in Fig. 1 is 315±82 μJy. Adding in the non-detections, and using the Kaplan-Meier estimator [15] shifts this to 186±40 μJy. Approximately 50% of all bursts have radio afterglows at 8.5 GHz above 110 μJy, while fewer than 10% exceed 500 μJy. The relatively small range of peak flux densities in Fig. 1 suggests that the fraction of "radio quiet" bursts is largely determined by instrumental sensitivities. With the arcsecond localizations provided by the *Swift* satellite (launch in 2004) it will be possible to routinely detect all afterglows with centimeter radio emission above 100 μJy. Increasing the fraction of detected radio afterglows significantly above 50% will require the sensitivity improvements provided by the *Expanded Very Large Array*[3] (complete in 2010).

[3] http://www.aoc.nrao.edu/evla/

From this sample of peak flux densities we also derive the peak spectral radio luminosity in Fig. 1 given by $L_\nu = 4\pi F_\nu\, d_L^2\, (1+z)^{1+\beta-\alpha}$, where $F_\nu \propto t^\alpha \nu^\beta$ and $\alpha = 1/2$ and $\beta = 1/3$ has been assumed, corresponding to an optically thin, rising light curve. The GRB redshifts lie in the range between z =0.36 to z=4.5. The peak of the distribution is centered on 10^{31} erg s^{-1} Hz^{-1} and is similar to low-luminosity FRI radio galaxies like M87. More interestingly, a comparison between this GRB sample and a sample of Type Ib/c supernovae [9] shows that the later is four orders of magnitude less luminous. Since radio emission is sensitive to the relativistic energy content of the shock, independent of the initial geometry of the explosion, this has been used to argue that the majority (<97%) of nearby Type Ib/c supernovae do not produce a GRB-like event, such as that seen toward SN 1998bw [32].

3 Phenomenology and Interpretation

In this section we will follow the evolution a GRB and its radio afterglow depicted schematically in Fig. 2. The observations span four orders of magnitude in time (0.1-1000 days) and three orders of magnitude in frequency (0.8-660 GHz), so it should be no surprise that radio light curves exhibit a rich phenomenology. To interpret these observations we will rely on the highly successful "standard fireball model" [34]. In this model there is an impulsive release of kinetic energy ($\sim 10^{51}$ erg) from the GRB event which drives an ultra-relativistic outflow into the surrounding medium whose hydrodynamical evolution is governed by the kinetic energy released, the density structure of the circumburst medium and the geometry of the outflow. Synchrotron emission is produced by this relativistic shock which accelerates electrons to a power-law distribution. It is through the study of temporal (and spectral) evolution of afterglow light curves that we can gain insight into the physical conditions of the shock and the central engine that produced it.

Despite response times as short as 2 hrs, centimeter searches (§2) are rarely successful until a day or more after a burst. Broadband afterglow spectra show that centimeter emission is attenuated as a result of synchrotron self-absorption [26]. Typical observed values for the self-absorption frequency ν_a are 5-10 GHz. It is interesting to note that the flux density below ν_a has the form $\mathrm{F}_\nu \propto \nu^2$, not the 5/2 spectral slope usually seen toward most radio sources. This is because the relativistic shock accelerates electrons to a power-law distribution (with energy index p given by $\mathrm{N}(\gamma_e) \propto \gamma_e^{-p}$) above a minimum energy γ_m, which initially radiate their energy most of their energy at $\nu_m >> \nu_a$. The flux below ν_a depends only the angular size of the source and the fraction of the shock energy that goes into accelerating electrons [31], and thus it is a useful diagnostic of the ratio of the energy of the shock and the density of the circumburst medium (E/n).

As this optically thick radio source expands, a monotonic rise in the flux would be expected. It was therefore a considerable surprise when early

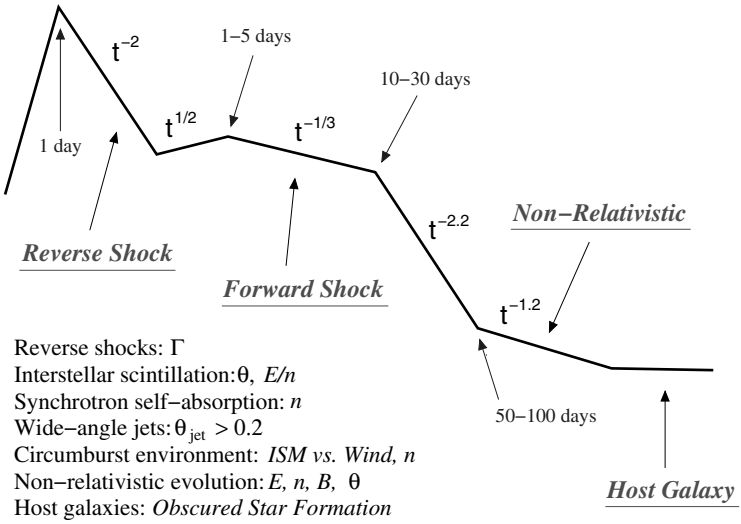

Fig. 2. A schematic radio afterglow light curve. Timescales and scalings for the temporal evolution are indicated. The list summarizes aspects of the flux evolution which are unique to the radio bands (Lorentz factor, Γ; source size, θ; energy, E; density, n; jet opening angle, $\theta_{\rm jet}$; density profile; magnetic field strength, B; and obscured star formation rate).

observations of GRB 970508 showed erratic, short term ($\sim$ hrs) and narrow band ($\sim$GHz) fluctuations in the centimeter emission [16]. The origin of these variations [25] was traced to the scattering of the radio emission, owing to the small angular size of the fireball, as it propagates through the turbulent ionized gas of our Galaxy. This is a large and complex subject [27, 41], but for the purpose of this review it is sufficient to note that for typical lines of sight the modulation of the flux densities is near a maximum at frequencies near 5-10 GHz. Coincidently, this is the same frequency range where ν_a typically lies and where the majority of radio observations are being made. While interstellar scintillation adds a certain degree of complexity to interpreting afterglow light curves, it also allows us to use the Galaxy as a large lens to effectively resolve the fireball. The observed "quenching" of diffractive scintillation from GRB 970708 four weeks after the burst [17, 45] lead to estimate of the angular size, demonstrating superluminal expansion and providing an early confirmation of the fireball model.

In many instances [7, 18, 29, 33, 48] bright, short-lived radio "flares" are detected at early times ($t < 3$ d). The emission is much brighter than expected from a backward extrapolation of the light curve, and the level of fluctuation is too great to be accounted for by interstellar scintillation. One of the best-known examples is the radio flare of GRB 990123 [33], which was accompanied by a 9th magnitude optical flash [1]. This prompt optical

and radio emission is thought to be produced in a strong reverse shock which adiabatically cools as it expands back through the relativistic ejecta [42]. The strength and lifetime of this reverse shock emission is sensitive to the initial Lorentz factor, $\Gamma_\circ$, of the shock and the density structure of the circumburst medium [7, 44]. To properly constrain these values requires that the peak of the emission be measured. This is difficult to do with optical observations, which require a response time on the order of the burst duration, while radio observations require a response time of only 12-48 hrs.

On a timescale of days to weeks after the burst, the subsequent evolution of the radio afterglow (Fig. 2) can be described by a slow rise to maximum, followed by a power-law decay. The radio peak is often accompanied by a sharp break in the optical (or X-ray) light curves [2, 28]. The most commonly accepted (but not universal) explanation for these achromatic breaks is that GRB outflows are collimated. The change in spectral slope, α, where $F_\nu \propto t^\alpha \nu^\beta$, occurs when the Γ of the shock drops below θ_j^{-1}, the inverse opening angle of the jet [40, 43]. Since the radio emission at ν_R initially lies below the synchrotron peak frequency ν_m the jet break signature is distinctly different than that at optical and X-ray wavelengths. Prior to the passage of ν_m the jet break is expected to give rise to a shallow decay $t^{-1/3}$ or plateau t^0, in the optical thin ($\nu_a < \nu_R$) or thick ($\nu_a > \nu_R$) regimes, respectively. Another recognizable radio signature of a jet-like geometry is the "peak flux cascade", in which successively smaller frequencies reach lower peak fluxes (i.e. $F_m \propto \nu_m^{1/2}$). Taken together, these observational signatures can be used to infer the opening angles θ_j of wide angle jets. Such jets are hard to detect at optical wavelengths because the break is masked by the host galaxy, which typically dominates the light curve between a week and a month after the burst [4, 22]. Once the real geometry of the outflow is known [10, 20] the energy released in the GRB phase and the afterglow phase can be determined.

As noted above, the radio band is fortuitously located close to ν_a and as such it is a sensitive probe of the density structure of the circumburst medium. Extensive broadband modeling [37] has yielded densities in the range 0.1 cm^{-3} < n< 100 cm^{-3}, with a canonical value of order n$\simeq$10 cm^{-3}. Such densities are found in the diffuse interstellar clouds of our Galaxy, commonly associated with star-forming regions. A density of order 5-30 cm^{-3} is also characteristic of the interclump medium of molecular clouds, as inferred from observations of supernova remnants in our Galaxy (e.g., [11] and references therein). Based on X-ray and optical observations alone, there have been claims of high n$\gg 10^4$ cm^{-3} [13, 50] or low n$\ll 10^{-3}$ cm^{-3} [36] circumburst densities. However, in several of these cases when the radio data has been added to the broadband modeling (i.e. constraining ν_a), there is no longer any support for either extreme of density [22, 29].

One unsolved problem on the structure of the circumburst environment is the absence of an unambiguous signature of mass loss from the presumed massive progenitor star in afterglow light curves [12]. Although there are some

notable exceptions (e.g., [39]), most GRB light curves are best fit by a jet expanding into a *constant* density medium instead of a radial density gradient, $\rho \propto r^{-2}$ [37]. Part of the solution may lie in reduced mass loss rates due to metalicity effects, or the motion of the star through a dense molecular cloud [47], both of which act to shrink the radius that the pre-burst wind is freely expanding. It is equally likely that our failure to distinguish between different models of the circumburst medium is due to the lack of early afterglow flux measurements, especially at millimeter and submillimeter wavelengths where the largest differences arise [35, 49]. The resolution of this conflict is important as it goes to the heart of the GRB progenitor question.

At sufficiently late times, when the rest mass energy swept up by the expanding shock becomes comparable to the initial kinetic energy of the ejecta (∼100 days), the expanding shock may slow to non-relativistic speeds [46]. A change in the temporal slope is expected at this time (Fig. 2) with $\alpha_{NR} = (21 - 15p)/10$ for a constant density medium, independent of geometry. This dynamical transition provides a simple and powerful method to derive the kinetic energy of the outflow which has expanded to be quasi-spherical at this time. In contrast, most energy estimates made at early times require knowledge of the *geometry* of the outflow [8, 10, 36]. Using the late-time radio light curves and the robust Taylor-Sedov formulation for the dynamics we can infer quantities such as the kinetic energy, ambient density, magnetic field strength, and the size of the fireball. The radius can be checked for consistency with the equipartition radius and the interstellar scintillation radius. This method has been used for GRB 970508 [17] and for GRB 980703 (Berger, private communication), yielding energies of order $few \times 10^{50}$ erg, in agreement with other estimates.

Finally, the radio light curves at late times may flatten due to the presence of an underlying host galaxy. Most GRBs studied to date have optical/NIR hosts but only about 20% have been seen at centimeter and submillimeter wavelengths [3, 6, 21]. This radio emission, if produced by star formation, implies star formation rates SRF~ 500 $M_\odot$ yr^{-1} and $L_{bol} > 10^{12}$ $L_\odot$, clearly identifies these GRB hosts as ultraluminous starburst galaxies which are all but obscured by dust at optical wavelengths. This is an emerging area with great potential for studying cosmic star formation with a sample of galaxies selected quite differently than other methods. Preliminary studies have already shown that GRB-selected galaxies are significantly bluer than other radio-selected samples [6].

Acknowledgement. DAF would like to thank his many collaborators in the radio afterglow network, especially Shri Kulkarni and Edo Berger.

References

1. C. Akerlof et al. : Nature **398**, 400 (1999)

2. E. Berger et al. : Astrophys. J. **545**, 56 (2000)
3. E. Berger, S. Kulkarni, D.A. Frail: Astrophys. J. **560**, 652 (2001)
4. E. Berger et al. : Astrophys. J. **556**, 556 (2001)
5. E. Berger et al. : Astrophys. J. **581**, 981 (2002)
6. E. Berger et al. : Astrophys. J. **588**, 99 (2003)
7. E. Berger et al. : Astrophys. J. Lett. **587**, L5 (2003)
8. E. Berger, S.R. Kulkarni, D.A. Frail: Astrophys. J. **590**, 379 (2003)
9. E. Berger et al. : astro-ph 0307228
10. J.S. Bloom, D.A. Frail, S.R. Kulkarni: astro-ph 0302210
11. R.A. Chevalier: Astrophys. J. **511**, 798 (1999)
12. R.A. Chevalier, Z. Li: Astrophys. J. **536**, 195 (2000)
13. Z.G. Dai, T. Lu: Astrophys. J. **537**, 803 (2000)
14. S.G. Djorgovski et al. : Astrophys. J. **562**, 654 (2001)
15. E.D. Feigelson, P.I. Nelson: Astrophys. J. **293**, 192 (1985)
16. D.A. Frail et al. : Nature **389**, 261 (1997)
17. D.A. Frail, E. Waxman, S.R. Kulkarni: Astrophys. J. **537**, 191 (2000)
18. D.A. Frail et al. : Astrophys. J. Lett. **538**, L129 (2000)
19. D.A. Frail et al. : In *AIP Conf. Proc. 526: Gamma-ray Bursts, 5th Huntsville Symposium*, p. 298 (2000)
20. D.A. Frail et al. : Astrophys. J. Lett. **562**, L55 (2001)
21. D.A. Frail et al. : Astrophys. J. **565**, 829 (2002)
22. D.A. Frail et al. : Astrophys. J. **590**, 992 (2003)
23. D.A. Frail et al. : Astron. J. **125**, 2299 (2003)
24. J.U. Fynbo et al. : Astron. Astrophys. **369**, 373 (2001)
25. J. Goodman: New Astron. **2 (5)**, 449 (1997)
26. T.J. Galama et al. : Astrophys. J. Lett. **541**, L45 (2000)
27. T.J. Galama et al. : Astrophys. J. **585**, 899 (2003)
28. F.A. Harrison et al. : Astrophys. J. Lett. **523**, L121 (1999)
29. F.A. Harrison et al. : Astrophys. J. **559**, 123 (2001)
30. K. Hurley et al. : Astrophys. J. **567**, 447 (2002)
31. J.L. Katz, T. Piran: Astrophys. J. **490**, 772 (1997)
32. S.R. Kulkarni et al. : Nature **395**, 663 (1998)
33. S.R. Kulkarni et al. : Astrophys. J. Lett. **522**, L97 (1999)
34. P. Mészáros: Ann. Rev. Astron. Astrophys. **40**, 137 (2002)
35. A. Panaitescu, P. Kumar: Astrophys. J. **543**, 66 (2000)
36. A. Panaitescu, P. Kumar: Astrophys. J. **554**, 667 (2001)
37. A. Panaitescu, P. Kumar: Astrophys. J. **571**, 779 (2002)
38. L. Piro et al. : Astrophys. J. **577**, 680 (2002)
39. P.A. Price et al. : Astrophys. J. Lett. **572**, L51 (2002)
40. J.E. Rhoads: Astrophys. J. **525**, 737 (1999)
41. B.J. Rickett: Ann. Rev. Astron. Astrophys. **28**, 561 (1990)
42. R. Sari, T. Piran: Astrophys. J. Lett. **517**, L109 (1999)
43. R. Sari, T. Piran, J.P. Halpern: Astrophys. J. Lett. **519**, L17 (1999)
44. A.M. Soderberg, E. Ramirez-Ruiz: astro-ph 0210524
45. E. Waxman, S.R. Kulkarni, D.A.Frail: Astrophys. J. **497**, 288 (1998)
46. R.A.M.J. Wijers, M.J. Rees, P. Mészáros: Mon. Not. R. Astron. Soc. **288**, L51 (1997)
47. R.A.M.J. Wijers: In *Gamma-ray Bursts in the Afterglow Era* p. 306 (2001)
48. S.A. Yost et al. : Astrophys. J. **577**, 155 (2002)
49. S. Yost et al. : astro-ph 0307056
50. J. in' t Zand et al. : Astrophys. J. **559**, 710 (2001)

Gamma-ray Bursts

Alberto J. Castro-Tirado

Instituto de Astrofísica de Andalucía (IAA-CSIC), P.O. Box 03004, 18080 Granada, Spain;
ajct@iaa.es

Summary. Since their discovery in 1967, Gamma-ray bursts (GRBs) have been puzzling to astrophysicists. With the advent of a new generation of X–ray satellites in the late 90's, it was possible to carry out deep multi-wavelength observations of the counterparts associated with the long duration GRBs class just within a few hours of occurrence, thanks to the observation of the fading X-ray emission that follows the more energetic gamma-ray photons once the GRB event has ended. The fact that this emission (the afterglow) extends at longer wavelengths, led to the discovery of optical/IR/radio counterparts in 1997-2003, greatly improving our understanding of these sources. The classical, long duration GRBs, have been observed to originate at cosmological distances in a range of redshifts with $0.1685 \leq z \leq 4.50$ implying energy releases of $\sim 10^{51}$ ergs. The recent results on GRB 021004 and GRB 030329 confirm that the central engines that power these extraordinary events are due to be collapse of massive stars rather than the merging of compact objects as previously also suggested. Short GRBs still remain a mystery as no counterparts have been detected so far.

1 Introduction

In 1967-73 the four VELA spacecraft, that where originally designed for verifying whether the former Soviet Union abided by the Limited Nuclear Test Ban Treaty of 1963, observed 16 peculiarly strong events [6, 39]. On the basis of arrival time differences, it was determined that they were related neither to the Earth nor to the Sun, but they were of cosmic origin. Therefore they were named cosmic Gamma-Ray Bursts (GRBs hereafter). Nearly 4000 events have been detected to date.

2 Observational Facts and Implications

2.1 GRBs in the Gamma-ray Domain

GRBs appear as brief flashes of cosmic high energy photons, carrying the bulk of their energy above ≈ 0.1 MeV (Fig. 1). The KONUS instrument on *Venera 11* and *12* gave the first indication that GRB sources were isotropically distributed in the sky [3, 44]. Based on a much larger sample, this result was

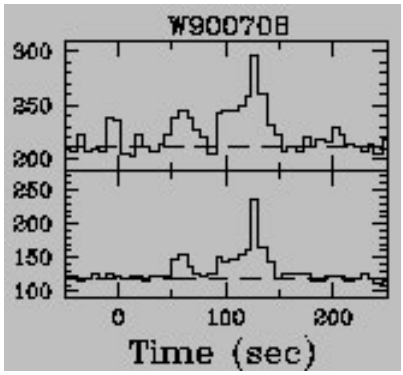

Fig. 1. One of the typical long-duration GRBs detected by WATCH on *GRANAT*, lasting for about 150-s in the 8-20 keV range (above) and in the 20-60 keV range (below). From [42].

nicely confirmed by BATSE on board the *CGRO* satellite [45]. In general, there was no evidence of periodicity in the time histories of GRBs. However there was indication of a bimodal distribution of burst durations, with ∼25% of bursts having durations around 0.2 s (the short/hard GRB class) and ∼75% with durations around 30 s (the long/soft GRB class). A deficiency of weak events was noticed in the log N-log S diagram, as the GRB distribution deviates from the -3/2 slope of the straight line expected for an homogeneous distribution of sources assuming an Euclidean geometry. However, the GRB distance scale had to remain unknown for 30 years. A comprehensive review of these observational characteristics can be seen in [22].

2.2 Long-duration GRBs in the Electromagnetic Spectrum

It was well known that an important clue for solving the GRB puzzle was going to be the detection of transient emission -at longer wavelengths- associated with the bursts. A review on the unsuccessful search for counterparts prior to 1997 can be seen in [10] and references therein.

Solving the Distance Scale

After the discovery of the first X-ray and optical afterglows (OA) for GRB 970228 detected by *BeppoSAX* [18, 67], the second OA associated to a GRB was detected within the GRB 970508 error box [5, 52]. The GRB 970508 OA light curve reached a peak in two days (R = 19.7, [21]) and was followed by a power-law decay F $\propto t^{-1.2}$ [11]. Optical spectroscopy obtained during the maximum allowed a direct determination of a lower limit for the redshift of GRB 970805 ($z \geq 0.835$), implying an isotropic energy release E $\geq 7 \times 10^{51}$ erg [47]. It was the first proof that GRB sources lie at cosmological

distances. The flattening of the decay in late August 1997 [52, 62] revealed the contribution of a constant brightness source -the host galaxy- that was revealed in late-time imaging obtained in 1998 [7, 12, 70]. The maximum observed 1-day after the burst has not been detected in other GRBs so far and it was interpreted by a delayed energy injection or by an axially symmetric jet surrounded by a less energetic outflow [51]. The luminosity of the galaxy is well below the knee of the galaxy luminosity function, L $\approx 0.12\ L^*$, and the detection of deep Mg I absorption (during the bursting episode) and strong [O II] 3727 Å emission (the latter mainly arising in H II regions within the host galaxy) confirmed $z = 0.835$ and suggested that the host could be a normal dwarf galaxy [53], with a star formation rate (SFR) of $\sim 1.0\ M_\odot\ \mathrm{year}^{-1}$ [7]. Prompt observations at cm and mm wavelengths led to the detection of the counterpart at these wavelengths [8, 23, 56]. The fluctuations could be the result of strong scattering by the irregularities in the ionized Galactic interstellar gas, with the damping of the fluctuations with time indicating that the source expanded to a significantly larger size. However VLBI observations did not resolve the object [66]. A Fe Kα line redshifted at $z = 0.835$ in the X-ray afterglow spectrum [54] was attributed to a thick torus of material surrounding the central engine [46].

About 35 host galaxies for classical, long duration GRBs, have been detected so far, in the range $0.1685 \leq z \leq 4.50$ (if ESO 184-G82 is excluded). None of the hosts are brighter than the knee of the luminosity function L^* at their redshift, but the GRB hosts are noticeable bluer than typical galaxies of similar magnitude [63].

The Existence of Collimated Emission

GRB 990123 was the first event for which contemporaneous optical emission was found simultaneous to the gamma-ray burst, reaching V $\sim$ 9 [1]. This optical flash did not track the gamma-rays and did not fit the extrapolation of the *BeppoSAX* and BATSE spectra towards longer wavelengths. This optical emission was interpreted as the signature of a reverse shock moving into the ejecta [60]. A brief radio transient was also detected [24] coincident with the optical counterpart [49] and spectroscopy indicated z = 1.599 [2]. A break observed in the light curve $\sim$ 1.5 days after the high energy event suggested the presence of a beamed outflow [13, 25, 41], thus reducing the energy release by $\sim 10^2$. A weak magnetic field in the forward shock region could account for the observed multiwavelength spectrum in contrast to the high-field magnetic field for GRB 970508 and it seems that the emission from the three regions was first seen in this event [28]: the internal, reverse and forward shocks.

Further support for a jet-like outflow came for GRB 990510, the first burst for which polarized optical emission was detected ($\Pi = 1.7 \pm 0.2$ %, [19, 68]). This confirmed the synchrotron origin of the blast wave itself and represented another case for a jet-like outflow [64], as has been later seen in other events.

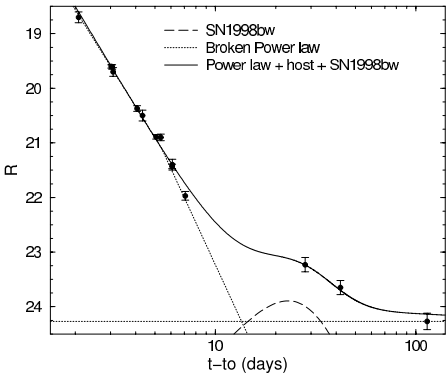

Fig. 2. The GRB 991208 R-band light curve (solid line) fitted with a SN1998 bw-like component at $z = 0.706$ (long dashed line) superposed to the broken power-law OA light curve displaying the second break at $t_{break} \sim 5$ *d* (with $\alpha_1 = -2.3$ and $\alpha_2 = -3.2$, short dotted lines) and the constant contribution of the host galaxy (R = 24.27 ±0.15, dotted line). From [15].

Dark GRBs

Following the unsuccessful search for an OA for GRB 970111 [9], intensive work was conducted for GRB 000210, a burst that was followed up by *CHANDRA*. The fact that no OA was detected despite of deep optical searches down to R $\sim$ 23.5 implied to classify the event as a another "dark" GRB. A constant brightness optical counterpart (R = 23.5, [32]) was coincident with the 1.6″ error box derived by *CHANDRA* [30] implying that this was the likely host galaxy. A radio transient was discovered with the VLA and from the X-ray spectrum, it was derived that either the gas is local to the GRB or that the gas is located in a dusty, gas-rich region of the galaxy [55], which is observed to harbor considering star formation [33].

In at least another three cases (GRB 981226, GRB 990506 and GRB 001109), radio transients were detected without accompanying optical/IR transients.The observed fraction of dark GRBs detected so far is $\sim$ 40%. This could be due to intrinsic faintness because of a low density medium, high absorption in a dusty environment, or Lyman limit absorption in high redshift galaxies (z > 7). If GRBs are tightly related to star-formation, a substantial fraction of them should occur in highly obscured regions. For instance, most of star formation in the Hubble Deep Field is so enshrouded by dust that starlight from the galaxies detected by SCUBA is attenuated by a factor of $\sim 10^2$ [38].

The Detection of X-ray Lines

The GRB 011211 (at z = 2.14), displayed rapid variations in the R-band light curve approximately 0.5 days after the burst, suggesting that they were

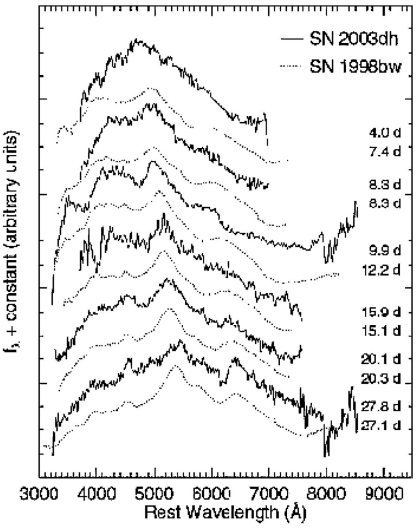

Fig. 3. Spectral evolution of the combined GRB 030329, the associated SN 2003dh and its host galaxy (no reddening correction applied). The lower spectra, dominated by SN 2003dh, reveals the typical broad-band SN signatures. To ease comparison, the spectrum of SN 1998bw at 33 days after the explosion is shown at the GRB 030329 redshift. From [36].

due to density fluctuations near the central engine on spatial scales of approximately 40-125 AU [37]. The early afterglow spectrum was obtained by *XMM-Newton*, which observed 11 hours after the initial burst, and appeared to reveal decaying H-like K emission lines of Mg, Si, S, Ar and Ca, arising in enriched material with an outflow velocity of order ~ 0.1c [57]. This was attributed to matter ejected from a massive stellar progenitor occurring shortly before the burst itself. Thermal emission, from an optically thin plasma, is the most plausible model that could account for the soft X-ray emission. The X-ray spectrum evolved with time over the first 12 ksec, suggesting that thermal emission dominated the early afterglow spectrum, whilst a power-law component dominated the latter stages. This implies that the progenitor of the GRB was a massive star and that the mass of the ejected material in GRB 011211 was estimated to be $\sim$ 4-20 $M_{\odot}$ [58].

The GRB-SN Connection

A peculiar Type Ic supernova (SN 1998bw) was found in the error box for the soft GRB 980425 by Galama et al. [27]. The SN lies was associated to the galaxy ESO 184-G82, an actively star forming SBc sub-luminous galaxy at $z = 0.0085$. The fact that the SN event occurred within $\pm$ 1 day of the GRB event, together with the relativistic expansion speed derived from the

The total energy released would be 8×10^{47} erg which is about $\sim 10^5$ smaller than derived for "classical" GRBs. Follow-up *HST* observations of ESO 184-G82 2.1 yr after the event, revealed an object consistent with being a point source within the astrometric uncertainty of $0.018''$ of the SN position. The object is located inside a star- forming region and is at least one magnitude brighter than expected for the SN based on a simple radioactive decay model, implying either a significant flattening of the light curve or a contribution from an underlying star cluster [26].

Independently, Castro-Tirado and Gorosabel [14] and Bloom et al. [4] also suggested the presence of an underlying SN in GRB 980326. Reichart [59] also proposed that a type Ib/c supernova lay "behind" another GRB (GRB 970228), overtaking the light curve two weeks after. This fact seems to be confirmed by a following work [29]. Further evidences have been found for another bursts [15, 20, 31, 34, 43]. See Fig. 2.

For GRB 021004, at least seven absorption line complexes spanning a velocity range of about 3000 km/s were found in the vicinity of the host galaxy, at z = 2.33 [16]. This observational evidence was interpreted as the presence of a multiple shell structure formed by the winds around the massive star progenitor, which it is thought to have been a Wolf-Rayet star [16, 48, 61].

GRB 030329 is the nearest classical, long duration GRB detected so far, at z = 0.1685. Due to its proximity, spectroscopic campaigns started already 1 day after the event, which led to the detection of SN absorption features superposed on the power-law OA spectrum. These signatures increased with time and resembled remarkably those of the SN1998bw/GRB 980425 spectrum. Thus, in spite of no optical bump being present in the optical/NIR light curve [35], the underlying object was dubbed SN2003dh (type Ic) [65] and from VLT spectroscopy, a photospheric expansion velocity of ~ 0.1c one week after the GRB was derived [36], comparable to the value found for SN1998bw. This event is therefore considered as the smoking gun that has allowed to definitively connect the collapse of massive stars with the long-duration GRBs, as was already proposed in 1974 [17] amongst the more than 100 theoretical models for explaining their origin.

It is possible then, in these powerful supernovae also dubbed "hypernovae" [50], that the explosions will be asymmetric and we are observing the GRB produced by a relativistic jet propagating along the rotation axis of the massive progenitor [69].

Acknowledgement. I am very grateful to M. E. Alcoholado-Feltström for her continuous support. This work has been partially financed by the Spanish Ministerio de Ciencia y Tecnología research project PNAYA 2002-0802, which makes use of the EU FEDER funds.

References

1. C. Akerloff et al. : Nature **398**, 400 (1999)
2. M. Andersen et al. : Science **283**, 2075 (1999)
3. J.-L. Atteia et al. : Astrophys. J. Suppl. **64**, 305 (1987)
4. J.S. Bloom et al. : Nature **401**, 453 (1999)
5. H. Bond: IAUC 6655 (1997)
6. J.T. Bonnell, R.W. Klebesadel: In: *Gamma-Ray Bursts, 3rd Huntsville Workshop*. ed. C. Kouveliotou et al. (AIP 384, 1996) p. 977
7. J.S. Bloom et al. : Astrophys. J. Lett. **507**, L25 (1998)
8. M. Bremer et al. : Astron. Astrophys. **332**, L13 (1998)
9. A.J. Castro-Tirado et al. : IAUC 6598 (1997)
10. A.J. Castro-Tirado: In: *Ultraviolet Astrophysics: Beyond the IUE Final Archive*. ed. R. Gonzalez-Riestra et al. (ESA Conf. Proc. SP-413, 1998) p. 659.
11. A.J. Castro-Tirado et al. : Science **279**, 1011 (1998)
12. A.J. Castro-Tirado et al. : IAUC 6848 (1998)
13. A.J. Castro-Tirado et al. : Science **283**, 2069 (1999)
14. A.J. Castro-Tirado, J. Gorosabel: Astron. Astrophys. Suppl. **138**, 449 (1999)
15. A.J. Castro-Tirado et al. : Astron. Astrophys. **370**, 398 (2001)
16. A.J. Castro-Tirado et al. : In preparation
17. S.A. Colgate: Astrophys. J. **187**, 333 (1974)
18. E. Costa et al. : Nature **387**, 783 (1997)
19. S. Covino et al. : Astron. Astrophys. **348**, L1 (1999)
20. M. Della Valle et al. : Astron. Astrophys. **406**, L33 (2003)
21. S.G. Djorgovski et al. : Nature **387**, 876 (1997)
22. G.J. Fishman, C.A. Meegan: Ann. Rev. Astron. Astrophys. **33**, 415 (1995)
23. D.A. Frail et al. : Nature **389**, 261 (1997)
24. D. Frail et al. : GCN 211 (1999)
25. A. Fruchter et al. : Astrophys. J. Lett. **519**, L13 (1999)
26. J.P. Fynbo et al. : Astrophys. J. Lett. **542**, L89 (2000)
27. T. Galama et al. : Nature **395**, 670 (1998)
28. T. Galama et al. : Nature **398**, 394 (1999)
29. T. Galama et al. : Astrophys. J. **536**, 185 (2000)
30. M. Garcia et al. : GCN 548 (2000)
31. P.M. Garnavich et al. : Astrophys. J. **582**, 924 (2003)
32. J. Gorosabel et al. : GCN 783 (2000)
33. J. Gorosabel et al. : Astron. Astrophys. **400**, 127 (2003)
34. J. Greiner et al. : Astrophys. J., in press
35. S. Guziy et al. : In preparation
36. J. Hjorth et al. : Nature **423**, 847 (2003)
37. S.T. Holland et al. : Astron. J. **124**, 639 (2002)
38. D.H. Hughes, J.S. and Dunlop: In: *Highly Redshifted Radio Lines*. eds. C.L. Carilli et al. (ASP Conf. Series 156, 1999) p. 99
39. R. Klebesadel, I. Strong, R. Olson: Astrophys. J. Lett. **182**, L85 (1973)
40. S. Kulkarni et al. : Nature **395**, 663 (1998)
41. S. Kulkarni et al. : Nature **398**, 389 (1999)
42. N. Lund, S. Brandt, A.J. Castro-Tirado: In: *Gamma-Ray Bursts, 1st Huntsville Workshop*. eds. G.J. Fishman et al. (1992) p. 53
43. N. Masetti et al. : Astron. Astrophys. **404**, 465 (2003)

44. E.P. Mazets et al. : Astrophys. Space Sci. **80**, 3 (1981)
45. C.A. Meegan et al. : Nature **355**, 143 (1992)
46. P. Mészáros, M.J. Rees: Mon. Not. R. Astron. Soc. **299**, L10 (1998)
47. M.R. Metzger et al. : Nature **387**, 878 (1997)
48. N. Mirabal et al. : astro-ph 0303616 (2003)
49. S.C. Odewahn et al. : GCN 201 (1999)
50. B. Paczyński: Astrophys. J. Lett. **494**, L45 (1998)
51. A. Panaitescu, P. Mészáros, M.J. Rees: Astrophys. J. Lett. **503**, L314 (1998)
52. H. Pedersen et al. : Astrophys. J. **496**, 311 (1998)
53. E. Pian et al. : Astrophys. J. Lett. **492**, L103 (1998)
54. L. Piro et al. : Astrophys. J. Lett. **514**, L73 (1999)
55. L. Piro et al. : Astrophys. J. **577**, 680 (2002)
56. G. Pooley, D. Green: IAUC 6670 (1997)
57. J.N. Reeves et al. : Nature **416**, 512 (2002)
58. J.N. Reeves et al. : Astron. Astrophys. **403**, 463 (2003)
59. D. Reichart: Astrophys. J. Lett. **521**, L111 (1999)
60. R. Sari, T. Piran: Astrophys. J. Lett. **520**, L641 (1999)
61. B.E. Schaefer et al. : Astrophys. J. **588**, 387 (2003)
62. V.V. Sokolov et al. : Astron. Astrophys. **334**, 117 (1998)
63. V.V. Sokolov et al. : Astron. Astrophys. **372**, 438 (2001)
64. K.Z. Stanek et al. : Astrophys. J. Lett. **522**, L39 (1999)
65. K.Z. Stanek et al. : Astrophys. J. Lett. **591**, L17 (2003)
66. G.B. Taylor et al. : Nature **389**, 263 (1997)
67. J. van Paradijs et al. : Nature **386**, 686 (1997)
68. R.A.M.J. Wijers et al. : Astrophys. J. Lett. **523**, L33 (1999)
69. S.E. Woosley: Astrophys. J. **405**, 273 (1993)
70. S.V. Zharikov, V.V. Sokolov, Yu.V. Barishev: Astron. Astrophys. **337**, 356 (1998)

X-ray Emission from Gamma-Ray Bursts

Filippo Frontera[1,2]

[1] University of Ferrara, Physics Dept., Via Paradiso 12, 44100 Ferrara, Italy;
frontera@fe.infn.it
[2] Istituto Astrofisica Spaziale e Fisica Cosmica, INAF, Via Gobetti, 101, 40129 Bologna, Italy
frontera@bo.iasf.cnr.it

Summary. In this paper I will present and discuss some of the relevant results obtained with the Italian satellite *BeppoSAX* on the prompt and afterglow emission of Gamma Ray Bursts (GRBs).

1 Introduction

After about 30 years of mystery, the distance scale issue of Gamma Ray Bursts (GRBs) has been definitely settled thanks to the X–ray astronomy mission *BeppoSAX*, an Italian satellite with Dutch participation [7]. *BeppoSAX* not only has permitted this issue to be resolved but has also provided most of the exciting results of the last seven years in GRB astronomy. The satellite, launched on 1996 April 30, was switched off on April 29, 2002, after 6 years of operational life. The high performance of *BeppoSAX* for GRB studies was due to a particularly well-matched configuration of its payload, with both wide field instruments (WFIs) and narrow field telescopes (NFTs).

After the exciting results obtained on GRBs in 1997 (e.g., [10, 11, 12, 15, 27, 31]), many other GRB events were discovered with *BeppoSAX* during its operational life: 1082 events were detected with the GRBM (catalog in preparation), 669 of them (corresponding to 62%) were recognized by the on-board logic and 413 (corresponding to 38%) were identified with the ground software. Light curves with high time resolution (up to 0.5 ms) are available only for the GRBs identified by the on-board logic, while for the other ones, only 1 s ratemeters are available. Of the 1082 events, 168 (corresponding to $\sim$ 16%) are short (<2 s) GRBs, 141 of which recognized by the on-board logic. The most outstanding results were obtained from the 51 GRBs which were simultaneously detected with the GRBM and WFCs, 37 of which were followed-up with the *BeppoSAX* NFTs. Gamma-ray fluence of these GRBs ranges from 1.9×10^{-4} erg cm^{-2} down to 2.5×10^{-7} erg cm^{-2}, while their duration is longer than 2 s ('long GRBs'). X-ray afterglows were discovered in $\sim$ 90% of the followed-on GRBs. However only $\sim$ 50% of the followed-up GRBs are detected in the optical band and $\sim$ 40% in the radio band. This lower rate raises the question about the origin of the so called "dark" GRBs (i.e., GRBs with no optical counterparts). Likely some of them have origin in stellar formation regions with high mass densities, which likely absorb the

ultraviolet radiation (in the rest frame of the GRB source). However, many of the dark GRBs could have origin in galaxies at very high redshifts (>5). In these cases the darkness is due to the absorption of the optical radiation by the intergalactic hydrogen.

2 Some Highlight Results

I will summarize here some of the most relevant results on GRBs obtained with *BeppoSAX*. They concern both the prompt GRB phenomenon, the afterglow emission and the GRB environment.

2.1 Prompt Emission Spectra

Thanks to the broad energy band (2–700 keV) covered by WFCs plus GRBM, *BeppoSAX* has allowed un unbiased determination of the prompt emission spectra. We found [2] that most of the time averaged spectra are well fit, down to 2 keV, with a smoothly broken power-law proposed by Band et al. [6]. In the remaining cases a simple power-law fits the data. In many cases ($\sim 70\%$) an optically thin synchrotron shock model (OTSSM) [39] fits the data. A confirmation of this result comes from the recent polarization measurement of the prompt emission from GRB021206 [9].

A more constraining test of the emission mechanism is the study of the spectral evolution of the GRB prompt emission. This investigation shows [16, 20] that there is a general evolution of the spectra, from hard to soft, except for the most intense events, whose hardness either mimics the GRB time profile (e.g., GRB990123) or does not evolve with time (e.g., GRB011121) [20]. A clear example of the hard-to-soft spectral evolution is given in Fig. 1, which shows the $EF(E)$ spectra of GRB970111 in the 10 contiguous time intervals (from A to J) in which we subdivided the GRB time profile. As it can be seen, the fit with an OTSSM is acceptable for the almost the entire duration, except at early times. This property has been found in several GRBs and shows that at early times some other emission mechanism (likely Inverse Compton, as discussed by Frontera et al. [16]) is at work.

2.2 Afterglow Spectra

In general, the late afterglow spectra, at least in the time interval during which the X–ray observations are possible, are consistent with a power law ($I(E) \propto E^{-\Gamma}$) with a photon index Γ distributed according to a Gaussian function with mean value $\Gamma_m = 1.93$ and standard deviation $\sigma = 0.35$ [18]. The emission mechanism is likely synchrotron radiation at least in some cases (e.g., GRB970508 [21]), but in other cases a synchrotron self Compton mechanism appears to be at work (e.g., GRB000926 [23]). This mechanism implies

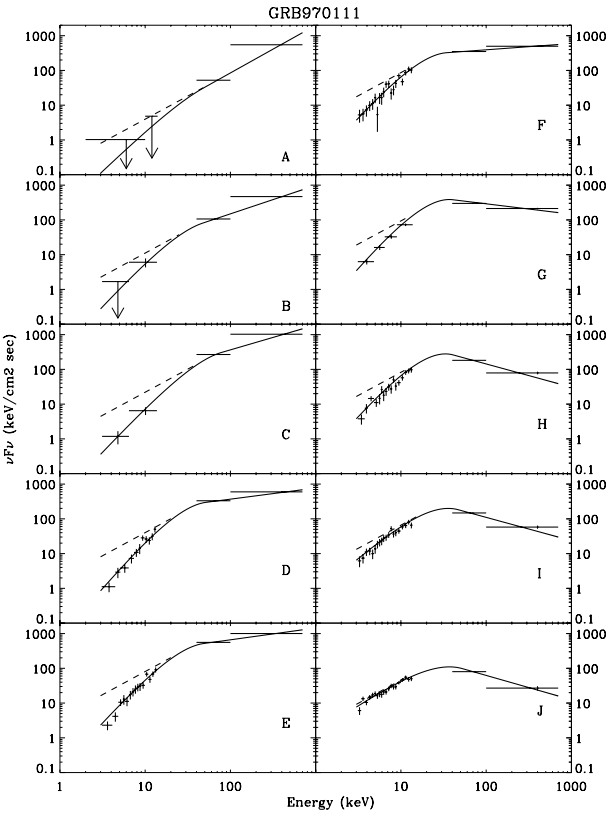

Fig. 1. $EF(E)$ spectrum of the GRB970111 prompt emission in the 10 contiguous time intervals (from A to J) in which the GRB time profile was subdivided. The GRB time duration in gamma–rays is 47 s. The dashed line shows the maximum spectral slope which can be expected, below the energy peak, in the case of the OTSSM. The continuous line shows the best fit with a Band function. Reprinted from Frontera et al. [16].

a medium denser than a typical interstellar medium in the X–ray production region. In the case of GRB000926, the inferred mass density is about 30 cm^{-3}. Multiwavelength spectra, from the radio to X–rays, are crucial to establish the emission mechanisms at work.

Recently also thermal models have been found to better fit the X–ray afterglow spectra of a few GRBs observed with the *XMM–Newton* and *Chandra* X–ray satellites: GRB001025A [41], GRB011211[34, 35], and GRB020813 [8]. In these cases an emitting plasma in collisional ionization equilibrium gives the best description of the data.

2.3 Fading Law of the Afterglow Emission and Its Geometry

In general, in the time intervals in which the X–ray observations have been possible, we find a consistency of the fading law of the X–ray afterglow emission with a single power–law ($F(t) \propto t^{-\delta}$), with distribution of the power-law index δ consistent with a Gaussian with centroid $\delta_m = 1.33$ and standard deviation $\sigma = 0.33$ [18]. However, specially in the optical band, breaks in the afterglow light curves of several GRBs have been observed [14]. These breaks, in some cases, are also visible in the X–ray data, if the tail of the prompt X–ray emission is assumed to already be X–ray afterglow emission (e.g., GRB010222 [45]). In fact this assumption has been demonstrated to be true by Frontera et al. [16], who found a correlation between X–ray fluence of the tail of the prompt emission and that of the late afterglow. The fading breaks and their time of occurrence, within the statistical uncertainties, appear to be independent of the photon energies.

The interpretation of these achromatic breaks has been discussed by various authors (e.g., [36, 37]). In the framework of the fireball model, a break is expected to occur if the relativistically expanding material is concentrated within a cone with angular width θ_c. As long as the Lorentz factor γ of the out flowing material is larger than $1/\theta_c$, due to relativistic beaming, the radiation is emitted within an angle $\theta_b = 1/\gamma$ from the cone axis, with $\theta_b < \theta_c$. When γ drops below $1/\theta_c$, the observer begins to see the edge of the cone and then the effect of the collimated outflow: a light curve steepening. Assuming a jet geometry and a uniform distribution of the energy within the jet, from the available data, Frail et al. [14] found that the distribution of the released energy per GRB is centered at 5×10^{50} erg, a value almost compatible with the energy released in a supernova explosion.

From the time behavior of the X-ray afterglow light curves, we can infer only a lower limit to the jet angle. This is a few degrees, which is consistent with the lowest opening angles derived by Frail et al. [14]. A stronger constraint on the opening angle is now found by the polarization measurement of GRB021206: about 0.4 degrees [9].

2.4 The E_p vs. E_{rad} Relationship

An investigation devoted to search out correlations between parameters derived from the redshift–corrected energy spectra of GRBs with known redshift has permitted us to discover [3] a power–law relation between intrinsic peak energy E_p of the $\nu F(\nu)$ spectra and isotropic electromagnetic energy E_{rad} released in the GRB event:

$$E_p \propto E_{rad}^{0.52 \pm 0.06} \tag{1}$$

This relation is now confirmed [4] by more *BeppoSAX* and HETE-2 results (see Fig. 2). It puts strong constraints to the GRB emission models: independently of the radiation pattern geometry, the E_p vs. E_{rad} relation has to

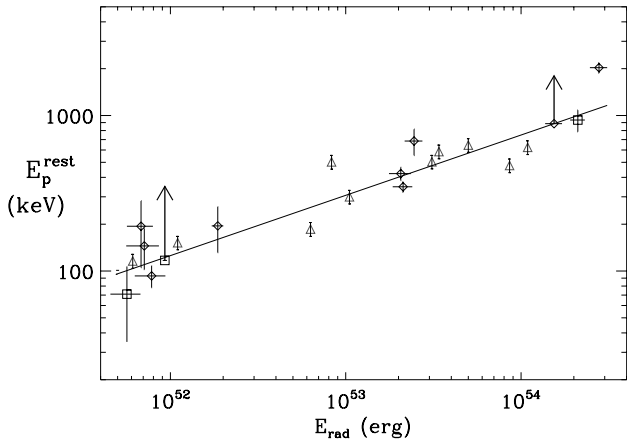

Fig. 2. Peak energy E_p of the redshift-corrected energy $EF(E)$ spectra of GRBs with known redshift as a function of the isotropic gamma–ray energy released during prompt emission. Reprinted from Amati [4].

be satisfied. The optically thin synchrotron shock model expects a similar relation, but only with too simplified assumptions, like the same duration of all GRBs [26]. A discussion on the possible interpretations of the above relation is given by Zhang and Mészáros [46] within the internal and external shock scenario.

2.5 The GRB Environment

Two main probes of the GRB environment are offered by the X–ray data: detection of absorption cutoffs in the GRB continuum spectra of the prompt and/or afterglow emission, detection of emission and/or absorption spectral features. Both these probes not only give information on the circumburst environment, but are an important tool to unveil the nature of the GRB progenitors.

Time variable $N_{\rm H}$ have been discovered in the prompt emission of 4 GRBs: GRB980329 [16], GRB990705 [1], and GRB000528 [20] and GRB010214 [22]. Also in the case of the X–ray afterglow emission, evidence of a hydrogen column density higher than that Galactic one, has been reported for GRB980329 [44], GRB980703 [40] and GRB010222 [45].

Evidence of X-ray emission features has been found in the afterglow spectra of 8 GRBs. The lines found with *BeppoSAX* concern 2 GRBs (970508 [32], and 000214 [5]), those found with *Chandra* concern GRB991216 [33] and GRB020813 [8], while those found with *XMM–Newton* concern GRB001025A, [41], GRB011211 [34, 35] and GRB030227 [42]. A line from GRB970828 [43] was detected with the Japanese X–ray satellite *ASCA*. Independently of the specific identification, all the detected lines point to the presence of ionized

metals at the time of the afterglow measurements, with the ionizing radiation likely being due to the GRB power output. The relative metal abundance inferred for the lines is very large: about 10 in the case of the light metals (e.g., [8]), values ≥ 60 in the case of Iron (e.g., [33]). Thus X-ray lines rule out the NS merger models and strongly point to an environment typical of a young supernova explosion.

Evidence of transient X–ray absorption features in the prompt emission has been found for two events: GRB990705 [1] and GRB011211 [19]. The absorption feature from GRB990705 was interpreted by Amati et al. [1] as a cosmologically redshifted K edge due to neutral Fe around the GRB location, and by Lazzati et al. [25] as an absorption line due to resonant scattering of GRB photons on H-like Iron (transition 1s-2p, $E_{rest} = 6.927$ keV). In both scenarios, the observed feature points to the presence of an iron-rich environment.

In the case of the transient line feature from GRB011211, the scenario is much more complex. Given that the redshift of the GRB optical counterpart is known ($z = 2.14$), if the line feature is interpreted as due to resonant scattering of GRB photons off , e.g., H–like Ni XXVIII (rest frame energy of 8.1 keV), the measured line energy implies a very high blue-shift (by $0.75c$) of the absorbing material. A possible interpretation of the feature is discussed by Frontera et al. [19].

2.6 GRB-SN Connection

The conclusions of the last two sections strongly point to a connection between supernovae and GRBs. The most direct evidence of this connection has been recently obtained in the case of GRB030329/SN2003dh [24, 38]: nine days after the burst the optical afterglow spectrum of GRB030329 appears to be the superposition of a power-law continuum plus a spectrum consistent with that observed from Type Ic supernova SN1998bw, which was associated with GRB980425 [28] on the basis of a positional and temporal coincidence. Thus the GRB030329/SN2003dh connection has shed light also on the GRB980425/SN1998bw connection issue (see, e.g., [29] and references therein). On the basis of the results on GRB030329, also the connection of GRB980425 with SN1998bw appears strongly enforced. Also the recent *XMM–Newton* observation of SN1998bw enforces such connection. Indeed, combining the *XMM–Newton* data with the *BeppoSAX* data, the X-ray light curve of GRB980425/SN1998bw appears to be the superposition of two components, the GRB power–law fading emission plus the emission from a peculiar type Ic supernova [30].

3 Conclusions

In spite of the big step forward accomplished in the last 7 years after the discovery of the first X-ray afterglows, many questions about the GRB phenomenon are still open, which can only be answered with further X–ray observations. A thorough discussion of the open issues can be found elsewhere [18]. Many of these issues are expected to be settled in the coming years, mainly with the launch of the SWIFT satellite. But a relevant contribution is expected also to be given by INTEGRAL, AGILE, and GLAST satellites, and later by the LOBSTER experiment aboard the International Space Station.

References

1. L. Amati et al. : Science **290**, 953 (2000)
2. L. Amati et al. : In: *Gamma–Ray Bursts in the Afterglow Era,* ed. by E. Costa, F. Frontera, J. Hjorth (Springer: Berlin, Heidelberg, 2001) pp. 34-36
3. L. Amati et al. : Astron. Astrophys. **390**, 81 (2002)
4. L. Amati: In: *Proc. of the Frascati Workshop on Multiwavelength observations of Cosmic X–ray Sources*, ed. by F. Giovannelli, L. Sabau-Graziati (Chinese J. of Astron. Astrophys., in press)
5. L.A. Antonelli et al. : Astrophys. J. Lett. **545**, L39 (2000)
6. D. Band et al. : Astrophys. J. **413**, 281 (1993)
7. G. Boella et al. : Astron. Astrophys. Suppl. **122**, 299 (1997)
8. N.R. Butler, H.L. Marshall: astro-ph 0303539 (2003)
9. W. Coburn, S.E. Boggs: Nature **423**, 415 (2003)
10. E. Costa et al. : Nature **387**, 783 (1997)
11. D. Dal Fiume et al. : Astron. Astrophys. **355**, 454 (2000)
12. M. Feroci et al. : Astron. Astrophys. **332**, L29 (1998)
13. D.A. Frail et al. : Nature **389**, 261 (1997)
14. D.A. Frail et al. : Astrophys. J. **562**, L55 (2001)
15. F. Frontera et al. : Astron. Astrophys. **334**, L69 (1998)
16. F. Frontera et al. : Astrophys. J. Suppl. **127**, 59 (2000)
17. F. Frontera et al. : In: *Gamma Ray Bursts in the Afterglow Era*, ed. by E. Costa, F. Frontera, J. Hjorth (Springer: Berlin, Heidelberg, 2001) p. 106
18. F. Frontera: In: *Supernovae and Gamma–Ray Bursters*, ed. by K.W. Weiler (Springer: Berlin Heidelberg, 2003) pp. 317-342
19. F. Frontera et al. : Astrophys. J. submitted
20. F. Frontera et al. : In preparation
21. T.J. Galama et al. : Astrophys. J. Lett. **500**, L97 (1998)
22. C. Guidorzi et al. : Astron. Astrophys. **401**, 491 (2003)
23. F.A. Harrison et al. : Astrophys. J. **559**, 123 (2001)
24. J. Hjorth et al. : Nature **423**, 847 (2003)
25. D. Lazzati et al. : Astrophys. J. **556**, 471 (2001)
26. N.M. Lloyd et al. : Astrophys. J. **534**, 227 (2000)
27. M.R. Metzger et al. : Nature **387**, 878 (1997)
28. F. Patat et al. : Astrophys. J. **555**, 900 (2001)
29. E. Pian et al. : Astrophys. J. **536**, 778 (2000)

30. E. Pian et al. : In preparation
31. L. Piro et al. : Astron. Astrophys. **331**, L41 (1998)
32. L. Piro et al. : Astrophys. J. Lett. **514**, L73 (1999)
33. L. Piro et al. : Science **290**, 955 (2000)
34. J.N. Reeves et al. : Nature **416**, 512 (2002)
35. J.N. Reeves et al. : Astron. Astrophys. **403**, 463 (2003)
36. J.E. Rhoads: Astrophys. J. Lett. **487**, L1 (1997)
37. R. Sari, T. Piran, J.P. Halpern: Astrophys. J. Lett. **519**, L17 (1999)
38. K.Z. Stanek.: Astrophys. J. Lett. **591**, L17 (2003)
39. M. Tavani: Astrophys. J. **466**, 768 (1996)
40. P.M. Vreeswijk et al. : Astrophys. J. **523**, 171 (1999)
41. D. Watson et al. : Astron. Astrophys. **393**, L1 (2002)
42. D. Watson et al. : Astron. Astrophys. **595**, L29 (2003)
43. A. Yoshida et al. : Astron. Astrophys. Suppl. **,, 138** 433 (1999)
44. J.J.M. in't Zand et al. : Astrophys. J. Lett. **505**, L119 (2001)
45. J.J.M. in't Zand et al. : Astrophys. J. **559**, 710 (2001)
46. B. Zhang, P. Mészáros: Astrophys. J. **581**, 1236 (2002)

Particle Acceleration in Gamma-Ray Bursts

J.G. Kirk

Max-Planck-Institut für Kernphysik, Postfach 10 39 80, 69029 Heidelberg, Germany;
john.kirk@mpi-hd.mpg.de

Summary. Simple kinematic theories of particle acceleration at relativistic shocks lead to the prediction of a high-energy spectral index of -1.1 for the energy flux of synchrotron photons. However, several effects can change this picture. In this paper I discuss the effect of magnetic field generation at the shock front and, by analogy with the Crab Nebula, suggest that an intrinsic break in the injection spectrum should be expected where the electron gyro radius is comparable to that of protons thermalized by the shock.

1 Introduction

The process or processes which accelerate the particles responsible for the nonthermal emission observed in gamma-ray bursts and in their after-glows are still unknown. However, the only proposed mechanism with significant predictive power is the first-order Fermi process operating at a shock front. In nonrelativistic flows, this mechanism has been applied in a wide variety of astrophysical situations and has been the subject of considerable theoretical effort – with interest currently focused on nonlinear aspects [16]. The relativistic outflow from a gamma-ray burst, on the other hand, demands a different approach [11], which is able to account for the intrinsic anisotropy of the particle distribution functions. In this paper I briefly review the status of the relativistic theory, present some new calculations of test-particle acceleration in the presence of shock-generated magnetic field, and discuss the application of the process to the modeling of GRB after-glow spectra, stressing an analogy with models of the relativistic termination shock of the wind from the Crab pulsar.

2 Kinematics

The kinematic problem of particle acceleration at a relativistic shock, i.e., that of finding the distribution of a collection of test particles undergoing small-angle, random, elastic (in the plasma frame) deflections in the vicinity of a discontinuity in the (relativistic) plasma velocity is well-understood. An analytic method based on an eigenvalue decomposition is available which

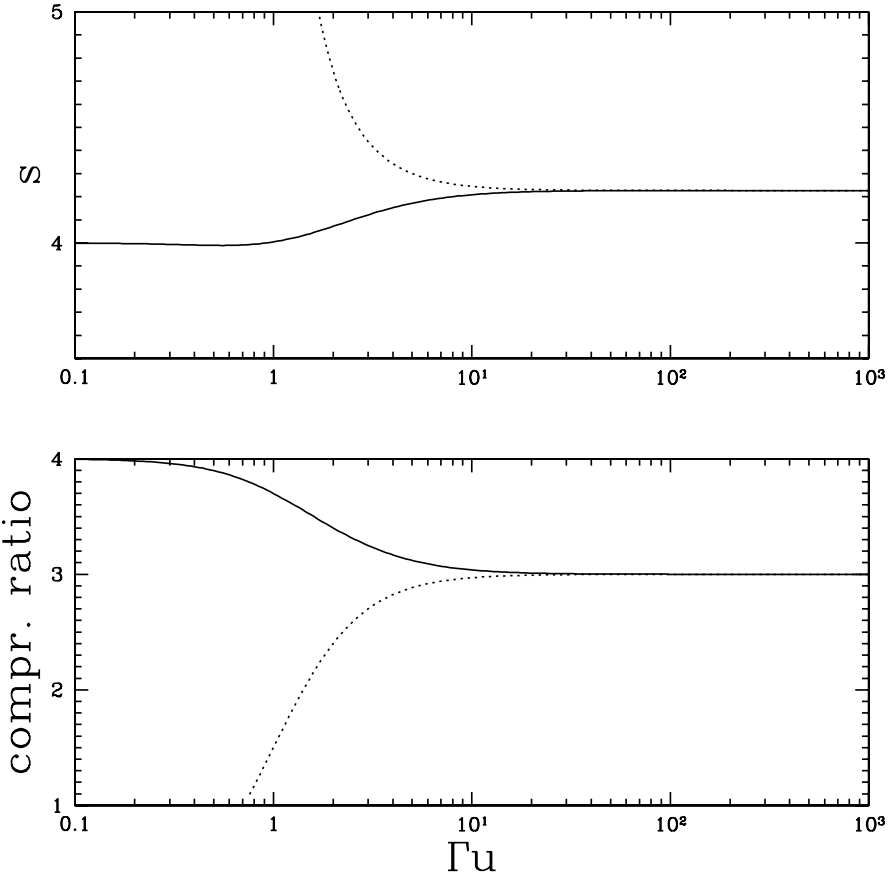

Fig. 1. The high-energy power-law index s (upper panel) and compression ratio (lower panel) as a function of the spatial component of the upstream four speed Γu. The dotted line refers to a shock in a gas with negligible rest-mass and the solid line to a strong shock (i.e., cold upstream medium) in an ideal gas with adiabatic index 5/3.

gives the spectrum and angular dependence of the distribution function at energies well above those of injection for arbitrary shock speeds [12]. In addition, Monte-Carlo simulations have been performed, finding results which are in good agreement with the analytic approach [1, 3]. These results are illustrated in Figs. 1 and 2. Well above the injection energy the phase-space density f is a power-law in momentum: $f \propto p^{-s}$ and at the shock front the angular dependence is well-approximated by the simple expression

$$f \propto (1-\mu_{\rm s}u)^{-s} \exp\left(-\frac{1+\mu_{\rm s}}{1-\mu_{\rm s}u}\right) \qquad (1)$$

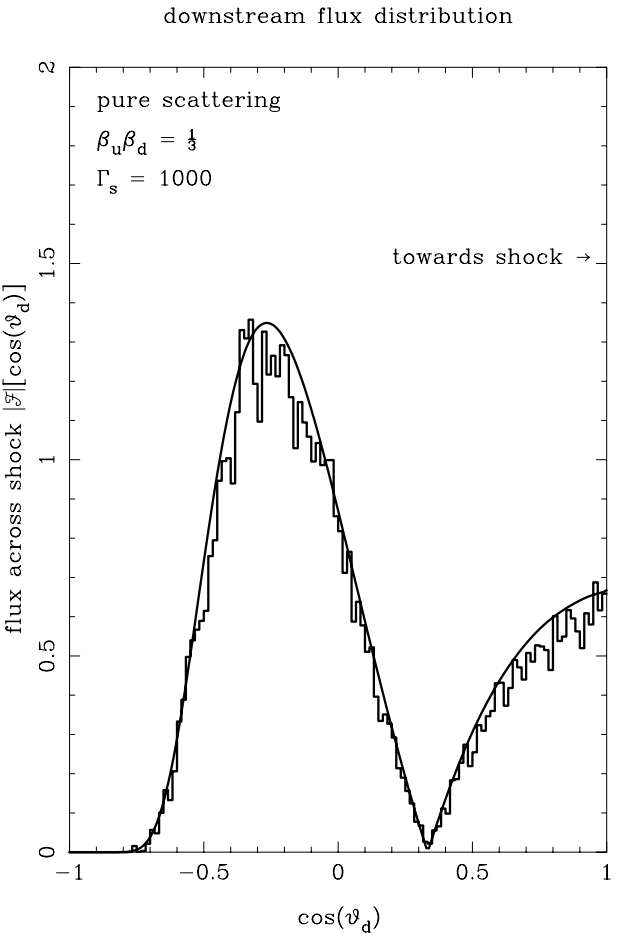

Fig. 2. A comparison (from [1]) between a Monte-Carlo simulation and the analytic result for the particle flux across a shock front as a function of the cosine of the angle θ_d between the particle velocity and the shock normal measured in the frame in which the downstream plasma is at rest. $\theta_d = 0$ corresponds to motion along the normal from downstream to upstream. Jump conditions for a relativistic gas are used and the upstream plasma has a Lorentz factor $\Gamma = 1000$.

where μ_s is the cosine of the angle between the shock normal and the particle velocity $c\boldsymbol{u}$ measured in the frame in which the shock is at rest and the upstream plasma flows along the shock normal. Fig. 1 shows the compression ratio and the high-energy power-law index s as a function of the spatial component of the 4-speed Γu of the upstream plasma, where $\Gamma = (1-u^2)^{-1/2}$.

For gamma-ray bursts, an interesting aspect of these results is that the power-law index tends asymptotically to the value $s \approx 4.23$ for large shock Lorentz factors (or, equivalently, upstream Lorentz factors), independent of

the equation of state of the plasma. This asymptotic value is essentially fixed by the compression ratio of the shock and depends only weakly on the form of the scattering operator used to describe the small-angle deflections [12].

There is an important difference between the scattering operator conventionally used in nonrelativistic theory and that used for relativistic shocks. The nonrelativistic picture assumes it is reasonable to define the trajectory of a particle between scatterings (the unperturbed motion) in terms of the motion of its guiding center. Scatterings cause a change in the pitch-angle, leading to the diffusion of particles along magnetic field lines. Cross-field diffusion is suppressed in this picture. However, as seen in the frame of the downstream medium, the magnetic field carried towards a shock by an upstream plasma flowing at high Lorentz factor appears to lie almost in the plane of the shock front. As a consequence, relativistic shocks are perpendicular shocks [4] which cannot be multiply crossed by particles diffusing along field lines. The first-order Fermi mechanism does not operate in this configuration unless cross-field diffusion is effective.

In a uniform field, a particle which crosses a relativistic shock front from downstream to upstream will be recaptured by the front after executing a fraction of roughly $\sim 1/\Gamma$ of a gyration. Thus, if scattering plays a role, it is reasonable to describe the unperturbed trajectory not as a helix, but as a straight line. This is especially true if, as expected (see next section), the field is highly nonuniform on the length scale of a gyro radius. In this case the role of the average field (if it exists) ceases to be important, and the description of the stochastic trajectory is in terms of deflections of the velocity, rather than changes in pitch angle. This is the form of operator used in the analytic approach. In Monte-Carlo treatments, it is possible to retain the effect of an average field [1, 18]. Provided the turbulence remains strong, little difference is found. However, as expected, the acceleration mechanism becomes less effective as the turbulence diminishes [19]. Explicit calculations of particle motion in a random magnetic field have also been performed [2, 5] and used to compute the acceleration around a relativistic shock for Lorentz factors $\Gamma \leq 5$ [2] and, more recently, for $\Gamma \leq 100$ [14]. The latter find good agreement with the analytic result on the asymptotic power-law index.

3 Nonlinear Effects and Magnetic Field Generation

In contrast with the situation in nonrelativistic shocks [16], the nonlinear modification of relativistic shock does not affect the asymptotic power-law index. There are two reasons for this: firstly, isotropized, accelerated particles behave like a relativistic gas with adiabatic index 4/3, so that the overall compression ratio of an ultra-relativistic shock front remains 3, even when a significant part of the overall energy and momentum flux is carried by these particles. Secondly, the asymptotic power-law index in the test-particle picture is soft (i.e., $s > 4$). This means that it is possible to consider a

Lorentz factor above which the test-particle approximation is valid, because the energy density in the remaining accelerated particles is indeed small. Nevertheless, a strong nonlinear effect can be exerted by particles of lower energies, whose mean free path to scattering is comparable to the size of internal structures in the shock transition [7].

Although there are strong indications that collisional processes may be important in the inner parts of a GRB fireball $r < 10^{16}$ cm [6, 23], the plasma responsible for the after-glow is probably best treated as collisionless. The most promising way of forming a relativistic shock in such a plasma is by the Weibel instability [17, 25, 26], which generates downstream magnetic field perpendicular to the streaming motion of the plasma i.e., in the plane of the incipient shock. A full simulation of this situation has not yet been performed, but recent 3D-PIC simulations of colliding plasma shells [8, 21, 22] suggest that magnetic field can be generated with a strength up to $\sigma \approx 1\%$. (Here the magnetization parameter σ is defined as the ratio of the magnetic energy density to twice the total enthalpy density (including rest mass) as measured in the plasma rest frame). This is encouraging, since it is roughly the level implied by spectral modeling [20] of GRB after-glows.

The spectrum of accelerated particles is certainly closely tied to the evolution of the turbulent magnetic field. However, if we are interested only in high energy particles of long mean free path, the power-law index predicted by the first-order Fermi mechanism can be calculated simply by modifying the shock jump conditions to account for the generated field. To do this, we consider time-averaged conditions, so that linear functions of the electromagnetic field vanish. The stress-energy tensor in the plasma frame is

$$T^{\mu\nu} = \left(w + \frac{B^2}{4\pi}\right) u^\mu u^\nu + \left(p + \frac{B^2}{8\pi}\right) g^{\mu\nu} - \frac{B^\mu B^\nu}{4\pi} \tag{2}$$

(for notation see [11]) and the last term on the right hand side does not contribute to the fluxes across the shock front if the magnetic field lies in the shock plane. As a result, the jump conditions are the same as those of an unmagnetized fluid, provided the magnetic enthalpy density $B^2/4\pi$ and pressure $B^2/8\pi$ are taken into account [15]. For a relativistic gas, this gives an effective adiabatic index

$$\gamma_{\rm eff} = \frac{4(1+\sigma)}{(3+\sigma)} \tag{3}$$

leading to an asymptotic compression ratio of $1/(\gamma_{\rm eff} - 1)$ and a relative speed of the upstream medium with respect to the downstream medium corresponding to the Lorentz factor $\Gamma_{\rm rel} = \Gamma\sqrt{(2-\gamma_{\rm eff})/\gamma_{\rm eff}}$ (where Γ is the Lorentz factor of the shock front seen in the upstream medium). As σ increases, the compression ratio of the shock decreases and the high-energy power-law softens, as shown in Fig. 3.

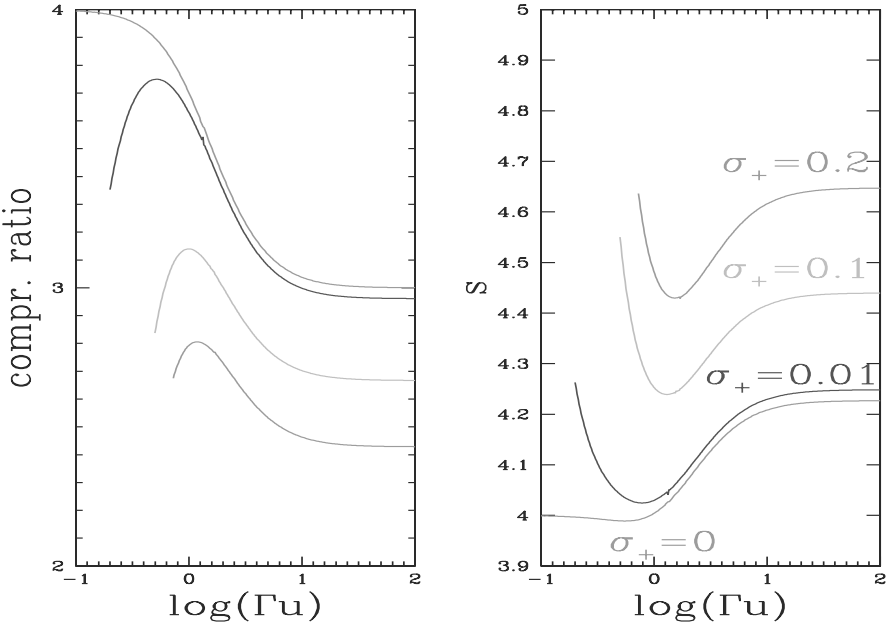

Fig. 3. The compression ratio and power-law index s for a gas of adiabatic index 5/3 in which a magnetic field is generated downstream to the level $\sigma = \sigma_+$ (see text for notation).

4 Learning from the Crab

A relativistic wind carries energy from the Crab pulsar out to the Nebula. This is released into nonthermal particles at a termination shock, which is probably the best observed relativistic shock in the universe. The average Lorentz factor of the upstream plasma can be estimated from the spin-down luminosity of the pulsar and the total number of electrons and positrons which have accumulated in the Nebula [13] to be between $\sim 10^4$ and 10^6. This is well into the asymptotic region of high Γ as far as the first-order Fermi process is concerned, and the X-ray synchrotron emission [24] indeed corresponds to the predicted power-law index of $s = 4.2$ for a plasma in which the magnetic energy plays no dynamical role [9].

However, the integrated synchrotron spectrum displays not only the expected "cooling break", at a frequency where the characteristic cooling time corresponds roughly to the age of the object, but also a second break at higher frequency [9]. This is presumably due to an intrinsic feature of the acceleration process and probably characterizes the transition between two different mechanisms. One possibility is that the break energy reflects the different spatial scales associated with ions and electrons/positrons. Regarded as distinct fluids, these components would be expected to produce shock structures

each on the scale of the thermal gyro radius: $\Gamma Mc^2/eB$ and $\Gamma mc^2/eB$, respectively. However, strong heating of the electron/positron gas, perhaps via the maser mechanism proposed by Hoshino et al. [10], should result in a smearing out of the smaller of these two scales. Below Lorentz factors of roughly $\Gamma M/m$, the hard ($s \approx 3$) maser mechanism should dominate over the first-order mechanism for electrons and positrons. An alternative explanation, which assumes the ions in the Crab wind carry very little of the energy flux, is that magnetic field dissipation within the shock front is responsible [15].

Whichever (if any) of these speculations is correct, the implications for GRB models are that the intrinsic spectrum is unlikely to be a single power-law. Hard spectra ($s < 4$) concentrate energy at the highest Lorentz factors and are not expected from the first-order Fermi mechanism at a relativistic shock. The signature of the latter is a softer spectrum extending above the bulk of the distribution with a power-law index which ranges from 4.2 to about 4.4, depending on the efficiency of magnetic field generation.

References

1. A. Achterberg, Y.A. Gallant, J.G. Kirk, A.W. Guthmann: Mon. Not. R. Astron. Soc. **328**, 393 (2001)
2. K.R. Ballard, A.F. Heavens: Mon. Not. R. Astron. Soc. **259**, 89 (1992)
3. J. Bednarz, M. Ostrowski: Phys. Rev. Lett. **80**, 3911 (1998)
4. M.C. Begelman, J.G. Kirk: Astrophys. J. **353**, 66 (1990)
5. F. Casse, M. Lemoine, G. Pelletier: Phys. Rev. D **65**, 023002 (2002)
6. E.V. Derishev, F.A. Aharonian, V.V. Kocharovsky, Vl.V. Kocharovsky: astro-ph 0301263 (2003)
7. D.C. Ellison, G.P. Double: Astropart. Phys. **18**, 213 (2002)
8. R.A. Fonseca, L.O. Silva, J.W. Tonge, W.B. Mori, J.M. Dawson: Phys. Plasmas **10**, 1979 (2003)
9. Y. Gallant, E. van der Swaluw, J.G. Kirk, A. Achterberg: "Modeling plerion spectra and their evolution." In: *Neutron Stars in Supernova Remnants.* eds. P.O. Slane, B.M. Gaensler (ASP Conf. Series: Vol. **271**, 2001) p. 161
10. M. Hoshino, J. Arons, Y.A. Gallant, A.B. Langdon: Astrophys. J. **390**, 454 (1992)
11. J.G. Kirk, P. Duffy: J. Phys. G: Nucl. Part. Phys. **25**, R163 (1999)
12. J.G. Kirk, A.W. Guthmann, Y.A. Gallant, A. Achterberg: Astrophys. J. **542**, 235 (2000)
13. J.G. Kirk, O. Skjæraasen: Astrophys. J. **591**, 366 (2003)
14. M. Lemoine, G. Pelletier: Astrophys. J. **589**, L73 (2003)
15. Y. Lyubarsky: astro-ph 0306435 (2003)
16. M. Malkov, L.O'C. Drury: Rep. Prog. Phys. **64**, 429 (2001)
17. M.V. Medvedev, A. Loeb: Astrophys. J. **526**, 679 (1999)
18. M. Ostrowski: Mon. Not. R. Astron. Soc. **264**, 248 (1993)
19. M. Ostrowski, J. Bednarz: Astron. Astrophys. **394**, 1141 (2002)
20. A. Panaitescu, P. Kumar: Astrophys. J. **571**, 779 (2002)

21. J. Sakai, T. Nakayama, Y. Kazimura, S. Bulanov: J. Phys. Soc. Japan **69**, 2503 (2000)
22. L.O. Silva, R.A. Fonseca, J.W. Tonge, J.M. Dawson, W.B. Mori, M.V. Medvedev: astro-ph 0307500 (2003)
23. B.E. Stern: astro-ph 0301384 (2003)
24. R. Willingale, B. Aschenbach, R.G. Griffiths, S. Sembay, R.S. Warwick, W. Becker, A.F. Abbey, J.M. Bonnet-Bidaud: Astron. Astrophys. **365**, L212 (2001)
25. T.Y.B. Yang, Y. Gallant, J. Arons, A.B. Langdon: Phys. Fluids **5**, 3369 (1993)
26. T.Y.B. Yang, J. Arons, A.B. Langdon: Phys. Plasmas **1**, 3059 (1994)

The First Steps in the Life of a GRB

Miguel A. Aloy

Max-Planck-Institut für Astrophysik, Karl-Schwarzschild-Str. 1, 85741 Garching, Germany
maa@mpa-garching.mpg.de

Summary. We present some preliminary results of relativistic hydrodynamic simulations of post-neutron star merger disks as potential candidates for progenitors of short-lasting gamma-ray bursts. We discuss some of the generic conditions under which a gamma-ray burst can be initiated in this kind of progenitor and the main characteristics of the resulting outflow.

1 Introduction

Gamma-ray bursts (GRBs) are sudden releases of energy which are, most probably, linked with catastrophic collapse events of massive stars (collapsars [17]; hypernovae, [13]) or with mergers of compact binaries [5, 6, 11, 12]. In all these models a fraction of the gravitational binding energy released by accretion of matter from a thick torus girding a stellar mass black hole (BH) is thought to power a pair fireball. Assuming that the baryon load of the fireball is not too large, the baryons are accelerated together with the $e^+ e^-$ pairs to Lorentz factors $> 10^2$ [4].

Due to their different duration and spectral properties GRBs are commonly divided in two classes: short ($\leq 2\,$s) and long ($\geq 2\,$s) GRBs [9]. The long subtype of GRBs has been quite extensively observed and there is a relatively large number of afterglow multi band observations from radio to X-rays. These observations have shed some light on the kind of progenitors and environments in which such progenitors reside. From the numerical point of view, the generation and early evolution of long GRBs in the framework of the collapsar model has been studied using 2D Newtonian [10] and relativistic hydrodynamics [2, 3, 18]. Observations of short GRBs are less numerous and it has not been possible to detect them in multi frequency searches.

The scenario arising after the merging process of a compact binary system consists of a central BH of a few solar masses girded by a thick accretion torus whose mass is of $0.05 - 0.3\ M_\odot$ [14, 8]. Once the thick disk is formed, up to $\sim 10^{51}$ erg can be released above the poles of the BH in a region that contains less than $10^{-5}\ M_\odot$ of baryonic matter due to the release of energy via ν–$\bar{\nu}$ annihilations. In principle, this may lead to the acceleration of this matter to ultrarelativistic speeds accounting for a successful GRB. If the duration of the event is related to the lifetime of the system [15] this kind of events can

only belong to the class of short GRBs because the expected time scale on which the BH engulfs the disk is fractions of a second [14].

In this work we address the question of whether a local deposition of energy around the remnant left over from the merger of two neutron stars can yield the formation of a pair of relativistic, collimated plasma outflows in opposite directions that can account for short GRBs. We employ 2D general relativistic hydrodynamic numerical simulations to study the properties of the outflows generated when pure thermal energy is released in a wide angle cone around the rotation axis of the system consisting of a stellar mass BH surrounded by a thick accretion torus. We use the high-resolution shock-capturing code GENESIS [1] to integrate the general relativistic hydrodynamic equations in 2.5D (i.e., in spherical (r, θ) coordinates assuming that there is no ϕ dependence of any physical quantity although the ϕ components of any vector can have non-zero values). Among the issues that we want to study are: the viability of the scenario of compact object mergers for producing ultrarelativistic outflows: the mechanism that can account for collimation (if any) of the outflowing plasma; the expected duration of GRB events generated in this framework; and the relation to the time during which the source of energy is active.

2 Initial Model and Numerical Set Up

We have constructed two initial models in which the gravitational field is provided by a Schwarzschild BH of 3 $M_\odot$ (models type-A) and 2.44 $M_\odot$ (models type-B) located at the center of the system (effects on the dynamics due to the self-gravity of the accretion torus or the external environment are neglected). These black holes are surrounded by thick accretion disks for which the initial configurations are built either by guidance through the data of Ruffert & Janka [14] and then letting the model relax until a torus of 0.1 $M_\odot$ is obtained (type-A), or by analytically following a prescription very close to that of Font & Daigne [7] in order to build an equilibrium torus of 0.07 $M_\odot$ around a Schwarzschild BH (type-B). The initial models include an environment which is of high density and non uniform in type-A models. In type-B models it is spherically symmetric, with low density which decreases with radius ($\rho \sim r^{-3.4}$) and that has a total mass of 2.52×10^{-7} $M_\odot$. These initial configurations, although they are *ad hoc* (i.e., not the result of a full computation of the merger epoch), mimic the expected state of a remnant of the merger of a compact binary system sufficiently well for our purposes. We assume equatorial symmetry, and we cover 90° in the angular θ-direction with 200 uniform zones. In the r–direction the computational grid consists of 400 (type-A) or 500 (type-B) zones spaced logarithmically between the inner boundary and an outermost radius of $R_{\rm max} = 2 \times 10^{10}$ cm (thus, we can study the evolution of any outflow up to ~ 0.5 s). The equation of state includes the contributions of non-relativistic nucleons treated as a mixture

of Boltzmann gases, radiation, and an approximate correction due to e^+e^-–pairs [16]. Complete ionization is assumed, and the effects due to degeneracy are neglected.

In a consistent post neutron star merger model an outflow will be powered by any process which gives rise to a local deposition of energy and/or momentum, as e.g., $\nu\bar{\nu}$–annihilation, or magneto-hydrodynamic processes. We mimic such a process by releasing pure thermal energy in a prescribed cone around the rotational axis of our system. In the radial direction the deposition region extends from the inner grid boundary located at 2 gravitational radii ($R_g = GM/c^2$; G, M and c being the gravitational constant, the mass of the BH and the speed of light in vacuum, respectively) to the outer radial boundary. In the angular direction, the opening half–angle of the deposition cone (θ_0) was chosen to be in the range $30° - 75°$. From the annihilation rate distribution computed in [14] and [8], we infer a power law distribution for the energy deposited per unit of volume in the surrounding of the system whose explicit form was approximated as $\dot{q} = \dot{q_0} z^{-n}$, where z is the distance along the rotation axis, n is the power law index ($n = 5$ hereafter) and $\dot{q_0}$ is a normalization factor that we use to fix the total energy deposition rate ($\dot{E}$).

3 Results

We have done a parameter study addressing three different aspects of the morphology and dynamics of outflows resulting from neutron star merger remnants. The first one is the question for the consequences of increasing $\dot{E}$ from 5×10^{49} erg s^{-1} to 5×10^{51} erg s^{-1}, using a fixed value of the opening half–angle (θ_0) of the deposition region. The second aspect is the dependence of the results when varying θ_0 while keeping the rest of the parameters fixed. Finally, we compare models having the same rate of energy deposition per unit of volume.

For energy deposition rates larger than a certain threshold $\dot{E}_{\rm th}$, all the models lead to either relativistic jets or ultrarelativistic winds (i.e., fireballs). The threshold is due to the need of overcoming the ram pressure $p_{\rm ram}$ that is exerted by the infalling external medium onto the new born fireball close to its initiation site. If the amount of energy per unit of volume pumped into the deposition region (in an interval of about of the free falling time of the fluid located at distances of the order of the radius of the torus) is not larger than $p_{\rm ram}$, the fireball is swallowed by the BH. The precise value of the threshold is model dependent as long as the densities and accretion velocities outside the thick torus depend on the details of the merger phase. For type-A models we find $\dot{E}_{\rm th} \sim 10^{49}$ erg s^{-1}, while for type-B models $\dot{E}_{\rm th} \lesssim 10^{48}$ erg s^{-1}. The smaller value in type-B models is due to their smaller ambient density.

Depending on the energy deposition rate and on the ambient density we find that the outflows are either jets (i.e., outflows where the lateral boundaries are causally connected) having a very small opening angle ($\lesssim 8°$) or

relatively wide opening angle ($\lesssim 25^\circ$) winds (i.e., the lateral boundaries are not causally connected). Models close to the thresholds of the energy deposition rate or with a high density environment tend to form relativistic ($\Gamma \sim 10$), low density, knotty jets whose head propagates at mildly relativistic speeds ($\sim 0.6c$). In contrast, models well above the threshold with dense environments or, independent of the deposition rate, in case of diluted environments either tend to form conical, ultrarelativistic ($\Gamma \gtrsim 400$) winds which are smooth, propagate at relativistic speeds ($\sim 0.97c$) and can be fitted by analytic power laws in case of models of type-A, or they propagate at ultrarelativistic speeds ($\gtrsim 0.9999c$) being rather irregular due to the effect of large Kelvin-Helmholtz (KH) instabilities originating from their interaction either with the torus, or with the environment in case of type-B. Indeed, the growth of KH modes determines whether the profiles of the physical variables are smooth and monotonically decreasing in the r-direction (type-A), or non-smooth and non monotonic (type-B). The larger growth of surface instabilities in models of type-B is due to the larger density contrast with respect to the environment in these type of models. An effect of the KH instabilities is to entrain mass into the relativistic outflows of type-B models. The amount of entrained mass is comparable with that of models of type-A. However, in type-B models, the amount of matter piled up ahead of the outflow is much smaller (because there is much less mass in the ambient) leading to a highly relativistic propagation velocity of the fireballs of type-B models, while only allowing for mildly relativistic speeds in type-A models. Indeed, the speed of propagation of the fireball is so large that models of type-B will lead to successful GRBs (in contrast to models of type-A; see below).

Increasing the energy deposition rate yields, independently of the model, an increase of the average Lorentz factor, and a decrease of the average density of the outflow at any given time. In models of type-A, the increase of $\dot{E}$ results in a transition in the outflow morphology from relativistic jets ($\dot{E} < 10^{51}$ erg s^{-1}) to ultrarelativistic wind-like outflows ($\dot{E} > 10^{51}$ erg s^{-1}). In models of type-B, we find ultrarelativistic winds for all energy deposition rates considered ($\dot{E} > 5 \times 10^{48}$ erg s^{-1}). For energy deposition rates leading to conical wind structures, the opening angle of the outflow (θ_w) is quite insensitive to the exact value of $\dot{E}$ (although it slightly increases with increasing $\dot{E}$), its value being $\sim 20^\circ - 30^\circ$.

In type-A models, decreasing θ_0 produces a transition from narrow jets to wide angle winds. In type-B models there is almost no difference in the opening angle of the wind when we vary θ_0 between 30° and 75°. However, there is a slight decrease of θ_w and an increase of the mass entrained (because of the development of KH instabilities) with increasing θ_0. In general, increasing θ_0 while keeping $\dot{E}$ constant leads to smaller average Lorentz factors in the resulting outflow.

Releasing the same total energy per unit of volume and time leads in models of both types to a larger baryon loading, when both θ_0 and $\dot{E}$ are

increased. In type-A models this also implies that there is a trend to form relativistic jets instead of winds, when we increase θ_0. In type-B models we always form winds but they have more baryon loading with increasing θ_0 and $\dot{E}$. The reason for this is that although the total energy deposition per unit of volume is the same, the model having the smallest deposition angle sweeps up less ambient mass (and drags less mass from the torus) than the model having the largest deposition angle and energy deposition rate.

We conclude that the opening angle of the resulting outflow, provided it is a jet, is set by the environmental conditions (mainly, the density). If the generated outflow is a wind, then the complete collimation process happens in less than 1 ms (approximately, the light crossing time of the torus) and θ_w is set by the opening angle of the torus, and neither by the external medium (which has much less inertia in type-B models because it is much more rarefied), nor by the angular size of the deposition region.

We have checked the evolution of two models after the shut down of the energy deposition. It turns out that outflows propagating in high density environments (type-A) will not yield successful GRBs while models with diluted environments (type-B) can do so. The reason being that, in type-B models, the speed of propagation of the leading radial edge of the fireball is faster than the rear one when the energy deposition is shut down. This is not the case in type-A models because they sweep up more ambient mass and the leading front of the outflow slows down. We find that in type-B models the fireball even stretches substantially in radial direction, because the propagation velocity of its leading front is larger than its rear edge. This points to the possibility that the duration of the GRB emission can be much larger than the time of the activity (i.e., of release of energy) of the central source.

References

1. M.A. Aloy, J.M. Ibáñez, J.M. Martí, E. Müller: Astrophys. J. Suppl. **122**, 151 (1999)
2. M.A. Aloy, E. Müller, J.M. Ibáñez, J.M. Martí, A.I. MacFadyen: Astrophys. J. Lett. **531**, L119 (2000)
3. M.A. Aloy, J.M. Ibáñez, J.A. Miralles, V. Urpin: Astron. Astrophys. **396**, 693 (2002)
4. G. Cavallo, M.J. Rees: Mon. Not. R. Astron. Soc. **183**, 359 (1978)
5. D. Eichler, M. Livio, T. Piran, D.N. Schramm: Nature **340**, 126 (1989)
6. J. Goodman: Astrophys. J. Lett. **308**, L47 (1986)
7. J.A. Font, F. Daigne: Mon. Not. R. Astron. Soc. **334**, 383 (2002)
8. H.-Th. Janka, Th. Eberl, M. Ruffert, C.L. Fryer: Astrophys. J. Lett. **527**, L39 (1999)
9. C. Kouveliotou et al. : Astrophys. J. Lett. **413**, L101 (1993)
10. A.I. MacFadyen, S.E. Woosley: Astrophys. J. **524**, 262 (1999)
11. R. Mochkovitch, M. Hernanz, J. Isern, X. Martin: Nature **361**, 236 (1993)
12. B. Pacyński: Astrophys. J. Lett. **308**, L43 (1986)

13. B. Pacyński: Astrophys. J. **494**, L45 (1998)
14. M. Ruffert, H.-Th. Janka: Astron. Astrophys. **344**, 573 (1999)
15. R. Sari, T. Piran: Astrophys. J. **485**, 270 (1997)
16. J. Witti, H.-Th. Janka, K. Takahashi: Astron. Astrophys. **286**, 841 (1994)
17. S.E. Woosley: Astrophys. J. **405**, 273 (1993)
18. W. Zhang, S.E. Woosley, A.I. MacFadyen: Astrophys. J. **586**, 356 (2003)

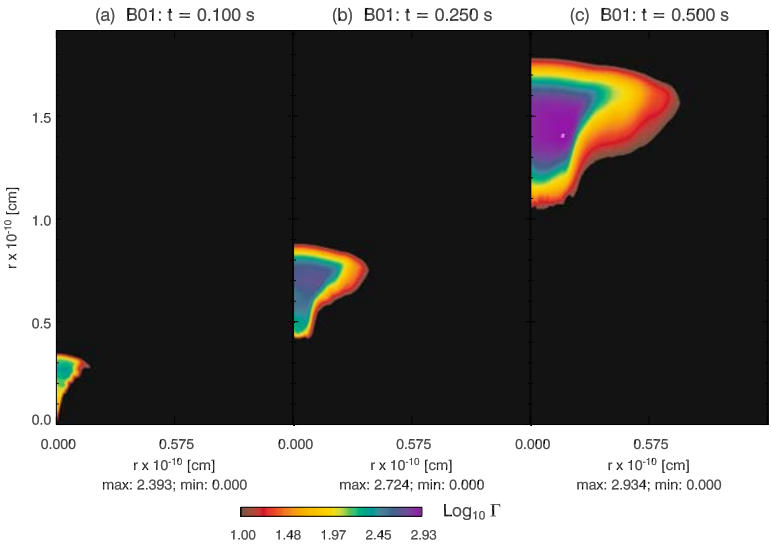

Evolution of the Lorentz factor (in logarithmic scale) of the outflow after the central energy release shut–off. The time of each snapshot is printed on top of each panel. The scale is limited to enhance the variations in the ultra–relativistic core of the outflow. The values of the minimum logarithm of the Lorentz factor a at each time are shown below each panel. In this model, thermal energy has been released during 100 ms at a rate of $2 \cdot 10^{50}$ erg/s in a conical region around the symmetry axis of half–opening angle 45 deg in the vicinity of a 2.44 $M_{\odot}$ black hole. Comparing the middle and right panels with the left one, it is noticeable the radial stretching of the ultrarelativistic core of the fireball. A possible consequence of this stretching is that the duration of the GRB event can be larger than the time of activity of the source. At the final computed time (0.5s) the Lorentz factor of the fireball is still increasing and does not show any sign of saturation yet.

Plate (Aloy)

Plate 5.

Physical Restrictions to Cosmological Gamma-Ray Burst Models*

G.S. Bisnovatyi-Kogan

Space Research Institute, Russian Academy of Science, Profsoyuznaya 84/32, Moscow 117997, Russia
gkogan@mx.iki.rssi.ru

Summary. The present common view about GRB origin is related to cosmology, and is based on statistical analysis, and on measurements of the redshifts in the GRB optical afterglows of long GRB. No correlation is found between redshifts, GRB spectrum, and total GRB fluence. Comparison of KONUS and BATSE data about statistics and hard X-ray lines is done, and some differences are noted. Hard gamma-ray afterglows, prompt optical spectra, hard X-ray lines, polarization measurements could be very important for farther insight into GRB origin. Possible connection of short GRB with soft gamma repeaters is discussed.

1 GRB Models

It is generally accepted now that cosmic gamma-ray bursts (GRB) have a cosmological origin. The first cosmological model, based on explosions in active galactic nuclei (AGN) was suggested in [25]. A mechanism of the GRB origin in the vicinity of a collapsing object based on neutrino-antineutrino annihilation was analyzed in [5]. GRB production in supernova explosion was discussed in [7]. The GRB models may be classified by two levels. The upper one is related directly to the observational appearance, and include 3 main models" 1) Fireball, 2) Cannon Ball, and 3) Precessing Jets.

The main restrictions are connected with the next (basic) level of GRB model, which is related to energy source, producing a huge energy output necessary for a cosmological GRB model. This class contains 5 main models:

1. (NS+NS), (NS+BH) mergers. This mechanism was investigated numerically in [27, 28]. Gamma radiation is produced here by $(\nu, \tilde{\nu})$ annihilation, and the energy output is not enough to explain most powerful GRB even with account of strong beaming. The energy emitted in the isotropic optical afterglow of GRB 990123 [1, 18] is about an order of magnitude larger than the total radiation energy output in this model.
2. Magnetorotational explosion. Magnetorotational explosion, proposed in [23] for a cosmological GRB, had been suggested earlier for the supernova

* This work is partly supported by RFFI grant 02-02-16900, INTAS/ESA grant 99-120, INTAS grant 00-491

explosion in [6]. Numerical calculations gave the efficiency of a transformation of the rotational energy into the kinetic one at the level of few percent [3, 4]. This is enough for the supernovae energy output, but is too low for cosmological GRB.

3. Hypernova. This model, suggested in [23] is popular now, because traces of the supernova explosions are believed to be found in the optical afterglows of several GRB [13, 35]. The hypernova model is based on a collapse of a massive core, formation of a black hole $M_{bh} \sim 20 M_{\odot}$, surrounded by a massive disk with a rapid accretion and appearance of GRB [19]. This model seems to be most promising now.
4. Magnetized disks around rotating (Kerr) black holes (RBH). This model is based on extraction of rotating energy of RBH when magnetic field is connecting the RBH with the surrounding accretion disk or accretion torus [37].
5. A model proposed in [29] creates the GRB by the pair-electromagnetic pulse from an electrically charged black hole surrounded by a baryonic remnant. The main problem here is how to form such a strongly charged BH.

2 Basic Data

2.1 Statistics

Statistical arguments in favor of the cosmological origin of GRB are based on a visual isotropy of GRB distribution on the sky in combination with a strong deviation of $\log N - \log S$ distribution obtained in BATSE observations [22] from the euclidian uniform distribution with the slope 3/2. Similar properties have been obtained in KONUS experiment [20] where the authors explained deviations from 3/2 slope by selection effects. The analysis of KONUS data with account of selection effects made in [17] gave the average value $< V/V_{max} >= 0.45 \pm 0.03$; the value 0.5 corresponds to pure uniform distribution. KONUS data had been obtained in conditions of constant background. Similar analysis [31] of BATSE data, obtained in conditions of substantially variable background, gave resulting $< V/V_{max} >= 0.334 \pm 0.008$. These two results seems to be in contradiction, because KONUS sensitivity was only 3 times less than that of BATSE, where deviations from the uniform distribution in BATSE data are sill large [15].

Statistical analysis and of BATSE data, divided in 4 classes according to their hardness and calculation of $< V/V_{max} >$ for different classes have been done in [32]. In the cosmological model we may expect smaller value of $< V/V_{max} >$ for softer GRB in the case of a uniform sample, because larger red shifts would correspond to softer spectra. The result is quite opposite, and soft GRB have larger $< V/V_{max} >$ than the hard ones, 0.47 and 0.27

respectively. It is supposed in [32] such a strong excess of luminosity in hard GRB, which overcomes the tendency of the uniform sample.

The influence of statistical errors in presence of the threshold was analyzed in [8]. The $\log N - \log S$ curve in presence of statistical errors on the level of average 10 thresholds has a similarity with the BATSE distribution.

2.2 Optical Afterglows and Red Shifted Lines

The spectra of optical afterglows have shown large red shifts z, up to 4.5, indicating to the cosmological origin of GRB and their enormous energy outputs. In most cases the red shifts have been measured in the faint host galaxies. The list of red shift measurements is given in [10, 14]. The redshift data from [14] are listed in [10] by total GRB fluences. Huge energy output during a short time (0.1 - few 100 seconds) create problems for the cosmological interpretation.

2.3 Collimation

To avoid a huge energy production, strong collimation is suggested in the radiation of GRBs. The restriction to the collimation angle follows from the analysis of the probability of appearance of the orphan optical afterglow [26], which should have lower or no collimation. The absence of any variable orphan afterglow in a search poses restriction $\Omega_{opt}/\Omega_\gamma << 1/2100$. At radio wavelengths published source counts and variability studies have been used in [24] to place a limit on the collimation angle, $\theta_\gamma \geq 5^\circ$.

Comparison of the red shifts and fluences presented in [10] shows no correlation between distance and observed flux (see Fig. 1). It is explained by strong collimation, and strong scattering is connected with different sight angles in the beam. If the collimation is connected with the relativistic bulk motion [13], then strong correlation between GRB duration and their power should exist: stronger GRB should be shorter. Absence of such correlation excludes models based on the relativistic bulk motion collimation.

2.4 Prompt Optical Afterglows

The prompt optical afterglow of GRB 990123 was caught by optical observations 22 seconds after the onset of the burst [1, 2]. GRB 990123 was detected by BATSE on 1999 January 23.407594. The event was strong and lasted $\geq$100 s. The T50 and T90 durations are 29.82 ($\pm$ 0.10) s and 63.30 ($\pm$ 0.26) s, respectively. The maximum optical brightness 8.95^m was reached 30s after the GRB beginning, and after 95s it was already at 14.5^m. So the gamma ray maximum almost coincides with the optical one. The observed optical luminosity, related to the redshift $z = 1.61$ reaches $L_{opt} \approx 4 \cdot 10^{49}$ ergs/s, what is about 5 orders of magnitude brighter than optical luminosity of any

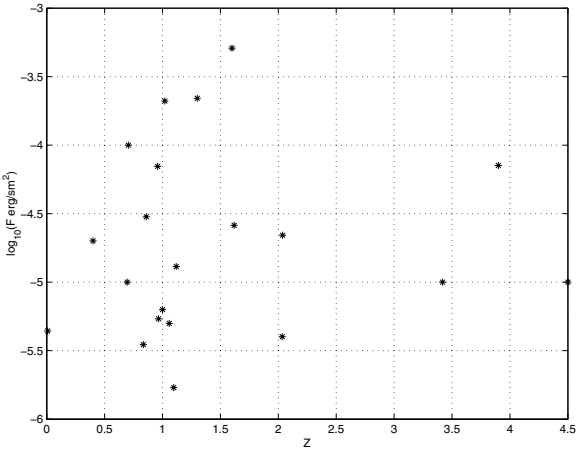

Fig. 1. Fluence F versus redshift z for GRB data from [10].

observed supernova. The energy of the prompt optical emission reaches 10^{51} ergs, and the isotropic gamma-ray flux is about $2.3 \cdot 10^{54}$ ergs, what exceeds the rest energy of the Sun [1, 18]. Another bright afterglows have been observed in GRB 021004 (15^m, z=2.3), GRB 030329 (12.4^m, z=0.168) and GRB 030418 (16.9^m). Brightest visual magnitude and redshift are given in brackets. Among those, the most remarkable afterglow observed by many observatories was in GRB 030329 (see e.g. [12, 30]), where the supernova was probably detected by the features of the optical spectra [36].

2.5 High-energy Afterglow

EGRET observations on CGRO have shown that GRB emit also very hard gamma photons up to 20 GeV [15]. The number of GRB with detected hard gamma radiation is about 10, from them 5 bursts had registered photon energies over 100 MeV [33]. Hard gamma emission, as a rule, continues longer than the main (soft) gamma ray burst, up to 1.5 hours in the GRB940217. Comparison of the angular aperture of EGRET and BATSE leads to conclusion that hard gamma radiation could be observed in large fraction (about one half) of all GRB. Spectral slope in hard gamma region lays between (-2) and (-3.7), and varies rapidly, becoming softer with time (GRB920622 in [34]).

2.6 Hard X-ray Lines

Hard gamma-ray lines in GRB spectra had been discovered by KONUS [21]. They had been interpreted there as cyclotron lines, and have been seen in 20-30% of the GRB. These spectra had shown a distinct variability: the visible

absorption decreases with time. In BATSE data [11] 13 statistically significant line candidates have been found from 117 GRBs. The only interpretation of hard spectral feature in the cosmological model [16] is based on the blue-shifted ($\Gamma = 25 - 100$) spectrum of the gas cloud illuminated by the gamma radiation of the fireball, and seems rather artificial.

3 Discussion

The investigation of orphan optical bursts by all-sky optical monitoring could be useful for putting better limits for the collimation. It is important to obtain prompt optical spectra of the GRB afterglows when the optical counterpart is still luminous, to investigate the polarization of the optical and X-ray afterglow for clarification of the radiation mechanism, and get more data on the hard gamma-ray afterglows.

The statistical analysis reveals at least two separate samples consisting of long ($>\sim 2$ s) and short bursts. Optical afterglows and redshift measurements have been done only for long bursts. Therefore, it is not excluded that short bursts have different (may be galactic) origin. It is interesting to compare the properties of short GRB with giant bursts from soft gamma-repeaters (SGR) inside the Galaxy. From the larger distance only giant bursts would be registered, which could be attributed to the short GRB. The existence of the giant bursts in the SGR (3 in 4 firmly known SGR in the Galaxy and LMC) implies a possibility for observation of giant bursts, which appear as short GRB, in other neighboring galaxies. The estimation gives more than 10 expected "short GRB" of this type from M 31 and other close neighbors [9]. The absence of any GRB projecting on the local group galaxies may indicate that SGR are more close and less luminous objects, than it is now accepted [9].

References

1. C.W. Akerlof et al. : Nature **398**, 400 (1999)
2. C.W. Akerlof, T.A. McKay: GCN 205 (1999)
3. N.V.Ardeljan, G.S. Bisnovatyi-Kogan, S.G. Moiseenko: Physics-Uspekhi **40**, 1076 (1997)
4. N.V. Ardeljan, G.S. Bisnovatyi-Kogan, S.G. Moiseenko: Astron. Astrophys. **355**, 1181 (2000)
5. V.S. Berezinsky, O.F. Prilutsky,: Astron. Astrophys. **175**, 309 (1987)
6. G.S. Bisnovatyi-Kogan: Sov. Astron. **14**, 652 (1971)
7. G.S. Bisnovatyi-Kogan, V.S. Imshennik, D.K. Nadyozhin, V.M. Chechetkin: Astrophys. Space Sci. **35**, 23 (1975)
8. G.S. Bisnovatyi-Kogan: Astron. Astrophys. **324**, 573 (1997)
9. G.S. Bisnovatyi-Kogan: Mem. Soc. Astron. It. **73**, 318 (2002)
10. G.S. Bisnovatyi-Kogan: astro-ph 0310361 (2003)

11. M.S. Briggs et al. : astro-ph 9901224 (1999)
12. R. Burenin et al. : GCN 2001 (2003)
13. S. Dado, A. Dar, A. De Rújula: Astron. Astrophys. **388**, 1079 (2002)
14. S.G. Djorgovski et al. : astro-ph 0107535 (2001)
15. G.J. Fishman, C.A. Meegan: Ann. Rev. Astron. Astrophys. **33**, 415 (1995)
16. C.J. Hailey, F.A. Harrison, K. Mori: Astrophys. J. Lett. **520**, L25 (1999)
17. J.C. Higdon, M. Schmidt: Astrophys. J. **355**, 13 (1990)
18. S. Kulkarni et al. : Nature **398**, 389 (1999)
19. A.I. MacFadyen, S.E. Woosley: Astrophys. J. **524**, 262 (1999)
20. E.P. Mazets et al. : Sov. Astron. Lett. **6**, 318 (1980)
21. E.P. Mazets et al. : Astrophys. Space Sci. **82**, 261 (1982)
22. C. Meegan et al. : Nature **355**, 143 (1992)
23. B. Paczynski: Astrophys. J. Lett. **494**, L45 (1998)
24. R. Perna, A. Loeb: Astrophys. J. Lett. **509**, L85 (1998)
25. O.F. Prilutsky, V.V. Usov: Astrophys. Space Sci. **34**, 387 (1975)
26. J.E. Rhoads: astro-ph 0103028 (2001)
27. M. Ruffert, H.-Th. Janka: Astron. Astrophys. **338**, 535 (1998)
28. M. Ruffert, H.-Th. Janka: Astron. Astrophys. **344**, 573 (1999)
29. R. Ruffini et al: Astron. Astrophys. **359**, 855 (2000)
30. V. Rumjantsev et al. : GCN 2005 (2003)
31. M. Schmidt: Astrophys. J. Lett. **523**, L117 (1999)
32. M. Schmidt: astro-ph 0101163 (2001)
33. E.J. Schneid et al. : NY Acad. Sci. Ann. **759**, 421 (1995)
34. E.J. Schneid et al. : Astrophys. J. **453**, 95 (1995)
35. V.V. Sokolov: astro-ph 0102492 (2001)
36. K.Z. Stanek et al. : astro-ph 0304173 (2003)
37. M.H.P.M. van Putten: Phys. Rep. **345**, 1 (2001)

Dynamical Evolution of ν-cooled Disks Following Compact Binary Mergers

William H. Lee[1]

Instituto de Astronomía, UNAM, Apdo. Postal 70-264, Cd. Universitaria, México; wlee@astroscu.unam.mx

Summary. Understanding the dynamical evolution of post-merger accretion disks over a long timescale (comparable to their lifetimes) is essential to determine if these can power short GRBs. Here we present preliminary results of such a study, spanning 0.2 seconds, by using a realistic equation of state and taking into consideration the effects of neutrino cooling (the main agent, given the physical conditions in the disks).

1 Introduction

The central engines of cosmological gamma ray bursts remain a mystery, but the veil that shrouds them has begun to lift, following the discovery of X-ray, optical and radio afterglows since 1997. It appears now that long GRBs, lasting more than a few seconds – and the only ones for which we have afterglow observations – originate from the collapse of massive stars. This is based partly on the fact that they are associated with regions of inferred high star formation rates in the putative host galaxies [7]. The exact mechanism by which the GRB is created is not entirely clear, but is most likely driven by hypercritical accretion onto a newly formed black hole following the collapse of the star.

Counterparts to short GRBs ($t_{dur} \leq 2$ s) have eluded observations so far, and so there is less information to go on, but it seems plausible to assume that they also originate at cosmological distances. One possibility is that they are the product of compact binary mergers, involving the final coalescence process of a double neutron star binary, or one containing a black hole. The merger timescale of these binaries (after the formation of the two compact objects) is a matter of current investigation and not yet settled [1, 8]. It could be that the lack of afterglows so far is due to the fact that this class of GRBs go off in a low-density environment (outside the host galaxy), making a counterpart harder to find. This scenario also involves hypercritical accretion onto a supramassive neutron star or a stellar mass black hole, following the tidal disruption of the secondary and the formation of an accretion disk.

In previous work, we have investigated precisely the outcome of the binary merger of a neutron star with a stellar mass black hole, using a 3D hydrodynamics code [3]. The calculation was only carried out for 20 ms or

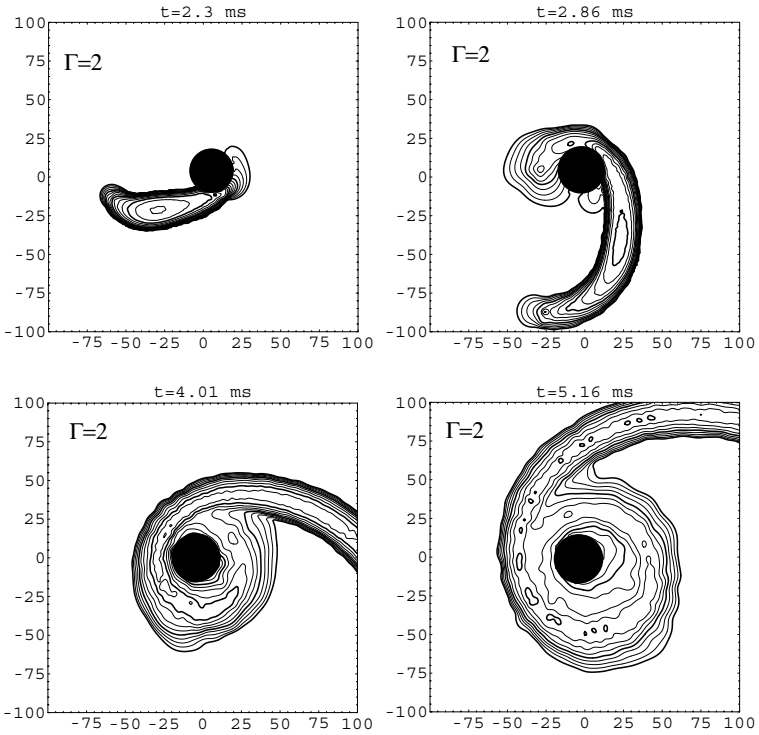

Fig. 1. First stages in the coalescence of a black hole-neutron star binary. The logarithmic contours are for density in the orbital plane. The rapid formation of an accretion structure close to azimuthal symmetry is clear. The axes are labeled in km.

so, due to computational limitations. A typical sequence of events is shown in Fig. 1, for an initial mass ratio M_{NS}/M_{BH}=0.31 using an ideal gas equation of state with adiabatic index $\Gamma = 2$. After a few orbital timescales, the accretion torus is nearly axisymmetric, contains a few tenths of a solar mass and is typically 400 km across. We refer the reader to [3] for further details of this calculation.

The dynamical timescale (ms) in such a system is much too short to account for even short GRBs, and its evolution needs to be understood for a longer period. We have addressed this, sacrificing one dimension in the problem by assuming azimuthal symmetry and modeling the disk in cylindrical coordinates (r, z) for 0.2 s. The first results of these calculations, reported in [4], took the initial conditions from an azimuthal average of the 3D results mentioned above, assumed an equally simple equation of state (ideal gas, $\gamma = 4/3$) and used an α-viscosity to account for the transport angular momentum.

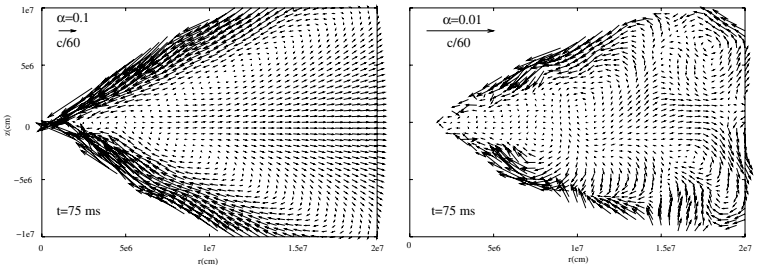

Fig. 2. Velocity field in the inner region of the accretion disk for α=0.1 (left) and $\alpha = 0.01$ (right) at $t = 75$ ms. The circulation patterns are clearly seen in both cases.

Here we describe a new set of more realistic calculations for the same initial configurations, having improved both the equation of state, and taking into account the cooling of the disk through neutrino emission.

2 Post-merger Evolution of the Disk

2.1 Physical Conditions and Equation of State

The accretion structures that are formed following the disruption of the neutron star are typically very dense ($\rho \geq 10^{11}$ g cm^{-3}) and hot ($T \geq 5$ MeV). Nuclei are entirely photodisintegrated, and the gas consists of non-degenerate free neutrons and protons, together with an extremely relativistic degenerate electron gas and photons. With these assumptions the pressure is given by

$$P = \rho kT/m_p + K(\rho/\mu_e)^{4/3} + aT^4/3 \qquad (1)$$

Note that even though the temperature is well above the threshold for pair creation, the number of these pairs is extremely small because of the degeneracy. Thus they do not contribute to the last term in the above equation. Steady state solutions to this type of disk have been recently considered [2, 5]. The time dependent evolution however, has not, and is of great importance, since the disk is not being fed matter or angular momentum by any external agent.

The timescale for the gas to achieve β-equilibrium, τ_β, is shorter than the accretion timescale, τ_{acc}. The electron fraction Y_e (and immediately also μ_e) is hence computed by assuming β-equilibrium, to maintain consistency. The photons cannot cool the gas, since τ_{acc} is itself shorter than their diffusion time, τ_{dif}. However, neutrinos are emitted in copious amounts (our calculations consider neutrino bremsstrahlung, plasmon decay, pair annihilation and electron and positron capture onto nucleons), and are the main source of cooling (the rates are as given in [2]). We do not consider explicitly the effects

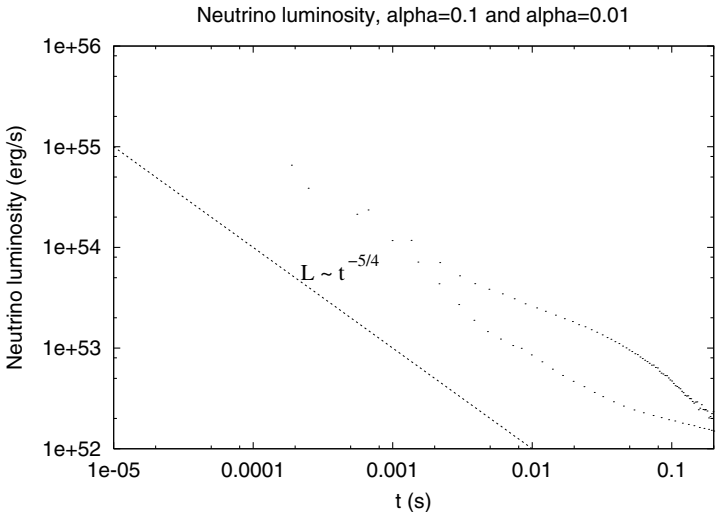

Fig. 3. Neutrino luminosity L_ν as a function of time for $\alpha = 0.1$ (upper solid line) and $\alpha = 0.01$ (lower solid line). The dashed line is a reference power law $L_\nu \propto t^{-5/4}$.

of neutrino transport, but simply assume that the optical depth of the fluid is small enough that they can escape freely. A crude *a posteriori* estimate of where the neutrino-surface lies indicates that $\tau_\nu \simeq 1$ at $\rho \simeq 10^{11}$ g cm^{-3} (based on the scattering off free nucleons (e.g., [6]). So the innermost region of the accretion disk becomes optically thick to neutrinos, and diffusive effects are expected to be important. This is something that clearly needs to be addressed in future work. For now, our assumptions allow us to compute upper limits to the neutrino luminosity in such disks.

2.2 Numerical Modeling

The actual dynamical evolution calculations are carried out using the same Smooth Particle Hydrodynamics (SPH) code used in previous studies of such disks [4]. The code solves the equations of motion for the fluid in the presence of a central mass (the black hole) in azimuthal symmetry. The equation of state has been modified, and neutrino cooling has been implemented, according to the discussion in section 2.1. The central mass produces a Newtonian point-mass potential, and the event horizon is modeled by an absorbing boundary at the Schwarzschild radius $r_g = 2GM_{\rm BH}/c^2$. The disk accretes because of the transport of angular momentum, modeled with an α-viscosity. The disks have initially between 20,000 and 80,000 SPH particles. We show here results for calculations that used $\alpha = 0.01$ and $\alpha = 0.1$, lasting 0.2 s.

2.3 Results

Figure 2 shows the velocity field in the inner regions of the accretion disks for two values of the viscosity parameter. The circulation patterns that are seen are similar to what we obtained in previous calculations. For large α the circulation has a vertical scale that is comparable to the radial coordinate, while for small α the cells are much smaller. The pattern persists throughout the calculations, diminishing in strength progressively.

Figure 3 shows the neutrino luminosities as functions of time for the same calculations. Roughly, $L_\nu \propto t^{-5/4}$, with slight differences between the two cases at late times. These are basically due to the fact that the high-viscosity disk dissipates more energy and is thus able to maintain higher luminosities. It is worth mentioning that for the physical conditions in the disk, electron and positron capture onto free nucleons gives the dominant contribution to the cooling rate.

3 Conclusions

From the curves shown in Fig. 3 one can in principle compute the energy deposition rates through ν-$\overline{\nu}$ annihilation, as a function of time, and investigate whether this process can drive a relativistic outflow.

Regardless of this particular aspect, after 0.2 s, the disk still contains several tenths of a solar mass, and densities in the inner regions reach 10^{11} g cm^{-3}. Were the magnetic field in such a plasma to reach equipartition values, the field strength would be $B \simeq 10^{15-16}$ G, sufficient to be able to drain the energy of the disk (or of the black hole) and power a short GRB.

Acknowledgement. It is a pleasure to thank W. Kluzniak and E. Ramírez-Ruiz for discussions and collaboration. This work is supported in part by Contract (36632-E).

References

1. N. Ivanova, K. Belczynski, V. Kalogera, F.A. Rasio, R.E. Taam: Astrophys. J. **592**, 475 (2003)
2. K. Kohri, S. Mineshige: Astrophys. J. **577**, 311 (2002)
3. W.H. Lee: Mon. Not. R. Astron. Soc. **328**, 583 (2001)
4. W.H. Lee, E. Ramirez-Ruiz: Astrophys. J. **577**, 893 (2002)
5. R. Narayan, T. Piran, P. Kumar: Astrophys. J. **557**, 949 (2001)
6. S.L. Shapiro, S.A. Teukolsky: In: *Black holes, white dwarfs, and neutron stars.* (Wiley Interscience: New York, 1983) p. 663
7. J. van Paradijs, C. Kouveliotou, R.A.M.J. Wijers: Ann. Rev. Astron. Astrophys. **38**, 379 (2000)
8. R.Voss, T.M. Tauris: Mon. Not. R. Astron. Soc. **342**, 1169 (2003)

On the Central Engine of Short Gamma-ray Bursts

Stephan Rosswog[1] and Enrico Ramírez-Ruiz[2]

[1] Dept. Physics & Astronomy, University of Leicester, Leicester LE1 7RH, UK; sro@astro.le.ac.uk
[2] Institute of Astronomy, Cambridge, CB3 OHA, UK; enrico@ast.cam.ac.uk

Summary. We assess the ability of neutron star binary coalescence to produce short gamma-ray bursts (GRBs). We find that the neutrino annihilation above the merged remnant will drive bipolar, relativistic jets along the initial binary rotation axis. This outflow can be collimated by the energetic, neutrino-driven baryonic wind that is blown off the remnant. Despite the narrow neutron star mass distribution the apparent luminosities will be spread over a broad range from $\sim 10^{49}$ to $\sim 10^{52}$ erg s^{-1}, typical jet opening half-angles are around 5 degrees. If the central core of the merger remnant does not collapse immediately convective dynamo action will set in and the available kinetic energy can be transformed into magnetic fields in excess of 10^{17} G. The corresponding spin-down time scale is ~ 0.2 s, just about the duration of a short GRB.

1 Introduction

While there is so far no direct evidence linking coalescence of double neutron star systems to gamma-ray bursts (GRBs), there can be no doubt about the plausibility of this system, at least for the subclass of short GRBs. Neutron star binaries can provide huge reservoirs of gravitational binding energy and are expected to lead naturally to short overall durations with variations on millisecond time scales. In the following we want to asses two popular mechanisms to launch a GRB.

2 Numerical Method and Simulations

We have performed global, 3D simulations of the last stages prior to the coalescence and followed the subsequent hydrodynamical evolution for about 15 ms. We use a temperature and composition dependent nuclear equation of state that covers the whole relevant parameter space in density, temperature and composition [16, 24, 25]. In addition, a detailed, multi-flavor neutrino treatment has been applied to account for energy losses and compositional changes due to neutrino processes. The neutrino treatment and the results concerning the neutrino emission have been described in detail in [18]. To

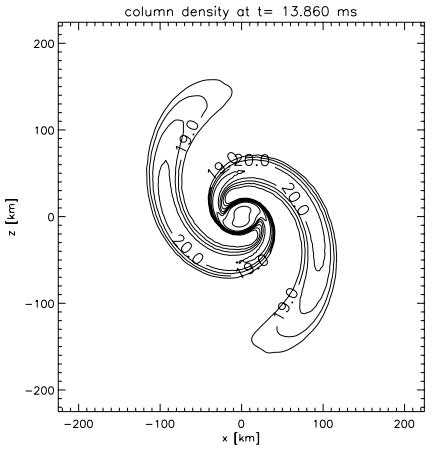

Fig. 1. Column density of an initially corotating neutron star binary system. For this simulation more than 10^6 SPH particles have been used.

solve the hydrodynamic equations we use the smoothed particle hydrodynamics method (SPH), the simulations are performed with up to more than a million SPH particles, see Fig. 1. The details of the production runs as well as those of several test runs can be found in [16, 18, 19]. Results focusing particularly on gamma-ray bursts have been presented in [17, 19, 20].

3 Assessment of the GRB Mechanisms

The energy released in a GRB represents just a minor fraction of the released gravitational binding energy (several times 10^{53} erg). This allows (in principle) for a plethora of possible burst mechanisms. The most popular of these are neutrino annihilation [1, 2, 5, 11, 15, 21, 22, 23] and the extraction of rotational energy via magnetic fields [6, 9, 10, 12, 14, 26, 28, 29].

3.1 Neutrino Annihilation

We find the merger remnant to emit neutrinos at a total luminosity of $\sim 2 \times 10^{53}$ erg s^{-1}. The luminosities are dominated by electron anti-neutrinos, followed by electron neutrinos and -slightly less luminous- the heavy lepton neutrinos. Their rms energies are around 15, 8, and 20 MeV, respectively. The bulk of the neutrino emission comes from the inner regions of the hot torus that has formed around the central object of the merger remnant (see [18] for details). In this context we consider two phenomena: 1) neutrinos and anti-neutrinos that annihilate above the merger remnant into $e^{\pm}$ pairs and 2) like in the case of a newborn proto-neutron star the neutrinos will blow off a strong baryonic wind from the remnant.

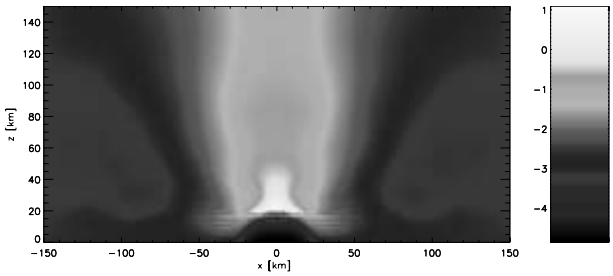

Fig. 2. Relativistic jet launched from a merger remnant via $\nu\bar{\nu}$ annihilation (upper half-plane; for details see [20]). Grey scale coded is the logarithm of the attainable Lorentz factor.

The thick disk with its geometry that is favorable for head-on neutrino collisions and its low baryon density along the original binary rotation axis launches a pair of relativistic jets [17]. An example of such a jet is shown in Fig. 2.

The typical energy provided in this way ($\sim 10^{48}$ erg), however, is way below the isotropic energy estimates for short GRBs ($\sim 10^{51}$ erg) at a redshift of $z = 1$ [7, 13] and therefore neutrino annihilation can only be a viable GRB mechanism if it goes along with a substantial collimation of the resulting outflow.

Such a collimation can be obtained via the ram pressure of the neutrino-driven, baryonic wind. This hydrodynamic collimation mechanism has been suggested by Levinson and Eichler [8]. They find that the jet half opening angle at large distances from the source, θ, is determined by the ratio of jet and wind luminosity, $\theta \propto L_j/L_w$. Since the luminosity in the wind exceeds that of the jet by far, the outflow is collimated into a narrow solid angle. Using the theoretical neutron star mass distribution of [4], calculating the neutrino emission as a function of the binary system mass and parameterizing the dependence of the wind luminosity as a function of the neutrino luminosity, $L_w \propto L_\nu^\alpha$, $\alpha = 3.2...3.4$ [27], we find the distributions of opening angles and luminosities shown in Figure 3. The broad distribution of opening angles is centered around 6 degrees, the luminosities around a few times 10^{50} erg s^{-1}. This is compatible with both the observational constraints on the luminosities of short GRBs and the estimated neutron star merger rates [19].

3.2 Magnetic Processes

The violent fluid motion within the merger remnant will almost certainly amplify the initial neutron star seed fields tremendously. To date, we are still lacking detailed MHD calculations of a neutron star coalescence, so we still have to wave our hands and draw conclusions from either simplified analytical models or purely hydrodynamic calculations.

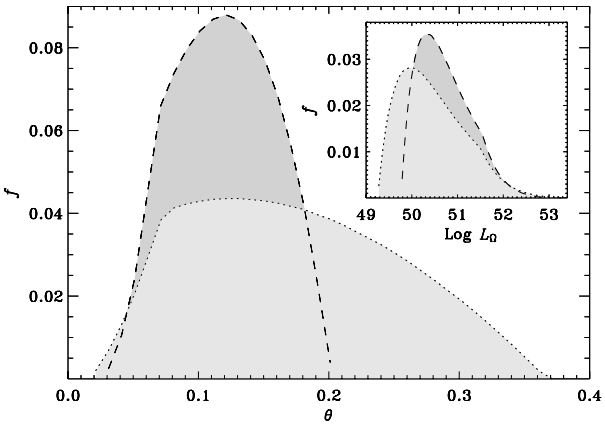

Fig. 3. Distribution of opening angles and apparent luminosities (inset) for GRBs launched via $\nu\bar{\nu}$ annihilation and collimated by means of a baryonic wind. (The dashed lines refer to $\alpha = 3.2$, the dotted to $\alpha = 3.4$; see text).

The equipartition field strength, $B^{\rm eq} = \sqrt{8\pi\rho c_s^2}$ in the central object of the merger remnant is (depending on the exact position) between 10^{16} G and 10^{18} G, and 10^{14} to 10^{16} G in the surrounding torus [20]. If just the relatively slow wrapping of the field lines via differential rotation (and no feedback onto the fluid) is assumed, equipartition will be reached in the central object within a few tens of seconds (provided it remains stable for long enough) and in the torus in around 4 s. Other field amplification mechanisms are expected to amplify the field exponentially leading to much shorter time scales. The fluid motion within the central object exhibits "convective cells" with sizes of ~ 1 km and velocities of $\sim 10^8$ cm s^{-1}. Moreover, the neutrino emission will, like in a proto-neutron star, establish a negative entropy and lepton number gradient and therefore drive vigorous convection (e.g., [3]). We find Rossby numbers (ratio of rotational and convective time scales), $Ro \equiv T_{\rm rot}/\tau_{\rm conv}$, substantially below unity (down to 0.1) and therefore expect that the system can sustain a large scale dynamo. Such a dynamo will increase the magnetic field exponentially with an e-folding time close to the convective time scale. Using the numbers determined from our simulations we find that equipartition will be reached within tens of milliseconds. The kinetic energy of the central object, $E_{\rm kin}$, is large enough for an average field strength $\langle B\rangle_{\rm co} = \sqrt{3\cdot E_{\rm kin}/R_{\rm co}^3} \approx 3\times 10^{17}$ G, where $R_{\rm co}$ is the radius of the central object. With this average field strength the spin-down time scale is $\tau_{\rm sd} = E_{\rm kin}/L_{\rm md} \approx 0.2$ s, where $L_{\rm md}$ is the magnetic dipole luminosity, i.e. $\tau_{\rm sd}$ is of the order of the typical duration of a short GRB.

A discussion of further possible magnetic mechanisms can be found in [20]. All of these mechanisms yield luminosities in excess of a few times 10^{52} erg s^{-1}and therefore yield typical time scales of order 1 s.

4 Conclusions

We have assessed the two most popular mechanisms to produce short GRBs from the coalescence of neutron star binaries, namely the annihilation of neutrino anti-neutrino pairs and magnetic energy extraction mechanisms. We find that $\nu\bar{\nu}$ annihilation provides the driving stresses to launch a pair of relativistic, bipolar jets. To explain the expected isotropic energies the jets have to be narrowly collimated. This collimation can be provided by the energetic, neutrino-driven baryonic outflow that goes along with the coalescence. Due to the sensitivity to the neutrino luminosities even a narrow mass spectrum results in a broad distribution of opening angles and apparent GRB luminosities.

We further expect the initial neutron star magnetic fields to be amplified to values close to equipartition within fractions of a second. The estimates of the various investigated magnetic mechanisms all yield very large luminosities that do not require any beaming. If the current picture turns out to be correct, short GRBs should be composed of two distinct components: the one resulting from neutrino annihilation plus wind collimation is narrowly beamed and the other, much more energetic, and possibly uncollimated component results from the plethora of magnetic mechanisms.

References

1. K. Asano, T. Fukuyama: Astrophys. J. **531**, 949 (2000)
2. K. Asano, T. Fukuyama: Astrophys. J. **546**, 1019 (2001)
3. R.I. Epstein: Mon. Not. R. Astron. Soc. **188**, 305 (1979)
4. C.L. Fryer, V. Kalogera: Astrophys. J. **554**, 548 (2001)
5. M. Jaroszinski: Acta Astronomica **43**, 183 (1993)
6. J.I. Katz: Astrophys. J. **490**, 772 (1997)
7. D. Lazzati, E. Ramírez-Ruiz, G. Ghisellini: Astron. Astrophys. **379**, L39 (2000)
8. A. Levinson, D. Eichler: Phys. Rev. Lett. **85**, 236 (2000)
9. P. Mészáros, M.J. Rees: Astrophys. J. Lett. **482**, L29 (1997)
10. P. Mészáros: Ann. Rev. Astron. Astrophys. **40**, 137 (2002)
11. R. Mochkovitch, M. Hernanz, J. Isern, X. Martin: Nature **361**, 236 (1993)
12. R. Narayan, B. Paczyński, T. Piran: Astrophys. J. Lett. **395**, L83 (1992)
13. A. Panaitescu, P. Kumar, R. Narayan: Astrophys. J. Lett. **561**, L171 (2001)
14. T. Piran: Phys. Rep. **314**, 575 (1999)
15. R. Popham, S.E. Woosley, C. Fryer: Astrophys. J. **518**, 356 (1999)
16. S. Rosswog, M.B. Davies: Mon. Not. R. Astron. Soc. **334**, 481 (2002)
17. S. Rosswog, E. Ramírez-Ruiz: Mon. Not. R. Astron. Soc. **336**, L7 (2002)
18. S. Rosswog, M. Liebendörfer: Mon. Not. R. Astron. Soc. **342,**, 673 (2003)
19. S. Rosswog, E. Ramírez-Ruiz: Mon. Not. R. Astron. Soc. **343,**, L36 (2003)
20. S. Rosswog, E. Ramírez-Ruiz, M.B. Davies: Mon. Not. R. Astron. Soc. **345**, 1077 (2003)
21. M. Ruffert, H.-T. Janka, K. Takahashi, G. Schäfer: Astron. Astrophys. **319**, 122 (1997)

22. M. Ruffert, H.-T. Janka: Astron. Astrophys. **344**, 573 (1999)
23. J.D. Salmonson, J.R. Wilson: Astrophys. J. **561**, 950 (2001)
24. H. Shen, H. Toki, K. Oyamatsu, K.!Sumiyoshi: Nuc. Phys. **637**, 435 (1998)
25. H. Shen, H. Toki, K. Oyamatsu, K. Sumiyoshi: Prog. Theor. Phys. **100**, 1013 (1998)
26. C. Thompson, R.C. Duncan: Astrophys. J. **408**, 194 (1993)
27. T.A. Thompson, A. Burrows, B.S. Meyer: Astrophys. J. **562**, 887 (2001)
28. V.V. Usov: Nature **357**, 472 (1992)
29. V.V. Usov: Mon. Not. R. Astron. Soc. **267**, 1035 (1994)

Part VIII

Supernovae, Gamma-Ray Bursters, and Cosmology

The Expanding and Accelerating Universe

Brian P. Schmidt

Research School of Astronomy and Astrophysics, Mt. Stromlo Observatory, The Australian National University, via Cotter Rd, Weston Creek, ACT 2611, Australia;
brian@mso.anu.edu.au

Summary. Measuring distances back to a significant portion of the look back time probes the make-up of the Universe, through the effects of different types of matter on the cosmological geometry and expansion. Over the past five years two teams have used type Ia supernovae to trace the expansion of the Universe to a look back time more than 70% of the age of the Universe. These observations show an accelerating Universe which is best explained by a cosmological constant, or other form of dark energy with an equation of state near $w = p/\rho = -1$. There are many possible lurking systematic effects. However, while difficult to completely eliminate, none of these appears large enough to challenge current results. However, as future experiments attempt to better characterize the equation of state of the matter leading to the observed acceleration, these systematic effects will ultimately limit progress.

1 The Cosmological Paradigm

Astronomers use a standard model for understanding the Universe and its evolution. The assumptions of this standard model, that General Relativity is correct, and the Universe is isotropic and homogenous on large scales, are not proven beyond a reasonable doubt - but they are well tested, and they do form the basis of our current understanding of the Universe. If these pillars of our standard model are wrong, then any inferences using this model about the Universe around us may be severely flawed, or irrelevant.

The standard model for describing the global evolution of the Universe is based on two equations that make some simple, and hopefully valid, assumptions. If the universe is isotropic and homogenous on large scales, the Robertson-Walker Metric gives the line element distance between two objects separated in space and time. The dynamic evolution of the Universe needs to be input into the Robertson-Walker Metric by the specification of the scale factor $a(t)$, which gives the radius of curvature of the Universe over time - or more simply, provides the relative size of a piece of space at any time. This description of the dynamics of the Universe is derived from General Relativity, and is known as the Friedman equation.

In cosmology, there are many types of distance, with the luminosity distance, D_L, being the most relevant to supernova observers. D_L is defined as the apparent brightness of an object as a function of its redshift, z. If we

assume the Universe is composed of a set of matter components, each having a fraction Ω_i of the critical density

$$\Omega_i = \frac{\rho_i}{\rho_{crit}} = \frac{\rho_i}{\frac{3H_0^2}{8\pi G}}, \quad (1)$$

with an equation of state which relates the density ρ_i and pressure p_i as $w_i = p_i/\rho_i$, then D_L is given by the numerically integrable equation,

$$D_L = D_A(1+z)^2 = \frac{c}{H_0}(1+z)\kappa_0^{-1/2} S\{\kappa_0^{1/2} \int_0^z dz' [\sum_i \Omega_i (1+z')^{3+3w_i} - \kappa_0 (1+z')^2]^{-1/2}\} \quad (2)$$

Here we define $S(x) = \sin(x)$, x, or $\sinh(x)$ for closed, flat, and open models respectively, and the curvature parameter κ_0, is defined as $\kappa_0 = \sum_i \Omega_i - 1$.

At low z, D_L scales linearly with redshift, with H_0 serving as the constant of proportionality. In the more distant Universe, D_L depends first order on whether on the rate of acceleration/deceleration (often referred to as q_0), or equivalently, the amount and types of matter that it is made up of. However, by observing objects over a range of high redshift (e.g. $0.3 > z > 1.0$), this degeneracy can be broken, providing a measurement of the absolute fractions of Ω_M and Ω_Λ [15].

To illustrate the effect of cosmological parameters on the luminosity distance, in Fig. 1 we plot a series of models for both Λ and non-Λ Universes. In the Left Panel, Top, the various models show the same linear behavior at $z < 0.1$ with models with the same H_0 indistinguishable to a few percent. By $z = 0.5$, the models with significant Λ are clearly separated, with distances that are significantly further than the zero-Λ universes. Unfortunately, two perfectly reasonable universes, given our knowledge of the local matter density of the Universe ($\Omega_M \sim 0.25$), one with a large cosmological constant, Ω_Λ=0.7, $\Omega_M = 0.3$, and one with no cosmological constant, $\Omega_M = 0.2$, show differences of less than 10%, even to redshifts of $z > 5$. Interestingly, the maximum difference between the two models is at $z \sim 0.8$, not at large z.

Figure 1 illustrates the effect of changing the equation of state of the non $w = 0$ matter component, assuming a flat universe $\Omega_{tot} = 1$. If we are to discriminate a dark energy component that is not a cosmological constant, measurements better than 5% are clearly required, especially since the differences in this diagram include the assumption of flatness, and also fix the value of Ω_M.

2 Type Ia Supernovae as Distance Indicators

SN Ia have been used as extragalactic distance indicators since Kowal first published his Hubble diagram ($\sigma = 0.6$ mag) for SNe I in 1968 [28]. We

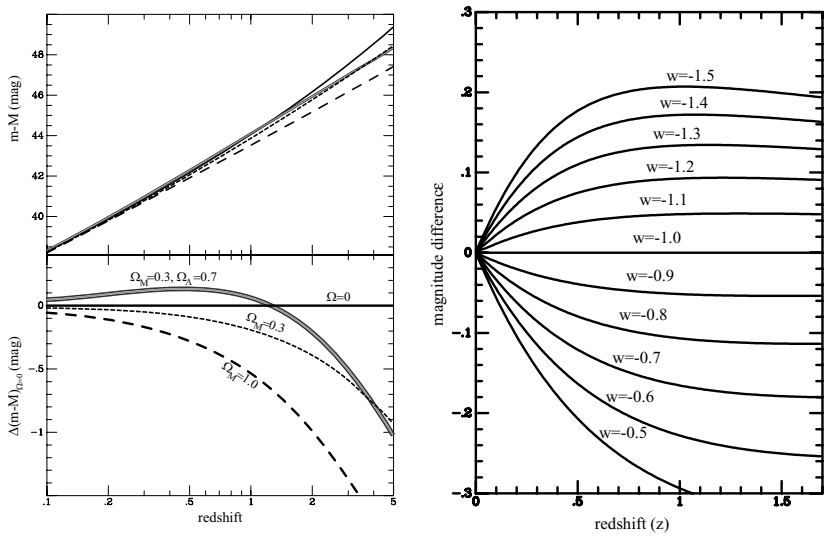

Fig. 1. Left Panel, Top: D_L expressed as distance modulus $(m-M)$ for four relevant cosmological models; $\Omega_M = 0$, $\Omega_\Lambda = 0$ (empty Universe); $\Omega_M = 0.3$, $\Omega_\Lambda = 0$; $\Omega_M = 0.3$, $\Omega_\Lambda = 0.7$; and $\Omega_M = 1.0$, $\Omega_\Lambda = 0$. In the Left Panel, Bottom, the empty universe has been subtracted from the other models to highlight the differences. Right Panel: D_L for a variety of cosmological models containing $\Omega_M = 0.3$ and $\Omega_x = 0.7$ with equation of state w_x. The $w_x = -1$ model has been subtracted off to highlight the differences of the various models.

now recognize that the old SNe I spectroscopic class is comprised of two distinct physical entities: SN Ib/c which are massive stars that undergo core collapse (or in some rare cases might undergo a thermonuclear detonation in their cores) after losing their hydrogen atmospheres, and the SN Ia which are most likely thermonuclear explosions of white dwarfs. In the mid-1980s, it was recognized that studies of the Type I supernova sample had been confused by these similar-appearing supernovae, which were henceforth classified as Type Ib [35, 57, 61] and Type Ic [23]). By the late 1980s/early 1990s, a strong case was being made that the vast majority of the true Type Ia supernovae had strikingly similar lightcurve shapes [5, 29, 30, 31], spectral time series [3, 8, 16, 38], and absolute magnitudes [30, 33]. There were a small minority of clearly peculiar Type Ia supernovae, e.g. SN 1986G [43], SN 1991bg [9, 32], and SN 1991T [9, 44], but these could be identified and "weeded out" by unusual spectral features.

Realizing the subject was generating a large amount of rhetoric despite not having a sizeable well-observed data set, a group of Astronomers based in Chile started the Calan/Tololo Supernova Search in 1990 [17]. This work took the field a dramatic step forward by obtaining a crucial set of high-quality supernova lightcurves and spectra. By targeting a magnitude range

that would discover Type Ia supernovae in the redshift range between 0.01 and 0.1, the Calan/Tololo search was able to compare the peak magnitudes of supernovae whose relative distance could be deduced from their Hubble velocities.

The Calan/Tololo Supernova Search observed some 25 fields (out of a total sample of 45 fields) twice a month for over $3\frac{1}{2}$ years with photographic plates or film at the CTIO Curtis Schmidt telescope, and then organized extensive follow-up photometry campaigns primarily on the CTIO 0.9m telescope, and spectroscopic observation on either the CTIO 4m or 1.5m. The search was a major success; it created a sample of 30 new Type Ia supernova lightcurves, most out in the Hubble flow, with an almost unprecedented control of measurement uncertainties [18].

In 1993 Phillips, in anticipation of the results he could see coming in as part of the Calan/Tololo search (he was a member of this team), looked for a relationship between the rate at which the Type Ia supernova's luminosity declines and its absolute magnitude. He found a tight correlation between these parameters using a sample of nearby objects, where he plotted the absolute magnitude of the existing set of nearby SN Ia which had dense photoelectric or CCD coverage, versus the parameter $\Delta m_{15}(B)$, the amount the SN decreased in brightness in the B band over the 15 days following maximum light [45]. For this work, Phillips used a heterogenous mixture of other distance indicators to provide relative distances, and while the general results were accepted by most, skepticism about the scatter and shape of the correlation remained. The Calan/Tololo search presented their first results in 1995 when Hamuy et al. showed a Hubble diagram of 13 objects at $cz > 5000$ km/s that displayed the generic features of the Phillips (1993) relationship [18]. It also demonstrated that the intrinsic dispersion of SN Ia using the $\Delta m_{15}(B)$ method was better than 0.15 mag.

The community more or less settled on the notion that including the effect of light curve shape was important for measuring distances with SN Ia when in 1996 Hamuy et al. showed the scatter in the Hubble diagram dropped from $\sigma \sim 0.38$ mag in B to $\sigma \sim 0.17$ mag for their sample of nearly 30 SN Ia at $cz > 3000$ km/s using the $\Delta m_{15}(B)$ correlation [20] .

Impressed by the success of the $\Delta m_{15}(B)$ parameter, Riess, Press and Kirshner developed the multi-color light curve shape method (MLCS), which parameterizes the shape of SN lightcurves as a function of their absolute magnitude at maximum [47]. This method also included a sophisticated error model, and fitted observations in all colors simultaneously, allowing a color excess to be included. This color excess, which we attribute to intervening dust, enables the extinction to be measured.

Another method that has been used widely in cosmological measurements with SN Ia is the "stretch" method, described by Perlmutter et al. [40, 42]. This method is based on the observation that the entire range of SN Ia lightcurves, at least in the B and V bands, can be represented with a

simple time-stretching (or shrinking) of a canonical light curve. The coupled stretched B and V light curves serve as a parameterized set of light curve shapes, providing many of the benefits of the MLCS method, but as a much simpler (and constrained) set. This method, as well as recent implementations of $\Delta m_{15}(B)$ [13, 46], and template fitting [56] also allow extinction to be directly incorporated into the SN Ia distance measurement. Other methods that correct for intrinsic luminosity differences or limit the input sample by various criteria have also been proposed to increase the precision of SNe Ia as distance indicators [2, 10, 55, 58], while these latter techniques are not as developed as the $\Delta m_{15}(B)$, MLCS, and stretch methods, they all provide distances that are comparable in precision, roughly $\sigma = 0.18$ mag about the inverse square law, equating to a fundamental precision of SN Ia distance being 6% (0.12 mag), once photometric uncertainties and peculiar velocities are removed.

3 The Measurement of Acceleration by SN Ia

The intrinsic brightness of SN Ia allow them to be discovered to $z > 1.5$. Fig. 1 shows that the differences in luminosity distances due to different cosmological models at this redshift are roughly 0.2 mag. For SN Ia, with a dispersion 0.2 mag, 10 well observed objects should provide a 3σ separation between the various cosmological models. It should be noted that the uncertainty described above in measuring H_0, is not important in measuring other cosmological parameters, because it is only the relative brightness of objects near and far that is being exploited in Eq. 2 - the value of H_0 scales out.

The first distant SN search was started by a Danish team. With significant effort and large amounts of telescope time spread over more than two years, they discovered a single SN Ia in a $z = 0.3$ cluster of galaxies (and one SN II at $z = 0.2$) [22, 34]. The SN Ia was discovered well after maximum light, and was only marginally useful for cosmology itself.

Just before this first discovery in 1988, a search for high-redshift Type Ia supernovae was begun at the Lawrence Berkeley National Laboratory (LBNL) and the Center for Particle Astrophysics, at Berkeley. This search, now known as the Supernova Cosmological Project (SCP), targeted SN at $z > 0.3$. In 1994, the SCP brought on the high-Z SN Ia era, developing the techniques which enabled them to discover 7 SN at $z > 0.3$ in just a few months.

The High-Z SN Search (HZSNS) was conceived at the end of 1994, when this group of astronomers became convinced that it was both possible to discover SN Ia in large numbers at $z > 0.3$ by the efforts of Perlmutter [39], and also use them as precision distance indicators as demonstrated by the Calan/Tololo group [18]. Since 1995, the SCP and HZSNS have both been working feverishly to obtain a significant set of high-redshift SN Ia.

3.1 Discovering SN Ia

Quantitatively, type Ia supernovae are rare events on an astronomer's time scale – they occur in a galaxy like the Milky Way a few times per millennium [6, 36, 37, 56]. With modern instruments on 4 meter-class telescopes, which scan 1/3 of a square degree to $R = 24$ magnitude in less than 10 minutes, it is possible to search a million galaxies to $z < 0.5$ for SN Ia in a single night.

Since SN Ia take approximately 20 days to rise from nothingness to maximum light [49], the three-week separation between "before and after" observations (which equates to 14 rest frame days at $z = 0.5$) is a good filter to catch the supernovae on the rise. The supernovae are not always easily identified as new stars on galaxies - most of the time they are buried in their hosts, and we must use a relatively sophisticated process to identify them. In this process, the imaging data that we take in a night, is aligned with the previous epoch, with the image star profiles matched (through convolution) and scaled between the two epochs to make the two images as identical as possible. The difference between these two images is then searched for new objects which stand out against the static sources that have been largely removed in the differencing process [40, 52]. The dramatic increase in computing power in the 1980s was thus an important element in the development of this search technique, as was the construction of wide-field cameras with ever-larger CCD detectors or mosaics of such detectors.

3.2 Obstacles to Measuring Luminosity Distances at High-Z

As shown above, the distances measured to SN Ia are well characterized at $z < 0.1$, but comparing these objects to their more distant counterparts requires great care. Selection effects can introduce systematic errors as a function of redshift, as can uncertain K-corrections, and an evolution of the SN Ia progenitor population as a function of look-back time. These effects, if they are large and not constrained or corrected with measurements, will limit our ability to accurately measure relative luminosity distances, and have the potential to undermine the potency of high-z SN Ia at measuring cosmology [27, 40, 42, 48, 52, 56].

K-Corrections

As SN are observed at larger and larger redshifts, their light is shifted to longer wavelengths. Since astronomical observations are normally made in fixed bandpasses on Earth, corrections need to be made to account for the differences caused by the spectrum of a SN Ia shifting within these bandpasses. K-correction errors depend critically on several separate uncertainties, including, the accuracy of spectrophotometry of SN; the accuracy of the absolute calibration of the fundamental astronomical standard systems; and using spectrophotometry for appropriate objects to calculate the corrections.

Extinction

In the nearby Universe we see SN Ia in a variety of environments, and about 10% have significant extinction [21]. Since we can correct for extinction by observing two or more wavelengths, it is possible to remove any first order effects caused by the average extinction properties of SN Ia changing as a function of z. However, second order effects, such as the evolution of the average properties of intervening dust could still introduce systematic errors. This problem can also be addressed by observing distant SN Ia over a decade or so of wavelength, in order to measure the extinction law to individual objects, but this is observationally expensive. An additional problem is the existence of a thin veil of dust around the Milky Way. Measurements from the COBE satellite have measured the relative amount of dust around the Galaxy accurately [51], but there is an uncertainty in the absolute amount of extinction of about 2% or 3% [4]. This uncertainty is not normally a problem; it affects everything in the sky more or less equally. However, as we observe SN at higher and higher redshifts, the light from the objects is shifted to the red, and is less affected by the galactic dust.

Selection Effects

As we discover SN, we are subject to a variety of selection effects, both in our nearby and distant searches. The most significant effect is Malmquist Bias - a selection effect which leads magnitude limited searches finding brighter than average objects near their distance limit; brighter objects can be seen in a larger volume relative to their fainter counterparts. Malmquist bias errors are proportional to the square of the intrinsic dispersion of the distance method, and because SN Ia are such accurate distance indicators, these errors are quite small - approximately 0.04 mag. Monte Carlo simulations can be used to estimate these effects, and to remove them from our data sets [42, 52].

Gravitational Lensing

Several authors have pointed out that the radiation from any object, as it traverses the large scale structure between where it was emitted, and where it is detected, will be weakly lensed as it encounters fluctuations in the gravitational potential [24, 26, 60]. Generally, most light paths go through underdense regions, and objects appear de-magnified. Occasionally the photons from a distant object encounter dense regions, and these lines of sight become magnified. The distribution of observed fluxes for sources is skewed by this process, such that the vast majority of objects appear slightly fainter than the canonical luminosity distance, with the few highly magnified events making the mean of all paths unbiased. Unfortunately, since we do not observe enough objects to capture the entire distribution, unless we know and include the skewed shape of the lensing, a bias will occur. At $z = 0.5$, this

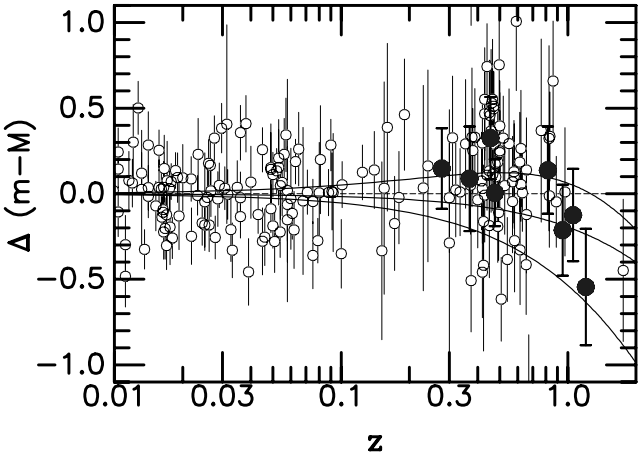

Fig. 2. Data as summarized in Tonry 2003 with points shown in a residual Hubble diagram with respect to an empty universe. In this plot the highlighted points correspond to median values in six redshift bins. From top to bottom the curves show $\Omega_M, \Omega_\Lambda = 0.3, 0.7$, $\Omega_M, \Omega_\Lambda = 0.3, 0.0$, and $\Omega_M, \Omega_\Lambda = 1.0, 0.0$.

lensing is not a significant problem, however, the effect scales roughly as z^2, and by $z = 1.5$, the effect can be as large as 25% [25]. While corrections can be derived by measuring the distortion on background galaxies in the line-of-site region around each SN, at $z > 1$, this problem may be one which ultimately limits the accuracy of luminosity distance measurements, unless a large enough set of SN at each redshift can be used to characterize the lensing distribution and average out the effect.

Evolution

SN Ia are seen to evolve in the nearby Universe. Hamuy et al. plotted the shape of the SN light curves against the type of host galaxy [19]. Early hosts (ones without recent star formation), consistently show light curves which rise and fade more quickly than those objects which occur in late-type hosts (objects with on-going star formation). However, once corrected for light curve shape, the corrected luminosity shows no bias as a function of host type. This empirical investigation provides confidence in using SN Ia over a variety of stellar population ages. It is possible, of course, to devise scenarios where some of the more distant supernovae do not have nearby analogues; therefore, at increasingly higher redshifts it can become important to obtain sufficiently detailed spectroscopic and photometric observations of each distant supernova to recognize and reject such examples that have no nearby analogues.

In principle, it could be possible to use the differences in the spectra and light curves between nearby and distant samples to correct any differences

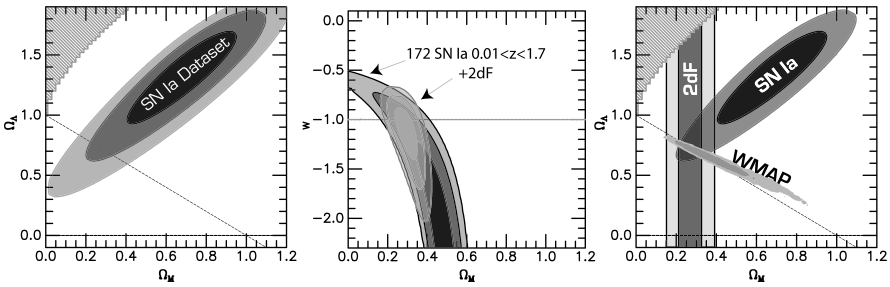

Fig. 3. Left Panel: The joint confidence contours for Ω_M, Ω_Λ using the Tonry et al. compilation of objects. Center Panel: Contours of Ω_M versus w_x from current observational data, where $\Omega_M + \Omega_x = 1$ has been used as a prior overlaid by contours including the current value of Ω_M from the 2dF redshift survey as an additional prior. Right Panel: Contours of Ω_M versus Ω_Λ from three current observational experiments; High-Z SN Ia [56], WMAP [53], and the 2dF redshift survey [59].

in absolute magnitude. Unfortunately theoretical investigations are not yet advanced enough to precisely quantify the effect of these differences on the absolute magnitude. A different empirical approach to handle SN evolution is to divide the supernovae into subsamples of very closely matched events, based on the details of the object's light curve, spectral time series, host galaxy properties, etc. A separate Hubble diagram can then be constructed for each subsample of supernovae, and each will yield an independent measurement of the cosmological parameters [1]. The agreement (or disagreement) between the results from the separate subsamples is an indicator of the total effect of evolution. A simple, first attempt at this kind of test has been performed comparing the results for supernovae found in elliptical host galaxies to supernovae found in late spirals or irregular hosts; the cosmological results from these subsamples were found to agree well [54].

Finally, it is possible to move to higher redshift and see if the SN deviate from the predictions of Eq. 2. At a gross level, we expect an accelerating Universe to be decelerating in the past because the matter density of the Universe increases with redshift, whereas the density of any dark energy leading to acceleration will increase at a slower rate than this (or not at all in the case of a Cosmological Constant). If the observed acceleration is caused by some sort of systematic effect, it is likely to continue to increase (or at least remain steady) with look-back time, rather than disappear like the effects of dark energy. A first comparison has been made with SN 1997ff [14] at $z \sim 1.7$, and it seems consistent with a decelerating Universe at this epoch [50]. More objects are necessary for a definitive answer, and these should be provided by a large program using the Hubble Space Telescope in 2002-3 by Riess and collaborators.

3.3 High Redshift SN Ia Observations

The SCP in 1997 announced their first results with 7 objects at a redshift around $z = 0.4$ [40]. These objects hinted to a decelerating Universe with a measurement of $\Omega_M = 0.88^{+0.69}_{-0.60}$, but were not definitive. Soon after, a $z \sim 0.8$ object observed with HST [41], and the first five objects of the HZSNS [11, 52] ruled out a $\Omega_M = 1$ universe with greater than 95% significance. These results were again superceded dramatically when both the HZSNS [48] and the SCP [42] announced results that showed not only were the SN observations incompatible with a $\Omega_M = 1$ universe, they were also incompatible with a Universe containing only normal matter. Both samples show that SN are, on average, fainter than what would be expected for even an empty Universe, indicating that the Universe is accelerating. The agreement between the two teams experimental results is spectacular, especially considering the two programs have worked in near complete isolation.

The easiest solution to explain the observed acceleration is to include an additional component of matter with an equation-of-state parameter more negative than $w < -1/3$; the most familiar being the Cosmological constant ($w = -1$). If we assume the universe is composed only of normal matter and a cosmological constant, then with greater than 99.9% confidence, the Universe has a cosmological constant.

Since 1998, many new objects have been added and these can be used to further test past conclusions. Tonry et al. has compiled current data (Fig. 2), and used only the new data to re-measure Ω_M, Ω_Λ, and find, more constrained, but perfectly compatible set of values with the SCP and High-Z 1998/99 results [56]. A similar study has been done with a set of objects observed using the Hubble Space Telescope by Knop et al. which also find concordance between the old data and new observations [27]. The 1998 results were not a statistical fluke, these independent sets of SN Ia still show acceleration. Tonry et al. has compiled all useful data from all sources (both teams) and provides the tightest constraints of SN Ia data so far [56]. These are shown in Fig. 3.

Of course, we do not know the form of dark energy which is leading to the acceleration, and it is worthwhile investigating what other forms of energy are possible second components [12, 42]. Fig. 3 shows the joint confidence contours for Ω_M and w_x (the equation of state of the unknown component causing the acceleration) using the current compiled data set [56]. Because this introduces an extra parameter, we apply the additional constraint that $\Omega_M + \Omega_x = 1$, as indicated by the Cosmic Microwave Background Experiments [7, 53]. The cosmological constant is preferred, but anything with a $w < -0.73$ is acceptable.

Additionally, we can add information about the value of Ω_M, as supplied by recent 2dF redshift survey results [59], as shown in the 2nd panel, where the constraint strengthens to $w < -0.73$ at 95% confidence. As a further test, if we assume a flat Λ universe, and derive Ω_M, independent of other

methods, the SN Ia data give $\Omega_M = 0.28 \pm 0.05$, in perfect accord with the 2dF results. These results are essentially identical, both in value and in size of uncertainty, to those obtained from the recent WMAP experiment [53] when they combine their experiment with the 2dF results. Taken in whole, we have three cosmological experiments — SN Ia, Large Scale Structure, and the Cosmic Microwave Background, each probing parameter space in a slightly different way, and each agreeing with each other. Fig. 3 shows that in order for the accelerating Universe to go away, two of these three experiments must both have severe systematic errors, and have these errors conspire in a way to overlap with each other to give a coherent story.

4 The Future

How far can we push the SN measurements? Finding more and more SN allows us to beat down statistical errors to arbitrarily small amounts, but ultimately systematic effects will limit the precision by which SN Ia distances can be applied to measure distances. A careful inspection of Fig. 3 show the best fitting SN Ia cosmology, does not lie on the $\Omega_{tot} = 1$ line, but rather at higher Ω_M, and Ω_Λ. This is because, at a statistical significance of 1.5σ, the SN data show the onset and departure of deceleration (centered around $z = 0.5$) occurs faster than the flat model allows. The total size of the effect is roughly 0.04 mag, which is within the current allowable systematic uncertainties that this data set allows. So while this may be a real effect, it could equally plausibly be a systematic error, or just a statistical fluke.

Our best estimate is that it is possible to control systematic effects from a ground based experiment to a level of 0.03 mag. A carefully controlled ground based experiment of 200 SN will reach this statistical uncertainty in $z = 0.1$ redshift bins, and is achievable in a five year time frame. The Essence project and CFHT Legacy survey are such experiments, and should provide answers over the coming years.

The Supernova/Acceleration Probe (SNAP) collaboration has proposed to launch a dedicated Cosmology satellite - the ultimate SN Ia experiment. This device, will, if funded, scan many square degrees of sky, discovering a thousand SN Ia in a year, and obtain spectra and lightcurves of objects out to $z = 1.8$. Besides the large numbers of objects and their extended redshift range, space also provides the opportunity to control many systematic effects better than from the ground.

With rapidly improving CMB data from interferometers, the satellites MAP and Planck, and balloon based instrumentation planned for the next several years, CMB measurements promise dramatic improvements in precision on many of the cosmological parameters. However, the CMB measurements are relatively insensitive to the dark energy and the epoch of cosmic acceleration. SN Ia are currently the only way to directly study this

acceleration epoch with sufficient precision (and control on systematic uncertainties) that we can investigate the properties of the dark energy, and any time-dependence in these properties. This ambitious goal will require complementary and cross-checking measurements of, for example, Ω_M from CMB, weak lensing, and large scale structure. The supernova measurements will also provide a test of the cosmological results independent from these other techniques (since CMB and weak lensing measurements are, of course, not themselves immune to systematic effects). By moving forward simultaneously on these experimental fronts, we have the plausible and exciting possibility of achieving a comprehensive measurement of the fundamental properties of our Universe.

References

1. D. Branch, S. Perlmutter, E. Baron, P. Nugent: In *R*esource Book on Dark Energy, ed. E.V. Linder, astro-ph 0109070
2. D. Branch, A. Fisher, E. Baron, P. Nugent: Astrophys. J. Lett. **470**, 7 (1996)
3. D. Branch: In *Encycolpedia of Astronomy and Astrophysics* (San Diego: Academic, 1989) p. 733
4. D. Burstein: astro-ph 030659
5. R. Cadonau: PhD thesis, Univ. Basel (1987)
6. E. Cappellaro et al. : Astron. Astrophys. **322**, 431 (1997)
7. P. de Bernardis et al. : Nature **404**, 955 (2000)
8. A.V. Filippenko: In *SN 1987A and Other Supernovae*, ed. I.J. Danziger, K. Kjar (Garching: ESO, 1991) p. 343
9. A.V. Fillipenko et al. : Astrophys. J. Lett. **384**, 15 (1992)
10. A. Fisher, D. Branch, P. Hoeflich, A. Khokhlov: Astrophys. J. Lett. **447**, 73 (1995)
11. P. Garnavich et al. : Astrophys. J. Lett. **493**, 53 (1998)
12. P. Garnavich et al. : Astrophys. J. **509**, 74 (1998)
13. L.G. Germany, A.G. Riess, B.P. Schmidt, N.B. Suntzeff: in press
14. R.L. Gilliland, P.E. Nugent, M.M. Phillips: Astrophys. J. **521**, 30 (1999)
15. A. Goobar, S. Perlmutter: Astrophys. J. **450**, 14 (1995)
16. M. Hamuy et al. : Astron. J. **102**, 208 (1991)
17. M. Hamuy et al. : Astron. J. **106**, 2392 (1993)
18. M. Hamuy, M.M. Phillips, J. Maza, N.B. Suntzeff, R.A. Schommer, R. Aviles: Astron. J. **109**, 1 (1995)
19. M. Hamuy et al. : Astron. J. **112**, 2391 (1996)
20. M. Hamuy et al. : Astron. J. **112**, 2408 (1996)
21. M. Hamuy P.A. Pinto: Astron. J. **117**, 1185 (1999)
22. L. Hansen, H.E. Jorgensen, H.U. Norgaard-Nielsen, R.S. Ellis, W.J. Couch: Astron. Astrophys. **211**, L9 (1989)
23. R.P. Harkness, J.C. Wheeler: In *Supernovae*, ed. A.G. Petschek (New York: Springer-Verlag, 1990) p. 1
24. D.E. Holz, R.M. Wald: Phys. Rev. **D58**, 063501 (1998)
25. D.E. Holz: Astrophys. J. **506**, 1 (1998)
26. R. Kantowski, T. Vaughan, D. Branch: Astrophys. J. **447**, 35 (1995)

27. R.A. Knop et al. : astro-ph 0309368
28. C.T. Kowal: Astron. J. **272**, 1021 (1968)
29. B. Leibundgut: PhD thesis, Univ. Basel, (1988)
30. B. Leibundgut G.A. Tammann: Astron. Astrophys. **230**, 81 (1990)
31. B. Leibundgut, G.A. Tammann, R. Cadonau, D. Cerrito: Astron. Astrophys. Suppl. **89**, 537 (1991)
32. B. Leibundgut et al. : Astron. J. **105**, 301 (1993)
33. D.L. Miller, D. Branch: Astron. J. **100**, 530 (1990)
34. H.U. Norgaard-Nielsen, L. Hansen, H.E. Jorgensen, A. Salamanca, R.S. Ellis: Nature **339**, 523 (1989)
35. N. Panagia: In *Supernovae as Distance Indicators*, ed. N. Bartel (Berlin: Springer-Verlag, 1985) p. 14
36. R. Pain et al. : Astrophys. J. **473**, 356 (1996)
37. R. Pain et al. : Ap.J. in press
38. G. Pearce, B. Patchett, J. Allington-Smith, I. Parry: Astrophys. Space Sci. **150**, 267 (1988)
39. S. Perlmutter et al. : IAUC 5956, 6263, 6270
40. S. Perlmutter et al. : Astrophys. J. **483**, 565 (1997)
41. S. Perlmutter et al. : Nature **391**, 51 (1998)
42. S. Perlmutter et al. : Astrophys. J. **517**, 565 (1999)
43. M.M. Phillips et al. : Pub. Astron. Soc. Pacific **99**, 592 (1987)
44. M.M. Phillips et al. : Astron. J. **103**, 1632 (1992)
45. M.M. Phillips: Astrophys. J. Lett. **413**, 105 (1993)
46. M.M. Phillips, P. Lira, N.B. Suntzeff, R.A. Schommer, M. Hamuy, J. Maza: Astron. J. **118**, 1766 (1999)
47. A.G. Riess, W.H. Press, R.P. Kirshner: Astrophys. J. **473**, 88 (1996)
48. A.G. Riess et al. : Astron. J. **116**, 1009 (1998)
49. A.G. Riess, A.V. Filippenko, W. Li, B.P. Schmidt: Astron. J. **118**, 2668 (1999)
50. A.G. Riess et al. : Astrophys. J. **560**, 49 (2001)
51. D.J. Schlegel, D.P. Finkbeiner, M. Davis: Astrophys. J. **500**, 525 (1998)
52. B. Schmidt et al. : Astrophys. J. **507**, 46 (1998)
53. D.N. Spergel et al. : Astrophys. J. Suppl. **148**, 175 (2003)
54. M. Sullivan et al. : Mon. Not. R. Astron. Soc. **340**, 1057 (2003)
55. G.A. Tammann, A. Sandage: Astrophys. J. **452**, 16 (1995)
56. J.L. Tonry et al. : Astrophys. J. **594**, 1 (2003)
57. A. Uomoto, R.P. Kirshner: Astron. Astrophys. **149**, L7 (1985)
58. S. van den Bergh: Astrophys. J. Lett. **453**, 55 (1995)
59. L. Verde et al. : Mon. Not. R. Astron. Soc. **335**, 432 (2002)
60. J. Wambsgabss, R. Cen, X. Guohong, J. Ostriker: Astrophys. J. Lett. **475**, 81 (1997)
61. J.C. Wheeler, R. Levreault: Astrophys. J. Lett. **294**, 17 (1985)

Observations of Type Ia Supernovae and Challenges for Cosmology

Weidong Li and Alexei V. Filippenko

Department of Astronomy, University of California, Berkeley, CA 94720-3411, USA;
wli@astro.berkeley.edu, alex@astro.berkeley.edu

Summary. Observations of Type Ia supernovae (SNe Ia) reveal correlations between their luminosities and light-curve shapes, and between their spectral sequence and photometric sequence. Assuming SNe Ia do not evolve at different redshifts, the Hubble diagram of SNe Ia may indicate an accelerating Universe, the signature of a cosmological constant or other forms of dark energy. Several studies raise concerns about the evolution of SNe Ia (e.g., the peculiarity rate, the rise time, and the color of SNe Ia at different redshifts), but all these studies suffer from the difficulties of obtaining high-quality spectroscopy and photometry for SNe Ia at high redshifts. There are also some troubling cases of SNe Ia that provide counterexamples to the observed correlations, suggesting that a secondary parameter is necessary to describe the whole SN Ia family. Understanding SNe Ia both observationally and theoretically will be the key to boosting confidence in the SN Ia cosmological results.

1 Observations of SNe Ia and the Accelerating Universe

Spectroscopic observations of nearby Type Ia supernovae (SNe Ia) reveal that they can be divided into several subclasses: the majority are the so-called "normal" or "Branch normal" SNe Ia [6], while the others are "peculiar" SNe Ia which can be further divided into SN 1991T-like or SN 1991bg-like objects (see [11] and references therein). Li et al. [27] discuss SN 1999aa-like objects as another potential subclass of the peculiar SNe Ia. The classification is based on the spectra of SNe Ia before or near maximum light: normal SNe Ia show conspicuous features of Si II, Ca II, and other intermediate-mass elements (IMEs; e.g., S II, O I); SN 1991T-like objects show unusually weak IME lines, yet prominent high-excitation features of Fe III; SN 1991bg-like objects have strong IME features, plus a broad Ti II absorption trough around 4100 Å and enhanced Si II/Ti II λ5800 absorptions. SN 1999aa-like objects are similar to the SN 1991T-like ones, but with significant Ca II H & K absorption lines.

Photometric observations of nearby SNe Ia also reveal a correlation between the peak luminosity and light-curve shape (LLCS correlation, hereafter). This was first convincingly demonstrated by Phillips (1993), and subsequently exploited by [16, 34, 37, 38]. The slower, broader light curves are intrinsically brighter at peak than the faster, narrower light curves. Various

parameters have been proposed to quantify the "speed" of the light curve, such as $\Delta m_{15}(B)$ (the decline in magnitudes between peak brightness and 15 days later in the B band), Δ (the difference in magnitudes between the peak brightness of a SN Ia and a nominal standard SN Ia), s ("stretch factor," the amount of stretch applied to the light curve (generally B band) of a SN Ia to match those of a nominal standard SN Ia), and various empirical methods have been developed to calibrate the peak absolute magnitudes of SNe Ia [16, 23, 34, 36, 38, 51]. The multi-color light-curve shape (MLCS) method, for example, has demonstrated the ability to achieve a scatter in the calibrated absolute magnitudes of SNe Ia to $\sim$0.15 mag [38].

By assuming that the observed correlation for nearby SNe Ia also applies to the objects at high redshift, utilizing the empirical calibration methods developed from nearby SNe Ia, and studying the Hubble diagram for SNe Ia at both low and high redshifts, the High-z SN Search Team [45] and the SN Cosmology Project [34] have measured that high-redshift SNe Ia are fainter than expected, and interpreted this result as evidence that the expansion of the Universe is accelerating, due perhaps to a non-zero cosmological constant or some other forms of dark energy (e.g., [24, 35, 39, 47].

2 Challenges of the Accelerating Universe

The observational fact is that the SNe Ia at $z \approx 0.5$ are $\sim$0.28 mag dimmer ($\sim$14% farther) than expected in a Universe with $\Omega_M = 0.3$ and no cosmological constant. Besides the interpretation of a positive cosmological constant, other possible alternatives have been proposed as follows.

1. Luminosity evolution. Two important questions are (a) whether the high-redshift SNe Ia follow the same LLCS correlation for the nearby objects, and (b) whether the SNe Ia at $z \approx 0.5$ are intrinsically fainter than nearby SNe Ia by 0.28 mag after correction for the LLCS correlation.
2. Interstellar dust, which produces more extinction of the high-redshift SNe Ia and makes them look apparently fainter.
3. Selection bias: preferentially fainter SNe Ia are observed at high redshift.
4. Gravitational lensing: the inhomogeneous distribution of matter in the Universe deamplifies the observed brightness of most high-redshift SNe Ia.

Among these, ordinary dust is not considered a viable option, as it introduces too much reddening in the colors of SNe Ia at high redshift [41, 42] and more dispersion in the distance measurements than is currently observed. "Grey" dust [1, 2], which leaves little or no imprint on the spectral energy distribution of a SN Ia, could be more pernicious, but the amount of grey dust required to explain the faintness of high-redshift SNe Ia would also distort the cosmic microwave background, an effect which has not been seen. Moreover, it still introduces more distance dispersion than is currently observed.

Tonry et al. [47] also provided evidence that a systematic effect which goes as a power law of $(1+z)$, such as extinction by dust, is not likely to match the SN Ia data. No known selection bias favors detection of intrinsically fainter SNe Ia at high redshift. Malmquist bias may afflict the nearby SN Ia sample so preferentially brighter objects were observed, but the effect is shown to be small [35, 39]. Moreover, the high-redshift SN Ia sample should be subject to the same bias to a greater extent, since most high-redshift SN searches are magnitude-limited. Gravitational lensing deamplification [4, 32], typically $\sim$ 2% at $z = 0.5$, is much smaller than the cosmological effect.

Luminosity evolution is arguably the most serious challenge to the cosmological interpretation of high-redshift SNe Ia. The cause of this is somewhat embarrassing: despite being the most luminous type of SN, SNe Ia have not been completely understood theoretically (see [25] for a review), or have the progenitor system conclusively identified (see [30] for a review). Consequently, theory cannot provide conclusive guidance on whether or how SNe Ia and their progenitor systems evolve at different redshifts. Nevertheless, theorists have provided some insights into this question by studying the effects of metallicity and the C/O ratio of a white dwarf (WD), the agreed precursor to a SN Ia (e.g., [22, 33, 48, 49]). Höflich, Wheeler, & Thielemann [22] suggested that the effect of changing metallicity on the rest-frame visual and blue light curves is small, and as the C/O ratio of a WD becomes progressively lower at higher redshift, the luminosity of the resulting SN Ia becomes brighter for the same light-curve shape, an effect that is contrary to the cosmological result from SNe Ia. Umeda et al. [48] and Nomoto et al. [33] use the variation in the C/O ratio in the WD to explain the distribution of SN Ia brightness, but suggest that the diversity can be normalized by applying the LLCS correlation.

Answers to the question of whether SNe Ia evolve have also been sought from observations of them at different redshifts. The nearby sample is an excellent laboratory for studying possible luminosity evolution, since SNe Ia have been observed in a wide range of host-galaxy morphologies including ellipticals, spirals, irregulars, and dwarf galaxies. In fact, the range of metallicity, stellar age, and interstellar environments probed by the nearby SN Ia sample is much greater than the mean evolution in these properties for individual galaxies between $z = 0$ and $z = 0.5$. Some variation of the observed characteristics of SNe Ia has been noticed; for example, luminous events occur preferentially in metal-poor environments [19], and the luminosity of SNe Ia correlates with the projected distance from the host nucleus [50]. However, after correction for the LLCS correlation and extinction, the observed residuals from the Hubble flow do not correlate with host-galaxy morphology or the projected radial distances [41, 42, 46]. This suggests that the LLCS correlation applies to a wide range of stellar environments and is a strong argument against significant evolution to $z = 0.5$ [45].

The empirical test of luminosity evolution at high redshift has been focused on getting high-quality spectra and light curves, and comparing them with those of nearby SNe Ia. The assumption of this test is that significant luminosity evolution would be accompanied by other visibly altered observables of the SNe. Comparison of high-quality spectra between nearby and high-redshift SN Ia have revealed remarkable similarity [8, 35, 39, 47]. Riess et al. [41, 42] also obtained the rest-frame I-band light curve of the high-redshift SN Ia 1999Q, which displayed the secondary maximum that is typical of normal nearby SNe Ia.

To date, there is no clear, direct evidence that suggests significant luminosity evolution for SNe Ia at different redshift. To rest the case of luminosity evolution, however, we need to fully understand the models of SNe Ia and how they evolve at different redshifts. Without a firm theoretical footing, we must conservatively demand that all observables of high-redshift SNe Ia be statistically consistent with their nearby counterparts.

In the following sections, we discuss in more detail some of the recent comparisons done on the observables and characteristics of SNe Ia at different redshifts, which mag suggest possible differences between high-redshift SNe Ia and their nearby counterparts.

2.1 Peculiarity Rate at Different Redshifts

The rate of "peculiar SNe Ia" in the nearby sample has been recently measured by [27]. They used a distance-limited sample of SNe Ia from the Lick Observatory Supernova Search (LOSS; [12]) and performed Monte Carlo simulations [26] demonstrating that essentially all SNe Ia should have been discovered in the sample galaxies of LOSS. Within this unbiased sample they found a rate of $\sim$20% for the SN 1991T/1999aa-like objects and $\sim$16% for the SN 1991bg-like objects, for a total peculiarity rate of $\sim$36%.

However, in the now more than 100 spectroscopically classified SNe Ia at high redshift, there has not been a single unambiguously peculiar SN Ia reported. While the lack of SN 1991bg-like objects could be explained by their intrinsic faintness and low expected rate in magnitude-limited searches, the lack of SN 1991T/1999aa-like objects is puzzling.

Li et al. [27] offered several possible explanations for the difference between the peculiarity rate of SNe Ia at different redshifts: extinction toward the SN 1991T/1999aa-like objects, difficulty in identifying peculiarities in poor-quality spectra of the high-redshift SNe Ia, and most importantly, the "age bias": the peculiarity of SN 1991T/1999aa-like objects can only be easily identified in early-time spectra. This same bias may also explain why the Calán/Tololo survey, a nearby magnitude-limited SN search, yielded no SN 1991T/1999aa-like objects among 29 SNe Ia [17].

If, however, these observational biases are not to blame, the absence of peculiar SNe Ia at high redshift could result from an evolution of the population of progenitor systems: certain progenitor channels at high redshift

may be lost due to a redshift-dependent variation in the mass, composition, and metallicity of SN Ia progenitors (e.g., [30, 44]). It is thus an important challenge to observationally identify some peculiar SNe Ia at high redshifts, to definitively rule out luminosity evolution as the cause of the difference in the peculiarity rate of SNe Ia at different redshifts.

2.2 Rise Time at Different Redshifts

The rise time is defined as the time interval between the explosion and the maximum brightness of a SN Ia. Precise knowledge of the SN Ia rise time, which is sensitive to the ejecta opacity and the distribution of ^{56}Ni, provides constraints on models of SN Ia progenitors. A comparison of the rise time for high-redshift and nearby SNe Ia is thus a valuable test of luminosity evolution.

The rise time for the nearby SNe Ia was measured by [40]. They collected about 25 measurements of SNe Ia between 10 and 18 days before B maximum, normalized them to a fiducial rise time curve, and measured a rise time of 19.98 ± 0.15 days. A preliminary rise time for the high-redshift SNe Ia was measured by [15] from the Supernova Cosmological Project (SCP) data as 17.50 ± 0.40 days, which is discrepant from the nearby rise time at a statistical likelihood greater than 99.99% (5.8σ). Aldering, Knop, & Nugent [3], however, refined the rise time for the high-redshift SNe Ia in the SCP data to 17.50 ± 1.20 days, a $\sim 2\sigma$ difference from the nearby measurement. They also suggested that under extreme situations the rise time could be biased up to 2–3 days due to observational biases and fitting methods.

It remains to be seen whether the rise times of high-redshift and nearby SNe Ia are statistically inconsistent when a better rise time measurement is derived for the high-redshift SNe Ia. It should also be noted that even if the two rise times are inconsistent with each other, it is unclear whether the difference in rise time could be translated into a difference in peak luminosity: most current theoretical models have difficulties in reproducing the observed rise times and the correlation between rise time and peak luminosity.

2.3 Intrinsic Color at Different Redshifts

To date, there is no consensus on the precise intrinsic colors of SNe Ia with different photometric behaviors. As a result, there is not a good theoretical or empirical method to accurately determine host-galaxy extinction to SNe Ia, and observers often have to resort to priors such as applying the Galactic reddening law to the host galaxies of SNe Ia, and assuming all SNe Ia have the same intrinsic color at maximum. Phillips et al. [37] proposed a method to estimate the host-galaxy reddening to a SN Ia by using its color at 30–60 days past maximum, but [28] showed that this method does not apply to all objects. The extinction correction is a major source of uncertainty in

the current empirical fitting methods. To circumvent this difficulty, people often use subsamples that are likely to have low extinction at both low and high redshifts. Fortunately, [21] showed that most SNe Ia should have low extinction.

Different methods for treating the extinction correction in the fitting process yield different results in the intrinsic color comparison of SNe Ia at a range of redshifts. Leibundgut [25] and Falco et al. [10] suggested that there is evidence from the $E(B-V)$ values in [39] that high-redshift SNe Ia are statistically bluer than their nearby counterparts, but analysis by [35] showed no such effect, nor did a recent compilation of 11 high-redshift SNe Ia observed by the *Hubble Space Telescope* [24]. The problem of extinction correction will continue to plague the empirical fitting methods until a better understanding of the intrinsic colors of SNe Ia is achieved, and the influence of extinction corrections on the cosmological conclusions needs to be investigated in more detail. Drell, Loredo, & Wasserman [9], for example, attributed the difference in colors to luminosity evolution, while [24] suggested that reasonable changes in colors do not have a significant impact on the cosmological results.

2.4 Peculiar Nearby SNe Ia

A fundamental assumption of the current empirical fitting methods is that the light curves of all normal SNe Ia can be represented by a single parameter such as $\Delta m_{15}(B)$, Δ, or s. However, there is growing evidence that not all SNe Ia form a one-parameter family. Branch [5] showed that normal SNe Ia could have very different expansion velocities. Hamuy et al. [18] showed that some light curves with similar decline rates have significant differences in particular details. Hatano et al. [21] also demonstrated that the spectroscopic diversity among SNe Ia is multi-dimensional.

The SN 1991T-like and SN 1991bg-like objects, though categorized as peculiar SNe Ia, generally follow the LLCS correlation and the spectrum–luminosity sequence – i.e., they seem to be an extension of the one-parameter description of normal SNe Ia. Some more disturbing cases of peculiar nearby SNe Ia that fail the one-parameter description are SN 2000cx [7, 26], SN 2002cx [29], SN 2001ay (Nugent et al. in preparation), and SN 2002ic [20].

The peculiarity of SN 2000cx is that its light curves cannot be fit well by the existing fitting methods. There is an apparent asymmetry in the B-band peak, in which the premaximum brightening is relatively fast (similar to that of the normal SN 1994D), but the postmaximum decline is relatively slow (similar to that of the overluminous SN 1991T). SN 2000cx has very blue colors and also unique spectral evolution. Its premaximum spectra are similar to those of SN 1991T-like objects, but the high-excitation Fe III lines remain prominent until well after maximum. The expansion velocities derived from the absorption features are unusually high and evolve differently than normal. Though it has a slow light curve, its estimated luminosity is average [26] or even slightly subluminous [7].

SN 2002cx has many properties that are the opposite of those of SN 2000cx. It has a premaximum spectrum similar to that of SN 1991T, a decline rate in the B-band similar to that of normal SNe Ia, but a luminosity similar to that of the very subluminous SN 1991bg. It has a very red color evolution, and has extremely low expansion velocities measured from spectral features. The R and I-band light curves have a peculiar plateau phase around maximum. The late-time decline rate in all $BVRI$ bands is unusually slow. SN 2003gq [13] may be another event that is similar to SN 2002cx.

SN 2001ay has a normal near-maximum spectrum, except that it has very high expansion velocities. The light curves of SN 2001ay are the slowest ever recorded, yet it has a normal luminosity. It also has a peculiar red color evolution until 30 days after maximum.

SN 2002ic is the only SN Ia to have shown direct evidence of SN ejecta interacting with the circumstellar medium (CSM). Its near-maximum spectrum is similar to that of SN 1991T, but diluted in strength. There are remarkable Balmer lines in later spectra, with $H\alpha$ showing an unresolved component (FWHM < 300 km s^{-1}) superimposed on a broad resolved base (FWHM ≈ 1800 km s^{-1}), similar to those observed in Type IIn SNe [11]. The spectral features and photometric behavior of SN 2002ic suggest that it has a very dense CSM. Based on these observations, [20] ruled out the double-degenerate model for SN 2002ic, and suggested that the progenitor system involves a white dwarf and an asymptotic giant branch star. Livio & Riess [31], however, argued that the opposite may be true: SN 2002ic results from a rare circumstance in which the SN Ia ejecta interact with the previously ejected common envelope of a double-degenerate system.

Although the frequency of these peculiar SNe Ia is low, and statistically they will not challenge the established empirical correlations, we need to understand why they are peculiar, and how they can be fit into the whole picture of SN Ia theories and observations. These objects with unusual properties might represent the general models of SNe Ia under extreme conditions, and studying them will provide clues to the theoretical models and progenitor systems. It is interesting to note that three of the four peculiar SNe Ia (SNe 2000cx, 2002cx, and 2001ay) all have very unusual expansion velocities, and three (SNe 2000cx, 2002cx, and 2002ic) show spectral features similar to those of SN 1991T. The subclass of SN 1991T/1999aa-like objects may thus be more heterogeneous than other SNe Ia, and objects with unusual expansion velocities should be treated with caution when used as cosmological tools.

3 Conclusions

Many alternatives have been proposed to explain the SN Ia data at different redshifts, but so far none has seriously challenged the accelerating Universe

result. We have found no clear, direct evidence that SNe Ia at different redshifts evolve, though some studies show that there may exist some differences in their peculiarity rate, rise time, or colors.

The key to boosting confidence in the cosmological results from SNe Ia is to understand SNe Ia both theoretically and observationally. We need to theoretically identify the elusive progenitor systems for SNe Ia, and find out the cause of the diversity of SNe Ia. Similarly, we need to continue to search for SN/CSM interactions such as that observed in SN 2002ic, and place stringent constraints on the accretion history of SN Ia progenitors. We also need to re-examine existing observations of SNe IIn, to investigate whether SN 2002ic is an isolated case, or whether some additional SNe IIn are actually SNe Ia with strong SN/CSM interaction. For nearby SNe Ia, we need to develop better methods to measure host-galaxy extinction than currently available, study the environmental effects, find more empirical correlations, and develop a subclassification scheme that possibly links to different progenitor channels. We should continue to study those SNe Ia that are clearly discrepant. For high-redshift SNe Ia, we need to identify some peculiar SN 1991T-like or SN 1991bg-like objects, get better rise time measurements, obtain more high-quality spectra and light curves, and compare them with those of nearby SNe Ia. The ESSENCE project (e.g., [14]), SNAP satellite (*http://snap.lbl.gov/*), and the higher-z project [43] are prime examples of current and future extensive studies of high-redshift SNe Ia.

Acknowledgement. Our research is currently supported by NSF grants AST-0206329 and AST-0307894, by the Sylvia & Jim Katzman Foundation, and by NASA grants GO-8641, GO-9114, and GO-9352 from the Space Telescope Science Institute, which is operated by AURA, Inc., under NASA contract NAS 5-26555. We thank the conference organizers for partial travel funds.

References

1. A.N. Aguirre: Astrophys. J. Lett. **512**, L19 (1999)
2. A.N. Aguirre: Astrophys. J. **525**, 583 (1999)
3. G. Aldering, R. Knop, P. Nugent: Astron. J. **119**, 2110 (2000)
4. A.J. Barber: Mon. Not. R. Astron. Soc. **318**, 195 (2000)
5. D. Branch: Astrophys. J. Lett. **316**, L81 (1987)
6. D. Branch, A. Fisher, P. Nugent: Astron. J. **106**, 2383 (1993)
7. P. Candia et al. : Pub. Astron. Soc. Pacific **115**, 277 (2003)
8. A. Coil et al. : Astrophys. J. Lett. **544**, L111 (2000)
9. P.S. Drell, T.J. Loredo, I. Wasserman: Astrophys. J. **530**, 593 (2000)
10. E. Falco et al. : Astrophys. J. **523**, 617 (1999)
11. A.V. Filippenko: Ann. Rev. Astron. Astrophys. **35**, 309 (1997)
12. A.V. Filippenko, W.D. Li, R.R. Treffers, M. Modjaz: In: *Small-Telescope Astronomy on Global Scales*, eds. W.P. Chen, C. Lemme, B. Paczyński (San Francisco: Astron. Soc. Pac., 2001) p. 121

13. A.V. Filippenko, R. Foley, R.: IAUC (2003)
14. P.M. Garnavich et al. : Bull. Am. Astron. Soc. **201**, 7809 (2002)
15. G. Goldhaber: Bull. Am. Astron. Soc. **193**, 4713 (1998)
16. M. Hamuy et al. : Astron. J. **112**, 2391 (1996)
17. M. Hamuy et al. : Astron. J. **112**, 2408 (1996)
18. M. Hamuy et al. : Astron. J. **112**, 2438 (1996)
19. M. Hamuy et al. : Astron. J. **120**, 1479 (2000)
20. M. Hamuy et al. : Nature **424** 651 (2003)
21. K. Hatano, D. Branch, J. Deaton: Astrophys. J. **502**, 177 (1998)
22. P. Höflich, J.C. Wheeler, F.-K. Thielemann: Astrophys. J. **502**, 177 (1998)
23. S. Jha: PhD thesis, Harvard Univ. (2002)
24. R.A. Knop et al. : astro-ph 0309368
25. B. Leibundgut: Ann. Rev. Astron. Astrophys. **39**, 67 (2001)
26. W. Li, A.V. Filippenko, A.G. Riess: Astrophys. J. **546**, 719 (2001)
27. W. Li et al. : Astrophys. J. **546**, 734 (2001)
28. W. Li et al. : Pub. Astron. Soc. Pacific **113**, 1178 (2001)
29. W. Li et al. : Pub. Astron. Soc. Pacific **115**, 453 (2003)
30. M. Livio: In: *Type Ia Supernovae, Theory and Cosmology*, eds. J.C. Niemeyer, J.W. Truran (Cambridge University Press, 2000) p. 33
31. M. Livio, A.G. Riess: Astrophys. J. Lett. **594**, L93 (2003)
32. R.B. Metcalf: Mon. Not. R. Astron. Soc. **305**, 746 (1999)
33. K. Nomoto et al. : In: *From Twilight to Highlight: The Physics of Supernovae*, eds. W. Hillebrandt, B. Leibundgut (Berlin: Springer, 2003) p. 115
34. S. Perlmutter et al. : Astrophys. J. **483**, 565 (1997)
35. S. Perlmutter et al. : Astrophys. J. **517**, 565 (1999)
36. M.M. Phillips: Astrophys. J. Lett. **413**, L105 (1993)
37. M.M. Phillips et al. : Astron. J. **118**, 1766 (1999)
38. A.G. Riess, W.H. Press, R.P. Kirshner: Astrophys. J. **473**, 88 (1996)
39. A.G. Riess et al. : Astron. J. **116**, 1009 (1998)
40. A.G. Riess et al. : Astron. J. **118**, 2675 (1999)
41. A.G. Riess: Pub. Astron. Soc. Pacific **112**, 1284 (2000)
42. A.G. Riess et al. : Astrophys. J. **536**, 62 (2000)
43. A.G. Riess: Bull. Am. Astron. Soc. **201**, 3901 (2002)
44. P. Ruiz-Lapuente, R. Canal: Astrophys. J. **497**, 57 (1998)
45. B.P. Schmidt et al. : Astrophys. J. **507**, 46 (1998)
46. M. Sullivan et al. : Mon. Not. R. Astron. Soc. **340**, 1057 (2003)
47. J.L. Tonry et al. : Astrophys. J. **594**, 1 (2003)
48. H. Umeda et al. : Astrophys. J. **522**, 43 (1999)
49. T. von Hippel, G.D. Bothun, R.A. Schommer: Astron. J. **114**, 1154 (1997)
50. L. Wang, P. Höflich, J.C. Wheeler: Astrophys. J. **483**, 29 (1997)
51. L. Wang, G. Goldhaber, G. Aldering, S. Perlmutter: Astrophys. J. **590**, 944 (2003)

The Standard Candle Method for Type II Supernovae and the Hubble Constant

Mario Hamuy

The Observatories of the Carnegie Institution of Washington
mhamuy@ociw.edu

Summary. The "standard candle method" for Type II plateau supernovae produces a Hubble diagram with a dispersion of 0.3 mag, which implies that this technique can produce distances with a precision of 15%. Using four nearby supernovae with Cepheid distances I find $H_0(V)$=75±7, and $H_0(I)$=65±12.

1 Introduction

Type II supernovae are exploding stars characterized by strong hydrogen spectral lines and their proximity to star forming regions, presumably resulting from the gravitational collapse of the cores of massive stars (M_{ZAMS}>8 $M_{\odot}$). These objects display great variations in their spectra and lightcurves depending on the properties of their progenitors at the time of core collapse and the density of the medium in which they explode [6]. The plateau subclass (SNe IIP) constitutes a well-defined family which can be distinguished by 1) a characteristic "plateau" lightcurve [1], 2) Balmer lines exhibiting broad P-Cygni profiles, and 3) low radio emission [15]. These SNe are thought to have red supergiant progenitors that do not experience significant mass loss and are able to retain most of their H-rich envelopes before explosion.

Although SNe IIP display a wide range in luminosity, rendering their use as standard candles difficult, Hamuy & Pinto [5] (HP02) used a sample of 17 SNe II to show that the relative luminosities of these objects can be standardized from a spectroscopic measurement of the SN ejecta velocity. Recently, I confirmed the luminosity-velocity relation [7] (H03) from a sample of 24 SNe IIP. This study showed that the "standard candle method" (SCM) yields a Hubble diagram with a dispersion of 0.3 mag, which implies that SNe IIP can be used to derive extragalactic distances with a precision of 15%. Since the work of H03, Cepheid distances to two SNe IIP have been published, bringing to four the total number of SNe IIP with Cepheid distances. In this paper I use these four objects to improve the calibration of the Hubble diagram, and solve for the value of the Hubble constant.

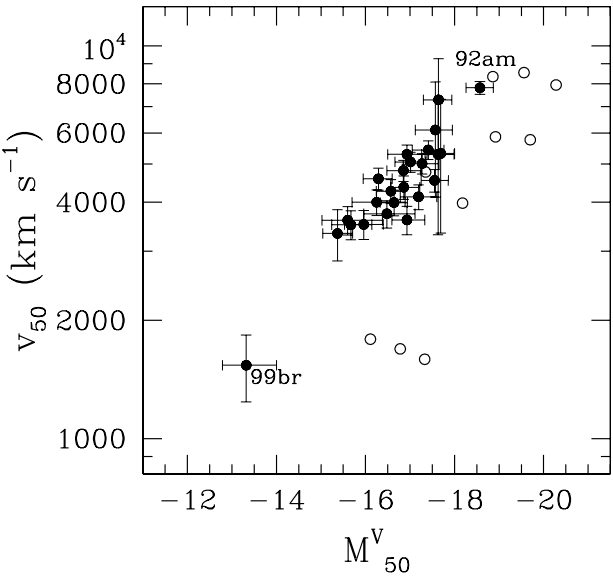

Fig. 1. Envelope velocity versus absolute plateau V magnitude for 24 SNe IIP, both measured in the middle of the plateau (day 50) (filled circles). The expansion velocities were obtained from the minimum of the Fe II λ5169 lines. The absolute magnitudes were derived from redshift-based distances and observed magnitudes corrected for dust extinction. Open circles correspond to explosion models computed by [9] and [10] for stars with $M_{ZAMS} \geq 8\ M_{\odot}$.

2 The Luminosity-Velocity Relation

The SCM is based on the luminosity-velocity relation, which permits one to standardize the relative luminosities of SNe IIP. Figure 1 shows the latest version, based on 24 genuine SNe IIP. This plot reveals the well-known fact that SNe IIP encompass a wide range ($\sim$5 mag) in luminosities. This correlation reflects the fact that while the explosion energy increases, so do the kinetic energy and internal energies. Also plotted in this figure with open circles are the explosion models computed by [9] and [10] for stars with $M_{ZAMS} \geq 8$ $M_{\odot}$, which reveals a reasonable agreement with observations.

3 The Hubble Diagram

In a uniform and isotropic Universe we expect locally a linear relation between distance and redshift. A perfect standard candle should describe a straight line in the magnitude-log(z) Hubble diagram, so the observed scatter is a measure of how standard the candle is. Next I assess the performance of the SCM based on the Hubble diagram constructed with the magnitudes and redshifts given in Table 1 for 24 SNe.

Table 1. Redshifts, Extinction, Magnitudes, and Ejecta Velocities of the 24 Type II Supernovae

SN	v_{CMB} (km s^{-1})	$A_{GAL}(V)$	$A_{host}(V)$	V_{50}	I_{50}	v_{50} (km s^{-1})
	±187	±0.06	±0.3			
1968L	321	0.219	0.00	12.03(08)	...	4020(300)
1969L	784	0.205	0.00	13.35(06)	...	4841(300)
1970G	580	0.028	0.00	12.10(15)	...	5041(300)
1973R	808	0.107	1.40	14.56(05)	...	5092(300)
1986I	1333	0.129	0.20	14.55(20)	14.05(09)	3623(300)
1986L	1466	0.099	0.30	14.57(05)	...	4150(300)
1988A	1332	0.136	0.00	15.00(05)	...	4613(300)
1989L	1332	0.123	0.15	15.47(05)	14.54(05)	3529(300)
1990E	1426	0.082	1.45	15.90(20)	14.56(20)	5324(300)
1990K	1818	0.047	0.20	14.50(20)	13.90(05)	6142(2000)
1991al	4484	0.168	0.00	16.62(05)	16.16(05)	7330(2000)
1991G	1152	0.065	0.00	15.53(07)	15.05(09)	3347(500)
1992H	2305	0.054	0.00	14.99(04)	...	5463(300)
1992af	5438	0.171	0.00	17.06(20)	16.56(20)	5322(2000)
1992am	14009	0.164	0.28	18.44(05)	17.99(05)	7868(300)
1992ba	1192	0.193	0.00	15.43(05)	14.76(05)	3523(300)
1993A	8933	0.572	0.05	19.64(05)	18.89(05)	4290(300)
1993S	9649	0.054	0.70	18.96(05)	18.25(05)	4569(300)
1999br	848	0.078	0.65	17.58(05)	16.71(05)	1545(300)
1999ca	3105	0.361	0.68	16.65(05)	15.77(05)	5353(2000)
1999cr	6376	0.324	0.00	18.33(05)	17.63(05)	4389(300)
1999eg	6494	0.388	0.00	18.65(05)	17.94(05)	4012(300)
1999em	838	0.130	0.18	13.98(05)	13.35(05)	3757(300)
1999gi	706	0.055	0.68	14.91(05)	13.98(05)	3617(300)

The CMB redshifts of the SN host galaxies were derived from the observed heliocentric redshifts. For the 16 SNe with cz<3000 km s^{-1} I corrected the redshifts for the peculiar motion of the SN hosts using the parametric model for peculiar flows of [14] (see H03 for details). In all cases I assigned an uncertainty of ±187 km s^{-1}, which corresponds to the cosmic thermal velocity yielded by the parametric model.

A convenient choice for SNe IIP is to use magnitudes in the middle of the plateau, so I interpolated the observed V and I fluxes to the time corresponding to 50 days after explosion. In order to use SNe IIP as standardized candles it proves necessary to correct the observed fluxes for dust absorption. The determination of Galactic extinction is under good control thanks to the IR dust maps of [12], which permit one to estimate $A_{GAL}(V)$ to ±0.06 mag. The determination of absorption in the host galaxy, on the other hand, is difficult. In H03 I described a method which assumes that SNe IIP should all reach the same color toward the end of the plateau phase. The underlying assumption is that the opacity in SNe IIP is dominated by e^- scattering, so they should

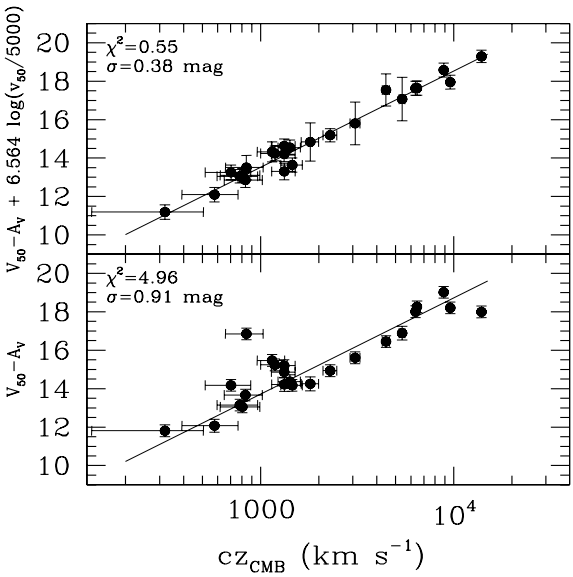

Fig. 2. (bottom) Raw Hubble diagram from SNe II plateau V magnitudes. (top) Hubble diagram from V magnitudes corrected for envelope expansion velocities.

all reach the temperature of hydrogen recombination as they evolve [2]. The method is not fully satisfactory since some discrepancies were obtained from $B-V$ and $V-I$ (probably caused by metallicity variations from SN to SN). An uncertainty of ± 0.3 mag can be assigned to this technique based on the reddening difference yielded by both colors.

The ejecta velocities come from the minimum of the Fe II λ5169 lines interpolated to day 50, which is good to ± 300 km s^{-1} [4]. In the four cases where I had to extrapolate velocities I adopted an uncertainty of ± 2000 km s^{-1}.

The bottom panel of Fig. 2 shows the Hubble diagram in the V band, after correcting the apparent magnitudes for the reddening values, while the top panel shows the same magnitudes after correction for expansion velocities. A least-squares fit to the data in the top panel yields the following solution,

$$V_{50} - A_V + 6.564(\pm 0.88)\ log(v_{50}/5000) = 5\ log(cz) - 1.478(\pm 0.11). \quad (1)$$

The scatter drops from 0.91 mag to 0.38 mag, thus demonstrating that the correction for ejecta velocities standardizes the luminosities of SNe IIP significantly. It is interesting to note that part of the spread comes from the nearby SNe which are potentially more affected by peculiar motions of their host galaxies. When the sample is restricted to the eight objects with cz>3,000 km s^{-1}, the scatter drops to only 0.33 mag. The corresponding fit for the restricted sample is,

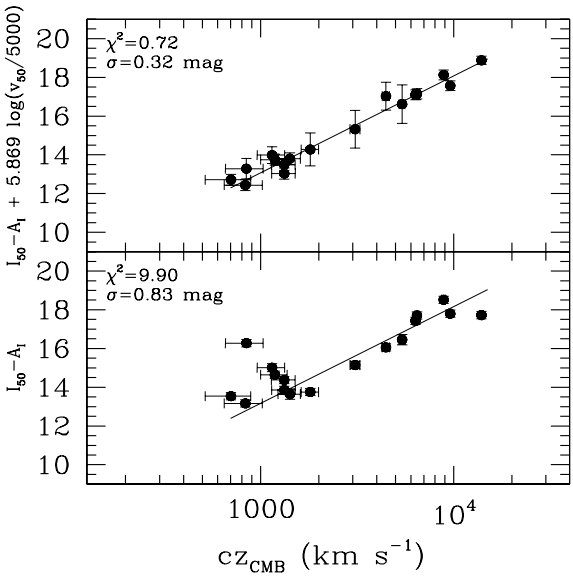

Fig. 3. (bottom) Raw Hubble diagram from SNe II plateau I magnitudes. (top) Hubble diagram from I magnitudes corrected for envelope expansion velocities.

$$V_{50} - A_V + 6.249(\pm 1.35)\ log(v_{50}/5000) = 5\ log(cz) - 1.464(\pm 0.15). \quad (2)$$

Figure 3 shows the same analysis but in the I band. In this case the scatter in the raw Hubble diagram is 0.83 mag, which drops to 0.32 mag after correction for ejecta velocities. This is even smaller that the 0.38 spread in the V band, possibly due to the fact that the effects of dust extinction are smaller at these wavelengths. The least-squares fit yields the following solution,

$$I_{50} - A_I + 5.869(\pm 0.68)\ log(v_{50}/5000) = 5\ log(cz) - 1.926(\pm 0.09). \quad (3)$$

When the eight most distant objects are employed the spread is 0.29 mag, similar to that obtained from the V magnitudes and the same sample, and the solution is,

$$I_{50} - A_I + 5.445(\pm 0.91)\ log(v_{50}/5000) = 5\ log(cz) - 1.923(\pm 0.11). \quad (4)$$

Table 2. The Hubble Constant

SN	Distance Modulus	Reference	$H_0(V)$ (km s^{-1} Mpc^{-1})	$H_0(I)$ (km s^{-1} Mpc^{-1})
1968L	28.25(15)	[13]	77±15	...
1970G	29.13(11)	[3]	77±13	...
1973R	29.86(08)	[3]	87±15	...
1999em	30.34(19)	[8]	64±13	65±12
Average			75±7	65±12

4 The Value of the Hubble Constant

The SCM can be used to solve for the Hubble constant, provided the distance to a nearby SN is known. If the distance D of the calibrator is known, and the distant sample is adopted, the Hubble constant is given by

$$H_0(V) = \frac{10^{V_{50} - A_V + 6.249 log(v_{50}/5000) + 1.464}}{D}, \tag{5}$$

$$H_0(I) = \frac{10^{I_{50} - A_I + 5.445 log(v_{50}/5000) + 1.923}}{D}. \tag{6}$$

Among the objects of our sample SN 1968L, SN 1970G, SN 1973R, and SN 1999em have precise Cepheid distances. The distances and the corresponding H_0 values are summarized in Table 2. SN 1999em is the only object that provides independent values from the V and I bands, and the results agree remarkably well. Within the uncertainties the values derived from the V-band magnitudes are in good agreement for all four objects, and the average proves to be $H_0(V)$=75±7 km s^{-1} Mpc^{-1}.

Currently, the most precise extragalactic distance indicators are the peak luminosities of SNe Ia. While the HST Key Project yielded a value of H_0=71±2 [3], Sandage and collaborators derived H_0=59±6 [11]. The difference is mostly due to systematic uncertainties in the Cepheid distances of the calibrating SNe. Since SCM is mainly calibrated with Cepheid distances of the HST Key Project, I conclude that both SNe Ia and SNe IIP give consistent results, which lends further credibility to the SCM.

HP02 found a value of H_0=55±12 based on one calibrator (SN 1987A), which proves significantly lower than the current 65-75 range. The main reason for this difference is that SN 1987A is not a plateau event and should not have been included in the HP02 sample since the physics of its lightcurve is different than that of SNe IIP.

5 Conclusions and Discussion

This sample of 24 SNe IIP shows that the luminosity-velocity relation can be used to standardize the luminosities of these objects. The resulting Hubble

diagram has a dispersion of 0.3 mag, which implies that SNe IIP can produce distances with a precision of 15%. Using four nearby SNe with Cepheid distances I find $H_0(V)$=75±7 and $H_0(I)$=65±12. These values compare with H_0=71±2 derived from SNe Ia [3], which lends further credibility to the SCM.

This study confirms that SNe IIP offer great potential as distance indicators. The recently launched Carnegie Supernova Program at Las Campanas Observatory has already targeted ∼20 such SNe and in the next years it will produce an unprecedented database of spectroscopy and photometry for ∼100 nearby SNe, which will be ideally suited for cosmological studies.

Although the precision of the SCM is only half as good as that produced by SNe Ia, with the 8-m class telescopes currently in operation it should be possible to get spectroscopy of SNe IIP down to V∼23 and start populating the Hubble diagram up to z∼0.3. A handful of SNe IIP will allow us to get and independent check on the distances to SNe Ia.

Acknowledgement. Support for this work was provided by NASA through Hubble Fellowship grant HST-HF-01139.01-A awarded by the Space Telescope Science Institute, which is operated by the Association of Universities for Research in Astronomy, Inc., for NASA, under contract NAS 5-26555.

References

1. R. Barbon, F. Ciatti, L. Rosino: Astron. Astrophys. **72**, 287 (1979)
2. R.G. Eastman, B.P. Schmidt, R. Kirshner: Astrophys. J. **466**, 911 (1996)
3. W.L. Freedman et al. : Astrophys. J. **553**, 47 (2001)
4. M. Hamuy: "Type II supernovae as distance indicators." Ph.D. Thesis, Univ. Arizona, Tucson (2001)
5. M. Hamuy, P.A. Pinto: Astrophys. J. Lett. **566**, L63 (2002) (HP02)
6. M. Hamuy: astro-ph 0301006 (2003)
7. M. Hamuy: astro-ph 0301281 (2003) (H03)
8. D.C. Leonard, S.M. Kanbur, C.C. Ngeow, N.R. Tanvir: astro-ph 0305259 (2003)
9. I.Y. Litvinova, D.K. Nadezhin: Astrophys. Space Sci. **89**, 89 (1983)
10. I.Y. Litvinova, D.K. Nadezhin: Sov. Astron. Lett. **11**, 145 (1985)
11. B.R. Parodi, A. Saha, A. Sandage, G.A. Tammann: Astrophys. J. **540**, 634 (2000)
12. D.J. Schlegel, D.P. Finkbeiner, M. Davis: Astrophys. J. **500**, 525 (1998)
13. F. Thim et al. : Astrophys. J. **590**, 256 (2003)
14. J.L. Tonry, J.P. Blakeslee, E.A. Ajhar, A. Dressler: Astrophys. J. **530**, 625 (2000)
15. K.W. Weiler, N. Panagia, M.J. Montes, R.A. Sramek: Ann. Rev. Astron. Astrophys. **40**, 387 (2002)

Observing the First Stars, One Star at a Time

Abraham Loeb

Astronomy Department, Harvard University, 60 Garden Street, Cambridge, MA 02138, USA;
aloeb@cfa.harvard.edu

Summary. Gamma-Ray Bursts (GRBs) are believed to originate in compact remnants (black holes or neutron stars) of massive stars. Their high luminosities make them detectable out to the edge of the visible universe. We describe the many advantages of GRB afterglows relative to quasars as probes of the intergalactic medium during the epoch of reionization. The Swift satellite, planned for launch by the end of 2004, will likely open a new era in observations of the high redshift universe.

1 Stellar Explosions at the Edge of the Visible Universe

Gamma-Ray Bursts (GRBs) are believed to originate in compact remnants (black holes or neutron stars) of massive stars. Their high luminosities make them detectable out to the edge of the visible universe [13, 24]. GRBs offer the opportunity to detect the most distant (and hence earliest[1]) population of massive stars, one star at a time. In the hierarchical assembly process of halos which are dominated by cold dark matter, the first galaxies should have had lower masses (and lower stellar luminosities) than their low-redshift counterparts. Consequently, the characteristic luminosity of galaxies or quasars is expected to decline with increasing redshift. GRB afterglows, which already produce a peak flux comparable to that of quasars or starburst galaxies at $z \sim 1-2$, are therefore expected to outshine any competing source at the highest redshifts, when the first dwarf galaxies have formed in the universe.

Preliminary polarization data from the *Wilkinson Microwave Background Probe* (*WMAP*) indicates an optical depth to electron scattering of $\sim 17 \pm 4\%$ after cosmological recombination [30]. This implies that the first stars must have formed at a redshift $z \sim 20$ [11, 12, 14, 29, 35, 36] and reionized a substantial fraction of the intergalactic hydrogen around that time. Early reionization can be achieved with plausible star formation parameters in the standard ΛCDM cosmology; in fact, the required optical depth can be achieved in a variety of very different ionization histories (since *WMAP* places only an integral constraint on these histories [20]). One would like to probe the

[1] Observational cosmology resembles archaeology. By probing deeper into the universe, one reveals layers of it that are more ancient (due to the finite speed of light).

full history of reionization in order to disentangle the properties and formation history of the stars that are responsible for it. GRB afterglows offer the opportunity to detect stars as well as to probe the ionization state [5] and metal enrichment level [17] of the intervening intergalactic medium (IGM).

GRBs, the electromagnetically-brightest explosions in the universe, should be detectable out to redshifts $z > 10$ [13, 24]. High-redshift GRBs can be easily identified through infrared photometry, based on the Lyα break induced by absorption of their spectrum at wavelengths below $1.216\,\mu\mathrm{m}\,[(1+z)/10]$. Follow-up spectroscopy of high-redshift candidates can then be performed on a 10-meter-class telescope. There are four main advantages of GRBs relative to traditional cosmic sources such as quasars:

- The GRB afterglow flux at a given observed time lag after the γ-ray trigger is not expected to fade significantly with increasing redshift, since higher redshifts translate to earlier times in the source frame, during which the afterglow is intrinsically brighter [13]. For standard afterglow lightcurves and spectra, the increase in the luminosity distance with redshift is compensated by this "cosmological time-stretching" effect.
- As already mentioned, in the standard ΛCDM cosmology, galaxies form hierarchically, starting from small masses and increasing their average mass with cosmic time. Hence, the characteristic mass of quasar black holes and the total stellar mass of a galaxy were smaller at higher redshifts, making these sources intrinsically fainter [34]. However, GRBs are believed to originate from a stellar mass progenitor and so the intrinsic luminosity of their engine should not depend on the mass of their host galaxy. GRB afterglows are therefore expected to outshine their host galaxies by a factor that gets larger with increasing redshift.
- Since the progenitors of GRBs are believed to be stellar, they likely originate in the most common star-forming galaxies at a given redshift rather than in the most massive host galaxies, as is the case for bright quasars [5]. Low-mass host galaxies induce only a weak ionization effect on the surrounding IGM and do not greatly perturb the Hubble flow around them. Hence, the Lyα damping wing should be closer to the idealized unperturbed IGM case [27] and its detailed spectral shape should be easier to interpret. Note also that unlike the case of a quasar, a GRB afterglow can itself ionize at most $\sim 4\times10^4 E_{51} M_\odot$ of hydrogen if its UV energy is E_{51} in units of 10^{51} ergs (based on the available number of ionizing photons), and so it should have a negligible cosmic effect on the surrounding IGM.
- GRB afterglows have smooth (broken power-law) continuum spectra unlike quasars which show strong spectral features (such as broad emission lines or the so-called "blue bump") that complicate the extraction of IGM absorption features. In particular, the continuum extrapolation into the Lyα damping wing (the Gunn-Peterson [19] absorption trough) during the epoch of reionization is much more straightforward for the smooth

UV spectra of GRB afterglows than for quasars with an underlying broad Lyα emission line [4, 5].

Although the nature of the central engine that powers the relativistic jets of GRBs is unknown, recent evidence indicates that GRBs trace the formation of massive stars [6, 7, 23, 32, 33], and in particular that long-duration GRBs are associated with Type Ib/c supernovae [31]. Since the first stars in the universe are predicted to be predominantly massive [1, 8], their death might give rise to large numbers of GRBs at high redshifts.

2 GRB Afterglows at High Redshifts

2.1 Motivation

In difference from quasars of comparable brightness, GRB afterglows are short-lived and release ~ 10 orders of magnitude less energy into the surrounding IGM. Beyond the scale of their host galaxy, they have a negligible effect on their cosmological environment[2]. Consequently, they make ideal probes of the IGM during the reionization epoch. Their rest-frame UV spectra can be used to probe the ionization state of the IGM through the spectral shape of the Gunn-Peterson [19] (Lyα) absorption trough, or its metal enrichment history through the intersection of enriched bubbles of supernova ejecta from early galaxies[17]. Afterglows that are unusually bright (> 10mJy) at radio frequencies should also show a detectable forest of 21 cm absorption lines due to enhanced HI column densities in sheets, filaments, and collapsed mini-halos within the IGM [10, 16].

Another advantage of GRB afterglows is that once they fade away, one may search for their host galaxies. Hence, GRBs may serve as signposts of the earliest dwarf galaxies that are otherwise too faint or rare on their own for a dedicated search to find them. Detection of metal absorption lines from the host galaxy in the afterglow spectrum, offers an unusual opportunity to study the physical conditions (temperature, metallicity, ionization state, and kinematics) in the interstellar medium of these high-redshift galaxies.

2.2 Afterglow Flux at the Lyα Wavelength

Figure 1 shows the expected spectral flux from GRB afterglows as a function of observed time after the GRB trigger for a sequence of redshifts (assuming typical model parameters [5]). The flux is calculated at the rest-frame Lyα wavelength, where intergalactic HI should produce the Gunn-Peterson [19] trough prior to reionization. As already mentioned, the flux does not decline

[2] Note, however, that feedback from a single GRB or supernova on the gas confined within early dwarf galaxies could be dramatic, since the binding energy of most galaxies at $z > 10$ is lower than 10^{51} ergs [3, 25].

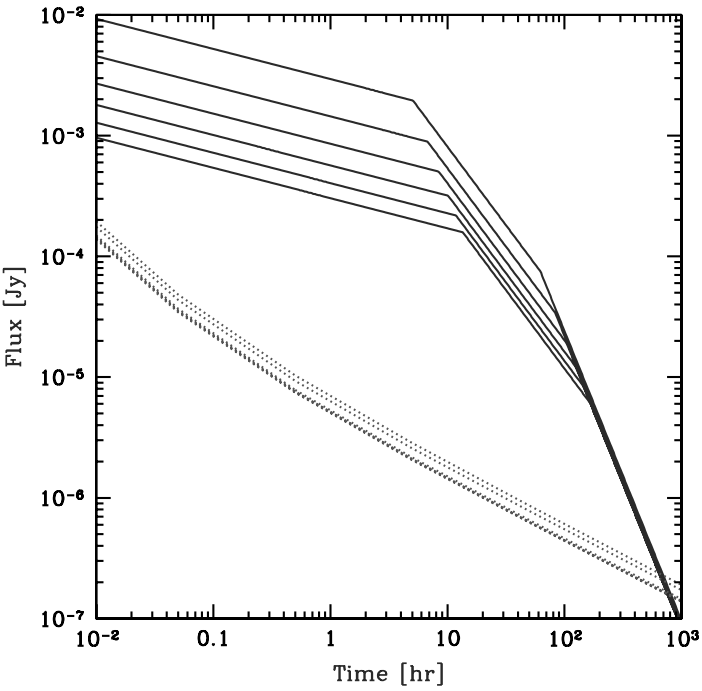

Fig. 1. GRB afterglow flux as a function of time since the γ-ray trigger in the observer frame (taken from [5]). The flux (solid curves) is calculated at the redshifted Lyα wavelength. The dotted curves show the planned detection threshold for the *James Webb Space Telescope* (*JWST*), assuming a spectral resolution $R = 5000$ with the near infrared spectrometer, a signal to noise ratio of 5 per spectral resolution element, and an exposure time equal to 20% of the time since the GRB explosion (see *http://www.ngst.stsci.edu/nms/main/*). Each set of curves shows a sequence of redshifts, namely $z = 5$, 7, 9, 11, 13, and 15, respectively, from top to bottom.

dramatically with increasing redshift since cosmic time stretching counteracts the luminosity distance increase.

The expected spectral shape of the Gunn-Peterson trough prior to the final overlap phase of HII regions in the IGM, is shown in Fig. 2. If GRBs trace the typical sites of star formation, then most of them should be hosted by dwarf galaxies at high redshifts. Low-mass hosts would perturb only weakly the surrounding IGM (radiatively through their ionizing flux, gravitationally [through cosmological infall, or hydrodynamically through their winds), in difference from the massive host galaxies of the brightest quasars at the same epoch [4, 5]. Consequently, the spectral shape of the Lyα trough (which is proportional to $e^{-\tau(\lambda)}$, where $\tau(\lambda)$ is the optical depth as a function of wavelength) is simpler to interpret for GRB afterglows than it is for quasars. The optical depth as a function of wavelength in the Lyα damping wing is

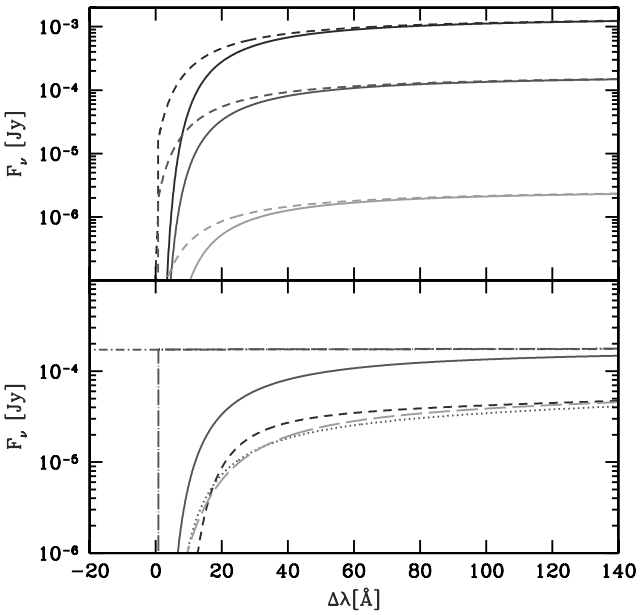

Fig. 2. Expected spectral shape of the Lyα absorption trough due to intergalactic absorption in GRB afterglows (taken from [5]). The spectrum is presented in terms of the flux density F_ν versus relative observed wavelength $\Delta\lambda$, for a source redshift $z = 7$ (assumed to be prior to the final reionization phase) and the typical halo mass $M = 4 \times 10^8 M_\odot$ expected for GRB host galaxies that cool via atomic transitions. *Top panel:* Two examples for the predicted spectrum including IGM HI absorption (both resonant and damping wing), for host galaxies with: (i) an age $t_S = 10^7$ yr, a UV escape fraction $f_{\rm esc} = 10\%$ and a Scalo initial mass function (IMF) in solid curves, or (ii) $t_S = 10^8$ yr, $f_{\rm esc} = 90\%$ and massive ($> 100 M_\odot$) Pop III stars in dashed curves. The observed time after the γ-ray trigger is one hour, one day, and ten days, from top to bottom, respectively. *Bottom panel:* Predicted spectra one day after a GRB for a host galaxy with $t_S = 10^7$ yr, $f_{\rm esc} = 10\%$ and a Scalo IMF. Shown is the unabsorbed GRB afterglow (dot-short dashed curve), the afterglow with resonant IGM absorption only (dot-long dashed curve), and the afterglow with full (resonant and damping wing) IGM absorption (solid curve). Also shown, with 1.7 magnitudes of extinction, are the afterglow with full IGM absorption (dotted curve), and attempts to reproduce this profile with a damped Lyα absorption system in the host galaxy (dashed curves). (Note, however, that damped absorption of this type could be suppressed by the ionizing effect of the afterglow UV radiation on the surrounding interstellar medium of its host galaxy [28].)

linearly proportional to the mean neutral fraction of the IGM, $x_{\rm HI}$, since its amplitude is normalized by the optical depth at the Lyα resonance, $\sim 6.75 \times 10^5 x_{\rm HI}[(1+z)/10]^{3/2}$ [3, 25, 27].

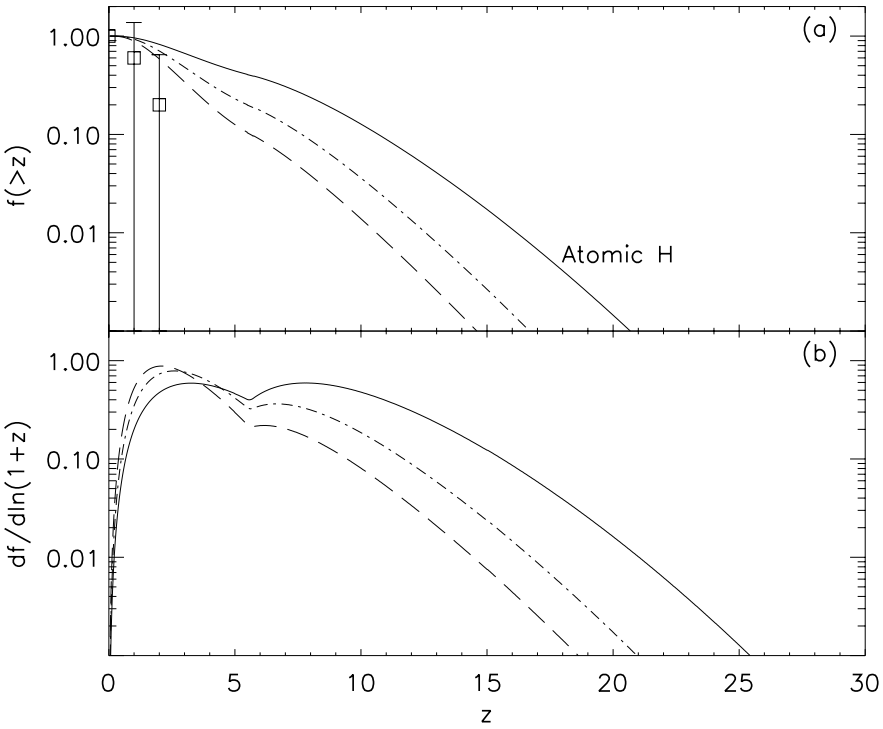

Fig. 3. Redshift distribution of all GRBs as compared to that measured by flux-limited surveys (taken from [9]). (*a*) Fraction of bursts that originate at a redshift higher than z vs. z. The data points reflect ~ 20 observed redshifts. (*b*) Fraction of bursts per logarithmic interval of $(1 + z)$ vs. z. *Solid lines*: All GRBs for star formation through atomic line cooling. *Dot-dashed lines*: Expected distribution for *Swift*. *Long-dashed lines*: Expected distribution for *BATSE*. Note that the curves for the two flux-limited surveys are very uncertain due to the poorly-determined GRB luminosity function. Nevertheless, GRB number counts could provide a rough measure of the cosmic formation rate of massive stars at high redshifts.

2.3 Statistics

The upcoming *Swift* satellite (see *http://swift.gsfc.nasa.gov/*), planned for launch by the end of 2003, is expected to detect about a hundred GRBs per year. Fig. 3 shows the expected redshift distribution of all GRBs (solid lines), under the assumption that the GRB rate is simply proportional to the star formation rate [9]. The long-dashed and the dot-dashed lines show the same rate, but taking into account the limited sensitivity of the *BATSE* and *Swift* detectors, respectively. This calculation implies that about a quarter of all GRBs detected by *Swift* should originate at $z > 5$. This estimate is rather uncertain because of the poorly determined GRB luminosity function [9].

In principle, the rate of high-redshift GRBs may be significantly suppressed if the early massive stars fail to launch a relativistic outflow. This is possible, since metal-free stars may experience negligible mass loss before exploding as a supernova. They would then retain their massive hydrogen envelope, and any relativistic jet might be quenched before escaping the star. However, localized metal enrichment is expected to occur rapidly (on a timescale much shorter than the age of the then-young universe) due to starbursts in the first galaxies and so even the second generation of star formation could occur in an interstellar medium with a significant metal content, resulting in massive stars that resemble more closely the counterparts of low-redshift GRB progenitors.

We note that the known population of optically-dark GRBs [23] is most likely associated with dust-obscured GRBs at low redshifts, although a small fraction of these bursts could be optically-dark due to Lyα absorption by the IGM at high-redshift.

2.4 Progenitors

In the previous section, we have assumed for simplicity a constant efficiency of forming GRBs per unit mass of stars. This simplifying assumption may either overestimate or underestimate the frequency of GRBs. Metal-free stars are thought to be massive [1, 8] and their extended envelopes may suppress central jets within them (which may be produced through the collapse of their core to a spinning black hole). On the other hand, low-metallicity stars are expected to have weak winds with little angular momentum loss during their evolution, and so they may preferentially yield rotating central configurations that produce GRB jets after core collapse [18, 22]. The basic question: "Should GRBs be common in the first generation of metal-free stars?" remains open for further study.

3 *Swift*: A Challenge for Infrared Follow-Ups

A small fraction ($\sim$ 10–25%) of the GRB afterglows detected by *Swift* are expected to originate at redshifts $z > 5$. This subset of afterglows can be selected photometrically using a small telescope, based on the Lyα break at a wavelength of $1.216\,\mu\mathrm{m}\,[(1+z)/10]$, caused by intergalactic HI absorption. The challenge in the upcoming years would be to follow-up on these candidates spectroscopically, using a large (10-meter class) telescope. A high-resolution spectrum can then be used to trace the ionization state (see Fig. 2) and metal enrichment state of the gas along the line-of-sight. For example, Fig. 4 illustrates the expected number of intersections of enriched bubbles of supernova ejecta from early galaxies, as a function of the equivalent width of the metal absorption lines they produce (see [17] for details). Measurement of this statistic for different metals can be used to constrain the initial mass

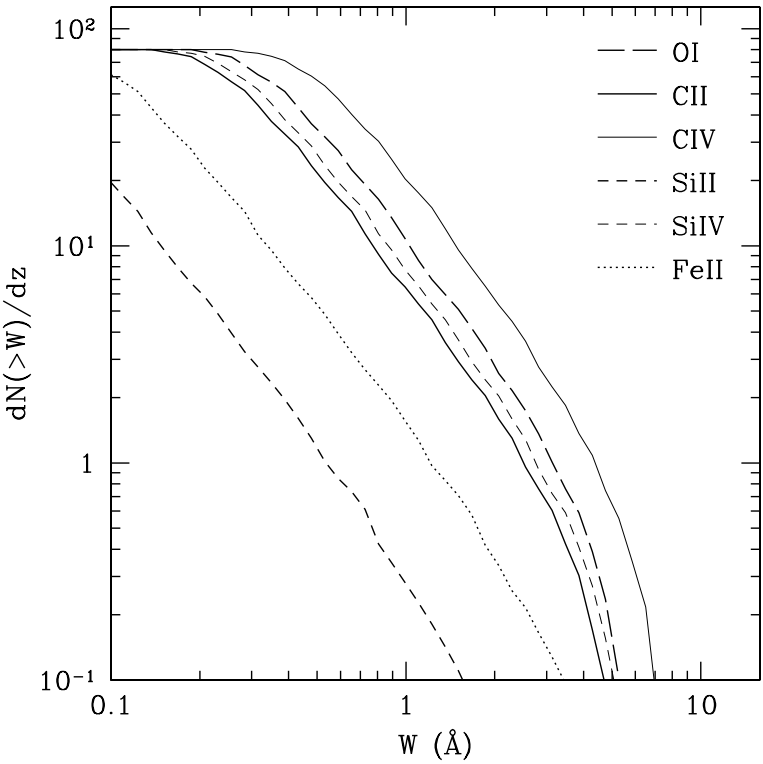

Fig. 4. Predicted number of line-of-sight intersections of metal-enriched bubbles around the first galaxies per redshift interval at a redshift $z = 8$ (taken from [17]). This statistic was calculated as a function of the equivalent width threshold of the metal absorption lines produced by these bubbles, for typical parameter choices of the theoretical model (see [17] for details). Thick solid, long-dashed, short-dashed, and dotted curves are for C II, O I, Si II, and Fe II metal lines, respectively. Thin solid and short-dashed curves are for C IV and Si IV, respectively.

function (through element abundances) and the mechanical energy output (through bubble sizes) of the first stars, as well as the significance of molecular H_2 cooling in forming stars within the first mini-halos (through the number density of small bubbles).

Based on the arguments mentioned in §1, GRB afterglows are likely to revolutionize observational cosmology and replace traditional sources like quasars, as probes of the IGM at $z > 5$. We caution, however, that this is a theoretical expectation (the highest redshift GRB detected so far [2] is at $z \sim 4.5$) and as such it is subject to uncertainties about the production of relativistic outflows by the first generation of stars.

However, note that even if GRB outflows are quenched in the massive envelopes of low-metallicity stars, one would expect them to appear at high

redshifts. This follows from the fact that metallicity obtains a large range of possible values (in different spatial regions) at any slice of cosmic time. For example, the broad emission lines of all known quasars show evidence for high metallicity gas [15, 21], and so it is clear that there are pockets of highly enriched gas near the centers of massive galaxies at $z > 6$, where star formation reached an advanced stage and GRB production should be as likely as it is in the local universe. The cores of the most massive galaxies at $z > 6$ simply predate the characteristic evolution of the rest of the universe at a much lower redshift, because these cores reside in unusually over dense cosmological environments [26]. Such environments are likely to produce GRB progenitors in the same way that less over dense cosmological regions produce them at a lower redshift. *Swift* has the potential to educate us whether GRBs are produced only within these massive galaxies or in the more common sites of star formation at early cosmic times, namely the low-metallicity dwarf galaxies.

In either case, the near future promises to be exciting for GRB astronomy as well as for studies of the high-redshift universe.

Acknowledgement. I am indebted to my collaborators for the various calculations mentioned in this overview: Rennan Barkana, Volker Bromm, Benedetta Ciardi, Steve Furlanetto, Jim Peebles, and Stuart Wyithe. This work was supported in part by NSF grants AST-0204514, AST-0071019, NASA grant ATP02-0004-0093, NATO grant PST.CLG.979414, and the John Simon Guggenheim Memorial Fellowship.

References

1. T. Abel, G.L. Bryan, M.L. Norman: Science **295**, 93 (2002)
2. M.I. Andersen et al. : Astron. Astrophys. **364**, L54 (2000)
3. R. Barkana, A. Loeb: Phys. Rep. **349**, 125 (2001)
4. R. Barkana, A. Loeb: Nature **421**, 341 (2003)
5. R. Barkana, A. Loeb: astro-ph 0305470 (2003)
6. A. W. Blain, P. Natarajan: Mon. Not. R. Astron. Soc. **312**, L35 (2000)
7. J.S. Bloom, S.R. Kulkarni, S.G. Djorgovski: Astron. J. **123**, 1111 (2002)
8. V. Bromm, P.S. Coppi, R.B. Larson: Astrophys. J. **564**, 23 (2002)
9. V. Bromm, A. Loeb: Astrophys. J. **575**, 111 (2002)
10. C.L. Carilli, N.Y. Gnedin, F. Owen: Astrophys. J. **577**, 22 (2002)
11. R. Cen: astro-ph 0210473 (2002)
12. R. Cen: astro-ph 0303236 (2003)
13. B. Ciardi, A. Loeb: Astrophys. J. **540**, 687 (2000)
14. B. Ciardi, A. Ferrara, S.D. M. White: astro-ph 0302451 (2003)
15. M. Dietrich, F. Hamann, I. Appenzeller, M. Vestergaard: astro-ph 0306584 (2003)
16. S.R. Furlanetto, A. Loeb: Astrophys. J. **579**, 1 (2002)
17. S.R. Furlanetto, A. Loeb: Astrophys. J. **588**, 18 (2003)
18. J.P.U. Fynbo et al. : astro-ph 0306403 (2003)

19. J.E. Gunn, B.A. Peterson: Astrophys. J. **142**, 1633 (1965)
20. Z. Haiman, G. Holder: astro-ph 0302403 (2003)
21. F. Hamann, M. Dietrich, B. Sabra, C. Warner: In: *Origin and Evolution of the Elements*, eds. A. McWilliam, M. Rauch (Proc. Carnegie Observ. Astrophys. Series, Vol. **4**, 2003); astro-ph 0306068 (2003)
22. A. Heger, C.L. Fryer, S.E. Woosley, N. Langer, D.H. Hartmann: Astrophys. J. **591**, 288 (2003)
23. S.R. Kulkarni et al. : SPIE **4005**, 9 (2000)
24. D.Q. Lamb, D.E. Reichart: Astrophys. J. **536**, 1 (2000)
25. A. Loeb, R. Barkana: Ann. Rev. Astron. Astrophys. **39**, 19 (2001)
26. A. Loeb, P.J.E. Peebles: Astrophys. J. **589**, 29 (2003)
27. J. Miralda-Escudé: Astrophys. J. **501**, 15 (1998)
28. R. Perna, A. Loeb: Astrophys. J. **501**, 467 (1998)
29. R. Somerville, M. Livio: astro-ph 030301 (2003)
30. D.N. Spergel et al. : astro-ph 0302209 (2003)
31. K.Z. Stanek et al. : Astrophys. J. Lett. **591**, L17 (2003)
32. T. Totani: Astrophys. J. Lett. **486**, L71 (1997)
33. R.A.M.J. Wijers, J.S. Bloom, J.S. Bagla, P. Natarajan: Mon. Not. R. Astron. Soc. **294**, L13 (1998)
34. J.S.B. Wyithe, A. Loeb: Astrophys. J. **581**, 886 (2002)
35. J.S.B. Wyithe, A. Loeb: Astrophys. J. **586**, 693 (2003)
36. J.S.B. Wyithe, A. Loeb: Astrophys. J. Lett. **588**, L69 (2003)

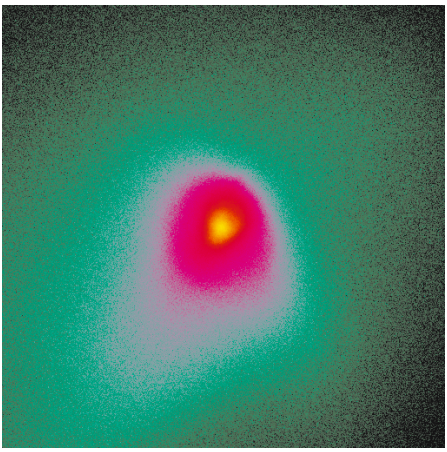

a) The coarse−grained morphology in a box with a linear physical size of 23.5 pc. At this time, a gravitationally−bound clump has formed with a mass of ~1000 $M_\odot$

b) The fine−grained morphology in a box with a linear physical size of 0.5 pc. The central density peak accretes mass vigorously,and is accompanied by a secondary clump.

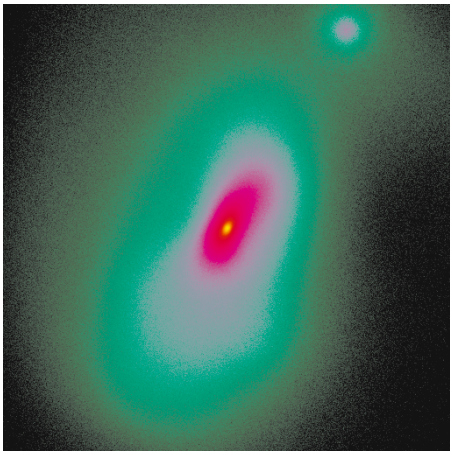

Numerical simulation of the collapse and fragmentation of a primordial cloud in 3D. We show the projected gas density at a redshift z ~ 21.5, shortly after gravitational runaway collapse has converged at the center of the cloud. (From Bromm,V., & Loeb, A., New Astronomy, 9, 353−364 (2004); astro−ph/0312456)

Plate (Loeb)

Plate 6.

The Host Galaxies of High-Redshift Type Ia Supernovae

Mark Sullivan[1], Richard Ellis[2], and the Supernova Cosmology Project[3]

[1] University of Durham, South Road, Durham, DH1 3LE, UK;
mark.sullivan@durham.ac.uk
[2] 105-24 Astronomy, Caltech, Pasadena, CA 91152, USA;
rse@astro.caltech.edu
[3] saul@lbl.gov**

Summary. We present new results on the Hubble diagram of distant type Ia supernovae (SNe Ia) segregated according to the type of host galaxy. This makes it possible to check earlier evidence for a cosmological constant by explicitly comparing SNe residing in galaxies likely to contain negligible dust with the larger sample. The cosmological parameters derived from these SNe Ia hosted by presumed dust-free early-type galaxies support earlier claims for a cosmological constant, which we demonstrate at $\simeq 5\sigma$ significance, and the internal extinction implied is small even for late-type systems ($A_B < 0.2$). Furthermore, the scatter observed in the SNe Ia Hubble diagrams correlates closely with host galaxy morphology. We find this scatter is smallest for SNe Ia occurring in early-type hosts and largest for those in late-type galaxies. Moreover, SNe residing in late-type hosts appear fainter in their light-curve-width-corrected luminosity than those in early-type hosts, as expected if a modest amount of dust extinction is a contributing factor. Thus, our data demonstrate that host galaxy extinction is unlikely to systematically dim distant SNe Ia in a manner that would produce a spurious cosmological constant.

1 Introduction

Type Ia supernovae (SNe Ia) have emerged as important probes of the cosmological world-model. Empirical relationships between the peak intrinsic luminosity and the light-curve decay time can reduce the dispersion in their photometric properties to $\simeq 0.17$ mag, making them excellent "calibrated candles" over a wide range in redshift. Systematic detection and calibration of high redshift SNe Ia over the last 10 years has led to two independent SN Ia Hubble diagrams, published by the Supernova Cosmology Project [3] (SCP) and the High-Redshift Supernova Search Team [6]. Data from both teams convincingly reject the deceleration expected from an Einstein–de Sitter (EdS) Universe, and provide evidence for a cosmic acceleration in a low mass-density Universe consistent with a non-zero vacuum energy density.

Such important results demand excellent supporting evidence, examining the homogeneity, environmental trends and evolutionary behavior of SNe Ia. Systematic differences in the peak magnitudes between high and low-redshift

** *http://supernova.lbl.gov/*

Table 1. The best-fitting cosmologies for SNe residing in each host galaxy type

SNe Subset	Best Ω_Λ	Mean dispersion	DOF	χ^2 /DOF	Probability that: $\Omega_\Lambda > 0$	$\Omega_\Lambda \geq \frac{\Omega_M}{2}$
All SNe	$0.72^{+0.09}_{-0.08}$	0.199	51	1.121	99.79	99.59
E/S0	$0.57\,(0.58)^{+0.12}_{-0.11}$	0.159	12	0.680	97.09	94.80
Spirals	$0.67\,(0.66)^{+0.07}_{-0.06}$	0.235	46	1.590	99.85	99.75
Early	$0.50\,(0.50)^{+0.12}_{-0.11}$	0.200	22	1.309	92.46	86.83
Late	$0.77\,(0.78)^{+0.08}_{-0.07}$	0.272	23	1.761	99.98	99.97

SNe, arising either from evolutionary effects in the SNe progenitors or via subtle differences in the environments of the low and high-redshift galaxies in which SNe are produced, could mimic the cosmic acceleration without necessarily destroying the small dispersion seen in existing Hubble diagrams. Here, we present the results of a study examining the dependence of SN properties on host galaxy morphology via Hubble Space Telescope (HST) imaging and Keck spectroscopy. Disc and spheroidal stellar populations represent different star-formation histories, metallicities and, most importantly, dust content, and we might expect that SNe Ia progenitor composition and peak magnitudes/light-curve properties could be affected accordingly. In particular, we investigate how existing Hubble diagrams are affected by SNe lying in different types of host galaxy where the dust content of the hosts varies from type to type, and thus examine the effect of host galaxy extinction on the determination of the cosmological parameters.

2 Datasets

In this analysis we use the high-redshift SNe sample taken from the SCP [3]. We have three diagnostics available for the high-redshift sample: i) HST-STIS/WFPC2 imaging providing morphology and SN location within the host, ii) Keck-II/ESI spectroscopy addressing the star-formation characteristics of the host galaxies, and iii) Ground-based R, I imaging from the original SN discovery campaigns which acts as a consistency check on the other two diagnostics. We classify each host as either a spheroidal (E/S0), an early-type spiral (Sa-Sbc), or a late-type spiral/irregular (Scd and later types). In total, 93% of the high-redshift SNe sample can be classified using these data. We combine this high-redshift sample with existing low-redshift samples [1, 5] using published host galaxy classifications [2].

3 Main Results

The Hubble diagram for the high-redshift SNe Ia as a function of host galaxy type can be found in Fig. 1, and the results of the cosmological fits for the

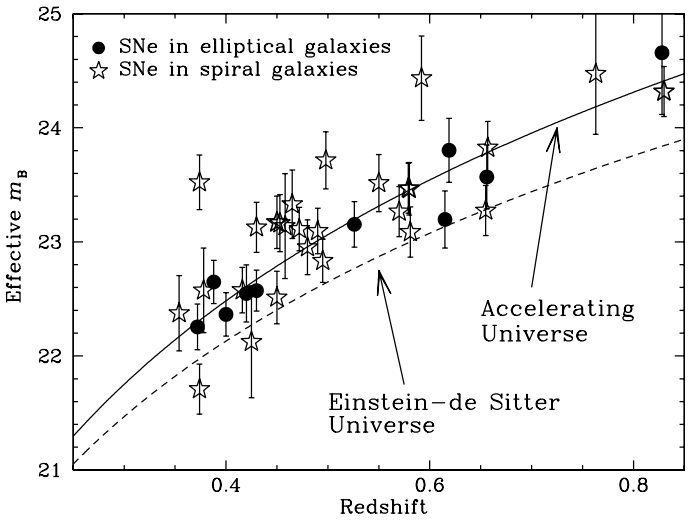

Fig. 1. The stretch-corrected high-redshift SNe Ia Hubble diagram plotted according to the class of the host galaxy. The expected brightness in both EdS and accelerating Universes are shown.

different SNe sub-classes are listed in Table 1 (see [7] for the full set of results). The principle finding is that all of the SNe subgroups strongly support cosmologies with $\Omega_\Lambda > 0$, and the best-fitting cosmological models for each SN sub-group are broadly consistent within the error-bars.

Furthermore, SNe residing in E/S0 galaxies provide 'tighter' cosmological fits, with smaller dispersions and χ^2/DOFs than the fits for SNe residing in later-type galaxies. The likely explanation for this result is that elliptical galaxies form a very homogeneous class of objects, being regular and usually dust-free when compared to the typically dusty nature of later-type galaxies. This hypothesis allows us to estimate the intrinsic spread in the peak magnitude of E/S0 SNe compared to those residing in other classes of galaxy. Currently, each SNe error contains a contribution of 0.17 mag added in quadrature to allow for the uncertainty in the light-curve-width-luminosity correction, regardless of the host class. As some of this dispersion arises from host galaxy extinction, we can use the (presumed) dust-free E/S0 SNe population to estimate the intrinsic dispersion for this class of SNe. For SNe in each host type, we therefore repeat the cosmological fits, altering the intrinsic dispersion until the χ^2/DOF for each fit is equal to one.

The intrinsic dispersions are (in magnitudes) 0.10, 0.25, and 0.24 for E/S0, early and late-type spirals/irregulars respectively. This small intrinsic dispersion seen for SNe in E/S0 matches very closely the dispersion seen in low-redshift SNe after a technique correcting for the effects of reddening has been applied (0.11 mag) [4]. The implication from this small dataset is clear:

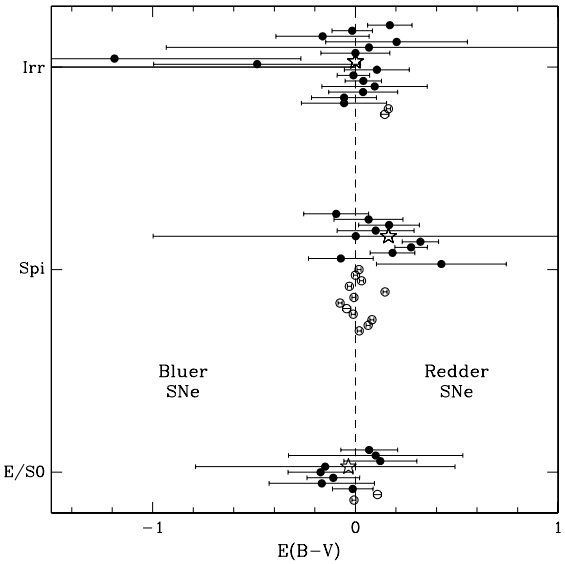

Fig. 2. The SN rest-frame "color excess" ($E(B-V)$) plotted as a function of the host galaxy type. The error-weighted mean of each distribution are shown as stars. The vertical offsets for each plotted SN is used to avoid over-plotting the data points and is illustrative only. High-redshift SNe are shown as filled circles, low-redshift SNe as open circles.

SNe residing in E/S0 hosts are superior "standard candles" than those in later-type galaxies due to the small amount of extinction affecting them.

We can further investigate the important issue of dust extinction on the SNe sample in two ways. Firstly, we can search for any differential extinction between the low and high-redshift samples by examining the distribution of the color excesses of the SNe (see [3, 7] for further details on how the color excess is measured), with larger color excesses representing redder SNe and hence likely higher extinctions. The distributions of the color excess at low and high-redshift are shown in Fig. 2, and appear very similar, with no clear offsets between the two populations. The mean color excess in E/S0 galaxies is $\simeq 0$, indicating that this population is largely dust-free. In spiral galaxies the color excess is more significant at $\simeq 0.07$ – but this value is dominated by two red SNe which are excluded from the principle cosmological fit of [3]. When these two SNe are removed, the color excess drops to 0.03 in spiral galaxies [7].

The second test on the effect of dust on the SNe properties investigates the dust content of spiral galaxies compared to E/S0 galaxies. When using SNe Ia as standard candles, an intrinsic absolute magnitude for the SNe is fit for – but this intrinsic magnitude contains not just information on the

brightness of the SN, but also information about the environment of each SN, in particular the amount of dust that may be dimming the SN light. To investigate this, we re-fit the cosmologies for SNe in the different sub-groups, but this time fitting only for this intrinsic SN magnitude, and holding the cosmology fixed at the values derived for SNe in E/S0 galaxies.

We find only a small difference between the brightness of SNe in E/S0s and spirals of 0.07 ± 0.08 magnitudes – the largest difference is between E/S0 and late-type spirals at 0.14 ± 0.09. These values are only marginally significant, and provide little evidence for an increased reddening between SNe in E/S0 and spiral galaxies.

4 Summary

We have investigated the Hubble diagram of SNe Ia by classifying 39 high-redshift events according to the their host galaxies as revealed by HST imaging, intermediate dispersion spectroscopy and broad-band colors. Together with morphological data for the host galaxies of local SNe drawn from the literature, we find the following.

1. SNe in all galaxy sub-groups provide convincing evidence for $\Omega_\Lambda > 0$, though the scatter on the Hubble diagram does correlate closely with the host galaxy type. This scatter is minimal for SNe occurring in host galaxies classed as early-type, and increases towards later classes. The correlation does not depend on whether the SN are corrected for differences in light-curve shape.
2. We compare the color excesses of distant SNe Ia with those observed locally and see no evidence for an increased extinction at higher-redshift. We see slight evidence for a type-dependent color excess, with, on average, spirals hosting the redder SNe.
3. SNe occurring in the later types are on average only marginally fainter than those in E/S0 galaxies, with a difference in the absolute peak luminosities between SNe in late-type spirals and E/S0s of only 0.14 ± 0.09 mag. This drops to 0.07 ± 0.08 mag when the spirals are taken as a whole.

We interpret these results according to the hypothesis that dust extinction in the host galaxy is the significant cause of the scatter in the Hubble diagram. Most importantly, the Hubble diagram confined to SNe Ia occurring in early-type host galaxies with presumed minimal internal extinction presents a very tight relationship and provides a $\simeq 5\sigma$ confirmation of a non-zero cosmological constant, assuming a flat Universe. When no assumption about the flatness of the Universe is made, SNe in E/S0 galaxies imply $\Omega_\Lambda > 0$ at nearly 98 per cent probability. Furthermore, the trends in extinction by host galaxy morphology and between low and high-redshift examples implies only

modest extinctions in spirals, though with a large galaxy-to-galaxy scatter. Our study is a good illustration of how ancillary data on host galaxies can be used to examine the nature and reliability of SNe as probes of the cosmological expansion history. We show that internal dust extinction cannot be a primary contaminant and that SNe Ia, particularly those occurring in spheroidal galaxies which can be readily screened with spectroscopic, colors and morphological data, represent a very powerful cosmological probe.

References

1. M. Hamuy et al. : Astron. J. **112**, 2408 (1996)
2. M. Hamuy et al. : Astron. J. **120**, 1479 (2000)
3. S. Perlmutter et al. : Astrophys. J. **517**, 565 (1999)
4. M.M. Phillips et al. : Astron. J. **118**, 1766 (1999)
5. A.G. Riess et al. : Astron. J. **117**, 707 (1999)
6. B.P. Schmidt et al. : Astrophys. J. **507**, 46 (1998)
7. M. Sullivan et al. : Mon. Not. R. Astron. Soc. **340**, 1057 (2003)

Constraints on SN Ia Progenitors and ICM Enrichment from Field and Cluster SN Rates

D. Maoz and A. Gal-Yam

School of Physics and Astronomy, Tel Aviv University, Tel Aviv, Israel;
dani@wise.tau.ac.il, avishay@wise.tau.ac.il

Summary. The iron mass in galaxy clusters is about 6 times larger than could have been produced by core-collapse SNe, assuming the stars in cluster galaxies formed with a standard IMF. Type-Ia SNe have been proposed as the alternative dominant iron source. We use our HST measurements of the cluster SN-Ia rate at high redshift to study the cluster iron enrichment scenario. The measurements can constrain the star-formation epoch and the SN-Ia progenitor models via the mean delay time between the formation of a stellar population and the explosion of some of its members as SNe-Ia. The low observed rate of cluster SNe-Ia at $z \sim 1$ pushes back the star-formation epoch in clusters to $z > 2$, and implies a short delay time. We also show a related analysis for high-z field SNe which implies, under some conditions, a long SN-Ia delay time. Thus, cluster enrichment by core-collapse SNe from a top-heavy IMF may remain the only viable option.

1 The SN Ia Rate in $z \leq 1$ Galaxy Clusters and the Source of Cluster Iron

The iron mass in galaxy clusters is about 6 times larger than could have been produced by core-collapse supernovae (SNe), assuming the stars in the cluster formed with a standard initial mass function (IMF; e.g., [10]). SNe Ia have been proposed as the alternative dominant iron source. Different SN Ia progenitor models predict different "delay functions", between the formation of a stellar population and the explosion of some of its members as SNe Ia. We use updated measurements of the total iron mass-to-light ratio in rich clusters to normalize the predicted SN Ia rate in clusters vs. redshift, using the delay function parameterization of [6]. We then use our previous measurements of the cluster SN Ia rate at high redshift [2] to constrain SN Ia progenitor models and the star-formation epoch in clusters. The low observed rate of cluster SNe Ia at $z \sim 0 - 1$ (Fig. 1) means that, if SNe Ia produced the observed amount of iron, they must have exploded at even higher z. This puts a $> 95\%$ upper limit on the mean SN Ia delay time of $\tau < 2$ Gyr (< 5 Gyr) if the stars in clusters formed at $z_f < 2$ ($z_f < 3$), assuming $H_o = 70$ km s^{-1} Mpc^{-1} (see [5] for full details). In the next section, we show that, for some current versions of cosmic (field) star formation history (SFH), observations of field

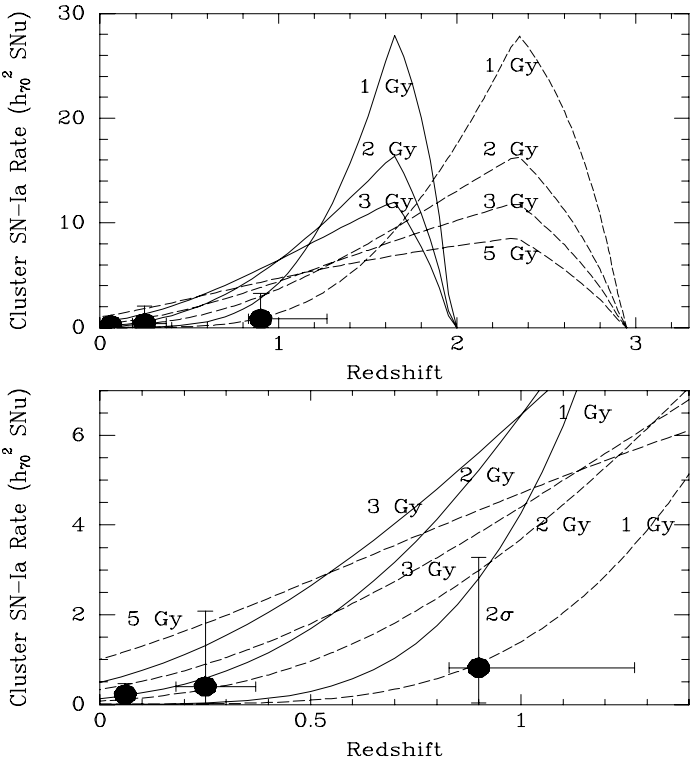

Fig. 1. Predicted SN Ia rates vs redshift, if most of the iron mass in clusters is produced by type-Ia SNe following a brief burst of star formation at redshift $z_f = 2$ (solid curves) and $z_f = 3$ (dashed curves). The bottom panel is a zoom on the low-z region of the top panel. The different curves are for SN Ia transfer functions with mean delay times, τ, as marked. Cluster SN Ia rate measurements are by [2, 9]. The latter are shown with 95%-confidence vertical error bars. The horizontal error bars give the visibility-time-weighted redshift ranges of the cluster samples. The $z_f = 2$ models (solid curves) with $\tau \geq 2$ Gyr are clearly ruled out by the $z \sim 1$ SN-rate measurement, even after accounting for a 30% uncertainty in the normalization of the models. The $z_f = 3$ model (dashed curves) with $\tau = 5$ Gyr predicts unacceptably high rates at low z.

SNe Ia place a *lower* bound on the delay time, $\tau > 3$ Gyr. If these SFHs are confirmed, the entire range of τ will be ruled out. Cluster enrichment by core-collapse SNe from a top-heavy IMF will then remain the only viable option.

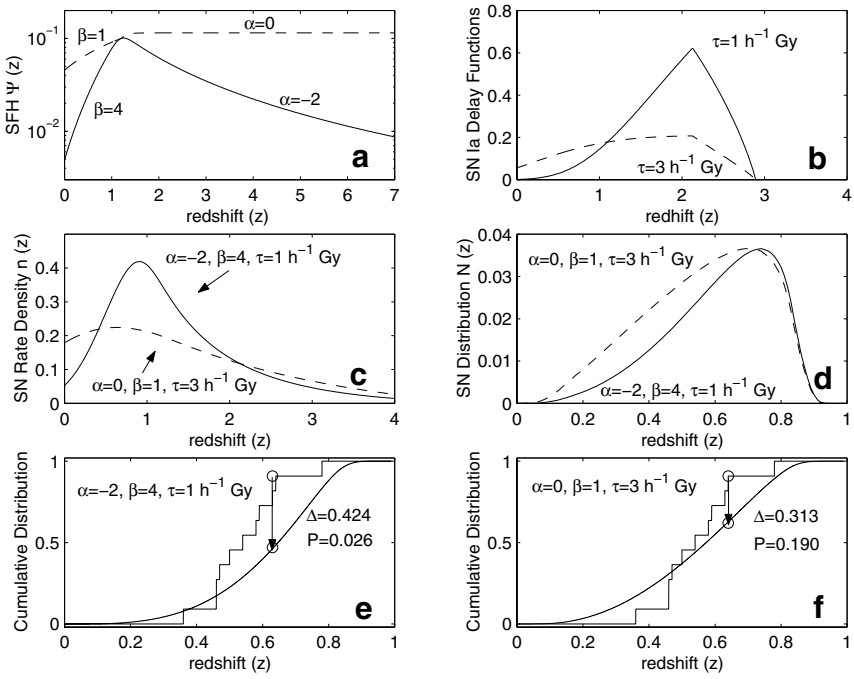

Fig. 2. Illustration of the modeling and comparison to data. The SFH ($\Psi(z)$) is modeled by two power laws, smoothly joined at $z = 1.2$. We denote the high-z index with α and the low-z index with β. Panel **a** shows two examples, a "Madau" SFH, with a peak at $z = 1.2$ (solid curve), and a shallower model (dashed curve) reflecting the proposed modifications by [1, 11]. Panel **b** shows two examples of the expected SN Ia rate density following a brief burst of star formation. These delay functions are calculated using the prescription of [6], with characteristic exponential delay times of $\tau = 1h^{-1}$ Gyr (solid) and $\tau = 3h^{-1}$ Gyr (dashed). For display purposes, an arbitrary redshift of $z = 3$ has been chosen for the burst of star formation. SFH models are convolved with a delay function, and the resulting SN rate densities $n(z)$ for a "Madau" SFH with $\tau = 1h^{-1}$ Gyr (solid) and a "Cowie-Steidel" SFH with $\tau = 3h^{-1}$ Gyr (dashed) are shown in panel **c**. Panel **d** shows the predicted SN distributions, $N(z)$, for the models of panel **c**, in a survey with the same observational parameters of the SCP search. KS tests show that the cumulative version of $N(z)$ from a model combining a "Madau" SFH with a typical delay time of $\tau = 1h^{-1}$ Gyr (panel **e**) is ruled out by the data, while a model with "Cowie-Steidel" SFH and $\tau = 3h^{-1}$ Gyr is consistent with the data (panel **f**). This "forward modeling" type of analysis is more powerful than the derivation of an observed SN rate at a mean z from the data (e.g., [8, 12]) and comparison to predictions (as in panel **c**), since no binning over redshift is carried out. Vertical axis units are arbitrary in panels **a**-**d**.

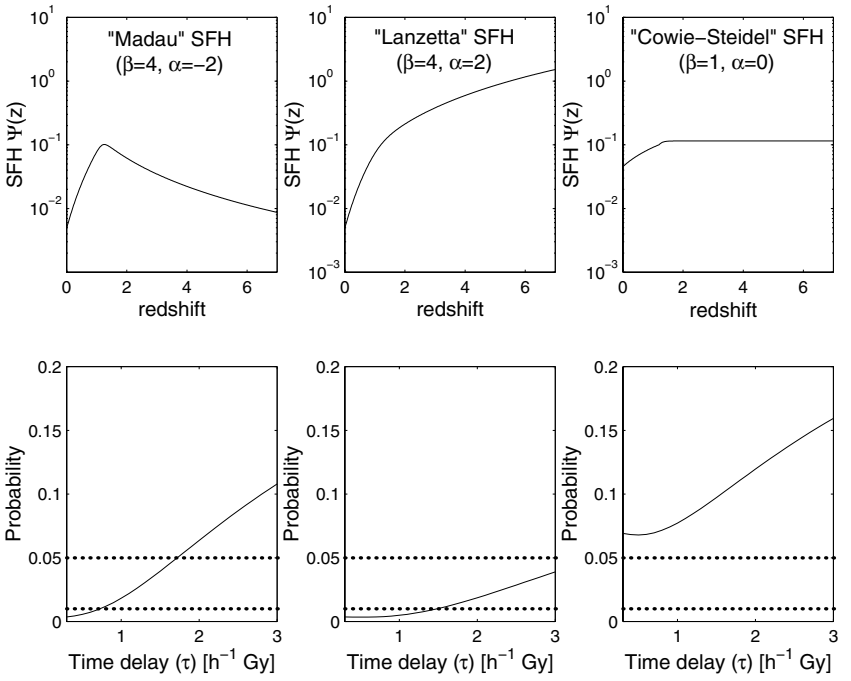

Fig. 3. Probability of SN Ia time delay values τ, given the data, for particular SFH models. Assuming the SFH models shown in the upper panels, we can constrain the allowed values of τ by the probability derived from the KS test (lower panels). Points below the upper and lower dotted lines are ruled out at 95% and 99% confidence, respectively.

2 The Redshift Distribution of Field SNe Ia: Constraints on Progenitors and Cosmic Star Formation History

In this section, we use the redshift distribution of SNe Ia discovered by the Supernova Cosmology Project (Pain et al. 2002) to constrain the star formation history (SFH) of the Universe and SN Ia progenitor models. Fig. 2 illustrates how, for a given choice of parameters describing the SFH and SN Ia delay time, we predict the observed cumulative (i.e., unbinned) redshift distribution in a given survey, and compare it to the data. Given some of the recent determinations of the SFH, the observed SN Ia redshift distribution indicates a long ($\gtrsim 1h^{-1}$ Gyr) mean delay time between the formation of a stellar population and the explosion of some of its members as SNe Ia (Fig. 3). For example, if the Madau et al. (1998) SFH is assumed, the delay time τ is constrained to be $\tau \geq 1.7(\tau \geq 0.7)h^{-1}$ Gyr at the 95%(99%) confidence level (CL). SFHs that rise at high redshift, similar to those advocated by Lanzetta et al. (2002), are inconsistent with the data at the 95% CL unless $\tau > 3.5h^{-1}$

Gyr. Long time delays disfavor progenitor models such as edge-lit detonation of a white dwarf accreting from a giant donor, and the carbon core ignition of a white dwarf passing the Chandrasekhar mass due to accretion from a subgiant (e.g., [13]). The SN Ia delay may be shorter, thereby relaxing some of these constraints, if the field star formation rate falls, between $z = 1$ and the present, less sharply than implied, e.g., by the original Madau plot. The discovery of larger samples of high-z SNe Ia by forthcoming observational projects should yield strong constraints on the progenitor models and the SFH (see [3] for full details). In the previous section we have demonstrated that if SNe Ia produce most of the iron in galaxy clusters, and the stars in clusters formed at $z \sim 2$, the SN Ia delay time must be *lower* than 2 Gyr. If so, then the Lanzetta et al. [4] SFH is inconsistent with the data presented here (Fig. 3).

3 Conclusions

The large mass of iron in clusters, combined with the low SN Ia rate we have measured in $z \sim 1$ clusters, require that, if SNe Ia are the dominant iron source, their delay time must be short. This would cast doubt, e.g., on the double degenerate models. The observed redshift distribution of field SNe Ia implies a slowly changing field SNR(z) for SNe Ia. For several popular star-formation histories, this then indicates a long delay time. Taken together, these constraints may suggest that the iron in clusters is from core-collapse SNe, from an early stellar population with a top-heavy IMF.

References

1. L.L. Cowie, A. Songaila, A.J. Barger: Astron. J. **118**, 603 (1999)
2. A. Gal-Yam, D. Maoz, K. Sharon: Mon. Not. R. Astron. Soc. **332**, 37 (2002)
3. A. Gal-Yam D. Maoz: Mon. Not. R. Astron. Soc. **347**, 942 (2004)
4. K.M. Lanzetta et al. : Astrophys. J. **570**, 492 (2002)
5. D. Maoz, A. Gal-Yam: Mon. Not. R. Astron. Soc. **347**, 951 (2004)
6. P. Madau, M. Della Valle, N. Panagia: Mon. Not. R. Astron. Soc. **297**, L17 (1998)
7. P. Madau et al. : Mon. Not. R. Astron. Soc. **283**, 1388 (1998)
8. R. Pain et al. : Astrophys. J. **577**, 120 (2002)
9. D. Reiss: *The Rate of Supernovae in the Nearby and Distant Universe.* Ph.D. Thesis (Univ. Washington: Seattle, 2000)
10. A. Renzini: Astrophys. J. **488**, 35 (1997)
11. C.C. Steidel et al. : Astrophys. J. **519**, 1 (1999)
12. J.L. Tonry et al. : Astrophys. J. **594**, 1 (2003)
13. L.R. Yungelson, M. Livio: Astrophys. J. **528**, 108 (2000)

Expected Changes of SNe with Redshift due to Evolution of Their Progenitors

Inma Domínguez,[1] Peter Höflich,[2] Oscar Straniero,[3] Marco Limongi[4] and Alessandro Chieffi[5]

[1] Universidad de Granada, Granada, Spain
inma@ugr.es
[2] Universidad de Texas, Austin, USA
[3] INAF-Osservatorio Astronomico di Collurania, Teramo, Italy
[4] INAF-Osservatorio Astronomico di Roma, Monteporzio, Italy
[5] Istituto di Astrofisica Spaziale, CNR, Roma, Italy

Summary. We have analyzed the influence of the stellar populations, from which SN progenitors come, on the observational outcome, including the metal free Pop. III. We use our models to study the evolution of the progenitor, the subsequent explosion and the light curves. For Type Ia, the variation of the main sequence mass of the progenitor of the exploding WD produces an offset in the maximum-decline relation of 0.2 mag. This effect is critical for the use of high redshift Type Ia SNe as cosmological standard candles. In contrast, the metallicity does not change the above relation (at maximum, $\Delta M_V \leq 0.06$ mag). For Type II, we find a dependence of the light curve properties with both main sequence mass and metallicity of the progenitor, and we identify a rather homogeneous subclass, "Extreme II-P," that may be used as a quasi-standard candle. Note that, although not as good as Type Ia for distance determinations, Type II are expected to have occurred since the first stars were formed.

1 Introduction

Due to their high brightness, SNe are among the best candidates to measure distances on cosmological scales; in particular, Type Ia SNe (SNe Ia) are the favorites as they are brighter by about 1 to 2 magnitudes than other class of SNe and show very homogeneous properties. Recently, SNe Ia observed at high redshifts, z, (see [31, 35]) have provided results that are consistent with a Universe composed mainly of "dark energy" or, equivalent, with a positive cosmological constant, $\Omega_\Lambda \sim 0.7$. Note that this conclusion relies on the application of an empirical relation between light curve (LC) shape and maximum luminosity which is obtained for the well observed nearby SNe Ia occurring in galaxies at known distance [31, 34].

To understand the nature of this dark energy, we need to observe standard-candles at high z. The quantity and quality of the data is increasing due to systematic searches, space telescopes and 8m-class ground telescopes. However, SNe or other standard-candles are calibrated locally, and their application to very high z may be limited by evolutionary effects. In fact, there is

observational evidence indicating a correlation of SN properties with those of their host galaxies [2, 3, 11, 22, 38].

SNe Ia are thought to be the thermonuclear explosion of CO white-dwarfs [20] triggered by mass accretion from a companion. The proposed scenarios are merging of WDs by gravitational radiation (double degenerate) [21, 39], and accretion of H and/or He from a non-degenerate companion (single degenerate) [40]. Moreover, they occur in elliptical galaxies indicating that some of their progenitors, at least, have evolutionary time-scales comparable to the Hubble time and, thus, at high z SNe Ia should be rare.

The other class of SNe, core collapse SNe, are thought to be the explosion of massive stars (greater than $\sim 10 M_{\odot}$) caused by the collapse of its central parts into a neutron star or a black hole. Their evolutionary time scales are short compared to the age of the universe even at high z [26, 37, 42]. Core collapse SNe show a wide range of brightness, up to 6 magnitudes, and properties of their light curves [10, 30, 43] which prevents their use as standard-candles. However, our knowledge of the event is improving and it may be possible to derive the absolute magnitude in a similar way as Type Ia if appropriate empirical correlations can be identified (see Hamuy, this volume and [12]). These objects will occur soon after the initial star formation period and, therefore, can be used to probe the structure of the universe at high z (e.g., at $z \sim 5$). At that epoch, galaxies are expected to be small and dim and core collapse supernovae may be the brightest objects in the Universe [27].

It is expected that, going back in time, the stellar population of the SN progenitors would be composed of more low metallicity and rapidly evolving, more massive, stars. In this work we focus, mainly, on the exploration of the sensitivity of the light curve characteristics on the underlying progenitor properties: initial mass and metallicity (Z).

2 Numerical Models

2.1 Stellar Evolution

The evolution of selected models in the mass range from 1.5 to 25 $M_{\odot}$ and Z between 0 (Pop.III) and 0.02 (solar) have been computed from the pre-main sequence to the TP-AGB phase in the case of the low and intermediate mass stars and to the onset of core collapse for the massive stars. We have not included rotation neither mass loss.

All models have been computed by means of the evolutionary code FRANEC (rev 4.2) and are extensively described in [7, 9, 25]. The details of the FRANEC has been presented in [4, 5, 36].

2.2 Explosions and Light Curves

Based on the previous models, the explosion, detailed post-processing and light curves are computed by means of a 1D radiation-hydrodynamic code (see [7, 9, 16]). All parameters are fixed in order to analyze the sensitivity of the observed properties to the initial mass and metallicity of the progenitors.

For Type Ia we have considered delayed detonation explosions because models based on this explosion mechanism reproduce monochromatic light curves and spectra reasonable well, including the maximum-LC shape relation (see for example [14, 15, 24, 29, 41]. The description of the velocity of the deflagration front is based on 3D simulations [8, 23, 28]; model parameters, transition density and ignition density, are fixed and have been chosen to reproduce a typical SN Ia.

For Type II, the explosion is triggered artificially by depositing energy above the mass cut, fulfilling the requirement that the final kinetic energy and the ^{56}Ni mass is the same in all models.

3 Results

3.1 Type Ia

We have connected the initial mass and metallicity of the WD progenitor to the light curves and spectral properties of SNe Ia. All the potential progenitors of the WD have been studied. The key parameter is the integrated C/O ratio, the fuel, within the Chandrasekhar mass WD. In general, changes are small because the nuclear energy released by a complete burning (into iron group ashes) of a pure Carbon WD is about 10 % larger than that released by a pure Oxygen WD with the same mass.

We find that the initial mass of the progenitor modifies the average C/O in the WD up to a 22 % and, as a consequence, the ^{56}Ni mass produced by the explosion and the kinetic energy (for details see [9] and also [17]). Progenitors with greater masses (smaller C/O rate within the WD and consequently less amount of ^{56}Ni) produce less luminous and slightly faster decline LCs. In particular, the initial mass alters the maximum-LC shape relation, which may be offset by up to 0.2 mag. Notice that for a detailed analysis of the nature of the dark energy an accuracy of 0.05 mag is required [1].

In addition, for these massive progenitors, kinetic energies and expansion velocities are also smaller, down to 2000 km/s. This correlation between LC shape and expansion velocity may be used to reduce the scatter in the empirical relation from which the maximum luminosity is obtained.

The dependence of the total C/O on the initial mass is mainly due to the different extension of the convective core during the central He burning phase. In fact, the internal structure of an exploding WD may be schematically divided in two distinct regions: an internal one, where C is significantly

depleted (about 25 % C and 75 % O) and an external one, where C/O is about 1. The internal region is built in during the core He-burning phase, while the external one is left by the shell burning (AGB or accretion phase). Since the extension of the central region (C depleted) coincides with the convective core of the He-burning progenitor, and since more massive progenitors have a larger convective cores, the larger is the progenitor mass, the smaller is the final (pre-explosive) C/O.

In contrast, the dependence of the size of this inner C-depleted region with metallicity is much weaker and not monotonic. In fact, the metallicity of the progenitor does not influence the average C/O ratio within the WD; changes are smaller than 9 % and, as a consequence, the amount of ^{56}Ni produced in the explosion and the kinetic energies are rather similar (however, see also [18]). For this reason, metallicity does not influence the maximum luminosity ($\Delta M_V \leq$0.06 mag), nor the LC shape.

Finally, we want to stress, that the final integrated C/O ratio within the pre-explosive Chandrasekhar mass WD depends on the scenario; mergers (double degenerate) are expected to have a smaller C/O ratio compared to single degenerates. The reason is that, in the case of merging, two central carbon depleted region corresponding to the two WDs, are added.

3.2 Type II

First, we want to mention the limitation of our theoretical study; we have explored a very limited parameter space (see Hamuy, these Proceedings, and [13]) and to compare with observations, different ^{56}Ni masses and kinetic energies should be considered and mass loss included during the evolution of the progenitor.

We find (see [7, 19] for details) that all the Pop. III models end up as Blue Super Giants (BSG) while all the solar metallicity ones end up as Red Super Giants (RSG). At intermediate Z, the more massive stars end up as BSG while the less massive ones end up as RSG. The limiting mass depends on Z. In general, the stellar radius depends on the opacity of the envelope; the lower the metallicity, the lower the opacity and, as a consequence, the structure is more compact.

If the progenitor is a RSG, the brightness during the plateau phase, which lasts more than 50 days, is nearly constant, $M_V \sim$ -17.5, and quite insensitive to changes of the initial mass ($\Delta M_V \leq$0.07 mag). Increasing the kinetic energy by a factor of 2, results in a slightly brighter plateau, $\Delta M_V \leq$0.3 mag. This makes this sub-class, which we call "Extreme II-P," a quasi-standard candle.

The similarity of the LCs is caused by the similarity of the density structures of the RSG envelopes, which show flat density gradients at the photosphere, which during the plateau phase is located at the H-recombination front. A self-regulating mechanism is at work: an increase in the energy release causes a heating of the photosphere and a reduction of the energy production

rate and vice versa. Because the density slope of the photosphere is flat and slowly changing, the luminosity profile of the light curves is rather flat.

Moreover, the unique light curves of Extreme II-P allow photometric identification and so, permit their observation from ground 8m-class telescopes up to a redshift of $z \sim 3$. Space telescopes, like SIRTF, would push this limit even further and the NGST is expected to detect SNII up to $z \sim 10$.

BSG progenitors produce sub-luminous events, 1.5 magnitudes fainter than SNII which come from RSGs. The light curve presents, instead of the plateau, a long-lasting phase of increasing brightness. In this case the self-regulating mechanism does not work due to the steep density gradients.

Finally, these studies are very preliminary, key problems, concerning the identification of the progenitors (Type Ia) and the explosion mechanisms (Type Ia and Type II), are still to be solved, and, besides, we do not know how the stellar populations evolve with redshift.

References

1. A. Albrecht, J. Weller: Astron. Astrophys. Suppl. **197**, 6106 (2000)
2. D. Branch, W. Romanishing, E. Baron: Astrophys. J. **465**, 73 (1996)
3. E. Cappellaro et al. : Astron. Astrophys. **322**, 421 (1997)
4. A. Chieffi, O. Straniero: Astrophys. J. Suppl. **71**, 48 (1989)
5. A. Chieffi, M. Limongi, O. Straniero: Astrophys. J. **502**, 737 (1998)
6. A. Chieffi, M. Limongi: Astrophys. J. **577**, 281 (2002)
7. A. Chieffi, I. Domínguez, P. Höflich, M. Limongi, O. Straniero: Mon. Not. R. Astron. Soc. **345**, 111 (2003)
8. I. Domínguez, P. Höflich: Astrophys. J. **528**, 854 (2000)
9. I. Domínguez, P. Höflich, O. Straniero: Astrophys. J. **557**, 279 (2001)
10. A.V. Filippenko: In: *Cosmic Explosions*. eds. S. Holt, W.W. Zhang (AIP: New York, 2000)
11. M. Hamuy et al. : Astron. J. **120**, 1479 (2000)
12. M. Hamuy, P.A. Pinto: Astrophys. J. Lett. **566**, L63 (2002)
13. M. Hamuy: Astrophys. J. **582**, 905 (2003)
14. P. Höflich: Astrophys. J. **443**, 89 (1995)
15. P. Höflich, A. Khokhlov, J.C. Wheeler: Astrophys. J. **444**, 831 (1995)
16. P. Höflich, A. Khokhlov: Astrophys. J. **457**, 500 (1996)
17. P. Höflich, J.C. Wheeler, F.K. Thielemann: Astrophys. J. **495**, 617 (1998)
18. P. Höflich, K. Nomoto, H. Umeda, J.C. Wheeler: Astrophys. J. **528**, 590 (2000)
19. P. Höflich, O. Straniero, M. Limongi, I. Domínguez, A. Chieffi: Rev. Mex. Astron. Astrofis. Conf. Series **10**, 157 (2001)
20. P. Hoyle, W.A. Fowler: Astrophys. J. **132**, 565 (1960)
21. I.J. Iben, A.V. Tutukov: Astrophys. J. Suppl. **54**, 335 (1984)
22. V.D. Ivanov, M. Hamuy, P.A. Pinto: Astrophys. J. **542**, 588 (2000)
23. A. Khokhlov: Astrophys. J. **457**, 695 (1995)
24. E.J. Lentz, E. Baron, D. Branch, P. Hauschildt, P.E. Nugent: Astrophys. J. **530**, 966 (2000)
25. M. Limongi A. Chieffi A., O. Straniero: Astrophys. J. Suppl. **129**, 625L (2000)

26. J. Maza S. van den Bergh: Astrophys. J. **204**, 519 (1976)
27. J. Miralda-Escudé, M.J. Rees: Astrophys. J. **478**, 57 (1997)
28. J.C. Niemeyer, W. Hillebrandt: Astrophys. J. **452**, 779 (1995)
29. P.E. Nugent, E. Baron, P. Hauschildt, D. Branch: Astrophys. J. **485**, 812 (1997)
30. F. Patat, R. Barbon, E. Cappellaro, M. Turatto: Astron. Astrophys. **282**, 731 (1994)
31. S. Perlmutter et al. : Astrophys. J. **517**, 565 (1999)
32. M.M. Phillips et al. : Pub. Astron. Soc. Pacific **90**, 592 (1987)
33. M.M. Phillips P. Lira, N.B. Suntzeff, R.A. Schommer, M. Hamuy, J. Maza: Astron. J. **118**, 1766 (1999)
34. A.G. Riess, W.H. Press, R.P. Kirshner: Astrophys. J. **473**, 588 (1996)
35. B.P. Schmidt et al. : Astrophys. J. **507**, 46 (1998)
36. O. Straniero, A. Chieffi, M. Limongi: Astrophys. J. **490**, 425 (1997)
37. G. Tammann: In: *NATO-ASI on Supernovae: A Survey of Current Research.* eds. M.J. Rees, R.J. Stoneham (Reidel: Dordrecht, 1982) p. 371
38. L. Wang, P. Höflich, J.C. Wheeler: Astrophys. J. Lett. **487**, L29 (1997)
39. R.F. Webbink: Astrophys. J. **277**, 355 (1984)
40. J. Whelan, I. Iben, Jr.: Astrophys. J. **186**, 1007 (1973)
41. J.C. Wheeler, P. Höflich, R. Harkness, J. Spyromilio: Astrophys. J. **496**, 908 (1998)
42. S.E. Woosley, T.A. Weaver: Ann. Rev. Astron. Astrophys. **24**, 205 (1986)
43. T.R. Young, D. Branch: Astrophys. J. Lett. **342**, L79 (1989)

Dark Energy: Nature and Robustness

A. Blanchard[1] and Y. Zolnierowski[1,2]

[1] LAOMP, 14, Av. E.Belin, 31 400 Toulouse, France
alain.blanchard@ast.obs-mip.fr
[2] LAPP, IN2P3-C.N.R.S., B.P. 110, 74941 Annecy-le-Vieux cédex, France

Summary. Supernovae have provided the evidence for the existence of a dominant dark energy component of the Universe. The commonly accepted form of such a component is the quintessence. Here, we show that the possible nature of this component is rather well constrained by combining the various existing observational cosmological data. However, relaxing some of the various hypothesis can lead to somewhat different results.

1 Introduction

In a couple of years the so-called concordance model, i.e. $\Omega_M \sim 0.3$ $\Omega_\Lambda = 1. - \Omega_M \sim 0.7$ and $H_0 \sim 72$ km/s/Mpc has become almost the standard model of modern cosmology. Its ability to reproduce several major observations of cosmological relevance is actually remarkable. In addition the WMAP signal is fully consistent with such a model which has therefore gained in strength. However, it requires the introduction of a non-zero cosmological constant which represents the actual dominant contribution to the density of the Universe. Although such a possibility has been advocating by Einstein for cosmological purpose since 1917, cosmologists have been reluctant to take seriously into account such a term during the last eighty years! The question of whether there is an actual non-zero cosmological constant (or something similar), dominating the density of the Universe and producing its acceleration is certainly one of the most important and surprising question of modern physics. Here we would like to point out that direct evidence for a cosmological constant is very limited.

2 The Cosmological Constant: a Strange Object

The presence of a positive cosmological constant dominating the density of the Universe has rather dramatic consequences: the vacuum is actually the dominant component of the density of the Universe with a negative gravitational force inducing acceleration of the Universe. Indeed, within general relativity the source of gravity is:

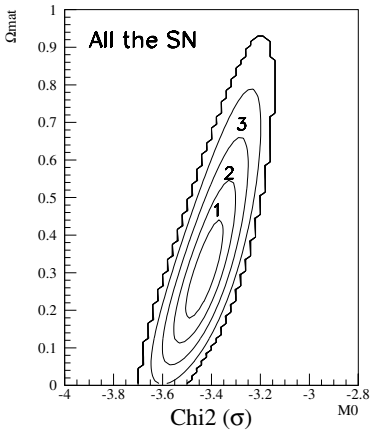

Fig. 1. Classical 1, 2, 3 σ contours in the plane Ω_M, Ω_λ from the Hubble diagram of SNIa using the SCP supernovae set (Perlmutter et al., 1999).

$$\rho + \frac{3p}{c^2} \tag{1}$$

ρ being the density and p the pressure. The vacuum has the following equation of state:

$$p = -\rho c^2 \tag{2}$$

leading to a negative source of gravity. A first puzzling aspect of the concordance model is that we are at a very specific period of the Universe at which the vacuum starts to dominate the density of the Universe. For instance at the typical redshift of distant supernovae ($z \sim 0.5$) the cosmological constant is not dominant any more over matter density. At redshift $z \sim 1.$, the matter density parameter is already $\Omega_m \sim 0.75$. So that supernovae hunters [7, 8] were lucky enough that the acceleration was not so obvious that it will have been noticed from first cosmological observations, and that still the cosmological constant is not small enough to have escape observational detection! Whether this argument is a valid concern or not is certainly subject to discussion, but it should be remembered that this type of concern leads to one of the original argument in Guth's paper [4] to advocate inflation.

3 Quintessence

One of the physically motivated alternatives to the cosmological constant is known as quintessence. In this scenario it is assumed that a scalar field is actually dominating the density of the Universe [6, 12]. No better idea has been produced since, and the quintessence scenario is very popular, as

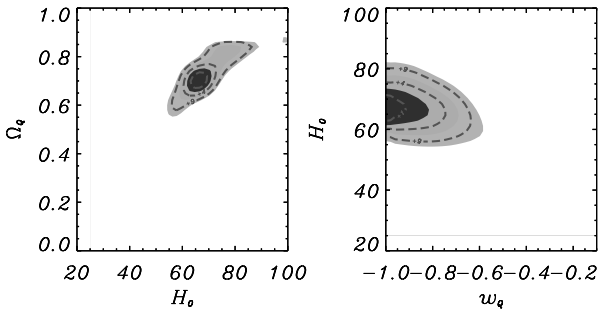

Fig. 2. 1, 2, 3 σ contours in the planes H_0, Ω_M and w_Q, H_0 from combining cosmological constraints including the Archeops CMB data [1].

being the only reasonable explanation of the acceleration of the Universe. The density of an homogenous scalar field is given by:

$$\rho_Q = \frac{1}{2}\dot{\Phi}^2 + V(\Phi) \tag{3}$$

while the pressure is:

$$p_Q = \frac{1}{2}\dot{\Phi}^2 - V(\Phi) \tag{4}$$

Such a field allows an arbitrary equation of state:

$$p_Q = w(z)\rho_Q \tag{5}$$

which is specified once the potential $V(\Phi)$ is given. Usually, $-1 \leq w$, although the region $w < -1$ is not forbidden. If $w < -1/3$ the expansion is accelerating. However, the various cosmological constraints (HST Hubble constant, Hubble diagram of distant supernovae, CMB, amplitude of matter fluctuations from clusters) allow to set severe constraints on this type of scenario, as shown on Fig. 2 [1]. The addition of the new WMAP data results in only a slight improvement [10]. This is an illustration of the fact that the standard scenario is very tightly constrained by existing data of cosmological relevance.

4 Casting Doubts on the Concordance Model

However, most of observational constraints used are subject to either some doubts from an observational point of view or to different interpretation when some simple hypotheses are relaxed. Moreover the concordance model conflicts with the observed abundance of high redshift clusters as analyzed in [2]. Probably the most important point is to remember that the CMB fluctuations, as observed by WMAP, do not require the introduction of a cosmological constant provided that the single power law assumption is relaxed.

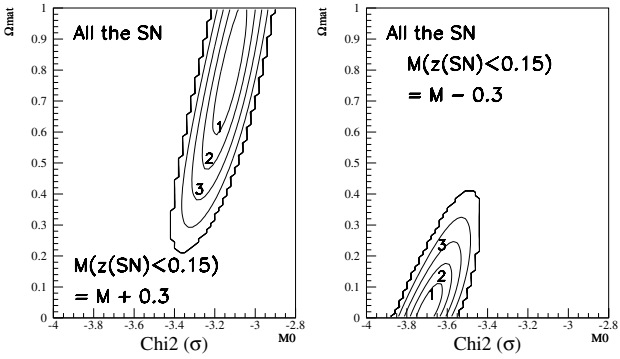

Fig. 3. Same contours than in figure 1, but after shifting the magnitude of distant SNIa (> 0.15) by ± 0.3 mag.

Furthermore, the introduction of a additional small amount of dark matter, $\Omega_{DM} \sim 0.1$, which does not cluster on small scale, like massive neutrinos with $m_\nu \sim 1$ eV or quintessence with $w \sim 0$, allows to reproduce the matter amplitude ($\sigma_8 \sim 0.55$ for $\Omega_M = 1$); such models then reproduce large scale structure data as well as a concordance model. One may consider that such a model is not as simple as the concordance, but there is some subjectivity in such an appreciation. One can alternatively consider that the introduction of a cosmological constant is extremely ugly.

4.1 Concerns with the Interpretation of Supernovae Hubble Diagram

It is important to remember that the only direct evidence for an accelerating Universe comes from the observational fact that distant supernovae appear fainter than those observed at low redshift. The amplitude of this dimming is not large: the signal is between 0.3 and 0.5 mag. Let us examine two possible concerns here: dust extinction [9] and selection biases. A first surprising result is that the High Z team found a couple of distant supernova with $B - V \sim -0.2$ the average being clearly bluer than their low redshift counterpart [5]. At first, this could be interpreted as an indication that distant are less dusty. As the color indices differ by something of the order of 0.1 mag, it would mean that distant SNIa are $\sim 0.3 - 0.5$ intrinsically brighter, pushing cosmological density parameter down to zero (see Fig. 2). However, the recent observation of [11] indicates no clear statistical difference in the average color of distant supernovae. Furthermore, local supernovae are never as blue as those present in the High Z team sample, even when their dust content is estimated to be zero. This therefore suggests a color evolution which is compensated by a larger dust extinction. So the apparent identical color hide a large dust extinction. This would therefore imply that intrinsic evolution

is hiding the greater dust obscuration. This is possible without requiring an exact cancelation given the large dispersion of existing data on SNIa. In such a case distant SNIa might well be fainter because of a larger dust extinction and not because of cosmological dimming. Assuming that SNIa with $z > 0.15$ are dimmed by 0.3 mag by such a process essentially cancel the need for a non-zero cosmological constant (see Fig. 3). Finally let us turn to the possible selection biases. One is first concerned by the fact that distant supernovae might be affected by the standard Malmquist bias:

$$\Delta m \approx 1.4\sigma^2 \tag{6}$$

Estimation of the amplitude of this bias is generally performed on the basis of the intrinsic dispersion of the luminosity after correction of the correlation between light curve and intrinsic luminosity. Taking a more conservative point of view and using the dispersion of the population implies that the amplitude of the possible bias could be:

$$\Delta m \approx 1.4(0.3 - 0.5)^2 \approx 0.125 - 0.35 \tag{7}$$

meaning that selection bias could be a real concern. At first look it seems that this bias if affecting the distant supernovae, would imply that the average population is intrinsically fainter. However, the procedure to identify distant SNIa is such that the correlation between peak magnitude and magnitude detection is small, therefore distant supernovae are likely to be weakly affected by this bias while local supernovae are more probably affected [7]. Again this would mean that distant SNIa appear fainter just because of selection biases, not because of cosmological dimming.

5 Conclusions

As we have summarized, although the concordance model is certainly the simplest way to reproduce a large set of existing data of cosmological relevance, direct evidence for the existence of cosmological constant is only coming from Supernovae Hubble diagram of SNIa, with a signal which is of the order of the intrinsic dispersion of the population. This means that moderate biases or/and astrophysical effects may significantly alter the significance of this result.

References

1. A. Benoît et al. : Astron. Astrophys. **399**, L25 (2003)
2. A. Blanchard, R. Sadat, J. Bartlett, M. Le Dour: Astron. Astrophys. **412**, 35 (2000)

3. A. Blanchard, M. Douspis, M. Rowan-Robinson, S. Sarkar: Astron. Astrophys. **412**, 35 (2003)
4. A. Guth: Phys. Rev. D **23**, 347 (1981)
5. B. Leibundgut: Ann. Rev. Astron. Astrophys. **39**, 67 (2001)
6. P.J.E. Peebles, B. Ratra: Astrophys. J. Lett. **325**, L17 (1998)
7. S. Perlmutter et al. : Astrophys. J. **517**, 565 (1999)
8. A.G. Riess et al. : Astron. J. **332**, 252 (2002)
9. M. Rowan-Robinson: Mon. Not. R. Astron. Soc. **332**, 252 (2002)
10. D.N. Spergel et al. : Astrophys. J. Suppl. **148**, 175 (2003)
11. M. Sullivan et al. : Mon. Not. R. Astron. Soc. **340**, 1057 (2003)
12. C. Wetterich: Nuc. Phys. **B302**, 668 (1988)

Brane Universes Tested by Supernovae

Włodzimierz Godłowski and Marek Szydłowski

Astronomical Observatory, Jagiellonian University, 30-244 Krakow, Orla 171, Poland;
godlows@oa.uj.edu.pl

Summary. We discuss observational constrains coming from supernovae Ia imposed on the behavior of the Randall-Sundrum models. It is interesting that brane models predict brighter galaxies for such redshifts which is in agreement with the measurement of the $z = 1.7$ supernova. We also demonstrate that the fit to supernovae data can also be obtained, if we admit the "super-negative" dark energy $p = -(4/3)\varrho$ on the brane, where the dark energy in a way mimics the influence of the cosmological constant.

1 Introduction

In recent times a lot of effort has been done on the idea that our Universe is a boundary of a higher-dimensional spacetime manifold [1]. Among superstring theories which may unify all interactions M-theory is a strong candidate for description of the real world. In this theory, gravity is a higher-dimensional theory, becoming effectively 4-dimensional at lower energies. In the standard model matter fields are confined to the 3-brane while gravity can, by its universal character, propagate in all extra dimensions. In the brane world models inspired by string/M theory [3, 4] new two parameters are introduced, namely brane tension λ and dark radiation U.

We should mention that before Randall and Sundrum (R-S) work [3, 4], where they proposed a mechanism to solve the hierarchy problem by a small extra dimension, large extra dimensions were proposed to solve this problem [1]. This gives an interesting feature because TeV gravity might be realistic and quantum gravity effects could be observed by next generation particle colliders. The Newtonian gravity potential on the brane is recovered at lowest order $V(r) = \frac{GM}{r}(1 + \frac{2l^2}{3r^2})$.

In this paper we demonstrate that if the brane world in the R-S version is realistic, we may find some evidence of higher-dimensions.

2 Brane Universes

In [7] we gave the formalism to express dynamical equations in terms of dimensionless observational density parameters Ω_i. In this notation the Friedman equation for brane universes takes the form:

$$\frac{1}{a^2}\left(\frac{da}{dt}\right)^2 = \frac{C_\gamma}{a^{3\gamma}} + \frac{C_\lambda}{a^{6\gamma}} - \frac{k}{a^2} + \frac{\Lambda_{(4)}}{3} + \frac{C_{\mathcal{U}}}{a^4}, \tag{1}$$

where $a(t)$ is the scale factor, $k = 0, \pm 1$ the curvature index (here we use natural system of units in which $8\pi G = c = 1$), $\Lambda_{(4)}$ the 4-dimensional cosmological constant, and γ the barotropic index ($p = (\gamma - 1)\varrho$ ($p =$ the pressure, $\varrho =$ the energy density). The constants are $C_\lambda = 1/6\lambda \cdot a^{6\gamma}\varrho^2$ and $C_{\mathcal{U}} = 2/\lambda \cdot a^4\mathcal{U}$; C_λ comes as a contribution from the brane tension λ, and $C_{\mathcal{U}}$ as a contribution from the dark radiation.

Because the ρ^2 term and dark radiation term do not appear in the standard cosmology, such terms could provide a small window to see the extra dimensions. It is useful to rewrite Eq. 1 to the dimensionless form. The brane universe can be interpreted as the standard Universe filled with the mixture of matter with the equation of state $p_i = (\gamma_i - 1)\rho_i$. Then we obtain a basic equation in the form:

$$\frac{\dot{x}^2}{2} = \frac{1}{2}\Omega_{k,0} + \frac{1}{2}\sum_i \Omega_{i,0}x^{2-3\gamma_i} = -V(x) \tag{2}$$

$$\ddot{x} = -\frac{1}{2}\sum_i \Omega_{i,0}(2 - 3\gamma_i)x^{1-3\gamma_i} = -\frac{\partial V(x)}{\partial x} \tag{3}$$

where $i = (\gamma, \lambda, \Lambda, U)$, and $x \equiv \frac{a}{a_0}$, $T \equiv |H_0|t$, $\dot{} \equiv \frac{d}{dT}$, t is the original cosmological time, and V is the potential function. Therefore the dynamics of the considered model is equivalent to introducing fictitious fluids which mimic the ρ^2 contribution and the dark energy term.

The above relations allow one to write down an explicit redshift-magnitude relation for the brane models to study their compatibility with astronomical data which is the subject of the present paper. Obviously, the luminosity of galaxies depends on the present densities of the different components of matter content, Ω_i, and their equations of state reflected by the value of the barotropic index, γ_i.

If the apparent luminosity of the source as measured by the observer is $l = L/4\pi d_L^2$, then the luminosity distance d_L of the source is defined by the relation

$$d_L = (1 + z)a_0 r_1 \equiv \frac{\mathcal{D}_L(z)}{H_0}, \tag{4}$$

and $\mathcal{D}_L$ is the dimensionless luminosity distance.

The observed and absolute luminosities are defined in terms of K-corrected apparent and absolute magnitudes m and M. When written in terms of m and M, we obtain

$$m(z) = \mathcal{M} + 5\log_{10}[\mathcal{D}_L(z)], \tag{5}$$

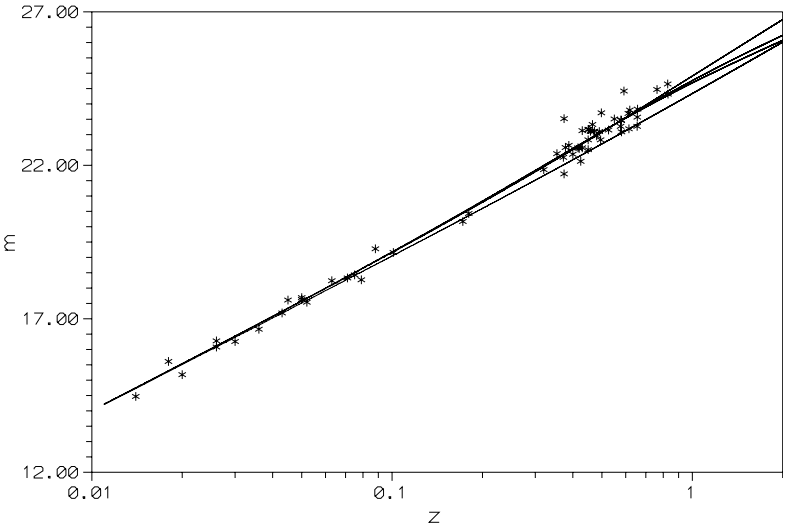

Fig. 1. The Redshift-magnitude relation for $\gamma = 1$ brane universes (dust on the brane). The top line is the best-fit Perlmutter model. The bottom line is a flat model with $\Omega_{m,0} = 1$. Between these two lines there are brane models with $\Omega_{\lambda,0} \neq 0$: lower–the best-fit non-flat model; higher–the best-fit flat model.

where $\mathcal{M} = M - 5\log_{10} H_0 + 25$. For the homogeneous and isotropic Friedman models one gets

$$\mathcal{D}_L(z) = \frac{(1+z)}{\sqrt{\mathcal{K}}} S(\chi) \tag{6}$$

where $S(\chi) = \sin\chi$ for $\mathcal{K} = -\Omega_{k,0}$; $S(\chi) = \chi$ for $\mathcal{K} = 1$; $S(\chi) = \sinh$ for $\mathcal{K} = \Omega_{k,0}$. The dimensionless parameters are $\Omega_k = -\frac{k}{H^2 a^2}$, $\Omega_\gamma = \frac{1}{3H^2}\varrho$, $\Omega_\lambda = \frac{1}{6H^2\lambda}\varrho^2$, $\Omega_{\Lambda_{(4)}} = \frac{\Lambda_{(4)}}{3H^2}$, and $\Omega_{\mathcal{U}} = \frac{2}{H^2\lambda}\mathcal{U}$.

3 Testing Brane Models

Now we test brane models using the Perlmutter sample [2]. In order to avoid any possible selection effects, we use the full sample called sample A (usually, one excludes two data points as outliers and another two points, presumably reddened, from the full sample of 60 supernovae).

First of all, we estimated the value of $\mathcal{M}$ from the sample of 18 low redshift supernovae, also testing our result by the full sample of 60 supernovae. We should note that, in fact, we have an ellipsoid of admissible models in a three-dimensional parameter space $\Omega_{m,0}$, $\Omega_{\lambda,0}$, $\Omega_{\Lambda_{(4)},0}$ at hand. Then, we have more freedom than in the Perlmutter et al. [2] analysis where they had only an ellipse in a two-dimensional parameter space $\Omega_{m,0}$, $\Omega_{\Lambda_{(4)},0}$. For a flat model

$\Omega_{k,0} = 0$ we obtain "corridors" of possible models. Formally, the best-fit flat model is $\Omega_{m,0} = 0.01$, $\Omega_{\lambda,0} = 0.09$ $\chi^2 = 94.7$ which is again unrealistic. In the realistic case we obtain for a flat model $\Omega_{m,0} = 0.25$, $\Omega_{\lambda,0} = 0.02$, $\Omega_{\Lambda_{(4)},0} = 0.73$ with $\chi^2 = 95.6$. One should note that all realistic brane models require also the presence of the positive 4-dimensional cosmological constant ($\Omega_{\Lambda_{(4)},0} \sim 0.7$).

In Fig. 1 we present plots of the redshift-magnitude relation against the supernovae data. One can observe that in both cases (best-fit and best-fit flat models) the difference between brane models and a flat model with $\Omega_{\Lambda_{(4)},0} = 0$ is largest for $0.6 < z < 0.7$ while it significantly decreases for the higher redshifts. It gives us a possibility to discriminate between the Perlmutter model and brane models when the data from high-redshift supernovae $z > 1$ are available. It is interesting that brane models predict brighter galaxies for such redshifts which is in agreement with the measurement of the $z = 1.7$ supernova [5, 6]. In other words, if the distant ($z > 1$) supernovae were brighter, the brane universes would be favored.

For completeness, we also made our analysis using samples B and C. It emerged that it does not significantly changes our results, although it increases the quality of the fit.

Formally, the best fit for the sample B is (56 supernovae) ($\chi^2 = 57.3$): $\Omega_{k,0} = -0.1$, $\Omega_{m,0} = 0.17$, $\Omega_{\lambda,0} = 0.06$, $\Omega_{\Lambda_{(4)},0} = 0.87$. For the flat model we obtain ($\chi^2 = 57.3$): $\Omega_{m,0} = 0.12$, $\Omega_{\lambda,0} = 0.06$, $\Omega_{\Lambda_{(4)},0} = 0.82$, while for a "realistic" model we obtain ($\chi^2 = 57.6$): $\Omega_{m,0} = 0.25$, $\Omega_{\lambda,0} = 0.02$.

Formally, the best fit for the sample C (54 supernovae) ($\chi^2 = 53.5$) gives $\Omega_{k,0} = 0$ (flat) $\Omega_{m,0} = 0.21$, $\Omega_{\lambda,0} = 0.04$, $\Omega_{\Lambda_{(4)},0} = 0.75$, while for a "realistic" model ($\chi^2 = 53.6$): $\Omega_{m,0} = 0.27$, $\Omega_{\lambda,0} = 0.02$.

One should note that we have also separately estimated the value of $\mathcal{M}$ for sample B and C. We obtained $\mathcal{M} = -3.42$. However, if we use this value in our analysis it does not change significantly the results (χ^2 does not change more than 1, which is a marginal effect for χ^2 distribution for 53 or 55 degrees of freedom).

In Fig. 2 we present a redshift-magnitude relation for brane models with dark energy ($\gamma = -1/3$). Note that the theoretical curves are very close to that of Perlmutter's which means that the dark energy cancels the positive-pressure influence of the ϱ^2 term and can simulate the negative-pressure influence of the cosmological constant to cause cosmic acceleration. From the formal point of view the best fit is ($\chi^2 = 95.4$): $\Omega_{k,0} = 0.2$, $\Omega_{d,0} = 0.7$, $\Omega_{\lambda,0} = -0.1$, $\Omega_{\mathcal{U}} = 0.2$, $\Omega_{\Lambda_{(4)},0} = 0$, which means that the cosmological constant must necessarily vanish. From this result we can conclude that the dark energy $p = -(4/3)\varrho$ can mimic the contribution from the $\Lambda_{(4)}$-term in standard models. For the best-fit flat model ($\Omega_{k,0} = 0$) we have ($\chi^2 = 95.4$): $\Omega_{d,0} = 0.2$, $\Omega_{\lambda,0} = -0.1$, $\Omega_{\mathcal{U}} = 0.2$, $\Omega_{\Lambda_{(4)},0} = 0.7$.

Finally, let us study the angular diameter test for brane universes. The angular diameter of a galaxy is defined by

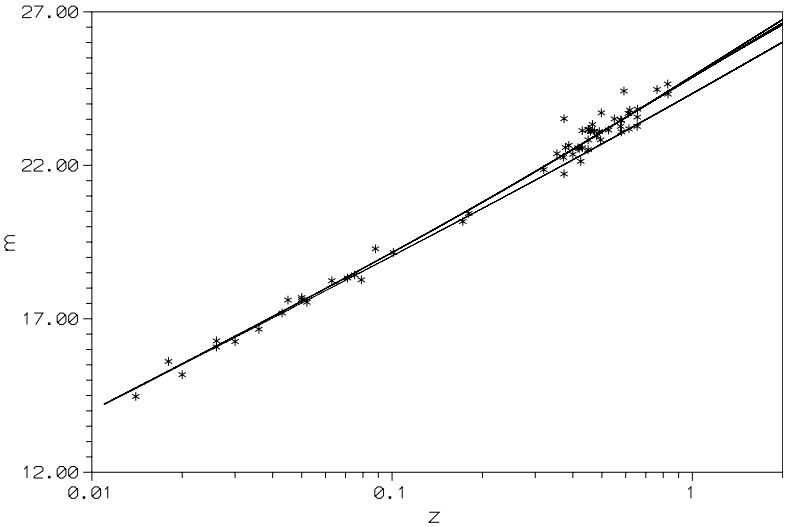

Fig. 2. The redshift-magnitude relation for $\gamma = -1/3$ brane universes (phantom on the brane). The top line is the Perlmutter model and the bottom line is the Einstein-de Sitter model. In the middle are two overlapping lines for the best-fitted and best-fitted flat brane models.

$$\theta = \frac{d(z+1)^2}{d_L}, \tag{7}$$

where d is a linear size of the galaxy. In a flat dust ($\gamma = 1$) universe θ has the minimum value $z_{min} = 5/4$. The dark radiation can enlarge the minimum value of θ while the ordinary radiation lowers this value $z_{min} = (\Omega_{\mathcal{U}} - 1 + \sqrt{3\Omega_{\mathcal{U}} + 1})/2\mathcal{U} \geq \frac{5}{4}$ for $\Omega_{\mathcal{U}} \leq 0$. This is a general influence of negative dark radiation onto the angular diameter size for brane models.

More detailed analytic and numerical studies show that the increase of z_{min} is even more sensitive to negative values of $\Omega_{\lambda,0}$ (ϱ^2 contribution). Similarly as for the dark radiation $\Omega_{\mathcal{U}}$, the minimum disappears for some large negative Ω_λ. Positive $\Omega_{\mathcal{U}}$ and Ω_λ make z_{min} decrease.

Finally, we also obtain that at high redshifts the expected luminosity of supernovae Ia should be brighter than in Perlmutter model. For the best fit value we obtain $\Omega_{\lambda,0} \simeq 0.01$ which seems to be unrealistic.

This occurs because, in the R-S model, there is a constraint on the parameter $\Omega_{\lambda,0}$ from the requirement of not violating the four-dimensional gravity on sufficiently large spatial scale. This constraint requires that the value of λ is less than about $(100\ \mathrm{GeV})^4$, which means that during the late epoch the ρ^2 term in the model should be small. Thus, the obtained value of $\Omega_{\lambda,0} \sim 0.01$ is the observational limit which is not based on theoretical model assumptions.

Acknowledgement. MS was supported by the KBN No. 1PO3D00326.

References

1. N. Arkani-Hamed, S. Dimopoulos, G. Dvali: Phys. Lett. B **429**, 263 (1998)
2. S. Perlmutter et al. : Astrophys. J. **517**, 565 (1999)
3. L. Randall, R. Sundrum: Phys. Rev. Lett. **83**, 3370 (1999)
4. L. Randall, R. Sundrum: Phys. Rev. Lett. **83**, 4690 (1999)
5. A.G. Riess et al. : Astron. J. **116**, 1009 (1998)
6. A.G. Riess et al. : Astrophys. J. **560**, 49 (2001)
7. M. Szydłowski, M.P. Dąbrowski, A. Krawiec: Phys. Rev. D **66**, 064003 (2002)

A Geometric Determination of the Distance to SN 1987A and the LMC

Nino Panagia[1,2]

[1] Space Telescope Science Institute, 3700 San Martin Drive, Baltimore, MD 21218, USA;
panagia@stsci.edu
[2] Affiliated with the Space Telescope Division of the European Space Agency, ESTEC, Noordwijk, Netherlands

Summary. Using the definitive reductions of the IUE light curves by [15] and an extensive set of *HST* images of SN 1987A we have repeated and improved our original analysis [8, 9] to derive a better determination of the distance to the supernova. In this way we have obtained an absolute size of the ring $R_{\rm abs} = (6.23 \pm 0.08) \times 10^{17}$ cm and an angular size $R'' = 808 \pm 17$ mas, which give a distance to the supernova $d(SN1987A) = 51.4 \pm 1.2$ kpc and a distance modulus $(m-M)_{SN1987A} = 18.55 \pm 0.05$. Allowing for a displacement of SN 1987A position relative to the LMC center, the distance to the barycenter of the Large Magellanic Cloud is also estimated to be $d(LMC) = 51.7 \pm 1.3$ kpc, which corresponds to a distance modulus of $(m - M)_{LMC} = 18.56 \pm 0.05$.

1 Introduction

Cepheid variables are possibly the most reliable, and certainly the most widely used secondary distance indicators to measure distances up to several tens of Mpc. Because of this they play a crucial role in the determination of the cosmological distance scale (for a review see the proceedings of the STScI Symposium *The Extragalactic Distance Scale*, [6]). On the other hand, the calibration of Cepheids as distance indicators is based on the study of Cepheid variables in the LMC and, therefore, determining the distance to the Large Magellanic Cloud is a fundamental step in establishing a cosmological distance scale because the zero point of the Cepheid calibration relies crucially on the calibration of the LMC distance.

Various methods have been employed to measure the distance to the LMC, with various degrees of success and/or accuracy (e.g., [7]). All methods, however, are indirect in that they all depend on the calibration of other distance indicators, and, therefore, have only a statistical value. Moreover, different distance indicators appear to give discordant results that are not compatible with each other, thus making the distance issue very slippery.

The presence of the famous circumstellar ring around SN 1987A has provided a unique opportunity to determine the distance to the LMC directly by using a purely geometric method: it consists in measuring the angular size of the ring from high resolution images and comparing it to the absolute size as

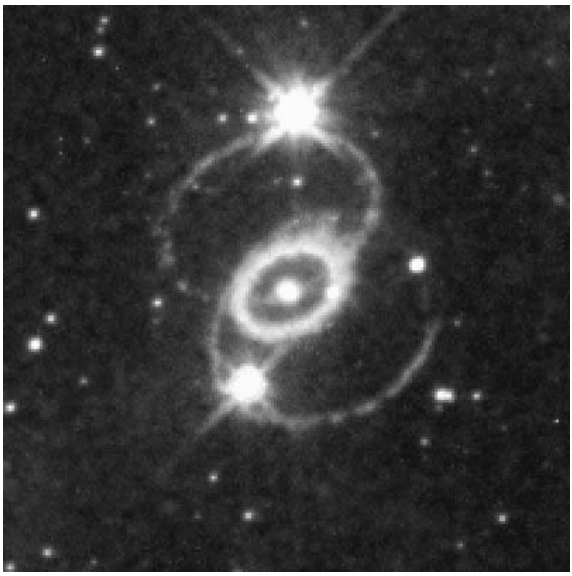

Fig. 1. An $8'' \times 8''$ region centered on SN 1987A as observed on September 24, 1994, with the *HST-WFPC2* in an [OIII] 5007 Å filter. In addition to the supernova, this figure shows clearly the presence of the three circumstellar rings, a brighter equatorial ring and two fainter, larger rings that are loosely aligned along the polar axis.

estimated from the evolution of emission lines produced by the ring ionized gas (see, e.g., [1, 2, 8, 9]).

In 1991 Panagia et al. [8, 9] estimated the distance to SN 1987A (51.2 ± 3.1 *kpc*) from a comparison of the angular size of the inner circumstellar ring as measured with the *HST-FOC* in August 1990 [5], with the ring absolute size as determined from the peaks of its UV emission line light curves.

More recently, Gould re-examined the problem adopting an infinitely narrow ring geometry and retaining Panagia et al. [8, 9] assumption of an exponential law for the line emissivity [2, 3]. Thus, using the same data as in Panagia et al. [8, 9] and Sonneborn et al. [15], respectively, but including only the NIV] and NIII] light curves, and adopting the average [OIII] ring size as measured by Plait et al. [11] over the period August 1990 – May 1993, Gould concluded that the distance to SN 1987A be less than 47 kpc.

The new reductions of the IUE spectra, done by Sonneborn et al. [15], have produced more accurate and reliable light curves. Therefore, we have decided to repeat our analysis using the new data set and including a more accurate and realistic estimate of the ring angular size obtained from the study of an extensive set of HST images of SN 1987A. Here, we present a brief outline of our analysis and the main results of our study. A complete account of this work will be presented in a forthcoming paper [10].

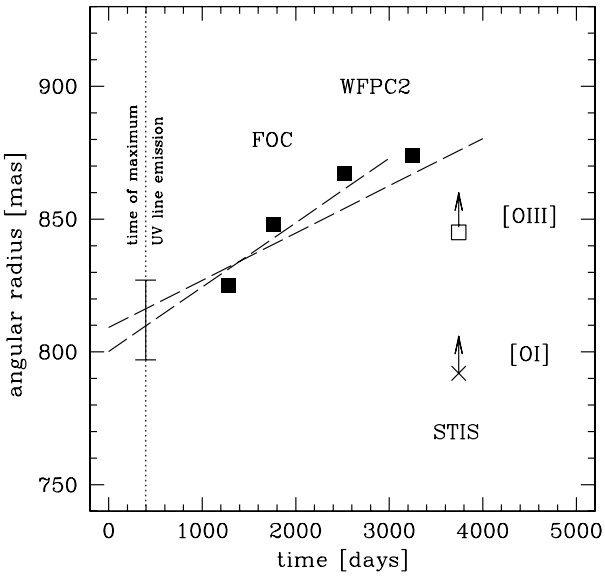

Fig. 2. The surface brightness averaged radius of the ring as measured in *FOC* and *WFPC2* images taken with a narrow band [OIII] filter, and the recent measurements made with the STIS in the light of the [OIII] 5007 Å and [OI] 6300 Å lines [16]. The two straight lines are the best fits to the *FOC+WFPC2* points only, and to the *FOC+WFPC2+STIS* [OIII] sizes, respectively. The error bar represents the range of possible values of the radius at the time of the UV maximum.

2 The Angular Size of the Ring

The inner circumstellar ring is clearly extended with a HPW of about 1/7 its radius (e.g. [5, 10]). The finite width of the ring makes the definition of an average size a very delicate one, which, if done improperly, may introduce errors as large as, say, half the HPW, i.e. as much as 7% or more.

Also, to derive the distance to SN 1987A one should compare the absolute ring size, determined from the light curves of twice ionized N and C and three times ionized N, with the angular size of the ring as measured at the time of the peak for radiation emitted by ions of comparable ionization stages.

While the images obtained with *HST* in the [OIII] line filter (see e.g. Fig. 1) satisfy the second requirement (comparable ions), they fail to satisfy the first one (comparable epochs). On the other hand, the analysis of both *FOC* and *WFPC2* images have revealed that the ring angular size, as estimated from [OIII] images, appears to increase with time ([10, 11]; see Fig. 2) while the one derived from Hβ and [NII] images remains constant in time and virtually coincides with the size measured in the earliest [OIII] image. This is the effect of both cooling and recombination of the OIII ion, that cause the [OIII] 5007 Å line intensity to decline more quickly at the inner edge of the

ring where the density is believed to be higher. An experimental confirmation of this effect is provided by HST-STIS imaging-spectroscopy of SN 1987A, obtained in April 1997 [16], that has shown an appreciably smaller ring size in the [OI] 6300 Å line than it is in the [OIII] 5007 Å line.

Therefore, the best value of the ring angular size to compare with the absolute size determined from the UV lines is an extrapolation of the observed sizes, as measured with *HST* in the [OIII] 5007 Å filter, back to the epoch of maximum UV line emission (approximately 400 days after the explosion, i.e. around early April 1988; cf. Fig. 3). In this way we obtain:

$$R'' = 808 \pm 17\,\mathrm{mas}\,.$$

3 The Absolute Size of the Ring

It has been shown [1, 2, 8, 9] that under the assumption of an infinitely narrow width the absolute radius of the ring can be derived from measurements of the onset time of the UV line emission, $t_\circ$, and the time of maximum UV line emission $t_{\max}$ because they correspond to the times when the near side and the far side of the ring start shining as a result of the ionization due to the initial UV flash from the supernova explosion. A simple geometric argument gives

$$R = c(t_\circ + t_{\max})/2\,.$$

As mentioned before, one has to measure the absolute size for the same emitting ion for which one can measure the angular size. In addition, one has also to take into account that the ring is clearly extended with a width $\delta R \simeq R/7$. Therefore, we have limited our analysis to the UV light curves of twice ionized ions, namely OIII, NIII and CIII, and we have compared them to theoretical light curves computed under the following assumptions:

- The ring is circular and has a Gaussian width with HPW of 14% the ring radius.
- The intrinsic emission of each ion decays exponentially with time.
- The free parameters are the radius and the inclination angle of the ring, the specific emissivity at time $t = 0$ and the decay time of each line.

The best fits to the light curves for the OIII] 1666 Å, NIII] 1750 Å, and CIII] 1909 Å lines are shown in Fig. 3.

We also show the composite light curve, sum of the OIII], NIII] and CIII] line intensities, and its best model fit: we note that the scatter in the composite light curve is greatly reduced relative to the three light curves, indicating that most of the fluctuation is actually noise. The individual determinations of the absolute radius fall in the range 230 to 248 light-days, or 6.0 to 6.4×10^{17} cm, with uncertainties of about 4% for OIII] and CIII], and slightly above 1% for NIII], resulting in an average value of

$$R = (6.23 \pm 0.08) \times 10^{17}\,\mathrm{cm}\,.$$

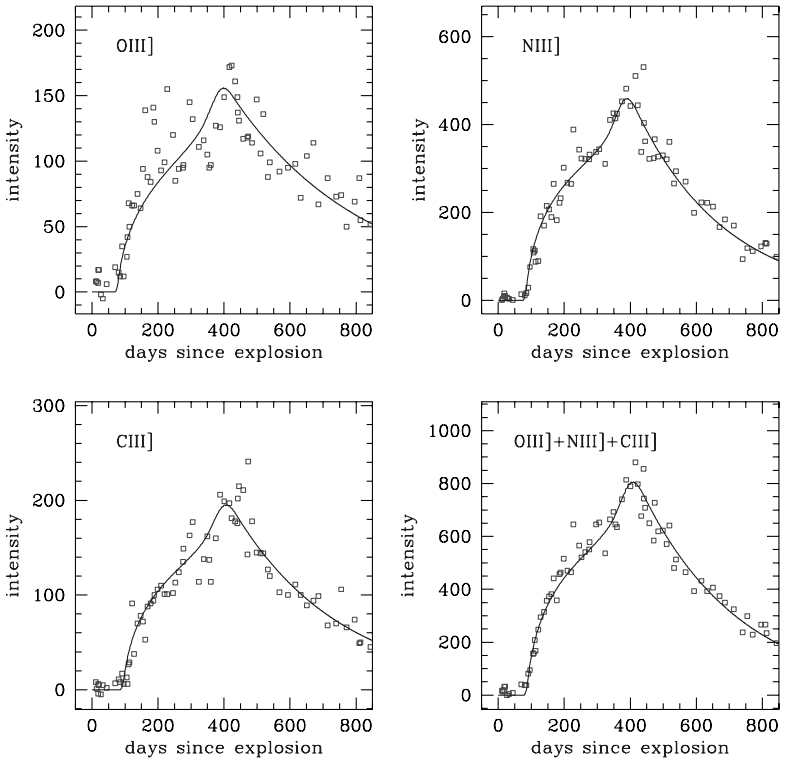

Fig. 3. The observed intensities (in units of 10^{-15} erg cm^{-2} s^{-1}) of the OIII] 1666 Å, NIII] 1750 Å, and CIII] 1909 Å lines and their straight sum are presented and compared to their best-fit model light curves.

4 Distance Determination

Comparing the absolute size of the circumstellar ring to its angular size, we derive a distance to SN 1987A

$$d(SN1987A) = 51.4 \pm 1.2\, kpc \qquad (m-M)_{\rm SN1987A} = 18.55 \pm 0.05\,.$$

This value is very close to our original determination [8, 9] but is considerably more accurate. Actually, it could still be an underestimate to the true distance to SN 1987A, because if the ring is not perfectly circular, as hinted by the marginal discrepancy between the inclinations determined from light curve fitting ($i \simeq 42^\circ$) and from the major to minor axis ratio ($i \simeq 44^\circ$), then the distance may have to be increased by as much as 2% [3].

Allowing for the difference of position of SN 1987A relative to the LMC barycenter [17] the best estimate of the distance to the center of mass of the LMC is found to be

Table 1. Summary of SN 1987A distance determinations based on UV line light curves and *HST* imaging

Authors	Emission Lines/Ions	$t_{\max}$ days	R″ mas	(m-M) SN 1987A
Prelim. IUE reductions				
Panagia et al. 1991 [8, 9]	NIII], NIV], NV, CIII]	413 ± 24	825 ± 17	18.55 ± 0.13
Gould 1995 [2]	NIII], NIV]	390 ± 2	858 ± 11	18.35 ± 0.04
Final IUE reductions				
Sonneborn et al. 1997 [15]	NIII]	399 ± 15	858 ± 11	18.43 ± 0.10
Gould & Uza 1998 [3]	NIII], NIV]	378 ± 5	858 ± 11	18.37 ± 0.04
Panagia et al. 2003 [10]	NIII], CIII], OIII]	395 ± 5	808 ± 17	18.55 ± 0.05

$$d(LMC) = 51.7 \pm 1.3\, kpc \qquad (m - M)_{\rm LMC} = 18.56 \pm 0.05\,.$$

The error includes the uncertainties on the SN 1987A distance (± 1.2 kpc) as well as those on the depth toward SN 1987A (± 0.2 kpc) and the relative position of the LMC barycenter (± 0.3 kpc).

5 Discussion and Consequences for the Cosmological Distance Scale

In the literature one finds a number of determinations of SN 1987A distance which are all based on the analysis of UV line light curves and *HST* imaging but provide values that may be quite discrepant with each other. Table 1 summarizes most of the "independent" analyses of such data, listing the authors (column 1), the emission lines considered (column 2), the derived time of the onset of the far side emission (column 3), the adopted/measured angular size of the ring (column 4) and, finally, the resulting distance modulus (column 5).

One sees immediately that most of the discrepancy can be attributed to the different angular size adopted and/or to the selection of UV emission lines that were employed to estimate the absolute size.

In particular, the "high" value of the angular size, 858 mas, is the average of the sizes measured by [11] on *FOC* images taken mostly with the [OIII] filter between August 1990 and October 1993. Since the apparent size of the ring increases with time, such an average represent a gross overestimate (about 6%) of the ring size at the time of the UV maximum which leads to an underestimate of the distance modulus of 0.13 magnitudes: this effect alone accounts for most of the discrepancies.

The second point to consider is the time of the far side emission onset, $t_{\max}$. As mentioned in Sec. 2, light curves of different ions give different values

of $t_{\max}$. This is due to both measurement uncertainties and physical effects, such as:

- different ions recombine at different rates;
- different lines react faster or slower to a general temperature decline, i.e. cooling, depending on their excitation potential;
- the ring is made of a multitude of condensations with a wide range of densities and temperatures, with the effect that intrinsic, and possibly large fluctuations add on top of the measurement errors to distort the average behavior of light curves.

To minimize these effects, one has to combine the results of as many light curves as possible but selecting only of ions with similar characteristics, which is what we have done in our study.

The conclusion is that all apparent discrepancies can be explained in terms of less-than-perfect selections of the data to compare with each other.

Our geometric determination of the LMC distance modulus is in excellent agreement with the recent determinations by Romaniello et al. [13] that are based on a study of both Red Clump stars and TRGB stars measured in multi-band HST images of SN 1987A field. In particular, they obtained $(m - M)_{RC} = 18.59 \pm 0.04 \pm 0.08$ and $(m - M)_{TRGB} = 18.69 \pm 0.25 \pm 0.06$ (the quoted errors are the statistical and systematic ones , respectively), whose weighted average is $< (m - M) >_{\text{LMC field}} = 18.60 \pm 0.04 \pm 0.08$.

It is apparent that the true LMC distance modulus must be around 18.60 and that values lower than 18.48 and higher than 18.72 are to be excluded with high confidence.

The main consequence of our distance determination is that all Cepheid distances based on the canonical value of 18.50 for the LMC (e.g., [7]) should be increased by about 3%. And, of course, all values of H_0 based directly or indirectly on Cepheid distances should be reduced by the same amount.

In this light, I like to assess the consequences for the determination of H_0 based on a Cepheid calibration of the peak brightness of type Ia supernovae (SNIa) relatively nearby (up to $\sim$25 Mpc) and comparison of Hubble diagrams of more distant SNIa. In a long term HST project led by Sandage, Saha and Tammann, 9 SNIa in spiral galaxies have been calibrated with Cepheid variables, resulting in average absolute magnitudes for type Ia supernovae $M_{\rm B} = -19.47 \pm 0.07$ and $M_{\rm V} = -19.46 \pm 0.06$ with the assumption of a LMC distance modulus of 18.50 [14]. Entering these values into the Hubble diagram of more distant SNIa leads to values of the Hubble constant around $H_0 = 61 \pm 6\,\mathrm{km\ s^{-1}\,Mpc^{-1}}$ for an adopted cosmological model with $\Omega_M = 0.3$, $\Omega_\Lambda = 0.7$ [14].

As said above, the new LMC distance modulus would imply a reduced value of the Hubble constant, by about 3%. However, one has to take into account reddening corrections for distant supernovae in the Hubble diagram (this problem was partly bypassed in Sandage et al. analysis by considering a Hubble diagram that included only SNIa affected by little reddening) whose

effect may increase the value of H_0 by as much as +7% (see e.g. [4, 12]). Combining the two competing effects in an approximate way results in a Hubble constant of

$$H_0 = 63 \pm 7 \,\mathrm{km\ s^{-1}\,Mpc^{-1}}\,.$$

Although it is obtained with a simplified analysis which can, and will be refined, I regard this as a rather robust result that is not likely to change much in the years to come, and that offers the pleasant feature of not violating any constraint posed by old stars and the evolution of the Universe.

References

1. E. Dwek, J.E. Felten: Astrophys. J. **387**, 551 (1992)
2. A. Gould: Astrophys. J. **452**, 189 (1995)
3. A. Gould, O. Uza: Astrophys. J. **494**, 118 (1998)
4. M. Hamuy, M.M. Phillips, N.B. Suntzeff, R.A. Schommer, J. Maza, R. Aviles: Astron. J. **112**, 2391 (1996)
5. P. Jakobsen et al. : Astrophys. J. Lett. **369**, L63 (1991)
6. M. Livio, M. Donahue, N. Panagia: In: "The Extragalactic Distance Scale," eds. M. Livio, M. Donahue, N. Panagia (Cambridge Univ. Press: Cambridge, 1997)
7. B. Madore, W. Freedman: Pub. Astron. Soc. Pacific **103**, 933 (1991)
8. N. Panagia, R. Gilmozzi, F. Macchetto, H.-M. Adorf, R.P. Kirshner: Astrophys. J. **380**, L23 (1991)
9. N. Panagia, R. Gilmozzi, F. Macchetto, H.-M. Adorf, R.P. Kirshner: Astrophys. J. Lett. **386**, L31 (1992)
10. N. Panagia, R. Gilmozzi, R.P. Kirshner, C.S.J. Pun, G. Sonneborn: in preparation
11. P.C. Plait, P. Lundqvist, R.A. Chevalier, R.P. Kirshner: Astrophys. J. **439**, 730 (1995)
12. A.G Riess, W.H. Press, R. P. Kirshner: Astrophys. J. **473**, 588 (1996)
13. M. Romaniello, M. Salaris, S. Cassisi, N. Panagia: Astrophys. J. **530**, 738 (2000)
14. A. Saha, A. Sandage, G.A. Tammann, A.E. Dolphin, J. Christensen, N. Panagia, F.D. Macchetto: Astrophys. J. **562**, 314 (2001)
15. G. Sonneborn et al. : Astrophys. J. **477**, 848 (1997)
16. G. Sonneborn et al. : Astrophys. J. Lett. **492**, L139 (1998)
17. R. van der Marel, M.-R.L Cioni: Astron. J. **122**, 1807 (2001)

SPRINGER PROCEEDINGS IN PHYSICS

46 **Cellular Automata and Modeling of Complex Physical Systems**
Editors: P. Manneville, N. Boccara, G.Y. Vichniac, and R. Bidaux

47 **Number Theory and Physics**
Editors: J.-M. Luck, P. Moussa, and M. Waldschmidt

48 **Many-Atom Interactions in Solids**
Editors: R.M. Nieminen, M.J. Puska, and M.J. Manninen

49 **Ultrafast Phenomena in Spectroscopy**
Editors: E. Klose and B. Wilhelmi

50 **Magnetic Properties of Low-Dimensional Systems II**
New Developments
Editors: L.M. Falicov, F. Mejía-Lira, and J.L. Morán-López

51 **The Physics and Chemistry of Organic Superconductors**
Editors: G. Saito and S. Kagoshima

52 **Dynamics and Patterns in Complex Fluids**
New Aspects of the Physics–Chemistry Interface
Editors: A. Onuki and K. Kawasaki

53 **Computer Simulation Studies in Condensed-Matter Physics III**
Editors: D.P. Landau, K.K. Mon, and H.-B. Schüttler

54 **Polycrystalline Semiconducturs II**
Editors: J.H. Werner and H.P. Strunk

55 **Nonlinear Dynamics and Quantum Phenomena in Optical Systems**
Editors: R. Vilaseca and R. Corbalán

56 **Amorphous and Crystalline Silicon Carbide III, and Other Group IV–IV Materials**
Editors: G.L. Harris, M.G. Spencer, and C.Y. Yang

57 **Evolutionaly Trends in the Physical Sciences**
Editors: M. Suzuki and R. Kubo

58 **New Trends in Nuclear Collective Dynamics**
Editors: Y. Abe, H. Horiuchi, and K. Matsuyanagi

59 **Exotic Atoms in Condensed Matter**
Editors: G. Benedek and H. Schneuwly

60 **The Physics and Chemistry of Oxide Superconductors**
Editors: Y. Iye and H. Yasuoka

61 **Surface X-Ray and Neutron Scattering**
Editors: H. Zabel and I.K. Robinson

62 **Surface Science**
Lectures on Basic Concepts and Applications
Editors: F.A. Ponce and M. Cardona

63 **Coherent Raman Spectroscopy**
Recent Advances
Editors: G. Marowsky and V.V. Smirnov

64 **Superconducting Devices and Their Applications**
Editors: H. Koch and H. Lübbing

65 **Present and Future of High-Energy Physics**
Editors: K.-I. Aoki and M. Kobayashi

66 **The Structure and Conformation of Amphiphilic Membranes**
Editors: R. Lipowsky, D. Richter, and K. Kremer

67 **Nonlinearity with Disorder**
Editors: F. Abdullaev, A.R. Bishop, and S. Pnevmatikos

68 **Time-Resolved Vibrational Spectroscopy V**
Editor: H. Takahashi

69 **Evolution of Dynamical Structures in Complex Systems**
Editors: R. Friedrich and A. Wunderlin

70 **Computational Approaches in Condensed-Matter Physics**
Editors: S. Miyashita, M. Imada, and H. Takayama

71 **Amorphous and Crystalline Silicon Carbide IV**
Editors: C.Y. Yang, M.M. Rahman, and G.L. Harris

72 **Computer Simulation Studies in Condensed-Matter Physics IV**
Editors: D.P. Landau, K.K. Mon, and H.-B. Schüttler

73 **Surface Science**
Principles and Applications
Editors: R.F. Howe, R.N: Lamb, and K. Wandelt

74 **Time-Resolved Vibrational Spectroscopy VI**
Editors: A. Lau, F. Siebert, and W. Werncke